RUHR-UNIVERSITÄT BOCHUM

Patrick Staubach

Contributions to the numerical modelling of pile installation processes and high-cyclic loading of soils

Bochum 2022

Heft 73

Schriftenreihe des Lehrstuhls für
Bodenmechanik, Grundbau und Umweltgeotechnik

Herausgeber: Torsten Wichtmann

ISSN 2699-1020

Patrick Staubach Numerical modelling of pile installation processes 73

ISSN 2699-1020

Ruhr-Universität Bochum
Schriftenreihe Bodenmechanik, Grundbau und Umweltgeotechnik
Heft 73

Herausgeber:
Prof. Dr.-Ing. habil. Torsten Wichtmann
Ruhr-Universität Bochum
Fakultät für Bau- und Umweltingenieurwissenschaften
Lehrstuhl für Bodenmechanik, Grundbau und Umweltgeotechnik
44801 Bochum
Telefon: 0234/ 3226135
Telefax: 0234/ 3214236
Internet: www.bgu.ruhr-uni-bochum.de

ISSN 2699-1020

Contributions to the numerical modelling of pile installation processes and high-cyclic loading of soils

Dissertation

as a requirement of the degree of
Doktor-Ingenieur (Dr.-Ing.)

at the Faculty of
Civil and Environmental Engineering
Ruhr-Universität Bochum

submitted by

Patrick Staubach

from Aschaffenburg, Germany

Reviewers:

Prof. Dr.-Ing. habil. Torsten Wichtmann

Prof. Dr.-Ing. Britta Bienen

Prof. Dr.-Ing. habil. Sascha Henke

Bochum, 2022

Preface of the editor

The installation of offshore wind parks represents a main contribution to the development of renewable energy sources. Most of the offshore wind turbines (OWT) are founded on monopiles, i.e. single piles with large diameter. The installation of theses piles in the seabed by either impact driving or vibration causes changes of the soil state (density and effective stress), which may influence the bearing capacity and the deformation behaviour of the pile under subsequent loading. Under offshore conditions the high-cyclic loading caused by wind and waves is of particular interest. During the lifetime of an OWT millions of load cycles of different amplitude act on the pile foundation, which may lead to an accumulation of deformation in the soil and thus to a permanent tilting of the OWT endangering its serviceability.

The dissertation of Patrick Staubach concentrates on the numerical investigation of the influences of the installation-induced changes on the long-term deformations of OWT pile foundations under high-cyclic loading. To enable realistic simulations of pile installation several numerical tools have been further developed and combined. A **u**-p-**U** finite element considering relative accelerations between the fluid and the solid phase was implemented. A semi-empirical approach based on soil permeability and loading frequency developed in the thesis allows to judge if such elements are necessary or if the simpler **u**-p formulations are sufficient for dynamic simulations considering consolidation. Furthermore, element- and segment-based Mortar discretization techniques for the pile-soil contact were developed and adopted to the pile installation problem. An existing approach to apply arbitrary continuum constitutive models as constitutive contact model was enhanced in order to guarantee the consistency of all stress components between the contact and the adjacent continuum elements. A hydromechanically coupled Coupled Eulerian Lagrangian (CEL) approach for large deformations was supplemented by the consideration of fluid acceleration.

The fields of state variables at the end of the simulation of installation were transferred to a second FE model which predicts the long-term deformations by means of a high-cycle accumulation (HCA) model. The HCA simulations were improved by the incorporation of an adaptive strain amplitude. This novel approach allows an automated update of the field of the strain amplitude during simulations with a HCA model. Furthermore, a HCA model for clay was introduced. All numerical tools were incorporated in the in-house FE code `numgeo` developed by Jan Machaček and Patrick Staubach. They were validated by the back analysis of various model tests. A good agreement between the numerical predictions and measurements could be confirmed for interface shear tests in which wall segments of different roughness were moved against the soil, for vibratory pile driving tests in water-saturated sand and for piles installed in dry sand subjected to lateral high-cyclic loading.

A parametric study on typical OWT piles in either sand or clay reveals that the installation-induced changes may either increase or decrease the long-term pile deformations depending on the soil type, the installation method (impact driving or vibration) and drainage conditions. Therefore, wished-in-place simulations may not be conservative in all cases.

The dissertation of Patrick Staubach represents the most complete and realistic numerical study to date on the influence of installation-induced changes in soil state on the long-term deformations of piles subjected to high-cyclic loading. Furthermore, the numerical tools developed in the framework of this thesis will be very helpful to solve other problems of geotechnical research in future.

Torsten Wichtmann

Acknowledgement

This thesis presents the development of advanced numerical tools for the analysis of soil-structure interactions, pile installation processes and soils subjected to high-cyclic loading. The work has been carried out while being a research assistant at Bauhaus Universität Weimar (BUW) from $2018-2022$ and Ruhr-Universität Bochum (RUB) from $2020-2022$.

I want to thank my first supervisor, Prof. Torsten Wichtmann, for the trust he has shown in me, starting from my time as an undergraduate student, and the opportunities he has given me since then. I have benefited greatly from his knowledge, unconditionally support and encouragement.

I also thank my co-advisor Prof. Britta Bienen for the interest she has shown in my research, even at the very beginning of my academic work, and the valuable input she has given me. I highly anticipate future joined projects. I am thankful to my co-advisor Prof. Sascha Henke, who has shown equal interest and has provided many helpful comments to my thesis. Prof. Daniel Balzani I thank for chairing my doctoral committee and for the honest interest in my work.

I owe special thanks to Dr. Jan Machaček. For the joined work on `numgeo` and the opportunity to critically discuss the subjects of this work, I thank him. Working together on a larger goal kept me motivated during months of bug-fixing of code. I thank all my former lecturers from the Karlsruher Institute of Technology (KIT), in particular Prof. Andrzej Niemunis, Dr. Gerhard Huber, Prof. Carlos Grandas and Prof. Theodoros Triantafyllidis, for awakening my interest in (numerical) geomechanics. In addition, I thank Dr. Stylianos Chrisopoulos, Dr. Ivo Kimmig and Dr. Lukas Knittel from the KIT. I am indebted to Dr. Jakob Vogelsang, who supplied me with countless results of high-quality experiments. I thank my (former) colleagues from BUW: Maria Noack, Paul Winkler, Hennes Jentsch, Dr. Detlef Rütz, Dr. Gunther Aselmeyer, Dr. Robert Wudtke, Frank Hoppe, Lisa Tschirschky and Cristian Rodríguez. Thanks to Annett Schumacher for her kindness and helpfulness. I am grateful to all colleagues from RUB, in particular to Dr. Merita Tafili, for supplying implementations of sophisticated constitutive models for clay, the enthusiasm she shows for `numgeo` and for joined projects. In addition, I want to thank Antonia Nitsch, Dr. Felipe Prada and Christoph Schmüdderich from the RUB, the latter in particular for his interest in and contributions to `numgeo`. I am grateful to Doris Traas from RUB for her help, especially in cases where I would have had to travel to Bochum without it. I thank Dr. Benjamin Cerfontaine for the input he has given me during his stay in Weimar. I am grateful to Prof. Hauke Zachert for his interest in my work and his support of the `numgeo` project. The constructive comments of anonymous reviewers of publications which are incorporated in this work are acknowledged as well.

I have to thank many supervised students of BUW contributing to this work, most notably Lisa Tschirschky, Maria Caridad Moscoso, Ella Hedwig-Albrecht, Josefine Skowronek, Dristi Lamichhane, Uta Junghans, Midia Ibrahim, Johanna Höschler, Hamed Farhadinasl, Moustafa Imbabi, Mohamed Ramadan Ragab Aly, Paul Malsch, Paul Müting, David Gonsior, Lukas Rentzsch, Xiaoqing Yang, Yichen Sui, Chris Bierschenk, Raihan Sharif and Raphael Schröder.

Lastly, I thank my friends and family for their continuous support.

Patrick Staubach

Abstract

This work presents contributions to the numerical modelling of the installation process and subsequent high-cyclic loading of piles, such as relevant for pile foundations for offshore wind turbines (OWTs). The developed numerical tools are implemented in the finite element code `numgeo` (`www.numgeo.de`), which is available for download.

The influence of relative acceleration between soil grains and pore fluid, neglected by the most common hydro-mechanically coupled finite element formulation (**u**-p formulation) but relevant for pile driving processes with high frequencies, is investigated by a novel analytical solution and various finite elements discretising the fluid displacements in addition to the fluid pressures. It is found that only for very large frequencies (> 50 Hz) with simultaneously high values of hydraulic conductivity ($> 10^{-3}$ m/s) the relative acceleration is of importance. Therefore, the **u**-p formulation is found to be applicable for the analysis of vibratory pile driving.

Constitutive models for the prediction of the mechanical response of soils to millions of load cycles (so-called high-cycle accumulation (HCA) models) are extended to be applicable for partially drained conditions by incorporation of a so-called adaptive strain amplitude, taking into account changes in soil stiffness during the high-cyclic loading. A HCA model for clay is implemented and applied to the analysis of monopiles for OWTs subjected to cyclic lateral loading with numerous load cycles.

Two different mortar contact discretisation techniques are developed and implemented in the finite element code `numgeo`. It is demonstrated that a segment-based mortar contact discretisation technique can be superior to an element-based technique in terms of numerical stability for vibratory pile driving in water-saturated soil. A general framework for the formulation of constitutive interface models based on constitutive continuum models is presented. Interface models based on Hypoplasticity with intergranular strain extension, the Sanisand model and the HCA model are formulated. In contrast to existing formulations, the boundary conditions are not only satisfied for the continuum but also for the interface zone, considering all stress and strain components in the interface. The simulation of large-scale cyclic interface shear tests shows that only the novel interface formulations allows to correctly consider the stress conditions in the interface zone.

The simulation of the pile installation process using a (hydro-mechanically coupled) Coupled Eulerian-Lagrangian method, which is extended to dynamic analyses, shows that for dry sand the installation-induced changes in the soil state result in a stiffer response of the pile to subsequent loading compared to simulations without consideration of the installation process.

Less permanent deformation is accumulated when the pile is subjected to high-cyclic loading using the HCA model following the installation process. However, for water-saturated initially dense sand and larger pile diameters, such as encountered for foundations for OWTs, less influence of the installation process is found. The better the drainage conditions during driving, the lower the accumulation of permanent deformations during subsequent high-cyclic loading. Lower accumulation of permanent deformations occurs if ideally drained conditions during driving are assumed. In case of clay, jacked piles show less accumulation of deformations when subjected to lateral cyclic loading compared to simulations neglecting the installation process, especially for a larger number of load cycles and for initially overconsolidated soils.

Zusammenfassung

In dieser Arbeit werden Beiträge zur numerischen Modellierung des Installationsprozesses und der anschließenden hochzyklischen Belastung von Pfählen vorgestellt, wie sie für Pfahlgründungen für Offshore-Windenergieanlagen (OWA) relevant ist. Die entwickelten numerischen Werkzeuge sind in dem Finite Elemente Programm `numgeo` (`www.numgeo.de`) implementiert, welches zum Download zur Verfügung steht.

Der Einfluss der relativen Beschleunigung zwischen Bodenkörnern und Porenflüssigkeit, welcher von der etablierten hydraulisch-mechanisch gekoppelten Finite Elemente Formulierung (**u**-p Formulierung) vernachlässigt wird, aber für Rammvorgänge mit hohen Frequenzen relevant ist, wird mit einer neuartigen analytischen Lösung und verschiedenen Finiten Elementen untersucht, die zusätzlich zu den Fluiddrücken auch die Fluidverschiebungen diskretisieren. Es zeigt sich, dass die relative Beschleunigung nur für sehr große Frequenzen (> 50 Hz) bei gleichzeitig hohen Werten der hydraulischen Durchlässigkeit ($> 10^{-3}$ m/s) von Bedeutung ist. Die **u**-p-Formulierung ist dementsprechend für die Simulation der Vibrationsrammung geeignet.

Stoffmodelle für die Modellierung des Bodenverhaltens bei einer Belastung mit Millionen von Lastzyklen (sogenannte hochzyklische Akkumulationsmodelle (HCA) Modelle) werden erweitert, so dass sie auch für partiell dränierte Bedingungen anwendbar sind. Dafür wird eine adaptive Dehnungsamplitude entwickelt, welche die Änderungen der Bodensteifigkeit während der hochzyklischen Belastung berücksichtigt. Ein HCA-Modell für Ton wird implementiert und für die Langzeitprognose von Monopiles für OWA eingesetzt, welche einer zyklischen lateralen Belastung mit einer großen Anzahl von Lastzyklen ausgesetzt sind.

Es werden zwei verschiedene mortar-Kontakt Diskretisierungen entwickelt und in `numgeo` implementiert. Es wird gezeigt, dass eine Segment-basierte mortar Methode einer Element-basierten Technik in Bezug auf die numerische Stabilität der Simulation der Vibrationsrammung in wassergesättigtem Boden überlegen sein kann. Eine neuartige Formulierung von konstitutiven Interface-Modellen auf der Grundlage von Kontinuumsmodellen wird vorgestellt. Es werden Interface-Modelle auf der Grundlage der Hypoplastizität mit Erweiterung um intergranulare Dehnungen, dem Sanisand-Modell und dem HCA-Modell formuliert. Im Gegensatz zu bestehenden Formulierungen werden die Randbedingungen nicht nur für das Kontinuum, sondern auch für die Interface-Zone erfüllt, wobei alle Spannungs- und Dehnungskomponenten in der Interface-Zone berücksichtigt werden. Die Simulation von zyklischen großmaßstäblichen Interface-Scherversuchen zeigt, dass nur die neuartigen Interface-Formulierungen eine korrekte Berücksichtigung der Spannungszustände in der Interface-Zone ermöglichen.

Die Simulation des Rammvorgangs mit einer (hydraulisch-mechanisch gekoppelten) Coupled Eulerian-Lagrangian Methode, welche auf dynamische Analysen erweitert wird, zeigt, dass bei trockenem Sand die durch die Installation induzierten Änderungen des Bodengefüges zu einer steiferen Reaktion des Pfahls auf nachfolgende Belastungen führen. Wenn der Pfahl nach dem Einbau hochzyklisch belastet wird, prognostizieren die Simulationen mit dem HCA-Modell eine geringere bleibende Verformung, wenn der Installationsprozess berücksichtigt wird. Für wassergesättigten, anfänglich dicht gelagerten Sand und größeren Pfahldurchmessern, wie sie bei OWA anzutreffen sind, wird jedoch ein geringerer Einfluss des Installationsprozesses festgestellt. Je besser die Dränagebedingungen während des Rammvorgangs sind, desto geringer ist die Akkumulation bleibender Verformungen bei der anschließenden hochzyklischen Belastung. Eine vergleichsweise geringere Akkumulation von bleibenden Verformungen tritt auf, wenn während der Rammung ideal dränierte Bedingungen angenommen werden. Bei Pfählen in Ton zeigen Simulationen mit Berücksichtigung des Installationsprozesses eine geringere Akkumulation von Verformungen, wenn sie einer lateralen zyklischen Belastung ausgesetzt sind, verglichen mit Simulationen, die den Einbauprozess vernachlässigen, insbesondere für eine größere Anzahl von Lastzyklen und für anfänglich überkonsolidierte Böden.

Contents

Chapter 1

Introduction

1.1 Motivation

The installation of piles changes the state of the surrounding soil. It is known from experimental investigations that the pile response to loading following the installation process is influenced by the installation method [114, 18, 362, 5]. For instance, vibratory driven piles in water-saturated soils are often reported to have less load capacity compared to impact driven or jacked piles [75, 282, 245, 144, 5] (see Fig. 1.1a for vibratory pile driving). In addition, vibratory driven piles tend to accumulate more deformation when subjected to cyclic lateral loading compared to impact driven piles [198, 362]. The lower resistance of vibratory driven piles is also mentioned in the German guidelines for piles "EA Pfähle" [94]. However, no guidelines for the estimation of the amount of reduction are given in [94], which shall be determined by a geotechnical expert. The Overseas Coastal Area Development Institute of Japan [380] incorporates similar advises as the "EA Pfähle" by recommending to switch to impact driving for the final phase of the vibratory driving process of a pile in order to ensure its bearing capacity.

The spatial distribution of relative density following the installation of a pile in initially dense sand obtained from a numerical simulation (further explained in Section 8.2) is displayed in Fig. 1.1b. It is well visible that the installation causes strong compaction of the sand in the vicinity of the pile tip, whereas a loosening is observed close to the pile shaft. This installation-induced alteration of the soil state influences the response of the pile once in service.

Following their installation, piles are frequently used to transfer cyclic loads from a structure to the subsoil. The analysis of the serviceability of pile foundations is of special interest for offshore

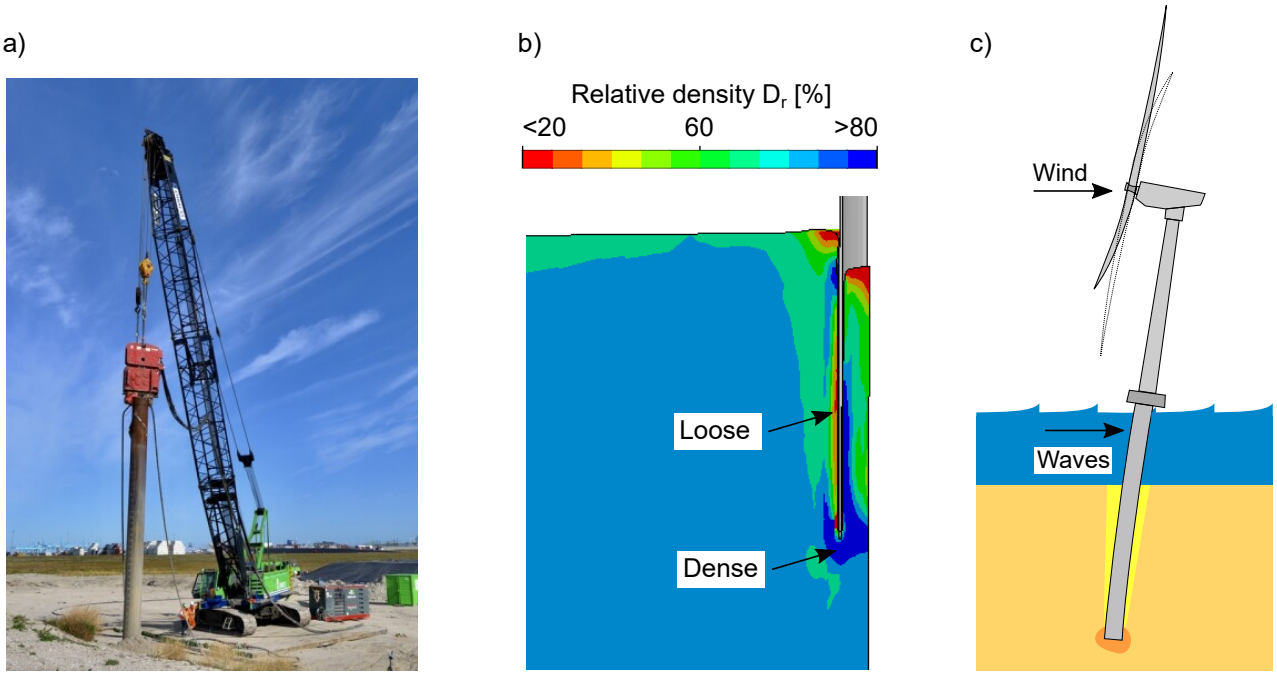

Figure 1.1: a) Vibratory driving of instrumented piles performed by the company Hottinger Brüel & Kjaer at the Maasvlakte (Rotterdam, Netherlands) in September 2020 in order to investigate the suitability of the vibratory driving technique for offshore foundations [172]. b) Relative density in the vicinity of a pile after installation (obtained from a numerical simulation). c) Loading of a monopile foundation for OWT by wind and water waves.

wind turbine (OWT) foundations (see Fig. 1.1c for a monopile foundation), which typically have only a small tolerance towards tilting. Since they are continuously loaded by wind and water waves over a long time period, methods to estimate the long-term deformations are required. Numerical simulations using special constitutive models for the high-cyclic loading are one possibility. Up to now, the installation effects are, however, usually not accounted for in numerical analyses of piles [4, 6, 233, 78, 84, 401, 191, 23, 39, 65, 74, 62, 215, 279, 280, 58, 7, 357, 188, 281, 441, 130, 175, 190]. It is unclear if this practice is conservative or not.

The installation of the foundations for OWTs has to be carried out under strict environmental and nature conservation conditions; in particular, the sound emissions during installation have to be limited to protect marine mammals. The usual installation method of impact pile driving can only meet these requirements by using additional technical solutions to reduce pile driving noise. Due to the lower noise emission, there is an increasing interest in the investigation of the applicability of vibratory driving and alternative driving methods, such as "Gentle Driving of Piles" [386] amongst others, for the installation of monopiles for OWTs. It is, however, yet

unclear if the current design practices for the lateral loading of the foundation can be applied to vibratory driven piles since the methods applied are based on experience from impact driven piles.

To improve the understanding of the mechanisms during pile installation and the impact on the (cyclic lateral) loading behaviour of the pile once in service, numerical methods can be applied. There is, however, no *state of the art* method for the simulation of pile driving. Especially in case of water-saturated soils, only a few numerical studies exist, which often simplify the physical processes strongly (e.g. only ideally drained/ideally undrained conditions, no friction between pile and soil or no consideration of inertia [145, 158, 165, 159, 161, 68, 67, 349, 275, 86, 277]). Many different challenging aspects are met for the numerical analysis of pile driving. Those are namely large deformations of the soil, contact constraints between pile and soil, hydro-mechanically coupled processes and (high frequency) dynamics in case of impact and vibratory pile driving. Different finite element formulations for the numerical analysis of hydro-mechanically coupled processes exist, but not all are necessarily suitable for dynamics with high wave frequencies [451, 310]. A (purely) Lagrangian representation of the soil may also be of disadvantage, since finite element formulations established in a classical Lagrangian framework are conventionally limited to merely small deformations. Special numerical schemes such as the *Material-Point-Method* (MPM) [3, 133] or Eulerian element techniques [27] are required to model the large deformations occurring during the simulation of pile installation.

The soil-pile interface behaviour plays a mayor role during pile driving [209, 293, 387, 182, 328]. Great care should be taken in the numerical treatment of the contact constraints since they add severe non-linearities to the problem at hand [336, 123]. This includes the discretisation of the contacts, the enforcement of the contact constraints and the constitutive description of the interface subjected to shearing. Due to cyclic interface shearing in case of impact or vibratory pile driving, the constitutive interface models utilised should be able to reproduce the soil response to cyclic loading. Numerically stable contact modelling techniques capable to take into account large deformations are required for the simulation of pile installation, which places high demands on the numerical code utilised. Even though being directly linked, most research work has either focused on the continuum mechanical aspects of contact mechanics (i.e. discretisation of the contacts and enforcement of constraints) or the geomechanical aspects (i.e. constitutive interface behaviour). This work aims to bridge both aspects.

For the numerical analysis of pile installation processes, different finite element formulations, constitutive (interface) models and contact discretisation techniques are developed and implemented in the finite element code `numgeo` [238], which is a joint project of Machaček [242] and the author of this work, in the scope of this dissertation. To estimate the deformation of piles

subjected to (long-term) cyclic loading with a large number of loading cycles following their installation process, the *high-cycle accumulation* (HCA) model [267] is applied. It is furthermore extended by a so-called adaptive strain amplitude, allowing for the analysis of high-cyclic loading accompanied by rapid changes of soil stiffness (e.g. relevant for foundations of OWTs in soils with low hydraulic conductivity due to built-up of excess pore water pressures caused by the cyclic loading). Moreover, a HCA model for clay is implemented and subsequently used for the prediction of the long-term response of monopile foundations for OWTs subjected to a large number of lateral load cycles.

1.2 Outline

A literature review regarding the effect of pile installation on the surrounding soil and the pile response to cyclic loading is given in Chapter 2. In addition, existing numerical approaches for modelling the installation as well as the cyclic loading of piles are recapped.

The adopted continuum mechanical model for the description of the multi-phase material soil and the basic governing equations are introduced in Chapter 3.

The discretisation of the governing equations using different hydro-mechanically coupled finite element formulations based on the Lagrangian framework is presented in Chapter 4. Attention is paid to the treatment of the *relative acceleration* between pore fluid and grains relevant for analyses with high wave frequency. A novel semi-analytical solution for the wave propagation in a fluid-saturated medium is presented for this purpose, which allows to express the influence of the relative acceleration solely in terms of hydraulic conductivity and highest wave frequency. Different hydro-mechanically coupled element formulations are evaluated based on the derived semi-analytical solution. In addition to Lagrangian finite element formulations, a hydro-mechanically coupled Eulerian formulation for the analysis of large deformations is presented.

The constitutive soil models which are applied and extended in the framework of this thesis are introduced in Chapter 5. An adaptive definition of the strain amplitude for the HCA models, taking into account the change of soil stiffness during the high-cyclic loading, is proposed.

Chapter 6 is devoted to contact mechanics. The development of two mortar contact discretisation techniques is presented. Advanced constitutive interface models based on the Hypoplasticity and the Sanisand model are developed. A novel constitutive contact model for the simulation of high-cyclic shearing of interfaces using the HCA model is proposed.

The finite element code `numgeo` is introduced in Chapter 7. Notes about the implementation of the numerical methods presented in the previous chapters are provided. The performance of the code is exemplary shown for different boundary value problems (BVPs).

In Chapter 8, the developed numerical tools are validated and the influence of the pile installation process on the pile behaviour during subsequent loading is investigated. The proposed constitutive interface models are applied to the simulation of large-scale cyclic interface shear tests. Numerical simulations of (vibratory) pile driving using the developed Lagrangian and Eulerian element formulations in conjunction with the developed contact discretisation techniques and constitutive contact models are presented. The influence of the installation process on the response of piles to subsequent (cyclic) loading is investigated by the back-analysis of model tests and for monopile foundations for OWT. The long-term behaviour of vibratory driven piles is compared to impact driven piles. The adaptive strain amplitude definition for the HCA models is applied to the investigation of the long-term behaviour of monopile foundations in soil with low hydraulic conductivity. The HCA model for clay is validated by a back-analysis of centrifuge tests on monopiles subjected to cyclic lateral loading. Following, the long-term behaviour of monopile foundations for OWTs in clay is investigated in a parametric study. Finally, the installation of a monopile in clay is simulated and the pile response to subsequent (high-cyclic) lateral loading is compared to a simulation without consideration of the installation process.

1.3 Notation

The following notation is used: Vectors and second order tensors are written with bold font, e.g. $\boldsymbol{a}$ and $\mathbf{A}$. A Cartesian coordinate system with the orthogonal unit vectors $\boldsymbol{e}_i$ for $i = 1, 2, 3$ is used. This system may be subjected to a rotation then given by unit vectors $\boldsymbol{e}'_i$. Fourth order tensors are written sans serif, e.g. E. The divergence is $\mathrm{div}(\boldsymbol{a}) = a_{i,i}$ for $i = 1, 2, 3$ and the gradient $\mathrm{grad}(\boldsymbol{a}) = a_{i,j}$ for $i, j = 1, 2, 3$. For the vector product $(\cdot)$, $\boldsymbol{a} \cdot \boldsymbol{b} = a_i b_i$ holds. The trace of a tensor is $\mathrm{tr}(\mathbf{A}) = A_{ii}$ for $i = 1, 2, 3$. Contraction of tensors is written with a colon for second order tensors $\mathbf{A} : \mathbf{B} = \mathrm{tr}(\mathbf{A} \cdot \mathbf{B}^T) = A_{ij} B_{ij}$, and for fourth order tensors $\mathsf{E} :: \mathsf{E} = E_{ijkl} E_{ijkl}$. Dyadic multiplication is written $\mathbf{A} \otimes \mathbf{A} = A_{ij} A_{kl}$. The euclidean norm $\|\mathbf{A}\| = \sqrt{\mathbf{A} : \mathbf{A}}$ is used. Normalisation is denoted by $\mathbf{A}^{\rightarrow} = \mathbf{A}/\|\mathbf{A}\|$. The deviator is defined by $\mathbf{A}^* = \mathbf{A} - \frac{1}{3}\mathrm{tr}(\mathbf{A})\mathbf{I}$, where $\mathbf{I} = \mathrm{diag}[1, 1, 1]$. If not stated otherwise, the mechanical sign convention for stress and strain is applied. The mean stress $p = -\frac{1}{3}\mathrm{tr}(\boldsymbol{\sigma})$ of the (effective) stress tensor $\boldsymbol{\sigma}$ and the scalar stress deviator $q = \sqrt{\frac{2}{3}}\|\boldsymbol{\sigma}^*\|$ are used.

Chapter 2

Pile response to cyclic loading and the influence of the installation process

An overview of the most relevant findings with respect to the influence of the pile installation process on the surrounding soil, the response of piles to cyclic loading and the impact of the installation process on the response of piles to subsequent loading is given in the following. In addition, existing numerical approaches for the analysis of the pile installation process and for the modelling of the (high-)cyclic loading behaviour of piles are recapped. The focus is on piles installed in sandy soils. Piles installed in clay are briefly addressed. Note that for other topics covered in this work (e.g. finite element formulations and contact mechanics) separate literature reviews are given in the corresponding chapters.

2.1 Experimental studies

2.1.1 Pile installation process

Impact pile driving is the most widespread pile installation method for foundations of OWTs and thus there is extensive experience in driving and estimating the pile response to subsequent loading. High levels of (underwater) noise are emitted during the driving process [164, 143], which can be problematic when installing offshore piles. For instance, the German Federal Environment Agency enforces a restriction of noise level to 190 dB for installation of offshore structures [389]. Impact driving can lead to sound levels well over 200 dB [314], which affects the local fauna [148].

Monotonic jacking is conventionally only used for piles with small dimensions. The installation of long piles or piles with a large cross-section would require a very strong abutment, making the method uneconomical.

Compared to impact driving, vibratory driving exhibits lower noise emissions. The cyclic movement of the pile during driving reduces the resistance in the soil such that the pile can be driven with relatively low static forces. Vibratory driving is often used in case of water-saturated soil, or it is combined with impact driving in case the penetration resistance can not be overcome during the installation process.

Piles in sand

The effects of pile driving on the state of the soil in the vicinity of the pile have so far been investigated primarily for jacking and impact driving. From experiments in dry sand it is known that the stress below the pile tip increases significantly and grain crushing can occur [432]. Once the pile tip passes the soil, a sharp reduction of effective (radial) stress acting on the pile shaft was observed in experiments [404, 432, 307, 181, 57]. This effect has been described by [403] and was later referred to as the "cavity expansion-contraction" mechanism [183]. A schematic of the development of the radial stress in the soil close to the pile shaft is given in Fig. 2.1a (based on [403]). Large radial stress acts in the soil close to the pile tip. Immediately after passing of the pile tip, the radial stress reduces sharply close to the shaft.

With increasing distance h (measured from the pile tip directed to the ground surface), the radial stress tends to reduce further, which is known as *friction fatigue* [155] or h/R effect [51] (in some papers, the term h/R effect is used to describe a general change of the soil state with h, not necessarily a reduction of radial stress). A schematic of this phenomenon is given in Fig. 2.1b based on [183]. The h/R effect is more pronounced in case of cyclic shearing as occurring during vibratory pile driving. In general, cyclic interface shearing is observed to lead to larger contraction of the soil in the interface zone compared to monotonic shearing [90, 92, 256].

The large increase in radial stress and the subsequent sharp reduction in the interface zone during the pile installation process are well visible from the results of a numerical simulation of the jacking of a pile in dry sand displayed in Fig. 2.1c. The simulations are documented in [359] and were performed using the Coupled Eulerian-Lagrangian (CEL) method. In addition, the friction fatigue effect is well visible in the plot on the far right.

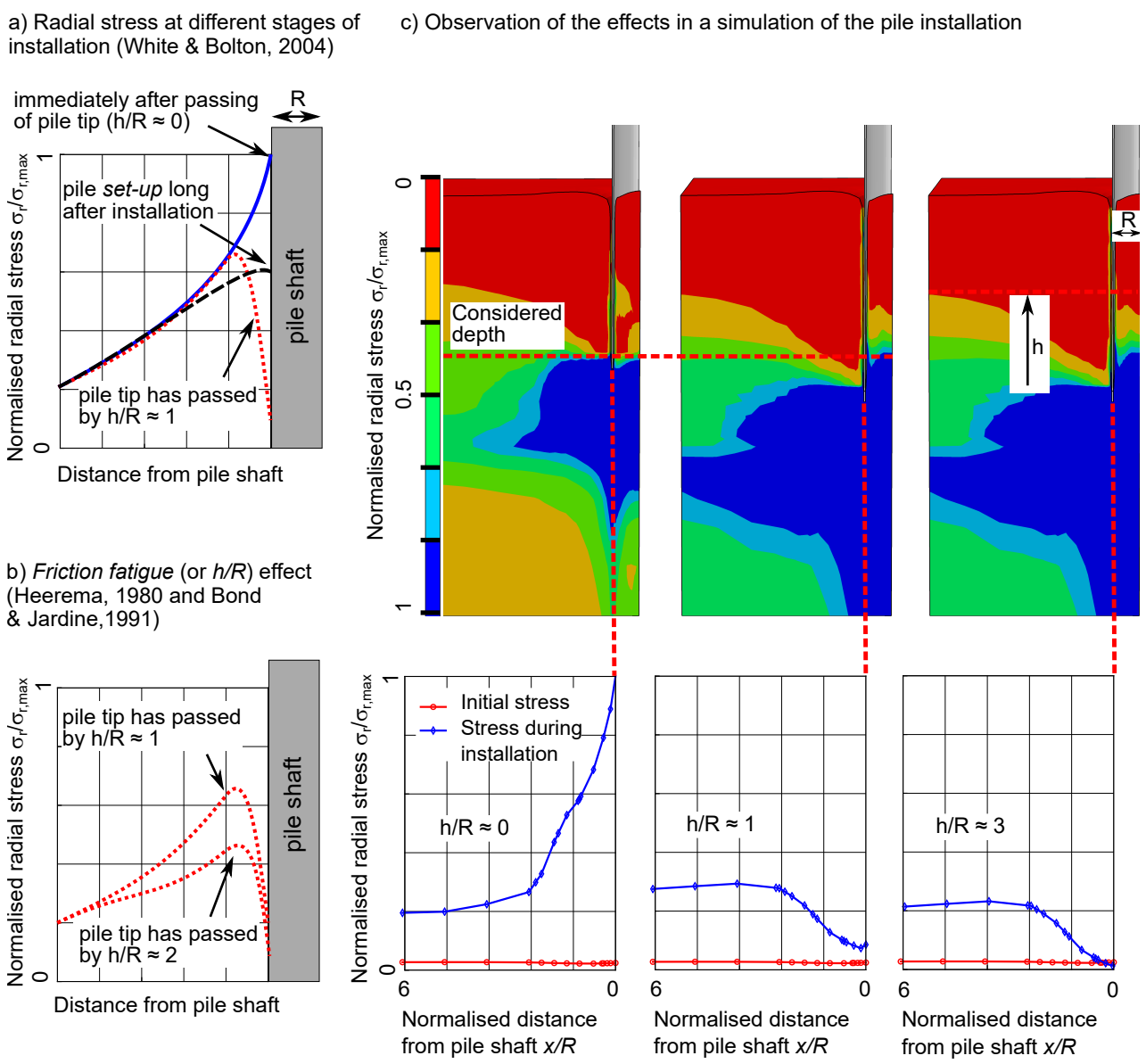

Figure 2.1: a) Schematic of the development of effective normalised radial stress $\sigma_r/\sigma_{r,\max}$ acting in the soil in the vicinity of the pile shaft with respect to the distance h from the pile tip divided by the pile radius R (modified from [403]). b) Reduction of $\sigma_r/\sigma_{r,\max}$ with ongoing pile penetration known as *friction fatigue* or h/R effect (modified from [183]). c) $\sigma_r/\sigma_{r,\max}$ during a simulation of jacking of a pile in a small-scale model test using the CEL method (x: distance from pile shaft). The distributions of $\sigma_r/\sigma_{r,\max}$ at different times of the pile penetration process and at different depths are given with respect to the normalised distance from the pile shaft (after [359]).

Over time, the effective radial stress acting normal to the pile shaft, reduced by the installation process, may increase again. This, however, is not connected to excess pore water pressure dissipation but attributed to a reduction of the high stress gradients in the vicinity of the pile shaft [66, 223]. This phenomenon is referred to as *set-up* effect and is for instance described in [66, 403]. The set-up effect is schematically shown in Fig. 2.1a. Even though the literature on set-up effects of driven piles is extensive (e.g. [329, 135, 207, 9, 152]), the impact of the installation method on the increase of pile resistance due to the set-up has not been quantified yet. The only study mentioning an influence of the installation method is [223, 222], stating that the set-up effect is stronger in case of impact driven piles compared to jacked piles. No study regarding the set-up effect of vibratory driven piles exists yet. However, there is no consensus in the literature for which conditions set-up effects occur and which processes cause them (see e.g. [207, 383] for a comprehensive overview regarding set-up effects). The recently performed study reported in [383], investigating possible set-up effects following jacking in dry sand in a calibration chamber, did not observe any stress redistribution nor any movement of soil particles using digital image correlation.

During installation of an open-ended pile, the rate of pile penetration may be higher than the rate of soil entering the inner of the pile. In dense soil and for piles with small diameters the soil may become plugged in the pile causing the so-called *soil plugging* effect [89, 158, 160, 162]. In this case, the response of the pile during the installation process becomes similar to a closed-ended pile and the penetration resistance increases sharply. Therefore, if the soil plugging effect is not properly accommodated for, the dimension of the chosen pile driver may not be appropriate. Furthermore, the bearing capacity of the installed pile is significantly higher if soil plugging occurred. For the dimensioning of driven piles subjected to vertical loads, the German guidelines for piles "EA Pfähle" [94] assume a fully plugged state, using the outlined area of the pile tip to calculate the vertical resistance of the pile. The occurrence of soil plugging depends, however, largely on the drainage conditions during driving. Fast driving in soil with low hydraulic conductivity leads to less soil plugging since the effective radial stresses inside the pile, leading to arching and impaction of the soil, are reduced [306]. In addition, the wall friction angle and hence the interface behaviour influences soil plugging. In a series of centrifuge tests, jacked piles were observed to show less tendency towards formation of a soil plug compared to impact driven piles in loose sand [157]. Opposite tendencies are reported in [304], which are explained by the inertia of the soil inside the pile, absent in case of jacking, causing the soil to resist moving together with the pile. In numerical studies presented in [158], jacked piles are also found to show high radial effective stresses inside the pile, while impact and vibratory driving lead to merely small increases in stress. Field tests reported in

[163] show that impact driven piles tend to show soil plugging, while vibratory driven piles do not. This can be attributed to the development of larger excess pore water pressure inside the pile in case of vibratory driving, reducing the effective radial stresses inside the pile.

Piles in clay

Numerous research studies have been conducted to investigate the installation-induced changes during pile driving in clay, mostly through field testing. Comprehensive reviews of the major findings can be found in [304, 99, 87]. In the following, the most relevant aspects for the research conducted in this work are briefly recapped.

During installation, an increase in (total) stresses and pore water pressure close to the pile tip occurs [72, 305]. While installation in overconsolidated soils results in an increase in total and effective radial stresses [51], there is little or no increase in effective radial stress at low values of initial overconsolidation ratio (OCR) [211]. For larger values of initial OCR, negative excess pore water pressures may develop near the pile shaft [51, 304]. As the distance h of the soil from the pile tip increases, the total stress decreases. In contrast to the installation in sand, the h/R effect does not necessarily describe a reduction of effective radial stress with increasing h/R for piles in clay [73, 210].

After the installation is finished, the total stresses decrease, in particular close to the pile tip [211]. The dissipation of excess pore water pressure after installation results in an increase in effective radial stresses in normally consolidated or slightly overconsolidated clay once the consolidation process is complete [211]. In contrast, a reduction in effective radial stresses may occur in highly overconsolidated clay during the consolidation phase [51, 210]. Results of field tests comparing open and closed-ended piles indicate that the effective radial stresses are not influenced by the different pile configurations [98].

2.1.2 Pile response to cyclic (lateral) loading

Piles in sand

The behaviour of piles under cyclic lateral loading has been subject of numerous experimental investigations: Small-scale experiments with constant load amplitude and uni-directional loading are documented in [76, 79, 77, 206, 287, 23, 126, 308, 435]. In order to investigate the pile behaviour under realistic stress conditions, while maintaining controlled boundary conditions, a series of centrifuge model tests have been carried out in addition [320, 40, 385].

Model tests to investigate the influence of alternating loading directions can be found in [320, 318, 316, 319]. In many of these experimental studies, the aim was to model the installation of the pile prior to cyclic lateral loading as realistically as possible (e.g. impact pile driving by using a light plastic hammer in [206]). In other model test series, the effect of the installation was completely neglected or not represented realistically. In these cases, the soil was either installed around the pile or the installation was carried out before the centrifuge was spun-up (i.e. pile installation at 1 g) [320].

Even though important findings regarding the influence of installation on the bearing behaviour of piles were obtained from the model tests, their transferability to real-scale piles is not unconditional. In particular, this concerns the installation process itself: while in situ tens of thousands blows are often needed during impact pile driving to bring the pile to its final depth (in particular for monopile foundations for OWT), in the laboratory a few hundred blows are usually sufficient to drive the pile to its final embedment depth [206, 316].

A specific investigation of the influence of the pile installation process on the lateral bearing behaviour was undertaken in [114, 194, 103] using centrifuge model tests. Klinkvort [194] investigated the jacking of piles in dense homogeneous Fontainebleau sand with an initial relative density of approximately 90 % in a centrifuge. The piles were installed both at 1 g and after the centrifuge was spun-up to the value used for the lateral loading of the pile. Figure 2.2a shows the dimensionless lateral load versus the dimensionless deflection of the two piles installed at 1 g and after spin-up, respectively. The lateral resistance of the pile installed at 1 g is less compared to the resistance of the pile installed following the spin-up. This is due to the alteration of the stress in the vicinity of the pile caused by the installation process, which is less in case of installation at 1 g since the subsequent spin-up reduces the installation-induced stress compared to the overburden stress. Similar observations have been made in [103, 114]. In [114], the influence of the pile installation technique on the response to subsequent monotonic lateral loading has been investigated in a centrifuge. The piles have been installed after spin-up of the centrifuge. Compared to jacked piles, impact driven piles showed less displacement at the same applied lateral loading. In contrast, in recently performed field tests comparable response to lateral loading of jacked and impact driven piles was observed [18]. The differences in these findings are likely to be caused by an influence of pile geometry, initial soil state and specifications of the applied driver.

Recently, field tests to investigate the influence of the pile installation technique on the response to lateral loading have been performed in a test pit at the Institute of Geomechanics and Geotechnics at Braunschweig University [362]. The piles had a diameter of 0.61 m and were

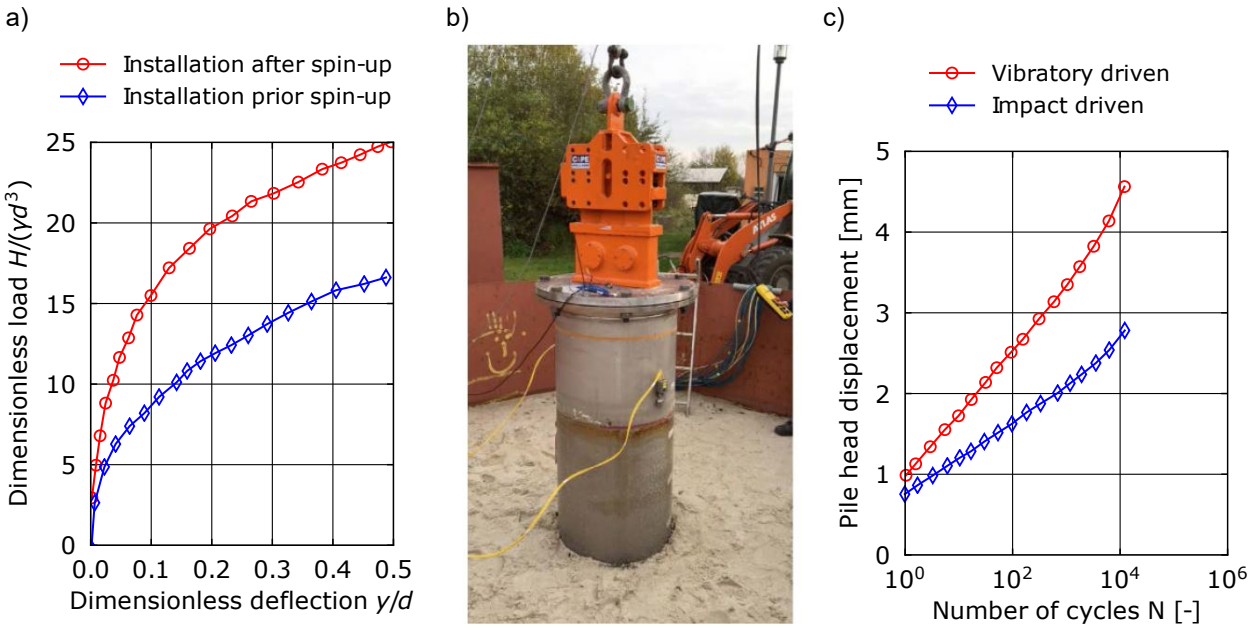

Figure 2.2: a) Lateral loading resistance of piles in centrifuge tests jacked either prior to the spin-up of the centrifuge or after spin-up (H: horizontal force, γ: dead weight of soil, d: pile diameter, y: lateral deflection) [194]. b) Field tests on vibratory driven piles performed at Technische Universität Braunschweig [362]. c) Horizontal pile head displacement during cyclic lateral loading following the installation by impact and vibratory driving, respectively [362].

driven 2.4 m in water-saturated sand with an initial relative density of approximately 70 %. The hydraulic conductivity of the sand was approximately $5 \cdot 10^{-4}$ m/s. A photo of the set-up of the vibratory pile driving test is given in Fig. 2.2b. Vibratory driving was either performed in a free-riding manner or crane-guided. In contrast to impact driven piles, for which an increase in effective radial stress in the vicinity of the pile tip was observed, the effective stress did not change as significantly for the crane-guided vibrated piles. However, piles vibrated in a free-riding manner showed similar increase in effective stress as the impact driven piles. With regard to the monotonic lateral load behaviour, significant differences were found between impact driven and crane-guided vibrated piles. A stiffer response was observed for the impact driven pile. The results of the lateral cyclic loading tests following the pile installation process are depicted in Fig. 2.2c. The pile head displacement versus number of applied load cycles is displayed. The impact driven pile shows significantly lower accumulation of deformation under the cyclic load compared to the crane-guided vibrated pile. Free-riding vibrated piles showed accumulated displacements in between those of impact driven and crane-guided vibrated piles. For all piles, a steady increase in the system stiffness with increasing number of load cycles was observed. As a result of the cyclic lateral loading of the pile, stress redistribution occurred

in the soil close to the pile. However, the increased radial stress close to the pile tip caused by the installation process by impact driving was still present after 10,000 lateral load cycles.

The results of [362] are in accordance with those of another recent field test campaign conducted by Achmus et al. [5], where the lateral load behaviour of vibrated piles was compared to impact driven piles. The subsoil at the test side close to Cuxhaven (Germany) consisted mainly of fine to medium coarse silica sands in a medium dense to dense initial state. The water table was located 4.2 m below the ground surface. The piles had a diameter of 4.3 m and were driven to a depth of approximately 19 m. When subjected to monotonic lateral loading following the installation, the secant stiffness of the vibrated pile was in maximum 60 % lower than that of the impact driven pile. A large influence of the specifications of the vibrator on the response to lateral loading was found. Piles vibrated over larger span of time, applying a vibrator with less power, showed larger resistance to lateral loading compared to piles which were vibrated faster.

In contrast to these studies, another recent field test campaign found that vibratory driven piles had a slightly higher resistance to lateral monotonic loading than impact driven piles [18]. It was hypothesised that the higher resistance was due to greater compaction of the soil caused by vibratory driving. In these tests, the soil consisted of medium dense unsaturated sand. Similarly to the results of these field tests, vibratory driven piles in a small-scale 1 g model test set-up with water-saturated dense sand showed a comparable behaviour to cyclic lateral loading for a number of load cycles larger than 10 [169] or even a lower accumulation of deformations compared to impact driven piles [204].

Piles in clay

Due to cyclic lateral loading, a reduction in stiffness of the soil surrounding the pile with increasing number of cycles occurs, which is mainly a result of a built-up of excess pore water pressure. This has for instance been observed in field tests with up to one thousand lateral load cycles on piles (diameter $D = 0.273$ m and $D = 1.22$ m) in stiff overconsolidated clay [101]. Similar results were obtained in recent field tests on monopile foundations with a diameter of 2.2 m in soft clay reported in [448] as well as in the pioneer work of Matlock [248] (in soft clay) and Reese et al. [313] (in heavily overconsolidated clay). In [397] a strong degradation of the lateral stiffness of the pile ($D = 0.8$ m, founded in soft clay) was observed during the cyclic loading as soon as the magnitude of the load was larger than a certain threshold level. The largest degradation occurred during the first five cycles followed by a stagnation of degradation. In case of cyclic loading with higher load magnitude, the rate of reduction

of pile stiffness increased with increasing number of applied cycles. Similar observations were made for piles with a diameter of $D = 0.153$ m in overconsolidated clay reported in [447]. Recently, Yang et al. [431] performed centrifuge tests on monopile foundations ($D = 5.9$ m in prototype scale) in soft kaolin clay subjected to lateral cyclic loading with hundreds of load cycles. In accordance with the observations documented in [299, 300], the cyclic loading lead to an increase in the magnitude of the bending moment and a decrease in the pile stiffness. Small scale model tests on piles ($D = 50$ mm) in marine clay with several thousand lateral load cycles reported in [220] showed an increasing permanent deflection of the pile with increasing number of load cycles for cyclic amplitudes in the range of 30 % to 60 % of the ultimate lateral resistance. Alternate cyclic loading with phases of reconsolidation between the cyclic events in centrifuge tests on monopiles ($D = 4$ m and $D = 6$ m in prototype scale) in soft clay revealed a partial recovery of the degraded lateral pile stiffness due to the resting period [200]. However, within each cyclic load package, the cumulative lateral displacement of the pile increased with number of applied load cycles.

A reduction of soil reaction force with ongoing cyclic lateral loading is incorporated in a simplified manner in the cyclic p-y curves of the American Petroleum Institute (API) [19], which are based on field tests [248]. Since the API cyclic p-y curves do not allow for a consideration of the number of applied load cycles or the load characteristics (e.g. the ratio of average and cyclic load), many modifications have been proposed over the span of the last decades. Such improved cyclic p-y curves have for instant recently been presented in [446], where the reduction of the soil reaction with ongoing cyclic loading has been incorporated using cyclic strain contour diagrams obtained from direct simple shear tests (see [16]).

Field tests reported in [131] show that the shear strength of clay is significantly altered by the installation process. As mentioned in [384], there is neither a comprehensive experimental nor a numerical study quantifying the influence of the installation process on the lateral loading behaviour of piles in clay. In centrifuge tests on piles in clay, the installation is usually performed at 1 g [171, 431, 200, 196], often justified by referring to earlier work adopting the same procedure. The installation at 1 g of course reduces the uncertainty, in particular relevant for numerical back-analysis of the tests [102], but does not reflect the processes taking place in reality. In [304] it is argued that any approach predicting the shaft capacity of a driven pile must consider: (1) the installation-induced changes in the soil state, (2) the following dissipation of excess pore water pressure and (3) the load-induced changes in the soil state.

To the author's best knowledge no comprehensive study regarding the influence of the installation technique on the response of piles to subsequent loading exists for clay.

2.2 Numerical studies

2.2.1 Modelling of the pile installation process

As mentioned in the introduction, special numerical techniques are required to model the pile installation process properly. Simulations based on the (updated Lagrangian) finite element method (FEM) [123, 158, 67, 349, 145], the Coupled Eulerian-Lagrangian (CEL) method [303, 161, 151, 397, 353, 354], the (Multi-Material) Arbitrary Lagrangian Eulerian (MMALE or ALE) method [232, 95, 28, 397, 32, 86, 382, 433], the Material Point Method (MPM) [292, 63, 149, 133, 255, 141, 246], the Particle FEM (PFEM) [153, 252, 445], the Discrete Element Method (DEM) [70, 214] and the Smoothed Particle Hydrodynamics (SPH) method [81, 345] are reported in the literature. In general, the applied method has to be able to account for both, large deformations in the soil and contact between pile and soil. Not all techniques are well suited to incorporate both aspects. Simulations based on the classical FEM are mostly (but not only) limited to closed-profile piles and the simulation of cone-penetration tests [395, 67, 349, 153, 252, 445], for which so-called *zipper-techniques* are employed [45, 75, 165, 245, 159]. This technique is also applied in this work and is explained in Section 8.2.1. An application of zipper-techniques to the simulation of the installation of pipe piles is presented in [159].

The limitations of the classical Lagrangian FEM with respect to large intrinsic deformations can be overcome by separating mesh and material points (employed by the PFEM and the MPM), the representation of the soil in an Eulerian framework (CEL and MMALE/ALE) or by methods not based on the FEM (DEM and SPH). So far, no method has proven to be superior to all other approaches. In addition, the choice for a method also depends on the aspects of pile driving which are to be studied. A discussion on the advantages of the different methods for the general application to geomechanical BVPs with large deformations can be found in [49, 344, 31]. In [397] some of the above mentioned large deformation techniques have been investigated and compared for geomechanical benchmark BVPs. Most of the existing studies did not consider hydro-mechanically coupled processes or neglected inertia. Especially for the analysis of vibratory pile driving in water-saturated soil only a very limited number of studies exist [67, 349, 240, 141].

2.2.2 Lateral cyclic loading of piles

Existing numerical studies focus mainly on the pile behaviour under a low number of load cycles (see e.g. [78] for a finite element approach or [279] for a macro-element approach).

Numerical investigations on the pile behaviour under high-cyclic loading are rare, because of limitations of the existing approaches and constitutive models. A conventional calculation with a constitutive model formulated in terms of stress and strain rates is normally only suitable for the simulation of a small number of cycles.

A simplified procedure to account for high-cyclic loading is employed by the "Strain Degradation Model" (SDM) by Achmus et al. [4, 6, 8]. Permanent deformations due to cyclic loading are captured by reducing Young's modulus of the soil from its value E_0 for monotonic loading to $E_N = E_0 \cdot N^{-a}$. The parameter a can be determined from cyclic triaxial tests. The stiffness degradation contradicts the actual physical processes, since the bedding modulus of the pile usually increases due to the repeated loading [1, 205]. A more detailed description of the SDM and comparison with other approaches (e.g. the API approach [13], the "Strain Wedge Model" [274, 26, 24, 25] and the "Enhanced Strain Wedge Model" developed by Taşan [377, 376]) can be found in [402]. In addition to the methods listed above, the cyclic degradation method [15, 16] developed by the Norwegian Geotechnical Institute can be used for the prediction of the tilting of monopile foundations under a large number of loading cycles [40].

The high-cycle accumulation (HCA) model by Niemunis et al. [268] is a constitutive model specifically tailored for the analysis of the soil response to high-cyclic loading and has a more profound physical basis compared to the models listed previously. In addition, it is not limited to the analysis of piles but can be used for arbitrary BVPs involving high-cyclic loading. In the framework of the HCA model only the average response of the soil due to cyclic loading with many repetitions is predicted. The model has been developed and verified by a comprehensive experimental study reported in [405, 414, 409, 412, 410, 413, 416, 417, 421]. The parameters of the HCA model can be determined from experiments [411, 419] or estimated based on granulometry or simple index quantities [415, 419]. The HCA model has been validated based on back-analysis of model tests on monopiles and shallow foundations [346, 435] and on a field test on a prototye of a gravity base foundation for OWTs [436, 437, 438]. A back-analysis of centrifuge tests on monopiles reported in [281] showed a good agreement with the experimental results although the material parameters of the HCA model were only estimated based on granulometry and simple index quantities. Furthermore, the cumulative deformations measured at a ship lock over two decades were successfully reproduced in simulations with the HCA model [239]. The HCA model has been used for a parametric study on the long-term deformations of monopile foundations for OWTs in [357].

Recently, so-called *memory surface* enhanced elasto-plastic models have been proposed [42, 227, 226, 225, 430], which can (in dependence of the formulation) account for the cyclic load history and are thus able to reproduce the response of soil to high-cyclic loading calculating

every individual load cycle. Liu et al. [225] proposed an extended Sanisand [82] model enhanced by a memory surface which could successfully reproduce the measured accumulated deformations in the triaxial tests with up to 10^4 cycles documented in [405]. In [228] this constitutive model has been applied for the simulation of a monopile under loading with up to 10^4 cycles. However, since each individual cycle must be simulated, it is open to question if this approach is suitable for models with a large number of finite elements and millions of loading cycles.

Houlsby et al. [173] presented a thermodynamically consistent model based on the framework of hyperplasticity which is able to describe cumulative effects due to a large number of cycles using "accelerated" ratcheting. In this approach only a few cycles are calculated conventionally with the hyperplastic model, and the resulting permanent deformations are increased in dependence of the maximum number of cycles to be considered in the high-cycle problem. No calculation of a strain amplitude, as required for the HCA model, is necessary in such simulations which may be advantageous for complicated loading paths during individual cycles. However, this model has yet not been applied for the analysis of the response of piles to cyclic loading.

Similar to the pile driving process, the drainage conditions are of particular importance for the pile response under cyclic loading. These are the practically most relevant conditions with respect to OWT foundations, which is highlighted by the considerable research volume on this topic [84, 74, 39, 189, 215, 188].

In all of the above listed schemes developed to analysis the pile response to cyclic loading, the installation process of the pile has not been accounted for. As has been shown in [115, 113, 112, 353, 352] and in the experimental investigations recapped in Section 2.1.2, the installation can have a distinct impact on the response of the pile to subsequent loading. Therefore, an incorporation of the installation-induced changes in soil state is judged to be of great importance for numerical analyses.

Chapter 3

Governing continuum mechanics equations

The governing equations required for the description of the hydro-mechanically coupled behaviour of soil in a continuum mechanics framework are defined in this chapter.

3.1 Continuum mechanical description of the multi-phase material soil

Conventional soil mechanics considers the soil as a multi-phase porous medium which consists of solid grains, water and air. As a rule, the soil is then often idealised in a further step as a dry medium, i.e. only the phase of solid and air are present, or a water-saturated medium, i.e. only solid and water are present. However, the mechanical behaviour of soil is significantly affected by its water content or degree of saturation, respectively, and its consideration is in many cases of great importance. For some problems with unsaturated states, where the soil is for instance subjected to large suction, a further distinction within the fluid phase has to be made in order to correctly describe the hydraulic and mechanical properties of the soil. This additional splitting is necessary because the behaviour of the fluid phase changes when it becomes discontinuous. Therefore, in the context of this work, the multi-phase porous medium soil includes a further distinction of the fluid phases into the so-called residual and free fluid phases.

The theoretical origin of the extended subdivision of the unsaturated soil zone lies in the hydrologic study of soil field capacity, which describes the ability of the soil to hold water

above the water table. The unsaturated zone can be conceptionally divided into three zones [364, 363]:

- **closed capillary zone**: Area immediately above the groundwater level. No continuous air phase exists. If air is present, it is of discontinuous form, e.g. bubbles enclosed by a continuous water phase.
- **open capillary zone**: Both the pore air and the pore water can exist as continuous or discontinuous phases, respectively. This region can be understood as the unsaturated soil zone in the classical sense.
- **unsaturated zone above the open capillary zone**: The pore water is discontinuous as a residual phase. The pore air phase is continuous.

The extended subdivision of the soil into five phases following the work of [127, 242] is adopted. The phases are:

- **solid** ($\sqcup^s$): Solid grains of soil. They are assumed to be assembled "continuously", forming the soil skeleton, such that gradients can be defined at every point.
- **free water** ($\sqcup^{wf}$): Continuous water phase occupying the pores of the soil. It is connected between the grain structure without interruptions within a *representative volume element*. By the condition of continuity, the momentum balance of the pore water is applicable.
- **residual water** ($\sqcup^{wr}$): Discontinuous water phase that cannot separate from the solid due to electrostatic binding forces. It is assumed to move with the solid and thus does not require its own motion field for the continuum mechanical description. Regardless of the magnitude of suction, it always remains present in the unsaturated region. In this work, the residual water phase does not directly influence the mechanical behaviour of the soil, but it is considered in the hydraulic description.
- **free air** ($\sqcup^{af}$): Continuous air phase within the grain skeleton. The momentum balance of air applies.
- **residual air** ($\sqcup^{ar}$): Trapped, confined gas bubbles. In this work, they are assumed to be trapped in the pore space and thus move with the same motion field as the solid. No production terms are accounted for in this work, i.e. the volume fraction of residual air is constant over time.

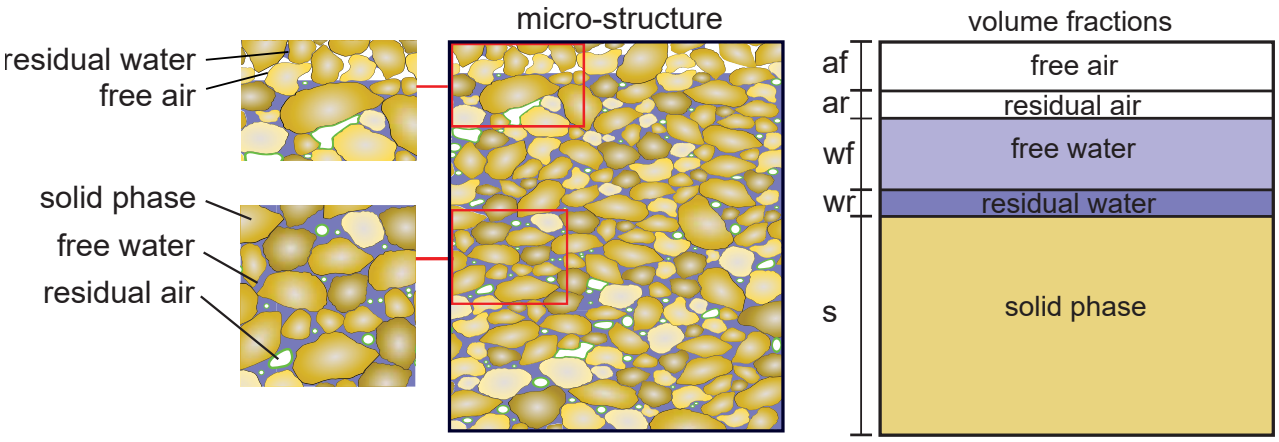

Figure 3.1: Micro-structure of the soil and division in volume fractions using a five-phase model (modified from [242])

The constituents and their arrangement on the micro-scale are schematically shown in Fig. 3.1.

The macroscopic description of heterogeneous substances idealised as a continuum can be done with the help of the *Theory of Porous Media* (TPM) (see [48, 54, 104, 106, 146, 105, 332]). In the framework of the TPM, the heterogeneous body is decomposed into homogeneous sub-bodies, forming a statistical surrogate model. Figure 3.1 shows the volume fractions of the adopted five-phase model. The considered region must be chosen large enough for a statistical statement to be admissible. The resulting superposed continuum allows both the mechanical and hydraulic description with the help of the proportional phase fractions of the total mixture.

The soil is composed of the individual phases $\alpha = \{s, wr, wf, ar, af\}$. The total volume of the mixture is therefore the sum over the partial volumes of the single phases

$$V = \sum_{\alpha} V^{\alpha}. \tag{3.1}$$

Similar, the total mass is the sum of the partial masses

$$m = \sum_{\alpha} m^{\alpha}. \tag{3.2}$$

The volume fractions φ^{α} are

$$\varphi^{\alpha} = \frac{V^{\alpha}}{V}. \tag{3.3}$$

The unit volume of the mixture is the sum of the partial unit volumes, viz.

$$\varphi = \sum_{\alpha} \varphi^{\alpha} = \varphi^{s} + \varphi^{wr} + \varphi^{wf} + \varphi^{ar} + \varphi^{af} = 1. \tag{3.4}$$

The specific (or material) density $\bar{\rho}^\alpha$ and the partial density ρ^α are

$$\bar{\rho}^\alpha = \frac{m^\alpha}{V^\alpha} \quad \text{and} \quad \rho^\alpha = \frac{m^\alpha}{V}, \tag{3.5}$$

where $\rho^\alpha = \varphi^\alpha \bar{\rho}^\alpha$. The porosity n is given by

$$n = 1 - \varphi^s. \tag{3.6}$$

The effective porosity n^e does not include the residual phases and is defined by

$$n^e = \varphi^{wf} + \varphi^{af} = 1 - \varphi^s - \varphi^{wr} - \varphi^{ar}. \tag{3.7}$$

The effective volume fraction S_e^γ, which is the ratio of the volume of the free fluid phase $\gamma = \{wf, af\}$ and the effective porosity n^e, is defined by

$$S_e^\gamma = \frac{\varphi^\gamma}{n^e} \tag{3.8}$$

The sum of S_e^γ over γ is one and is thus in sum constant over time

$$\sum_\gamma S_e^\gamma = 1 \quad \text{and} \quad \sum_\gamma \frac{\partial S_e^\gamma}{\partial t} = 0. \tag{3.9}$$

The effective saturation, which takes into account the residual phases, results from the consideration of S^{wr} proposed by [129, 127]

$$S^e = \frac{S^w - S^{wr}}{1 - S^{wr}}, \tag{3.10}$$

with the degree of saturation of the water S^w and the residual water saturation S^{wr} [216]

$$S^w = \frac{V^{wf} + V^{wr}}{V - V^s} = \frac{\varphi^{wf} + \varphi^{wr}}{1 - \varphi^s} \quad \text{and} \quad S^{wr} = \frac{V^{wr}}{V - V^s} = \frac{\varphi^{wr}}{1 - \varphi^s}. \tag{3.11}$$

The following assumptions underlie the continuum mechanical description:

- The free fluid phases are continuous, such that balance equations may be formulated. This condition is approximately satisfied for effective degrees of saturation in the range $0 \leq S^e \lessapprox 0.85$ [251]. Above the upper limit, the pore air is discontinuous and the mechanical and hydraulic description must not be carried out assuming a continuum. The same holds for effective degrees of saturation below the residual water saturation S^{wr}, where the pore water is discontinuous.

- The representative volume element used to describe the soil is large compared to the grain size and the size of the pore spaces.

The assumption of a constant hydraulic conductivity of the soil to pore fluids is only justified for completely saturated or completely dry conditions. For unsaturated soil, the coexistence of pore water and pore air must be taken into account, as the cross-sectional area of the pores available for flow is reduced [125]. The reduced hydraulic conductivity is taken into account by a factor, the relative permeability $k^{\mathrm{rel},\gamma}$ ($\gamma = \{wf,\ af\}$), whose value range is between 0 and 1. The hydraulic conductivity of the soil with respect to the phase γ is then calculated by

$$k_{ij}^{\gamma} = k^{\mathrm{rel},\gamma} \frac{\bar{K}_{ij}^{\mathrm{perm},\gamma} \|\boldsymbol{b}\| \bar{\rho}^{\gamma}}{\mu^{\gamma}}, \tag{3.12}$$

where $\bar{K}_{ij}^{\mathrm{perm},\gamma}$ corresponds to the permeability to pore fluids. μ^{γ} is the dynamic viscosity and $\boldsymbol{b}$ the gravity vector. The relative permeability can be a function of the degree of saturation S^w or the effective degree of saturation S^e. Empirical models for the relative permeability are found in [137, 263, 125].

Throughout the work, the general conditions of an unsaturated state and three phases with independent fields of motion (solid and two fluids) are considered. For the application of the derived numerical schemes at the end of the thesis, however, mostly water-saturated or dry soil conditions are studied. Having future extensions of the numerical schemes proposed in the subsequent chapters in mind, the governing equations, building the foundation of the numerical schemes, are formulated as general as possible for why the five phase model is chosen as basis.

3.2 Kinematics

Using a fixed coordinate system, the position vector of phase α in the reference configuration is given by $\boldsymbol{X}^{\alpha}$. Due to deformation, the position changes to the current configuration given by $\boldsymbol{x}^{\alpha} = \boldsymbol{x}^{\alpha}(\boldsymbol{X}^{\alpha}, t)$. Note that throughout the work the spatial coordinate $\boldsymbol{x}^{\alpha}$, the displacement $\boldsymbol{u}^{\alpha}$, the velocity $\dot{\boldsymbol{u}}^{\alpha}$ and the acceleration $\ddot{\boldsymbol{u}}^{\alpha}$ of phase α are intrinsic values. Therefore, $\bar{\square}$ is dropped for these quantities for the sake of convenience. Considering large deformations, a distinction between *material* (field variables in terms of reference configuration) and *spatial* (field variables in terms of current configuration) description has to be made. While a Lagrangian description is also often referred to as material description, an Eulerian description is also called spatial.

The mapping from reference to current configuration has to be continuous and bijective, which is secured by a positive and non-zero determinant of the deformation gradient $\mathbf{F}$ defined by

$$\mathbf{F}^{\alpha} = \frac{\partial \boldsymbol{x}^{\alpha}(\boldsymbol{X}^{\alpha}, t)}{\partial \boldsymbol{X}^{\alpha}} \tag{3.13}$$

and its inverse

$$(\mathbf{F}^\alpha)^{-1} = \frac{\partial \boldsymbol{X}^\alpha}{\partial \boldsymbol{x}^\alpha(\boldsymbol{X}^\alpha, t)}. \tag{3.14}$$

Given any quantity $\sqcup$ of phase α, the *material time derivative* is given by

$$\frac{\mathrm{d}^\alpha \sqcup^\alpha (\boldsymbol{x}^\alpha, t)}{\mathrm{d}t} = \frac{\partial \sqcup^\alpha (\boldsymbol{x}^\alpha, t)}{\partial t} + \frac{\partial \sqcup^\alpha (\boldsymbol{x}^\alpha, t)}{\partial \boldsymbol{x}^\alpha} \cdot \bar{\boldsymbol{v}}^\alpha(\boldsymbol{X}^\alpha, t), \tag{3.15}$$

where the first term is often denoted as *local* and the second as *convective* derivative. In Eq. (3.15), $\bar{\boldsymbol{v}}^\alpha(\boldsymbol{X}^\alpha, t) = \dfrac{\mathrm{d}^\alpha \boldsymbol{x}^\alpha(\boldsymbol{X}^\alpha, t)}{\mathrm{d}t}$ holds. The acceleration $\bar{\boldsymbol{a}}^\alpha(\boldsymbol{X}^\alpha, t)$ is defined analogously.
If the material time derivative is to be taken with respect to the moving phase γ but the variable itself is moving with the field α, the convective term describes the movement with respect to the field of γ, which is denoted using the operator $\mathrm{d}^\gamma/\mathrm{d}t$ [332], defined by

$$\frac{\mathrm{d}^\gamma \sqcup^\alpha (\boldsymbol{x}^\alpha, t)}{\mathrm{d}t} = \frac{\mathrm{d}^\alpha \sqcup^\alpha (\boldsymbol{x}^\alpha, t)}{\mathrm{d}t} + \frac{\partial \sqcup^\alpha (\boldsymbol{x}^\alpha, t)}{\partial \boldsymbol{x}^\alpha} \cdot \bar{\boldsymbol{w}}^\gamma(\boldsymbol{X}^\gamma, t), \tag{3.16}$$

where $\bar{\boldsymbol{w}}^\gamma = \bar{\boldsymbol{v}}^\gamma - \bar{\boldsymbol{v}}^\alpha$ expresses the velocity of the phase γ relative to the phase α. The solid phase is chosen as the reference field of motion. The material time derivative of the fluid phases is then defined by

$$\frac{\mathrm{d}^\gamma \sqcup^\alpha (\boldsymbol{x}^\alpha, t)}{\mathrm{d}t} = \frac{\mathrm{d}^s \sqcup^\alpha (\boldsymbol{x}^\alpha, t)}{\mathrm{d}t} + \frac{\partial \sqcup^\alpha (\boldsymbol{x}^\alpha, t)}{\partial \boldsymbol{x}^\alpha} \cdot \bar{\boldsymbol{w}}^\gamma(\boldsymbol{X}^\gamma, t), \tag{3.17}$$

with $\bar{\boldsymbol{w}}^\gamma = \bar{\boldsymbol{v}}^\gamma - \bar{\boldsymbol{v}}^s$. For sake of convenience $\dfrac{\mathrm{d}^s \sqcup^\alpha (\boldsymbol{x}^\alpha, t)}{\mathrm{d}t} = \dfrac{\mathrm{d} \sqcup^\alpha (\boldsymbol{x}^\alpha, t)}{\mathrm{d}t}$ is agreed in the following.

In an *updated Lagrange* formulation, as employed in this thesis, the reference configuration is taken to be the state of the previous calculation increment, hence $\boldsymbol{X}^\alpha = \boldsymbol{x}^\alpha(t)$. The deformation gradient is therefore

$$\mathbf{F}^\alpha = \frac{\partial \boldsymbol{x}^{t+\Delta t,\alpha}(\boldsymbol{x}^{t,\alpha}, t)}{\partial \boldsymbol{x}^{t,\alpha}}. \tag{3.18}$$

3.3 Definition of strain

Every motion of a body can be decomposed in a pure stretch in direction of the three orthogonal axes and a pure rigid rotation, which is expressed by the polar decomposition theorem given by

$$\mathbf{F} = \mathbf{R} \cdot \mathbf{U} = \mathbf{V} \cdot \mathbf{R}, \tag{3.19}$$

wherein the deformation gradient is split into the right stretch tensor $\mathbf{U}$ or left stretch tensor $\mathbf{V}$ (symmetric and positive definite) and the rotation tensor $\mathbf{R}$ (orthogonal, i.e. $\mathbf{R}^T = \mathbf{R}^{-1}$). The velocity gradient is given by

$$\mathbf{L} = \dot{\mathbf{F}} \cdot \mathbf{F}^{-1}, \tag{3.20}$$

where

$$\dot{\mathbf{F}} = \frac{\partial \dot{\boldsymbol{u}}(\boldsymbol{X}, t)}{\partial \boldsymbol{X}}. \tag{3.21}$$

The velocity gradient can be decomposed in its symmetric part $\mathbf{D}$ and non-symmetric part $\mathbf{W}$, viz.

$$\mathbf{L} = \frac{1}{2}(\mathbf{L} + \mathbf{L}^T) + \frac{1}{2}(\mathbf{L} - \mathbf{L}^T) = \mathbf{D} + \mathbf{W}, \tag{3.22}$$

where $\mathbf{D}$ is the strain rate. The total strain can be calculated using Green's strain given by

$$\boldsymbol{\varepsilon}^G = \frac{1}{2}(\mathbf{F}^T \cdot \mathbf{F} - \mathbf{I}) = \frac{1}{2}(\underbrace{\mathbf{C}}_{\mathbf{U}^2} - \mathbf{I}) \tag{3.23}$$

or using the Hencky (logarithmic) strain defined by

$$\boldsymbol{\varepsilon}^H = \ln \mathbf{V}. \tag{3.24}$$

Most finite element codes (including the commercial finite element code `Abaqus`) use Hencky strain. The logarithmic strain has different advantages over other strain measures [271]:

- Strain can be added without the need to define a reference configuration, which is advantageous for an updated Lagrangian framework.
- An integration over time is easily possible.
- If the trace of strain is zero, the volume stays constant, which is not necessarily the case if the small-strain ("engineer strain") definition is used.

To determine the left stretch tensor $\mathbf{V}$ in Eq. (3.24), a polar decomposition of the deformation gradient has to be performed. Numerically, $\mathbf{V}$ can be determined using the *singular value decomposition*, where a quadratic tensor $\mathbf{A}$ is decomposed into three separate tensors, viz.

$$\mathbf{A} = \mathbf{B} \cdot \mathbf{D} \cdot \mathbf{C}^T. \tag{3.25}$$

The polar decomposition according to Eq. (3.19) is then

$$\mathbf{V} = \mathbf{B} \cdot \mathbf{C}^T \quad \text{and} \quad \mathbf{R} = \mathbf{C} \cdot \mathbf{D} \cdot \mathbf{C}^T. \tag{3.26}$$

Alternatively, $\mathbf{V}$ may be calculated using the relation

$$\mathbf{V} \cdot \mathbf{V} = \mathbf{F} \cdot \mathbf{F}^T = \mathbf{B}, \tag{3.27}$$

where the square root of the Left-Cauchy-Green tensor $\mathbf{B}$ has to be computed. In general, the square root of a tensor is not uniquely defined. However, in case the tensor is *positive semi-definite*, only one square root exists, which is called the *principal square root*. Since the Left-Cauchy-Green tensor is even *positive definite*, a unique solution exists. To compute the square root of $\mathbf{B}$ the following steps are performed:

- Diagonalise $\mathbf{B}$ to a form $\mathbf{B} = \mathbf{Z} \cdot \mathbf{D} \cdot \mathbf{Z}^T$ where $\mathbf{D}$ is the diagonal matrix (with the Eigenvalues of $\mathbf{B}$ alongside the diagonal axis) and $\mathbf{Z}$ an orthogonal matrix.
- Calculate the square root of $\mathbf{D}$ by taking the square root of the Eigenvalues which yields the tensor $\mathbf{D}'$.
- Perform $\mathbf{B}' = \mathbf{Z} \cdot \mathbf{D}' \cdot \mathbf{Z}^T$.

3.4 Definition of stress

Stress as force per unit area in the current configuration is denoted as Cauchy stress $\boldsymbol{\sigma}$ or *true* stress. It relates the traction $\boldsymbol{t}$ (a stress vector) with the normal vector $\boldsymbol{n}$ of a surface, viz.

$$\boldsymbol{t}(\boldsymbol{n}) = \boldsymbol{n} \cdot \boldsymbol{\sigma}. \tag{3.28}$$

The stress tensor is assumed symmetric throughout the work, i.e. $\boldsymbol{\sigma} = \boldsymbol{\sigma}^T$. This allows to adopt the *Voigt* notation for the stress tensor, being used in Chapter 4.

For the constitutive description, an *objective* (a rigid rotation does not cause any change in stress) definition of the stress rate is necessary [52]. While the stress tensor is an objective quantity, the rate of stress is not. Note that the strain rate is objective in contrast. To obtain an objective stress rate, the *Zaremba-Jaumann* [439, 184] stress rate is applied in this work, which is given by

$$\mathring{\boldsymbol{\sigma}} = \dot{\boldsymbol{\sigma}} + \boldsymbol{\sigma} \cdot \mathbf{W} - \mathbf{W} \cdot \boldsymbol{\sigma}, \tag{3.29}$$

where the objective stress rate $\mathring{\boldsymbol{\sigma}}$ is introduced. $\mathbf{W}$ is the spin-tensor introduced in Eq. (3.22).

To integrate Eq. (3.29), the *Hughes-Winget* algorithm [178] is applied. The update of stress is performed using

$$\boldsymbol{\sigma}^{t+\Delta t} = \hat{\boldsymbol{\sigma}}^{t+\Delta t} + \Delta\boldsymbol{\sigma} \tag{3.30}$$

where

$$\hat{\boldsymbol{\sigma}}^{t+\Delta t} = \mathbf{Q}\cdot\boldsymbol{\sigma}^{t}\cdot\mathbf{Q}^{T} \quad \text{and} \quad \mathbf{Q} = \big(\mathbf{I} - \frac{1}{2}\mathbf{W}\big)^{-1}\cdot\big(\mathbf{I} + \frac{1}{2}\mathbf{W}\big). \tag{3.31}$$

To evaluate $\mathbf{D}$ and $\mathbf{W}$ a midpoint rule is applied, defining $\mathbf{D}(\mathbf{x}^{t+\Delta t/2})$ and $\mathbf{W}(\mathbf{x}^{t+\Delta t/2})$ using the midpoint between the current coordinate of the previous increment $\boldsymbol{x}^{t}$ and the current coordinate of the present increment $\boldsymbol{x}^{t+\Delta t}$ (updated coordinate). In Eq. (3.30), $\Delta\boldsymbol{\sigma}$ denotes the increment in stress computed by the constitutive model.

The effective (grain-to-grain) stress is given by

$$\boldsymbol{\sigma} = \boldsymbol{\sigma}^{\mathrm{tot}} + B(\bar{p}^{af} - \chi s)\mathbf{I}, \tag{3.32}$$

where the parameters χ, B and the suction $s = \bar{p}^{af} - \bar{p}^{wf}$ are introduced. $\boldsymbol{\sigma}^{\mathrm{tot}}$ is the total stress and $\bar{p}^{af}$ and $\bar{p}^{wf}$ are the intrinsic pore air and pore water pressures, respectively. Following [129, 242], the assumption $\chi = S^{e}$ is made [11, 12]. In Eq. (3.32), B denotes the Biot constant, which is calculated by $B = 1 - K/K^{s}$, where K is the bulk modulus of the grain skeleton and K^{s} the bulk modulus of individual grains.

3.5 Compressibility

The specific density $\bar{\rho}^{\alpha}$ of phase α is a function of the acting (intrinsic) pressure $\bar{p}^{\alpha}$ and the bulk modulus $\bar{K}^{\alpha}$. The change of the pressure with time is calculated by (see e.g. [332, 213])

$$\frac{\mathrm{d}^{\alpha}\bar{p}^{\alpha}}{\mathrm{d}t} = \frac{\bar{K}^{\alpha}}{\bar{\rho}^{\alpha}}\frac{\mathrm{d}^{\alpha}\bar{\rho}^{\alpha}}{\mathrm{d}t}. \tag{3.33}$$

Using Eq. (3.16), the change of density with respect to time is

$$\frac{\mathrm{d}^{\alpha}\bar{\rho}^{\alpha}}{\mathrm{d}t} = \frac{\partial\bar{\rho}^{\alpha}}{\partial t} + \mathrm{grad}(\bar{\rho}^{\alpha})\cdot\bar{\boldsymbol{v}}^{\alpha}, \tag{3.34}$$

Eq. (3.34) is inserted into Eq. (3.33) yielding

$$\frac{\mathrm{d}^{\alpha}\bar{p}^{\alpha}}{\mathrm{d}t} = \frac{\bar{K}^{\alpha}}{\bar{\rho}^{\alpha}}\left[\frac{\partial\bar{\rho}^{\alpha}}{\partial t} + \mathrm{grad}(\bar{\rho}^{\alpha})\cdot\bar{\boldsymbol{v}}^{\alpha}\right]. \tag{3.35}$$

The change of the partial density with respect to time $\frac{\mathrm{d}^\alpha \rho^\alpha}{\mathrm{d}t}$ is

$$\begin{aligned}
\frac{\mathrm{d}^\alpha \rho^\alpha}{\mathrm{d}t} &= \varphi^\alpha \frac{\mathrm{d}^\alpha \bar{\rho}^\alpha}{\mathrm{d}t} + \bar{\rho}^\alpha \frac{\mathrm{d}^\alpha \varphi^\alpha}{\mathrm{d}t} \\
&= \varphi^\alpha \left[\frac{\partial \bar{\rho}^\alpha}{\partial t} + \operatorname{grad}(\bar{\rho}^\alpha) \cdot \bar{\boldsymbol{v}}^\alpha \right] + \bar{\rho}^\alpha \left[\frac{\partial \varphi^\alpha}{\partial t} + \operatorname{grad}(\varphi^\alpha) \cdot \bar{\boldsymbol{v}}^\alpha \right] \\
&= \varphi^\alpha \frac{\bar{\rho}^\alpha}{\bar{K}^\alpha} \frac{\mathrm{d}^\alpha \bar{p}^\alpha}{\mathrm{d}t} + \bar{\rho}^\alpha \left[\frac{\partial \varphi^\alpha}{\partial t} + \operatorname{grad}(\varphi^\alpha) \cdot \bar{\boldsymbol{v}}^\alpha \right] \\
&= \varphi^\alpha \frac{\bar{\rho}^\alpha}{\bar{K}^\alpha} \frac{\partial \bar{p}^\alpha}{\partial t} + \frac{\bar{\rho}^\alpha}{\bar{K}^\alpha} \operatorname{grad}(\bar{p}^\alpha) \cdot \bar{\boldsymbol{v}}^\alpha + \bar{\rho}^\alpha \left[\frac{\partial \varphi^\alpha}{\partial t} + \operatorname{grad}(\varphi^\alpha) \cdot \bar{\boldsymbol{v}}^\alpha \right].
\end{aligned} \tag{3.36}$$

3.6 Conservation of mass

The mass m^α of phase α of a body that fills the volume V results from the integration of its density ρ^α, viz.

$$m^\alpha = \int_{V^\alpha} \bar{\rho}^\alpha \mathrm{dV}^\alpha = \int_V \rho^\alpha \, \mathrm{dV} \,. \tag{3.37}$$

Assuming that no production nor any exchange of mass occurs and that the control volume is moving with the considered body, the mass must remain unchanged with respect to time, which leads to

$$\frac{\mathrm{d}^\alpha}{\mathrm{d}t} m^\alpha = \int_V \frac{\mathrm{d}^\alpha \rho^\alpha}{\mathrm{d}t} + \rho^\alpha \operatorname{div}(\bar{\boldsymbol{v}}^\alpha) \, \mathrm{dV} = 0. \tag{3.38}$$

Since the volume is arbitrary, Eq. (3.38) can be written to

$$\frac{\mathrm{d}^\alpha \rho^\alpha}{\mathrm{d}t} + \rho^\alpha \operatorname{div}(\bar{\boldsymbol{v}}^\alpha) = 0. \tag{3.39}$$

3.6.1 Solid, residual water and residual air

Using Eq. (3.39), the mass balance of the solid, the residual water and the residual air phase ($\eta = \{s, wr, ar\}$) is given by

$$\frac{\mathrm{d}\rho^\eta}{\mathrm{d}t} + \rho^\eta \operatorname{div}(\bar{\boldsymbol{v}}^s) = 0. \tag{3.40}$$

Note that Eq. (3.40) implies the assumption that the residual fluid phases move with the velocity of the solid phase. Using Eq. (3.36) and $\rho^\eta = \varphi^\eta \bar{\rho}^\eta$ yields

$$\varphi^\eta \frac{\bar{\rho}^\eta}{\bar{K}^\eta} \frac{\partial \bar{p}^\eta}{\partial t} + \varphi^\eta \frac{\bar{\rho}^\eta}{\bar{K}^\eta} \operatorname{grad}(\bar{p}^\eta) \cdot \bar{\boldsymbol{v}}^s + \bar{\rho}^\eta \left[\frac{\partial \varphi^\eta}{\partial t} + \operatorname{grad}(\varphi^\eta) \cdot \bar{\boldsymbol{v}}^s \right] + \rho^\eta \operatorname{div}(\bar{\boldsymbol{v}}^s) = 0. \tag{3.41}$$

Assuming the phase η to be incompressible[1], neglecting the gradient of the volume fraction φ^η and dividing by $\bar{\rho}^\eta$ results in

$$\frac{\partial \varphi^\eta}{\partial t} + \varphi^\eta \operatorname{div}(\bar{\boldsymbol{v}}^s) = 0. \tag{3.42}$$

Eq. (3.42) has to be met for every phase η. Therefore, the sum over the exponent $\eta = \{s, wr, ar\}$ has to be equal to zero as well, viz.

$$\frac{\partial \varphi^s}{\partial t} + \frac{\partial \varphi^{wr}}{\partial t} + \frac{\partial \varphi^{ar}}{\partial t} + \varphi^s \operatorname{div}(\bar{\boldsymbol{v}}^s) + \varphi^{wr} \operatorname{div}(\bar{\boldsymbol{v}}^s) + \varphi^{ar} \operatorname{div}(\bar{\boldsymbol{v}}^s) = 0. \tag{3.43}$$

Using the definition of the effective porosity n^e given by Eq. (3.7), the conservation of mass for the solid, residual water and residual air phase is given by

$$\dot{n}^e = (1 - n^e) \operatorname{div}(\bar{\boldsymbol{v}}^s). \tag{3.44}$$

3.6.2 Free water and free air

For the mass balance of the free water phase, Eq. (3.39) is

$$\frac{\mathrm{d}^{wf} \rho^{wf}}{\mathrm{d}t} + \rho^{wf} \operatorname{div}(\bar{\boldsymbol{v}}^{wf}) = 0. \tag{3.45}$$

Using Eqs. (3.17, 3.36), Eq. (3.45) yields

$$\begin{aligned} &\varphi^{wf} \frac{\bar{\rho}^{wf}}{\bar{K}^{wf}} \frac{\mathrm{d}\bar{p}^{wf}}{\mathrm{d}t} + \varphi^{wf} \frac{\bar{\rho}^{wf}}{\bar{K}^{wf}} \operatorname{grad}(\bar{p}^{wf}) \cdot \bar{\boldsymbol{w}}^{wf} + \bar{\rho}^{wf} \frac{\mathrm{d}\varphi^{wf}}{\mathrm{d}t} + \bar{\rho}^{wf} \operatorname{grad}(\varphi^{wf}) \cdot \bar{\boldsymbol{w}}^{wf} \\ &+ \rho^{wf} \operatorname{div}(\bar{\boldsymbol{v}}^{wf}) = 0. \end{aligned} \tag{3.46}$$

Rearranging and division by $\bar{\rho}^{wf}$ results in

$$-\frac{\mathrm{d}\varphi^{wf}}{\mathrm{d}t} = \frac{\varphi^{wf}}{\bar{K}^{wf}} \frac{\mathrm{d}\bar{p}^{wf}}{\mathrm{d}t} + \frac{\varphi^{wf}}{\bar{K}^{wf}} \operatorname{grad}(\bar{p}^{wf}) \cdot \bar{\boldsymbol{w}}^{wf} + \operatorname{grad}(\varphi^{wf}) \cdot \bar{\boldsymbol{w}}^{wf} + \varphi^{wf} \operatorname{div}(\bar{\boldsymbol{v}}^{wf}). \tag{3.47}$$

Using the differentiation of φ^γ with respect to time given by

$$\frac{\mathrm{d}\varphi^\gamma}{\mathrm{d}t} = \frac{\mathrm{d}S_e^\gamma}{\mathrm{d}t} \left[1 - (\varphi^s + \varphi^{wr} + \varphi^{ar})\right] - S_e^\gamma \left(\frac{\mathrm{d}\varphi^s}{\mathrm{d}t} + \frac{\mathrm{d}\varphi^{wr}}{\mathrm{d}t} + \frac{\mathrm{d}\varphi^{ar}}{\mathrm{d}t}\right) \tag{3.48}$$

as well as Eq. (3.8) leads to

$$\begin{aligned} S_e^{wf} \left(\frac{\mathrm{d}\varphi^s}{\mathrm{d}t} + \frac{\mathrm{d}\varphi^{wr}}{\mathrm{d}t} + \frac{\mathrm{d}\varphi^{ar}}{\mathrm{d}t}\right) - \frac{\mathrm{d}S_e^{wf}}{\mathrm{d}t} n^e = \frac{\varphi^{wf}}{\bar{K}^{wf}} \frac{\mathrm{d}\bar{p}^{wf}}{\mathrm{d}t} + \frac{\varphi^{wf}}{\bar{K}^{wf}} \operatorname{grad}(\bar{p}^{wf}) \cdot \bar{\boldsymbol{w}}^{wf} \\ + \operatorname{grad}(\varphi^{wf}) \cdot \bar{\boldsymbol{w}}^{wf} + \varphi^{wf} \operatorname{div}(\bar{\boldsymbol{v}}^{wf}). \end{aligned} \tag{3.49}$$

[1]The assumption of incompressibility is questionable for the residual air phase. [242] presented an approach taking into account the compressibility of the residual air and mass transfer between free and residual air. In future work, this approach could also be implemented in the balance equations employed in this thesis.

Eq. (3.42) is inserted into Eq. (3.49) resulting in

$$
\begin{aligned}
&- S_e^{wf}\left(\varphi^s + \varphi^{wr} + \varphi^{ar}\right)\operatorname{div}(\bar{\boldsymbol{v}}^s) - \frac{\mathrm{d}S_e^{wf}}{\mathrm{d}t} n^e \\
&= \frac{\varphi^{wf}}{\bar{K}^{wf}} \frac{\mathrm{d}\bar{p}^{wf}}{\mathrm{d}t} + \frac{\varphi^{wf}}{\bar{K}^{wf}} \operatorname{grad}(\bar{p}^{wf}) \cdot \bar{\boldsymbol{w}}^{wf} + \operatorname{grad}(\varphi^{wf}) \cdot \bar{\boldsymbol{w}}^{wf} + \varphi^{wf} \operatorname{div}(\bar{\boldsymbol{v}}^{wf}).
\end{aligned} \tag{3.50}
$$

Using

$$
\operatorname{div}(\boldsymbol{w}^\alpha) = \operatorname{grad}(\varphi^\alpha) \cdot \bar{\boldsymbol{w}}^\alpha + \varphi^\alpha \operatorname{div}(\bar{\boldsymbol{v}}^\alpha) - \varphi^\alpha \operatorname{div}(\bar{\boldsymbol{v}}^s) \tag{3.51}
$$

and the relation $\varphi^{wf} = S_e^{wf} n^e = S_e^{wf}\left[1 - \left(\varphi^s + \varphi^{wr} + \varphi^{ar}\right)\right]$, the final form of the mass balance of the free water phase is

$$
\frac{\varphi^{wf}}{\bar{K}^{wf}} \frac{\mathrm{d}\bar{p}^{wf}}{\mathrm{d}t} + \frac{1}{\bar{K}^{wf}} \operatorname{grad}(\bar{p}^{wf}) \cdot \boldsymbol{w}^{wf} + \frac{\mathrm{d}S_e^{wf}}{\mathrm{d}t} n^e + S_e^{wf} \operatorname{div}(\bar{\boldsymbol{v}}^s) + \operatorname{div}(\boldsymbol{w}^{wf}) = 0. \tag{3.52}
$$

Proceeding analogously, the mass balance of the free air phase reads

$$
\frac{\varphi^{af}}{\bar{K}^{af}} \frac{\mathrm{d}\bar{p}^{af}}{\mathrm{d}t} + \frac{1}{\bar{K}^{af}} \operatorname{grad}(\bar{p}^{af}) \cdot \boldsymbol{w}^{af} + \frac{\mathrm{d}S_e^{af}}{\mathrm{d}t} n^e + S_e^{af} \operatorname{div}(\bar{\boldsymbol{v}}^s) + \operatorname{div}(\boldsymbol{w}^{af}) = 0. \tag{3.53}
$$

3.7 Conservation of linear momentum

The balance of linear momentum of phase α is defined by [333]

$$
\operatorname{div}(\boldsymbol{\sigma}^\alpha) + \rho^\alpha \boldsymbol{b} = \rho^\alpha \frac{\mathrm{d}^\alpha \bar{\boldsymbol{v}}^\alpha}{\mathrm{d}t}. \tag{3.54}
$$

$\boldsymbol{\sigma}^\alpha$ is the partial stress tensor of phase α.

3.7.1 Balance of linear momentum of the mixture

The linear momentum of the mixture is obtained by summation of all phases $\sum_\alpha$ using Eq. (3.54), viz.

$$
\operatorname{div}(\boldsymbol{\sigma}^{tot}) + \rho^{tot}\boldsymbol{b} = \left(\varphi^s \bar{\rho}^s + \varphi^{wr}\bar{\rho}^{wr} + \varphi^{ar}\bar{\rho}^{ar}\right)\frac{\mathrm{d}\bar{\boldsymbol{v}}^s}{\mathrm{d}t} + \varphi^{wf}\bar{\rho}^{wf}\frac{\mathrm{d}^{wf}\bar{\boldsymbol{v}}^{wf}}{\mathrm{d}t} + \varphi^{af}\bar{\rho}^{af}\frac{\mathrm{d}^{af}\bar{\boldsymbol{v}}^{af}}{\mathrm{d}t}. \tag{3.55}
$$

Using Eqs. (3.15, 3.17) accounting for the movement of the free fluid phases relative to the movement of the solid, Eq. (3.55) yields

$$
\begin{aligned}
\operatorname{div}(\boldsymbol{\sigma}^{tot}) + \rho^{tot}\boldsymbol{b} = &\left(\varphi^s \bar{\rho}^s + \varphi^{wr}\bar{\rho}^{wr} + \varphi^{ar}\bar{\rho}^{ar}\right)\frac{\mathrm{d}\bar{\boldsymbol{v}}^s}{\mathrm{d}t} + \varphi^{wf}\bar{\rho}^{wf}\left[\frac{\mathrm{d}\bar{\boldsymbol{v}}^{wf}}{\mathrm{d}t} + \operatorname{grad}(\bar{\boldsymbol{v}}^{wf})\cdot\bar{\boldsymbol{w}}^{wf}\right] \\
&+ \varphi^{af}\bar{\rho}^{af}\left[\frac{\mathrm{d}\bar{\boldsymbol{v}}^{af}}{\mathrm{d}t} + \operatorname{grad}(\bar{\boldsymbol{v}}^{af})\cdot\bar{\boldsymbol{w}}^{af}\right].
\end{aligned} \tag{3.56}
$$

Eq. (3.56) is equivalent to

$$\begin{aligned}\operatorname{div}(\boldsymbol{\sigma}^{tot}) + \rho^{tot}\boldsymbol{b} = (\varphi^s\bar{\rho}^s + \varphi^{wr}\bar{\rho}^{wr} + \varphi^{ar}\bar{\rho}^{ar})\left[\frac{\partial\bar{\boldsymbol{v}}^s}{\partial t} + \operatorname{grad}(\bar{\boldsymbol{v}}^s)\cdot\bar{\boldsymbol{v}}^s\right] \\ + \varphi^{wf}\bar{\rho}^{wf}\left[\frac{\partial\bar{\boldsymbol{v}}^{wf}}{\partial t} + \operatorname{grad}(\bar{\boldsymbol{v}}^{wf})\cdot\bar{\boldsymbol{w}}^{wf} + \operatorname{grad}(\bar{\boldsymbol{v}}^{wf})\cdot\bar{\boldsymbol{v}}^s\right] \\ + \varphi^{af}\bar{\rho}^{af}\left[\frac{\partial\bar{\boldsymbol{v}}^{af}}{\partial t} + \operatorname{grad}(\bar{\boldsymbol{v}}^{af})\cdot\bar{\boldsymbol{w}}^{af} + \operatorname{grad}(\bar{\boldsymbol{v}}^{af})\cdot\bar{\boldsymbol{v}}^s\right]. \qquad (3.57)\end{aligned}$$

Using the definition of effective (grain-to-grain) stress introduced in Eq. (3.32) and assuming that the convective terms are of negligible magnitude (see [451, 309, 452]), the final form of the balance of linear momentum of the mixture is

$$\begin{aligned}\operatorname{div}[\boldsymbol{\sigma} - B(\bar{p}^{af} - S^e s)\mathbf{1}] + \rho^{tot}\boldsymbol{b} = (\varphi^s\bar{\rho}^s + \varphi^{wr}\bar{\rho}^{wr} + \varphi^{ar}\bar{\rho}^{ar})\frac{\mathrm{d}\bar{\boldsymbol{v}}^s}{\mathrm{d}t} + \varphi^{wf}\bar{\rho}^{wf}\frac{\mathrm{d}\bar{\boldsymbol{v}}^{wf}}{\mathrm{d}t} \\ + \varphi^{af}\bar{\rho}^{af}\frac{\mathrm{d}\bar{\boldsymbol{v}}^{af}}{\mathrm{d}t}. \qquad (3.58)\end{aligned}$$

3.7.2 Balance of linear momentum of the free fluid phases

The balance of linear momentum of the free water phase is obtained analogously to the balance of linear momentum of the mixture but takes into account the drag forces between the solid and the fluid. Note that the drag forces between solid and free fluid phases have opposite sign but identical magnitude for why no drag forces are considered in the balance of linear momentum of the mixture (the terms cancel each other out). The balance of linear momentum of the free water phase is given by

$$\operatorname{div}(\bar{p}^{wf}\mathbf{I}) - \bar{\rho}^{wf}\boldsymbol{b} + \bar{\rho}^{wf}\left[\frac{\mathrm{d}\bar{\boldsymbol{v}}^{wf}}{\mathrm{d}t} + \operatorname{grad}(\bar{\boldsymbol{v}}^{wf})\cdot\bar{\boldsymbol{w}}^{wf}\right] = -\frac{\varphi^{wf}\eta^w}{k^{\mathrm{rel},w}}(\mathbf{K}^{\mathrm{Perm},w})^{-1}\cdot\bar{\boldsymbol{w}}^{wf}, \quad (3.59)$$

where the definition $\boldsymbol{\sigma}^{wf} = -\varphi^{wf}\bar{p}^{wf}\mathbf{I}$ is used. Note that in Eq. (3.59) all terms are already divided by φ^{wf} and the assumption $\operatorname{div}(\varphi^{wf}) = \mathbf{0}$ is used. Using $\operatorname{div}(\sqcup\mathbf{I}) = \operatorname{grad}(\sqcup)$ and neglecting the convective term, the final form of the balance of linear momentum of the free water phase is obtained by Eq. (3.60).

$$\operatorname{grad}(\bar{p}^{wf}) + \bar{\rho}^{wf}\frac{\mathrm{d}\bar{\boldsymbol{v}}^{wf}}{\mathrm{d}t} + \frac{\varphi^{wf}\eta^w}{k^{\mathrm{rel},w}}(\mathbf{K}^{\mathrm{Perm},w})^{-1}\cdot\bar{\boldsymbol{w}}^{wf} = \bar{\rho}^{wf}\boldsymbol{b} \qquad (3.60)$$

Analogously, the balance of linear momentum of the free air phase is given by

$$\operatorname{grad}(\bar{p}^{af}) + \bar{\rho}^{af}\frac{\mathrm{d}\bar{\boldsymbol{v}}^{af}}{\mathrm{d}t} + \frac{\varphi^{af}\eta^a}{k^{\mathrm{rel},a}}(\mathbf{K}^{\mathrm{Perm},a})^{-1}\cdot\bar{\boldsymbol{w}}^{af} = \bar{\rho}^{af}\boldsymbol{b}. \qquad (3.61)$$

Chapter 4

Finite element formulations

The spatial and temporal discretisation of the governing equations derived in the previous chapter are presented in the following. As already mentioned in the introduction, different element formulations for the discretisation of hydro-mechanically coupled balance equations exist, which differ in the variables that are spatially discretised. Choosing the displacement of the solid phase $\boldsymbol{u}^s$ and the two pore fluid pressures $\bar{p}^{wf}$ and $\bar{p}^{af}$ as *primary variables* (the underlying equations are solved with respect to them), the commonly applied **u**-p-p element formulation (denoted as **u**-p element formulation in the following for sake of convenience) [451] is obtained.

Using the **u**-p element formulation, the assumption of identical acceleration of all phases $\ddot{\boldsymbol{u}}^\gamma = \ddot{\boldsymbol{u}}^s$ is necessary, which is an intervention in the physical equations. The importance of the consideration of the relative acceleration between the phases has been mentioned in many numerical studies, in which high frequencies and pore fluid flow have been met concurrently [453, 310, 309, 213, 266, 234, 185, 108, 337, 78, 74, 254, 259, 20]. In addition, as the primary unknowns have varying physical dimensions and their values therefore differ considerably, the stiffness matrix of the **u**-p element is poorly conditioned [349]. To avoid excessive oscillation of the pore fluid pressure under nearly undrained conditions, the Ladyshenskaya-Babuška-Brezzi (LBB) condition [111] must be satisfied. This is generally ensured by discretising the pore fluid pressure with interpolation functions one order less than those used for the solid displacement. Without any additional artificial stabilisation, the formulation of a **u**-p element with linearly interpolated displacement *degree-of-freedom* (DOF) is therefore not recommended.

In the framework of this thesis, a **u**-p-**U** element formulation with two fluid phases (hence, a **u**-p-p-**U**-**U** element formulation but denoted as **u**-p-**U** element formulation in the following for sake of convenience) is developed, which is presented in this chapter. Opposite to the **u**-p

formulation, the **u**-p-**U** element formulation accounts for the relative acceleration. Note that a **u**-**U**(-**U**) element formulation has been previously developed by the author of this work as well, which has been documented in [241, 347]. Technically, the **u**-p-**U** and **u**-**U** element formulations are identical in regards to the underlying governing equations. The **u**-**U** element formulation, however, has three shortcomings compared to the **u**-p-**U** element formulation:

- An iterative calculation of the pore fluid pressure in case of unsaturated soils is necessary since the degree of saturation is a function of the pore fluid pressure and vice versa. The formulation of numerically stable iterative schemes is not trivial.
- **u**-**U** elements tend to suffer from volumetric locking of the fluid phase, which has been observed and documented by the author in detail in [349]. Even elements with selective reduced integration of the fluid pressure were found to show diverging integration point values for large volumetric strains.
- Incompressibility of the pore fluids can not be assumed.

An advantage of the **u**-**U** element formulation, compared to the other two formulations, is the superior conditioning of the stiffness matrix [349] and hence improved numerical stability. Recent investigations of [311, 238] show that a single point integration together with enhancement by an hourglass stiffness for the fluid phase can overcome the problems of volumetric locking of the **u**-**U** element formulation.

Despite the addressed shortcomings of the **u**-p and **u**-**U** element formulations, they are used at a later point for the simulation of different BVPs in order to show their performance in comparison to the **u**-p-**U** element formulation. In addition, a three-dimensional **u**-p element using tri-quadratic interpolation functions with 27 nodes is developed in Section 6.6, since the commonly employed 20-noded three-dimensional *serendipity* elements perform inferior in contact analyses.

This chapter is structured as follows: Section 4.1 introduces the mathematical operations required for the spatial discretisation of the continuum with the finite element method. The derivation of the **u**-p-**U** (Lagrangian) element formulation is presented in Section 4.2. Notes about the minimisation of the residuum, time integration and implementation of the element are provided in Section 4.3. The development of a novel semi-analytical solution for poro-elasto-dynamics allowing for the investigation of the influence of the aforementioned relative acceleration between solid and fluid phase is discussed in Section 4.4. The different element formulations are inspected regarding their numerical performance in more detail in Section 4.5.

The basics of an Eulerian element formulation and the implementation of a hydro-mechanically coupled and explicit (Coupled Eulerian-Lagrangian) method in the commercial finite element code `Abaqus` is presented in Section 4.6.

4.1 Finite element operations

The isoparametric description is used for the interpolation of the coordinates of the finite element. The global coordinate is calculated using

$$\boldsymbol{x}(\boldsymbol{\xi}) = \sum_I N_I(\boldsymbol{\xi}) \boldsymbol{x}_I, \tag{4.1}$$

where the interpolation function $N_I(\boldsymbol{\xi})$ at node I and the local coordinate $\boldsymbol{\xi}$ is used. $\boldsymbol{x}(\boldsymbol{\xi})$ is the global coordinate at the local coordinate $\boldsymbol{\xi}$ of the element and $\boldsymbol{x}_I$ is the global coordinate of node I. The interpolation function N_I is 1 at node I. The number of components of $\boldsymbol{\xi}$ is identical to the number of dimensions and the local coordinate has the components $\boldsymbol{\xi} = [\xi, \eta, \zeta]^{\mathrm{T}}$ for three-dimensional analyses. ξ and η are also employed as the local coordinate of element edges and faces, respectively. Where possible, the scalar components of the local coordinate are used in the following. The interpolation functions used are either termed linear, quadratic (serendipity shape functions), bi/tri-quadratic (standard Lagrange polynomials) or cubic according to their order of interpolation.

The derivation of the global coordinates with respect to the local coordinates is

$$\boldsymbol{x}_{,\xi}(\boldsymbol{\xi}) = \sum_I \frac{dN_I(\boldsymbol{\xi})}{d\boldsymbol{\xi}} \boldsymbol{x}_I, \tag{4.2}$$

which is also known as the element *Jacobian* $\mathbf{J}$. The normal vector $\boldsymbol{n}(\xi)$ at the edge of an element is given for 2D by

$$\boldsymbol{n}(\xi) = \frac{\boldsymbol{x}_{,\xi}(\xi) \times \boldsymbol{\tau}_3}{\|\boldsymbol{x}_{,\xi}(\xi)\|}, \tag{4.3}$$

where $\boldsymbol{\tau}_3 = [0, 0, 1]^T$ is used and $\boldsymbol{x}_{,\xi}(\xi)$ is the derivative of the global coordinate with respect to the local coordinate ξ evaluated at position ξ (only relevant for interpolation with order two or higher). $\times$ marks the cross product. For three-dimensional analyses, the normal vector is defined by

$$\boldsymbol{n}(\xi, \eta) = \frac{\boldsymbol{x}_{,\xi}(\xi, \eta) \times \boldsymbol{x}_{,\eta}(\xi, \eta)}{\|\boldsymbol{x}_{,\xi}(\xi, \eta) \times \boldsymbol{x}_{,\eta}(\xi, \eta)\|}. \tag{4.4}$$

The tangential vectors orientated in the local coordinate system are determined by

$$\boldsymbol{\tau}_1(\xi) = \frac{\boldsymbol{x}_{,\xi}(\xi)}{\|\boldsymbol{x}_{,\xi}(\xi)\|} \tag{4.5}$$

for 2D and by

$$\boldsymbol{\tau}_1(\xi,\eta) = \frac{\boldsymbol{x}_{,\xi}(\xi,\eta)}{\|\boldsymbol{x}_{,\xi}(\xi,\eta)\|} \quad \text{and} \quad \boldsymbol{\tau}_2(\xi,\eta) = \frac{\boldsymbol{x}_{,\eta}(\xi,\eta)}{\|\boldsymbol{x}_{,\eta}(\xi,\eta)\|} \tag{4.6}$$

for the 3D case.

The Voigt-notation for stress and strain is adopted. For geometrically linear (small strain) 3D analyses the strain is calculated using the symmetric portion of the displacement gradient

$$\boldsymbol{\varepsilon} = \begin{bmatrix} \varepsilon_{xx} \\ \varepsilon_{yy} \\ \varepsilon_{zz} \\ \gamma_{xy} \\ \gamma_{yz} \\ \gamma_{zx} \end{bmatrix} = \sum_I \underbrace{\begin{bmatrix} N_{I,x} & 0 & 0 \\ 0 & N_{I,y} & 0 \\ 0 & 0 & N_{I,z} \\ N_{I,y} & N_{I,x} & 0 \\ 0 & N_{I,z} & N_{I,y} \\ N_{I,z} & 0 & N_{I,x} \end{bmatrix}}_{\mathbf{B}_I} \begin{bmatrix} u_{Ix} \\ u_{Iy} \\ u_{Iz} \end{bmatrix}, \tag{4.7}$$

where the so-called *B-matrix* $\mathbf{B}_I$ is introduced. In the axisymmetric case the strain is calculated by

$$\boldsymbol{\varepsilon} = \begin{bmatrix} \varepsilon_{rr} \\ \varepsilon_{zz} \\ \varepsilon_{\theta\theta} \\ \gamma_{rz} \end{bmatrix} = \sum_I \underbrace{\begin{bmatrix} N_{I,r} & 0 \\ 0 & N_{I,z} \\ \frac{1}{r}N_I & 0 \\ N_{I,z} & N_{I,r} \end{bmatrix}}_{\mathbf{B}_I} \begin{bmatrix} u_{Ir} \\ u_{Iz} \end{bmatrix}, \tag{4.8}$$

where the radius r from the symmetry axis to the current point is calculated using

$$r(\boldsymbol{\xi}) = \sum_I N_I(\boldsymbol{\xi}) r_I. \tag{4.9}$$

For the numerical integration, the *Gauss-quadrature* is employed. To evaluate the weights based on a given value of the local coordinate ξ, the *Legendre-polynomial* defined by

$$p_N(\xi) = \frac{1}{2^N N!} \frac{d^N(\xi^2-1)^N}{d\xi^N} \tag{4.10}$$

is used. N is the order of interpolation and the coordinates of the integration points $\bar{\xi}_{\text{igp}}$ are obtained by computing $p_N(\bar{\xi}_{\text{igp}}) = 0$. The weight of the integration point is then given by

$$w_{\text{igp}} = \frac{2}{(1-\bar{\xi}_{\text{igp}}^2)\left[\dfrac{dp_N(\bar{\xi}_{\text{igp}})}{d\xi}\right]^2}. \tag{4.11}$$

The integration of a function $f(x,y,z)$ over a volume Ω is done numerically using

$$\begin{aligned}\int_\Omega f(x,y,z)\mathrm{d}\Omega &= \int_{-1}^{1}\int_{-1}^{1}\int_{-1}^{1} f[x(\xi,\eta,\zeta),y(\xi,\eta,\zeta),z(\xi,\eta,\zeta)]j(\xi,\eta,\zeta)\mathrm{d}\xi\mathrm{d}\eta\mathrm{d}\zeta \\ &= \sum_{k=1}^{n_{GP}}\sum_{j=1}^{n_{GP}}\sum_{l=1}^{n_{GP}} f[x(\xi_k,\eta_j,\zeta_l),y(\xi_k,\eta_j,\zeta_l),z(\xi_k,\eta_j,\zeta_l)]j(\xi_k,\eta_j,\zeta_l)w_k w_j w_l,\end{aligned} \tag{4.12}$$

where the determinant j of the Jacobian $\mathbf{J}$ introduced in Eq. (4.2) is used. In case of an axisymmetric analysis the numerical integration is given by

$$\begin{aligned}\int_\Omega f(r,z)\mathrm{d}\Omega &= 2\pi\int_{-1}^{1}\int_{-1}^{1} f[r(\xi,\eta),z(\xi,\eta)]r(\xi,\eta)J(\xi,\eta)\mathrm{d}\xi\mathrm{d}\eta \\ &= 2\pi\sum_{k=1}^{n_{GP}}\sum_{j=1}^{n_{GP}} f[r(\xi_k,\eta_j),z(\xi_k,\eta_j)]r(\xi_k,\eta_j)j(\xi_k,\eta_j)w_k w_j.\end{aligned} \tag{4.13}$$

4.2 Spatial discretisation using a u-p-U formulation

The primary variables are spatially discretised by

$$\boldsymbol{u}^\theta = \sum_I N_I^\theta(\boldsymbol{\xi})\boldsymbol{u}_I^\theta \quad \text{for} \quad \theta = \{s, wf, af\} \quad \text{and} \quad \bar{p}^\gamma = \sum_K N_K^\gamma(\boldsymbol{\xi})\bar{p}_K^\gamma \quad \text{for} \quad \gamma = \{wf, af\}.$$

The interpolation function $N_I^\theta(\boldsymbol{\xi})$ interpolates the displacement of phase $\theta = \{sf, wf, af\}$. Likewise, the pressure of phase $\gamma = \{wf, af\}$ is interpolated using $N_K^\gamma(\boldsymbol{\xi})$. For sake of convenience it is assumed that the fluid pressure of the different phases is interpolated utilising the same interpolation function N_K^p, i.e. the identical order of interpolation is used.

In order to discretise the balance equations introduced in Chapter 3 spatially, the equations are multiplied by so-called test functions $\delta\lambda$ and integrated over a finite volume. By this procedure the final set of discretised equations contain no spatial derivatives of the primary unknowns but only of their interpolation functions. For the discretisation, the relation

$$\mathrm{div}(\delta\lambda \sqcup) = \delta\lambda\,\mathrm{div}(\sqcup) + \mathrm{grad}(\delta\lambda)\sqcup \tag{4.14}$$

and the Gaussian integral theorem

$$\int_\Omega \mathrm{div}(\delta\lambda \sqcup)\mathrm{d}\Omega = \int_\Gamma \boldsymbol{n}\cdot\delta\lambda \sqcup \mathrm{d}\Gamma \tag{4.15}$$

are required. In Eq. (4.15), $\boldsymbol{n}$ denotes the normal vector on surface Γ. Note that the index notation is used in the following.

4.2.1 Balance of linear momentum of the mixture

Eq. (3.58) is multiplied by δu_i^s and integrated over a finite volume Ω yielding

$$\underbrace{\int_\Omega \delta u_i^s \sigma_{ij,j}^{tot}\mathrm{d}\Omega}_{A} + \int_\Omega \delta u_i^s \rho^{tot} b_i \mathrm{d}\Omega = \int_\Omega \delta u_i^s(\varphi^s\bar{\rho}^s + \varphi^{wr}\bar{\rho}^{wr} + \varphi^{ar}\bar{\rho}^{ar})\bar{a}_i^s\mathrm{d}\Omega + \int_\Omega \delta u_i^s \varphi^{wf}\bar{\rho}^{wf}\bar{a}_i^{wf}\mathrm{d}\Omega + \int_\Omega \delta u_i^s \varphi^{af}\bar{\rho}^{af}\bar{a}_i^{af}\mathrm{d}\Omega. \tag{4.16}$$

Using Eq. (4.15) and Eq. (4.14), term A in Eq. (4.16) yields

$$\int_\Omega \delta u_i^s \sigma_{ij,j}^{tot}\mathrm{d}\Omega = \int_\Gamma \delta u_i \hat{t}_i \mathrm{d}\Gamma - \int_\Omega \delta u_{i,j}^s \sigma_{ij}^{tot}\mathrm{d}\Omega, \tag{4.17}$$

where $\hat{t}_i$ is a prescribed traction force on the element surface. Using the definition of effective stress introduced in Eq. (3.32) and multiplying Eq. (4.16) by the test and interpolation functions leads to

$$\begin{aligned}\int_\Gamma \delta u_{Ii}^s N_I^s \hat{t}_i \mathrm{d}\Gamma - \int_\Omega \delta u_{Ii}^s N_{I,j}^s \sigma_{ij}\mathrm{d}\Omega + \int_\Omega \delta u_{Ii}^s N_{I,j}^s B[N_K^p\bar{p}_K^{af} - S^e(N_K^p\bar{p}_K^{af} - N_K^p\bar{p}_K^{wf})]\delta_{ij}\mathrm{d}\Omega \\ + \int_\Omega \delta u_{Ii}^s N_I^s \rho^{tot} b_i \mathrm{d}\Omega - \int_\Omega \delta u_{Ii}^s N_I^s(\varphi^s\bar{\rho}^s + \varphi^{wr}\bar{\rho}^{wr} + \varphi^{ar}\bar{\rho}^{ar})N_J^s\bar{a}_{Ji}^s\mathrm{d}\Omega \\ - \int_\Omega \delta u_{Ii}^s N_I^s \varphi^{wf}\bar{\rho}^{wf}N_J^{wf}\bar{a}_{Ji}^{wf}\mathrm{d}\Omega - \int_\Omega \delta u_{Ii}^s N_I^s \varphi^{af}\bar{\rho}^{af}N_J^{af}\bar{a}_{Ji}^{af}\mathrm{d}\Omega = 0.\end{aligned} \tag{4.18}$$

Since Eq. (4.18) has to hold for arbitrary test functions δu_{Ii}^α, the test functions can be cancelled. In the following, the *Voigt* notation is used for stress and strain, which is highlighted by using the index $\sqcup_m$ instead of $\sqcup_j$. Considering that Eq. (4.18) is non-linear with respect to the solid displacement and has to be iteratively solved, the residuum r_{Ii}^s is introduced, which has to be minimised during the iteration. The final form of the spatially disrectised balance of linear

momentum of the mixture is given by

$$
\begin{aligned}
r^s_{Ii} = &\int_\Omega B^s_{Imi}\sigma_m \mathrm{d}\Omega - \int_\Omega N^s_{I,j} B[N^p_K \bar{p}^{af}_K - S^e(N^p_K \bar{p}^{af}_K - N^p_K \bar{p}^{wf}_K)]\delta_{ij}\mathrm{d}\Omega \\
&- \int_\Omega N^s_I \rho^{tot} b_i \mathrm{d}\Omega + \int_\Omega N^s_I(\varphi^s \bar{\rho}^s + \varphi^{wr}\bar{\rho}^{wr} + \varphi^{ar}\bar{\rho}^{ar}) N^s_J \bar{a}^s_{Ji}\mathrm{d}\Omega \\
&+ \int_\Omega N^s_I S^e n^e \bar{\rho}^{wf} N^{wf}_J \bar{a}^{wf}_{Ji}\mathrm{d}\Omega + \int_\Omega N^s_I(1-S^e) n^e \bar{\rho}^{af} N^{af}_J \bar{a}^{af}_{Ji}\mathrm{d}\Omega - \int_\Gamma N^s_I \hat{t}_i \mathrm{d}\Gamma. \qquad (4.19)
\end{aligned}
$$

4.2.2 Balance of mass of the free fluid phases

By integration of Eq. (3.52) over a finite volume and multiplication with the interpolation function of the pore fluid pressure N^p_K, the spatially discretised balance of mass of the free water phase is given by

$$
\begin{aligned}
r^{pwf}_K = &\int_\Omega N^p_K n^e \frac{S^e}{\bar{K}^{wf}} N^p_L \dot{\bar{p}}^{wf}_L \mathrm{d}\Omega + \int_\Omega N^p_K \frac{1}{\bar{K}^{wf}} \bar{p}^{wf}_L N^p_{L,i} w^{wf}_i \mathrm{d}\Omega + \int_\Omega N^p_K \frac{\mathrm{d}S^e}{\mathrm{d}t} n^e \mathrm{d}\Omega \\
&+ \int_\Omega N^p_K S^e N^s_{J,i} \bar{v}^s_{Ji}\mathrm{d}\Omega + \int_\Omega N^p_K \varphi^{wf}\big(N^{wf}_{J,i}\bar{v}^{wf}_{Ji} - N^s_{J,i}\bar{v}^s_{Ji}\big)\mathrm{d}\Omega. \qquad (4.20)
\end{aligned}
$$

The spatially discretised balance of mass of the free air phase is obtained analogously, viz.

$$
\begin{aligned}
r^{paf}_K = &\int_\Omega N^p_K n^e \frac{1-S^e}{\bar{K}^{af}} N^p_L \dot{\bar{p}}^{af}_L \mathrm{d}\Omega + \int_\Omega N^p_K \frac{1}{\bar{K}^{af}} N^p_{L,i} \bar{p}^{af}_L w^{af}_i \mathrm{d}\Omega - \int_\Omega N^p_K \frac{\mathrm{d}S^e}{\mathrm{d}t} n^e \mathrm{d}\Omega \\
&+ \int_\Omega N^p_K (1-S^e) N^s_{J,i} \bar{v}^s_{Ji}\mathrm{d}\Omega + \int_\Omega N^p_K \varphi^{af}\big(N^{af}_{J,i}\bar{v}^{af}_{Ji} - N^s_{J,i}\bar{v}^s_{Ji}\big)\mathrm{d}\Omega. \qquad (4.21)
\end{aligned}
$$

4.2.3 Balance of linear momentum of the free fluid phases

Using analogous procedures as for the balance of linear momentum of the mixture, the spatially discretised balance of linear momentum of the free water phase is given by

$$
\begin{aligned}
r^{wf}_{Ii} = &\int_\Gamma N^w_I \hat{p}^{wf} n_i \mathrm{d}\Gamma - \int_\Omega N^{wf}_{I,i} N^p_K \bar{p}^{wf}_K \mathrm{d}\Omega + \int_\Omega N^w_I \bar{\rho}^{wf} N^{wf}_J \bar{a}^{wf}_{Ji}\mathrm{d}\Omega \\
&+ \int_\Omega N^{wf}_I \frac{n^e S^e \eta^w}{k^{\mathrm{rel},w}} (K^{\mathrm{Perm,w}}_{ij})^{-1} N^{wf}_J \bar{v}^{wf}_{Jj}\mathrm{d}\Omega - \int_\Omega N^{wf}_I \frac{n^e S^e \eta^w}{k^{\mathrm{rel},w}} (K^{\mathrm{Perm,w}}_{ij})^{-1} N^s_J \bar{v}^s_{Jj}\mathrm{d}\Omega \\
&- \int_\Omega N^{wf}_I \bar{\rho}^{wf} b_i \mathrm{d}\Omega, \qquad (4.22)
\end{aligned}
$$

where $\hat{p}^{wf}$ is a pore water traction on the surface (Neumann boundary condition). The discretised balance of linear momentum of the free air phase is given by

$$
\begin{aligned}
r_{Ii}^{af} = &\int_{\Gamma} N_I^{af} \hat{p}^{af} n_i \mathrm{d}\Gamma - \int_{\Omega} N_{I,i}^{af} N_K^p \bar{p}_K^{af} \mathrm{d}\Omega + \int_{\Omega} N_I^{af} \bar{\rho}^{af} N_J^{af} \bar{a}_{Ji}^{af} \mathrm{d}\Omega \\
&+ \int_{\Omega} N_I^{af} \frac{n^e (1 - S^e) \eta^a}{k^{\mathrm{rel},a}} (K_{ij}^{\mathrm{Perm,a}})^{-1} N_J^{af} \bar{v}_{Jj}^{af} \mathrm{d}\Omega \\
&- \int_{\Omega} N_I^{af} \frac{n^e (1 - S^e) \eta^a}{k^{\mathrm{rel},a}} (K_{ij}^{\mathrm{Perm,a}})^{-1} N_J^{s} \bar{v}_{Jj}^{s} \mathrm{d}\Omega - \int_{\Omega} N_I^{af} \bar{\rho}^{af} b_i \mathrm{d}\Omega.
\end{aligned} \tag{4.23}
$$

4.3 Solution procedure, temporal discretisation and implementation

To minimise the residuum $\boldsymbol{r}(\boldsymbol{d})$ (referred to as *right-hand-side*, RHS) which is a function of the DOF $\boldsymbol{d}$, the *Newton-Raphson* method is applied. At every i-th iteration, the correction $\boldsymbol{c}^{(i+1)}$ is added to the DOFs $\boldsymbol{d}^{(i)}$, such that $\boldsymbol{r}(\boldsymbol{d}^{(i)} + \boldsymbol{c}^{(i+1)}) \approx 0$ is eventually achieved. By expanding this equation in a Taylor series about $\boldsymbol{d}^{(i)}$, and linearising the obtained equation, a linear *system-of-equations* (SOE) is obtained, as follows:

$$
\frac{\partial \boldsymbol{r}\left(\boldsymbol{d}^{(i)}\right)}{\partial \boldsymbol{d}} \boldsymbol{c}^{(i+1)} = -\boldsymbol{r}\left(\boldsymbol{d}^{(i)}\right). \tag{4.24}
$$

Eq. (4.24) is computed until $\boldsymbol{c}^{(i+1)}$ and $\boldsymbol{r}(\boldsymbol{d}^{(i)})$ are smaller than a given tolerance. As is visible from Eq. (4.24), the partial derivatives of the residuum with respect to the discretised variables are required. The SOE that needs to be solved is given in Eq. (4.25).

$$
\begin{bmatrix}
\frac{\partial \boldsymbol{r}^s}{\partial \boldsymbol{u}^s} & \frac{\partial \boldsymbol{r}^s}{\partial p^{wf}} & \frac{\partial \boldsymbol{r}^s}{\partial p^{af}} & \frac{\partial \boldsymbol{r}^s}{\partial \boldsymbol{u}^{wf}} & \frac{\partial \boldsymbol{r}^s}{\partial \boldsymbol{u}^{af}} \\
\frac{\partial \boldsymbol{r}^{pwf}}{\partial \boldsymbol{u}^s} & \frac{\partial \boldsymbol{r}^{pwf}}{\partial p^{wf}} & \frac{\partial \boldsymbol{r}^{pwf}}{\partial p^{af}} & \frac{\partial \boldsymbol{r}^{pwf}}{\partial \boldsymbol{u}^{wf}} & \frac{\partial \boldsymbol{r}^{pwf}}{\partial \boldsymbol{u}^{af}} \\
\frac{\partial \boldsymbol{r}^{paf}}{\partial \boldsymbol{u}^s} & \frac{\partial \boldsymbol{r}^{paf}}{\partial p^{wf}} & \frac{\partial \boldsymbol{r}^{paf}}{\partial p^{af}} & \frac{\partial \boldsymbol{r}^{paf}}{\partial \boldsymbol{u}^{wf}} & \frac{\partial \boldsymbol{r}^{paf}}{\partial \boldsymbol{u}^{af}} \\
\frac{\partial \boldsymbol{r}^{wf}}{\partial \boldsymbol{u}^s} & \frac{\partial \boldsymbol{r}^{wf}}{\partial p^{wf}} & \frac{\partial \boldsymbol{r}^{wf}}{\partial p^{af}} & \frac{\partial \boldsymbol{r}^{wf}}{\partial \boldsymbol{u}^{wf}} & \frac{\partial \boldsymbol{r}^{wf}}{\partial \boldsymbol{u}^{af}} \\
\frac{\partial \boldsymbol{r}^{af}}{\partial \boldsymbol{u}^s} & \frac{\partial \boldsymbol{r}^{af}}{\partial p^{wf}} & \frac{\partial \boldsymbol{r}^{af}}{\partial p^{af}} & \frac{\partial \boldsymbol{r}^{af}}{\partial \boldsymbol{u}^{wf}} & \frac{\partial \boldsymbol{r}^{af}}{\partial \boldsymbol{u}^{af}}
\end{bmatrix}
\begin{bmatrix}
\boldsymbol{c}^s \\ \boldsymbol{c}^{pwf} \\ \boldsymbol{c}^{paf} \\ \boldsymbol{c}^{wf} \\ \boldsymbol{c}^{af}
\end{bmatrix}
= -
\begin{bmatrix}
\boldsymbol{r}^s \\ \boldsymbol{r}^{pwf} \\ \boldsymbol{r}^{paf} \\ \boldsymbol{r}^{wf} \\ \boldsymbol{r}^{af}
\end{bmatrix} \tag{4.25}
$$

The contributions to the *left-hand-side* $\partial \boldsymbol{r}\left(\boldsymbol{d}^{(i)}\right)/\partial \boldsymbol{d}$ (referred to as LHS) are not given in detail here. They can either be calculated analytically or determined using numerical differentiation, as is also explained later.

For the temporal discretisation, the *Hilber-Hughes-Taylor* time integration scheme [168] is utilised. The acceleration at the end of the increment $(t + \Delta t)$ is calculated using

$$\ddot{\boldsymbol{u}}^{(t+\Delta t)} = \frac{1}{\beta \Delta t^2} \left(\boldsymbol{u}^{(t+\Delta t)} - \boldsymbol{u}^{(t)} - \Delta t \dot{\boldsymbol{u}}^{(t)} \right) - \left(\frac{1}{2\beta} - 1 \right) \ddot{\boldsymbol{u}}^{(t)} \tag{4.26}$$

and the velocity by

$$\begin{aligned} \dot{\boldsymbol{u}}^{(t+\Delta t)} &= \dot{\boldsymbol{u}}^{(t)} + \Delta t \left[(1-\gamma)\, \ddot{\boldsymbol{u}}^{(t)} + \gamma \frac{1}{\beta \Delta t^2} \left(\boldsymbol{u}^{(t+\Delta t)} - \boldsymbol{u}^{(t)} - \Delta t \dot{\boldsymbol{u}}^{(t)} \right) - \gamma \left(\frac{1}{2\beta} - 1 \right) \ddot{\boldsymbol{u}}^{(t)} \right] \\ &= (1 - \frac{\gamma}{\beta}) \dot{\boldsymbol{u}}^{(t)} + \gamma \frac{1}{\beta \Delta t} \left(\boldsymbol{u}^{(t+\Delta t)} - \boldsymbol{u}^{(t)} \right) + \Delta t \frac{\beta - \gamma/2}{\beta} \ddot{\boldsymbol{u}}^{(t)}. \end{aligned} \tag{4.27}$$

β and γ are parameters controlling numerical dissipation. Typically, both parameters are expressed by α, for which $\beta = \frac{1}{4}(1+\alpha)^2$ and $\gamma = \frac{1}{2} + \alpha$ are defined. For numerical stability, α should be in a range of $\alpha \in [0, \frac{1}{3})$. The larger α is, the larger is the numerical damping. For most simulations performed in the framework of this thesis $\alpha = 0.1$ is set (except in Section 8.2.1, where $\alpha = 0.05$ is used), which results in moderate numerical damping.

The **u**-p-**U** element is implemented for 2D/3D and axisymmetric analyses in the in-house finite element code `numgeo`, which is introduced in detail in Chapter 7. An overview of the implemented elements is given in Table 4.1. The different elements are explained in more detail and inspected in Section 4.5, where comparisons with the **u**-p and **u**-**U** element formulations are provided. In addition, the *condition number* of the stiffness matrix, a measure for the numerical stability representing the accuracy of computing an inverse, of the **u**-p-**U** element is compared to those of the **u**-p and **u**-**U** element formulations in Section 8.2.2. The computational performance of the **u**-p and **u**-p-**U** element formulations for the simulation of vibratory pile driving is also evaluated in Section 8.2.2.

4.4 Novel semi-analytical solution for the wave propagation in a poro-elastic medium and investigation of the relative acceleration

The derivation of a novel semi-analytical solution for the wave propagation in a fluid-saturated elastic 1D medium is presented in this section (note that some of the following has already been published by the author in [349, 348]). Contrary to existing analytical solutions, a semi-analytical solution based on the **u**-**U** formulation (denoted as u-U formulation in this section

Element label	Dimension	Shape	Nodes	Interpolation **u**/**U**-p	ngp
2D elements					
`u6p3u6`	2D	triangle	6	quadratic-linear	3
`u8p4u8`	2D	rectangle	8	quadratic-linear	9
`u8p8u8`	2D	rectangle	8	quadratic-quadratic	9
`u4p4u4`	2D	rectangle	4	linear-linear	4
`u8p4u8-red`	2D	rectangle	8	quadratic-linear	4
Axisymmetric elements					
`u6p3u6-ax`	axisym.	triangle	6	quadratic-linear	3
`u8p4u8-ax`	axisym.	rectangle	8	quadratic-linear	9
`u8p4u8-ax-red`	axisym.	rectangle	8	quadratic-linear	4
3D elements					
`u20p8u20`	3D	brick	20	quadratic-linear	27
`u20p8u20-red`	3D	brick	20	quadratic-linear	8
`u27p8u27`	3D	brick	27	(tri-)quadratic-linear	27

Table 4.1: Different types of **u**-p-**U** elements implemented in `numgeo` (ngp: number of integration points)

because of the 1D reduction) is developed, which allows to investigate the influence of the relative acceleration. Note that a semi-analytical solution based on the **u**-p-**U** formulation is possible as well, but is mathematically more tedious due to the larger number of primary unknowns. The analytical solution is derived in discrete time and transformed back in physical time using an inverse Laplace transformation. Two different approaches for the inverse Laplace transformation are applied and compared to numerical solutions using the finite elements developed previously. After having validated the semi-analytical solution, a novel scheme to evaluate the influence of the relative acceleration solely in terms of highest compression wave frequency and hydraulic conductivity is presented.

4.4.1 Governing equations

In the following, the governing equations for the wave propagation in a fluid-saturated porous 1D column are given. The exponents $\sqcup^s$ for the solid and $\sqcup^f$ for the fluid phase are used. Only intrinsic values of fluid pressure are used, hence $\bar{p}^f$ is dropped for sake of convenience. No body forces are included, as the differential equations would be inhomogeneous otherwise.

The momentum balance of the mixture given by Eq. (3.58) reduces for 1D fluid-saturated conditions to

$$Du^s_{,xx} - Bp^f_{,x} = \varphi^s \bar{\rho}^s \ddot{u}^s + \varphi^f \bar{\rho}^f \ddot{u}^f, \tag{4.28}$$

with $D = E\frac{(1-\nu)}{(1+\nu)(1-2\nu)}$. E denotes Young's modulus and ν is the Poisson's ratio. $\sqcup_{,x}$ denotes the change of variable $\sqcup$ with respect to the coordinate x. Analogously, the momentum balance of the pore fluid phase is reduced to

$$p^f_{,x} + \bar{\rho}^f \ddot{u}^f + \frac{\varphi^f \eta^f}{K^{\text{perm}}}(\dot{u}^f - \dot{u}^s) = 0. \tag{4.29}$$

The pore fluid pressure is calculated using the mass balance of the pore fluid given by

$$\dot{p}^f \frac{\varphi^f}{\bar{K}^f} + \varphi^f \dot{u}^f_{,x} + (1-\varphi^f)\dot{u}^s_{,x} = 0. \tag{4.30}$$

For the u-U formulation, Eqs. (4.28, 4.29) have to be expressed in terms of displacement (and its time derivatives) alone. In order to substitute the pore fluid pressure in the momentum balance of the mixture, Eq. (4.30) has to be integrated in time. As this is not possible analytically, it is assumed that a reference state, where $p^f = u^s_{,x} = u^f_{,x} = 0$ holds, can be defined. Since every deformation is purely reversible for the elastic medium this simplification does not influence the solution. Eq. (4.30) now reads

$$p^f = -\frac{\bar{K}^f}{\varphi^f}\left[\varphi^f u^f_{,x} + (1-\varphi^f)u^s_{,x}\right], \tag{4.31}$$

which can then be substituted into Eq. (4.28) yielding

$$\underbrace{\left[D + B(1-\varphi^f)\frac{\bar{K}^f}{\varphi^f}\right]}_{\beta} u^s_{,xx} + B\bar{K}^f u^f_{,xx} = \rho^s \ddot{u}^s + \rho^f \ddot{u}^f. \tag{4.32}$$

In the framework of the analytical solution, the balance equations are solved in discrete time. The Laplace transformation is defined by

$$\hat{u}(x,t) = \int_{-\infty}^{\infty} u(x,t) e^{\lambda s t}\,\mathrm{dt}\,. \tag{4.33}$$

The primary variables $\hat{u}^s$ and $\hat{u}^f$ are given by exponential *ansatz* functions such as

$$\hat{u}^s(x) = U^s e^{\lambda s x} \quad \text{and} \quad \hat{u}^f(x) = U^f e^{\lambda s x}. \tag{4.34}$$

Using Eq. (4.34), Eq. (4.32) can be expressed in spectral form, viz.

$$\beta u^s_{,xx} + B\bar{K}^f u^f_{,xx} = s^2 \rho^s \hat{u}^s + s^2 \rho^f \hat{u}^f. \tag{4.35}$$

The momentum balance of the pore fluid is also substituted using Eq. (4.31), viz.

$$-\frac{\bar{K}^f}{\varphi^f}\left[\varphi^f \hat{u}^f_{,xx} + (1-\varphi^f)\hat{u}^s_{,xx}\right] + \bar{\rho}^f s^2 \hat{u}^f + \frac{\varphi^f \eta^f}{K^{\text{perm}}}(s\hat{u}^f - s\hat{u}^s) = 0. \tag{4.36}$$

Insertion of Eq. (4.34) in Eq. (4.35) and in Eq. (4.36) leads to a linear system of equations such as

$$\begin{bmatrix} \beta\lambda^2 - \rho^s & B\bar{K}^f\lambda^2 - \rho^f \\ -\dfrac{\varphi^f\eta^f}{K^{\text{perm}}}\dfrac{1}{s} - \dfrac{\bar{K}^f}{\varphi^f}(1-\varphi^f)\lambda^2 & \bar{\rho}^f + \dfrac{\varphi^f\eta^f}{K^{\text{perm}}}\dfrac{1}{s} - \bar{K}^f\lambda^2 \end{bmatrix} \begin{bmatrix} U^s \\ U^f \end{bmatrix} = \mathbf{0}. \tag{4.37}$$

The characteristic equation is given by

$$\lambda^4 \underbrace{\left[-\beta\bar{K}^f + B\bar{K}^f\frac{\bar{K}^f}{\varphi^f}(1-\varphi^f)\right]}_{a} + \lambda^2 \underbrace{\left[\beta\bar{\rho}^f + \bar{K}^f\rho^s + \beta\frac{\varphi^f\eta^f}{K^{\text{perm}}}\frac{1}{s} + B\bar{K}^f\frac{\varphi^f\eta^f}{K^{\text{perm}}}\frac{1}{s} - \rho^f\frac{\bar{K}^f}{\varphi^f}(1-\varphi^f)\right]}_{b}$$
$$+ \underbrace{\left(-\rho^s\frac{\varphi^f\eta^f}{K^{\text{perm}}}\frac{1}{s} - \rho^f\frac{\varphi^f\eta^f}{K^{\text{perm}}}\frac{1}{s} - \bar{\rho}^f\rho^s\right)}_{c} = 0. \tag{4.38}$$

The solution for λ is

$$\lambda_1 = -\lambda_3 = \sqrt{\frac{-b+\sqrt{b^2-4ac}}{2a}} \quad \text{and} \quad \lambda_2 = -\lambda_4 = \sqrt{\frac{-b-\sqrt{b^2-4ac}}{2a}}. \tag{4.39}$$

The primary variables are given by the fundamental system defined by

$$\hat{u}^s(x) = \sum_{i=1}^{4} U_i^s e^{\lambda_i s x} \quad \text{and} \quad \hat{u}^f(x) = \sum_{i=1}^{4} U_i^w e^{\lambda_i s x}. \tag{4.40}$$

The coefficients U_i^s and U_i^f are evaluated according to the boundary conditions. In order to investigate the relative acceleration in a forthcoming section, the u-U formulation with the assumption $\ddot{u}^s = \ddot{u}^f$ (i.e. no relative acceleration) is derived in addition. The system of equations for this case is defined by

$$\begin{bmatrix} \beta\lambda^2 - \rho^{\text{tot}} & B\bar{K}^f\lambda^2 \\ -\dfrac{\varphi^f\eta^f}{K^{\text{perm}}}\dfrac{1}{s} - \dfrac{\bar{K}^f}{\varphi^f}(1-\varphi^f)\lambda^2 + \bar{\rho}^f & \dfrac{\varphi^f\eta^f}{K^{\text{perm}}}\dfrac{1}{s} - \bar{K}^f\lambda^2 \end{bmatrix} \begin{bmatrix} U^s \\ U^f \end{bmatrix} = \mathbf{0}. \tag{4.41}$$

The characteristic equation is

$$\lambda^4 \underbrace{\left[-\beta\bar{K}^f + B\bar{K}^f\frac{\bar{K}^f}{\varphi^f}(1-\varphi^f)\right]}_{a} + \lambda^2 \underbrace{\left(\bar{K}^f\rho^{\text{tot}} + \beta\frac{\varphi^f\eta^f}{K^{\text{perm}}}\frac{1}{s} + B\bar{K}^f\frac{\varphi^f\eta^f}{K^{\text{perm}}}\frac{1}{s} - \bar{\rho}^f B\bar{K}^f\lambda^2\right)}_{b}$$
$$- \underbrace{\rho^{\text{tot}}\frac{\varphi^f\eta^f}{K^{\text{perm}}}\frac{1}{s}}_{c} = 0. \tag{4.42}$$

4.4.2 Solution for different boundary conditions in discrete time

A column with length l is considered. The coordinate x takes values from 0 to l. A Heaviside load $H(t) = \sigma_0$ is applied at $x = l$ instantaneously ($t = 0$ s). A schematic illustration of the column is given in Fig. 4.1. The Dirichlet boundary conditions are

$$\hat{u}^s(x = 0) = 0 \quad \text{and} \quad \hat{u}^f(x = 0) = 0. \tag{4.43}$$

Two additional Neumann boundary conditions are required, which are varied. They are

$$\hat{\sigma}^s(x = l) = 0 \text{ or } -\sigma_0 \quad \text{and} \quad \hat{p}^f(x = l) = 0 \text{ or } \sigma_0. \tag{4.44}$$

The solid phase is either not loaded or a pressure of magnitude σ_0 is assigned at $x = l$. The fluid phase is loaded analogously. Different solutions for the different Neumann boundary conditions are derived. The total stress is given by

$$\hat{\sigma}^{tot}(s, x) = D\hat{u}^s_{,x} - B\hat{p}^f = D\sum_{i=1}^{4} \lambda_i s U_i^s e^{\lambda_i s x} - B\hat{p}^f. \tag{4.45}$$

The pore fluid pressure is computed using Eq. (4.31), which is given in discrete time by

$$\hat{p}^f = -\frac{\bar{K}^f}{\varphi^f}\left[\varphi^f \hat{u}^f_{,x} + (1-\varphi^f)\hat{u}^s_{,x}\right] = -\frac{\bar{K}^f}{\varphi^f}\left[\varphi^f \sum_{i=1}^{4} \lambda_i s U_i^w e^{\lambda_i s x} + (1-\varphi^f)\sum_{i=1}^{4} \lambda_i s U_i^s e^{\lambda_i s x}\right]. \tag{4.46}$$

As the four boundary conditions are not sufficient to determine the eight constants in Eq. (4.40), one of the Eigenvectors of the system of equations (see Eq. (4.37)) is used in addition. The coefficient of the solid phase is

$$U_i^s = \underbrace{\frac{\rho^f - B\bar{K}^f\lambda_i^2}{\beta\lambda_i^2 - \rho^s}}_{f_i} U_i^f. \tag{4.47}$$

In case of the negligence of the relative acceleration, Eq. (4.41) is used. The coefficient of the solid phase for this case is

$$U_i^s = \frac{-B\bar{K}^f\lambda_i^2}{\beta\lambda_i^2 - \rho^{\mathrm{tot}}} U_i^f. \tag{4.48}$$

For all subsequent operations, Eq. (4.47) is used. The solution using Eq. (4.48) is obtained analogously.

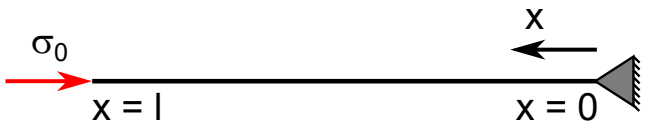

Figure 4.1: 1D column with boundary conditions

Together with the boundary conditions, Eq. (4.47) allows to determine all eight constants. In order to do so, Eq. (4.46) is substituted with Eq. (4.47) yielding

$$\begin{aligned}\hat{p}^f = -\frac{\bar{K}^f}{\varphi^f}\left[\varphi^f \hat{u}^f_{,x} + (1-\varphi^f)\hat{u}^s_{,x}\right] &= -\frac{\bar{K}^f}{\varphi^f}\left[\varphi^f \sum_{i=1}^{4} \lambda_i s \frac{1}{f_i} U_i^s e^{\lambda_i s x} + (1-\varphi^f)\sum_{i=1}^{4} \lambda_i s U_i^s e^{\lambda_i s x}\right] \\ &= -\sum_{i=1}^{4} \lambda_i s U_i^s e^{\lambda_i s x} \underbrace{\frac{\bar{K}^f}{\varphi^f}\left[\varphi^f \frac{1}{f_i} + (1-\varphi^f)\right]}_{b_i}. \end{aligned} \tag{4.49}$$

The effective stress is given by Eq. (4.45) and is calculated using

$$\hat{\sigma}^s(s,x) = D\sum_{i=1}^{4} \lambda_i s U_i^s e^{\lambda_i s x}. \tag{4.50}$$

Taking into account the Neumann boundary conditions with loading of both phases, the system of equations determining the four constants is given by

$$\begin{bmatrix} e^0 & e^0 & e^0 & e^0 \\ \frac{e^0}{f_1} & \frac{e^0}{f_2} & \frac{e^0}{f_1} & \frac{e^0}{f_2} \\ \lambda_1 e^{\lambda_1 s l} & \lambda_2 e^{\lambda_2 s l} & -\lambda_1 e^{-\lambda_1 s l} & -\lambda_2 e^{-\lambda_2 s l} \\ -\lambda_1 e^{\lambda_1 s l} b_1 & -\lambda_2 e^{\lambda_2 s l} b_2 & \lambda_1 e^{-\lambda_1 s l} b_1 & \lambda_2 e^{-\lambda_2 s l} b_2 \end{bmatrix} \begin{bmatrix} U_1^s \\ U_2^s \\ U_3^s \\ U_4^s \end{bmatrix} = \begin{bmatrix} 0 \\ 0 \\ -\frac{\sigma_0}{Ds} \\ \frac{\sigma_0}{s} \end{bmatrix}. \tag{4.51}$$

Note that all equations are already in a reduced form and the simplification $\lambda^2_{i=3,4} = \lambda^2_{i=1,2}$ is applied. Note in addition that the Eigenvalues are in general complex numbers. However, as all coefficients contain either the square of λ or no Eigenvalue at all, the sought variables are always non-complex. The system of equations given by Eq. (4.51) is solved using the computer algebra program `Mathematica`. The coefficients in case of $\hat{\sigma}^s(x=l) = -\sigma_0$ and $\hat{p}^f(x=l) = 0$ are:

$$\begin{aligned} U_1^s &= \frac{b_2\sigma_0}{D(b_1-b_2)(e^{\lambda_1 s l}+e^{-\lambda_1 s l})\lambda_1 s} \quad ; \quad U_2^s = \frac{-b_1\sigma_0}{D(b_1-b_2)(e^{\lambda_2 s l}+e^{-\lambda_2 s l})\lambda_2 s} \\ U_3^s &= \frac{-b_2\sigma_0}{D(b_1-b_2)(e^{\lambda_1 s l}+e^{-\lambda_1 s l})\lambda_1 s} \quad ; \quad U_4^s = \frac{b_1\sigma_0}{D(b_1-b_2)(e^{\lambda_2 s l}+e^{-\lambda_2 s l})\lambda_2 s} \end{aligned}$$

For $\hat{\sigma}^s(x=l) = -\sigma_0$ and $\hat{p}^f(x=l) = \sigma_0$ the coefficients are:

$$U_1^s = \frac{(b_2 - D)\sigma_0}{(b_1 - b_2)D(e^{\lambda_1 sl} + e^{-\lambda_1 sl})\lambda_1 s} \quad ; \quad U_2^s = \frac{(D - b_1)\sigma_0}{(b_1 - b_2)D(e^{\lambda_2 sl} + e^{-\lambda_2 sl})\lambda_2 s}$$
$$U_3^s = \frac{-(b_2 - D)\sigma_0}{(b_1 - b_2)D(e^{\lambda_1 sl} + e^{-\lambda_1 sl})\lambda_1 s} \quad ; \quad U_4^s = \frac{-(D - b_1)\sigma_0}{(b_1 - b_2)D(e^{\lambda_2 sl} + e^{-\lambda_2 sl})\lambda_2 s}$$

4.4.3 Fully analytical inverse Laplace transformation

In the following, $\hat{\sigma}^s(x=l) = -\sigma_0$ and $\hat{p}^f(x=l) = \sigma_0$ are considered as Neumann boundary condition exemplary. In that case the displacements given in Eq. (4.40) are defined by

$$\hat{u}^s = \frac{\sigma_0}{(b_1 - b_2)Ds}\left[\frac{(D - b_2)\left(e^{-\lambda_1 sx} - e^{\lambda_1 sx}\right)}{(e^{\lambda_1 sl} + e^{-\lambda_1 sl})\lambda_1} + \frac{(b_1 - D)\left(e^{-\lambda_2 sx} - e^{\lambda_2 sx}\right)}{(e^{\lambda_2 sl} + e^{-\lambda_2 sl})\lambda_2}\right] \quad \text{and} \tag{4.52}$$

$$\hat{u}^f = \frac{\sigma_0}{(b_1 - b_2)Ds}\left[\frac{(D - b_2)\left(e^{-\lambda_1 sx} - e^{\lambda_1 sx}\right)}{(e^{\lambda_1 sl} + e^{-\lambda_1 sl})\lambda_1 f_1} + \frac{(b_1 - D)\left(e^{-\lambda_2 sx} - e^{\lambda_2 sx}\right)}{(e^{\lambda_2 sl} + e^{-\lambda_2 sl})\lambda_2 f_2}\right]. \tag{4.53}$$

To transform the solution back into the time domain, the inverse Laplace transformation has to be performed. As the Eigenvalues λ depend on s, an analytical solution is not possible. $\lambda(s)$ results from the viscous interaction terms as can be seen from Eq. (4.38). Assuming negligible interaction forces, a fully analytical inverse Laplace scheme can be derived. The transformation to time domain using a fully analytical approach is presented in the following.

Before transforming Eqs. (4.52, 4.53) to the time domain, the exponential functions are further simplified to:

$$\hat{u}^s = \frac{\sigma_0}{(b_1 - b_2)Ds}\left[\frac{(D - b_2)\left(e^{-\lambda_1 s(x+l)} - e^{\lambda_1 s(x-l)}\right)}{(1 + e^{-2\lambda_1 sl})\lambda_1} + \frac{(b_1 - D)\left(e^{-\lambda_2 s(x+l)} - e^{\lambda_2 s(x-l)}\right)}{(1 + e^{-2\lambda_2 sl})\lambda_2}\right]$$
$$\hat{u}^f = \frac{\sigma_0}{(b_1 - b_2)Ds}\left[\frac{(D - b_2)\left(e^{-\lambda_1 s(x+l)} - e^{\lambda_1 s(x-l)}\right)}{(1 + e^{-2\lambda_1 sl})\lambda_1 f_1} + \frac{(b_1 - D)\left(e^{-\lambda_2 s(x+l)} - e^{\lambda_2 s(x-l)}\right)}{(1 + e^{-2\lambda_2 sl})\lambda_2 f_2}\right] \tag{4.54}$$

The following series expansion [330]

$$\frac{1}{1 + e^{-2\lambda_i sl}} = \sum_{n=0}^{\infty} (-1)^{-n} e^{-2\lambda_i sln} \tag{4.55}$$

is used, which is applied to Eq. (4.54) yielding

$$\frac{e^{-\lambda_1 s(x+l)} - e^{\lambda_1 s(x-l)}}{s(1 + e^{-2\lambda_1 sl})} = \sum_{n=0}^{\infty} (-1)^{-n} \frac{1}{s}\left(e^{-\lambda_1 s[x+l(1+2n)]} - e^{\lambda_1 s[x-l(1+2n)]}\right). \tag{4.56}$$

For the transformation back into time domain, the inverse Laplace transformation using the following convolution integral

$$u^s(t,x) = \int_0^t \mathscr{L}^{-1}\big[\hat{u}^s(s,x)\big](\tau,x) f(t-\tau) d\tau, \tag{4.57}$$

is calculated. $f(t) = H(t)$ is set in the present case. $H(t) = 1$ holds for arbitrary t since a Heaviside load is considered, which is applied instantaneously. Therefore, $f = 1$ can be set. The required Laplace transforms for Eq. (4.57) are defined by

$$\frac{1}{s} e^{-\lambda_i s[x+l(1+2n)]} \bullet\!\!-\!\!\circ\, H\left\{t - \lambda_i[x + l(1+2n)]\right\} \quad \text{and} \tag{4.58}$$

$$e^{-\lambda_i s[x+l(1+2n)]} \bullet\!\!-\!\!\circ\, \delta\left\{t - \lambda_i[x + l(1+2n)]\right\}, \tag{4.59}$$

which can be found in standard Laplace tables given in elementary mathematical textbooks. The derivation and integration rules for Eq. (4.58) needed are

$$\delta(x) = \frac{dH}{dx} \quad \text{and} \quad \int H(x)dx = xH(x). \tag{4.60}$$

Substitution of Eq. (4.56) with Eq. (4.58) leads to

$$\frac{e^{-\lambda_i s(x+l)} - e^{\lambda_i s(x-l)}}{s(1+e^{-2\lambda_i s l})} = \sum_{n=0}^{\infty} (-1)^{-n} \left(H\Big\{t - \lambda_i[x + l(1+2n)]\Big\} - H\Big\{t + \lambda_i[x - l(1+2n)]\Big\} \right). \tag{4.61}$$

Inserting Eq. (4.61) in Eq. (4.54) and in Eq. (4.57) using Eq. (4.60) defines the displacement of the solid in the time domain by

$$\begin{aligned} u^s = \frac{\sigma_0}{(b_1-b_2)D} \sum_{n=0}^{\infty} (-1)^{-n} \Bigg[& \frac{(D-b_2)}{\lambda_1} \Bigg(\big\{t - \lambda_1[x + l(1+2n)]\big\} H\big(t - \lambda_1[x + l(1+2n)]\big) \\ & - \big\{t + \lambda_1[x - l(1+2n)]\big\} H\big\{t + \lambda_1[x - l(1+2n)]\big\} \Bigg) \\ & + \frac{(b_1-D)}{\lambda_2} \Bigg(\big\{t - \lambda_2[x + l(1+2n)]\big\} H\big\{t - \lambda_2[x + l(1+2n)]\big\} \\ & - \big\{t + \lambda_2[x - l(1+2n)]\big\} H\big\{t + \lambda_2[x - l(1+2n)]\big\} \Bigg) \Bigg]. \end{aligned} \tag{4.62}$$

The displacement of the fluid is given accordingly by

$$\begin{aligned} u^f = \frac{\sigma_0}{(b_1-b_2)D} \sum_{n=0}^{\infty} (-1)^{-n} \Bigg[& \frac{(D-b_2)}{\lambda_1 f_1} \Bigg(\big\{t - \lambda_1[x + l(1+2n)]\big\} H\big(t - \lambda_1[x + l(1+2n)]\big) \\ & - \big\{t + \lambda_1[x - l(1+2n)]\big\} H\big\{t + \lambda_1[x - l(1+2n)]\big\} \Bigg) \\ & + \frac{(b_1-D)}{\lambda_2 f_2} \Bigg(\big\{t - \lambda_2[x + l(1+2n)]\big\} H\big\{t - \lambda_2[x + l(1+2n)]\big\} \\ & - \big\{t + \lambda_2[x - l(1+2n)]\big\} H\big\{t + \lambda_2[x - l(1+2n)]\big\} \Bigg) \Bigg]. \end{aligned} \tag{4.63}$$

The pore fluid pressure given in Eq. (4.49) is first substituted using Eq. (4.52) yielding

$$\begin{aligned}\hat{p}^f &= -\sum_{i=1}^{4} \lambda_i s U_i^s e^{\lambda_i s x} b_i \\ &= -\frac{\sigma_0}{(b_1-b_2)D}\left[\frac{b_1(D-b_2)\left(-e^{-\lambda_1 s(x+l)} - e^{\lambda_1 s(x-l)}\right)}{(1+e^{-2\lambda_1 s l})}\right. \\ &\left. + \frac{b_2(b_1-D)\left(-e^{-\lambda_2 s(x+l)} - e^{\lambda_2 s(x-l)}\right)}{(1+e^{-2\lambda_2 s l})}\right] \end{aligned} \tag{4.64}$$

and consequently transformed back to the time domain, which results in

$$\begin{aligned} p^f = \frac{\sigma_0}{(b_1-b_2)D}\sum_{n=0}^{\infty}(-1)^{-n}\Big[&b_1(D-b_2)\big(H\{t-\lambda_1[x+l(1+2n)]\}\big) \\ &+ H\{t+\lambda_1[x-l(1+2n)]\} + b_2(b_1-D)\big(H\{t-\lambda_2[x+l(1+2n)]\} \\ &+ H\{t+\lambda_2[x-l(1+2n)]\}\big)\Big]. \end{aligned} \tag{4.65}$$

Note that the changed signs in Eq. (4.64) are due to $\lambda_1 = -\lambda_3$.

To check if the analytical solution has been derived correctly, the wave propagation in a column of $l = 10$ m length consisting of one fluid only (no solid phase present) is studied first. The excess pore fluid pressure at the coordinate $x = 0$ m due to an external loading of $\hat{p}^f(x = l) = 1$ kPa is shown in Fig. 4.2. The compression wave reaches $x = 0$ m after 6.75 ms. With the velocity of the compression wave in the fluid defined by

$$\dot{u}^f = \sqrt{\frac{\bar{K}^f}{\bar{\rho}^f}}, \tag{4.66}$$

the velocity in the case of water $\dot{u}^f = \sqrt{\frac{2200000}{1}} = 1483.24$ m/s and the time needed to reach the bottom $t = \frac{l}{\dot{u}^f} = 0.00675$ s is calculated. The solution obtained by Eq. (4.65) is therefore correct in terms of wave velocity. An excess pore water pressure of 2 kPa is observed, which is due to the reflection of the compression wave at the Dirichlet boundary condition (same polarity of incident and reflected wave).

4.4.4 Semi-analytical inverse Laplace transformation using the convolution quadrature method

The negligence of the viscous interaction terms in the fully analytical scheme presented in the previous section is equivalent to a hydraulic conductivity tending to infinity. The fully analytical solution is thus only of limited usefulness for the investigation of the relative acceleration.

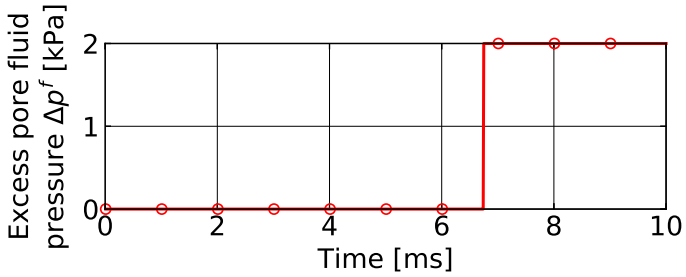

Figure 4.2: Excess pore fluid pressure for the Heaviside loading of pure water with 1 kPa ($\bar{K}^f = 2.2$ GPa and $l = 10$ m)

Therefore, a semi-analytical approach is developed, allowing to consider an arbitrary hydraulic conductivity.

The convolution integral given in Eq. (4.57) in case of $\lambda(s)$ can not be solved analytically. A numerical method has to be applied since the convolution integral can not be written with respect to Laplace and time domain simultaneously. A convolution quadrature method proposed by Lubich [235] solves the convolution integral using a series expansion of the form

$$u_x(t) = \int_0^t f(t-\tau)g(\tau)d\tau \quad \rightarrow \quad u_x(n\Delta t) = \sum_{k=0}^{n} w_{n-k}(\Delta t)g(k\Delta t), \quad n = 0, 1, ..., N. \tag{4.67}$$

The weights w are determined by

$$w_n(\Delta t) = \frac{\mathscr{R}^{-n}}{L} \sum_{l=0}^{L-1} \hat{u}_x \Bigg(\underbrace{\frac{\gamma\left(\mathscr{R}e^{il2\pi/L}\right)}{\Delta t}}_{s_l} \Bigg) e^{-inl2\pi/L}. \tag{4.68}$$

The fundamental solution in Laplace domain $\hat{u}_x(s, x)$ is evaluated using a multi-step method $\gamma(s)$. Schanz et al. [330, 331] use the quotient of the underlying characteristic polynomials $\gamma = 3/2 - 2z + 1/2z^2$, the radius of a circle in the *domain of analyticity* $\mathscr{R}^N = \sqrt{\varepsilon} = \sqrt{10^{-10}}$ and $L = N$ solving similar convolution integrals. Note that $\mathscr{R}$ must be in the range $0 < \mathscr{R} < 1$. Eq. (4.67) represents a time discretisation using a time step of Δt split in $N+1$ equal intervals.

Eqs. (4.67, 4.68) can be summed up yielding

$$u_x(n\Delta t) = \frac{\mathscr{R}^{-n}}{L+1} \sum_{l=0}^{L} \hat{u}_x(s_l) e^{inl2\pi/L}. \tag{4.69}$$

Eq. (4.69) can either directly be computed or a *discrete Fourier transformation* (DFT) defined as

$$f_m = \sum_{k=0}^{2n-1} x_k e^{-\frac{2\pi i}{2n}mk}, \quad m = 0, ..., 2n-1, \tag{4.70}$$

can be used. Therein, x_k is a vector filled by the entries of $\hat{u}_x(s_l)$ with respect to l (or k in the case of x_k).

The semi-analytical solution is implemented in a `Fortran` code. The quadrature method is implemented according to Eqs. (4.67, 4.68). Application of a DFT as given in Eq. (4.70) is tested as well due to the speed-up in terms of computational time but is not further applied due to immense noise in the output.

In order to validate the semi-analytical solution, a comparison with the **u**-p-**U** element formulation is made. The finite element simulation is performed using the finite element code `numgeo` (see Chapter 7) and two-dimensional elements with quadratically interpolated solid and fluid displacements and linearly interpolated fluid pressure. A soil column with a length of $l = 10$ m, discretised using 100 equally-spaced finite elements, is considered. The Heaviside loading is exclusively imposed on the solid phase and the boundary conditions are according to Eq. (4.43). The material parameters are given in Table 4.2. The time increment for the semi-analytical solution is chosen to $\Delta t = 10^{-6}$ s and $N = 10^5$, which proved to result in stable results not changing with smaller values for Δt. The corresponding $\mathscr{R}$ is 0.99988487740. The resulting excess pore fluid pressure history at $x = 0$ m during the wave propagation and the displacement of the column at $x = 10$ m are given in Fig. 4.3 in comparison with the **u**-p-**U** element formulation. Both the finite element simulation and the semi-analytical solution show oscillations in the excess pore fluid pressure but are in good agreement otherwise. As is further discussed in Section 8.2.2, the oscillations result (partly[1]) from the bad condition of the stiffness matrix of the **u**-p-**U** element formulation. In case of the semi-analytical solution the oscillations are caused by the convolution quadrature method, as is discussed in [330].

The displacement of the column at $x = l$ is in perfect accordance. The consolidation process occurring simultaneously to the wave propagation is well visible by the permanent displacement of the column, which increases with every wave passing.

4.4.5 Quantification of the influence of the relative acceleration based on the semi-analytical solution

The influence of relative acceleration between solid and fluid phase is investigated in this section using the developed semi-analytical solution. Having proposed the **u**-p element formu-

[1] The oscillations could also be reduced by choosing stricter convergence criteria for the pore fluid pressure DOF.

Parameter			Value	Unit
Young's modulus	E	=	15000	[kPa]
Poisson's ratio	ν	=	0.3	[-]
Bulk modulus fluid	$\bar{K}^f$	=	2.2	[GPa]
Permeability	K^{perm}	=	$1 \cdot 10^{-12}$	[m^2]
Dynamic viscosity	η^f	=	$1 \cdot 10^{-6}$	[kPas]
Gravity	g	=	10	[m/s^2]
Grain density	$\bar{\rho}^s$	=	2.7	[g/cm^3]
Fluid density	$\bar{\rho}^f$	=	1	[g/cm^3]
Porosity	n	=	0.5	[-]
Top loading	σ_0	=	1	[kPa]
Column length	l	=	10	[m]

Table 4.2: Set of parameters employed for the analysis of the wave propagation using the derived semi-analytical solution and the finite element approach. Note that the hydraulic conductivity is calculated using $k^f = g\rho^f K^{\text{perm}}/\eta^f$.

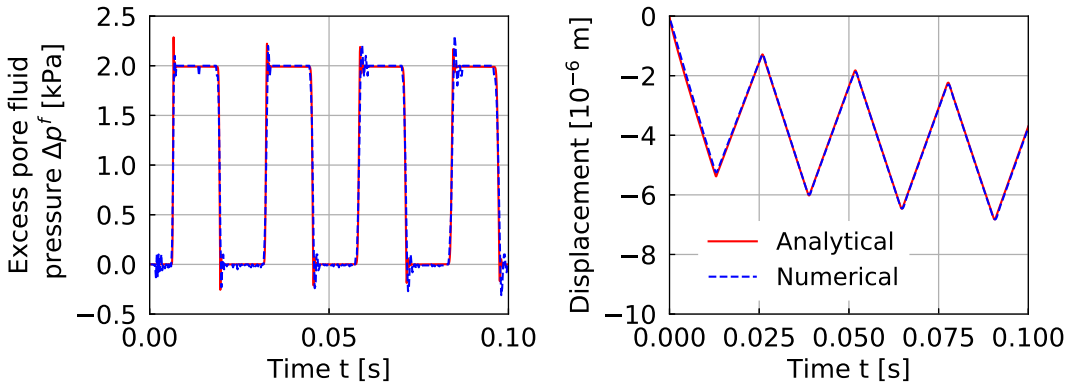

Figure 4.3: Excess pore fluid pressure at $x = 0$ m and displacement at $x = l$ using the parameters given in Table 4.2 for the semi-analytical solution and the **u**-p-**U** element formulation

lation, Zienkiewicz and co-workers have subsequently investigated the influence of the relative acceleration in [450], using an analytical approach. Zienkiewicz et al. proposed the diagram given in Fig. 4.5, quantifying the influence of relative acceleration. The constants required as input are the *characteristic length* l, the hydraulic conductivity k^f, the gravity g, the angular frequency ω, the total density ρ^{tot}, the density of the fluid $\bar{\rho}^f$ and the compression wave velocity v_c of the mixture. Two parameters are derived using these constants, quantifying the

influence of the relative acceleration. They are defined by

$$\pi_1 = \frac{k^f \rho^{\mathrm{tot}} v_c^2}{g \bar{\rho}^f \omega l^2} \quad \text{and} \quad \pi_2 = \frac{\omega^2 l^2}{v_c^2}. \tag{4.71}$$

These parameters are the coefficients of the accelerations in the Eqs. (4.28, 4.29) if the equations are rearranged and a periodic loading is assumed. The characteristic length l has no physical meaning and has been the length of the one-dimensional column considered in the analytical solution by Zienkiewicz et al. [450]. From Eq. (4.71) and Fig. 4.5 it is evident that a larger hydraulic conductivity increases π_1 and hence the influence of relative acceleration.

Using the novel semi-analytical solution with and without consideration of the relative acceleration, the excess pore fluid pressure vs. time using the parameters supplied in Table 4.2 is given in Fig. 4.4 using a hydraulic conductivity of $k^f = 10^{-5}$ m/s and $k^f = 10^{-3}$ m/s, respectively. In case of the low hydraulic conductivity the parameter π_1 is so small that the value is outside of the covered range of values. Hence, relative acceleration is of no importance according to Fig. 4.5. This is confirmed by the excess pore fluid pressure history displayed in Fig. 4.4a, where almost no difference between the results of the semi-analytical solution with and without consideration of the relative acceleration, respectively, is found. In case of the higher hydraulic conductivity the regime is marked in Fig. 4.5. Again, the diagram indicates that relative acceleration can be neglected. The development of the excess pore fluid pressure displayed in Fig. 4.4b shows, however, that the difference between the semi-analytical solution with and without consideration of the relative acceleration grows with ongoing wave propagation and a well identifiable deviation is visible after the third wave passing ($t \approx 0.08$ s).

As mentioned in the introduction to this chapter, numerous researchers have argued with the importance of the relative acceleration when deciding for a hydro-mechanically coupled finite element formulation. In most cases, however, the calculation of π_1 and π_2 and application of Fig. 4.5 would indicate that the relative acceleration is negligible for the analysis performed. One reason that the diagram is seldom referred to is likely the large number of variables and associated uncertainty required to calculate the two parameters given in Eq. (4.71) since the characteristic length has no physical meaning.

The novel semi-analytical solution derived herein allows to simplify the dimensionless parameters using the relation $\omega = \frac{\pi v_c}{l} \rightarrow l = \frac{\pi v_c}{\omega}$, as the frequency is equal to that of the first compression wave caused by the Heaviside load. The parameters π_1 and π_2 become

$$\pi_1 = \frac{k^f \rho^{\mathrm{tot}} \omega}{g \bar{\rho}^f \pi^2} \quad \text{and} \quad \pi_2 = \pi^2. \tag{4.72}$$

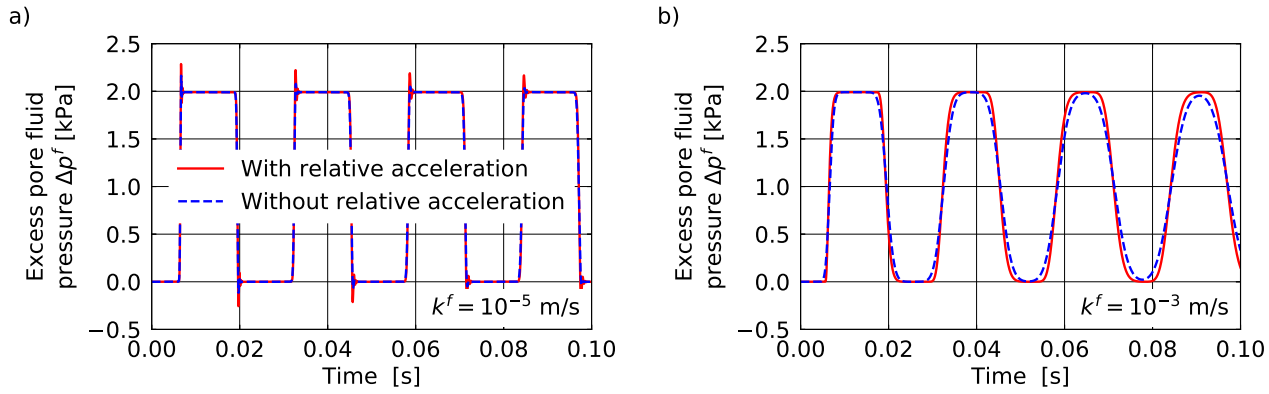

Figure 4.4: Excess pore fluid pressure at $x = 0$ m using the semi-analytical solution with and without consideration of the relative acceleration. The results displayed in plot a) are obtained using the parameters listed in Table 4.2. For plot b) an increased hydraulic conductivity of $k^f = 10^{-3}$ m/s is set.

The second parameter is now a constant and the main variables that influence the impact of relative acceleration are k^f and ω. The regime of negligible relative acceleration can therefore be evaluated by the variation of k^f and ω alone. For this purpose, the previously derived semi-analytical solution is applied with consideration of the relative acceleration and compared to the results without relative acceleration in a parametric study varying k^f and ω (the latter by varying the length of the column). The error between the two solutions is evaluated by comparing the differences in the excess pore fluid pressure and time shift of the propagating wave simultaneously. The tolerated relative error is set to 2 %. Larger discrepancies are classified in the regime of non-negligible relative acceleration, and consequently, in the regime in which the results obtained from the **u**-p formulation differ from those obtained using the full formulations (**u**-p-**U** and **u**-**U** element formulation). Owing to the considerable computational time, the individual calculations are performed until either (a) the error tolerance is exceeded or (b) the first peak of the pore pressure is reached by both formulations, without exceeding the error tolerance. The error increases with number of wave passings, leading to an underestimation of the error in this study if the waves pass several times as is visible from Fig. 4.4b.

Figure 4.6 presents the results of the parametric study, depicting the regime of negligible and non-negligible relative acceleration, respectively. The regimes are determined solely by the highest compression wave frequency and the hydraulic conductivity. Note that in Fig. 4.6 not the angular but the natural frequency is used. The parameters of the simulation given in Fig. 4.4b are marked by the blue circle. As expected, the influence of the relative acceleration

increases with increasing frequency and hydraulic conductivity. Therefore, in case of fine-grained soils, the influence of the relative acceleration is little to non-existent. This corresponds to so-called *high-viscous coupling* ($k^f/\eta^f \to 0$), meaning that the two-phase medium behaves like a one-phase medium during wave passaging (see [132]). For higher hydraulic conductivity than 10^{-4} m/s, the maximum frequency at which relative acceleration still can be neglected decreases over-linearly with the hydraulic conductivity. For a given hydraulic conductivity of $7 \cdot 10^{-4}$ m/s, a threshold frequency level of approximately 55 Hz is reached.

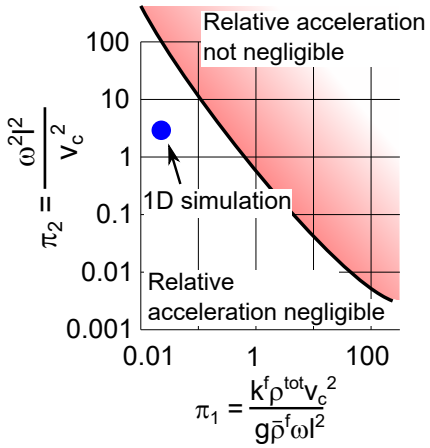

Figure 4.5: Influence of the relative acceleration in dependence of the two dimensionless parameters π_1 and π_2 defined in Eq. (4.71) (modified from [450]). The regime for the simulation displayed in Fig. 4.4b using a hydraulic conductivity of $k^f = 10^{-3}$ m/s is marked.

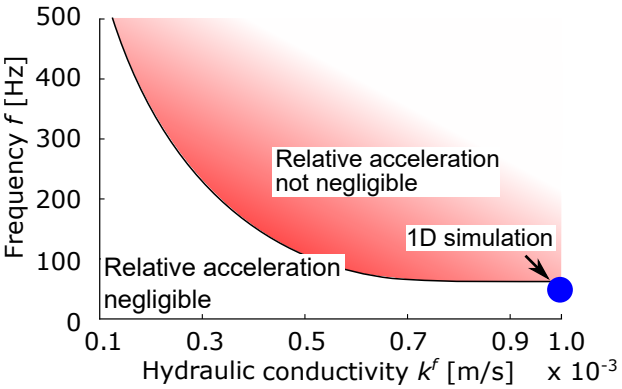

Figure 4.6: Influence of relative acceleration with respect to the frequency and the hydraulic conductivity based on the semi-analytical solution. Note that the frequency is used, and not the angular frequency. The regime for the simulation displayed in Fig. 4.4b using a hydraulic conductivity of $k^f = 10^{-3}$ m/s is marked.

Figure 4.6 indicates that using the parameters given in Tab. 4.2 with an increased hydraulic conductivity of $k^f = 10^{-3}$ m/s small deviations between simulations with and without consideration of relative acceleration have to be expected. This fits well to the excess pore fluid pressure time history given in Fig. 4.4b, where small deviations between the solutions are observed as well.

It is concluded that the proposed diagram allows to easily identify the applicability of the **u**-p element formulation in numerical analyses with multi-phase porous media and high frequency dynamics. Compared to the diagram by Zienkiewicz et al. [450], the uncertainty regarding the

influencing factors is significantly reduced since the definition of a characteristic length is not required. Somewhat surprisingly, the maximum frequency for which the relative acceleration is still found to be negligible is considerably higher than assumed by researchers [310, 185, 259, 244]. Figure 4.6 shows that the **u**-p formulation can be applied for almost all typical geomechanical BVPs, including vibratory pile driving (frequency typically higher than $f \gtrapprox 25$ Hz) in soils with comparably high hydraulic conductivity.

To investigate if the findings regarding the applicability of the **u**-p element formulation still hold if complex geometries and effects due to material damping are faced simultaneously, the simulation of vibratory pile driving tests is presented in Section 8.2.2 using the **u**-p and the **u**-p-**U** element formulation, respectively.

4.5 Performance of different hydro-mechanically coupled finite element formulations

The comparison of different hydro-mechanically coupled finite element formulations with the semi-analytical solution are given in Fig. 4.7. The semi-analytical solution with consideration of the relative acceleration is applied. The same geometrical specifications of the column and identical parameters as used in Section 4.4.4 (with $k^f = 10^{-5}$ m/s) are employed. The column is discretised using 100 finite elements for both 2D and 3D simulations as well as for elements with linearly and quadratically interpolated solid displacement. Note that all elements are implemented in the finite element code `numgeo`. The **u**-p element has been implemented by Machaček [243]. The implementations of the **u**-p-**U** and **u**-**U** element formulations done by the author are based on the implementation of the **u**-p element (see [349] for the implementation of the **u**-**U** element). More details on `numgeo` and the various finite element formulations available are given in Chapter 7. The following element formulations are compared in Fig. 4.7:

- `u8p4u8` element: **u**-p-**U** element formulation, two-dimensional, 8 nodes discretising solid displacement, 4 nodes discretising pore fluid pressure, 8 nodes discretising fluid displacement, serendipity formulation, integration with 9 integration points
- `u8p4u8-red` element: **u**-p-**U** element formulation, two-dimensional, 8 nodes discretising solid displacement, 4 nodes discretising pore fluid pressure, 8 nodes discretising fluid displacement, serendipity formulation, reduced integration with 4 integration points

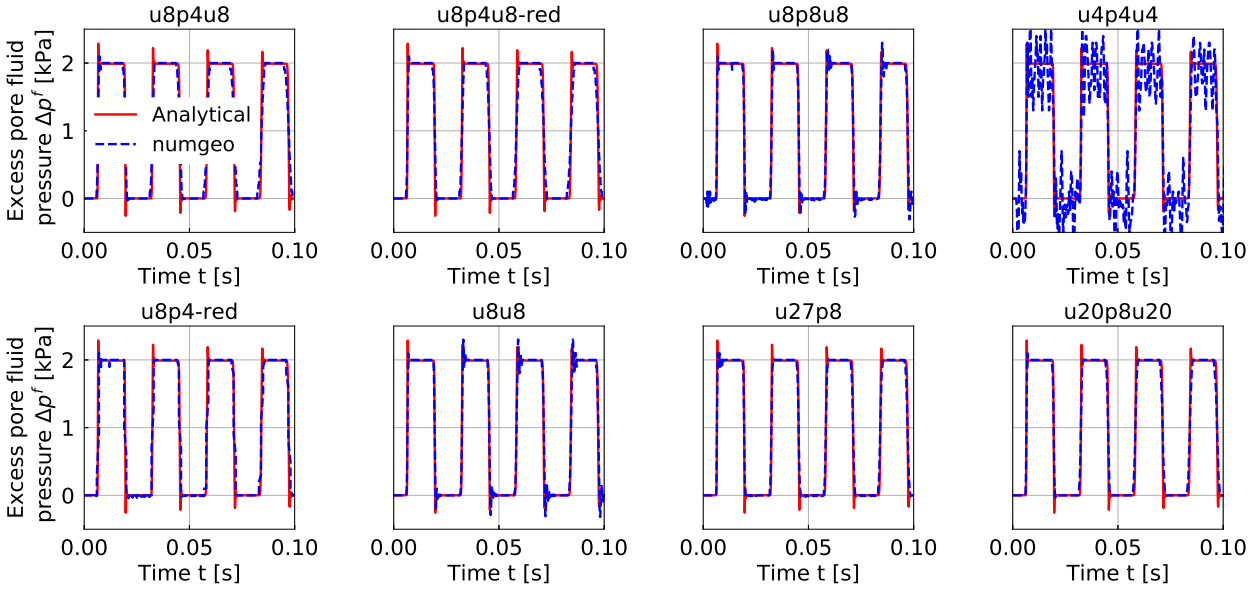

Figure 4.7: Excess pore fluid pressure at $x = 0$ m using different element formulations. The parameters listed in Table 4.2 are adopted.

- `u8p8u8` element: **u**-p-**U** element formulation, two-dimensional, 8 nodes discretising solid displacement, 8 nodes discretising pore fluid pressure, 8 nodes discretising fluid displacement, serendipity formulation, integration with 9 integration points
- `u4p4u4` element: **u**-p-**U** element formulation, two-dimensional, 4 nodes discretising solid displacement, 4 nodes discretising pore fluid pressure, 4 nodes discretising fluid displacement, integration with 4 integration points
- `u8p4-red` element: **u**-p element formulation, two-dimensional, 4 nodes discretising solid displacement, 4 nodes discretising pore fluid pressure, serendipity formulation, reduced integration with 4 integration points
- `u8u8` element: **u**-**U** element formulation, two-dimensional, 8 nodes discretising solid displacement, 8 nodes discretising fluid displacement, serendipity formulation, integration with 9 integration points
- `u27p8` element: **u**-p element formulation, three-dimensional, 27 nodes discretising solid displacement, 8 nodes discretising pore fluid pressure, tri-quadratic formulation, integration with 27 integration points
- `u20p8u20` element: **u**-p-**U** element formulation, three-dimensional, 20 nodes discretising solid displacement, 8 nodes discretising pore fluid pressure, 20 nodes discretising fluid displacement, serendipity formulation, integration with 8 integration points

Element label	Formulation	Shape	Nodes	Interpolation $\mathbf{u}(/\mathbf{U})$-p	ngp
2D Elements					
`u8p4u8`	**u**-p-**U**	rectangle	8	quadratic-linear	9
`u8p4u8-red`	**u**-p-**U**	rectangle	8	quadratic-linear	4
`u8p8u8`	**u**-p-**U**	rectangle	8	quadratic-quadratic	9
`u4p4u4`	**u**-p-**U**	rectangle	4	linear-linear	4
`u8p4-red`	**u**-p	rectangle	8	quadratic-linear	4
`u8u8`	**u**-**U**	rectangle	8	quadratic-quadratic	9
3D Elements					
`u27p8`	**u**-p	brick	27	(tri-)quadratic-linear	27
`u20p8u20`	**u**-p-**U**	brick	20	quadratic-linear	27

Table 4.3: Different types of elements used for the analysis of the wave propagation in a fluid-saturated column. The element formulation, the element shape, the number of nodes discretising the displacements, the interpolation order for displacement and pore pressure and the number of integration points (ngp) are given. Note that for the `u8u8` element a selective reduced integration scheme is adopted. Only 4 points are used for the integration of terms containing the fluid pressure.

The different element types, their formulation, shape, number of nodes discretising the displacements, interpolation order for displacement and pore pressure and number of integration points (ngp) are also provided in Table 4.3.

Except of the `u4p4u4` element all finite element formulations are in good agreement with the solution of the semi-analytical approach. Strong oscillations are observed using the `u4p4u4` element. The direct comparison with the other elements is, however, inequitable since the distance between the nodes is twice the value of the other two-dimensional elements. Among the quadratically interpolated **u**-p-**U** elements, the `u8p8u8` element performs the worst, since considerable oscillations in the curve of the excess pore fluid pressure are observed. As has been mentioned at the beginning of this chapter, an interpolation of the fluid pressure one order less than the solid displacement is recommended for the **u**-p element formulations in order to satisfy the LBB condition. Based on the work of Zienkiewicz [451], [185] states that the **u**-p-**U** elements, opposite to the **u**-p element formulation, do not require different order of interpolation. The results of the present study demonstrate that the `u8p8u8` and `u4p4u4`

elements show stronger oscillations compared to the u8p4u8 elements and their application can therefore not be recommended.

The u8p4u8-red element employs a reduced integration scheme for all contributions of the balance equations and is computationally advantageous to the fully integrated elements. Despite the reduced number of integration points, the u8p4u8-red element is in perfect agreement with the u8p4u8 element. The three-dimensional elements (u27p8 and u20p8u20 element) perform similarly as their two-dimensional counterparts. The u27p8 element, which uses tri-quadratic interpolation functions, unlike the u20p8u20 element, is investigated in more detail in Section 6.6. As mentioned earlier, the u27p8 element is considered because it is advantageous in contact analyses.

In a second comparison, the parameters are altered in the following way: $E = 10,000$ kPa, $\bar{K}^f = 1.1$ GPa, $k^f = 10^{-3}$ m/s and $\sigma_0 = 10$ kPa. A larger influence of the relative acceleration is expected compared to the first set of parameters. The results of this study are given in Fig. 4.8. Due to the higher hydraulic conductivity, the oscillations in the excess pore fluid pressure are reduced for most element formulations, except for the u8p8u8 and u4p4u4 elements, which solidifies the conclusions drawn from the simulation using the first set of parameters. The elements based on the **u**-p formulation show an increasing divergence from the solution of the semi-analytical approach with ongoing wave propagation as has already been observed earlier in Fig. 4.4. This error between the element formulations is in particular visible from Fig. 4.9, where the results of the u8p4 and the u8p4u8 element are compared for a time period between $t = 0.15$ s and $t = 0.2$ s. The u8p4u8 element is in perfect accordance with the semi-analytical solution whereas significant deviation is observed using the u8p4 element.

4.6 Eulerian finite element techniques

4.6.1 Basics

In an Eulerian analysis the mesh is fixed in space and the material moves through it. In contrast to a Lagrangian analysis, the elements are not necessarily completely occupied by material. An Eulerian approach is of advantage if large deformations are modelled since no mesh distortion occurs.

In most Eulerian codes, a calculation increment is conceptually divided into two steps. In the first step, the solution is progressed in time analogous to a Lagrangian analysis. In the second

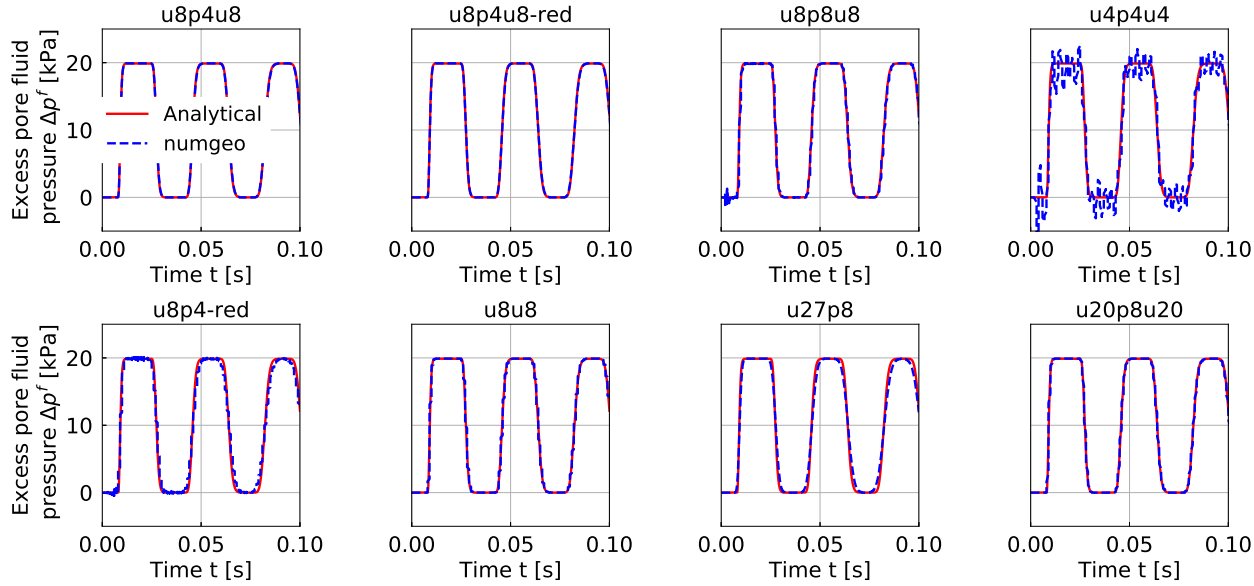

Figure 4.8: Excess pore fluid pressure at $x = 0$ m using different element formulations. The parameters listed in Table 4.2 are modified to: $E = 10,000$ kPa, $\bar{K}^f = 1.1$ GPa, $k^f = 10^{-3}$ m/s and $\sigma_0 = 10$ kPa.

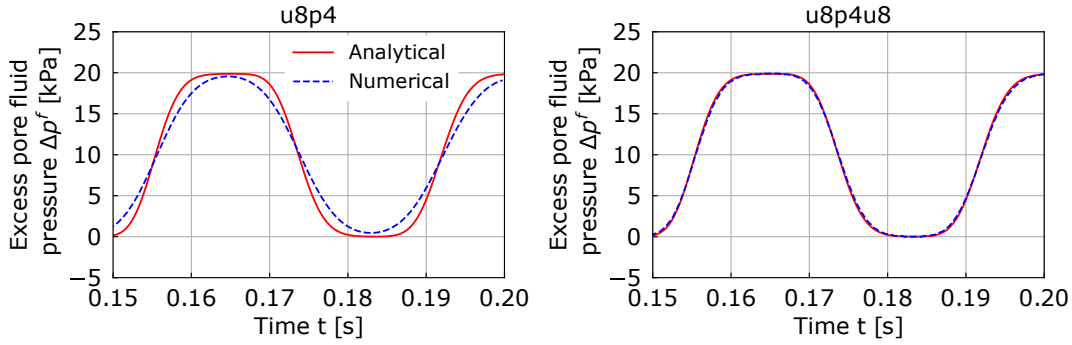

Figure 4.9: Excess pore fluid pressure at $x = 0$ m using the `u8p4` and `u8p4u8` elements. The parameters listed in Table 4.2 are modified: $E = 10,000$ kPa, $\bar{K}^f = 1.1$ GPa, $k^f = 10^{-3}$ m/s and $\sigma_0 = 10$ kPa.

step, the solution is then mapped back to the Eulerian mesh, which is called the *remap* or *advection* step. The strategy of solving the problem in two separate steps is often referred to as *operator split* since the underlying differential equations are solved term-by-term (see e.g. [43, 44, 396, 30]).

The balance equations introduced in Chapter 3 can generally be written by

$$\frac{\partial \square}{\partial t} + \operatorname{div}(\boldsymbol{\psi}) = S, \tag{4.73}$$

where S is the *source term* and $\boldsymbol{\psi}$ is the *flux function*. Using operator splitting, Eq. (4.73) is divided into two separate equations, which are

$$\frac{\partial \sqcup}{\partial t} - S = 0 \quad \text{and} \tag{4.74}$$

$$\frac{\partial \sqcup}{\partial t} + \operatorname{div}(\boldsymbol{\psi}) = 0. \tag{4.75}$$

Eqs. (4.74, 4.75) are solved sequentially. First, in the Lagrangian step, Eq. (4.74) is minimised. In order to solve Eq. (4.75), the nodes which have moved during the Lagrangian step are moved back to their original position and the material transport is computed. The Lagrangian solution variables such as the stress are accounted for using transport algorithms [43, 44]. The procedure of the operator split is illustrated in Fig. 4.10.

In earlier times, Eulerian calculations were attributed to be inaccurate due the poor resolution of material interfaces [43]. However, interface tracking techniques have improved over time and the use of second order advection algorithms, which calculate the material transport between elements, allow for a very accurate computation of the flowing material.

A method in which both Lagrangian and Eulerian elements are present and interact with each other is referred to as Coupled Eulerian-Lagrangian (CEL) method. In the finite element code `Abaqus` the CEL method is implemented using an explicit time integration scheme. Recently, the CEL method has gained increasing interest in numerical geomechanics due to its comparably easy accessibility through the commercial finite element code `Abaqus` and the increased computational resources available. The CEL method is in particular appealing for the simulation of pile driving, for which the pile is modelled using a Lagrangian description and the soil, undergoing large deformations, is modelled in the Eulerian framework. Successful applications of the CEL approach to geotechnical BVPs have been reported e.g. in [303, 17, 397, 156, 32]. However, these simulations were restricted to either perfectly drained or locally undrained conditions.

4.6.2 Hydro-mechanically coupled CEL method

To account for the change in pore fluid pressure and the resulting consolidation process, the CEL method is extended by the pore fluid pressure as an additional primary unknown. This is done based on an idea reported in [151, 150], where a coupled temperature-displacement analysis is performed with `Abaqus`. Therein, the temperature is replaced by the excess pore fluid pressure. In the following, this approach is elaborated in detail since an extension of the

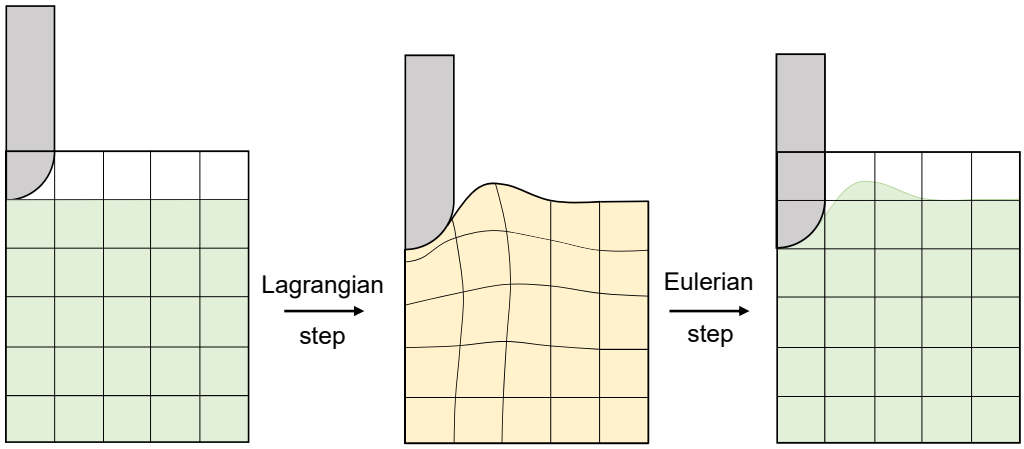

Figure 4.10: Sequences of steps in Eulerian analyses (modified from [32])

method used in [151, 150] is introduced, allowing to take into account the accelerations in the balance equation of linear momentum of the pore fluid. Note that the derivation of the hydro-mechanically coupled CEL method has already been published by the author in [353, 354]. In the following, instead of the exponent $\sqcup^{wf}$ and $\sqcup^{af}$ for the free water and free air phase, the exponent $\sqcup^{f}$ is used to indicate that a general fluid is considered. Note that only fluid-saturated conditions are taken into account.

Based on the conclusion that the influence of relative acceleration is negligible for most BVPs, the **u**-p formulation is used for the derivation of the hydro-mechanically coupled CEL method. For this purpose, the balance of linear momentum of the free fluid phase given by Eq. (3.60) is expressed in terms of relative velocity between fluid and solid phase. The relative velocity is defined by

$$\boldsymbol{w}^f = \frac{K^{\mathrm{Perm}}}{\eta^f}\Big[-\operatorname{grad}(p^f) + \bar{\rho}^f\,(\boldsymbol{b} - \ddot{\boldsymbol{u}}^s)\Big] \tag{4.76}$$

and inserted into the mass balance of the fluid given by Eq. (3.52), resulting in

$$\varphi^f \frac{1}{\bar{K}^f}\dot{p}^f + \operatorname{div}\left\{\frac{K^{\mathrm{Perm}}}{\eta^f}\Big[-\operatorname{grad}(p^f) + \bar{\rho}^f\,(\boldsymbol{b} - \ddot{\boldsymbol{u}}^s)\Big]\right\} + \operatorname{div}(\dot{\boldsymbol{u}}^s) = 0. \tag{4.77}$$

The similarity between Eq. (4.77) and the energy balance for the simulation of thermal processes is utilised to incorporate the hydro-mechanically coupled analyses in `Abaqus` [151, 150]. The energy balance is

$$\rho c\dot{\theta} + \lambda\,\operatorname{div}\Big[-\operatorname{grad}(\theta)\Big] = -\dot{m}_T, \tag{4.78}$$

where ρ is the total density, c the specific heat, θ the temperature, λ the thermal conductivity and $\dot{m}_T$ the internal heat production.

Using the relationship $\bar{\rho}^f \boldsymbol{b} - \mathrm{grad}(p^f) = -\mathrm{grad}(\Delta p^f)$ and expressing the pore fluid pressure rate only in terms of the change relative to the initial state ($\dot{p}^f = \Delta\dot{p}^f$), Eq. (4.77) can be rewritten to

$$\varphi^f \frac{\Delta\dot{p}^f}{\bar{K}^f} + \frac{K^{\mathrm{Perm}}}{\eta^f}\mathrm{div}\Big[-\mathrm{grad}(\Delta p^f)\Big] - \frac{K^{\mathrm{Perm}}}{\eta^f}\mathrm{div}\big(\ddot{\boldsymbol{u}}^s\big) + \mathrm{div}(\dot{\boldsymbol{u}}^s) = 0. \tag{4.79}$$

By (re)interpreting the temperature as the excess pore fluid pressure $\theta = \Delta p^f$, the following three matching terms can be identified from a comparison of Eq. (4.79) and Eq. (4.78)

$$c\rho\dot{\theta} = \varphi^f \frac{\Delta\dot{p}^f}{\bar{K}^f}, \tag{4.80}$$

$$\lambda\ \mathrm{div}\big[-\mathrm{grad}(\theta)\big] = \frac{K^{\mathrm{Perm}}}{\eta^f}\mathrm{div}\Big[-\mathrm{grad}(\Delta p^f)\Big] \quad \text{and} \tag{4.81}$$

$$\dot{m}_T = \mathrm{div}(\dot{\boldsymbol{u}}^s) - \frac{K^{\mathrm{Perm}}}{\eta^f}\mathrm{div}\big(\ddot{\boldsymbol{u}}^s\big). \tag{4.82}$$

Performing a thermal-displacement analysis with `Abaqus`, the constants in Eqs. (4.80) and (4.81) are set to

$$c = \frac{\varphi^f}{\bar{K}^f \rho} \quad \text{and} \quad \lambda = \frac{K^{\mathrm{Perm}}}{\eta^f} \tag{4.83}$$

and the heat production following Eq. (4.82) is defined in a user material subroutine (`VUMAT` in the present case). As the interface of the `VUMAT` provides no information on the acceleration of the solid phase, the divergence of the solid acceleration is approximated using an explicit mid-point rule

$$\mathrm{div}(\ddot{\boldsymbol{u}}^s)^{t+\Delta t} = \frac{\mathrm{tr}(\dot{\boldsymbol{\varepsilon}})^{t+\Delta t} - \mathrm{tr}(\dot{\boldsymbol{\varepsilon}})^t}{2\Delta t} + \frac{\mathrm{div}(\ddot{\boldsymbol{u}}^s)^t}{2}, \tag{4.84}$$

where $()^{t+\Delta t}$ corresponds to the current and $()^t$ to the previous time increment.

Contrary to [151, 150], the proposed method allows for the simulation of hydro-mechanically coupled problems using the full balance equations. One draw-back of this approach is the constant density employed by `Abaqus`, e.g. no changes of the density are considered. However, in case of fluid-saturated porous media the influence of a restriction to constant density is judged small compared to the restrictions of simulations assuming ideally drained/undrained conditions or neglecting the influence of inertia.

Since cavitation can occur during pile driving in water-saturated soils with low hydraulic conductivity, the internal heat production given by Eq. (4.82) for $p^f + \Delta p^f < p^f_{lim}$ is only computed if $\dot{m}_T < 0$. p^f_{lim} is the fluid pressure at which for a given temperature cavitation occurs.

The performance of the proposed fully coupled explicit approach is evaluated by comparison with the semi-analytical solution for the wave propagation in a poro-elastic medium derived in the previous sections. A Heaviside load of the solid phase is considered again. The parameters used for the numerical as well as for the semi-analytical approach are the same as used in Section 4.4.4 given in Table 4.2. For the semi-analytical solution and the explicit approach, the time increments are set to $\Delta t = 10^{-5}$ s and $\Delta t = 10^{-6}$ s, respectively. The soil column for the numerical analyses is either discretised using 100 elements or 1000 elements. For the explicit calculations a time scaling factor, which can be used to modify the maximum stable time increment of an explicit calculation, of 0.1 is used (see [340]).

The displacement-time history recorded at $x = l$ and the development of excess pore fluid pressure at $x = 0$ m are illustrated in Fig. 4.11a and Fig. 4.11b. For both the predicted excess pore fluid pressure Δp^f as well as the displacements u the semi-analytical solution matches the explicit numerical solution well.

Although the accordance with the semi-analytical solution is generally good, strong oscillations of the excess pore fluid pressure Δp^f are observed in the numerical solution in case of a discretisation with 100 elements. However, these oscillations are absent in case of the displacements. The oscillations can be noticeably reduced by refining the spatial discretisation, as evident from the results obtained with 1000 elements.

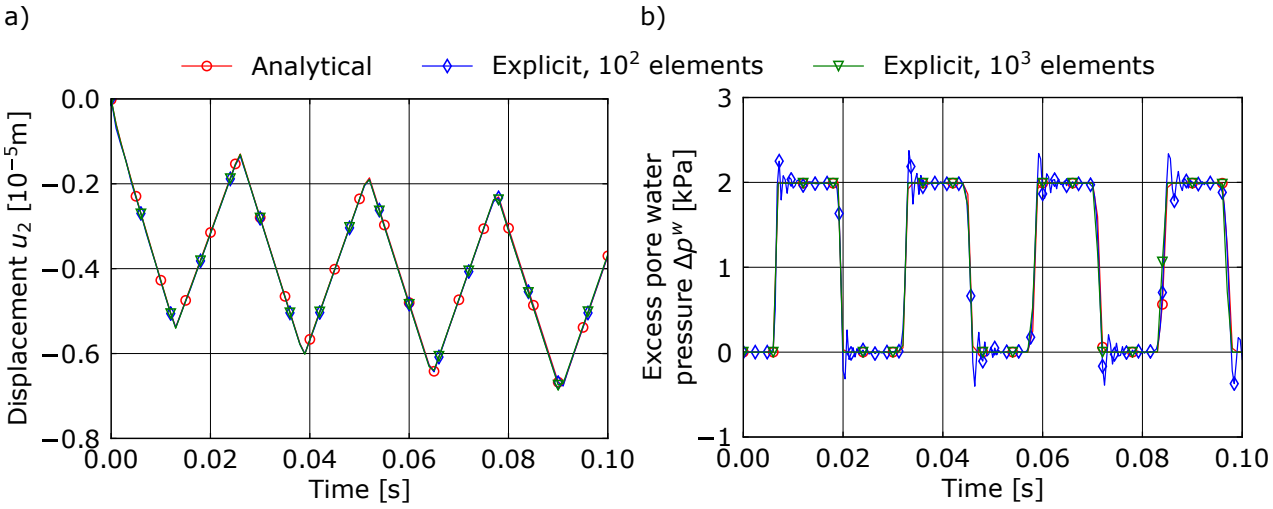

Figure 4.11: a) Comparison of numerical and semi-analytical results for the 1D wave propagation: Displacement-time history recorded at $x = l$. b) Comparison of numerical and semi-analytical results for the 1D wave propagation: Development of excess pore fluid pressure (Δp^f) at $x = 0$ m.

Note that the extension works for both, fully Lagrangian or Eulerian analyses with `Abaqus`. Using it in conjunction with the (Multi-Material) Arbitrary Lagrangian Eulerian (MMALE or ALE) method is possible as well. The presented extension has already been supplied to other researchers and was used e.g. for the simulation of vibro-compaction in water-saturated soil [192].

Chapter 5

Constitutive models

Different constitutive models to describe the mechanical behaviour of soil are used. A distinction between *conventional* models, used for analyses with monotonic and cyclic loading with up to $N \approx 10^2 - 10^4$ cycles, and *high-cycle* models, used for analyses with more than $10^2 - 10^4$ cycles, is made.

Four conventional constitutive soil models are employed in the scope of this thesis: the hypoplastic model with the intergranular strain extension [423, 269], the Sanisand model [82], the Modified-Cam-Clay (MCC) model [317] and the anisotropic visco-ISA (AVISA) model developed and implemented by M. Tafili [373, 374]. The first three models have been implemented anew into `numgeo` by the author with the aim of numerical stability even for strongly non-linear BVPs such as pile driving, which is not necessarily the case with implementations available. The constitutive equations, details on the numerical integration and implementation as well as comparisons of the results of the new implementations with existing implementations are given in Appendix A for the hypoplastic model and Sanisand.

The high-cycle models, namely the high-cycle accumulation (HCA) models for sand and clay, are described in the following. Both models have been implemented into `numgeo` as well. The enhancement of the HCA models by an adaptive strain amplitude, allowing to incorporate the influence of rapid changes in the soil stiffness during the high-cyclic loading, is presented in Section 5.2.

5.1 High-cycle accumulation models

The HCA model of Niemunis et al. [268] is a constitutive model for the prediction of the mechanical behaviour of granular media subjected to a large number of load cycles. In contrast to conventional constitutive models, the HCA model does not consider the response of the soil during individual cycles but predicts the average values (stress, strain and other additional state variables) at N applied cycles (see Fig. 5.1). Thus, no incremental application of individual cycles is necessary. Note that not only the HCA model is following this calculation strategy. Similar strategies are employed by the constitutive models proposed in [286, 59, 173] as well.

The characteristics of the cyclic loading are taken into account using a tensorial strain amplitude definition, which strongly influences the accumulation of deformation predicted by the HCA model. In order to obtain the strain amplitude, at least one individual loading cycle has to be simulated, using a conventional constitutive model. This calculation phase of the HCA model is denoted as the *low-cycle* mode of the model. Note that two cycles are usually simulated using the conventional constitutive model and the strain amplitude is calculated based on the recorded strain path of the second cycle (see Fig. 5.1). The first quarter of the first cycle represents an initial loading, while all further cycles represent un- and reloading. Hence, the first cycle is not used for the determination of the strain amplitude.

After the determination of the strain amplitude, the accumulation of permanent strain for each following load cycle is calculated in the high-cycle mode of the model. As is indicated in Fig. 5.1, the strain amplitude can be updated during the high-cycle mode of the HCA model using so-called *update cycles* in case the cyclic loading leads to a considerable change in the soil stiffness. These update cycles are calculated using the conventional constitutive model. During the update cycle the strain path is again recorded and an updated strain amplitude is calculated.

The approach followed by the HCA model has three major advantages over simulating a large number of loading cycles using conventional constitutive models:

- A simulation of millions of load cycles using the conventional approach requires an even larger number of calculation increments. For more complex BVPs, such as a monopile foundation, the computational resources required would exceed available resources.
- In dependence of the global error control as well as on the integration of the (non-linear) conventional constitutive model, an accumulation of numerical inaccuracies occurs. Since

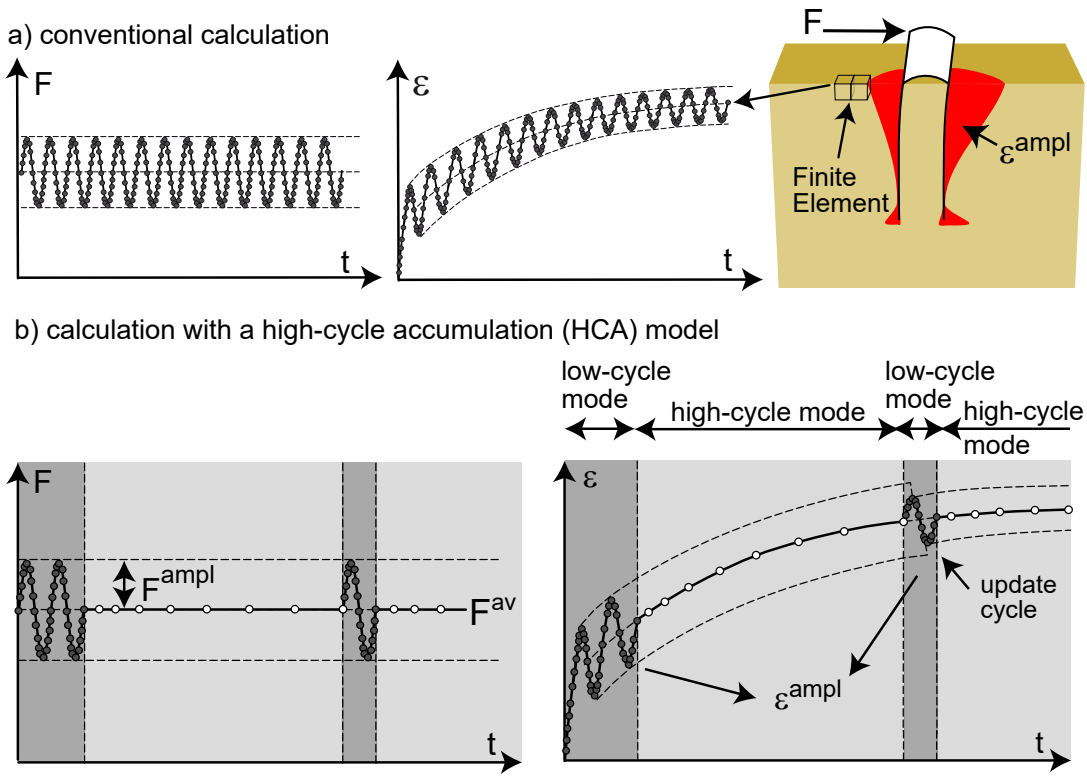

Figure 5.1: Calculation strategy in conventional analyses and in simulations using the HCA model (modified from [406]). For simulations with the HCA model the strain amplitude $\varepsilon^{\text{ampl}}$ is determined from the second load cycle calculated with a conventional constitutive model. It can be updated at a given number of cycles by interrupting the high-cycle mode by an additional conventional load cycle. During the high-cycle mode only the average loading is applied and the strain amplitude is assumed to be constant.

the permanent strain accumulated per cycle is extremely low for a larger number of load cycles, such inaccuracies can influence the solution considerably. Especially in case of simulations with severe non-linearities and many required iterations this accumulation may completely falsify the results of the simulation [268].

- The behaviour of granular media subjected to a large number of load cycles can not be captured adequately by most conventional constitutive models since the cyclic history is not taken into account. It is furthermore advantageous to separate the *low-cycle* modelling of the soil behaviour from the high-cycle modelling as it reduces the complexity of the constitutive model formulation. An example for a suitable conventional model for high-cyclic loading is the memory-surface enhanced Sanisand model proposed by Liu et al. [225] already mentioned in Chapter 2. However, due to the restrictions mentioned in the two previous raised points, constitutive models such as the HCA model are still

necessary for the incorporation of a larger number of loading cycles in complex BVPs with a large number of DOFs.

The basic equation of the HCA model reads

$$\mathring{\boldsymbol{\sigma}} = \mathsf{E} : (\dot{\boldsymbol{\varepsilon}} - \dot{\boldsymbol{\varepsilon}}^{\mathrm{acc}} - \dot{\boldsymbol{\varepsilon}}^{\mathrm{pl}}) \tag{5.1}$$

with the (objective) stress rate $\mathring{\boldsymbol{\sigma}}$ of the effective Cauchy stress $\boldsymbol{\sigma}$ (compression positive), the strain rate $\dot{\boldsymbol{\varepsilon}}$ (compression positive), the accumulation rate $\dot{\boldsymbol{\varepsilon}}^{\mathrm{acc}}$, a plastic strain rate $\dot{\boldsymbol{\varepsilon}}^{\mathrm{pl}}$ (necessary only for stress paths touching the yield surface) and the pressure-dependent elastic stiffness E. In the framework of HCA models the dot over a symbol denotes a derivative with respect to the number of cycles N, i.e. $\dot{\sqcup} = \partial \sqcup / \partial N$. Note that when integrating Eq. (5.1) numerically in a finite element analysis it has to be integrated over $\Delta N = \Delta t / t_{\mathrm{cycle}}$ where t_{cycle} is the duration of a single cycle (period) and Δt is the time increment applied by the finite element program. This is especially important for transient processes where time influences the solution, e.g. in case of partially drained conditions with a consolidation process running simultaneously. Depending on the boundary conditions, Eq. (5.1) predicts a change of stress ($\mathring{\boldsymbol{\sigma}} \neq \mathbf{0}$) and/or an accumulation of strain ($\dot{\boldsymbol{\varepsilon}} \neq \mathbf{0}$).

For $\dot{\boldsymbol{\varepsilon}}^{\mathrm{acc}}$ in Eq. (5.1) the multiplicative approach

$$\dot{\boldsymbol{\varepsilon}}^{\mathrm{acc}} = \dot{\varepsilon}^{\mathrm{acc}}\, \mathbf{m} \tag{5.2}$$

is used. The *direction* of strain accumulation (flow rule) is $\mathbf{m} = \dot{\boldsymbol{\varepsilon}}^{\mathrm{acc}} / \|\dot{\boldsymbol{\varepsilon}}^{\mathrm{acc}}\| = (\dot{\boldsymbol{\varepsilon}}^{\mathrm{acc}})^{\rightarrow}$ (unit tensor) and the *intensity* of strain accumulation $\dot{\varepsilon}^{\mathrm{acc}} = \|\dot{\boldsymbol{\varepsilon}}^{\mathrm{acc}}\|$. The flow rule of the Modified Cam Clay (MCC) model is applied for $\mathbf{m}$. It is given by

$$\mathbf{m} = \left[\frac{1}{3} \left(p^{\mathrm{av}} - \frac{(q^{\mathrm{av}})^2}{M^2 p^{\mathrm{av}}} \right) \mathbf{I} + \frac{3}{M^2} (\boldsymbol{\sigma}^{\mathrm{av}})^* \right]^{\rightarrow}, \tag{5.3}$$

where $\sqcup^{\rightarrow} = \sqcup / \| \sqcup \|$ denotes the normalisation of a tensorial quantity. $(\boldsymbol{\sigma}^{\mathrm{av}})^*$ denotes the deviatoric portion of the average effective stress tensor. p^{av} and q^{av} are the average mean effective and deviatoric stress, respectively. For the triaxial case the critical stress ratio $M = F\, M_{cc}$ is calculated by

$$F = \begin{cases} 1 + M_{ec}/3 & \text{for } \eta^{\mathrm{av}} \leq M_{ec} \\ 1 + \eta^{\mathrm{av}}/3 & \text{for } M_{ec} < \eta^{\mathrm{av}} < 0 \\ 1 & \text{for } \eta^{\mathrm{av}} \geq 0 \end{cases} \tag{5.4}$$

with

$$M_{cc} = \frac{6 \sin \varphi_{cc}}{3 - \sin \varphi_{cc}} \quad \text{and} \quad M_{ec} = -\frac{6 \sin \varphi_{cc}}{3 + \sin \varphi_{cc}}. \tag{5.5}$$

with the parameter φ_{cc}, which is similar but not necessarily identical to the critical friction angle φ_c derived from a shear test with monotonic loading. $\eta^{\mathrm{av}} = q^{\mathrm{av}}/p^{\mathrm{av}}$ in Eq. (5.4) is the average stress ratio.

The strain amplitude is calculated based on the recorded six-dimensional strain path (six independent components of the strain tensor for 3D cases) and is defined as the euclidean norm of six spans obtained by consecutive projection (degeneration) of the strain path on (hyper-)planes. For a one-dimensional cyclic loading path, the classical definition $\varepsilon^{\mathrm{ampl}} = (\varepsilon^{\mathrm{max}} - \varepsilon^{\mathrm{min}})/2$ is regained with $\varepsilon^{\mathrm{max/min}}$ denoting maximum/minimum strains. In order to derive a tensorial amplitude and subsequently a scalar amplitude descriptor, a sequence of projections of the strain loop is performed, each reducing the dimensionality of the strain loop by one (e.g. from 6D to 5D, from 5D to 4D, ..., from 2D to 1D). For the original loop and each of the projected loops, the two strain points with maximum distance are determined. The orientations $\vec{\boldsymbol{r}}^{(i)}$ with $i = 1, 2, ..., 6$ connecting both points as well as their corresponding scalar distance $2R^{(i)}$ are calculated. The following steps are performed to calculate the strain amplitude [265, 268, 272]:

- Determine the maximum distance $2R^{(i)}$ and the direction of the maximum distance $\vec{\boldsymbol{r}}^{(i)}$ of the strain points for each dimension i starting from the dimension corresponding to the total number of strain components for the considered BVP
- Project the strain path onto a hyperplane perpendicular to $\vec{\boldsymbol{r}}^{(i)}$. The strain path is reduced by one dimension using $\boldsymbol{\varepsilon}^{(i-1)} = \boldsymbol{\varepsilon}^{(i)} - \boldsymbol{\varepsilon}^{(i)}(\boldsymbol{\varepsilon}^{(i)} : \vec{\boldsymbol{r}}^{(i)})$, which leads to a "flattened" strain path
- Save $R^{(i)}$ and $\vec{\boldsymbol{r}}^{(i)}$
- Repeat until $R^{(1)}$ and $\vec{\boldsymbol{r}}^{(1)}$

The procedure is illustrated in Fig. 5.2 for a recorded strain path with three strain components for each recorded strain point. To simplify the illustrative example, only two strain components (ε_{11} and ε_{22}) are non-zero. Thus, the projection procedure has to be performed only two times since the recorded strain path is 2D. A third projection results in $R^{(1)} = 0$ since ε_{12} is zero for all points.

In general, having calculated $R^{(i)}$ and $\vec{\boldsymbol{r}}^{(i)}$ for each dimension, the tensorial amplitude A according to [265, 268] is calculated using

$$\mathsf{A} = \sum_{i=1}^{6} R^{(i)} \vec{\boldsymbol{r}}^{(i)} \otimes \vec{\boldsymbol{r}}^{(i)}. \tag{5.6}$$

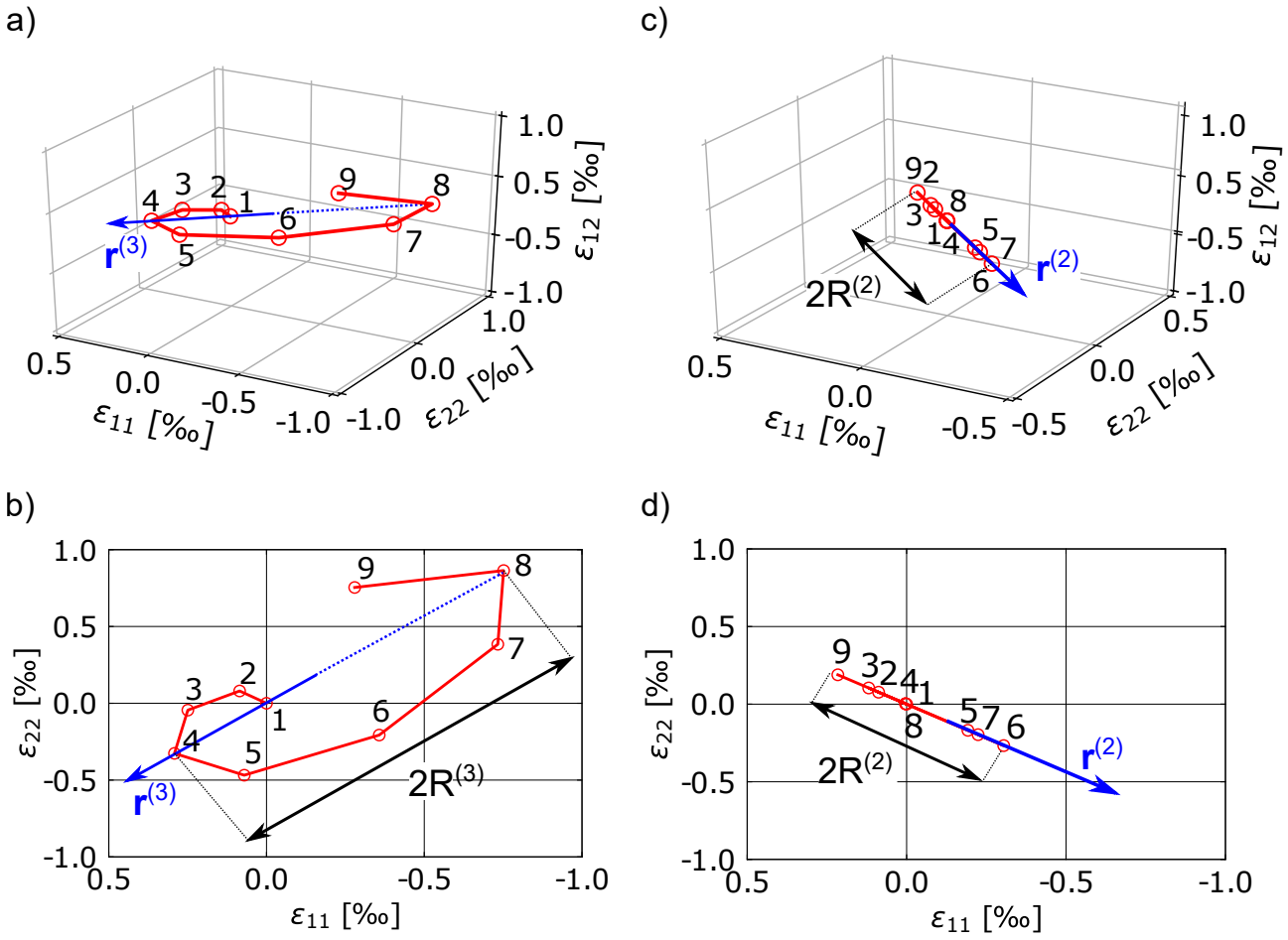

Figure 5.2: Illustrative example for the calculation of the strain amplitude from a recorded strain path in a 2D analysis. Plot a) shows the recorded strain path with 3 strain components for each strain point and the corresponding direction of maximum distance $\vec{\boldsymbol{r}}^{(3)}$ from strain point eight to four. Since $\varepsilon_{12} = 0$ is set for all points (to simplify the procedures for the illustrative example), the projection is performed in the $\varepsilon_{11} - \varepsilon_{22}$ plane as is visible from plot b). From that projection the scalar distance $2R^{(3)}$ is obtained. The reduced strain path is calculated using $\boldsymbol{\varepsilon}^{(2)} = \boldsymbol{\varepsilon}^{(3)} - \boldsymbol{\varepsilon}^{(3)}(\boldsymbol{\varepsilon}^{(3)} : \vec{\boldsymbol{r}}^{(3)})$ (performed for each recorded point) and is given in plot c). Again, the direction of maximum distance $\boldsymbol{r}^{(2)}$ from strain point nine to six and the scalar distance $2R^{(2)}$ are calculated. In plot d) the reduced strain path is displayed in the $\varepsilon_{11} - \varepsilon_{22}$ plane. Note that a subsequent flattening results in $R^{(1)} = 0$ for the present case since the original strain path had only two strain components with non-zero values. Note in addition that, contrary to the illustration, $\|\vec{\boldsymbol{r}}^{(i)}\| = 1$ holds.

The scalar value of the strain amplitude used for the function f_{ampl} is defined by

$$\varepsilon^{\text{ampl}} = \|\mathsf{A}\| = \sqrt{\sum_{i=1}^{6} (R^{(i)})^2}. \tag{5.7}$$

Recently, the utilised definition of the tensorial amplitude has been further validated by using hollow-cylinder tests applying cycles with an independent oscillation of four strain components and up to 10^4 cycles [408, 195].

5.1.1 HCA model for sand

For the HCA model for sand, the intensity of strain accumulation $\dot{\varepsilon}^{\text{acc}}$ in Eq. (5.2) is calculated according to Niemunis et al. [268] as a product of six functions given by

$$\dot{\varepsilon}^{\text{acc}} = f_{\text{ampl}}\ \dot{f}_N\ f_e\ f_p\ f_Y\ f_\pi. \tag{5.8}$$

Each function considers a single influencing parameter, i.e. the strain amplitude $\varepsilon^{\text{ampl}}$ (function f_{ampl}), the cyclic preloading g^A ($\dot{f}_N$), void ratio e (f_e), average mean pressure p^{av} (f_p), average stress ratio η^{av} or $\bar{Y}^{\text{av}}$ (f_Y) and the effect of polarization changes ($f_\pi = 1$ for a constant polarization). The definitions of the functions and the corresponding material constants are supplied in Table 5.1 and in Table 5.2. Note that the value of the function f_{ampl} is limited to $10^{C_{\text{ampl}}}$ in the model for sand. The determination of the state variable g^A is analysed in more detail in Section 5.2.

The normalised stress ratio $\bar{Y}^{\text{av}}$ used in f_Y is zero for isotropic stresses ($\eta^{\text{av}} = 0$) and one on the critical state line ($\eta^{\text{av}} = M_{cc}$ for triaxial compression). The function Y of Matsuoka & Nakai [249] is used for the calculation of $\bar{Y}^{\text{av}}$, which is defined by

$$\bar{Y}^{\text{av}} = \frac{Y^{\text{av}} - 9}{Y_c - 9} \quad \text{with} \quad Y_c = \frac{9 - \sin^2\varphi_{cc}}{1 - \sin^2\varphi_{cc}} \quad \text{and} \quad Y^{\text{av}} = \frac{27(3 + \eta^{\text{av}})}{(3 + 2\eta^{\text{av}})(3 - \eta^{\text{av}})}. \tag{5.9}$$

The plastic strain rate $\dot{\boldsymbol{\varepsilon}}^{pl}$ used in Eq. (5.1) is only required if the stress path reaches the Matsuoka & Nakai failure locus during the high-cyclic loading. This failure locus is given by

$$F = -\frac{I_1 I_2}{I_3} - 9 - 8\tan^2(\varphi) \leq 0, \tag{5.10}$$

where I_1, I_2, I_3 are the principal invariants of the effective stress tensor and φ is the density-dependent friction angle.

Function	Material constant	Ref. quant.
$f_{\text{ampl}} = \left(\dfrac{\varepsilon^{\text{ampl}}}{\varepsilon^{\text{ampl}}_{\text{ref}}} \right)^{C_{\text{ampl}}}$	C_{ampl}	$\varepsilon^{\text{ampl}}_{\text{ref}}$
$\dot{f}_N = \dot{f}^A_N + \dot{f}^B_N$	C_{N1}	
$\dot{f}^A_N = C_{N1} C_{N2} \exp\left(-\dfrac{g^A}{C_{N1} f_{\text{ampl}}} \right)$	C_{N2}	
$\dot{f}^B_N = C_{N1} C_{N3}$	C_{N3}	
$f_e = \dfrac{(C_e - e)^2}{1+e} \dfrac{1+e_{\text{ref}}}{(C_e - e_{\text{ref}})^2}$	C_e	e_{ref}

Table 5.1: Functions, material constants and reference quantities shared by the HCA models for sand and clay

Function	Material constant	Ref. quant.
$f_p = \exp\left[-C_p \left(\dfrac{p^{\text{av}}}{100\ \text{kPa}} - 1 \right) \right]$	C_p	
$f_Y = \exp\left(C_Y\ \bar{Y}^{\text{av}} \right)$	C_Y	φ_{cc}

Table 5.2: Additional functions, material constants and reference quantities to Table 5.1 solely used in the HCA model for sand

The formulation of the pressure-dependent elastic stiffness of the HCA model for sand required in Eq. (5.1) has been derived from numerous drained and undrained high-cyclic triaxial tests [410, 416] and can be found in [406]. The bulk modulus can be determined by comparison of the volumetric strain accumulation measured in drained cyclic triaxial tests with the accumulation of pore water pressure measured in undrained tests [406]. The Poisson's ratio may be obtained by performing strain-controlled undrained cyclic triaxial tests starting with an initial stress ratio $\eta \neq 0$ [406].

The parameters of the HCA model given in Table 5.2 can be determined from experiments [411, 419] or estimated based on granulometry or simple index quantities [415, 419].

5.1.2 HCA model for clay

Similar to sand, clay can show an accumulation of permanent strain due to cyclic loading with many repetitions. Based on data from an extensive laboratory testing program on kaolin under undrained cyclic loading [418], a HCA model for clay has been proposed in [406], which is discussed in the following.

Eq. (5.1) used in the HCA model for sand is adopted for the clay model as well. The stiffness E, the intensity of accumulation $\dot{\varepsilon}^{\mathrm{acc}}$ and the plastic strain rate $\dot{\boldsymbol{\varepsilon}}^{\mathrm{pl}}$ have to be adjusted for the clay model, however. Compared to sand, additional functions to take into account the overconsolidation ratio OCR (f_{OCR}) and the loading frequency (f_f) have to be added to the intensity of accumulation for the clay model. On the other hand, one of the functions f_e and f_p incorporated in the HCA model for sand can be omitted since in normally consolidated soils void ratio and pressure are directly interrelated to each other via the normal compression curve $e(p)$. The factor f_e is used in the HCA model for clay. The following multiplicative approach is employed for the intensity of strain accumulation [406, 358], viz.

$$\dot{\varepsilon}^{\mathrm{acc}} = f_{\mathrm{ampl}}\ \dot{f}_N\ f_e\ f_\eta\ f_{OCR}\ f_f. \tag{5.11}$$

In addition to the aforementioned modifications, the factor f_Y of the model for sand is replaced by f_η in Eq. (5.11). The functions and the corresponding material constants are given in Table 5.1 and Table 5.3. An overview of the complete model including the derivation of the constitutive equations, determination of the parameters and the simulation of element tests is given in [406, 358].

Function	Material constant
$f_\eta = \exp\left(C_\eta\ \lvert\eta^{\mathrm{av}}\rvert / M\right)$	C_η
$f_{\mathrm{OCR}} = \exp[-C_{\mathrm{OCR}}(\mathrm{OCR} - 1.0)]$	C_{OCR}
$f_f = 1$	-

Table 5.3: Additional functions and material constants to Table 5.1 solely used in the HCA model for clay

Analogous to the HCA model for sand, incorporation of a plastic strain rate is required since the stress can take un-physical values otherwise (e.g. far outside the failure locus). The isotropic yield surface of the MCC model is used for this purpose. The preloading surface is an ellipse

described by

$$p(p - p_e^+) + \left(\frac{q}{M}\right)^2 = 0, \tag{5.12}$$

with the critical stress ratio M. The equivalent pressure p_e^+ marks the intercept of the preloading surface with the p-axis. The overconsolidation ratio is defined as

$$\mathrm{OCR} = \frac{p_e}{p_e^+}, \tag{5.13}$$

where p_e is calculated from the virgin compression line as observed in isotropic compression tests given by

$$\ln\left(\frac{1 + e_{e0}}{1 + e}\right) = \lambda \ln\left(\frac{p_e}{p_{e0}}\right). \tag{5.14}$$

e_{e0} and p_{e0} are the referential void ratio and pressure, respectively, and λ is the inclination of the compression line in a diagram with log-log scale. Using an associative flow rule, the plastic strain can be calculated by

$$\dot{\boldsymbol{\varepsilon}}^{\mathrm{pl}} = \dot{\phi}\frac{\partial F}{\partial \boldsymbol{\sigma}}, \tag{5.15}$$

where $\dot{\phi} > 0$ is the *plastic potential* and F is the scalar value of the preloading surface in Eq. (5.12). $\dfrac{\partial F}{\partial \boldsymbol{\sigma}}$ is equivalent to $\mathbf{m}$ introduced in Eq. (5.3). The plastic strain is calculated iteratively using Newton's method. The increment in plastic strain is calculated by

$$\Delta\boldsymbol{\varepsilon}^{\mathrm{pl}} = \Delta\phi\frac{\partial F}{\partial \boldsymbol{\sigma}}. \tag{5.16}$$

$\Delta\phi$ is determined by computing the zero of Eq. (5.12) using Newton's method, viz.

$$\Delta\phi^{i+1} = \Delta\phi^i - \frac{F^i}{\dfrac{dF^i(\Delta\phi^i)}{d\Delta\phi}}. \tag{5.17}$$

Eq. (5.17) is solved in every iteration i until F is sufficiently close to zero. The derivative of F with respect to $\Delta\phi$ is

$$\frac{dF(\Delta\phi)}{d\Delta\phi} = \frac{\partial F}{\partial p}\frac{\partial p}{\partial \Delta\phi} + \frac{\partial F}{\partial q}\frac{\partial q}{\partial \Delta\phi} + \frac{\partial F}{\partial p_e^+}\frac{\partial p_e^+}{\partial \Delta\phi}. \tag{5.18}$$

The partial derivatives of mean effective stress p, deviatoric stress q and p_e^+ are defined by (see [53])

$$\frac{\partial p}{\partial \Delta\phi} = -K\frac{(2p - p_e^+)}{1 + (2K + \vartheta p_e^+)\Delta\phi}, \tag{5.19}$$

$$\frac{\partial q}{\partial \Delta\phi} = -\frac{q}{\Delta\phi + M^2/6\mu} \quad \text{and} \tag{5.20}$$

$$\frac{\partial p_e^+}{\partial \Delta\phi} = \vartheta p_e^+\frac{2p - p_e^+}{1 + (2K + \vartheta p_e^+)\Delta\phi}. \tag{5.21}$$

In Eq. (5.21) ϑ is defined by

$$\vartheta = \frac{1+e}{\lambda - \kappa}, \tag{5.22}$$

where the swelling index κ is used. For the HCA model for clay, a simple isotropic stiffness is used for E in Eq. (5.1) calculated by

$$\mathsf{E} = K\mathbf{1} \otimes \mathbf{1} + 2\mu\mathsf{I}, \tag{5.23}$$

where the scalar factors are defined as

$$K = \frac{1+e}{\kappa}p \quad \text{and} \quad \mu = \frac{3K(1-2\nu)}{2(1+\nu)}. \tag{5.24}$$

In Eq. (5.24) ν is the Poisson's ratio. I in Eq. (5.23) is the fourth order identity tensor. As has been outlined in [268], a hyper-elastic definition of stiffness is inessential for the HCA model since such models do not describe the course of stress and strain during individual cycles. Thus, no accumulation of artificial strain during closed stress cycles or vice versa occurs despite the hypo-elastic definition of stiffness.

5.2 Incorporation of an adaptive strain amplitude

In case of cyclic loading with significant change in effective stress, e.g. by relaxation of the stress due to contraction, the strain amplitude may change during the high-cycle phase of the HCA model as the result of the alteration of the soil stiffness. As already elaborated on in Section 5.1, a change in strain amplitude can be taken into account by the HCA model by incorporation of update cycles, which are performed with a conventional constitutive model. It is, however, a priori not known at which number of loading cycles an update cycle should be incorporated or what the correct number of required update cycles is. Furthermore, the strain amplitude may in some cases change so rapidly with number of loading cycles that many update cycles would be necessary which can considerably increase the run time of a simulation and thus diminish the main advantage of the HCA model. In [357] it was demonstrated that only by incorporation of many update cycles, the influence of the hydraulic conductivity on the long-term behaviour of a monopile foundation under partially drained conditions could be realistically taken into account (i.e. larger permanent deformation for lower hydraulic conductivity).

In addition to the aforementioned shortcoming, the use of update cycles requires a repeated change of the "active" constitutive model, which can lead to numerical difficulties. Because the cyclic history variable used in the HCA model is not considered by the conventional

constitutive model, a significantly larger permanent deformation can be predicted during the update cycle than would be predicted by the HCA model for one cycle. Acknowledging these disadvantages, an adaptive formulation of the strain amplitude, which takes into account the change in soil stiffness during cyclic loading, is developed in the following. The proposed modifications of the HCA model are then applied to the simulation of undrained cyclic triaxial tests.

5.2.1 Cyclic preloading ($\dot{f}_N$) and historiotropic state variable (g^A)

In case of a time-varying strain amplitude, the definition of $\dot{f}_N$ given in Table 5.1 has to be revised. Based on the measured response of sand in drained high-cyclic triaxial tests, a suitable function to describe the increase of accumulated strain with increasing number of cycles N was found to be [268]

$$f_N = C_{N1}[\ln(1 + C_{N2}N) + C_{N3}N]. \tag{5.25}$$

C_{N1}, C_{N2} and C_{N3} are material parameters. For the calculation of the rate of the intensity of accumulation with respect to N the derivative of f_N with respect to N is required

$$\dot{f}_N = \underbrace{\frac{C_{N1}C_{N2}}{1 + C_{N2}N}}_{\dot{f}_N^A} + \underbrace{C_{N1}C_{N3}}_{\dot{f}_N^B}. \tag{5.26}$$

However, the definition of $\dot{f}_N$ in Eq. (5.26) contradicts the Miner's rule, which is especially apparent when considering a case where the magnitude of the cyclic loading is negligible leading to virtually no accumulation of deformation but $\dot{f}_N$ decreases nevertheless as N increases. Eq. (5.26) thus has to incorporate the intensity of cyclic loading of the previous cycles N. For this purpose, a so-called *historiotropic* state variable g^A was introduced in the original model by Niemunis et al. $\dot{f}_N(N)$ is replaced by $\dot{f}_N(g^A)$ where $g^A = f(N, f_{\text{ampl}})$ is a function of the number of previous loading cycles and the strain amplitude of these previous cycles. The rate of g^A is calculated as the product of $\dot{f}_N$ and f_{ampl}. Integration of $\dot{g}^A$ with respect to N then gives the preloading state variable g^A:

$$g^A = \int \dot{g}^A \mathrm{d}N = \int \dot{f}_N^A f_{\text{ampl}} \mathrm{d}N. \tag{5.27}$$

If f_{ampl} is assumed to be constant over the studied number of cycles the definition

$$g^A = f_{\text{ampl}} C_{N1} \ln(1 + C_{N2}N) \tag{5.28}$$

is obtained. In order to replace N in Eq. (5.26), Eq. (5.28) is rearranged to

$$N = \frac{1}{C_{N2}} \left[\exp\left(\frac{g^A}{f_{\text{ampl}} C_{N1}} \right) - 1 \right]. \tag{5.29}$$

Eq. (5.26) now can be written as

$$\dot{f}_N = C_{N1} C_{N2} \exp\left(-\frac{g^A}{C_{N1} f_{\text{ampl}}} \right) + C_{N1} C_{N3}. \tag{5.30}$$

This definition of $\dot{f}_N$ is identical to the one given in Table 5.1.

For the general case of the strain amplitude being a function of the number of cycles $\varepsilon^{\text{ampl}}(N)$ this definition has to be revised. Assuming that the strain amplitude remains constant over the span of N_0 to N, one may integrate Eq. (5.27) to

$$g^A \Big|_{N=N_0}^{N=N} = \int_{N_0}^{N} \dot{f}_N f_{\text{ampl}} \mathrm{d}N = \ln \frac{1 + C_{N2} N}{1 + C_{N2} N_0} C_{N1} f_{\text{ampl}}. \tag{5.31}$$

Using $g^A(N) = \int_{N_0}^{N} \dot{g}^A \mathrm{d}N + g^A(N_0)$ and rearranging with respect to N yields

$$N = \frac{1}{C_{N2}} \left[\exp\left(\frac{g^A(N) - g^A(N_0)}{C_{N1} f_{\text{ampl}}} \right) \cdot (1 + C_{N2} N_0) - 1 \right]. \tag{5.32}$$

Eq. (5.26) becomes

$$\dot{f}_N = \frac{C_{N1} C_{N2}}{(1 + C_{N2} N_0)} \exp\left(\frac{g^A(N_0) - g^A(N)}{C_{N1} f_{\text{ampl}}} \right) + C_{N1} C_{N3}. \tag{5.33}$$

N_0 is the number of the cycle at which the strain amplitude was updated for the last time and $g^A(N_0)$ the cyclic preloading state variable at N_0. A similar definition of $\dot{f}_N$ for $f_{\text{ampl}} \neq \text{const.}$ has also been derived in [272].

Note that when using update cycles the definition of $\dot{f}_N$ in Eq. (5.33) should be applied and not Eq. (5.30). The error using Eq. (5.30) obviously increases with increasing change in f_{ampl}. In case of negligible change of f_{ampl} Eq. (5.30) still holds.

5.2.2 Adaptive strain amplitude definition

In order to take into account changes in the strain amplitude during high-cyclic loading, two different approaches are proposed and discussed in the following. Using the *local* approach, the strain amplitude is updated for each integration point independently. Thus, neither the geometrical specifications of the BVP nor the characteristics of the applied loading are accounted for. In contrast, the global SOE has to be solved in case of the *global* approach since the influence of geometry of the BVP is considered.

Local approach for the adaptive strain amplitude

The strain amplitude is a function of the soil stiffness and is assumed to change linearly with respect to it. The following relation between the tensorial strain amplitude and the soil stiffness is proposed

$$\mathsf{A}^N = \mathsf{A}^0 \frac{\|\mathsf{E}^0\|}{\|\mathsf{E}^N\|}. \tag{5.34}$$

A^N and E^N are the tensorial amplitude and the soil stiffness at N cycles, respectively. A^0 and E^0 are the corresponding reference values. Equation (5.34) is motivated by the assumption that the change in (mean value of) stiffness between the updates of the strain amplitude is large compared to the change of stiffness during an individual cycle such that it can be taken as representative.

Note that instead of Eq. (5.34), the updated scalar strain amplitude $\varepsilon^{\mathrm{ampl},N} = \varepsilon^{\mathrm{ampl},0} \frac{\|\mathsf{E}^0\|}{\|\mathsf{E}^N\|}$ can also directly be calculated alternatively. The soil stiffness E is obtained using the conventional constitutive model since it determines the strain amplitude. E^0 is the stiffness of the first converged increment of the cycle used to calculate the strain amplitude. The strain increment of this calculation increment is saved and later reused to evaluate the updated value of the soil stiffness E^N, which is obtained using the state variables at N applied loading cycles. Both E^0 and E^N are defined as secant stiffness. Alternatively, the tangent stiffness at mean loading, where $\mathsf{E} = \frac{\partial \Delta \boldsymbol{\sigma}}{\partial \Delta \boldsymbol{\varepsilon}}$ is calculated by a numerical differentiation scheme (as further elaborated on in Appendix A), may be used. Preliminary investigations showed no influence of the definition of the stiffness for the update of the strain amplitude.

A second, more sophisticated approach is to use the direction of maximum distance at the reference state for each dimension $\vec{\boldsymbol{r}}^{0(i)}$ introduced in Eq. (5.6) which is done using

$$\mathsf{A}^N = \sum_{i=1}^{6} R^{0(i)} \vec{\boldsymbol{r}}^{0(i)} \otimes \vec{\boldsymbol{r}}^{0(i)} \frac{\mathsf{E}^0 :: (\vec{\boldsymbol{r}}^{0(i)} \otimes \vec{\boldsymbol{r}}^{0(i)})}{\mathsf{E}^N :: (\vec{\boldsymbol{r}}^{0(i)} \otimes \vec{\boldsymbol{r}}^{0(i)})}, \tag{5.35}$$

where $\sqcup :: \sqcup = \sum_{i=1}^{3} \sum_{j=1}^{3} \sum_{k=1}^{3} \sum_{l=1}^{3} \sqcup_{ijkl} \sqcup_{ijkl}$. Eq. (5.35) has the advantage that the change of stiffness is only considered in the direction of the radius $R^{0(i)}$ at the reference state. By using Eq. (5.34), the change in stiffness is "smeared".

Preliminary investigations on the monopile simulations presented in Section 8.4 showed that both Eq. (5.34) and Eq. (5.35) are suitable for the incorporation of the influence of the change in soil stiffness on the strain amplitude and the differences in the updated scalar strain amplitude are minimal. Hence, the simpler Eq. (5.34) is used.

Due to its local character, some kind of nonlocal smoothing of the updated strain amplitude has to be performed using the local approach. Otherwise a localisation of the strain amplitude (*self-reinforcing* or *positive feedback phenomenon*) and a strong mesh-dependency is expected, similar to the localisation observed for strain softening materials [107, 288, 41, 186, 134, 370, 341]. Having obtained the scalar value of the updated strain amplitude $\varepsilon^{\mathrm{ampl},N}$, the spatially averaged value $\bar{\varepsilon}^{\mathrm{ampl},N}$ is defined by

$$\bar{\varepsilon}^{\mathrm{ampl},N}(\boldsymbol{x}_i) = \int w(\boldsymbol{x}_i, \boldsymbol{x}_j)\varepsilon^{\mathrm{ampl},N}(\boldsymbol{x}_j)\,\mathrm{dV}\,. \tag{5.36}$$

$\boldsymbol{x}_i$ is the coordinate of the integration point at which the smoothed value is calculated and $\boldsymbol{x}_j$ is the coordinate of all points considered for the smoothing (in other words, all integration points of the finite element model). $w(\boldsymbol{x}_i, \boldsymbol{x}_j)$ is a weight function. The weight function is defined such that for a uniform distribution, uniformity is preserved after smoothing [288], viz.

$$w(\boldsymbol{x}_i, \boldsymbol{x}_j) = \frac{w_0(\boldsymbol{x}_i, \boldsymbol{x}_j)}{\int w_0(\boldsymbol{x}_i, \boldsymbol{x}_j)\,\mathrm{dV}}. \tag{5.37}$$

$w_0(\boldsymbol{x}_i, \boldsymbol{x}_j)$ determines the dependency of the weighting on the distance between the points i and j. Points j closer to the coordinate $\boldsymbol{x}_i$ have larger values for $w_0(\boldsymbol{x}_i, \boldsymbol{x}_j)$ than points further away.

A commonly applied approach for $w_0(\boldsymbol{x}_i, \boldsymbol{x}_j)$ is the Gaussian function [288], for which the weighting is defined by

$$w_0(\boldsymbol{x}_i, \boldsymbol{x}_j) = \frac{1}{l_c\sqrt{\pi}} e^{-\left(\frac{\|\boldsymbol{x}_i - \boldsymbol{x}_j\|}{l_c}\right)^2}, \tag{5.38}$$

where the so-called *characteristic length* l_c is introduced. l_c influences the distance to other points which are considered for the smoothing. The larger l_c, the more points are considered in the averaging. For the application to nonlocal plasticity, l_c is often related to the grain size and depends additionally on the distance between integration points of the finite elements. No relation in terms of grain size exists for the application of the nonlocal smoothing algorithm to the smoothing of the strain amplitude. A lower boundary of l_c can, however, be estimated by the distance between integration points of the finite elements. l_c has to be large enough such that a sufficient number of points are located in the zone of smoothing. At least the integration points of the same finite element should be considered for the smoothing.

The smoothing of the strain amplitude is performed by evaluation of Eq. (5.36) for all inte-

gration points n_{igp}. The smoothed strain amplitude is

$$\bar{\varepsilon}^{\mathrm{ampl},N}(\boldsymbol{x}_i) = \sum_{j=1}^{n_{\mathrm{igp}}} w(\boldsymbol{x}_i, \boldsymbol{x}_j)\varepsilon^{\mathrm{ampl},N}(\boldsymbol{x}_j), \tag{5.39}$$

where the weighing is calculated by

$$w(\boldsymbol{x}_i, \boldsymbol{x}_j) = \frac{w_0(\boldsymbol{x}_i, \boldsymbol{x}_j)}{\sum_{k=1}^{n_{\mathrm{igp}}} w_0(\boldsymbol{x}_i, \boldsymbol{x}_k)}. \tag{5.40}$$

An efficient evaluation of Eq. (5.39) and Eq. (5.40) is crucial since the number of integration points n_{igp} of the model can be large and the computational effort increases with the square of n_{igp}. Fortunately, the outer loop over the integration points i can easily be evaluated using parallel computing with multiple threads, as is explained in Section 7.1.3. The influence of the smoothing is discussed in more detail in Section 8.4.3 for the application to the long-term behaviour of monopile foundations for OWTs.

Global approach for the adaptive strain amplitude

Eqs. (5.34, 5.35) can only account for the local change in soil stiffness (even though the nonlocal smoothing adds some global character to it). Given for instance a pile, no influence due to a change in the deformation mode caused by load re-distribution can be considered. Hence, an additional approach is proposed, which is similar to the usage of update cycles. During the high-cycle phase individual loading cycles are calculated using the conventional constitutive model in a purely "private" fashion parallel to the high-cyclic calculation using the HCA model, so that the applied loading and the resulting change in the soil state do not influence the solution of the high-cyclic phase directly. Only the updated strain amplitude is transferred to the high-cycle part of the simulation. The current state variables of soil are used in these individual loading cycles.

This has three advantages over the application of the "conventional" update cycles:

- The high-cycle phase of the HCA model is not interrupted. In simulations with severe non-linearities, the HCA model may in some cases fail to converge at the beginning of the accumulation phase due to the change of the constitutive model, which is avoided using the proposed global approach. Such instabilities are for instance observed for hydro-mechanically coupled simulations with **u**-p elements or **u**-p-**U** elements where small time increments may cause oscillations in the pore fluid pressure (the conditioning of the stiffness matrices gets worse with smaller time increments, see Section 8.2.2 for a

comparison of the condition numbers of **u**-p and **u**-p-**U** elements with the condition number of the better conditioned matrix of the **u**-**U** elements). The advantage of the proposed definition over update cycles for such a case is demonstrated in Section 8.4.1.

- No manual incorporation of the update cycles in a separate calculation step is necessary, hence allowing to update the strain amplitude at an arbitrary number of applied load cycles in a more convenient way.

- Because the cyclic history variable used in the HCA model is not considered by the conventional constitutive model, a significant larger permanent deformation is often predicted during the update cycle than would be predicted by the HCA model equations for one cycle. This error is larger for update cycles performed at a larger number of pre-loading cycles, since the accumulation rate decreases with increasing value of the cyclic history variable.

The following outlines the procedures necessary for a global definition of the adaptive strain amplitude:

- At a given number of applied load cycles in the high-cycle phase an additional (separate) analysis (*submodel analysis*) is performed. The initial state of the submodel analysis corresponds to the current state of the parent analysis. This is done by saving all relevant state variables from the parent simulation, which are then used to initialise the submodel analysis.

- One individual load cycle is calculated in the submodel analysis and the strain path is recorded. The strain amplitude is calculated at the end of the cycle using Eq. (5.6).

- The parent analysis retrieves the updated strain amplitude from the submodel analysis. No other solution variables (displacement, strain, stress, state variables,...) are altered.

- The parent analysis is continued with the regular high-cycle phase using the updated strain amplitude.

A schematic illustration of these procedures is depicted in Fig. 5.3. Note that only the effective stress and the void ratio change during the high-cycle phase of the simulation. Other internal state variables of the conventional constitutive model used for the low-cycle phase, such as the intergranular strain tensor in case of the hypoplastic model or the back-stress and fabric tensor

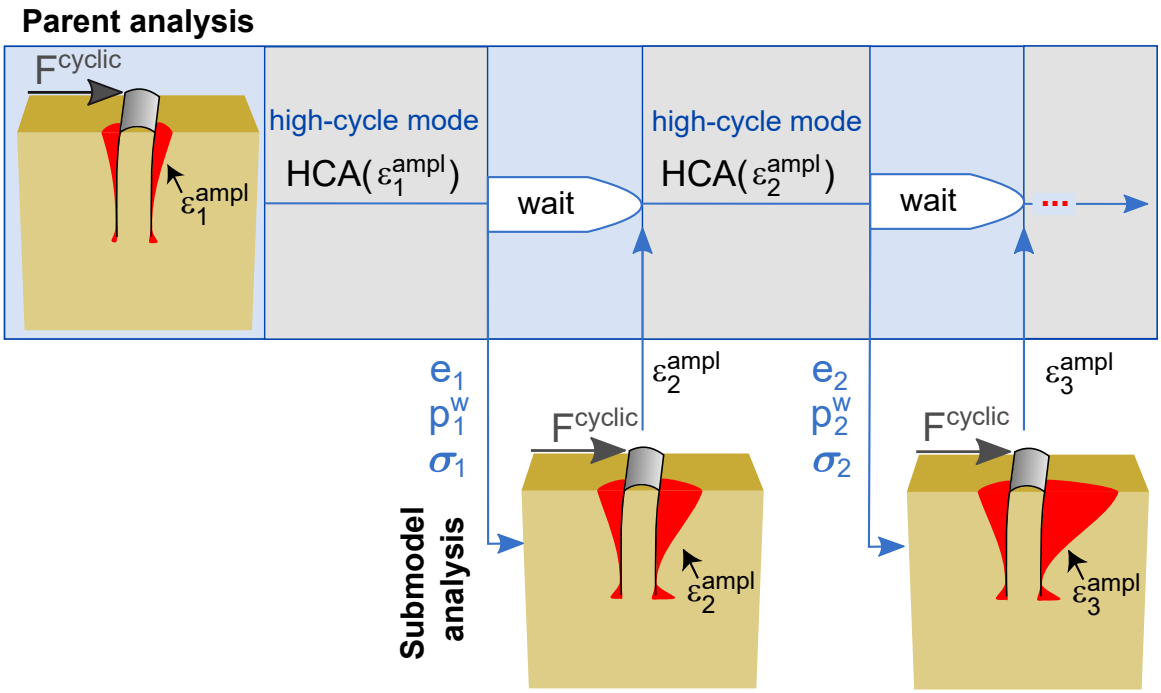

Figure 5.3: Schematic illustration of the procedures performed in a HCA simulation with a submodel analysis. After a given number of cycles the field of strain amplitude $\varepsilon^{\text{ampl}}$ is updated in a submodel analysis which obtains the state variables (e.g. void ratio e, pore water pressure p^w and effective stress $\boldsymbol{\sigma}$) from the parent analysis and calculates the updated strain amplitude $\varepsilon_2^{\text{ampl}}$. $\varepsilon_2^{\text{ampl}}$ is then used in the parent analysis for the next high-cycle phase.

of the Sanisand model, are not updated. Therefore, the values saved from the last increment of the last conventional load cycle are used.

The global approach, in contrast to the local approach, requires to assemble and solve the global SOE in many increments, analogous to the "conventional" update cycles. As will be outlined in Section 8.4.1, the global approach is nonetheless superior to the "conventional" update cycles in terms of computational performance and numerical stability.

5.2.3 Application to undrained cyclic triaxial tests

In order to show the influence of the change of strain amplitude and the suitability of the proposed adaptive strain amplitude for well controlled boundary conditions and simple geometry, undrained cyclic triaxial tests are analysed in this section. The tests have been performed in the laboratory of the Institute of Soil Mechanics and Rock Mechanics at KIT, Karlsruhe. A medium coarse sand ($d_{50} = 0.6$ mm, $C_u = 3$) was used as test material. The tests started

from an isotropic initial mean effective stress of $p_0 = 300$ kPa and an initial relative density of $D_r = 56$ %. Cycles with a deviatoric stress amplitude of $q^{\mathrm{ampl}} = 60$ kPa were then applied.

The simulations of the tests are performed using the HCA model in combination with the hypoplastic model with intergranular strain extension as conventional model. The parameters used are given for the hypoplastic model in Table 5.4 and for the HCA model in Table 5.5. The parameters of the HCA model have been calibrated in a preceding work using the same triaxial test data (see [406] for the general calibration procedure). Note that for this calibration, the strain amplitude $\varepsilon^{\mathrm{ampl}}(N)$ measured in the test was used as input for the HCA model. This is not done for the simulations presented in the following, for which the strain amplitude is either calculated by the hypoplastic model or updated using the proposed adaptive strain amplitude definition. For the pressure-dependent elastic stiffness E of the HCA model (see Eq. (5.1)) the bulk modulus is calculated according to [406] from

$$K = B\left(\frac{p^{\mathrm{av}}}{p_{\mathrm{atm}}}\right)^{n} p_{\mathrm{atm}},$$

with the parameters $B = 400$, $n = 0.5$ and $p_{\mathrm{atm}} = 100$ kPa [406]. During the high-cycle phase of the simulations the HCA model predicts the change in pore water pressure $\dot{p}^w = \sqrt{3}K\dot{\varepsilon}^{\mathrm{acc}}$ [406].

φ_c [-]	e_{i0} [-]	e_{c0} [-]	e_{d0} [-]	h_s [kPa]	n [-]	α [-]	β [-]	R [-]	m_R [-]	m_T [-]	β_R [-]	χ [-]
33.6°	0.953	0.829	0.474	$9 \cdot 10^6$	0.36	0.076	0.5	10^{-4}	2.3	1.15	0.1	5.5

Table 5.4: Parameters of Hypoplasticity with intergranular strain extension used for the simulation of the cyclic undrained triaxial test

C_{ampl}	C_e	C_p	C_Y	C_{N1}	C_{N2}	C_{N3}
1.6	0.48	0.005	3	$7{\cdot}10^{-4}$	0.06	$2.8 \cdot 10^{-4}$

Table 5.5: Parameters of the HCA model adopted for the simulation of the cyclic undrained triaxial test

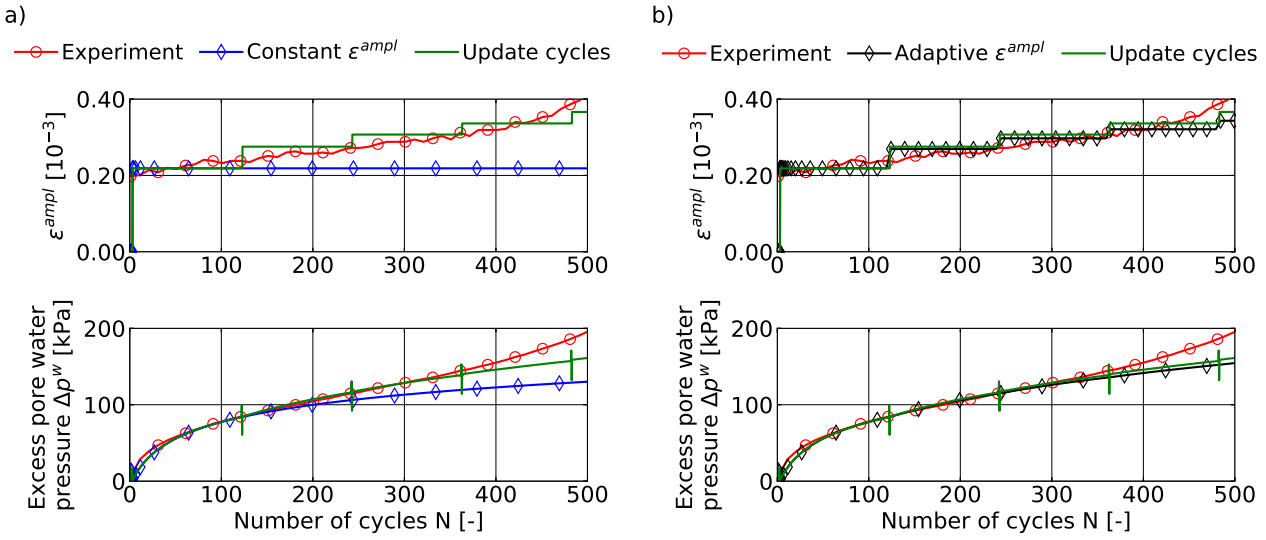

Figure 5.4: Strain amplitude $\varepsilon^{\text{ampl}}$ and excess pore water pressure Δp^w vs. number of loading cycles N measured in the experiment and obtained from the simulations. a) Simulations without update cycles (constant $\varepsilon^{\text{ampl}}$) and with update cycles. b) Simulations with adaptive strain amplitude $\varepsilon^{\text{ampl}}$ in the framework of the local approach and with update cycles. The update cycles and the update using the adaptive strain amplitude are performed at N =120, 240, 360, 480.

Fig. 5.4a displays the strain amplitude $\varepsilon^{\text{ampl}}$ and the excess pore water pressure Δp^w vs. number of loading cycles N for the experiment and a simulation with a constant strain amplitude $\varepsilon^{\text{ampl}}$. In addition, a simulation with incorporation of update cycles at N = 120, 240, 360, 480 is depicted. With ongoing cyclic loading the strain amplitude and the excess pore water pressure increase in the test. The increase of the strain amplitude is a consequence of the decrease in soil stiffness due to the reduction in effective stress (compression positive). Both simulations predict the excess pore water pressure well up to N = 200. For a higher number of cycles, however, the simulation with constant $\varepsilon^{\text{ampl}}$ underestimates the increase in excess pore water pressure compared to the experiment. The simulation with update cycles is able to capture the increase in $\varepsilon^{\text{ampl}}$, which in turn leads to the prediction of a faster accumulation of excess pore water pressure due to higher accumulation rates according to Eq. (5.8) (self-reinforcing or positive feedback phenomenon).

The simulation using the adaptive strain amplitude in the framework of the local approach and updating $\varepsilon^{\text{ampl}}$ at N = 120, 240, 360, 480 is given in Fig. 5.4b. In the ideal case, this simulation would coincide with the simulation employing update cycles. However, since the simulation using update cycles considers the full cycle whereas the adaptive strain amplitude estimates the secant stiffness at the mean loading, a small deviation of the simulations is observed.

The simulation using update cycles gives slightly larger strain amplitudes compared to the simulation using the adaptive strain amplitude. The difference increases with every update of the strain amplitude since larger strain amplitudes result in larger strain amplitudes at the next update due to stronger relaxation of effective stress.

The same simulations but with an update of the strain amplitude at every 5th cycle (the increment size is 5 cycles per increment and the strain amplitude is updated every increment) using the adaptive strain amplitude is given in Fig. 5.5. A slightly too large strain amplitude and a corresponding moderate overestimation of the excess pore water pressure accumulation for $N < 200$ are observed. For $N > 400$, however, the excess pore water pressure is now in better agreement with the experimental results.

The simulation of the cyclic undrained triaxial tests shows that the adaptive strain amplitude is able to capture the changes in strain amplitude with increasing excess pore water pressure. The application to the simulation of a monopile foundation for OWT foundations is presented in Section 8.4.

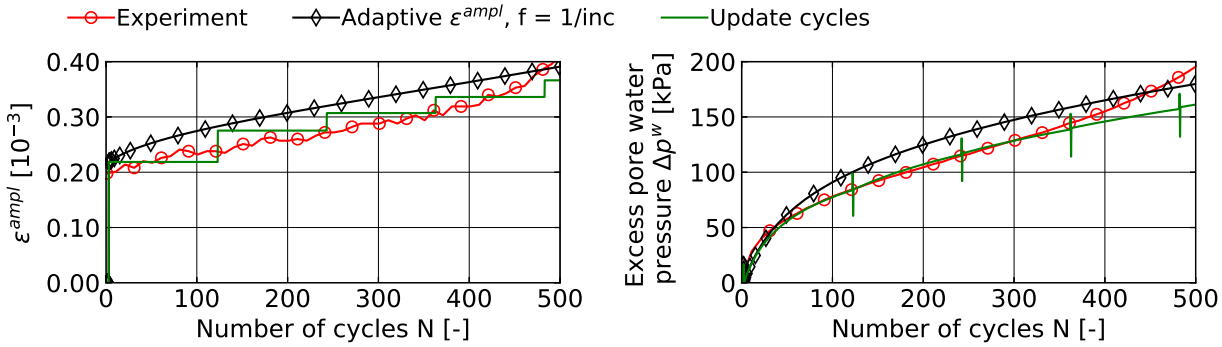

Figure 5.5: Strain amplitude $\varepsilon^{\text{ampl}}$ and excess pore water pressure Δp^w vs. number of loading cycles N measured in the experiment and obtained from the simulations with adaptive strain amplitude $\varepsilon^{\text{ampl}}$ and with update cycles. The strain amplitude is updated in every 5th cycle using the adaptive strain amplitude.

Chapter 6

Contact mechanics

Accounting for contacting bodies adds significant complexity to numerical analyses. Every contact analysis has to consider the change of the position of bodies and is hence geometrically non-linear by nature. The computational handling of contact analyses is nowadays an own branch of research in solid mechanics and is also very relevant in geomechanics, as soil-structure interaction has to be accounted for in many BVPs. Efficient contact search algorithms are also required for *discrete* methods such as the *discrete element method* (DEM), where the contact constraints between many discrete bodies have to be enforced [283, 262]. The performance of mixed finite element/DEM methods, where individual grains are discretised using conventional finite elements, also depends strongly on the applied contact algorithms [236].

Even though the present work is focused on geomechanical aspects, the following chapter covers both the solid-mechanics as well the constitutive modelling related aspects of contact mechanics. The contact discretisation detects the contacting bodies, determines the normal distance and the tangential slip and eventually integrates the contact contributions. The constitutive contact model calculates the change in contact stress based on the increment in relative surface movement computed by the contact discretisation method. One of the most advanced family of contact discretisation techniques are the so-called mortar methods. In general, mortar techniques can be divided into *segment-based* mortar (SBM) [301, 428, 302, 297] and *element-based* mortar (EBM) [122, 124, 388] techniques [117]. In the framework of the SBM technique, the surfaces of the contact pair are divided into finite segments, which are interpolated and integrated similarly as continuum finite elements (no discrete contact elements are introduced, however). In contrast, the EBM technique does not require the segmentation of the surface pair and uses the integration points (existing or potentially additionally created) of the edges/surfaces of the underlying finite elements for the surface integration, analogous

to the integration of regular (constant) external tractions.

In contrast to simpler contact discretisation techniques (e.g. the Node-to-Surface (NTS) method implemented in many finite element codes), both mortar techniques satisfy contact patch tests used to evaluate the performance of the contact discretisation technique [2]. The Babuška-Brezzi stability requirements can be satisfied as well [422]. In addition, determination and integration of the contact stresses using mortar methods is in general not (strongly) dependent on the discretisation of the underlying continuum and the methods are suitable for large-deformation analyses. Mortar methods allow for a local refinement of the geometry of the contacting surfaces, resulting in a smoother distribution of contact stresses compared to simpler contact discretisation techniques. A refinement is in particular appealing for the incorporation of state-dependent constitutive interface models, such as used for soils. This is due to their sensitivity towards small changes in strain (in particular changes of strain direction) caused by (spatially) discontinuous relative surface movements and jumps in contact stresses which can occur when using less advanced contact discretisation techniques. Furthermore, using quadratically interpolated finite elements, as often applied in computational geomechanics, is troublesome in combination with the NTS method [425], whereas such limitations are not faced using mortar methods.

Mortar methods have originally been proposed for the decomposition of domains [46] and were only later applied to contact mechanics. The first application of the mortar technique as contact discretisation method was reported by [339, 440, 285]. These early versions of the mortar technique have then been extended by [301, 428] to allow for frictional contact and consideration of large-deformations for 2D applications. [427] later developed a mortar method for self contact taking into account large-deformations as well. [302] presented a 3D mortar method and an extension for quadratically interpolated finite elements. [388] developed an EBM approach for 2D using Lagrange multipliers including frictional forces. The division of the surfaces into segments is not required, which saves computational time and makes the implementation more straightforward. A comparison of segment-based vs. element-based integration in the framework of the mortar method has been presented by [117], concluding that the SBM is slightly more accurate. [296] developed a mortar contact technique for fluid-structure interfaces using dual Lagrange multipliers [298], allowing for static condensation of the additional unknowns introduced by the Lagrange multiplier. In [342] the implementation of the mortar method in the open-source finite element code `Calculix`[1] has been presented. [116] proposed a 3D mortar method for refined analysis of sharp corners and edges. An overview

[1] `Calculix` is a finite element code for structural mechanics applications. The interested reader is referred to www.calculix.de.

over proposed mortar contact techniques can be found in [203]. Early applications of mortar methods in geomechanics are reported e.g. in [123]. In more recent work, mortar methods have also been used in combination with hydro-mechanically coupled finite elements considering partially drained conditions to study pile installation processes [326, 325]. In addition, the analysis of unsaturated soils employing mortar contact techniques has been reported in [140].

Both a 2D/3D large-deformation EBM and a 2D SBM contact discretisation method considering friction and using a numerical differentiation scheme for the calculation of a consistent Jacobian are developed and implemented in the framework of this thesis. The numerical differentiation scheme is advantageous in case complex interface models are used, for which no consistent Jacobian can be derived analytically. Both contact discretisation methods consider the state-dependency of the friction model such as necessary for a hypoplastic interface model. A zero-thickness contact element approach is used for both mortar methods[2]. The SBM contact discretisation technique is applied for the large-deformation analysis of vibratory pile driving in water-saturated soil considering friction and strongly non-linear constitutive (interface) models for the first time in this thesis. Compared to existing work, these simulations add complexity not only due to the additional non-linearities but also because of non-conforming meshes (i.e. differing element sizes of the paired surfaces) with frequently changing node connectivities due to the large penetration depth of the pile during the installation process. So far, it is unclear if the SBM method is superior in terms of efficiency to the less advanced EBM discretisation for such analyses since the required evaluation of the mortar segments has to be performed very frequently.

The second part of this chapter is devoted to constitutive contact modelling, also referred to as constitutive interface modelling. A novel procedure to use existing constitutive continuum models for the mechanical description of the constitutive interface behaviour is presented. In addition, an interface model for high-cyclic loading based on the HCA model is proposed. The novel interface models are validated using monotonic and cyclic simple interface shear tests.

6.1 Notation

The basic features of the mechanical description of the contact problem are presented first, whereby these apply independently of the chosen contact discretisation method. Classically,

[2]Nowadays, zero-thickness contact elements are the norm. Only very few finite element codes still use discrete contact elements. Discrete contact elements are limited to merely small relative tangential movements. Such restrictions do not exist for zero-thickness contact elements.

one surface of the pair is denoted as the slave ($\sqcup^{(1)}$) (i.e. the surface with the finer mesh) and the other as master ($\sqcup^{(2)}$) surface. Recalling Eq. (3.28), the surface traction is defined by

$$\boldsymbol{t} = \boldsymbol{\sigma} \cdot \boldsymbol{n}^{(1)}, \tag{6.1}$$

wherein $\boldsymbol{n}^{(1)}$ is the normal vector of the slave surface. The normal vector of the master surface $\boldsymbol{n}^{(2)}$ is given by

$$\boldsymbol{n}^{(2)} = -\boldsymbol{n}^{(1)}. \tag{6.2}$$

The contact stress of the contact pair can be separated in its normal and tangential components, viz.

$$\boldsymbol{t} = \boldsymbol{t}_N + \boldsymbol{t}_T. \tag{6.3}$$

The normal stress component t_N (negative for compression) and the normal stress vector $\boldsymbol{t}_N$ are

$$t_N = -\boldsymbol{n}^{(2)} \cdot \boldsymbol{\sigma} \cdot \boldsymbol{n}^{(1)} \quad \text{and} \quad \boldsymbol{t}_N = -\boldsymbol{n}^{(2)} t_N. \tag{6.4}$$

The (total) normal stress can be decomposed according to Terzaghi's principle in

$$t_N = t'_N - p^w, \tag{6.5}$$

where the effective normal stress t'_N and the (intrinsic) pore water pressure p^w (positive for compression) are introduced. The tangential stress vector is defined by

$$\boldsymbol{t}_T = \boldsymbol{t} - \boldsymbol{t}_N = (\mathbf{I} - \boldsymbol{n}^{(2)} \otimes \boldsymbol{n}^{(2)}) \cdot \boldsymbol{t}. \tag{6.6}$$

The minimum distance between slave and master nodes is evaluated by the euclidean norm

$$\boldsymbol{x}^{(2)}(\boldsymbol{x}^{(1)}) = \arg(\min \|\boldsymbol{x}^{(1)} - \boldsymbol{x}^{(2)}\|) \tag{6.7}$$

and the gap $\boldsymbol{g}$ calculated using

$$\boldsymbol{g} = \boldsymbol{X}^{(1)} + \boldsymbol{u}^{(1)} - (\boldsymbol{X}^{(2)} + \boldsymbol{u}^{(2)}) = \boldsymbol{g}_0 + \boldsymbol{u}^{(1)} - \boldsymbol{u}^{(2)}, \tag{6.8}$$

where $\boldsymbol{g}_0$ is the gap in the reference configuration and $\boldsymbol{u}$ the displacement. Similar to the contact stress, the contact gap has a normal

$$\boldsymbol{g}_N = \boldsymbol{n}^{(2)} \otimes \boldsymbol{n}^{(2)} \cdot \boldsymbol{g} \tag{6.9}$$

and a tangential part

$$\boldsymbol{g}_T = (\mathbf{I} - \boldsymbol{n}^{(2)} \otimes \boldsymbol{n}^{(2)}) \cdot \boldsymbol{g}. \tag{6.10}$$

Conventionally, the contact pair has to satisfy the following conditions:

- Only contact pressure is possible: $t_N \leq 0$
- A penetration is not allowed: $g_N \geq 0$
- If the surfaces are not in contact, the contact stress is zero. If the gap is zero, the stress is not equal to zero. These so-called *complementary conditions* are expressed by $g_N t_N = 0$

The three conditions are also known as the *Karush-Kuhn-Tucker* (KKT) conditions. The contact conditions are interpreted as constraints in mechanical terms. These constraints can represent a condition on the displacement of two contact points and prevent them from penetrating into each other. In water-saturated soil, a structure (e.g. a pile) can not separate from the water as long as no cavitation takes place allowing for positive values of t_N (and non-zero normal contact stress despite $g_N > 0$). This means that for positive values of g_N, the effective stress component t'_N is zero and the pore water pressure p^w takes negative values. Thus, $t_N = -p^w$ holds in this case.

For the contact constraint enforcement, the *penalty regularisation* and the *Lagrange multiplier* method are common approaches. Other methods such as the so-called *direct elimination*, *perturbated Lagrange* formulation and the *augmented Lagrange* method exist but are not considered in this work. For an overview over contact enforcement techniques and their advantages and disadvantages the interested reader is referred to [424]. The Lagrange multiplier method and the penalty regularisation are introduced in the following.

6.2 Contact constraint enforcement

In the general case, the weak form of the balance of linear momentum introduced in Eq. (3.54) is based on a variational formulation, which corresponds to an energy functional. For the introduction of the contact constraints $\boldsymbol{c}(\boldsymbol{u})$, the variational formulation is first considered. Mathematically, the stationarity solution of the potential $\pi(\boldsymbol{u})$ in the domain Ω under the constraint

$$\boldsymbol{c}(\boldsymbol{u}) = \boldsymbol{0} \tag{6.11}$$

is sought. The penalty regularisation and Lagrange multiplier method are used to enforce Eq. (6.11), which are introduced in the next sections. Following, a weak form in analogy to the form obtained in Chapter 3, which is used for the finite element discretisation, is obtained by variation.

6.2.1 Lagrange multiplier method

The constraint $\boldsymbol{c}(\boldsymbol{u})$ is added to the internal potential and multiplied by the Lagrange multiplier (LM) $\boldsymbol{\lambda}$, viz.

$$\bar{\pi}^{LM}(\boldsymbol{u}) = \pi^{\text{int}}(\boldsymbol{u}) + \int_{\Omega} \boldsymbol{\lambda} \cdot \boldsymbol{c}(\boldsymbol{u}) \mathrm{d}\Omega. \tag{6.12}$$

The weak form is obtained by variation with respect to the primary variables (the displacement $\boldsymbol{u}$ and the Lagrange multiplier $\boldsymbol{\lambda}$), which is obtained as

$$\delta\bar{\pi}^{LM}(\boldsymbol{u}, \boldsymbol{\lambda}) = \delta_u\bar{\pi}^{LM}(\boldsymbol{u}, \boldsymbol{\lambda}) + \delta_\lambda\bar{\pi}^{LM}(\boldsymbol{u}, \boldsymbol{\lambda}) \quad \text{with} \tag{6.13}$$

$$\delta_u\bar{\pi}^{LM}(\boldsymbol{u}, \boldsymbol{\lambda}) = \delta_u\pi^{\text{int}}(\boldsymbol{u}) + \int_{\Omega} \boldsymbol{\lambda} \cdot \delta_u\boldsymbol{c}(\boldsymbol{u}) \mathrm{d}\Omega \quad \text{and} \tag{6.14}$$

$$\delta_\lambda\bar{\pi}^{LM}(\boldsymbol{u}, \boldsymbol{\lambda}) = \int_{\Omega} \delta_\lambda\boldsymbol{\lambda} \cdot \boldsymbol{c}(\boldsymbol{u}) \mathrm{d}\Omega. \tag{6.15}$$

$\delta\pi^{\text{int}}(\boldsymbol{u})$ corresponds to the weak form of the balance equations derived in Chapter 4. Since the governing equations considered in this work do not only discretise the solid displacement but also the fluid displacements, $\delta\pi^{\text{int}}(\boldsymbol{u})$ can be the internal potential of any of those phases.

The Lagrange multipliers are spatially discretised at the contact nodes, which is done by the finite element method in the same manner as for other primary variables (h: discretised), i.e.

$$\boldsymbol{\lambda}_h = \sum_I N_I \boldsymbol{\lambda}_I \quad \text{and} \tag{6.16}$$

$$\delta\boldsymbol{\lambda}_h = \sum_I N_I \delta\boldsymbol{\lambda}_I. \tag{6.17}$$

The LM method gives, in contrast to the penalty regularisation, the exact contact stress enforcing the KKT conditions rigorously. However, it enlarges the SOE due to the additional primary variables and leads to a saddle point problem where the LHS can be ill-conditioned.

6.2.2 Penalty method

In analogy to the Lagrange multiplier method, the internal potential is expanded by the constraint $\boldsymbol{c}(\boldsymbol{u})$

$$\bar{\pi}^{\text{PM}}(\boldsymbol{u}) = \pi^{\text{int}}(\boldsymbol{u}) + \frac{1}{2}\varepsilon \int_{\Omega} \boldsymbol{c}(\boldsymbol{u}) \cdot \boldsymbol{c}(\boldsymbol{u}) \mathrm{d}\Omega \tag{6.18}$$

using the penalty factor ε. The weak form follows again by variation, noting that the penalty factor is a constant independent of the primary variables, viz.

$$\delta\bar{\pi}^{\text{PM}}(\boldsymbol{u}) = \delta\pi^{\text{int}}(\boldsymbol{u}) + \varepsilon \int_{\Omega} \boldsymbol{c}(\boldsymbol{u}) \cdot \delta\boldsymbol{c}(\boldsymbol{u}) \mathrm{d}\Omega. \tag{6.19}$$

Unlike the LM method, the penalty method does not increase the size of the SOE, but it can also lead to poor conditioning of the stiffness matrix depending on the value of the penalty factor. In addition, the solution may depend on ε if the value is poorly chosen.

6.2.3 Contribution to the balance equations

Enforcing the KKT conditions using the LM method and separating the contact stress in its normal and tangential part, the potential associated with contact enforcement is defined by

$$\bar{\pi}_c^{\mathrm{LM}} = \int_{\Gamma^c} (\lambda_N g_N + \boldsymbol{\lambda}_T \cdot \boldsymbol{g}_T) \mathrm{d}\Gamma^c, \tag{6.20}$$

where the Lagrange multipliers correspond to the normal stress $t_N = \lambda_N$ and the tangential stress $\boldsymbol{t}_T = \boldsymbol{\lambda}_T$. Note that the contact contribution is integrated over the active contact area Γ^c. Variation of the potential leads to the contact contribution to the spatially discretised balance equations introduced in Chapter 4 given by

$$R_c^{\mathrm{LM}} = \int_{\Gamma^c} (\lambda_N \delta g_N + \boldsymbol{\lambda} \cdot \delta \boldsymbol{g}_T) \mathrm{d}\Gamma^c + \int_{\Gamma^c} (\delta\lambda_N g_N + \delta\boldsymbol{\lambda}_T \cdot \boldsymbol{g}_T) \mathrm{d}\Gamma^c. \tag{6.21}$$

The potential associated with contact enforcement using the penalty method is defined as

$$\bar{\pi}_c^{\mathrm{PM}} = \frac{1}{2} \int_{\Gamma^c} (\varepsilon_N (g_N)^2 + \varepsilon_T \boldsymbol{g}_T \cdot \boldsymbol{g}_T) \mathrm{d}\Gamma^c \tag{6.22}$$

and variation leads to the contribution to the balance equations given by

$$R_c^{\mathrm{PM}} = \int_{\Gamma^c} (\varepsilon_N g_N \delta g_N + \varepsilon_T \boldsymbol{g}_T \cdot \delta \boldsymbol{g}_T) \mathrm{d}\Gamma^c. \tag{6.23}$$

The determination of the gap, stress as well as the integration over the active contact area depends on the contact discretisation technique used, which are introduced in the following.

6.3 Element-based mortar method

Initially, the node-to-node connectivity of the contacting bodies is evaluated using the minimum euclidean distance defined by Eq. (6.7). The node-to-node connectivity for a contact pair using quadratically interpolated 2D finite elements is schematically shown in Fig. 6.1. Note that the connectivity can change during an analysis due to movement of the two bodies.

Based on the node-to-node connectivity, the minimum distance between the master and the slave surface is calculated using the *convective coordinate* $\bar{\xi}$ (taking values from -1 to 1) along

the master surface, which is illustrated in Fig 6.2. An orthogonal projection of the coordinates $\boldsymbol{x}_I^{(1)}$ of slave node I onto the master surface $\Gamma_c^{(2)}$ is performed for this purpose. This is done by enforcing the tangential vector of the master surface $\boldsymbol{x}_{,\xi}^{(2)}(\bar{\xi}^{(2)})$ to be orthogonal to the normal gap vector with minimum magnitude between the master surface and slave node I. The projection is defined by

$$\Big[\sum_J^{\text{nnode}} N_J^{(2)}(\bar{\xi}^{(2)})\boldsymbol{x}_J^{(2)} - \boldsymbol{x}_I^{(1)}\Big] \cdot \boldsymbol{x}_{,\xi}^{(2)}(\bar{\xi}^{(2)}) = R \stackrel{!}{=} 0, \tag{6.24}$$

where the isoparametric description as introduced in Eq. (4.1) is used to calculate the coordinate of the master surface. To numerically find the solution of Eq. (6.24), Newton's method is applied. The required derivative of Eq. (6.24) is given by

$$\begin{aligned} K = \frac{\partial R}{\partial \xi} &= \frac{\partial \boldsymbol{g}_I(\bar{\xi}^{(2)})}{\partial \xi} \cdot \boldsymbol{x}_{,\xi}^{(2)}(\bar{\xi}^{(2)}) + \boldsymbol{g}_I(\bar{\xi}^{(2)}) \cdot \boldsymbol{x}_{,\xi\xi}^{(2)}(\bar{\xi}^{(2)}) \\ &= \sum_J^{\text{nnode}} N_{J,\xi}(\bar{\xi}^{(2)})\boldsymbol{x}_J^{(2)} \cdot \boldsymbol{x}_{,\xi}^{(2)}(\bar{\xi}^{(2)}) + \boldsymbol{g}_I(\bar{\xi}^{(2)}) \cdot \boldsymbol{x}_{,\xi\xi}^{(2)}(\bar{\xi}^{(2)}), \end{aligned} \tag{6.25}$$

with $\boldsymbol{g}_I(\bar{\xi}^{(2)}) = \Big[\sum_J^{\text{nnode}} N_J^{(2)}(\bar{\xi}^{(2)})\boldsymbol{x}_J^{(2)} - \boldsymbol{x}_I^{(1)}\Big]$. The second term in Eq. (6.25) is only relevant for quadratically interpolated finite elements since $\boldsymbol{x}_{,\xi\xi}^{(2)}(\bar{\xi}^{(2)})$ is zero otherwise. Note that using quadratically interpolated finite elements, a projection is performed for both *exterior* (located at the element corner) and *interior* (located at the element edge/on the element face) nodes (see Fig. 6.2).

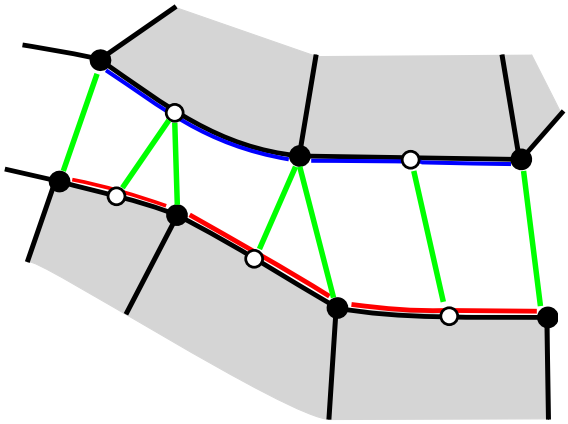

Figure 6.1: Evaluation of the node-to-node connectivity based on the euclidean distance

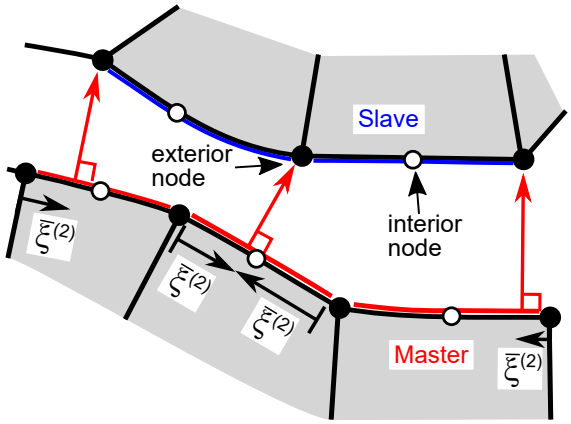

Figure 6.2: Determination of the minimum distance between the paired surfaces using the convective coordinate $\bar{\xi}$ along the master surface

After Eq. (6.24) is satisfied and $\bar{\xi}^{(2)}$ obtained, the normal respectively tangential components of the distance of the slave node are calculated by

$$g_{N,I}^{(1)} = \Big[\sum_{J}^{\text{nnode}} N_J^{(2)}(\bar{\xi}^{(2)}) \boldsymbol{x}_J^{(2)} - \boldsymbol{x}_I^{(1)} \Big] \cdot \boldsymbol{n}^{(2)}(\bar{\xi}^{(2)}) \quad \text{and} \tag{6.26}$$

$$\boldsymbol{g}_{T,I,\alpha}^{(1)} = \Big[\sum_{J}^{\text{nnode}} N_J^{(2)}(\bar{\xi}^{(2)}) \boldsymbol{x}_J^{(2)} - \boldsymbol{x}_I^{(1)} \Big] \cdot \Big[\boldsymbol{\tau}_\alpha^{(2)}(\bar{\xi}^{(2)}) \otimes \boldsymbol{\tau}_\alpha^{(2)}(\bar{\xi}^{(2)}) \Big]. \tag{6.27}$$

$\boldsymbol{n}^{(2)}(\bar{\xi}^{(2)})$ is the normal vector of the master surface at the local coordinate $\bar{\xi}^{(2)}$ and is defined by Eq. (4.4). $\boldsymbol{\tau}_\alpha^{(2)}(\bar{\xi}^{(2)})$ is the tangential vector in direction $\alpha = 1, 2$ (if the problem is three-dimensional) introduced in Eqs. (4.5, 4.6). For frictional problems, the increment of the tangential gap $\Delta \boldsymbol{g}_{T,\alpha}$ is required. It is calculated by

$$\Delta \boldsymbol{g}_{T,I,\alpha}^{(1)} = \Big[\sum_{J}^{\text{nnode}} N_J^{(2)}(\bar{\xi}^{(2)}) \Delta \boldsymbol{u}_J^{(2)} - \Delta \boldsymbol{u}_I^{(1)} \Big] \cdot \Big[\boldsymbol{\tau}_\alpha^{(2)}(\bar{\xi}^{(2)}) \otimes \boldsymbol{\tau}_\alpha^{(2)}(\bar{\xi}^{(2)}) \Big]. \tag{6.28}$$

$g_{N,I}$ and $\boldsymbol{g}_{T,I,\alpha}$ defined in Eqs. (6.26, 6.27) determine the contact distance for node I of the slave surface. In order to determine the respective values for the master node J, the convective coordinate $\bar{\xi}^{(1)}$ along the slave surface is computed, viz.

$$\Big[\sum_{I}^{\text{nnode}} N_I^{(1)}(\bar{\xi}^{(1)}) \boldsymbol{x}_I^{(1)} - \boldsymbol{x}_J^{(2)} \Big] \cdot \boldsymbol{x}_{,\xi}^{(1)}(\bar{\xi}^{(1)}) \stackrel{!}{=} 0. \tag{6.29}$$

The normal and tangential distances given by Eqs. (6.26, 6.27) are then evaluated using $\bar{\xi}^{(1)}$ to obtain $g_{N,J}^{(2)}$ and $\boldsymbol{g}_{T,J}^{(2)}$, defining the normal and tangential gap of the master node J.

For three-dimensional analyses, the convective coordinate has two components since the projection is performed on a face rather than a line. For the projection of the location of the slave node onto the face of the master surface, the convective coordinates $\bar{\xi}^{(2)}$ and $\bar{\eta}^{(2)}$ are evaluated by

$$\Big[\sum_{J}^{\text{nnode}} N_J^{(2)}(\bar{\xi}^{(2)}, \bar{\eta}^{(2)}) \boldsymbol{x}_J^{(2)} - \boldsymbol{x}_I^{(1)} \Big] \cdot \boldsymbol{x}_{,\xi}^{(2)}(\bar{\xi}^{(2)}, \bar{\eta}^{(2)}) \stackrel{!}{=} 0 \quad \text{and} \tag{6.30}$$

$$\Big[\sum_{J}^{\text{nnode}} N_J^{(2)}(\bar{\xi}^{(2)}, \bar{\eta}^{(2)}) \boldsymbol{x}_J^{(2)} - \boldsymbol{x}_I^{(1)} \Big] \cdot \boldsymbol{x}_{,\eta}^{(2)}(\bar{\xi}^{(2)}, \bar{\eta}^{(2)}) \stackrel{!}{=} 0. \tag{6.31}$$

Eqs. (6.30, 6.31) are solved simultaneously using Newton's method. The required derivatives of Eqs. (6.30, 6.31) in analogy to Eq. (6.25) build a two times two matrix in this case. The

local convective coordinates are updated every n-th iteration by

$$\begin{bmatrix} \bar{\xi}^{(2)} \\ \bar{\eta}^{(2)} \end{bmatrix}_{n+1} = \begin{bmatrix} \bar{\xi}^{(2)} \\ \bar{\eta}^{(2)} \end{bmatrix}_{n} - \begin{bmatrix} \boldsymbol{g}_I(\bar{\xi}^{(2)}, \bar{\eta}^{(2)}) \cdot \boldsymbol{x}^{(2)}_{,\xi}(\bar{\xi}^{(2)}, \bar{\eta}^{(2)}) & \boldsymbol{g}_I(\bar{\xi}^{(2)}, \bar{\eta}^{(2)}) \cdot \boldsymbol{x}^{(2)}_{,\eta}(\bar{\xi}^{(2)}, \bar{\eta}^{(2)}) \end{bmatrix}_n \cdot \begin{bmatrix} \frac{\partial}{\partial \bar{\xi}^{(2)}} \left[\boldsymbol{g}_I(\bar{\xi}^{(2)}, \bar{\eta}^{(2)}) \cdot \boldsymbol{x}^{(2)}_{,\xi}(\bar{\xi}^{(2)}, \bar{\eta}^{(2)}) \right] & \frac{\partial}{\partial \bar{\xi}^{(2)}} \left[\boldsymbol{g}_I(\bar{\xi}^{(2)}, \bar{\eta}^{(2)}) \cdot \boldsymbol{x}^{(2)}_{,\eta}(\bar{\xi}^{(2)}, \bar{\eta}^{(2)}) \right] \\ \frac{\partial}{\partial \bar{\eta}^{(2)}} \left[\boldsymbol{g}_I(\bar{\xi}^{(2)}, \bar{\eta}^{(2)}) \cdot \boldsymbol{x}^{(2)}_{,\xi}(\bar{\xi}^{(2)}, \bar{\eta}^{(2)}) \right] & \frac{\partial}{\partial \bar{\eta}^{(2)}} \left[\boldsymbol{g}_I(\bar{\xi}^{(2)}, \bar{\eta}^{(2)}) \cdot \boldsymbol{x}^{(2)}_{,\eta}(\bar{\xi}^{(2)}, \bar{\eta}^{(2)}) \right] \end{bmatrix}^{-1}_{n} . \tag{6.32}$$

In analogy to the EBM method for 2D analyses, the projection is also performed on the faces of the finite elements of the slave surface to evaluate the minimum distances of the master node. Hence, the equations

$$\left[\sum_{I}^{\text{nnode}} N^{(1)}_I(\bar{\xi}^{(1)}, \bar{\eta}^{(1)}) \boldsymbol{x}^{(1)}_I - \boldsymbol{x}^{(2)}_J \right] \cdot \boldsymbol{x}^{(1)}_{,\xi}(\bar{\xi}^{(2)}, \bar{\eta}^{(2)}) \stackrel{!}{=} 0 \quad \text{and} \tag{6.33}$$

$$\left[\sum_{I}^{\text{nnode}} N^{(1)}_I(\bar{\xi}^{(1)}, \bar{\eta}^{(1)}) \boldsymbol{x}^{(1)}_I - \boldsymbol{x}^{(2)}_J \right] \cdot \boldsymbol{x}^{(1)}_{,\eta}(\bar{\xi}^{(2)}, \bar{\eta}^{(2)}) \stackrel{!}{=} 0 \tag{6.34}$$

are iteratively solved.

The evaluation of the convective coordinates for 3D analyses is schematically shown in Fig. 6.3. The grey element face indicates the slave surface for which the local convective coordinates are evaluated solving Eqs. (6.33, 6.34) simultaneously using Newton's method. The convective coordinates are exemplary evaluated for 3 nodes of the master surface.

During the minimisation of Eqs. (6.30 - 6.34) the local coordinates may exceed the boundaries of the element ($\{\|\bar{\xi}\|, \|\bar{\eta}\|\} > 1$). In this case, the minimisation has to continue with the face of the next element to which the local coordinates point. Different cases have to be distinguished when evaluating the element face for which the projection continues depending on the value of the local coordinates and the local node label of the current element. If the convective coordinates reach a "natural" border, i.e. the coordinates are spatially outside the defined surface zone, the mechanism stops.

The normal contact distance and increment in relative tangential movement are determined at the surface nodes. For the integration of the resulting contact stress, an interpolation to the integration points of the surface is made. The integration of surface loads is performed analogously to the integration of finite elements defined by Eqs. (4.12, 4.13). Alternatively, the evaluation of the convective coordinates may be directly done for the coordinates of the integration points of the surface. $\boldsymbol{x}^{(1)}_I$ in Eqs. (6.30, 6.31) and $\boldsymbol{x}^{(2)}_J$ in Eqs. (6.33, 6.34) are replaced

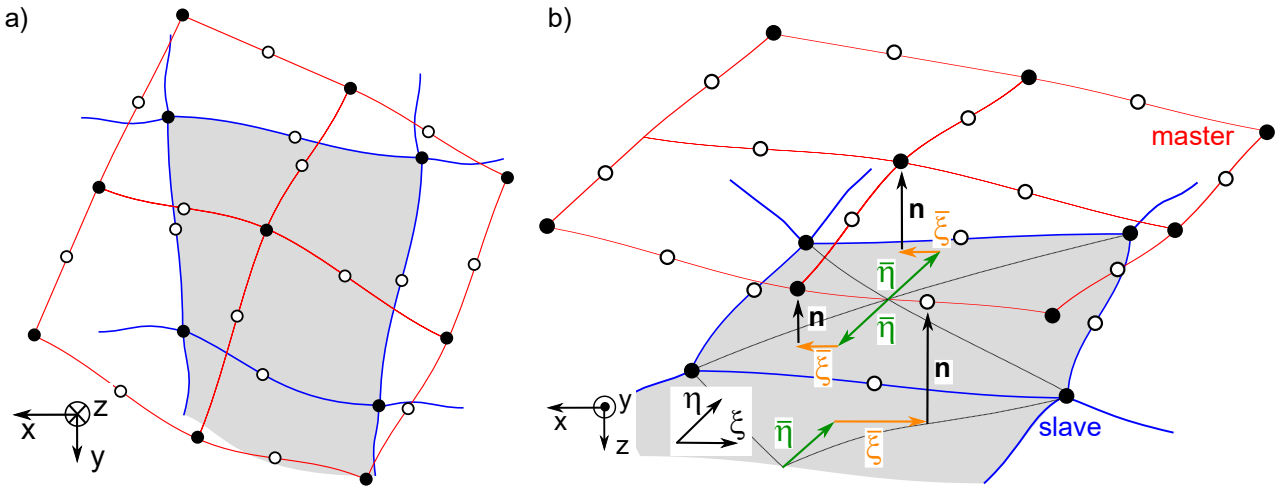

Figure 6.3: Evaluation of the convective coordinates of the slave surface for 3D analyses. Figure a) shows the top-view on the surfaces. The exemplary evaluation of the convective coordinates of the slave surface by projection to three master nodes is given in Fig. b).

by $\sum_I^{\text{nnode}} N_I^{(1)}(\xi_{\text{igp}}^{(1)}, \eta_{\text{igp}}^{(1)})\boldsymbol{x}_I^{(1)}$ and $\sum_J^{\text{nnode}} N_J^{(2)}(\xi_{\text{igp}}^{(2)}, \eta_{\text{igp}}^{(2)})\boldsymbol{x}_J^{(2)}$ in this case. An interpolation of the contact variables is not necessary using this approach. Both techniques are implemented in `numgeo`.

Using elements with linear interpolation, the surface geometry is a non-differentiable function leading to problems using the projection mechanism described in Eqs. (6.30 - 6.34) when kinks between faces of different finite elements exist. In case the local convective coordinates reach beyond the element border, the local tangential vector may jump. This can cause non-convergence of the projection algorithm and a wrong determination of the local convective coordinates. To prevent this, the change of the global coordinate with respect to the local coordinate $\boldsymbol{x}_{,\xi}$ is determined using quadratic interpolation functions even if linearly interpolated finite elements are used. The coordinates of the additional nodes for the quadratic interpolation are obtained by interpolation using the linear shape functions of the actual element. Using this approach, $\boldsymbol{x}_{,\xi}$ is a smooth function and the convergence of Eqs. (6.30 - 6.34) is secured[3].

The implemented EBM method allows adding additional nodes or integration points to the surface. This is beneficial, since the contact stress is in general non-constant with respect to the surface geometry. Its determination and integration is thus more precise if more discrete points on the surface are considered. For this, artificial nodes/integration points are generated at the surface, which are located at the local coordinates of the underlying finite elements at

[3]Note that in the literature an averaging of the normal/tangential vectors of the two faces of the linearly interpolated finite elements is conventionally performed [428, 297].

which integration points would exist if finite elements with higher order would be used. Hence, the surface operations are performed as if finite elements with a higher order of interpolation are used, but the drawback of higher computational effort in computation of the continuum using a larger number of discrete points is circumvented.

The EBM method is implemented in combination with the penalty regularisation introduced in Section 6.2.2. The normal contact contribution to the force equilibrium using the EBM discretisation technique is given by

$$\boldsymbol{r}_{N,I}^{(i)} = \sum_{\text{igp}}^{\text{ngp}} N_I^{(i)}(\xi_{\text{igp}}^{(i)}) t_{N,\text{igp}}^{(i)} \boldsymbol{n}_{\text{igp}}^{(i)} w_{\text{igp}}^{(i)} j_{\text{igp}}^{(i)} \quad \text{for} \quad i = \{1, 2\}, \tag{6.35}$$

if the contact stress is directly evaluated at the integration points of the finite-element edge or face. The normal contact stress $t_{N,\text{igp}}^{(i)}$ is calculated by multiplying the normal distance with the penalty factor in case of active contact.

For three-dimensional analyses, the contribution to the force equilibrium of the frictional contact forces $\boldsymbol{r}_{T,I}^{(i)}$ is calculated using

$$\boldsymbol{r}_{T,I}^{(i)} = \sum_{\alpha}^{\text{ndim-1}} \sum_{\text{igp}}^{\text{ngp}} N_I^{(i)}(\xi_{\text{igp}}^{(i)}) t_{T,\text{igp},\alpha}^{(i)} \boldsymbol{\tau}_{\text{igp},\alpha}^{(i)} w_{\text{igp}}^{(i)} j_{\text{igp}}^{(i)} \quad \text{for} \quad i = \{1, 2\}. \tag{6.36}$$

The required derivatives of Eqs. (6.35, 6.36) with respect to the primary variables for the LHS are given in Appendix B.2. In Section 6.7, a numerical differentiation scheme for the evaluation of the required derivations of the contact contributions with respect to the primary variables is presented. Validation of the implementation and evaluation of the performance of the EBM method is provided in Section 6.8.

6.4 Segment-based mortar method

The formulation of a segment-based mortar method is presented in the following. Note that some parts of the following section have already been published by the author in [360].

6.4.1 Evaluation of the convective coordinate

Prior to the *segmentation* of the contact surfaces, the evaluation of the convective coordinate $\bar{\xi}$, in analogy to the EBM method, is necessary. As proposed in [428], the projection is always performed using the normal vector at the master surface and not, as done in case of the

EBM method, using the normal vector at the slave and master surface, respectively. This is advantageous for the definitions of the segments as is demonstrated in Fig. 6.4. The exemplary contact pair, which has already been considered to explain the EBM method in Fig. 6.2, is divided into segments used for the SBM method. Figure 6.4a shows the determination of the segments using a definition of the convective coordinate where the tangential vector at both surfaces is used. As is indicated, some surface area at the blue slave surface of the green segment on the left-hand side is lost. The improved evaluation of the convective coordinate evaluating the tangential vectors only at the master surface (displayed in Fig. 6.4b) avoids this shortcoming. The convective coordinate of the slave surface $\bar{\xi}^{(1)}$ is thus calculated using

$$\Big[\sum_{I}^{\text{nnode}} N_I^{(1)}(\bar{\xi}^{(1)}) \boldsymbol{x}_I^{(1)} - \boldsymbol{x}_J^{(2)} \Big] \cdot \boldsymbol{x}_{J,\xi}^{(2)} \stackrel{!}{=} 0 \tag{6.37}$$

in case of the SBM contact discretisation and not by Eq. (6.29) employed by the EBM technique.

Fig. 6.4b also shows the case of two convective coordinates for one node (being the case for the slave node between the brown and aquamarine segment in the centre of the slave surface). This additional projection (*correction projection*) is required, if no projection is performed to a master node (the master node at the brown segment in Fig. 6.4a). Note that the lost surface area of the master surface on the far right-hand side of Fig. 6.4b would not occur in the actual analysis, as long as the hinted slave element on the far right-hand side would be included in the slave surface definition. If this element edge is not included in the surface definition, the surface area of the master surface would be lost, since no orthogonal projection to the master node on the far right-hand side is possible.

6.4.2 Determination of segments

Having determined the convective coordinates of both surfaces, the division of the contacting surfaces into finite segments, analogous to the division of a continuum in finite elements, has to be performed. This subdivision of the surfaces into segments is beneficial, because it allows to exactly determine and integrate the contact stress with a possibility of a locally refined spatial discretisation of the contact surfaces.

As displayed in Fig. 6.5, six different types of segments are identified, which differ in the way the borders of the segment are defined. The border of a segment is either an existing node or the value of the convective coordinate $\bar{\xi}^{(i)}$. Note that the segment is always defined according

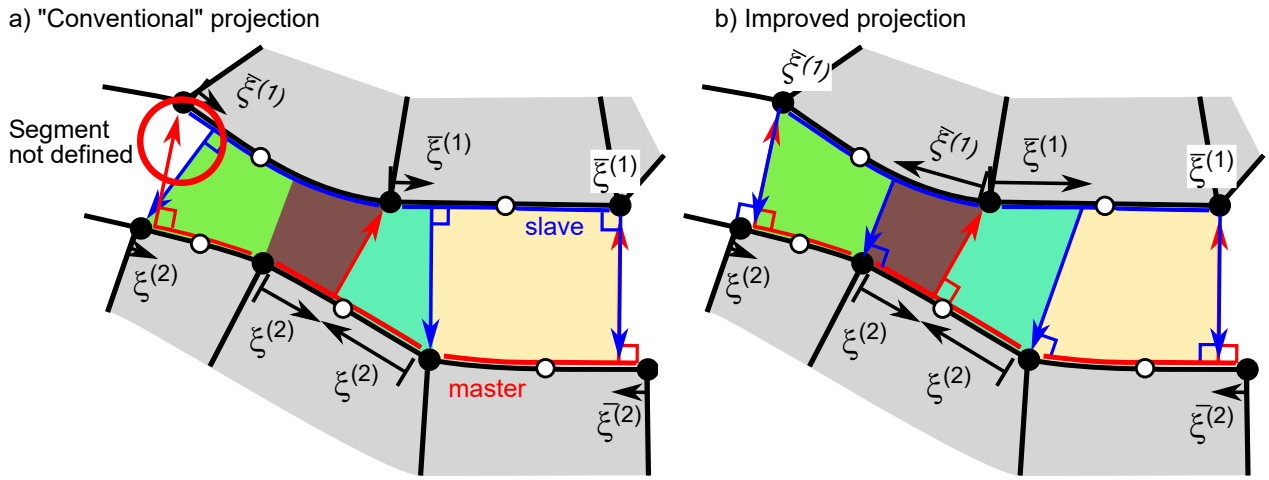

Figure 6.4: Contact discretisation using the SBM approach. a) Segmentation using the conventional projection scheme with normal vectors evaluated alongside the master and the slave surface, respectively. b) Improved scheme for which the normal vectors are evaluated only at the master surface using Eqs. (6.24, 6.37). The segments after evaluation of the convective coordinates are depicted as well.

to the nodes and convective coordinates at the slave surface, i.e. in Fig. 6.5 the criteria defining the type of segment refer to the convective coordinate evaluated at the slave surface. In case of the segment type I for instance, both convective coordinates of the finite element at the slave surface are outside the edge of the actual finite element. Hence, the segment is formed by two existing nodes on the slave surface. Both convective coordinates of the master surface, however, are on the same edge of the identical finite element.

The segment types V and VI are established by the same nodes as in case of types II and III, respectively. However, the convective coordinate for types III and V starts from the same node that forms the segment while in cases II and VI the convective coordinate of a different node is used. This distinction is only important in the context of the implementation. As proposed by [296], only exterior nodes are projected in case of finite elements with interpolation order two or higher. Interior nodes are not involved in the segmentation process and are located inside of the segments.

As stated in [424], the segmentation can be difficult to program. This is in particular the case when the numbers of nodes of both surfaces are comparable. In contrast to the EBM approach, a much finer disretisation of one surface is therefore not a potential source of errors but simplifies the evaluation of the segments of the SBM technique. If one surface has more nodes alongside its entire length than the other, an algorithm for the evaluation of the segments

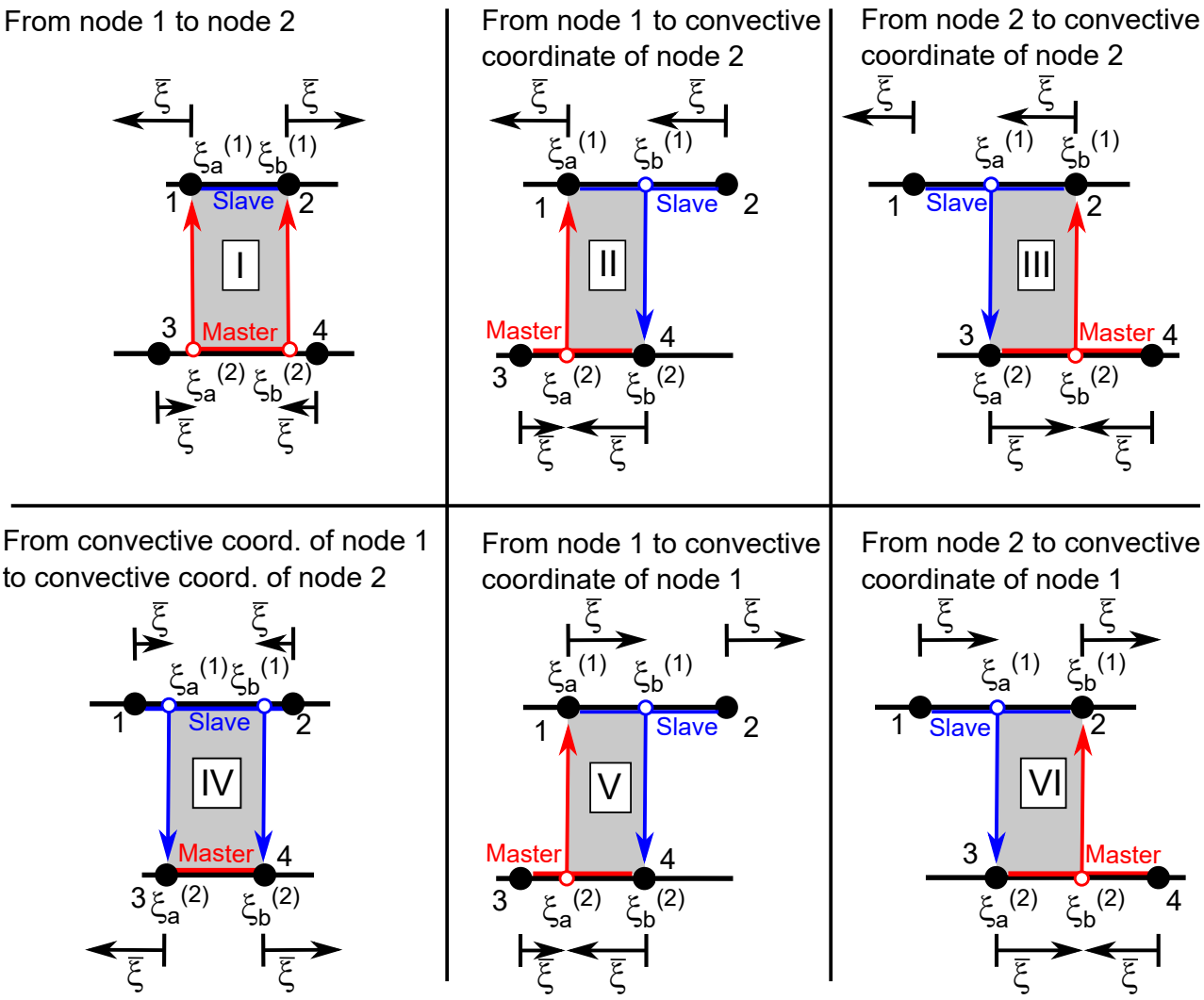

Figure 6.5: Definition of different types of segments in dependence of the arrangement of nodes and convective coordinates. An unfilled circle represents the location of the convective coordinate while filled dots are existing (exterior) nodes.

as formulated in Algorithm 1 can be applied. In some cases a node of the finer surface may be connected to a node of the coarser surface which is however connected to a another, third node of the finer surface. In this case the border of the segment is different for each surface and the segmentation mechanism fails. To prevent this, the already mentioned *correction projection* of the node of the coarser surface is performed with the premise that this node is now connected to the aforementioned first node of the finer surface.

If the number of nodes of the two surfaces differs significantly but no surface can be defined as being finer discretised for the entire contact zone, the herein adopted scheme, where the segmentation is performed based on the finer discretised surface (i.e. the slave surface), may

Algorithm 1: Evaluation of segments for simple cases (one surface finer than the paired surface)

Result: Segments S, type of the segments, node labels of the segments

1 **for** *$ielem^{(1)}$ in all finite elements of the finer surface (1)* **do**
2 Calculate the convective coordinates $\xi_a^{(1)}$ and $\xi_b^{(1)}$ of the exterior nodes for $ielem^{(1)}$
3 Determine the type of segment according to Fig. 6.5
4 Evaluate the segments S for $ielem^{(1)}$ based on $\xi_a^{(1)}$ and $\xi_b^{(1)}$
5 Save the nodes and convective coordinates of the finer (node number 1 and 2) as well as of the coarser (node number 3 and 4) surface (see Fig 6.5)
6 **end**

fail. It is worth mentioning that the segmentation increases in complexity in case of 3D analyses. Special algorithms, such as the *Sutherland-Hodgman* polygon clipping algorithm [371] employed by [342, 302] or Delaunay triangulation [167] have to be applied in that case.

6.4.3 Interpolation of segments

The variables within each segment are interpolated using the local coordinate η, which takes values from -1 to 1, analogously to the local coordinate of regular (rectangular/brick) finite elements. The order of the interpolation function is defined according to the number of existing and projected nodes forming the segment. The mapping from the local finite element edge coordinate $\xi^{(1)}$ of the slave surface to the local coordinate of the segment formed at the slave surface in case of linear finite elements is performed by

$$\xi^{(1)}(\eta) = \frac{1}{2}(1-\eta)\xi_a^{(1)} + \frac{1}{2}(1+\eta)\xi_b^{(1)}, \tag{6.38}$$

wherein $\xi_a^{(1)}$ is the first local coordinate of the segment and $\xi_b^{(1)}$ the second. As is indicated in Fig. 6.5, $\xi_a^{(1)}$ and $\xi_b^{(1)}$ can either represent projections using the convective coordinate or existing nodes. A similar interpolation rule is set up for the master side of the segment, viz.

$$\xi^{(2)}(\eta) = \frac{1}{2}(1-\eta)\xi_a^{(2)} + \frac{1}{2}(1+\eta)\xi_b^{(2)}. \tag{6.39}$$

In case of quadratically interpolated finite elements, the following interpolation of the local coordinate of the element with respect to the local coordinate of the segment is used

$$\xi^{(i)}(\eta) = -\frac{1}{2}\eta(1-\eta)\xi_a^{(i)} + \frac{1}{2}\eta(1+\eta)\xi_b^{(i)} + (1-\eta^2)\xi_c^{(i)}, \tag{6.40}$$

wherein $\xi_c^{(i)}$ is $(\xi_a^{(i)}+\xi_b^{(i)})/2$ and $i = \{1, 2\}$. As has been mentioned earlier, the contact contributions of the segments can be integrated using a different order as employed for the underlying finite element. Often, a higher order of integration of the segment compared to the order of integration of the finite element is applied [296]. This is advantageous since the distance between slave and master surface can vary strongly within one segment if the mesh is coarse. For higher order of integration, the distance is calculated in more integration points of the segment thus allowing for a more precise calculation of the gap and a better approximation of the contact stress, which is often spatially irregularly distributed.

For each integration point *igp* of the segment, the coordinates $\boldsymbol{x}_{\text{igp}}^{(i)}$ and contact stress $\boldsymbol{t}_{\text{igp}}$ are interpolated using

$$\boldsymbol{x}_{\text{igp}}^{(i)} = \sum_{L}^{\text{nnode}} N_L^{\text{seg}}(\eta_{\text{igp}}) \cdot \boldsymbol{x}_L^{(i)} \quad \text{and} \tag{6.41}$$

$$\boldsymbol{t}_{\text{igp}} = \sum_{L}^{\text{nnode}} N_L^{\text{seg}}(\eta_{\text{igp}}) \cdot \boldsymbol{t}_L. \tag{6.42}$$

η_{igp} is the local coordinate of the integration point, N^{seg} is the interpolation function of the segment, $\boldsymbol{x}_L$ is the (global) coordinate of a, possibly "imaginary", node L (unfilled circle in Fig. 6.5) and $\boldsymbol{t}_L$ is the (total) contact stress vector at node L from a previous calculation step. Note that for hydro-mechanically coupled analyses, the effective normal contact stress is required for the calculation of shear stresses. Therefore, the pore water pressure is interpolated from the nodes of the finite elements to the integration points of the segments to calculate the effective normal contact stress. The effective normal contact stress $t'_{N,\text{igp}}$ at the integration points of the segment is defined by

$$t'_{N,\text{igp}} = t_{N,\text{igp}} + p^w_{\text{igp}} = \sum_{L}^{\text{nnode}} N_L^{\text{seg}}(\eta_{\text{igp}})(t_{N,L} + p^w_L), \tag{6.43}$$

where the interpolation from the nodes introduced in Eq. (6.42) is used.

The nodes L are located at the border (at the local finite element coordinates $\xi_a^{(i)}$ and $\xi_b^{(i)}$) and, if the underlying finite element is quadratically interpolated, in the middle of the segment (at the local finite element coordinate $\xi_c^{(i)}$). They are either imaginary, if the local convective coordinate and the location of the existing finite element nodes are not identical, or identical to existing nodes I otherwise. In case of imaginary nodes, their values have to be obtained using a similar interpolation as in Eqs. (6.41, 6.42) but using the local convective coordinates $\bar{\xi}$ and the values at the existing finite element nodes I. Of course, it is also possible to directly interpolate the nodal values to the integration points of the segments without obtaining them at the borders of the segments first.

State variables are not saved at the integration points of the segments but at the nodes of the finite elements. The values of the integration points thus have to be obtained by interpolation from the nodes in every calculation step (i.e. every iteration) since any displacement of the surface pair changes the coordinates of the segments and hence the location of the integration points. In contrast to the integration points of regular finite elements, the integration points of the mortar segment are therefore not "permanent" but are newly created in every calculation step (i.e. in every iteration). Conceptually, this is similar to a (conventional) particle finite element method (PFEM) [179], where the existing nodes are newly connected thereby creating a new set of integration points for which the initial state variables are obtained by interpolation using the saved values at the nodes.

In addition to Eqs. (6.41, 6.42), the relative tangential displacement increment is interpolated, if a frictional contact definition is used. If the constitutive contact model incorporates additional state variables, an additional interpolation is required.

Once the (current) global coordinates of every integration point of the slave and the master side have been calculated, the distance between the integration points is determined for each of the points using

$$\boldsymbol{g}_{\text{igp}} = \boldsymbol{x}^{(2)}_{\text{igp}} - \boldsymbol{x}^{(1)}_{\text{igp}}. \tag{6.44}$$

The normal and tangential component of the distance are

$$g_{N,\text{igp}} = (\boldsymbol{x}^{(2)}_{\text{igp}} - \boldsymbol{x}^{(1)}_{\text{igp}}) \cdot \boldsymbol{n}^{(1)}_{\text{igp}} \quad \text{and} \tag{6.45}$$

$$\boldsymbol{g}_{T,\text{igp},\alpha} = (\boldsymbol{x}^{(2)}_{\text{igp}} - \boldsymbol{x}^{(1)}_{\text{igp}}) \cdot (\boldsymbol{\tau}^{(1)}_{\text{igp},\alpha} \otimes \boldsymbol{\tau}^{(1)}_{\text{igp},\alpha}), \tag{6.46}$$

where $\boldsymbol{\tau}_{\text{igp},\alpha}$ is the (normalised) tangential vector in direction $\alpha = 1, 2$ (if the problem is three-dimensional). In case of two-dimensional analyses, Eq. (6.46) can be rewritten to

$$g_{T,\text{igp}} = (\boldsymbol{x}^{(2)}_{\text{igp}} - \boldsymbol{x}^{(1)}_{\text{igp}}) \cdot \boldsymbol{\tau}^{(1)}_{\text{igp},1}. \tag{6.47}$$

For frictional analyses, an incremental formulation is required. Similar to Eq. (6.28), the increment in relative tangential movement $\Delta g_{T,\text{igp}}$ is calculated using

$$\Delta g_{T,\text{igp}} = (\Delta \boldsymbol{u}^{(2)}_{\text{igp}} - \Delta \boldsymbol{u}^{(1)}_{\text{igp}}) \cdot \boldsymbol{\tau}^{(1)}_{\text{igp},1}. \tag{6.48}$$

The increment of displacement $\Delta \boldsymbol{u}_{\text{igp}}$ in Eq. (6.48) is obtained using a similar interpolation as used in Eq. (6.41).

For the integration of the segments, 5 integration points are used for each segment as proposed in [428, 296]. The local coordinates and integration weights are calculated using Eqs. (4.10,

4.11). The higher integration order allows for a more refined determination of the, usually with respect to the local coordinate of the segment non-constant, distribution of the normal and tangential distances given by Eqs. (6.45, 6.46) and hence the contact stress. An integration with a larger number of integration points (7 and 9) is implemented as well. However, for typical meshes (i.e. for a typical number of nodes and elements required to represent a surface geometry adequately) used, 5 integration points have proven to be a good compromise between accuracy and computational cost. As mentioned earlier, the integration points are created in every calculation step, allowing to change the number of integration points at any time of the analysis. If strongly fluctuating values and complex geometries are obtained for a segment at a certain stage of an analysis, an increase of the number of integration points during the calculation is therefore possible.

6.4.4 Contribution to the balance equations, integration and extrapolation

The contribution to the balance equation of linear momentum in case of active contact is

$$\boldsymbol{r}_I^C = \int_{\Gamma^C} \boldsymbol{t}_I^C \mathrm{d}\Gamma^C, \tag{6.49}$$

wherein $\boldsymbol{r}_I^C$ is the contact force at node I, Γ^C is the contact area and $\boldsymbol{t}_I^C$ the contact stress. In analogy to the definition of the contact contribution to the balance equations provided in Section 6.2.3, the contact stress is split in normal and tangential stress

$$\boldsymbol{t}_I^C = t_{N,I}\boldsymbol{n}_I + \boldsymbol{t}_{T,I}. \tag{6.50}$$

Eq. (6.49) is numerically integrated for the slave ($i = 1$) and master ($i = 2$) surface using

$$\boldsymbol{r}_I^{C,(i)} = \sum_{\mathrm{igp}}^{\mathrm{ngp}} N_I^{(i)}[\xi^{(i)}(\eta_{\mathrm{igp}})]\boldsymbol{t}_{\mathrm{igp}}^{(i)} w_{\mathrm{igp}} j_{\mathrm{igp}}^{(i)}, \tag{6.51}$$

which is a 1D form of the general numerical integration scheme given in Eq. (4.12). Note that $N_I^{(i)}$ is the interpolation function of the edge of the finite element underlying the segment for the slave and master side, respectively. It is evaluated according to the local segment coordinate of the integration point of the segment. Note that the normal component of the contact stress $\boldsymbol{t}_{\mathrm{igp}}^{(i)}$ is the same for the slave and the master side in magnitude, but has opposite sign. The local segment coordinate η_{igp} and the integration point weights w_{igp} are shared by the surfaces and hence no exponent indicating the slave or master surface is necessary.

In Eq. (6.51), $j_{\mathrm{igp}}^{(i)} = \left|\left|\frac{\partial \boldsymbol{x}^{(i)}(\xi_{\mathrm{igp}})}{\partial \xi^{(i)}}\right|\right| \frac{\partial \xi^{(i)}(\eta_{\mathrm{igp}})}{\partial \eta}$ takes into account the mapping from the local to the global coordinate system. The second factor describing the change of the local element coordinate ξ with local segment coordinate η is necessary since the segment length differs from the length of the complete element edge in general. $\dfrac{\partial \xi^{(i)}}{\partial \eta}$ yields in case of linearly interpolated elements

$$\frac{\partial \xi^{(i)}}{\partial \eta} = \frac{1}{2}\left(\xi_b^{(i)} - \xi_a^{(i)}\right) \tag{6.52}$$

and in case of quadratically interpolated elements

$$\frac{\partial \xi^{(i)}}{\partial \eta} = -\frac{1}{2}(1-2\eta)\xi_a^{(i)} + \frac{1}{2}(1+2\eta)\xi_b^{(i)} - 2\eta\xi_c^{(i)}. \tag{6.53}$$

The integration of three segments formed at the edge of the quadratically interpolated finite element *ielem* is exemplary shown in Fig. 6.6. The values of the interpolation functions N_I with respect to the local coordinate of *ielem* are given in the plot. The segments I, II and III are also given with their borders according to the local coordinate. Each segment has 5 integration points, which are given in blue for segment I, red for segment II and green for segment III. Their location depends on the local coordinate of the segment η. In order to demonstrate the integration of an arbitrary variable given at the integration points of the segment, a variable with identical value for every integration point is considered. Its distribution with respect to the local coordinate of the element is given by the blue line. For the integration of the variable, the interpolation functions of the three nodes of the quadratically interpolated element *ielem* are evaluated at the location of the integration points of the segments using Eq. (6.40) and integrated using Eq. (6.51). The integrated values obtained at the nodes of *ielem* are given below the plot, being 0.3333 for the corner nodes and 1.3333 for the middle node. These values agree with those obtained by analytical integration of the constant variable with a value of 1 over a line length of 2. Of course, the example is only of academic nature.

After all contact variables (gap, stress and state variables) have been updated at the integration points of the segment, the values have to be extrapolated to the finite element nodes at which they are saved for the next calculation step. The extrapolation is performed in analogy to Eqs. (6.41, 6.42) using

$$\sqcup_L^{(i)} = \sum_{\mathrm{igp}}^{\mathrm{ngp}} N_{\mathrm{igp}}^{(i)}(\eta_L') \cdot \sqcup_{\mathrm{igp}}^{(i)}, \tag{6.54}$$

where η_L' is the *stretched* local coordinate of the point to which the integration point values are extrapolated. As already explained for the interpolation given by Eqs. (6.41, 6.42), the

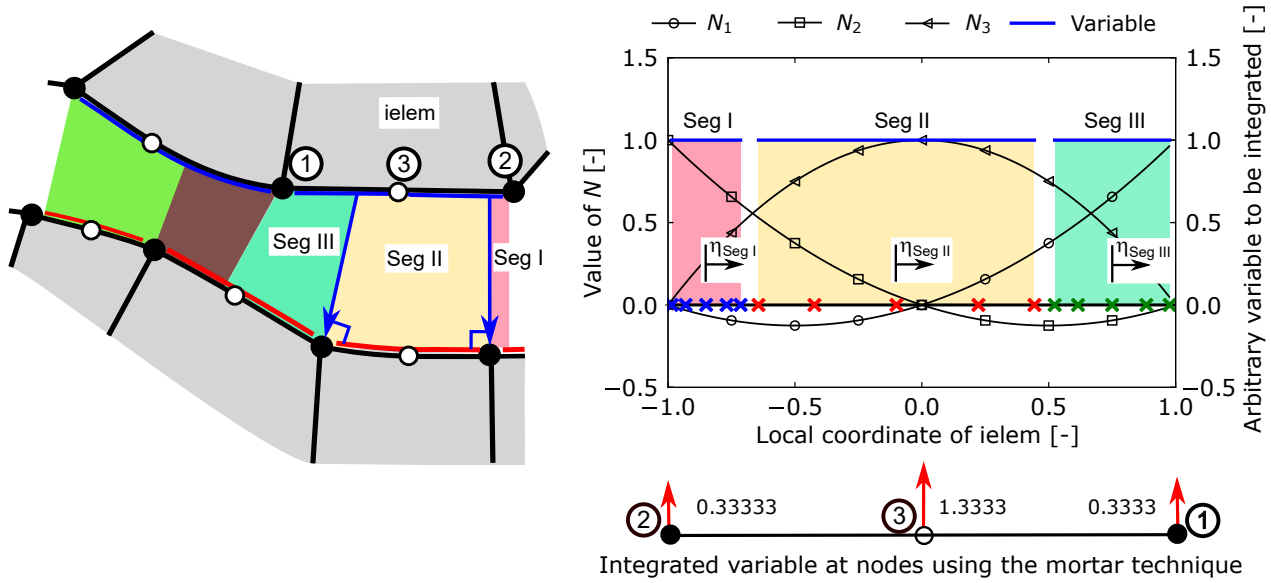

Figure 6.6: Example for the integration of segment variables to finite element node values. The left figure depicts the three segments at the element edge of the finite element *ielem*. The right plot shows the integration of the three segments for an exemplary distribution of an arbitrary variable given in blue. The variable takes the value one at every integration point of every segment to simplify the example. *ielem* is quadratically interpolated using the shape functions $N_{1,2,3}$ with their distributions given in the plot. The integration of each integration point value (given by blue, red and green crosses for each segment separately) is done using the shape functions of the finite element. Note that 5 integration points per segment are used. The integration using the proposed scheme gives the integrated values at the nodes of the finite element given below the plot. The obtained values at the nodes coincide with an analytical integration.

node L is either an imaginary segment border node or an existing node of a finite element. Only in case L is an existing node ($L = I$) an extrapolation is performed and the values are saved at node I.

For an implicit solving scheme using the Newton-Raphson method given in Eq. (4.24), the partial derivatives of the contact contributions with respect to the primary variables discretised in the finite element framework are required. The analytically calculated derivatives for the SBM discretisation technique for simple interface models can be found in Appendix B.2. However, if the constitutive interface model is complex an analytical derivation of the derivatives is not straight-forward and sometimes not even possible. For such cases, a numerical differentiation scheme is introduced in Section 6.7, which is applicable for both contact discretisation techniques, the EBM and the SBM method.

6.5 Contact iterations

Due to the added non-linearities, contact analyses may need special treatment of the constraints in order to achieve good convergence rates if two bodies come into contact driven by Neumann boundary conditions and one of the bodies is not constrained by any Dirichlet boundary condition (e.g. a pile driven by force into soil). If contacts open or close, entries in RHS and LHS with large values are removed or added, respectively. This causes jumps in the solution, causing the global Newton-Raphson iteration to fail to converge. Special *contact iterations* are introduced for such cases. During a contact iteration, the contact contributions to the global system of equations are iteratively refined until no nodes change their contact status and the change in contact stress from one contact iteration to the next is below a tolerance. As long as these two requirements are not met, the updated contact contributions are only added to the slave and not to the master surface. This procedure is given in Algorithm 2. Note that if a previous iteration involved a contact iteration, at least two additional iterations with consideration of the contact contributions to RHS and LHS of the master surfaces are required, i.e. the iteration is not finished in case of convergence if the contact contributions to the master surface are considered for the first time. This is defined in line 19 of Algorithm 2. Otherwise, the displacement of the master body following the first update of the contact contributions is only taken into account with the correction $\mathbf{c}^{(i)}$ and no subsequent call of the contact algorithms is made.

6.6 Integration of contact contributions using serendipity elements

Following the *Taylor-Hood* formulation [378], the solid displacement of the hydro-mechanically coupled finite element formulations ($\mathbf{u}$-p or $\mathbf{u}$-p-$\mathbf{U}$) presented in Chapter 4 is conventionally interpolated using quadratic interpolation functions. The fluid pressure is interpolated using linear interpolation functions. Otherwise, the LBB condition is not fulfilled and numerical stability not secured. For 3D elements, the interpolation functions using 20 nodes are usually applied for the interpolation of the displacement. This so-called *serendipity* element does not use the standard Lagrangian bi/tri-quadratic interpolation functions.

The integration of the shape functions used for quadratically interpolated serendipity elements can lead to a negative area/volume, which is not physical [56, 71]. This is problematic in contact

Algorithm 2: Contact iteration procedure

Result: Updated displacement $\boldsymbol{u}^{(i)}$ of global iteration i

1 **for** $i = 0, 1, 2, ..$ *until convergence* **do**
2 Set $\texttt{contact\_iteration}^{(i)}$ = .false.
3 Assemble element contributions to RHS $\boldsymbol{r}^{\mathrm{elem}(i)}(\boldsymbol{u}^{(i)})$ and LHS $\mathbf{L}^{\mathrm{elem}(i)}(\boldsymbol{u}^{(i)})$
4 Determine the contact contributions RHS $\boldsymbol{r}^{C(i)}(\boldsymbol{u}^{(i)})$ and LHS $\mathbf{L}^{C(i)}(\boldsymbol{u}^{(i)})$
5 **if** *Any nodes changed contact status from i-1 to i or any* $\|\boldsymbol{t}^{C(i)} - \boldsymbol{t}^{C(i-1)}\| > tol$ **then**
6 Set $\texttt{contact\_iteration}^{(i)}$ = .true.
7 Assemble $\boldsymbol{r}^{C(i)}$ and $\mathbf{L}^{C(i)}$ only for slave nodes
8 Add $\boldsymbol{r}^{C(i)}$ and $\mathbf{L}^{C(i)}$ to $\boldsymbol{r}^{\mathrm{elem}(i)}$ and $\mathbf{L}^{\mathrm{elem}(i)}$
9 Solve the SOE given by Eq. (4.25)
10 Update displacement according to Eq. (4.24): $\mathbf{u}^{(i+1)} = \mathbf{u}^{(i)} + \mathbf{c}^{(i)}$
11 Go to line 1
12 **else**
13 Assemble $\boldsymbol{r}^{C(i)}$ and LHS $\mathbf{L}^{C(i)}$ for both surfaces
14 Add $\boldsymbol{r}^{C(i)}$ and $\mathbf{L}^{C(i)}$ to $\boldsymbol{r}^{\mathrm{elem}(i)}$ and $\mathbf{L}^{\mathrm{elem}(i)}$
15 Solve the SOE given by Eq. (4.25)
16 Update displacement according to Eq. (4.24): $\mathbf{u}^{(i+1)} = \mathbf{u}^{(i)} + \mathbf{c}^{(i)}$
17 Check for global convergence
18 **end**
19 **if** $\texttt{contact\_iteration}^{(i-1)}$ = *.true.* **then**
20 Go to line 1
21 **else**
22 If global convergence: **leave**
23 **end**
24 **end**

analyses, as the convergence rate is heavily influenced by this error in the integration of the contact stress and contributions to LHS on the element faces [85]. However, the primarily used element type in geotechnical analysis with pore fluid pressure DOF is the quadratically interpolated serendipity element as has been pointed out in Chapter 4.

A solution for the problem of surface integration of 3D serendipity elements in contact analyses has been proposed by [56], adding an additional node to the face of the serendipity element being in contact. Note that both the shape functions used for the integration of the face as

well as the shape functions of the finite element have to be modified. It is not sufficient to only integrate the surface with an additional node, which has been tested in the course of this work. The approach by [56] requires a distinction during assembly of RHS and LHS, since finite elements with contact contributions have to be interpolated and integrated differently than regular finite elements. From a programming point of view this is not ideal. Therefore, a transformation of any serendipity element to a full tri-quadratically interpolated element using standard Lagrangian shape functions in case of 3D contact analyses is implemented. The interpolation functions are given in Appendix B.1. This element has 27 nodes and does not suffer from the aforementioned problems in contact analyses.

Since some pre-processors (e.g. `Abaqus CAE`) do not allow for the generation of 27-node brick elements (referred to as `u27` element), the generation of the additional nodes required for the transformation of the 20-node brick element (`u20`) to the 27-node element is implemented in `numgeo`. The additional nodes are also added automatically to existing node-set definitions.

To show the differences in terms of convergence rate between the `u20` and `u27` element, the change in the norm of residual energy (for definition see [36]) with respect to the number of iterations for a contact analysis with two elastic bodies coming in initial contact is given in Fig. 6.7. The `u27` element converges in one iteration yielding perfect equilibrium. The convergence rate of the `u20` element is considerably worse.

A major drawback of the `u27` elements, compared to the `u20` elements, is that a reduced numerical integration is not possible. The `u20` elements allow for an integration using 8 integration points instead of a "full" integration with 27 points without showing communicable hourglass modes. Contrary to that, `u27` elements show strong hourglassing for 8, 14 or 15 integration points (for the integration rules see [180]). All three integration rules have been tested and are found to be not feasible. To the author's best knowledge, no hourglass-stiffness enhanced reduced integrated `u27` element formulation is reported in the literature. In future research, the zero-energy modes of the reduced integrated `u27` element could be identified and suppressed by an artificial hourglass stiffness.

Note that the trouble of surface integration of serendipity elements exists only for 3D analyses. The integration of the element edge of 2D serendipity elements does not show the aforementioned errors since standard Lagrangian interpolation functions are used for the 1D edges.

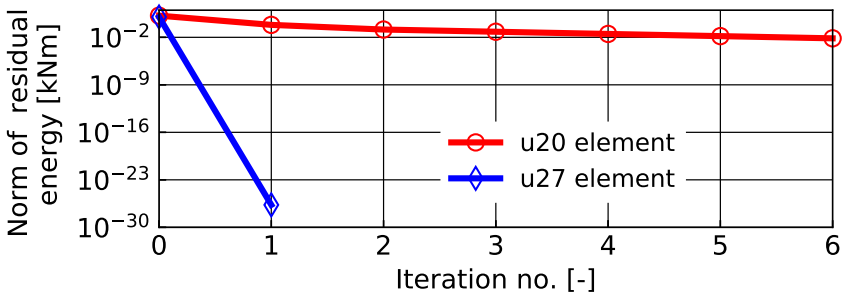

Figure 6.7: Change of the norm of residual energy with respect to number of iteration for the simulation of two elastic bodies coming into contact (a penalty factor of $\varepsilon = 100 \cdot E$ is used to enforce the non-penetration condition, where E is Young's modulus) for the `u20` and `u27` element, respectively

6.7 Numerical differentiation

As has been mentioned earlier, the derivative (referred to as Jacobian) of the contact contributions with respect to the spatially discretised variables is required for an implicit solving scheme using the Newton-Raphson method.

A consistent Jacobian of the contact contributions is crucial for the global iteration process and to achieve fast convergence. For complex constitutive interface models the determination of the derivatives is a tedious task and prone to errors. Depending on the interface model, the correct determination of the constitutive Jacobian may even be impossible (e.g. for the hypoplastic interface model proposed later in Section 6.10) and can only be approximated by simplifying the analytically calculated derivatives. Therefore, the Jacobian is determined using a numerical differentiation scheme. This scheme is similar to the one used for the implementation of the hypoplastic model presented in Appendix A and is based on the work reported in [120]. The numerical differentiation secures that a consistent Jacobian is obtained in any case, hence ensuring fast convergence. The numerical differentiation scheme is applicable for both the EBM and the SBM contact discretisation technique. In addition, it can be used in conjunction with any constitutive contact model without modifications. If not for the numerical differentiation scheme, for each constitutive contact model presented in Section 6.10 the Jacobian would have to be analytically calculated and implemented, which is a tedious task.

The derivative of the contact contribution given by Eq. (6.49) is first rewritten to

$$\frac{\partial \boldsymbol{r}_I^C}{\partial u_{iI}} = \left(\mathbf{J}_I^C\right)_i, \tag{6.55}$$

where a mixed index notation is used to highlight the derivative with respect to component i ($i = \{1, 2\}$ for 2D and $i = \{1, 2, 3\}$ for 3D analyses) at node I. Assuming that the contact contribution $\boldsymbol{r}_I^C$ of node I depends solely on the displacement, the Jacobian is calculated using

$$\left(\mathbf{J}_I^C\right)_i = \frac{1}{\vartheta}\Big[\boldsymbol{r}_I^C(\Delta\boldsymbol{u}_I + \vartheta\mathbf{I}_i) - \boldsymbol{r}_I^C(\Delta\boldsymbol{u}_I)\Big], \tag{6.56}$$

where the perturbation ϑ is introduced. Following [120], ϑ is determined by

$$\vartheta = \max(1, ||\Delta\boldsymbol{u}_I||) \cdot \sqrt{EPS}, \tag{6.57}$$

wherein $EPS \approx 10^{-16}$ is the machine precision. In Eq. (6.56), $\mathbf{I} = \mathrm{diag}[1, 1]$ is used for 2D and $\mathbf{I} = \mathrm{diag}[1, 1, 1]$ for 3D analyses. Note that the derivation of contact force at one node with respect to the displacement of the connected node of the paired surface ($\frac{\partial \boldsymbol{r}_I^{C,(1)}}{\partial \boldsymbol{u}_J^{(2)}}$ and $\frac{\partial \boldsymbol{r}_J^{C,(2)}}{\partial \boldsymbol{u}_I^{(1)}}$) has to be considered. Therefore, Eq. (6.56) has to be evaluated at least $2 \cdot ndim{+}1$ times, since the displacement of the connected point has to be perturbed as well. $ndim$ is the number of dimensions of the boundary value problem.

For advanced constitutive interface models, the contribution of the contact forces may further be a function of contact stress $\boldsymbol{t}$ and state variables $\boldsymbol{k}$, i.e. $\boldsymbol{r}_I^C(\Delta\boldsymbol{u}_I, \boldsymbol{t}_I, \boldsymbol{k}_I)$. The state variables change with respect to the displacement, the contact stress and the state variables, described by the function $\boldsymbol{f}_I(\Delta\boldsymbol{u}_I, \boldsymbol{t}_I, \boldsymbol{k}_I)$. For such interface models, the numerical differentiation should incorporate the change with respect to these variables as well. The jacobian can then be calculated using

$$\frac{\mathrm{d}}{\mathrm{d}t}\left(\mathbf{J}_I^C\right)_i = \frac{1}{\vartheta}\Big\{\boldsymbol{r}_I^C\big[\Delta\boldsymbol{u}_I + \vartheta\mathbf{I}_i, \boldsymbol{t}_I + \vartheta\big(\mathbf{J}_I^C\big)_i, \boldsymbol{k}_I + \vartheta\big(\mathbf{G}_I\big)_i\big] - \boldsymbol{r}_I^C(\Delta\boldsymbol{u}_I, \boldsymbol{t}_I, \boldsymbol{k}_I)\Big\}, \tag{6.58}$$

where

$$\frac{\mathrm{d}}{\mathrm{d}t}\left(\mathbf{G}_I\right)_i = \frac{1}{\vartheta}\Big\{\boldsymbol{f}_I\big[\Delta\boldsymbol{u}_I + \vartheta\mathbf{I}_i, \boldsymbol{t}_I + \vartheta\big(\mathbf{J}_I^C\big)_i, \boldsymbol{k}_I + \vartheta\big(\mathbf{G}_I\big)_i\big] - \boldsymbol{f}_I(\Delta\boldsymbol{u}_I, \boldsymbol{t}_I, \boldsymbol{k}_I)\Big\}. \tag{6.59}$$

Eq. (6.58) and Eq. (6.59) have to be solved simultaneously in an iterative scheme to secure consistency.

The numerical differentiation schemes are implemented for both EBM and SBM contact discretisation techniques. For contact analyses without friction or with a simple Couloumb friction model the analytically derived constitutive Jacobian is preferred since the contact algorithms have to be run only once.

As is demonstrated in Section 6.10.7 for the simulation of simple interface shear tests, using Eq. (6.56) alone leads to fast convergence rates despite the negligence of the change of state

variables with respect to displacement and stress. Eq. (6.56) is computational advantageous compared to Eq. (6.58), since it does not require any additional iterations and has to be performed only $2 \cdot ndim+1$ times. Therefore, Eq. (6.56) is used for the implementation of the numerical differentiation scheme.

6.8 Validation and comparison of the implemented contact discretisation methods

In order to compare the performance of the implemented EBM and SBM methods for a simple BVP as well as to validate the implementations, the Hertzian contact problem is studied. Note that no additional integration points are generated at the element edges using the EBM method for the simulations presented in this section.

Figure 6.8 shows the adopted mesh and the material properties (Young's modulus E and Poisson's ratio ν) of the deformable bodies. Only quadratically interpolated finite elements (serendipity formulation) are used. The upper sphere (radius $R = 8$ m) is loaded by an uniform vertical traction which is equivalent to a force of $F = 10$ kN when integrated over the diameter. An irregular meshing with reciprocal non-aligned surface nodes is used in order to better identify the differences between the contact discretisation techniques. The lower sphere (radius $R = 8$ m) has exactly two times larger element edges at the surface in the symmetry axis compared to the upper sphere.

The right-hand side of Fig. 6.8 displays the distribution of normal contact stress t_N with respect to the horizontal coordinate starting from the symmetry axis of the model for the analytical solution based on the Hertzian contact theory (see [187, 295]) and simulations using the implemented mortar methods. Both implemented contact discretisation techniques give results which are in good accordance with the results of the analytical solution. At the nodes which are close to come into contact, small deviations between the analytical solution and the EBM method are observed. These deviations are reduced using the SBM method due to the local refinement. Overall, however, the differences between the two contact discretisation techniques implemented in the framework of this thesis are small. In order to investigate this for the geometrically much more complex simulation of vibratory pile driving in water-saturated soil, both techniques are applied for this BVP in Section 8.2.3.

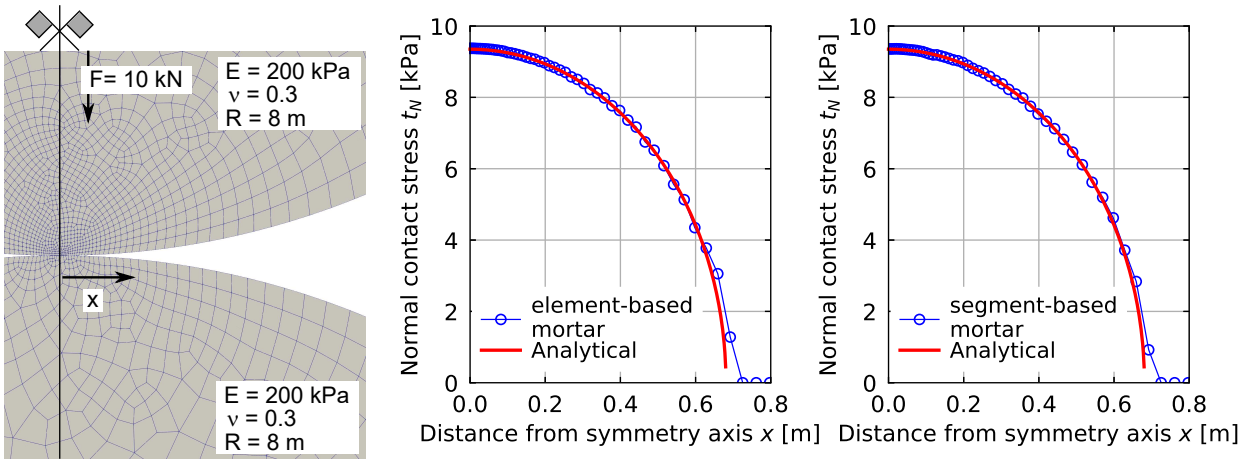

Figure 6.8: Model of the Hertzian contact problem (left) and normal contact stress vs. the horizontal coordinate starting from the symmetry axis of the model for the analytical solution based on the Hertzian contact theory and the simulations using the implemented element-based and segment-based mortar methods (right)

6.9 Contact of multi-phase media

The contact between objects with multiple phases requires special considerations for the contact enforcement. The contact treatment of the pore fluid depends on the element formulation used to discretise the continuum. While the **u**-p elements do not discretise the movement of the pore fluid explicitly, the **u**-**U** and **u**-p-**U** element formulations do. Therefore, the contact constraints have to be enforced for the pore fluid movement as well, i.e. the pore fluid has to be prevented to move into the paired object. For some BVPs, this can also be realised by coupling the solid movement to the fluid movement along the contact surface using multi-point constraints. However, a separation of the phases along the interface is then impossible. In addition, for most BVPs it is not possible to constrain the displacement only in normal direction of the contact, i.e. in case of a pile with constantly changing normal vector in circumferential direction.

In order to correctly model the interface using the **u**-**U** and **u**-p-**U** formulations, the contact discretisation and contact enforcement are performed separately for the solid and the fluid phases. Thus, contact forces are distinguishable and the constitutive contact behaviour can be treated separately. The total normal contact stress t_N is the sum of the effective normal contact stress t'_N and the normal fluid contact stress t^f_N, viz.

$$t_N = t'_N + t^f_N. \tag{6.60}$$

In order to determine t^f_N, the same contact discretisation and contact enforcement techniques

as for the solid phase are used. Eq. (6.49) is extended by the contribution of the fluid phase, yielding

$$\boldsymbol{r}_I^C = \int_{\Gamma^{C,s}} \boldsymbol{t}_I^{C,s} \mathrm{d}\Gamma^{C,s} + \int_{\Gamma^{C,f}} \boldsymbol{t}_I^{C,f} \mathrm{d}\Gamma^{C,f}, \tag{6.61}$$

where $\boldsymbol{t}_I^{C,s}$ is the contact stress of the solid phase and $\boldsymbol{t}_I^{C,f}$ the contact stress of the fluid phase. $\Gamma^{C,s}$ and $\Gamma^{C,f}$ are the active contact areas of the solid and the fluid phase, respectively. Note that $\Gamma^{C,s}$ and $\Gamma^{C,f}$ are not necessarily identical.

Essentially, the contact algorithms presented in the previous sections can directly be applied to the fluid phase as well. Conceptually, this can be viewed as if there were two meshes with identical numbers of nodes but different positions. The contact operations are performed for both meshes independently and the contact forces are distributed to the two phases according to the relative distance of each phase to the paired object.

In case of the **u**-p-**U** formulation, the normal fluid contact stress t_N^f, which is equivalent to a Neumann boundary condition, is for most cases equivalent to the (intrinsic) pore fluid pressure p^f of the contact node. Frictional contact is solely considered for the solid phase since the fluids are assumed to have negligible viscosity. Contact separation conditions can be set separately for the solid and the fluid.

In order to illustrate the concept of the multi-phase contact conditions, the Hertzian contact analysis of the previous section is repeated considering a deformable rectangle discretised by `u8p4` and `u8p4u8` elements, respectively. The sphere is discretised using solid elements (`u8`). The deformed configuration and the spatial distribution of normalised pore fluid pressure are given in Fig. 6.9. The EBM contact discretisation technique is used. The deformable body has a low hydraulic conductivity ($k^w = 10^{-13}$ m/s) and no drainage is possible at the borders of the model. The simulation can therefore be treated as almost ideally undrained. The distribution of total normal contact stress t_N, the pore fluid pressure p^f and the normal fluid contact stress t_N^f between the sphere and the deformable body are given on the right-hand side of Fig. 6.9. The normalised distance is defined as the distance from the symmetry axis divided by the radius of the sphere. In case of the `u8p4` element the contact conditions are enforced for the mixture of the solid and the fluid phase whereas both phases are treated separately in case of the `u8p4u8` elements. Hence, the normal fluid contact stress t_N^f is only available for this element formulation. The comparison of the two element formulations shows that they give the same results for the Hertzian contact problem. This is because the contact conditions are equivalent in terms of enforced constraints (the mixture can not penetrate into the sphere).

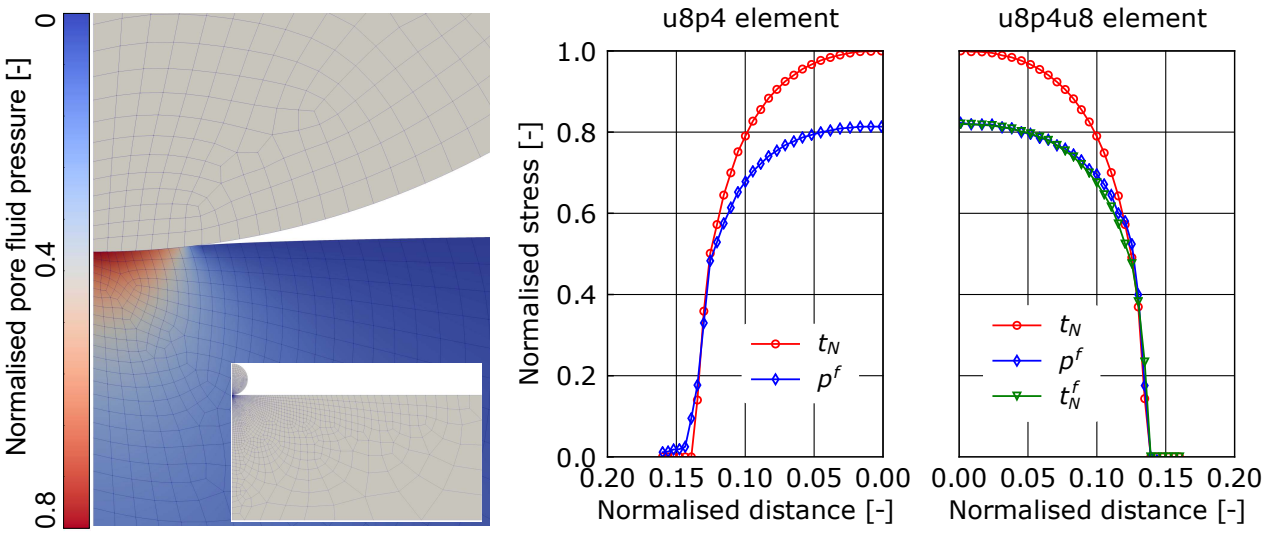

Figure 6.9: Spatial distribution of normalised pore fluid pressure and contact stress using the **u**-p and the **u**-p-**U** element formulation, respectively. The plots display the total normal contact stress t_N, the pore fluid pressure p^f and the normal contact fluid stress t_N^f (all normalised by the maximum value of t_N) with the horizontal coordinate starting in the symmetry axis of the model.

6.10 Advanced constitutive interface models for sand considering (high-)cyclic loading

The frictional stress between contacting surfaces with relative tangential movement is determined by the constitutive contact model, also termed the constitutive interface model in this thesis. For the modelling of pile driving processes or axial loading of piles in general, the adequate incorporation of frictional forces between pile and soil is a key point for the successful prediction of the overall process [209, 293, 387, 182, 328]. In most geomechanical analyses, a simple Coulomb interface model is used to consider friction. However, the constitutive behaviour of soil-structure interfaces is more complex than can be captured by the simple Coulomb friction model.

The mechanical behaviour of sand-structure interfaces is strongly influenced by the surface roughness κ. For relatively smooth surfaces the contact friction angle is often fully mobilised after a short shear path and remains almost constant after mobilisation [393]. For rough surfaces, however, the behaviour is similar to the response observed in simple shear or triaxial tests performed on dense sand, where the peak stress is followed by gradual softening with

ongoing shearing. Compared to smooth surfaces, the shear band is usually much broader for rough surfaces. These characteristics of the constitutive interface behaviour of sand are schematically shown in Fig. 6.10a.

Interface shear tests are performed to determine the mechanical properties of soil-structure interfaces and can, amongst other criteria, categorised according to their boundary conditions. Figure 6.10b displays schematics of simple interface shear tests with constant normal stiffness (K constant, CNS test) and constant normal load (t_N constant, CNL test). For most BVPs, constant normal stiffness conditions are believed to be more representative, since the shearing of the interface leads to volumetric strain and hence change in the normal contact stress. The influence of the constant normal stiffness and constant normal load boundary conditions on the shear stress vs. tangential displacement curves is also schematically shown in Fig. 6.10b. CNS tests do not exhibit a peak in the t_T vs. u_T plot and reach higher maximum shear stress with increasing normal stiffness. In case of CNL tests, the curves show a peak while higher normal load results in a higher maximum shear stress. Larger relative displacements between the soil sample and the structure are necessary in case of higher normal load to reach the peak value of t_T compared to lower normal load [321].

The aforementioned characteristics of the constitutive behaviour of sand-structure interfaces are confirmed by numerous monotonic (see e.g [110, 100, 247, 260, 118]) and cyclic interface shear tests (see e.g. [109, 442, 443, 121]) reported in the literature. In addition, these characteristics have also been reproduced using the discrete element method [444, 449, 177].

6.10.1 Modelling of interfaces using existing constitutive continuum models

For the numerical modelling of the mechanical behaviour of the interface zone (i.e. the friction model), two general approaches exist. The employed constitutive models are either specifically tailored for the application to interfaces and are solely used as friction models (see e.g. the models presented in [335, 257, 139, 174, 201, 229, 323, 324, 322, 429, 284, 230, 231]) or they are based on models originally developed for the constitutive modelling of the continuum (see e.g. [147, 21, 399, 367, 369, 366, 368, 365, 400]). For the second approach, the stress and strain in the interface have to be given in a global continuum setting (i.e. the full tensors), whereas in the first approach only the normal (contact) stress, the shear stress and the shear strain of the interface zone are conventionally considered. Using the second approach, a slight modification of the constitutive equations of the continuum model is often necessary to account for the

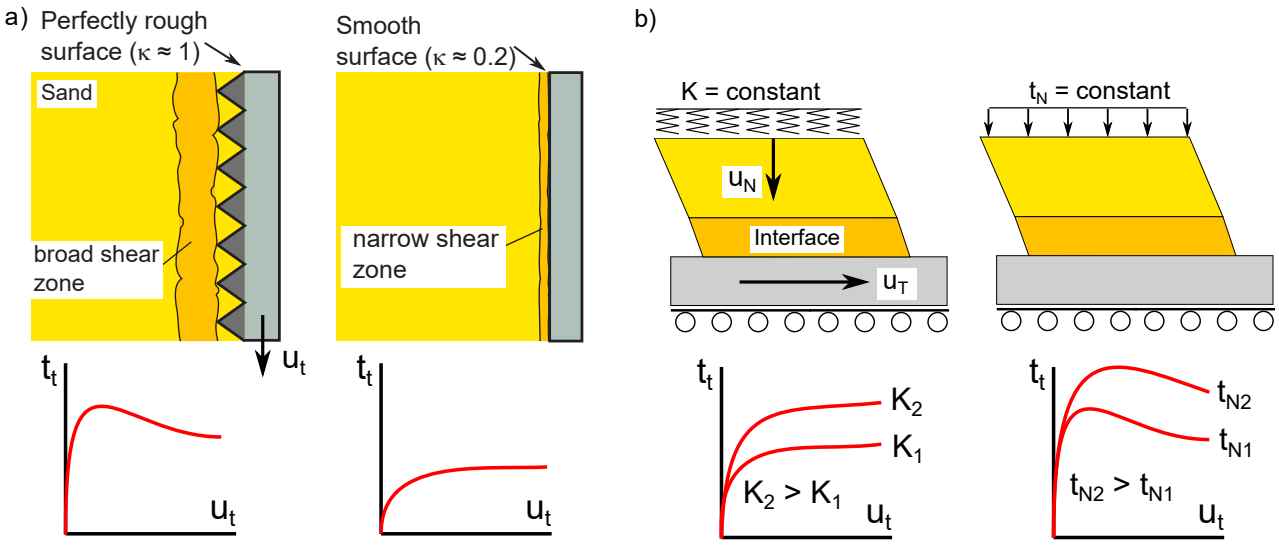

Figure 6.10: a) Schematic of the shear stress vs. tangential displacement response of soil-structure interfaces in dependence of the surface roughness (based on [393]). b) Different boundary conditions used in simple interface shear tests and their influence on the shear stress vs. tangential displacement response.

characteristics of the soil-structure interface, such as the surface roughness. Compared to the first approach, the application of existing continuum models to the modelling of interfaces has the advantage that the constitutive model needs not to be formulated completely new[4] [147, 22, 21]. Moreover, apart from the surface roughness and the shear band thickness, no additional constitutive parameters are usually required for the friction model since they are typically identical to those used for the continuum constitutive model. Therefore, additional interface shear tests to calibrate the parameters of the friction model are not required in all cases.

Herle & Nübel [166], Gutjahr [147] and Arnold & Herle [22, 21] were among the first to apply hypoplastic continuum models to the modelling of interfaces. They modified the hypoplastic relations such that they are applicable for plane conditions (Herle & Nübel, Gutjahr) or assumed identical normal stress components[5] $\sigma_{11}^{\text{interface}} = \sigma_{22}^{\text{interface}} = \sigma_{33}^{\text{interface}}$ (Arnold & Herle) in the hypoplastic interface element. The two approaches have different shortcomings, which

[4]This is not the case for the (first) approach presented in [399, 400], where a projection of the continuum model to the interface zone is used. This requires the assumption of Lode's angle to be zero and has thus far only been used together with rather simple elasto-plastic constitutive continuum models.

[5]The stress tensor of the interface $\boldsymbol{\sigma}^{\text{interface}}$ is not to be confused with the contact stress vector $\boldsymbol{t}$ and its components. When referring to the normal stress components of the interface, the diagonal values of $\boldsymbol{\sigma}^{\text{interface}}$ are meant. Normal contact stress refers to t_N.

are discussed by Stutz et al. [365, 367]. The recently presented approach by Stutz et al. [367, 369, 366, 368, 365] is more promising, because it is possible to consider the normal strain of the interface, which has been neglected in earlier schemes. In addition, differing normal stress components can be taken into account ($\sigma_{11}^{\text{interface}} \neq \sigma_{22}^{\text{interface}}$ and $\sigma_{11}^{\text{interface}} \neq \sigma_{33}^{\text{interface}}$). However, as will be shown in this work, the approach by Stutz et al. can violate the boundary conditions of a system, caused by non-realistic (initial) jumps in the normal stress components in the transition zone.

Apart from the application of (existing) constitutive continuum models, several stand-alone constitutive interface models have been proposed (see [335, 139, 174, 201, 229, 399, 400, 323, 322, 429]), which are all based on an additive split of elastic and plastic strains (i.e. elasto-plastic models). These models are of "Coulomb"-type with respect to the stress conditions in the interface, i.e. only normal and shear stress but no in-plane interface normal stress components are considered. Therefore, the interface shear stress rate is a function of the interface normal stress σ_N (identical to the normal contact stress t_N) and potentially some other state variables $\boldsymbol{\alpha}$ (including the shear stress $\boldsymbol{\tau}$), i.e. $\dot{\boldsymbol{\tau}} = f(\sigma_N, \boldsymbol{\alpha})$.

A general framework to apply existing constitutive continuum models as constitutive interface models is presented in the following. For this purpose, the approach by Stutz et al. is enhanced such that the normal stress components in the interface are not independent of the stress of the adjacent continuum, allowing to consider the boundary conditions of a BVP in the interface. Note that some of the following has already been published by the author in [361].

6.10.2 Stress and strain conditions in the interface element

As has already been mentioned in the previous sections, the interface element is formulated as zero-thickness element, without the need of additional discrete interface elements. This has the great advantage that sliding with large relative surface motions can be modelled without the need to re-create discrete interface elements. Figure 6.11 shows a schematic of a shear band with thickness d_s (Fig. 6.11a), the normal stress components acting in the shear band including the local coordinate system of the interface (Fig. 6.11b) and an idealised interface element in 2D subjected to the shear strain γ_1. The local coordinate system of the interface has the basis vector $\boldsymbol{n}$ for the normal direction and the two tangential basis vectors $\boldsymbol{t}_1$ and $\boldsymbol{t}_2$. The components of the normal stress of the interface element are likewise defined by σ_n for the normal and σ_{p1}, σ_{p2} for the two normal stress components in-plane. The interface element is further subjected to the two shear stress components τ_1 and τ_2 acting in the $\boldsymbol{n} - \boldsymbol{t}_1$ and $\boldsymbol{n} - \boldsymbol{t}_2$ plane, respectively.

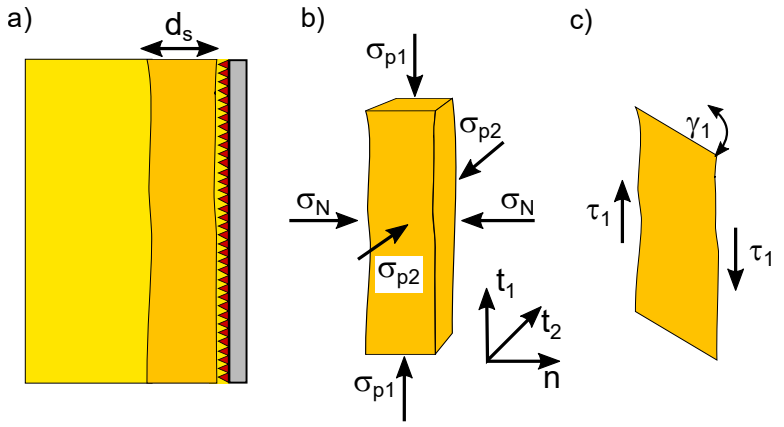

Figure 6.11: a) Shear band with thickness d_s formed at a soil-structure interface. b) Normal stress components acting in the shear band. c) Shear strain and stress in a 2D interface element.

In the approach by Stutz et al. [367], the following definitions of stress and strain tensors are used for the constitutive continuum model applied as interface model

$$\boldsymbol{\sigma}^{\text{interface}} = \begin{bmatrix} \sigma_N & \tau_1 & \tau_2 \\ \tau_1 & \sigma_{p1} & 0 \\ \tau_2 & 0 & \sigma_{p1} \end{bmatrix} \quad \text{and} \quad \boldsymbol{\varepsilon}^{\text{interface}} = \begin{bmatrix} \varepsilon_N & \gamma_1/2 & \gamma_2/2 \\ \gamma_1/2 & 0 & 0 \\ \gamma_2/2 & 0 & 0 \end{bmatrix}. \tag{6.62}$$

In contrast to the approaches by Gutjahr and Arnold & Herle, the normal strain ε_N of the interface is considered. To determine ε_N, the increment of normal contact stress Δt_N is enforced to be identical to the stress increment in normal direction of the interface $\Delta\sigma_N$ computed using the constitutive continuum model equations, viz.

$$\Delta\sigma_N - \Delta t_N \stackrel{!}{=} 0. \tag{6.63}$$

Therein, $\stackrel{!}{=}$ symbolises that Eq. (6.63) has to be enforced. Eq. (6.63) is solved using a Newton iteration in form of

$$\Delta\varepsilon_N^{n+1} = \Delta\varepsilon_N^n - \left(\Delta\sigma_N^n - \Delta t_N\right) / \frac{\partial\Delta\sigma_N^n}{\partial\Delta\varepsilon_N^n}. \tag{6.64}$$

The iteration is performed n-times until the left-hand side of Eq. (6.63) is sufficiently close to zero.

Since for most constitutive soil models $\dfrac{\partial\Delta\sigma_{ii}}{\partial\Delta\varepsilon_{11}} \neq 0_{ii}$ applies, the interface normal stress components σ_{p1} and σ_{p2} change with $\Delta\varepsilon_N$. In the same way the intergranular strain tensor, represent-

ing an important state variable of the hypoplastic model with intergranular strain extension, changes with $\Delta\varepsilon_N$ as well as with the shear strain increment $\Delta\boldsymbol{\gamma}$.

It is important to note that the constitutive response is influenced by the normal contact stress history since the normal stress components of the continuum model develop with increasing normal contact stress. Therefore, the contact behaviour should be described in all steps with the same constitutive contact model when applying the approach by Stutz et al. [367]. In the implementation by Stutz et al. [367], the assumption $\sigma_{p1} = \sigma_{p2}$ is made (see Eq. (6.62)). Due to restrictions of the closed-source software `Abaqus` used by Stutz et al. [367] for the implementation of the interface model, the initial normal stress components furthermore have to be set isotropically, i.e. $\sigma_{p1,0} = \sigma_{p2,0} = \sigma_{N,0}$ [366].

Using the approach by Stutz et al. [367], a *jump* in the stress tensor between continuum and interface generally exists. The following condition of the jump $[[\boldsymbol{\sigma}]] = \boldsymbol{\sigma}^{\text{interface}} - \boldsymbol{\sigma}^{\text{continuum}}$ has to be satisfied [390, 265]:

$$[[\boldsymbol{\sigma}]] \cdot \boldsymbol{n} = \mathbf{0}. \tag{6.65}$$

For plain-strain conditions, only one jump in the stress acting parallel to the discontinuity line is permitted (the other in-plane stress component is not governed by Eq. (6.65), but of course a jump is possible). For 3D, three jumps at the discontinuity plane are allowed by static considerations, which are the normal stress components σ_{p1} and σ_{p2} given in Fig. 6.11 as well as the shear stress component in the $\boldsymbol{t}_1 - \boldsymbol{t}_2$ plane.

Using the approach by Stutz et al. [367], both normal stress components orientated tangentially to the discontinuity plane may jump. This is allowed according to Eq. (6.65) but is not necessarily realistic. The approach by Stutz et al. [367] can violate the boundary conditions of a BVP. For instance, if a prescribed traction parallel to a discontinuity line exists, the corresponding stress component in the interface is not necessarily identical to it. Such a case is illustrated in Fig. 6.12. Even though a vertical traction is prescribed, the vertical stress in the interface zone is only governed by the interface strain in normal direction, which does in general not lead to a vertical stress in the interface being in equilibrium with the prescribed external loading. The developing normal interface stress components depend, among other influencing factors, on the lateral stress coefficient. Moreover, using the approach by Stutz et al. [367], no strain of the interface zone in direction of the vertical traction can be taken into account. This is a major disadvantage, considering that the hypoplastic model with intergranular strain extension is considerably influenced by the strain history. In addition, a jump already exists prior to shearing and the initial stress conditions might not be correctly reflected, which is further discussed in Section 6.10.7.

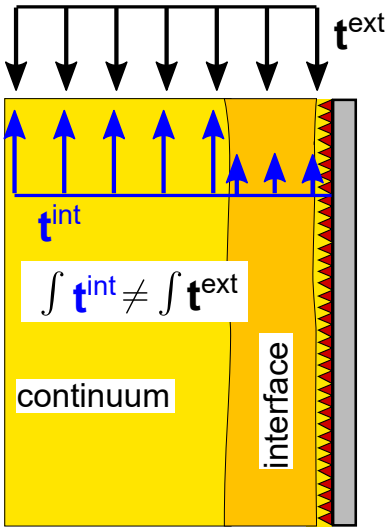

Figure 6.12: Illustration of the jump in the internal vertical stress vector $\boldsymbol{t}^{int}$ between continuum and interface in case of an external load ($\boldsymbol{t}^{ext}$) using the existing interface formulations

In order to address the shortcomings of the approach by Stutz et al. [367], it is assumed that all normal stress components of the interface are identical to the normal stress of the adjacent continuum and no jump in the stress exists. For this purpose the stress tensor of the adjacent continuum is extrapolated to the interface element, avoiding the (initial) jump. The extrapolation of the stress tensor from the integration points of the adjacent continuum elements to the surface nodes is performed by

$$\boldsymbol{\sigma}^{\text{extra}} = \sum_{\text{igp}}^{\text{ngp}} N_{\text{igp}}(\xi', \eta') \boldsymbol{\sigma}_{\text{igp}}^{\text{continuum}}, \tag{6.66}$$

where ξ' and η' are the stretched local coordinates (see Fig. 6.13b) of the adjacent continuum element from which the stress is retrieved. The stretched local coordinates are ≤ 1 at the location of the integration points and > 1 at the location of the contact points such that an extrapolation is performed. $\boldsymbol{\sigma}^{\text{extra}}$ is the extrapolated stress given in the global coordinate system and $\boldsymbol{\sigma}_{\text{igp}}^{\text{continuum}}$ is the stress in integration point *igp* of the adjacent continuum element. *ngp* is the number of all integration points of the considered continuum element. Note that if the point on the interface lies exactly between two or more continuum elements, the average values of the extrapolated stresses of all adjacent elements are computed. The stress has to be rotated according to the local coordinate system of the interface element. The rotation is defined by

$$\boldsymbol{\sigma}'^{\text{extra}} = \boldsymbol{\alpha} \cdot \boldsymbol{\sigma}^{\text{extra}} \cdot \boldsymbol{\alpha}^T, \tag{6.67}$$

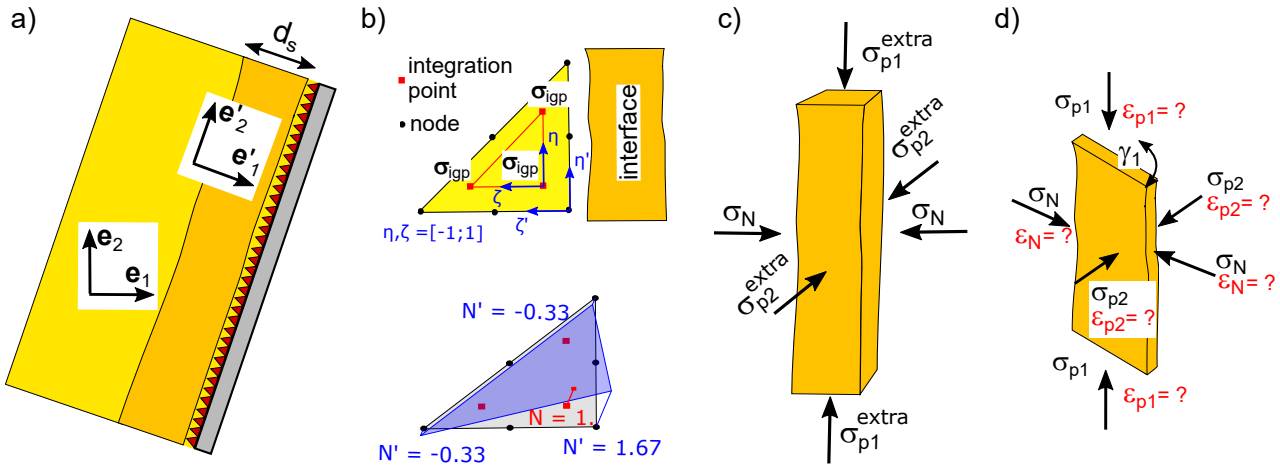

Figure 6.13: a) Global and local coordinate system of the interface. b) Extrapolation of the continuum stress to the interface. c) Normal stress components acting in the interface. d) Boundary conditions of the novel interface element formulation.

where

$$\alpha_{ij} = \boldsymbol{e}^{'(i)} \cdot \boldsymbol{e}^{(j)}. \tag{6.68}$$

$\boldsymbol{e}^{'(i)}$ is the i-th basis vector of the local interface coordinate system and $\boldsymbol{e}^{(j)}$ is the j-th basis vector of the global coordinate system. The rotation from global to local coordinate system is displayed in Fig. 6.13a. Only the interface normal stress components $\sigma_{p1}^{\text{extra}}$ and $\sigma_{p2}^{\text{extra}}$ of $\boldsymbol{\sigma}^{'\text{extra}}$ are of interest. The other components of the stress tensor (σ_N, τ_1, τ_2) are obtained using the contact stress vector $\boldsymbol{t}$ of the previous converged state (this is either the solution at the last global iteration or the solution at the last converged sub-increment, as is further explained in Section 6.10.4). The stress components of the interface element using the extrapolated stress are given in Fig. 6.13c. Using the proposed definitions for the stress state of the interface element, Eq. (6.62) is modified to Eq. (6.69):

$$\bar{\boldsymbol{\sigma}}^{\text{interface}} = \begin{bmatrix} \sigma_N & \tau_1 & \tau_2 \\ \tau_1 & \sigma_{p1} & 0 \\ \tau_2 & 0 & \sigma_{p2} \end{bmatrix} \quad \text{and} \quad \bar{\boldsymbol{\varepsilon}}^{\text{interface}} = \begin{bmatrix} \varepsilon_N & \gamma_1/2 & \gamma_2/2 \\ \gamma_1/2 & \varepsilon_{p1} & 0 \\ \gamma_2/2 & 0 & \varepsilon_{p2} \end{bmatrix} \tag{6.69}$$

Note that the assumption of $\sigma_{p1} = \sigma_{p2}$ is neither required nor made. In addition, the strains ε_{p1} and ε_{p2} are not necessarily zero as assumed by Stutz et al. [367], which is also indicated in Fig. 6.13d. For 2D plain-strain analyses, however, the normal strain component ε_{p2} is zero of course. It is important to note that the normal strain components ε_{p1} and ε_{p2} do not change

due to pure shearing of the interface, i.e. they are only governed by a change in stress caused not by interface shearing. This is of great importance because if the stress components σ_{p1} and σ_{p2} are fixed to the values obtained from the continuum but they change due to the shearing of the interface, an incompatibility occurs. Only a change in the stresses σ_{p1} and σ_{p2} due to some changes in the continuum stress not caused by the interface shearing leads to changes in ε_{p1} and ε_{p2} (e.g. some external loading parallel to the interface plane). If pure shearing of the interface occurs, the approach reduces to the approach by Stutz et al. [367] in terms of the strain tensor. An example for such conditions is given later with the simulation of simple interface shear tests.

Note that the second approach presented by [399] also considers all stress components similar to Eq. (6.69). However, in analogy to the approach by Stutz et al. [367], the stress is also not directly influenced by the adjacent continuum stress.

The contact normal stress t_N and the extrapolated (rotated) stress components ($\sigma_{p1}^{\text{extra}}$ and $\sigma_{p2}^{\text{extra}}$) have to be in equilibrium with the stress of the interface element. This is enforced by

$$\sigma_N - t_N \stackrel{!}{=} 0, \tag{6.70}$$

$$\sigma_{p1} - \sigma_{p1}^{\text{extra}} \stackrel{!}{=} 0 \quad \text{and} \tag{6.71}$$

$$\sigma_{p2} - \sigma_{p2}^{\text{extra}} \stackrel{!}{=} 0. \tag{6.72}$$

Note that the shear stress components of the continuum need not to be enforced to be in equilibrium with the contact shear stresses since they are identical by definition. Note in addition that Eqs. (6.70 - 6.72) are not formulated incrementally since stress equilibrium is enforced. According to the jump condition given by Eq. (6.65), Eqs. (6.71 - 6.72) need not necessarily be satisfied. They can be enforced according to the boundary conditions of the considered BVP. In general, however, Eqs. (6.70 - 6.72) should be satisfied initially (prior to shearing) if homogeneity is assumed.

Using the Jacobian $\mathbf{J}$ of the constitutive continuum model applied as interface model, Eqs. (6.70 - 6.72) are solved using Newton's method with iterative calculation of the unknown strain, viz.

$$\boldsymbol{\varepsilon}^{\text{interface},n+1} = \boldsymbol{\varepsilon}^{\text{interface},n} - \mathbf{J}^{-1} : \left(\boldsymbol{\sigma}^{\text{interface}} - \boldsymbol{\sigma}'^{\text{extra}} \right), \tag{6.73}$$

where $\boldsymbol{\sigma}'^{\text{extra}} = \text{diag}[t_N, \sigma_{p1}^{\text{extra}}, \sigma_{p2}^{\text{extra}}]$ and $\boldsymbol{\sigma}^{\text{interface}} = \text{diag}[\sigma_N, \sigma_{p1}, \sigma_{p2}]$.

Eq. (6.73) is solved in two steps. First,

$$\mathbf{J} : \Delta\boldsymbol{\varepsilon}^{\text{interface},n} = -\left(\boldsymbol{\sigma}^{\text{interface}} - \boldsymbol{\sigma}'^{\text{extra}} \right) \tag{6.74}$$

is solved for $\Delta\boldsymbol{\varepsilon}^{\text{interface},n} = \boldsymbol{\varepsilon}^{\text{interface},n+1} - \boldsymbol{\varepsilon}^{\text{interface},n}$ and then added to the total strain of iteration n, viz.

$$\boldsymbol{\varepsilon}^{\text{interface},n+1} = \boldsymbol{\varepsilon}^{\text{interface},n} + \Delta\boldsymbol{\varepsilon}^{\text{interface},n}. \tag{6.75}$$

In each iteration n, the shear stress components of the contact stress vector $\boldsymbol{t}$ from the last converged state are added to $\boldsymbol{\sigma}^{\text{interface}}$

$$\bar{\boldsymbol{\sigma}}^{\text{interface}} = \boldsymbol{\sigma}^{\text{interface}} + \mathbf{T}, \tag{6.76}$$

where $\mathbf{T} = \{[0, \tau_1, \tau_2]^T, [\tau_1, 0, 0]^T, [\tau_2, 0, 0]^T\}$. This is done because only the normal stress components are supposed to change during the iterative calculation of the increments of the normal strain components. During the update of the normal strains, the shear stresses are not considered in Eq. (6.74) but the constitutive model is called using $\bar{\boldsymbol{\sigma}}^{\text{interface}}$, including the shear stress components from the last converged iteration. Since the increment in shear strain is non-zero, the shear stress components change during the Newton iteration. The contact shear stress vector $\boldsymbol{t}_T$ is, however, only updated in case Eqs. (6.70 - 6.72) are satisfied. The definition of the shear strain components in $\bar{\boldsymbol{\varepsilon}}^{\text{interface}}$ is given in the next section.

6.10.3 Shear strain

Using zero-thickness interface elements, the increment in shear strain is calculated by

$$\tan \Delta\boldsymbol{\gamma} = \frac{\Delta\boldsymbol{g}_T}{d_s}, \tag{6.77}$$

where the interface thickness d_s and the increment in tangential gap $\Delta\boldsymbol{g}_T$ (see Eq. (6.28)) are used. For granular media, the interface thickness is usually assumed identical to the shear band thickness, which is a function of the grain size for cohesionless soils. According to laboratory observations [174, 92, 91, 247], the shear band developing at soil-structure interfaces during shearing has a thickness of approximately $5 - 10 \cdot d_{50}$, where d_{50} is the median grain size. It is important to note that the shear band thickness is usually not constant with respect to shear strain [258]. The definitions of the strain conditions in the interface element introduced in Section 6.10.2 allow to consider the change of the interface thickness with respect to the normal strain and hence enable to consider the dilatancy of the interface zone. The interface thickness is postulated to be calculated by

$$d_s = d_{s0} + \varepsilon_N \cdot d_{s0}, \tag{6.78}$$

where d_{s0} is the initial interface thickness, estimated using the aforementioned approximation based on experimental results. Note that the influence of the consideration of the change in

shear band thickness on the calculated shear strain is not large. For the simulations presented later the normal strain did not exceed 10 % in most cases, leading to comparably small changes in d_s. Note in addition that even though the shear band thickness introduces a parameter which is hard to estimate and may involve a great uncertainty, using a Coulomb friction model also requires the definition of a tangential penalty factor (or a relative tangential displacement at which the shear stress is fully mobilised as e.g. implemented in the commercial software `Abaqus` [372]). This parameter is equivalently hard to estimate as is estimating d_s.

In analogy to Eq. (6.76), the shear components of the strain tensor are added to $\bar{\boldsymbol{\varepsilon}}^{\text{interface}}$ in every iteration n, viz.

$$\bar{\boldsymbol{\varepsilon}}^{\text{interface}} = \boldsymbol{\varepsilon}^{\text{interface}} + \mathbf{E}, \tag{6.79}$$

where $\mathbf{E} = \{[0, \gamma_1/2, \gamma_2/2]^T, [\gamma_1/2, 0, 0]^T, [\gamma_2/2, 0, 0]^T\}$.

6.10.4 Implementation

The pseudocode of the implementation is given in Algorithm 3. An explicit sub-increment scheme with error control is applied, for which the shear strain increment is divided in *nsub* sub-increments in line 1. A fixed maximum sub-increment of $5 \cdot 10^{-6}$ for the increment in shear strain is used. During the Newton iteration, the strain increment is calculated using Eq. (6.79) with the sub-increment of shear strain and the increments of the normal strain components from the last iteration. The sub-increment of shear strain is constant. In each iteration, the state variables $\boldsymbol{\alpha}$ of the constitutive interface model and the full stress tensor are first set to the values of the previous converged sub-increment in lines 5 and 6. The constitutive continuum model updates the stress and the state variables in line 7 based on the strain increment $\Delta\bar{\boldsymbol{\varepsilon}}^{\text{interface},i}$. Using the updated stress tensor, the updated normal strain increment is calculated in line 8. Lastly, the error r is calculated using Eqs. (6.70 - 6.72). The tolerance *tol* for the error is chosen as $tol = 0.2$ %, which originates from experience when integrating the stress rate of the hypoplastic model (see Appendix A.1). The state variables and the updated stress tensor are saved after convergence in lines 12 and 13. Note that the algorithm is independent of the underlying constitutive continuum model applied.

Depending on the constitutive model used, the iterative procedure can be computationally expensive, which is further discussed in Section 8.2.3. The evaluation of the contact contributions implemented in `numgeo` can be performed in parallel using multiple threads. Since the required communication of the threads is little compared to the time spent in the update of the contact contributions, an almost linear scaling with respect to the number of applied threads

is achieved. A discussion on the numerical performance of the proposed interface formulation is given in Section 8.1.3 for the simulation of large-scale interface shear tests.

Algorithm 3: Iterative calculation of the interface normal strain components

Result: Updated interface strain $\bar{\boldsymbol{\varepsilon}}^{\text{interface}}$, stress $\bar{\boldsymbol{\sigma}}^{\text{interface}}$ and state variables $\boldsymbol{\alpha}$

Divide shear strain increment $\Delta\boldsymbol{\gamma}$ in $nsub$ sub-increments $\delta\boldsymbol{\gamma}$
for $i = 1, 2, ..$ *until* $nsub$ **do**
  for $n = 1, 2, ..$ *until* $r < tol$ **do**
    Calculate $\Delta\bar{\boldsymbol{\varepsilon}}^{\text{interface},i}$ using $\delta\boldsymbol{\gamma}$ and $\Delta\boldsymbol{\varepsilon}^{\text{interface},n}$
    $\boldsymbol{\alpha}^n = \boldsymbol{\alpha}^i$
    $\bar{\boldsymbol{\sigma}}^{\text{interface},n} = \bar{\boldsymbol{\sigma}}^{\text{interface},i}$
    Call const. continuum model $\bar{\boldsymbol{\sigma}}^{\text{interface},n} = f(\bar{\boldsymbol{\sigma}}^{\text{interface},n}, \Delta\bar{\boldsymbol{\varepsilon}}^{\text{interface},i}, \boldsymbol{\alpha}^n)$
    Calculate $\Delta\boldsymbol{\varepsilon}^{\text{interface},n}$ using Eq. (6.74)
    $r = \|\boldsymbol{\sigma}^{\text{interface},n} - \boldsymbol{\sigma}'^{\text{extra}}\| / \|\boldsymbol{\sigma}'^{\text{extra}}\|$
  end
  Save strain $\bar{\boldsymbol{\varepsilon}}^{\text{interface},i+1} = \bar{\boldsymbol{\varepsilon}}^{\text{interface},i} + \Delta\bar{\boldsymbol{\varepsilon}}^{\text{interface},i}$
  Save state variables $\boldsymbol{\alpha}^{i+1} = \boldsymbol{\alpha}^n$
  Save stress $\bar{\boldsymbol{\sigma}}^{\text{interface},i+1} = \bar{\boldsymbol{\sigma}}^{\text{interface},n}$
end

6.10.5 Modelling of high-cyclic interface shearing using HCA interface models

Similar to the soil-continuum, cyclic shearing of interfaces can lead to permanent strain accumulation even for comparably small strain amplitudes if the number of load cycles is large. In general, cyclic loading of soil-structure interfaces leads to an accumulation of negative volumetric strain (contraction) for both initially dense and initially loose soil in the interface [90, 92, 256]. Similar to the continuum soil behaviour, the contraction is more pronounced in case of initially loose sand [109]. For initially loose soil-structure interfaces, some researchers found an increase in maximum shear stress that can be mobilised in the contact due to the cyclic shearing [93, 335]. In case of initially dense interfaces, a relaxation of the normal contact stress components as well as the shear stress components usually occurs [93, 109].

Up to now, no constitutive interface model for high-cyclic loading of interfaces exists. For

instance, such a model could be relevant for the simulation of piles subjected to high-cyclic vertical loading or combined vertical and horizontal loading. The general framework of the interface element introduced in the previous sections allows for a straightforward formulation of a constitutive interface model for high-cyclic loading based on the HCA models introduced in Chapter 5.

During the recording step of the simulation with the HCA model, a strain point is only saved in case the strain calculated from the iterative procedure given in Eq. (6.74) leads to stress equilibrium of interface and adjacent continuum. During the high-cycle mode of the HCA model, the stress equilibrium has to be enforced using Eqs. (6.70 - 6.72) as well since the accumulated strain causes the interface stress to change.

6.10.6 Modifications of constitutive continuum models for the application to interfaces

Recalling the influence of the surface roughness κ on the constitutive response of the interface zone (see Fig. 6.10), κ has to be incorporated in the constitutive continuum models applied as interface models. κ is defined by [147]

$$\kappa = \frac{\tan(\varphi^{\text{interface}})}{\tan(\varphi_c)} \tag{6.80}$$

with $\varphi^{\text{interface}}$ being the friction angle of the interface and φ_c the critical friction angle of the soil, and can be estimated using

$$\kappa = 0.25 \log R_n + 1.05, \tag{6.81}$$

where R_n is the normalised surface roughness given by $R_n = \dfrac{R_{max}(L = d_{50})}{d_{50}}$ [193]. d_{50} is the median grain size of the soil and $R_{max}(L = d_{50})$ is the maximum surface roughness on a length $L = d_{50}$ of the interface.

It is not desirable that the parameter sets of constitutive continuum models calibrated with the intent to be applied as continuum models have to be re-calibrated based on interface shear tests when applied as interface models. Therefore, the surface roughness is incorporated as a modification of the parameters of the constitutive continuum models without the need to perform additional interface shear tests and re-calibrate the constitutive parameters for every case. Three different constitutive continuum models are applied as interface models in this work, for which the surface roughness is incorporated as follows:

- **Hypoplasticity with intergranular strain**: Following the work of [147], the critical friction angle φ_c used in the calculation of a given in Eq. (A.7) is multiplied by the roughness factor κ, viz.

$$a = \frac{\sqrt{3}\big[3 - \sin(\kappa\varphi_c)\big]}{2\sqrt{2}\sin(\kappa\varphi_c)}. \tag{6.82}$$

In addition, since the interface behaviour of rough surfaces is similar to initially dense sand while smooth surfaces tend to show a response similar to initially loose sand, the parameter α, influencing the peak in the stress-strain response and the dilatancy behaviour, is modified. The pyknotropic factor f_d (see Eq. (A.7)) is calculated using

$$f_d = \left(\frac{e - e_d}{e_c - e_d}\right)^{\alpha\kappa^2} \tag{6.83}$$

and the barotropic factor f_b (see Eq. (A.8)) is defined by

$$f_b = \frac{h_s}{n}\left(\frac{e_{i0}}{e_{c0}}\right)^{\beta}\frac{1+e_i}{e_i}\left(\frac{3p_s}{h_s}\right)^{1-n}\left[3 + a^2 - a\sqrt{3}\left(\frac{e_{i0} - e_{d0}}{e_{c0} - e_{d0}}\right)^{\alpha\kappa^2}\right]^{-1}. \tag{6.84}$$

- **Sanisand**: The critical stress ratios M_c and M_e are modified by

$$M_c = \frac{6\sin(\kappa\varphi_c)}{3 - \sin(\kappa\varphi_c)} \quad \text{and} \quad M_e = \frac{-6\sin(\kappa\varphi_c)}{3 + \sin(\kappa\varphi_c)}. \tag{6.85}$$

In analogy to the hypoplastic model, the parameter n_b in Eq. (A.24)

$$\boldsymbol{\alpha}_\theta^b = \sqrt{\frac{2}{3}}\Big[g(\theta, c)Me^{-n_b\kappa\psi} - m\Big]\boldsymbol{n} \tag{6.86}$$

influencing the peak behaviour and the parameter A_0 in Eq. (A.29)

$$A_d = A_0\kappa(1 + \langle \boldsymbol{z} : \boldsymbol{n}\rangle) \tag{6.87}$$

influencing the dilatancy are modified by κ.

- **HCA model for sand**: Since the available data for high-cyclic shearing of interfaces is limited, only the friction angle φ_{cc} used for the calculation of the critical stress ratio introduced in Eq. (5.5) is modified by κ. The factor f_Y, considering the effect of normalised stress ratio on the accumulation rate, is influenced by this modifications as well. Higher values of f_Y are obtained for lower surface roughness. In future work, high-cyclic interface tests with varying surface roughness should be performed in order to investigate the suitability of the present approach.

6.10.7 Simulation of simple interface shear tests

To show the performance of the proposed constitutive interface models, simple interface shear tests are simulated. A schematic sketch of the tests, the difference between simple and direct shear tests as well as the definition of the normal stress and strain components for the test conditions are given in Fig. 6.14. The considered tests have been performed by Fakharian [109] and Fakharian & Evgin [110]. The experimental campaign comprises tests with constant normal stress and tests with constant normal stiffness. The soil sample had dimensions of 100 $\times$ 100 $\times$ 20 mm.

Monotonic as well as cyclic tests with up to 50 cycles have been performed. Different soils have been studied but only tests using a crushed silica sand are considered for the numerical analyses. Since neither the material is available nor any triaxial test data exists, the material constants required for the constitutive interface models are estimated based on parameters for a similar material. A crushed quartz sand (termed "L4C"), which has a grain size distribution very similar to the silica sand used in the interface tests and the same $d_{50} = 0.6$ mm, is used. The parameters of Hypoplasticity with intergranular strain, determined based on laboratory tests (index, oedometer and triaxial tests), are provided in Table 6.1. The material constants for the HCA model have been calibrated based on triaxial tests documented in [420]. The HCA parameters are given in Table 6.2. Note that no "tuning" of the parameters is performed since the comparison of the different interface formulations is focused here and not the comparison with the experimental data. Note in addition that the investigations in this section are restricted to the hypoplastic and the HCA interface model. The Sanisand interface model is later applied in Section 8.1 for the simulation of large-scale interface shear tests.

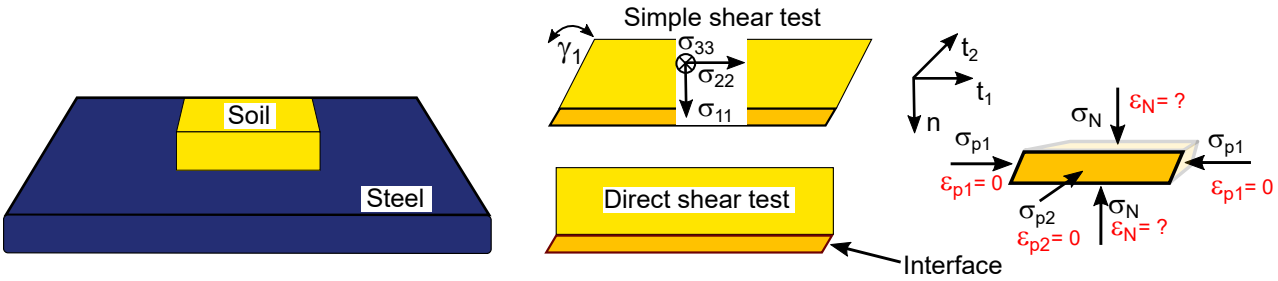

Figure 6.14: Schematic sketch of the interface shear tests, the different test conditions for simple and direct shear tests, the definition of the normal continuum stresses and the definition of the normal stress and strain components in the interface for the test conditions

φ_c	e_{i0}	e_{c0}	e_{d0}	h_s	n	α	β	R	m_R	m_T	β_R	χ
[°]	[-]	[-]	[-]	[kPa]	[-]	[-]	[-]	[-]	[-]	[-]	[-]	[-]
36	1.32	1.149	0.763	4516386	0.28	0094	1.2	10^{-4}	2.4	1.2	0.3	1.5

Table 6.1: Parameters of the hypoplastic model with intergranular strain extension for the crushed quartz sand "L4C"

C_{ampl}	C_e	C_p	C_Y	C_{N1} $[10^{-4}]$	C_{N2}	C_{N3}
0.95	0.48	-0.19	2.33	2.5	0.15	0

Table 6.2: Parameters of the HCA model for the crushed quartz sand "L4C"

Tests with monotonic loading

Only tests with comparatively modest values of normal contact stress are considered, excluding those with higher stress. Particle breakage occurred in the tests with higher stress, which can not be considered with the interface models developed in this work. Simple interface shear tests with constant normal stress of 100 kPa, an initial relative density of $D_{r0} = 0.88$ and sand-blasted steel surface are considered. The surface is assumed to be nearly perfectly rough ($\kappa = 0.9$) in the numerical analysis. An interface thickness of $5 \cdot d_{50} = 3$ mm is assumed. The intergranular strain tensor is assumed to be initially fully mobilised in the direction of shearing, such that no increased shear stiffness due to the intergranular strain extension exists initially. During the test, the intergranular strain tensor evolves due to strain in the normal interface direction. The initial stress in the continuum is calculated assuming a lateral stress coefficient of $K_0 = 0.5$.

Idealising the interface shear box as single element test (one linear finite element with one integration point[6]), the normal stress component σ_{p1} is non-constant and the corresponding strain is zero ($\varepsilon_{p1} = 0$) (see Fig. 6.14). The normal stress component σ_{p2} is also non-constant and for the strain $\varepsilon_{p2} = 0$ holds.

Note that due to the aforementioned boundary conditions of the shear test, only ε_N is non-zero using Eq. (6.74). The other normal strain components are zero since the normal stress components σ_{p1} and σ_{p2} develop identical to the corresponding continuum stresses. This does not need to be set manually for the novel interface formulation but results automatically from the stress and strain conditions. Note that this is due to the boundary conditions of

[6]Hourglass deformation modes are suppressed due to the Dirichlet boundary conditions

the simple interface shear test and not the case for more complex BVPs in general. For the numerical model, the vertical displacement of the top nodes is enforced to be identical by using a multi-point constraint. This constraint accounts for the rigid top plate used to apply the normal stress in the experiment. The implementation of the original approach by Stutz et al. [367] in `numgeo`, which is applied for comparison purposes in the following, utilises the same sub-increment scheme and error control as described in Section 6.10.4. Identical values for tolerated error and sub-increment size are used for both approaches. In addition, the identical implementation of the hypoplastic continuum model is utilised.

The results of the experiment and those of the simulations using the novel approach for the stress conditions in the interface element ($\sigma_{p1} = \sigma_{22}$ and $\sigma_{p2} = \sigma_{33}$) and the approach by Stutz et al. [367] are displayed in Fig. 6.15. The shear stress t_T and the normal stress components σ_{p1} and σ_{p2} of the interface are plotted vs. the tangential displacement of the steel plate. In case of the simulation with the novel approach both interface normal stress components are obtained from the continuum using the procedures described in Section 6.10.2. The normal continuum stress components σ_{22} and σ_{33} vs. the tangential displacement are given in Fig. 6.15d,e as well.

The shear stress vs. tangential displacement plot demonstrates that both interface formulations predict different peak and residual values of shear stress. The simulation using the approach by Stutz et al. [367] results in a lower peak and residual shear stress compared to the novel approach. Since the initial stiffness is higher due to the higher initial mean stress in the interface, the approach by Stutz et al. [367] furthermore results in an earlier peak in shear stress with respect to the tangential displacement. Compared to the experiment the peak is also underestimated using the novel interface formulation, which could be enhanced using a larger value of surface roughness κ or a larger value for the parameter α of the hypoplastic model. In case of the novel interface formulation using $\sigma_{p1} = \sigma_{22}$ and $\sigma_{p2} = \sigma_{33}$, the normal interface and normal continuum stress components match, as is visible from the comparisons of Fig. 6.15b with Fig. 6.15d and Fig. 6.15c with Fig. 6.15e. The approach by Stutz et al. [367] results in a strong jump of normal stress components between interface and continuum.

Despite the higher values of interface normal stress components (compared to the novel approach assuming $\sigma_{p1} = \sigma_{22}$ and $\sigma_{p2} = \sigma_{33}$), a slightly lower residual shear resistance is observed in case of the simulation using the approach by Stutz et al. [367]. This is due to the lower continuum normal stress components as is visible from Fig. 6.15d and Fig. 6.15e. Therefore, the continuum is the "weak link" (the interface and the continuum respond as in *series*, and not as in *parallel*) using the approach by Stutz et al. [367].

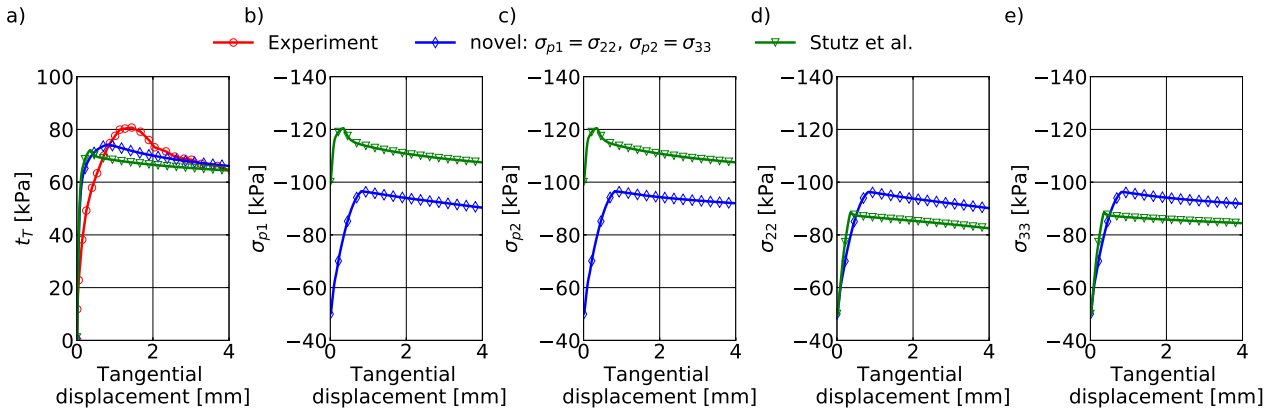

Figure 6.15: Results of the simulation of a simple interface shear test using either the novel approach for the calculation of the stress conditions in the interface element or the approach by Stutz et al. [367]. The interface shear stress and the interface normal stress components σ_{p1} and σ_{p2} vs. the tangential displacement u_T of the steel plate are displayed in plot a), b) and c), respectively. For the novel approach, the interface normal stress components σ_{p1} and σ_{p2} are obtained from the continuum ($\sigma_{p1} = \sigma_{22}$ and $\sigma_{p2} = \sigma_{33}$). In addition, the continuum normal stress components σ_{22} and σ_{33} vs. the tangential displacement are given in plots d) and e), respectively.

The comparison of the different interface formulations shows that the choice of the boundary conditions of the interface element influences the mechanical response. However, both formulations give reasonable results in terms of shear stress vs. tangential displacement compared to the results of the experiment. It is not surprising that only small differences in terms of shear stress exist, since the normal strain in the interface is almost identical to the normal strain of the adjacent continuum element (however, the approach by Stutz et al. [367] gives less normal strain in the interface compared to the continuum due to the higher mean stress in the interface). Since the shear stress in the interface and the continuum is also identical, but all other strain components are zero, the assumptions of the approach by Stutz et al. [367] hold. However, as is demonstrated for the large-scale cyclic interface shear tests in Section 8.1, the different approaches for the interface zone can have a distinct influence on the predicted shear stress, when the stress and strain conditions are more complex.

In order to judge the performance of the different interface models for perfectly rough conditions in comparison to a simulation without interface element, the simulations are repeated assuming perfectly rough conditions ($\kappa = 1$) and are compared to a simulation using only the hypoplastic continuum model and prescribing the displacement of the steel plate to the nodes of the soil sample. This modelling approach without interface element only works for

simulations with comparably small relative motions, since sliding can not be modelled without severe distortion of the continuum elements close to the interface zone (this aspect is important for the analysis of pile driving, for instance). The results are given in Fig. 6.16. Note that, as has also been outlined previously, the normal strains ε_{p1} and ε_{p2} are zero using the novel interface formulation since the interface in-plane normal stress components develop identical to the corresponding continuum stress components. This is due to the boundary conditions of the simple interface shear test and not generally the case. For the approach by Stutz et al. [367] two different cases for the initialisation of the normal stress components in the interface are studied. The stress components are either initialised according to the initial continuum stress ($\sigma_{p1,0} = \sigma_{22,0}$ and $\sigma_{p2,0} = \sigma_{33,0}$), which is directly possible using `numgeo`, or initialised to the value of initial normal contact stress ($\sigma_{p1,0} = t_{N,0}$ and $\sigma_{p2,0} = t_{N,0}$), which corresponds to the restriction when using `Abaqus`. In terms of shear stress vs. tangential displacement all interface approaches give results similar to the simulation without interface. However, the approach by Stutz et al. [367] setting $\sigma_{p1,0} = t_{N,0}$ and $\sigma_{p2,0} = t_{N,0}$ gives slightly higher values of shear stress. This is absent if the interface stress is initialised by the continuum stress. Very similar results for all stresses are obtained using the novel approach and the approach of Stutz et al. [367] setting $\sigma_{p1,0} = \sigma_{22,0}$ and $\sigma_{p2,0} = \sigma_{33,0}$. It is also well visible that using the approach of Stutz et al. [367] setting $\sigma_{p1,0} = \sigma_{22,0}$ and $\sigma_{p2,0} = \sigma_{33,0}$ almost no jump between the interface and the continuum stress develops. This, however, is only the case for the simple interface shear test considered here, since the normal strain component ε_N of the interface and of the continuum is almost identical. For more complicated BVPs, as considered in Section 8.1, when using the approach by Stutz et al. [367], the interface stress develops in general differently to the adjacent continuum stress.

To assess the superior convergence rate obtained using numerical differentiation (see Section 6.7) compared to analytical derivatives of the hypoplastic interface model, the change of the norm of residual energy with respect to the number of iterations is given in Fig. 6.17 for the simulation of the monotonic simple interface shear test. In case of the numerical differentiation scheme both approaches, the simplified Eq. (6.56) where only the displacement increment is perturbed, and Eqs. (6.58, 6.59), for which in addition all state variables are also perturbed, are used. The first increment of the monotonic shearing phase of the simulation is considered.

Note that the analytical derivatives of the hypoplastic model are not consistent, since an analytical calculation of a consistent derivative is not possible using the hypoplastic model considered here. However, the derivative can be approximated. In the following, the derivative used is shortly explained. The objective stress rate of the (continuum) hypoplastic model with

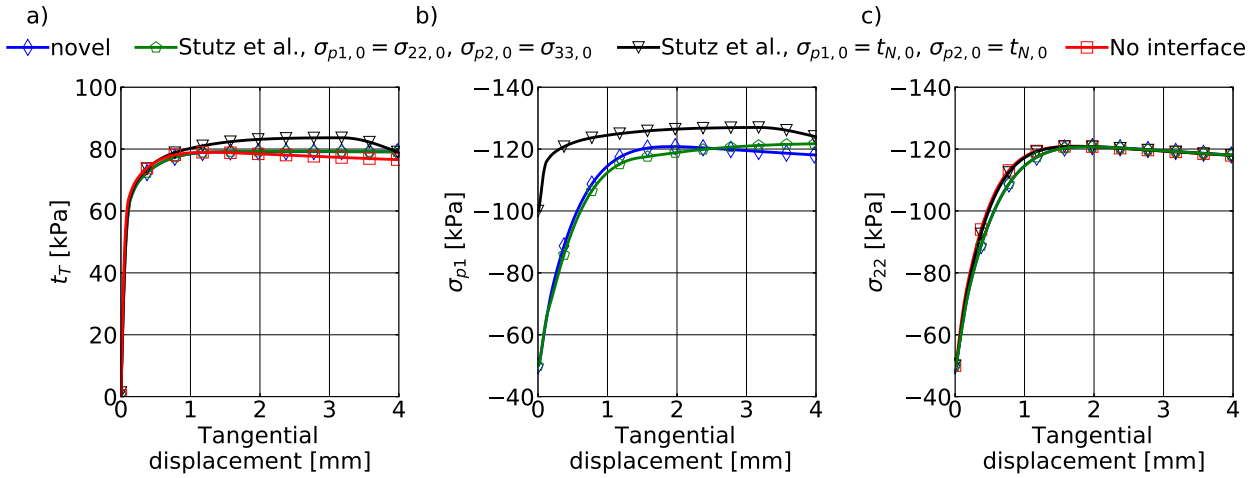

Figure 6.16: Results of the simulation of a simple interface shear test with perfectly rough ($\kappa = 1$) surface using the novel approach for the calculation of the stress conditions in the interface element, the approach by Stutz et al. [367] with different initialisation of the normal stress components in the interface and an approach without interface zone. The interface shear stress t_T and the interface normal stress component σ_{p1} vs. the tangential displacement u_T of the steel plate are displayed in plot a) and b). In addition, the continuum normal stress component σ_{22} vs. the tangential displacement is given in plot c). For the approach by Stutz et al. [367] the initial stress components are either initialised according to the initial continuum stress ($\sigma_{p1,0} = \sigma_{22,0}$ and $\sigma_{p2,0} = \sigma_{33,0}$) or to the value of initial normal contact stress ($\sigma_{p1,0} = t_{N,0}$ and $\sigma_{p2,0} = t_{N,0}$). In case of the simulation without interface, the displacement of the steel plate is prescribed to the nodes of the soil sample, using only the hypoplastic continuum model.

intergranular strain extension is given by [269] (see Eq. (A.1) in Appendix A.1)

$$\mathring{\boldsymbol{\sigma}} = \mathsf{M}(\boldsymbol{\sigma}, \mathbf{h}, e) : \dot{\boldsymbol{\varepsilon}}. \tag{6.88}$$

M is a fourth-order stiffness tensor, $\mathbf{h}$ is the intergranular strain tensor and e the void ratio. Discretising in time using finite increments, the derivative of Eq. (6.88) with respect to the strain increment is given by

$$\frac{\partial \Delta\sigma_{ij}}{\partial \Delta\varepsilon_{mn}} = M_{ijmn} + \frac{\partial M_{ijkl}}{\partial \Delta\sigma_{kl}} \frac{\partial \Delta\sigma_{kl}}{\partial \Delta\varepsilon_{mn}} \Delta\varepsilon_{kl} + \frac{\partial M_{ijkl}}{\partial \Delta h_{kl}} \frac{\partial \Delta h_{kl}}{\partial \Delta\varepsilon_{mn}} \Delta\varepsilon_{kl} + \frac{\partial M_{ijkl}}{\partial \Delta e} \frac{\partial \Delta e}{\partial \Delta\varepsilon_{mn}} \Delta\varepsilon_{kl}. \tag{6.89}$$

Only the first term of Eq. (6.89) is considered. For the use as interface model, the derivative is then given in Voigt notation by

$$J_{ik}^{\text{interface}} = \frac{\partial \Delta\sigma_i}{\partial \Delta\varepsilon_j} \frac{\partial \Delta\varepsilon_j}{\partial \Delta g_k} = M_{ij} \frac{\partial \Delta\varepsilon_j}{\partial \Delta g_k}, \tag{6.90}$$

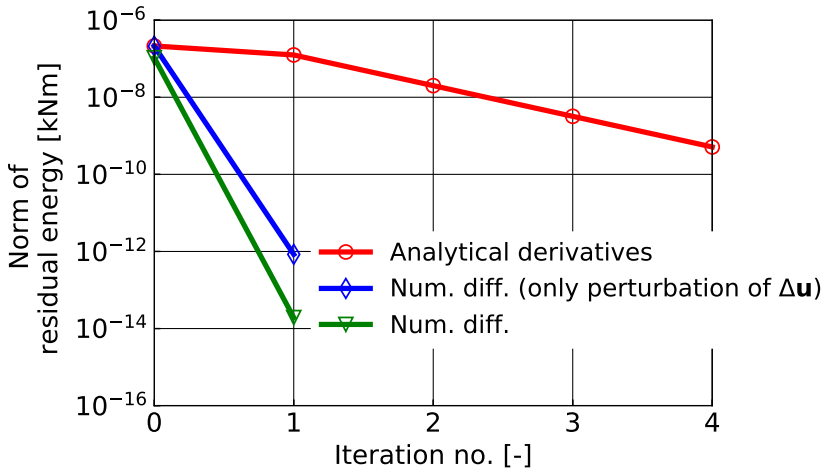

Figure 6.17: Change of the norm of residual energy with respect to the number of iterations for the simulation of the monotonic simple shear test using either analytical derivatives for the Jacobian of the hypoplastic interface model or the numerical differentiation schemes. For the numerical differentiation either only $\Delta \boldsymbol{u}$ is perturbed or all variables influencing the contact contributions (i.e. stress and other state variables) are perturbed.

where Δg_k is the increment of relative surface movement (see Eq. (6.28) for the definition of the tangential part). Figure 6.17 shows that using the numerical differentiation schemes presented in Section 6.7, the residual energy decreases much more rapidly compared to the approach using the analytical derivative. Compared to the simplified differentiation scheme where only the displacement increment is perturbed, the complete numerical differentiation scheme gives a slightly better convergence rate. However, considering the much larger computational effort of the complete scheme as explained in Section 6.7, the simplified scheme is used.

Tests with cyclic loading

The cyclic interface shear tests have been performed by Fakharian [109] and Fakharian & Evgin [110] as well. In contrast to the monotonic tests, constant normal stiffness conditions are considered. The initial normal stress is 300 kPa.

The simulation of a test with a normal stiffness of $K = 400$ kPa/mm and a tangential displacement amplitude $u_T^{\text{ampl}} = 0.75$ mm using the hypoplastic interface model is displayed in Fig. 6.18 for the novel formulation and the formulation by Stutz et al. [367]. Note that all normal stress components are initialised by the value of the normal contact stress using the approach by Stutz et al. [367]. Fig. 6.18a and Fig. 6.18c display the shear stress vs. tangential

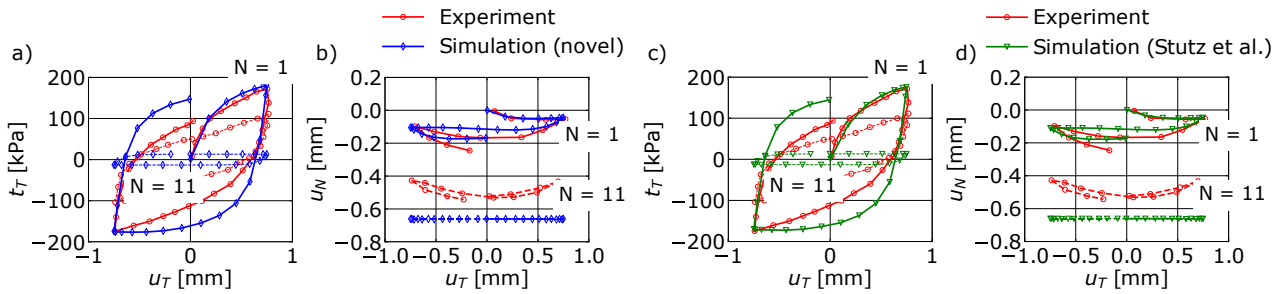

Figure 6.18: Results of the simulations of a cyclic simple interface shear test with constant normal stiffness using either the novel hypoplastic interface formulation (plot a and b) or the approach by Stutz et al. [367] (plot c and d) in comparison to the measurements made in the experiment. Plot a), c) and b), d) display the shear stress t_T and normal displacement u_N vs. tangential displacement u_T at $N = 1$ and $N = 11$ cycles, respectively.

displacement for the first ($N = 1$) and 11th ($N = 11$) cycle, comparing the results of the experiment and the simulations using the two approaches. The initial loading and un-loading is well reproduced by both simulations. The residual shear stress at the end of the first complete cycle is, however, too large compared to the measured value. Both the results of the simulations and the results of the experiment show much lower values of shear stress for the 11th cycle compared to the first cycle. In case of the simulations, the reduction of the shear stress is much more pronounced than for the experiment.

The normal displacement (of the entire soil sample and not of the interface alone) vs. tangential displacement plots given in Fig. 6.18b and Fig. 6.18d show that the compaction (negative values of u_N indicate reduction in soil volume) of the soil caused by the first cycle is well reproduced by both interface formulations. The compaction during the first quarter of the cycle is very well predicted, while the dilatancy during the third quarter is not well captured by the simulation. In addition, the compaction during the last quarter of the first cycle is underestimated. The compaction at the 11th cycle is overestimated, however. Larger normal displacement is predicted by the simulations in comparison to the experiment. During the 11th cycle almost no dilatancy and no accumulation of compaction occurs in the simulations, which stands in contrast to the curve of the experiment.

The results of the same test simulated using the novel HCA interface model are given in Fig. 6.19. In analogy to simulations with the continuum HCA model, the first two cycles are simulated using the hypoplastic interface model and the strain amplitude is calculated based on the recorded strain path of the second cycle. For the remaining 48 cycles only the mean trend is predicted by the HCA model. Therefore, the shear stress vs. tangential displacement plot is

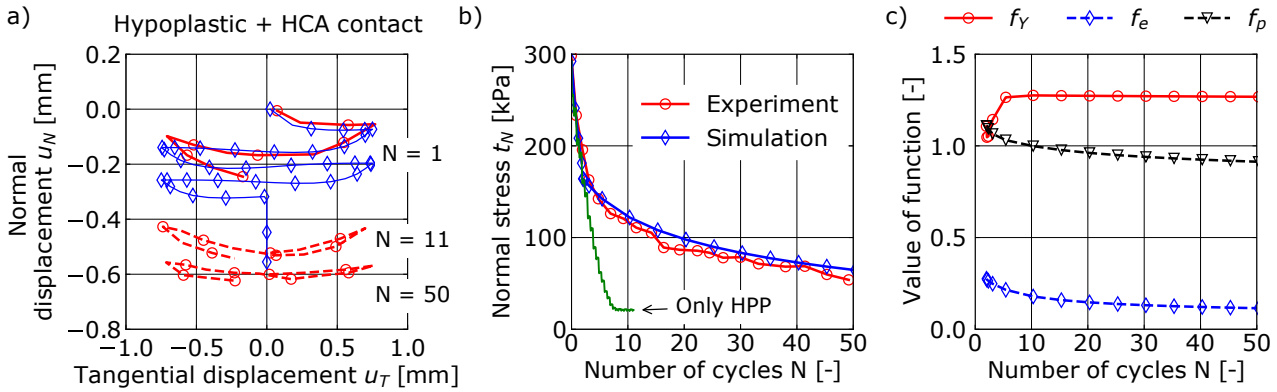

Figure 6.19: Results of the simulation of a cyclic simple interface shear test with constant normal stiffness using the novel HCA interface formulation in comparison to the measured values of the experiment. Plot a) displays the normal displacement vs. tangential displacement curves at $N = 1$, $N = 11$ and $N = 50$ cycles in case of the experiment and continuously for all load cycles in case of the simulation. Plot b) and plot c) depict the normal stress and the values of different functions of the HCA model vs. the number of applied cycles. In plot b) a simulation using only the hypoplastic interface model (HPP) is given in addition to the simulation with the HCA interface model.

not given for the simulation with the HCA model since the average tangential displacement is constant (zero in the present case) during the high-cycle phase. Note that the average value of shear stress reduces during the HCA phase. This tendency is also visible for the experiment from Fig. 6.18a.

The normal displacement vs. tangential displacement plot given in Fig. 6.19a shows the results of the experiment at $N = 1$, $N = 11$ and $N = 50$ cycles and the complete results of the simulation. During the HCA phase the normal displacement continuously increases in magnitude (the soil compacts) from $u_N \approx -0.3$ mm at $N = 2$ to $u_N \approx -0.55$ mm at $N = 50$. The final value is in good agreement with the results of the experiment at $N = 50$. The change of normal contact stress with the number of applied load cycles given in Fig. 6.19b shows that the simulation using the HCA model reproduces the results of the experiment very well and much more satisfactory than the simulation using the hypoplastic interface model alone. Note that the simulation with the hypoplastic interface model failed to converge for a number of cycles larger than 10 due to the low stress level reached.

Fig. 6.19c depicts the change of the functions f_Y, f_e and f_p of the HCA model with respect to the number of cycles. The function f_{ampl} considering the strain amplitude is not displayed

since it remains constant during the simulation (the adaptive definition of the strain amplitude proposed in Section 5.2.2 is not applied). Because the strain amplitude is comparably large in the present case ($\varepsilon^{\text{ampl}} \approx 0.05$), $f_{\text{ampl}} \approx 500$ is observed (note that the restriction $f_{\text{ampl}} < 10^{C_{\text{ampl}}}$ is not applied). Another test with a much smaller strain amplitude is presented later in this section. The function f_Y slightly increases at the beginning of the HCA phase due to the faster reduction of mean effective stress compared to the reduction of shear stress. For $N \geq 10$, the function stays constant indicating that the two effects outbalance each other. The factor f_e continuously decreases with the number of applied cycles due to the ongoing compaction of the soil in the interface. Because the parameter C_p is negative for the considered material, the factor f_p decreases with ongoing cyclic loading despite a decrease in mean effective stress of the interface. For most other soils, C_p is positive leading to an increase of f_p with decreasing mean effective stress.

The change of normal stress vs. the number of cycles for a test with a lower normal stiffness of $K = 200$ kPa/mm is given in Fig. 6.20a. Compared to the test with $K = 400$ kPa/mm, the normal stress reduces less during the cyclic shearing due to less contraction of the soil in the interface. The effect of the reduced normal stiffness is correctly represented by the simulation and the results fit well to the measurements of the experiment. The same comparison but now for a test with a reduced cyclic tangential displacement amplitude of $u_T^{\text{ampl}} = 0.25$ mm

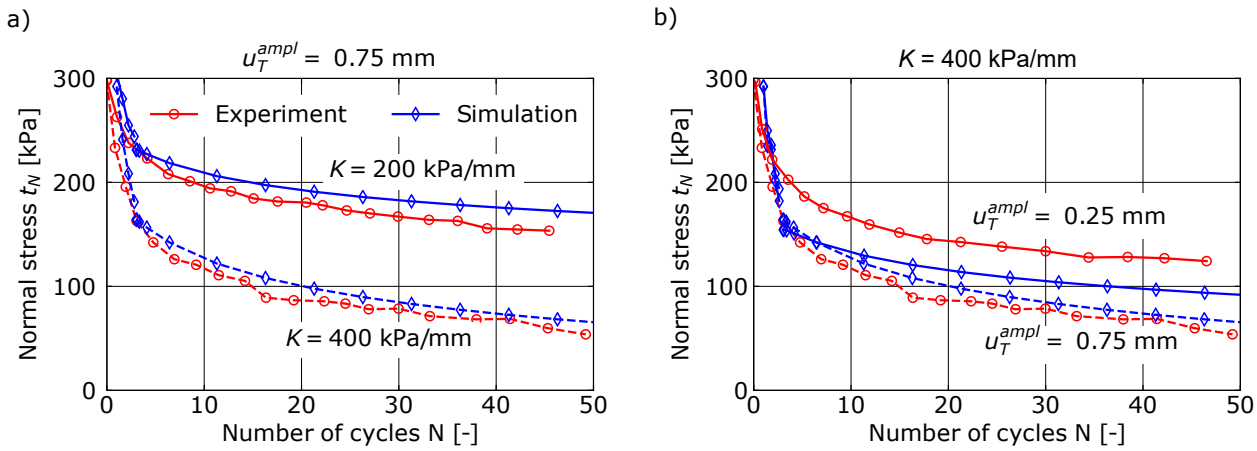

Figure 6.20: Results of the simulations of cyclic simple interface shear tests with constant normal stiffness using the novel HCA interface formulation in comparison to the measured values of the experiment. Plot a) depicts the normal stress vs. the number of applied cycles for two different values of normal stiffness using a cyclic tangential displacement amplitude of $u_T^{\text{ampl}} = 0.75$ mm. Plot b) shows the same as a) but for two tests with different cyclic tangential displacement amplitude and a normal stiffness of $K = 400$ kPa/mm.

($K = 400$ kPa/mm) is displayed in Fig. 6.20b. The strain amplitude in the simulation of this test is $\varepsilon^{\text{ampl}} \approx 0.01$ and the function $f_{\text{ampl}} \approx 100$. The lower tangential displacement amplitude results in less reduction of normal stress with respect to the number of load cycles for both the simulation and the experiment. In the simulation, however, only the change of normal stress during the HCA phase is influenced by the reduced tangential displacement amplitude, while no difference can be identified for the first two cycles where the hypoplastic interface model is applied. This results in an overestimation of the reduction of normal stress during the first two cycles compared to the experiment. The trend of normal stress after $N = 2$ (when the high-cycle phase starts) is very well reproduced by the simulation with the HCA interface model.

Chapter 7

numgeo: a finite element program for geomechanical applications

Jan Machaček started the programming of the finite element code numgeo during his PhD at KIT in Karlsruhe in 2017. The author of this work joined the project at the end of 2018. numgeo is a stand-alone and general finite element code with strong focus on geomechanics. Apart from the hydro-mechanically coupled CEL method implemented in Abaqus, all numerical schemes presented and discussed in the previous chapters are implemented in numgeo. Partly (e.g. in case of the novel constitutive interface models or the adaptive strain amplitude), an implementation of the proposed numerical schemes would be impossible using closed-source software, which highlights the advantages of in-house codes such as numgeo. In addition, most finite element codes do not offer hydro-mechanically coupled finite elements for the analysis of dynamic processes. Many researchers working in the field of geotechnics have therefore extended existing (closed-source) finite element codes by so-called user-defined elements [334, 67, 217, 218] or have proposed work-around solutions [151, 29, 351]. In many cases these extensions work only sub-optimal due to low performance or have some shortcomings due to restrictions of extensibility of the main code. Such shortcomings are circumvented with numgeo.

The most relevant features of numgeo are shown in Fig. 7.1. For further information on the numgeo project the interested reader is referred to www.numgeo.de and [238]. In addition, reference is made to the manuals distributed together with numgeo, which contain a list of available commands, an example manual as well as a material and an element guide. Note that the input file format, naming conventions and keywords are similar to those used by Abaqus. Therefore, users who are familiar with Abaqus can easily switch to numgeo. The compiled

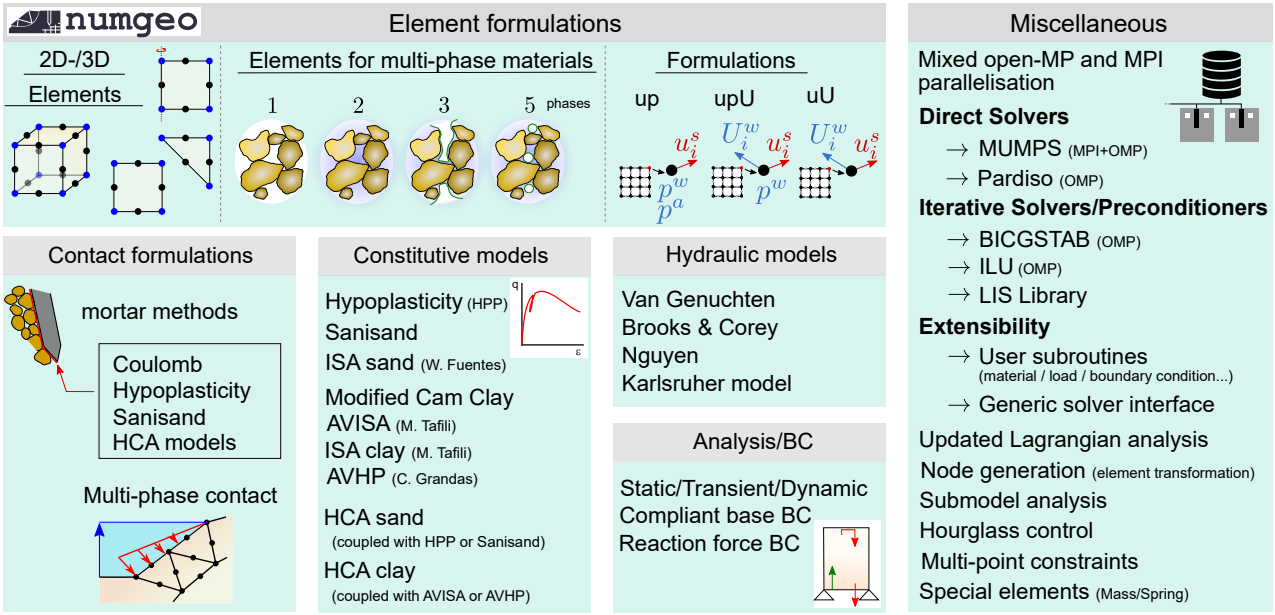

Figure 7.1: Key features of `numgeo`

program, in which almost all of the numerical schemes developed in the framework of this thesis are available[1], can be downloaded from `www.numgeo.de`.

This chapter gives insights into the implementation of some of the numerical schemes. In addition to source-code related subjects, comparisons with the results using the finite element program `Abaqus` are given for two benchmark simulations.

7.1 Implementations

`numgeo` is programmed in modern `Fortran`. Since `Fortran` 2003, object-oriented programming is possible, which allows to access globally defined variables at any point of the code avoiding the excessive use of local input-output variables of subroutines. An example of the object-oriented programming of the type `contact_node_obj` is given in Listing 7.1. This type carries all information of an individual contact node, e.g. the label of the connected node `connected_node` and the gap between the two nodes `gap`. The node object is part of the derived type `surface_obj`, as is defined in line 6 of Listing 7.1. Each surface has a list of nodes, all carrying the variables of `contact_node_obj`. The number of nodes of the surface is not known a priori, for why it is defined as allocatable array.

[1]The HCA model for clay and the interface models based on Sanisand and the HCA model for sand are yet not available in the public version.

```
type contact_node_obj
  integer(ik)                          :: connected_node
  real(rk), allocatable, dimension(:) :: gap
end type contact_node_obj

type surface_obj
  type(contact_node_obj), allocatable, dimension(:) :: node
end type surface_obj
```

Listing 7.1: Example of the object-oriented programming for the contact node type

`numgeo` uses a mixed MPI-OpenMP parallelisation. In general, every process has its own memory in case of MPI based parallelisation (*distributed-memory* processing). This makes the synchronisation of the different threads necessary. In addition, the complete program is run in parallel and not only individual parts of the code. In contrast, the memory is shared by all processes using OpenMP parallelisation (*shared-memory* processing). Only parts of the code are run with multiple threads, which are usually local loops with a large number of runs. OpenMP parallelisation is for instance used by `Yade`, which is a popular discrete element code [154].

Many loops in `numgeo` are parallelised using OpenMP (see [242]). Only one of the utilised direct-solvers, namely the `MUMPS` (MUltifrontal Massively Parallel sparse direct Solver) solver [14], uses a mixed MPI-OpenMP parallelisation. Similar hybrid approaches of mixed parallelisation are for instance used by `MOOSE` (Multiphysics Object Oriented Simulation Environment) [289].

In the following, pseudo-codes of the implementations of the proposed numerical schemes are presented and discussed exemplary. In particular, the multi-threaded computation of the SBM and EBM contact discretisation techniques as well as the nonlocal smoothing algorithm are presented.

7.1.1 Parallel computation of mortar segments

A pseudo-code of the implementation of the SBM contact discretisation is given in Listing 7.2. Having performed the initial contact pairing using the subroutine `get_contact_pairing` in line 0, the convective coordinate according to Section 6.4.1 is determined for every node (or integration point, depending on the algorithm) using the subroutine `convective_coordinate`. The segmentation as proposed in Section 6.4.2 is performed by the subroutine `mortar_segmentation`,

which allocates the derived type `contact%segment`, holding all *nseg* segments and their information. Up to this point, the program runs in serial (one thread) since the performed operations are not time consuming and only a few loops with a low number of runs exist.

```
0  call get_contact_pairing(...)
1  call convective_coordinate(...)
2  call mortar_segmentation(contact%segment,...)
3
4  !$omp parallel
5  !$omp private(iseg,...)
6  !$omp shared(contact,...)
7  !$omp do
8  do iseg = 1, size(contact%segment)
9  call interpolate_and_integrate_segment(iseg,...)
10 call save_segment_variables(iseg,...)
11 enddo
12 !$omp end do
13 !$omp end parallel
14
15 deallocate(contact%segment)
```

Listing 7.2: Pseudo-code for the SBM contact discretisation with parallel computation of the segments

The interpolation and integration of the segments being the most time consuming procedure, a parallel assembling of the segments using multiple threads is performed (`$omp parallel`). For the parallelisation using OpenMP, variables can either be declared as private variable, i.e. every thread has its own copy of the variable (line 5 of Listing 7.2), or shared, i.e. only one global copy of the variable exits (line 6 of Listing 7.2). For the parallel loop over all segments given in line 8 of Listing 7.2, the local iterator *iseg* is a private variable. The derived type `contact%segment` is shared since every thread writes to it. Every thread operates on a different segment, securing that no threads write to the same variable. Otherwise, so-called *race conditions*, where the solution is affected by the timing, or *data races*, where one thread operates on an object while another reads from it, could occur and the code would not be *thread-safe*. Of course, different threads are allowed to read the same variable at the same time.

After the integration of the segments, the contact variables are saved at the surface nodes (line 10). Finally, once the loop over the segments is finished, the derived type `contact%segment` is deallocated in line 14, since the number and order of segments can change from iteration to iteration.

Especially when using more advanced interface models such as the hypoplastic contact model proposed in Section 6.10, where the Newton iteration required to calculate the interface strain is computationally demanding, a considerable speed-up of the contact algorithms using multiple threads is achieved. Depending on the number of contact segments, number of integration points per segment and utilised number of threads, a nearly linear speed-up with respect to number of threads is accomplished.

7.1.2 Parallel computation using the EBM contact discretisation

Opposite to the SBM contact discretisation, the loop over the contact nodes of the surface *isurf* (derived type `contact%surface(isurf)%node`) is multi-threaded in case of the EBM contact discretisation. The pseudo-code is given in Listing 7.3. Because during the initial call of the subroutines thread-safety is not secured, the number of threads is limited to 1 as is given in line 0. This is because the node-to-node connectivity has yet not been evaluated. For all subsequent calls, the contact pairing, the evaluation of the convective coordinate and the update of the contact stress as defined in Section 6.3 can be performed using multiple threads. The integration and scattering to the SOE is currently not performed in parallel because it is much less computationally demanding than the update of the contact contributions.

```
0  if (first_call) call omp_set_num_threads(1)
1
2  !$omp parallel
3  !$omp private(inode,...)
4  !$omp shared(contact,...)
5  !$omp do
6  do inode = 1, size(contact%surface(isurf)%node)
7    call get_contact_pairing(inode,...)
8    call convective_coordinate(inode,..)
9    call update_stress(inode,...)
10 enddo
11 !$omp end do
12 !$omp end parallel
13
14 call integrate(...)
```

Listing 7.3: Pseudo-code for the EBM contact discretisation with parallel computation of the contact nodes

7.1.3 Parallel computation of the nonlocal smoothing algorithm

The nonlocal smoothing algorithm introduced in Section 5.2.2 used to smooth the field of the strain amplitude in a HCA simulation with adaptive strain amplitude is multi-threaded as well. The outer-loop over all elements *nelems* considered for the smoothing is performed in parallel, as is given in Listing 7.4. All local variables in the pseudo-code are private, whereas the global derived types `contact` and `element` are read from and written to by every thread in a shared manner. Having obtained the coordinates of two different integration points, the weighting function `weight_function` (e.g. a Gaussian function, see Eq. (5.38)) is called and the weight `alpha` obtained. The state variable `statev` is then multiplied by the weight in line 11. After all elements *nelems* in the *jelem* loop have been evaluated, the thread writes the private value to the shared object `element%no(ielem)%ip(jgauss)%statev(statev_no)`, in which the position *ielem* in the derived type is only accessed by the current thread.

```
0  !$omp parallel
1  !$omp private(ielem,igauss,jelem,jgauss,coordsi,coordsj,statev,alpha,...)
2  !$omp shared(contact,element,...)
3  !$omp do
4  do ielem = 1, nelems
5    do igauss = 1, ngpi
6    call ip_coords(coordsi,ielem,igauss,...)
7      do jelem = 1, nelems
8         do jgauss = 1, ngpj
9           call ip_coords(coordsj,jelem,jgauss,...)
10          call weight_function(coordsi,coordsj,alpha,...)
11          statev = statev + element%no(jelem)%ip(jgauss)%statev(statev_no)*alpha
12          sum_alpha += alpha
13        enddo
14     enddo
15     element%no(ielem)%ip(igauss)%statev(statev_no) = statev / sum_alpha
16   enddo
17 enddo
18 !$omp end do
19 !$omp end parallel
```

Listing 7.4: Pseudo-code for the nonlocal smoothing algorithm

The implementation is not limited to the smoothing of the strain amplitude for simulations with the HCA model but allows the smoothing of arbitrary state variables. The implementation of a nonlocal plasticity model such as proposed in [107, 288, 41, 186, 134, 370] is straightforward using the implementation given in Listing 7.4.

7.1.4 User-defined contact properties

`numgeo` supports the definition of so-called *user-defined subroutines*, allowing to customise parts of the code without having to recompile the source code, and thus enabling using a pre-compiled binary executable in combination with a code written by the user. For instance, such user-defined subroutines define user materials, user loads or user contact properties. The user-defined subroutines are called by the main program during run-time and have to be pre-compiled.

The user-subroutine for the definition of contact properties is given in Listing 7.5. Note that the implementation is based on the general framework by [242]. The subroutine is used to define the properties `props` of any constitutive interface model and allows to consider a time-dependency (`step_time`) or a dependency on the coordinate (`coords`) of the contact node (`node`). In addition, an influence of the displacement (`disp`) of the node and the coordinates (`coords_connected`) and displacement (`disp_connected`) of the connected node can be taken into account. Such dependencies are useful if e.g. the wall friction angle depends on the coordinate of the contact node or a reduction in time has to be accounted for.

```
0  subroutine user_contact_properties(istep,node,slave,nprops,interaction_type, &
1  step_time,coords,coords_connected,disp,disp_connected,props) &
2   bind(c,name='user_contact_properties')
3  use, intrinsic :: iso_c_binding
4  implicit none
5  integer(c_int)                    , intent(in)    :: istep
6  integer(c_int)                    , intent(in)    :: node
7  logical                           , intent(in)    :: slave
8  integer(c_int)                    , intent(in)    :: nprops
9  character(c_char)                 , intent(in)    :: interaction_type(*)
10 real(c_double)                    , intent(in)    :: step_time
11 real(c_double), dimension(3)      , intent(in)    :: coords
12 real(c_double), dimension(3)      , intent(in)    :: coords_connected
13 real(c_double), dimension(3)      , intent(in)    :: disp
14 real(c_double), dimension(3)      , intent(in)    :: disp_connected
15 real(c_double), dimension(nprops) , intent(inout) :: props
16
17 !user coding to define the contact properties props
18 write(*,*) 'WARNING: user_contact_properties is called without user coding'
19 props(:) = 0.0d0
20
21 end subroutine user_contact_properties
```

Listing 7.5: Subroutine for user-defined contact properties

7.2 Comparison of `numgeo` with `Abaqus`

Periodically, depending on the frequency of modifications made to the code, benchmark simulations are performed in order to secure the functionality of `numgeo`. Two of such benchmark simulations, which are in particular used to investigate the functionality of the contact algorithms, are presented in the following. The results using `numgeo` are compared to those using `Abaqus`. Only elastic simulations are considered in order to reduce the computational time of the benchmark simulation.

The results of the simulation of a large-scale interface shear test are shown in Fig. 7.2. The wall is moved downwards relative to the elastic body. A Coulomb model is used to account for friction. The identical mesh and type of elements is used for both finite element programs. Note that the benchmark is performed for different elements (2D/3D, linear and quadratic interpolation, full and reduced integration) and contact discretisation techniques but only the linear 2D case with full integration of the finite elements and the SBM contact discretisation is shown here. The other cases give the same results as presented in the following.

The normal and the shear contact stress histories at one node on the surface of the elastic body with respect to the displacement of the wall are given in Fig. 7.2a. For both contact

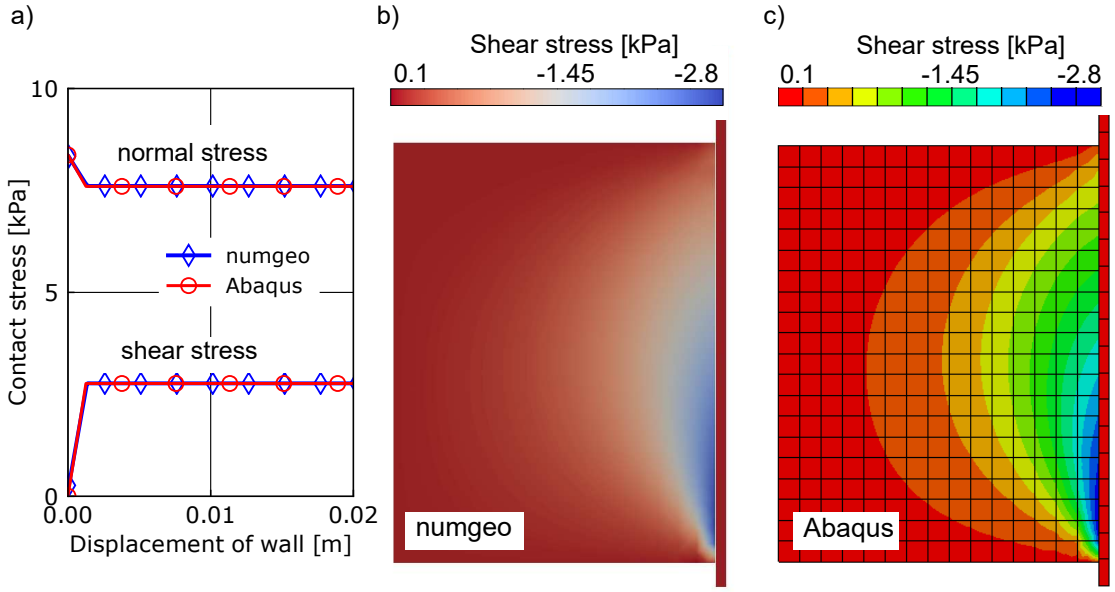

Figure 7.2: a) Normal and shear contact stress with respect to the displacement of the wall for the simulations using `numgeo` and `Abaqus`, respectively. b) and c) Spatial distribution of shear stress using `numgeo` and `Abaqus`, respectively.

stress components the results of `numgeo` and `Abaqus` coincide. Since no dilatancy is accounted for by the Coulomb friction model, the shear stress stays constant once fully mobilised. The spatial distribution of shear stress is given in Fig. 7.2b,c for `numgeo` and `Abaqus`, respectively. Due to the different post-processors, different colour maps are used. Despite the difference in visualisation, the distributions obtained using the two different finite element programs are in good accordance.

In order to show the performance of `numgeo` in three-dimensional contact analyses, the cyclic loading of a pile in elastic soil using `numgeo` and `Abaqus` is investigated. Figure 7.3a shows the comparison of the normalised pile head displacement ($u_1/u_{1,max}$) obtained from the simulations using `numgeo` and `Abaqus`, respectively. Note that $u_{1,max}$ is identical for the results of both programs. The results of the finite element programs are in good accordance, even if slightly larger deviations are observed compared to the interface test. The spatial distribution of normalised horizontal stress ($\sigma_{11}/\sigma_{11,max}$) and the deformed configuration at the maximum loading point is given in Fig. 7.3b using `numgeo` and in Fig. 7.3c using `Abaqus`. Note again that $\sigma_{11,max}$ is identical for the results of both programs. A direct comparison of the spatial distribution is difficult due to the different post-processors of the programs. Nevertheless, it is

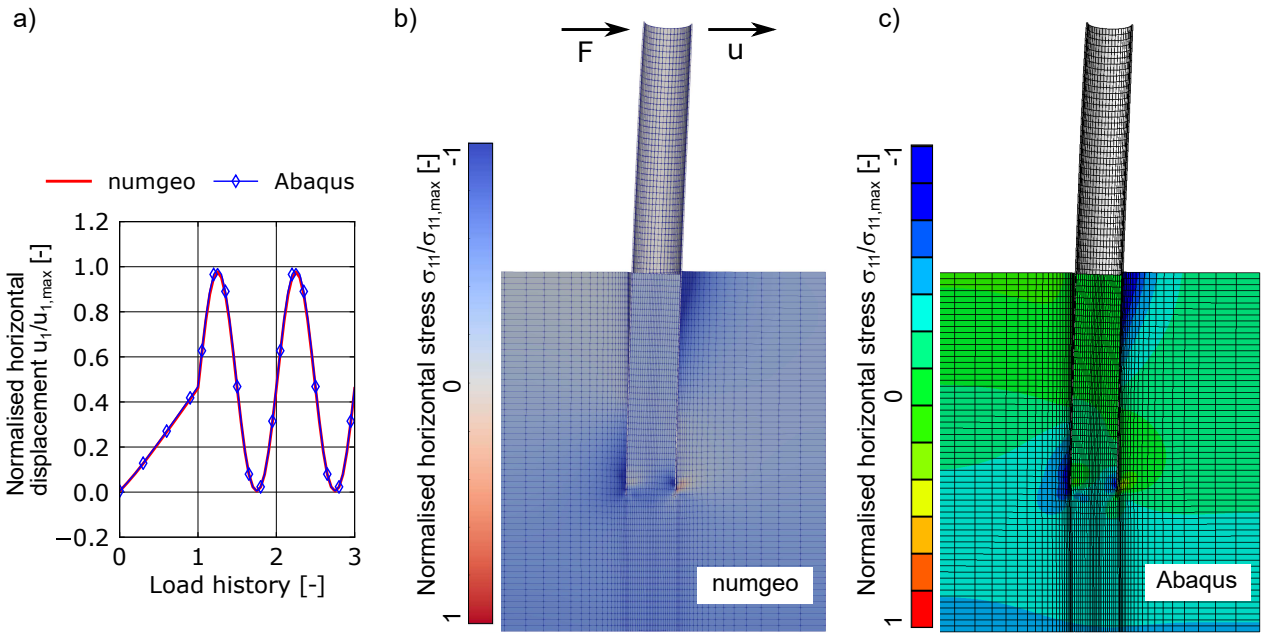

Figure 7.3: a) Normalised horizontal displacement ($u_{1,max}$ is identical for the results of both programs) at the pile head with respect to the load history using `numgeo` and `Abaqus`, respectively. b) and c) Spatial distribution of normalised horizontal stress ($\sigma_{11,max}$ is identical for the results of both programs) at the peak loading using `numgeo` and `Abaqus`, respectively.

visible that the magnitudes and the spatial distribution of the horizontal stress are comparable.

Additional comparisons of `numgeo` with `Abaqus` for the simulation of the lateral loading of piles using the hypoplastic model for the soil are reported by the author in [359]. Compared to the results displayed in Fig. 7.3, slightly larger differences between the two programs are observed, which are, however, judged to be within an acceptable range.

Note that `numgeo` has been benchmarked by a far larger number of BVPs than presented here. In particular, the results of simulations of monopile foundations for OWTs subjected to a large number of load cycles using the HCA model have been compared with the results obtained using `Abaqus`. The differences in the decisive output variables were in maximum 5 %.

Chapter 8

Application of the numerical tools and investigation of the influence of the pile installation on the response to subsequent loading

The numerical schemes developed in the Chapters 4 - 6 and implemented in `numgeo` are validated and employed for the simulation of pile installation and high-cyclic loading of piles in this chapter.

The proposed constitutive interface models presented in Section 6.10 are applied to the analysis of large-scale cyclic interface shear tests in Section 8.1. Simulations of vibratory pile driving experiments in water-saturated sand using the developed element formulations, contact discretisation techniques and the hydro-mechanically coupled CEL method are presented in Section 8.2.

Following the validation of the numerical methods for the simulation of the pile installation process, the influence of the installation on the response of piles to subsequent lateral (cyclic) loading is investigated in Section 8.3. The back-analysis of small-scale model tests on monopiles in sand subjected to up to 10,000 lateral load cycles using the HCA model is presented in Section 8.3.1. The long-term behaviour under cyclic lateral loading of vibratory driven piles in comparison to impact driven piles in dense sand is investigated in Section 8.3.2.

The application of the adaptive strain amplitude proposed in Section 5.2 to the simulation of the long-term behaviour of monopile foundations in soils with low hydraulic conductivity

is covered in Section 8.4. The HCA model for clay is validated based on the back-analysis of centrifuge tests on laterally loaded monopiles in Section 8.5. A parametric study on the long-term response of monopile foundations in clay is presented in Section 8.6. Finally, the effects of the installation process on the long-term deformations of monopile foundations in clay are investigated in Section 8.7.

8.1 Large-scale interface shear tests

The large-scale interface shear test set-up was originally developed by Rebstock [312] at the Institute of Soil Mechanics and Rock Mechanics at KIT, Karlsruhe. It has later been improved by Vogelsang [391, 393] and has been used to study the interface behaviour of soil for complex geometrical conditions and varying values of surface roughness.

8.1.1 Experimental set-up and numerical model

The dimensions of the test set-up are schematically shown in Fig. 8.1a. Dry sand has been pluviated in layers into the steel-framed box. The box is 1.2 m wide, 0.5 m deep and 2 m high. The wall on the right-hand side is made of four segments that can be shifted up- or downwards with a hydraulic drive. The resulting forces were measured with load cells attached to the segments in vertical and horizontal direction. Each segment has a width of 0.5 m and a height of 0.6 m. The second segment from below is sanded, thus its surface can be assumed as perfectly rough with $\kappa \approx 1$. The other three segments are made of stainless steel and have a smooth surface with a roughness of $\kappa \approx 0.35$ [393]. The imposed movement of the wall for the test considered for the numerical analysis is supplied in Fig. 8.1a. A cyclic displacement-time history with a 3 mm downwards phase followed by 1 mm upwards movement was used. The monotonic tests performed by Vogelsang are not considered here since the initial phase of the cyclic test is equivalent to the monotonic path and the results are therefore to some extent redundant. The considered test had an initial height of the sand volume of 1.56 m and a relative density of $D_{r0} = 70$ %. The segment at the bottom of the box overlapped the lower boundary of the sand volume by 9 cm at the start of the test.

Throughout the experiments performed by Vogelsang the so-called "Karlsruhe Sand", which is a medium coarse sand, has been used. The index parameters are supplied in Table 8.1. During the last decades, different sands have been referred to as "Karlsruhe Sand", which can differ

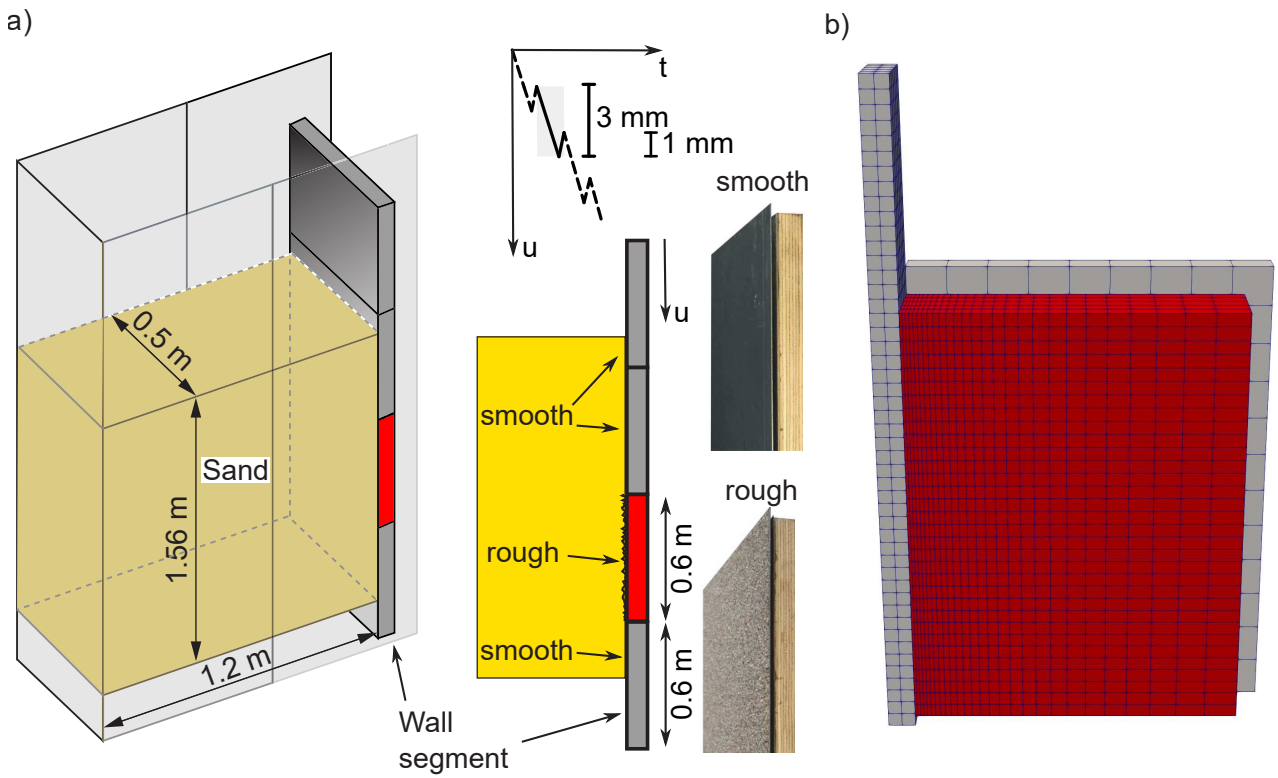

Figure 8.1: a) Large-scale interface test set-up (modified from [393]) with dimensions, photos of the surfaces of the different wall segments and imposed displacement-time history of the wall. b) Finite-element model adopted for the numerical analysis of the test.

significantly in their grain sizes and shapes. An extensive experimental study and description of the "Karlsruhe Sand" used in the experiments considered here is given in [391].

Parameter		Quantity	Unit
Grain density	$\bar{\rho}^s$	2.65	[g/cm^3]
Median grain size	d_{50}	0.55	[mm]
Coefficient of uniformity	C_U	1.5	[-]
Maximum void ratio	$e_{\max}$	0.857	[-]
Minimum void ratio	$e_{\min}$	0.555	[-]
Critical friction angle	φ_c	33.1	[°]

Table 8.1: Index parameters of "Karlsruhe Sand"

A 3D model with linearly interpolated and reduced integrated elements is used, which is displayed in Fig. 8.1b. The side wall is considered in the model in order to take into account the

friction at the soil-structure interface. The symmetry of the test is utilised such that only a soil volume of $0.25 \times 1.2 \times 1.56$ m is modelled. Vertical and horizontal displacement constraints are introduced at the bottom of the soil. The reason for constraining the horizontal displacement is the comparably rough surface of the bottom surface of the container. In accordance with the preliminary numerical analysis performed by Vogelsang using a simple Coulomb friction model [393], the pluviation of the soil is taken into account by incrementally increasing the gravity acting on the soil mass. The initial value of gravity $g = 2$ m/s^2 is increased by increments of 2 m/s^2 until $g = 10$ m/s^2 is reached. Discussion on the importance of incrementally increasing the gravity in order to correctly model the initial stress state can be found in [392, 393, 366]. The modelling of the pluviation process leads to lower final vertical and horizontal stresses because of the shear stresses developing at the sides of the container (arching effect). A geometrically non-linear calculation (updated Lagrangian) is performed. The Zaremba-Jaumann stress rate is used in order to ensure an objective stress rate. For the constitutive modelling of the interface either the hypoplastic model with intergranular strain extension, the Sanisand model or the Coulomb friction is used. The hypoplastic model is used for the continuum independently of the applied interface model. The novel formulation of the interface element according to Section 6.10.2 is used. Both normal stress components (σ_{p1} and σ_{p2}) are extrapolated from the continuum to the interface element. In addition, a simulation with the approach by Stutz et al. [367] is performed.

The constitutive parameters of the hypoplastic and the Sanisand model have been calibrated based on numerous oedometric compression, monotonic and cyclic triaxial tests on "Karlsruhe Sand" reported in [240]. Tests with low effective stress level have been used in order to best represent the conditions in the model tests. The parameters of the hypoplastic model are given in Table 8.2 and those for Sanisand in Table 8.3. If not stated otherwise, the shear band thickness is assumed to be $d_s = 6$ mm, which is $\approx 11 \cdot d_{50}$. This high value is chosen because the rough segment has a roughness of $\kappa = 1$, resulting in a very broad shear band. The initial lateral earth pressure coefficient for both directions prior to the incremental increase of gravity is assumed to be $K_0 = 0.5$. Friction at the smooth segments as well as the side wall is considered using the Coulomb friction model with a friction coefficient of $\mu = \tan(\delta) = 0.25$ ($\kappa \approx 0.35$) and a tangential stiffness of 6000 kN/m. In accordance with the observation that smooth surfaces can be adequately modelled using the Coulomb friction model (see Section 6.10), preliminary analyses using the sophisticated interface models also for the smooth segments and the side walls gave similar results as simulations using the Coulomb model. In addition, only 20 % of the total shear force of the moving wall originates from the smooth segments while 80 % is mobilized at the rough segment [393]. Therefore, due to the improved computational

performance, the Coulomb model is applied for the smooth surfaces.

φ_c	e_{i0}	e_{c0}	e_{d0}	h_s	n	α	β	m_R	m_T	R	β_R	χ
33.1°	0.979	0.851	0.549	19 GPa	0.285	0.1	0.32	2.4	1.2	$5 \cdot 10^{-5}$	0.08	7

Table 8.2: Parameters of the hypoplastic model with intergranular strain extension for "Karlsruhe Sand" [240]

p_a	e_0	λ_c	ξ	M_c	c	m	G_0
100 kPa	1.1	0.25	0.35	1.3	0.88	0.05	70
ν	h_0	c_h	n_b	A_0	n_d	$z_{\max}$	c_z
0.05	8	0.35	1.3	0.8	0.8	60	2000

Table 8.3: Parameters of the Sanisand model for "Karlsruhe Sand" [240]

To the author's best knowledge only very few of the advanced constitutive interface models proposed in the literature have been applied to complex BVPs with cyclic shearing such as the large-scale interface tests considered here. Examples for the application of advanced constitutive interface models to more complex BVPs can be found in [231, 324]. The rare application to complex BVPs is believed to be due to the inferior convergence rate faced when introducing strongly non-linear interface models in implicit calculations. These problems are to some extent circumvented in the numerical implementations used in the present work, since a consistent Jacobian is secured by the numerical differentiation scheme introduced in Section 6.7. It is worth noting that simulations of the large-scale interface tests using an analytically derived Jacobian of the contact contributions did not converge.

8.1.2 Results of the simulations

The results of the experiments and the simulations are evaluated in terms of (spatially) average shear and normal stress (positive values indicate compression in this and all forthcoming sections) measured at the rough segment. During the test, the forces acting normal and tangential to this segment were measured. Based on these forces, the average stress of the segment was calculated. The results of the tests and those of the simulations using the hypoplastic model

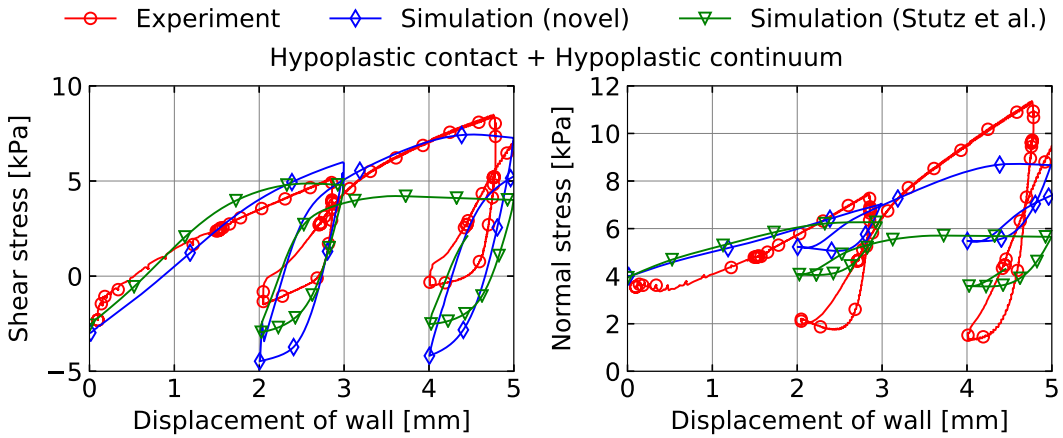

Figure 8.2: Average shear stress and normal stress of the rough segment vs. displacement of the wall for the values measured in the experiment and the simulations using the proposed hypoplastic interface model (novel) and the approach by Stutz et al. [367], respectively

for the interface as well as for the continuum are given in Fig. 8.2. Predictions by both the novel interface approach and the approach by Stutz et al. [367] are given. Two cyclic movement phases are studied. A positive value of wall displacement indicates downwards directed movement. Both simulations capture the slightly negative shear stress prior to the wall movement caused by the soil assembling process well. Likewise, the initial normal stress is in good accordance with the measurements of the experiment. Both the shear and the normal stress increase when the wall starts to move downwards, which is well predicted by both simulations qualitatively and quantitatively. The values reached at a wall movement of 3 mm are in good agreement with the measurements of the test. The approach by Stutz et al. [367] results in an earlier and lower peak of the shear stress reached before 3 mm wall displacement. When the wall movement is reversed, both the shear and the normal stress reduce. In case of the normal stress, both simulations capture the rapid reduction at the initial stage of the reversed movement but show much higher values compared to the measurements for larger wall displacement. Since the simulation using the approach by Stutz et al. [367] starts with a lower value of normal stress at the point of reversal, the minimum value reached at a wall displacement of 2 mm is also lower, fitting better to the experiment compared to the novel approach. Due to this overestimation of the normal stress by both simulations, the reduction in shear stress after reversal is in turn overestimated, since the yielding shear stress is in magnitude much higher compared to the experiment. The minimum shear stress reached during the upwards movement in the experiment is much higher due to the lower normal stress.

Similar observations are made for the second cycle. In terms of normal stress the discrepancies between the measurements and the results of the simulations increase for both the downwards and the upwards movement phase. For both wall movement phases the increase respectively decrease in normal stress is too small in the simulations compared to the measurements. Compared to the novel approach, the approach by Stutz et al. [367] shows much lower values of shear and normal stress during the second cycle, resulting in a worse accordance with the measured values. In addition, the continuous increase in both stress components during the downwards movement in the second cycle is not reflected. Overall, the novel approach leads to higher maximum shear stress, in particular for the second cycle. This is reasonable, since the vertical stress of the continuum is taken into account by the novel approach. Since the vertical stress is larger than the horizontal stress components, higher mean stresses act in the interface resulting in a higher shear resistance. This is also visible from Fig. 8.3, which depicts the development of the normal stress components in an interface point at the lower half of the rough segment for the two approaches. The component σ_{p1} corresponds to the horizontal stress component tangentially to the interface zone while σ_{p2} is acting in vertical direction (in this particular case the orientations of the normal stress components in the interface are identical to the global coordinate axes). Much larger values of σ_{p1} and σ_{p2} develop during the wall movement using the novel approach. Especially the vertical stress (σ_{p2}) increases significantly, which can be explained by an impaction of soil (i.e. a zone of stress concentration) between the rough segment and the bottom of the container during the downwards movement. This is visible from the spatial distribution of vertical stress given in Fig. 8.6, which is discussed in more detail later. Such influences resulting from the geometry and boundary conditions of the

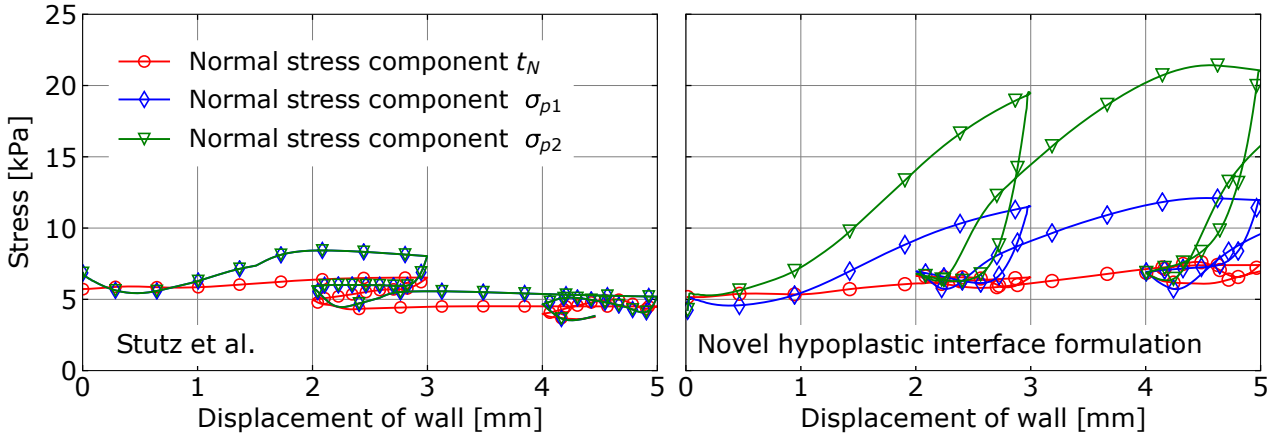

Figure 8.3: Development of the normal stress components in an interface point at the lower half of the rough segment for the approach by Stutz et al. [367] and the novel approach using the hypoplastic interface formulation

BVP are only indirectly considered by the approach of Stutz et al. [367]. The horizontal stress component (σ_{p1}) obtained with the novel approach, however, does not differ as significantly as the component σ_{p2} from the values obtained using the approach by Stutz et al. [367]. When the wall moves upwards, values lower than the initial state are observed. Slightly lower values are obtained for the approach by Stutz et al. [367] at maximum upwards movement, which explains the slightly lower absolute values of shear stress observed in Fig. 8.2. Figure 8.3 demonstrates that the normal stress components in the interface zone diverge considerably during shearing and the assumption of $\sigma_{p1} = \sigma_{p2}$ is not valid for this BVP.

The corresponding simulation using the Coulomb friction model for the rough segment is presented in Fig. 8.4. The normal and tangential stresses prior to the movement of the wall are again in good accordance with the measured values. Both the shear and normal stress increase less in the initial wall displacement phase compared to the simulation using the hypoplastic interface models. The maximum shear and normal stresses measured at a wall displacement of 3 mm in the experiment are both underestimated by the simulation. No sliding of the soil at the rough segment is encountered, which is visible by the steady increase in shear stress without approaching a constant maximum value. When the wall moves upwards again, both the shear and the normal stress reduce with almost the same inclination in the stress-displacement diagram as during the downwards movement. This is in contrast to the measured stress-displacement histories, which show a much stronger reduction in stress during the first $\approx$ 0.2 mm of upwards movement. The reduction in the normal stress during this phase is strongly underestimated by the simulation using the Coulomb interface model. The simulations using the hypoplastic models show a much better accordance with the experimental results, capturing the strong initial reduction in normal stress.

The results demonstrate the large influence of the constitutive interface model on the simulation results. Despite using the hypoplastic model for the continuum, the simulation using the Coulomb friction model is not capable to capture many aspects of the interface behaviour. The proposed hypoplastic interface model is able to predict the changes in the inclinations of the stress-displacement curves at reversals of the wall displacement direction as well as the significant increase in normal stress with downwards wall movement.

The shear band thickness is a parameter of the interface model which adds a considerable uncertainty due to its wide range of possible values (see Section 6.10.3). Therefore, a comparison for values of the shear band thickness of $d_s = 6$ mm and $d_s = 4$ mm $\approx 7 \cdot d_{50}$ is provided in Fig. 8.5. The hypoplastic model is used for the interface as well as for the continuum. Only the novel interface formulation is used. For the first phase of the wall movement both simulations

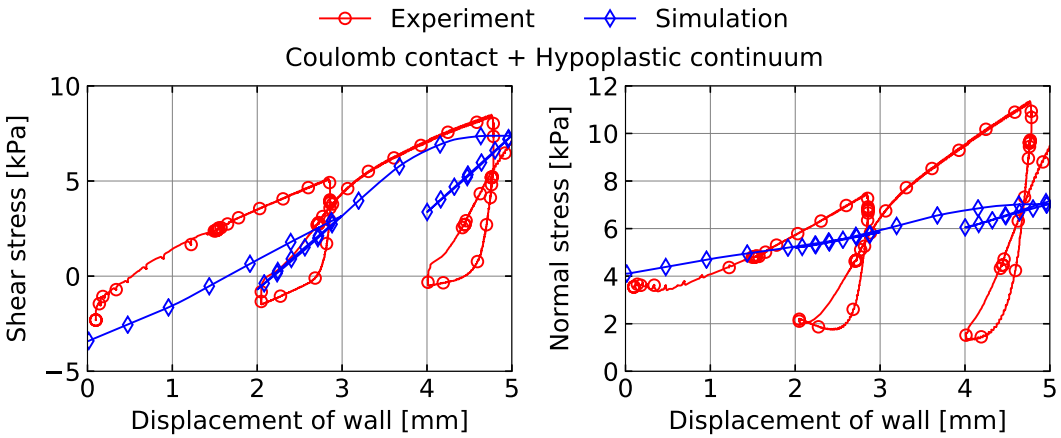

Figure 8.4: Comparison of the experimental results with a simulation using a Coulomb interface model

show a comparable change in shear and normal stress. A slightly faster mobilisation of stress is observed for $d_s = 4$ mm due to the higher shear strain in the interface element for the same wall movement. Furthermore, a slightly stronger reduction in normal stress during the first upwards phase is observed for $d_s = 4$ mm, which is in better accordance with the experimental values compared to the simulation using $d_s = 6$ mm. In the subsequent downwards movement of the wall, the simulation using $d_s = 4$ mm results in a lower magnitude of maximum shear stress compared to the simulation with $d_s = 6$ mm. The simulation with $d_s = 6$ mm shows larger amplitudes of shear stress compared to the simulation with $d_s = 4$ mm. This difference

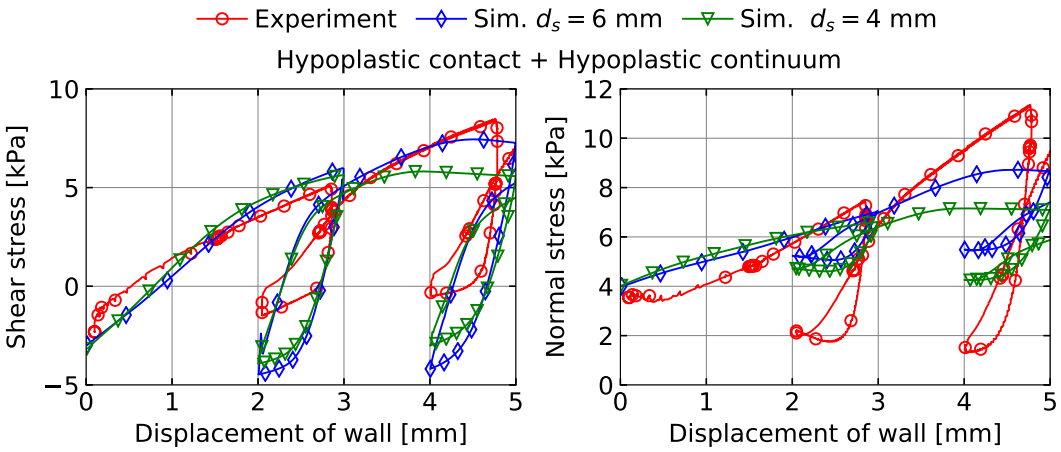

Figure 8.5: Average shear stress and normal stress of the rough segment vs. displacement of the wall for the values measured in the experiment and the simulations using the proposed hypoplastic interface model comparing two different values of shear band thickness d_s

seems to increase with ongoing cyclic wall movement since the differences in the shear stress amplitude are larger for the second cycle compared to the first one. It can be noted that the influence of the shear band thickness is low for the first cycle but seems to increase with ongoing cyclic loading.

The spatial distributions of the (continuum) shear stress component σ_{31}, of the horizontal stress σ_{11} and of the vertical stress σ_{33} are provided in Fig. 8.6 at the time of the maximum downwards movement of the wall in the first cycle. The hypoplastic model is applied for the contact and the continuum. Only the novel interface formulation is used. The rough segment is easily identifiable by the large shear stress acting in the soil adjacent to it. Merely small values are observed for the soil adjacent to the smooth segments. At the same wall movement, the horizontal and vertical stresses are also significantly increased in the vicinity of the rough segment. The horizontal stress acting close to the smooth segment below the rough segment is noticeably reduced due to the wall displacement. From the field of vertical stress, a zone in the shape of a triangle with high values of stress is visible (impacted soil zone). This has already been mentioned previously and is, since the vertical stress enters the interface formulation, one of the reasons why the novel interface formulation predicts higher shear stresses at the rough

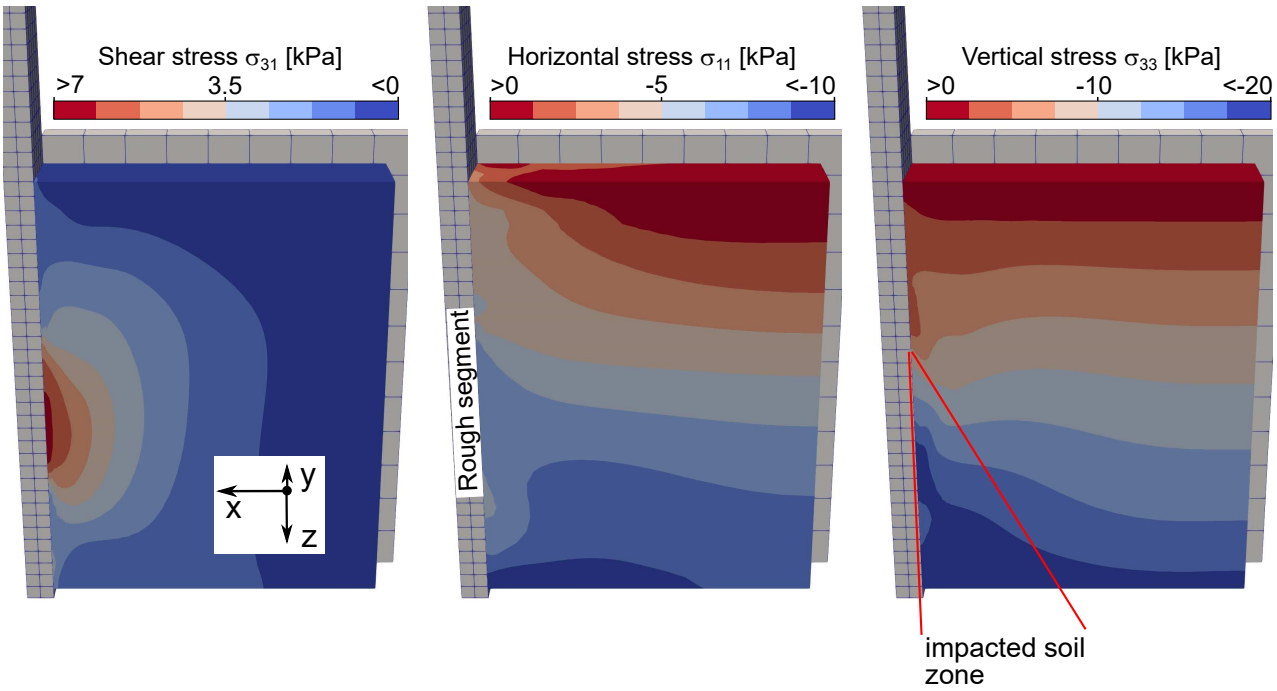

Figure 8.6: Spatial distribution of shear stress σ_{31}, horizontal stress σ_{11} and vertical stress σ_{33} at the time of maximum downwards movement of the wall in the first cycle using the hypoplastic model for both the interface and the continuum

segment during the downwards movement of the wall compared to the approach by Stutz et al. [367].

In another comparison, the Sanisand interface model proposed in Section 6.10.6 is applied. Note that the hypoplastic model is used for the continuum nevertheless. Simulations using Sanisand for both the interface and the continuum give similar results but the convergence using the Sanisand model for the continuum is worse compared to the application of the hypoplastic continuum model. Using the Sanisand interface model both the shear and the normal stress at the downwards movement phases of the wall are better captured than using the hypoplastic interface model as is visible from Fig. 8.7. During the upwards movement, however, the normal stress is overestimated in comparison to the values measured in the experiment as well.

The comparisons of the simulations with the results of the model tests show that the constitutive interface model is of great importance for the mechanical response of rough soil-structure interfaces. In particular, the stress development in the interface due to the cyclic movement of the wall cannot be adequately captured using a Coulomb friction model. The novel interface models proposed in this work are found to deliver a better reproduction of the measurements than the approach by Stutz et al. [367], highlighting the importance of the stress conditions in the interface element. However, independent of the employed interface formulation, the reduction of the normal stress at the rough segment at wall movement reversal is not well predicted by the numerical simulations. Since considerable shear strains are developing in the continuum during the wall movement, it would be interesting to study if a micro-polar contin-

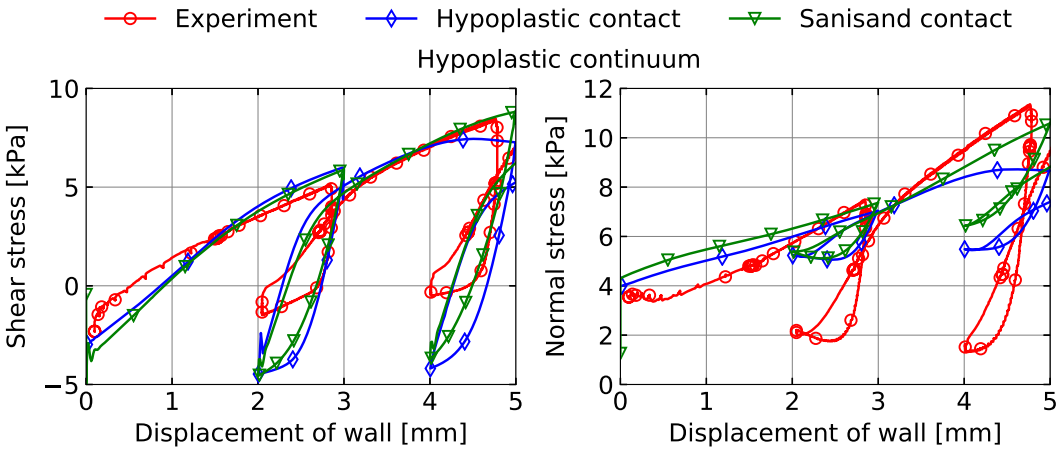

Figure 8.7: Comparison of the experimental results with a simulation using the hypoplastic and the Sanisand interface model in the framework of the novel interface formulation

uum formulation of the hypoplastic model (see e.g. [379, 38]) gives different results than the standard formulation employed herein.

8.1.3 Computational performance

Table 8.4 gives the total number of iterations, the total time to finish the calculation and the total time spent in the contact routines for the simulations of the large-scale interface shear test using the different interface models and formulations. Unsurprisingly, the Coulomb friction requires the fewest number of iterations and results in the shortest calculation time. The time spent in the contact routines is only 10 % of the total time of the simulation. For the novel hypoplastic interface formulation more iterations and much more time is required. The ratio of time spent in the contact routines to total time increases to 30 %. An even worse computational performance is observed using the novel interface formulation in combination with the Sanisand model, even though slightly less iterations are required. Approximately 40 % more time is spent in the contact routines compared to the hypoplastic interface model. These differences are not due to the formulation as interface models but result from the general formulation and implementation of the (continuum) constitutive models underlying the interface formulation. The implementation of the hypoplastic continuum model employs an adaptive sub-increment scheme with error control whereas for the Sanisand model an explicit sub-stepping scheme is used (see Appendix A for details on the implementation of the constitutive continuum models).

Simulation	No. of iterations	Total time [s]	Time contact [s]
Coulomb friction	2600	5969	618
Novel hypoplastic interface	2950	8540	2524
Novel Sanisand interface	2710	9343	3459
Hypoplastic interface by Stutz et al.	2730	8504	2463

Table 8.4: Number of (global) iterations, total (physical) time and (physical) time spent in the contact routines for the different interface models and formulations. The contact routines, element loop and the solver are all run with four native cores (one Intel®Core™ i9 9900K processor with four cores run with the base-frequency of 3.6 GHz without utilising Hyper-threading is used).

Compared to the novel hypoplastic interface formulation the approach by Stutz et al. [367] shows a slightly better numerical performance. This is because no extrapolation of stresses from the continuum is required. In addition, fewer global iterations are required, which can be explained by the lower values of shear stress developing at the rough segment, leading to less changes in strains and stresses in the continuum and the interface.

8.2 Vibratory pile driving in water-saturated sand: Back-analysis of model tests

The following investigations are made with reference to the simulation of vibratory pile driving model tests in water-saturated sand:

- Investigation of the influence of relative acceleration using the **u**-p and **u**-p-**U** element formulation (Section 8.2.2).
- Comparison of the two developed contact discretisation techniques (EBM and SBM methods) as well as a comparison of the Coulomb friction model with the proposed hypoplastic and Sanisand interface models in Section 8.2.3.
- Lastly, the hydro-mechanically coupled CEL method is compared to simulations using Lagrangian elements in Section 8.2.4.

Note that in addition to the investigations listed above, the influence of the constitutive soil model (using the hypoplastic model with intergranular strain, Sanisand and the hypoplastic model with intergranular strain anisotropy (ISA) [128, 294]) has been studied in [240, 237] for the vibratory pile driving model tests considered. From this study it was concluded that all three constitutive models can reproduce the most important aspects of the vibratory pile driving process. Therefore, only the hypoplastic model with intergranular strain is applied for the constitutive modelling of the continuum in this section.

The simulations are also performed using an iterative solver instead of the direct `MUMPS` solver [14] used for all other simulations in this section. The results using an iterative solver are discussed in Appendix C.1. Only when using a *multilevel incomplete LU factorization* (MILU) pre-conditioner with a very low *drop-tolerance* of the lower and upper triangular matrix numerical stable results can be achieved using an iterative solver. Since the computational effort increases significantly with decreasing drop-tolerance, the direct solver is found to be superior to the iterative solver.

8.2.1 Vibratory pile driving model tests

The small-scale model tests used for the back-analysis were performed by Vogelsang and are documented in [392, 394, 393]. A schematic sketch and a picture of the half-axisymmetric test device is displayed in Fig. 8.8. The vibrator was realised as a pair of unbalances mounted on top of the pile. A load cell was placed between the vibrator and the pile. Two pore pressure transducers (PPT A and PPT B, see Fig. 8.8) were installed at the front window. In analogy to the large-scale interface tests discussed in the previous section, "Karlsruhe Sand" has been used, which was pluviated into deaerated water and further densified through hammer blows against the container. The final relative density was 71 % which corresponds to a porosity of $n = 0.39$ and a total density of $\rho^{\mathrm{tot}} = 2.02$ g/cm^3. The index properties of "Karlsruhe Sand" are given in Table 8.1 in the previous section.

A closed-profile pile with a 60° pointed tip and a radius of 16.5 mm ($d^{Pile} = 33$ mm) was used in the experiments. The closed-profile was preferred over an open-profile in order to be able to simulate the experiments without mesh distortion using a fully Lagrangian analysis. The aluminium pile had a smooth surface and a wall friction angle of approximately $\delta \approx 1/3\varphi_c = 11°$, with φ_c being the critical friction angle of the sand. This results in a surface roughness of $\kappa = \tan(\delta)/\tan(\varphi_c) = 0.3$.

Prior to driving, the pile was pushed into the sand up to a depth of approximately 15 cm. During driving, the vibrator was free to move in vertical direction and its self-weight of 6.594 kg was completely carried by the pile. A guiding allowed movement of the pile in vertical direction only. The combined mass of the pile, the load cell and the vibrator was 7.881 kg.

Additional experiments with pile installation in a full cylindrical container have shown results very close to those obtained with the set-up shown in Fig. 8.8 as reported in [393]. Thus, the model test can be treated as an axisymmetric problem in the numerical simulations.

The mesh adopted for the Lagrangian simulations including boundary conditions and dimensions is given in Fig. 8.8c. A full axisymmetric model is used. The forces and masses are scaled to fit to the half-axisymmetric experimental set-up. The so-called zipper-method is used to avoid mesh distortion when the pile penetrates into the soil. This technique is established for axisymmetric penetration problems [45, 165]. Using this approach, the boundary of the soil in the symmetry axis below the pile tip is not constrained by Dirichlet boundary conditions in horizontal direction but by a contact constraint with a thin vertical extension of the pile directly in the symmetry axis (see red line in Fig. 8.8). When the pile penetrates into the soil this allows the elements below the tip to be pushed to the side by the pile which would not

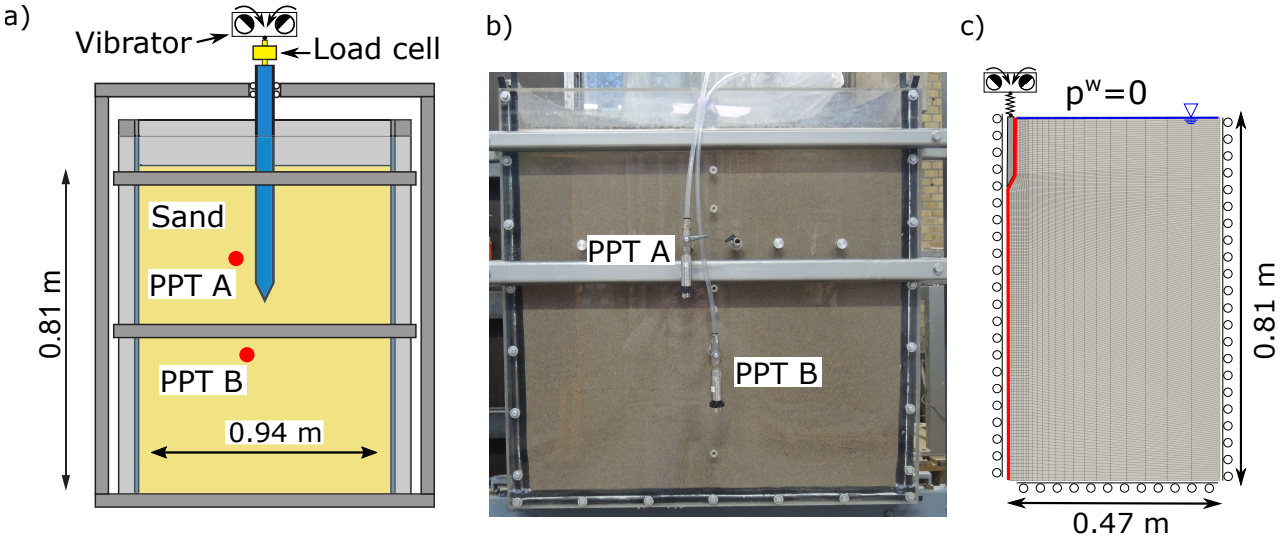

Figure 8.8: a) Schematic drawing of the front of the test device. b) Photo of the device (based on [392, 394]). c) Finite element model for the Lagrangian simulation. The red line in Fig. c) indicates the extension of the pile used for the zipper-method.

be possible if they would be constrained by a Dirichlet boundary condition.

The load cell is replaced by a spring with identical stiffness. The unbalances on top are idealised as a mass point. The driving force of the vibrator is applied on this mass point and transferred by the spring to the top of the pile. Using a vibratory frequency of 25 Hz, the amplitude of dynamic force F^{ampl} is 0.225 kN. The dynamic force exerted by the vibrator over time and the corresponding frequency are given in Fig. 8.9. Note that since the unbalances required a specific time to reach the desired frequency in the experiments, a linear increase in the force amplitude is assumed for the first 0.05 s.

A geometrically non-linear calculation is performed and the Zaremba-Jaumann stress rate (see Eq. (3.29)) is used. The EBM contact discretisation technique with 3 integration points per element edge is used for the investigation of the influence of relative acceleration in the subsequent section. The Coulomb friction model with a friction coefficient of $\mu = \tan(\delta) = 0.19$ is used. Note that the bulk modulus of the pore water is assumed to be $\bar{K}^w = 2.2$ GPa for the simulations presented in the next section. For the initial porosity of the considered test the hydraulic conductivity of "Karlsruhe Sand" is $k^w = 1.1 \cdot 10^{-3}$ m/s.

The Hilber-Hughes-Taylor (HHT) time integration scheme (see Section 4.3) with a damping parameter $\alpha = 0.05$ is used during the dynamic step. A constant time increment of $\Delta t = 0.001$ s is set.

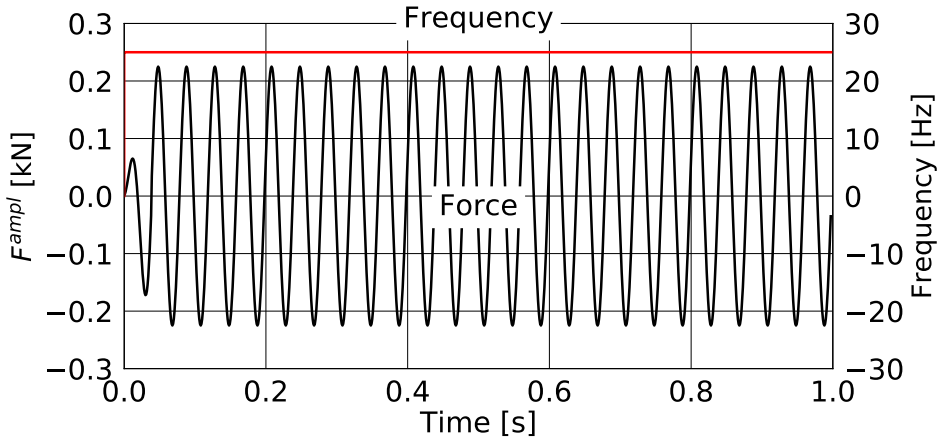

Figure 8.9: Vibratory driving force F^{ampl} and frequency over time

8.2.2 Comparison of different hydro-mechanically coupled finite element formulations and influence of relative acceleration

In order to verify the conclusions drawn on the influence of relative acceleration in Section 4.4 for a complex BVP, the vibratory pile driving model tests are simulated with two different finite element formulations in this section. As has been outlined in Chapter 4, the **u**-p finite element formulation assumes the relative acceleration to be negligible. The validity of this assumption depends on the wave frequency and the hydraulic conductivity of the soil, which has been discussed in detail in Section 4.4,. Since vibratory pile driving involves high frequencies and the "Karlsruhe Sand" used in the vibratory pile driving model tests has a relatively large hydraulic conductivity of $k^w > 10^{-3}$ m/s, the relative acceleration might have a large influence on the numerical solution. Therefore, the **u**-p-**U** element formulation derived in Section 4.2 is applied in addition to the **u**-p formulation. A comparison of the results using the two different element formulations allows to quantify the influence of the relative acceleration and hence the applicability of the **u**-p formulation.

Note that the results presented in the following have partly been already published by the author in [349, 348]. However, the simulations reported in these papers have been performed using `Abaqus` in conjunction with user-defined finite element implementations of the **u**-p, **u**-**U** and **u**-p-**U** formulations. The shortcomings of these simulations (e.g. only frictionless contact due to inability to distinguish between total and effective normal contact stress, see [349, 348]) are not faced in the simulations presented in the following using `numgeo`. The water displacement DOFs of the **u**-p-**U** elements are constrained with the solid displacement using a multi-point constraint based on the penalty technique in order to secure consistency with

the simulation using **u**-p elements. The fluid-phase contact introduced in Section 6.9 is not applied.

For the evaluation of the pile penetration the normalised pile displacement $\tilde{u}_y$ is used, which is defined by

$$\tilde{u}_y = \frac{u_y}{d^{Pile}}. \tag{8.1}$$

In Eq. (8.1), u_y is the vertical displacement of the pile and d^{Pile} is the pile diameter.

The normalised pile displacement vs. time of vibration is depicted in Fig. 8.10a for the experiment and the simulations using the **u**-p and **u**-p-**U** elements, respectively. In Fig. 8.10b and Fig. 8.10c the regime of the model tests is marked in the diagrams used to quantify the influence of relative acceleration. Fig. 8.10b shows the novel diagram proposed in Section 4.4.5, which allows to express the influence of relative acceleration solely in terms of highest wave frequency and hydraulic conductivity. The diagram suggests that the relative acceleration is negligible for the given specifications and the application of the **u**-p formulation is justified. Likewise, the diagram by Zienkiewicz et al. [450] given in Fig. 8.10b indicates that the relative acceleration can be neglected for the present BVP. A characteristic length of 0.5 m is assumed for the evaluation of the factors required for the diagram by Zienkiewicz et al., which is approximately the distance of the pile tip to the bottom of the soil container.

In accordance with the evaluation of the influence of relative acceleration based on the diagrams, the pile penetration rate is similar for the simulations using the two element formulations as can be seen from Fig. 8.10a. The **u**-p-**U** element formulation tends to predict a slightly faster penetration rate compared to the **u**-p elements, however. As has been outlined in Section 4.4.5, the differences between simulations with and without incorporation of relative acceleration increase with every wave passing. A similar effect is observed for the simulations of the vibratory pile driving process. However, despite the application of approximately 100 cycles of the rotating unbalances, the differences between the two element formulations remain comparably modest. Besides the finding that the influence of relative acceleration is nearly negligible for the predicted pile penetration, an acceptable agreement of the results of the simulations with the measured pile penetration is observed.

Figure 8.11 displays the pore water pressure measured in PPT A (see Fig. 8.8) for the values measured in the experiment and the simulations using the **u**-p and **u**-p-**U** element formulation, respectively. PPT A is passed by the pile tip at approximately 0.8 s of driving. At this time the oscillations in the pore water pressure reach their maximum for the experiment as well as for the two simulations. Both simulations predict the amplitude of pore water pressure well

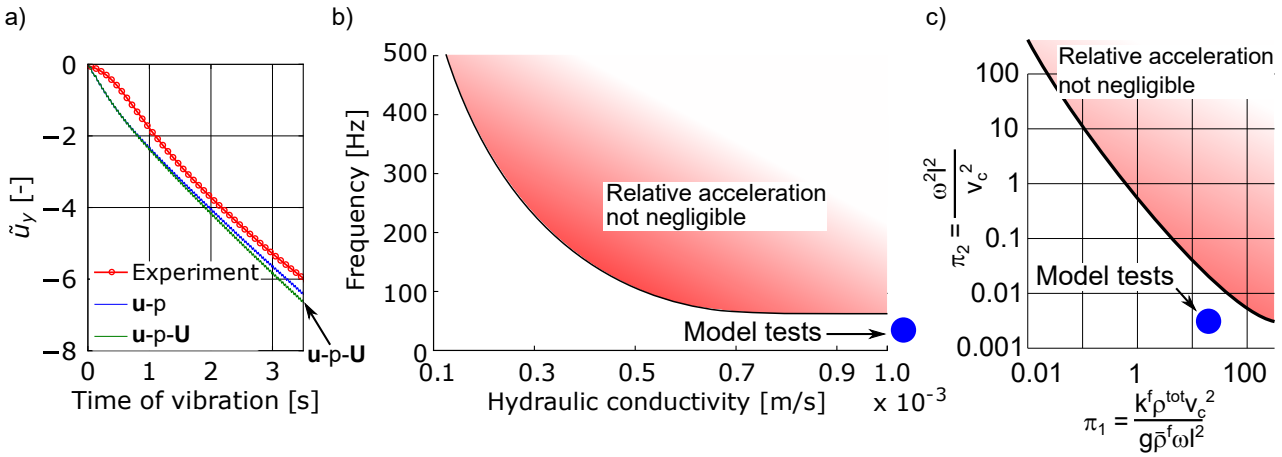

Figure 8.10: a) Normalised pile displacement with respect to time of vibration for the values measured in the experiment and the simulations using the **u**-p and **u**-p-**U** element formulation, respectively. b) Regime of the model tests marked in the diagram quantifying the influence of relative acceleration neglected by the **u**-p element formulation proposed in Section 4.4.5. c) Regime of the model tests marked in the diagram quantifying the influence of relative acceleration by Zienkiewicz et al. [450].

at this time of vibration. A doubling of frequency is observed in the curves of the pore water pressure for both simulations. A smaller amplitude in every second cycle is predicted which is not in accordance with the results of the experiment. This is also shown in more detail later in Fig. 8.22.

The amplitudes after passing of the transducer are too small for both simulations compared to the measured values. In accordance with the observations made based on the diagrams in Fig. 8.10b,c as well as with the pile penetration in Fig. 8.10a, the differences in the pore water pressure between the finite element formulations is not large. Interestingly, the most noticeably deviation between the formulations is observed for the aforementioned irregularity in the pore water pressure amplitudes. A shift of these irregular amplitudes between the two element formulations occurs.

It is concluded that the influence of relative acceleration on the decisive variables (pile penetration and pore water pressure) is small for the vibratory pile driving simulations, and the assumption of identical accelerations made by the **u**-p formulation is found to be valid. In addition, the threshold curve established by the proposed semi-analytical approach is confirmed. Overall, it may be concluded that the **u**-p element formulation is suitable for the simulation of vibratory pile driving in water-saturated soil, even if the hydraulic conductivity of the soil is

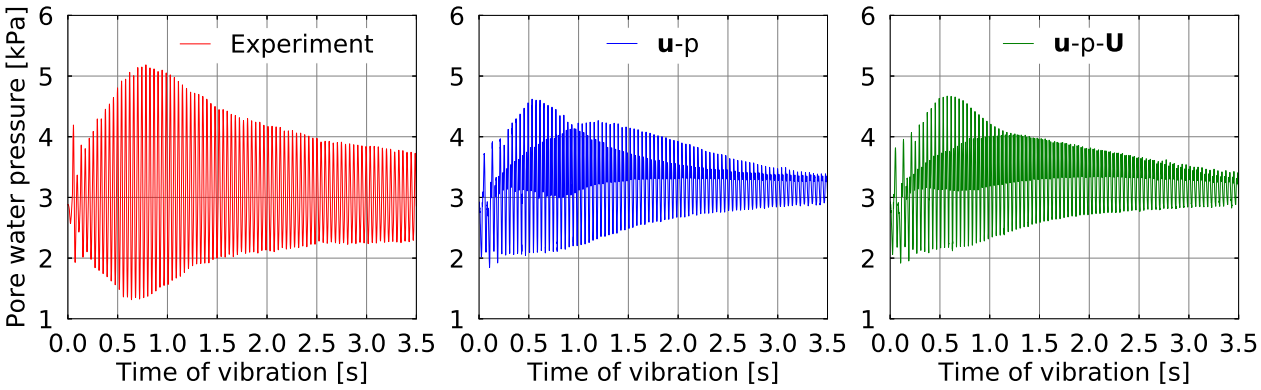

Figure 8.11: Pore water pressure in PPT A (see Fig. 8.8) for the measured values of the experiment and the results of the simulations using the **u**-p and **u**-p-**U** element formulation, respectively

comparably high. The computational much more demanding **u**-p-**U** element formulation (the **u**-p element formulation requires approximately half the time to complete the simulation) is not required in terms of consideration of the relative acceleration. In addition to the superior computational performance due to the reduced number of DOFs, the definition of the boundary condition is less complex using the **u**-p element formulation.

To compare the numerical effectiveness of the different hydro-mechanically coupled finite element formulations from a quantifiable perspective, the stiffness matrices and their corresponding condition numbers are evaluated. As has already been mentioned in Section 4.3, the condition number is a measure for the accuracy with which an inverse of a matrix can be calculated. Large values of the condition number indicate a loss of accuracy and hence possibly a poor numerical performance.

The stiffness matrices of an element in the centre of the numerical model are depicted in Fig. 8.12, ordered with respect to the DOFs. In addition to the **u**-p and **u**-p-**U** element formulations, the stiffness matrix using the **u**-**U** element formulation is given as well. The results in terms of pile penetration and pore water pressure of simulations using the **u**-**U** element formulation can be found in [349, 348]. They are similar to the results of the **u**-p and **u**-p-**U** element formulation but diverging values of pore water pressure at the integration points are predicted, caused by volumetric locking effects as is explained in Chapter 4.

The main observations obtained by the visualisation of the stiffness matrices can be summarised as follows:

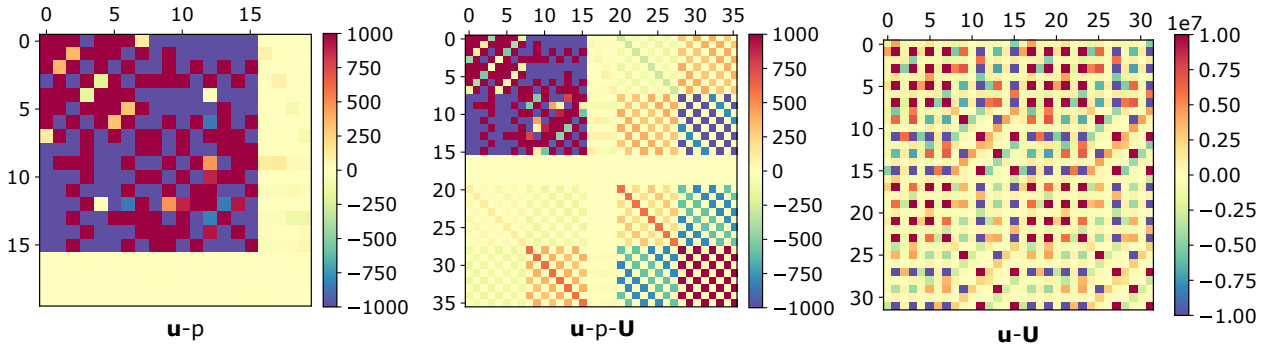

Figure 8.12: Stiffness matrices for one element during vibratory pile driving located in the model centre. Note that the matrices are ordered by DOFs, meaning that columns 1:16 are with respect to the solid displacement, columns 17:32 are with respect to the water displacement (**u**-**U**), columns 17:20 are with respect to the pore pressure (**u**-p and **u**-p-**U**), and columns 21:36 are with respect to the water displacement (**u**-p-**U**).

- The magnitudes of the entries of the **u**-**U** formulation are considerably larger than those of the **u**-p and **u**-p-**U** formulations. The latter two have the same magnitude ranges.
- The entries corresponding to the pore pressure are considerably smaller than those of the displacement (in the case of the **u**-p and **u**-p-**U** formulations), which strongly affects the conditioning.
- None of the matrices is symmetric, but compared to the **u**-p and **u**-p-**U** formulations, the **u**-**U** formulation yields a nearly-symmetric matrix.

The definition [452]

$$c = \|\mathbf{A}\| \, \|\mathbf{A}^{-1}\| \tag{8.2}$$

is used to determine the condition number c of the stiffness matrix $\mathbf{A}$. The condition numbers of the stiffness matrices for the different formulations are presented in Table 8.5. The condition number is large in all cases, meaning that the stiffness matrices $\mathbf{A}$ are poorly conditioned. If, in the case of the **u**-p formulation, only the part of the stiffness matrix containing the entries corresponding to the solid phase is considered, the condition number is approximately 2000, indicating considerably superior conditioning. The condition numbers of the matrices derived from the **u**-p and **u**-p-**U** formulations significantly exceed the condition number of the **u**-**U** formulation. Therefore, the **u**-**U** formulation gives a stiffness matrix for which it is easier to calculate an inverse.

Formulation	Condition number c [-]
u-**U**	$32 \cdot 10^5$
u-p	$46 \cdot 10^9$
u-p-**U**	$48 \cdot 10^9$

Table 8.5: Condition number c for different finite element formulations obtained by the matrices provided in Fig. 8.12

8.2.3 Influence of the contact discretisation technique and the interface model

The simulations presented in the previous section are repeated using the segment-based mortar (SBM) contact discretisation technique in conjunction with the **u**-p element formulation. If not stated otherwise, the SBM contact discretisation technique is used with 5 integration points per segment and the EBM method with 3 integration points per element edge. Additional simulations using the EBM method with 5 integration points are performed as well.

In addition to simulations using the Coulomb friction model, the proposed hypoplastic and Sanisand interface models are applied in this section. The surface roughness is set to $\kappa = 0.3$ and the interface thickness is estimated to be $d_s \approx 10 \cdot d_{50} = 5$ mm.

The Kozeny/Carman equation [197, 60] is used to account for the influence of the porosity n on the hydraulic conductivity for the simulations presented in this section. The required parameters have been derived experimentally by Vogelsang and are given in [394, 240]. The spatial distribution of the hydraulic conductivity during the pile driving process is given in Appendix C.2. Due to the loosening of the soil close to the pile, considerably larger values of hydraulic conductivity are obtained in the vicinity of the pile compared to the initial values. However, lower values are obtained in greater distance to the pile. The consideration of the change in hydraulic conductivity due to a change in porosity leads to higher pile penetration rates compared to constant values, which is also demonstrated in Appendix C.2.

The normalised pile displacement $\tilde{u}_y$ vs. time of vibration for the simulations using the two mortar techniques and the different interface models is given in Fig. 8.13. Note that for the experiment only the mean trend of pile penetration is depicted. Given the complexity of the BVP, the simulations reproduce the measured values well and the difference between the simulations is relatively small. The EBM method using the Coulomb interface model predicts the lowest pile penetration rate while the SBM method in combination with the Sanisand

interface model shows the highest pile penetration rate. In general, the SBM method gives higher pile penetration rates than the element-based method. The simulation employing the EBM method in conjunction with the Coulomb friction model and five integration points also shows a higher penetration rate in comparison to the corresponding simulation with three integration points for the first 4 s of driving. However, towards the end of the simulation, the two simulations reach almost identical values of $\tilde{u}_y$. At the beginning of the driving process ($t \approx 0.2$ s), the EBM method with the Coulomb interface model shows an irregular pattern of displacement amplitudes, which is absent in the results using the SBM method with the Coulomb friction model. Towards the end of the driving process both mortar methods incorporating the Sanisand interface model show irregular patterns of $\tilde{u}_y$ as well, with every second cycle showing a lower amplitude.

In order to better visualise the mentioned irregularities, the evolution of the normalised pile displacement is given in detail for the time frames *S1*, *S2* and *S3* (marked in Fig. 8.13) in Fig. 8.14, showing the results for all utilised interface models. For the time frames *S1* and *S2* all simulations show a harmonic sinusoidal pile displacement with almost constant amplitudes, whereas for time frame *S3* both mortar methods in combination with the Sanisand interface model show noticeable irregularities, with every second cycle showing a smaller amplitude. For both mortar techniques the Sanisand interface model shows a higher pile penetration at time frame *S3* compared to the simulations with the Coulomb interface model. Using the hypoplastic interface model, the results almost coincide with the results of the Coulomb interface model in case of the segment-based method but higher penetration rates for the EBM method are observed.

Compared to the results of the experiment, all simulations predict too large amplitudes of displacement. This deviation has also been observed for earlier simulations of the vibratory pile driving tests reported in [69] and its further investigation is not subject of the present work.

To further analyse the differences between the mortar methods, the pile force measured between vibrator and pile head is evaluated. Note that this force is not identical to the prescribed force at the mass point connected to the spring due to inertia forces. The normalised pile force is defined by

$$\tilde{F}^{Pile} = \frac{F^{Pile}}{F^{Pile}_{stat}}, \tag{8.3}$$

where F^{Pile}_{stat} is the static pile force resulting from the combined dead weight of the pile, the oscillator and the load cell. In the simulations, the pile force results mostly from the integration

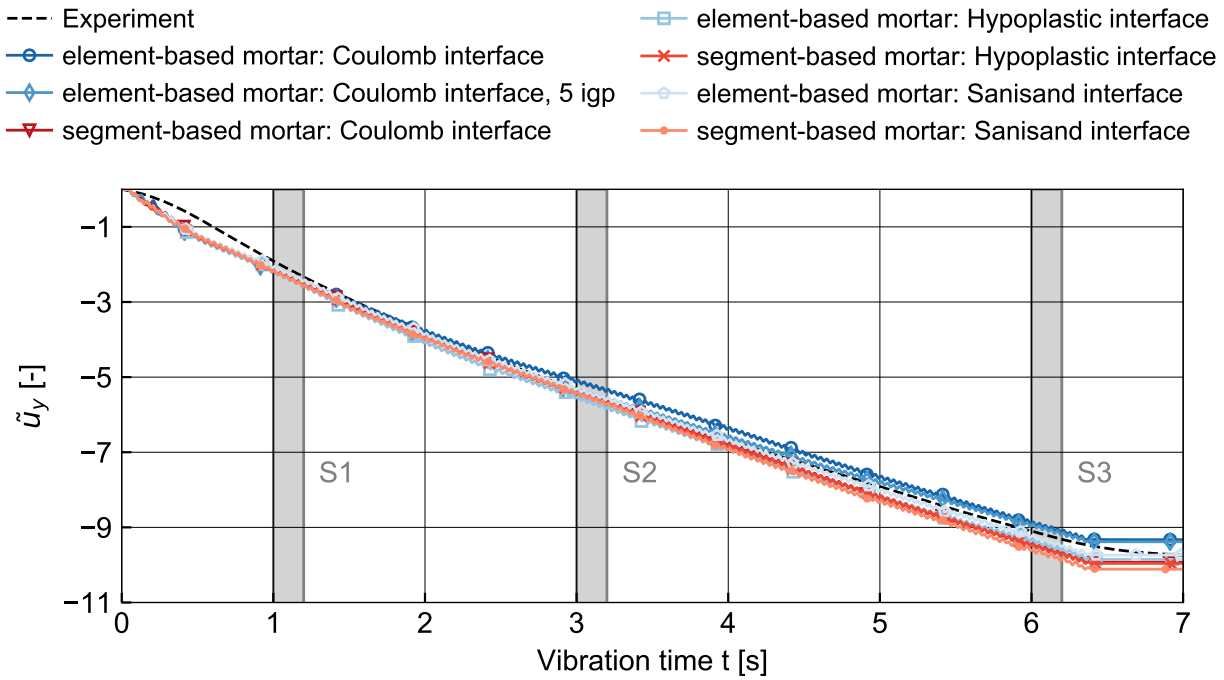

Figure 8.13: Comparison of normalised pile displacement $\tilde{u}_y$ vs. time of vibration for the measured values and the simulations using the EBM and the SBM contact discretisation technique in combination with the different interface models. In addition, one simulation using the element-based technique with five integration points per finite element edge instead of three is given.

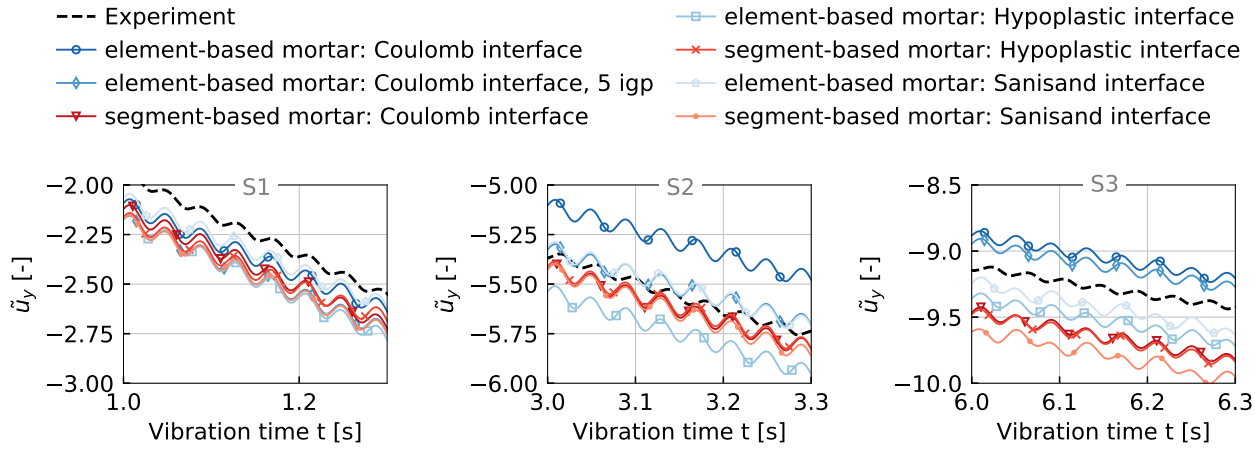

Figure 8.14: Normalised pile displacement $\tilde{u}_y$ vs. time of vibration for the time frames *S1*, *S2* and *S3* marked in Fig. 8.13 for the measured values and the simulations using the EBM and the SBM contact discretisation technique in combination with different interface models

of the contact stresses along the paired surfaces and is therefore strongly influenced by the contact discretisation technique. The normalised pile displacement $\tilde{u}_y$ vs. normalised pile force $\tilde{F}^{Pile}$ is given for the experiment and the simulations using the different mortar techniques with the Coulomb and the Sanisand interface model in Fig. 8.15 for the time frame *S2* and in Fig. 8.16 for the time frame *S3*. For all simulations the accordance of the results with the measured values is acceptable but the magnitude of normalised pile force is underestimated. The potential reason for this deviation is most likely the set of parameters of the hypoplastic model used for the modelling of the continuum. Simulations using a different parameter set for "Karlsruhe Sand" reported and used for the simulation of the vibratory pile driving tests in [69] result in a much better representation of the pile driving force. However, much too low excess pore water pressures are predicted using this (to some extend randomly chosen) parameter set. In addition, this parameter set does not reproduce results of undrained cyclic triaxial tests on "Karlsruhe Sand" well. The comparison of the measured excess pore water pressures with the values obtained by the simulations presented in this section is given in Fig. C.3 of the appendix.

Compared to the EBM method, the segment-based technique gives a more regular course of $\tilde{F}^{Pile}$ for both interface models. The better performance of the SBM method can be traced back to the finer surface discretisation, leading to a smoother distribution of contact stress and a more precise integration (to prove this, a simulation using the element-based approach with

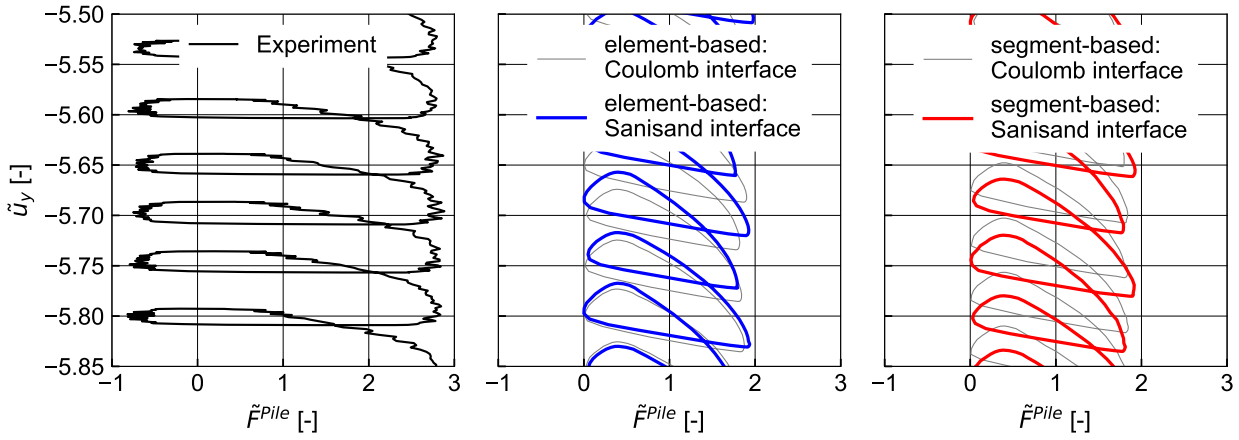

Figure 8.15: Normalised pile displacement $\tilde{u}_y$ vs. normalised pile force $\tilde{F}^{Pile}$ during time frame *S2* (marked in Fig. 8.13) for the values measured in the experiment and the simulations using the EBM and the SBM contact discretisation technique in combination with the Coulomb and the Sanisand interface model, respectively

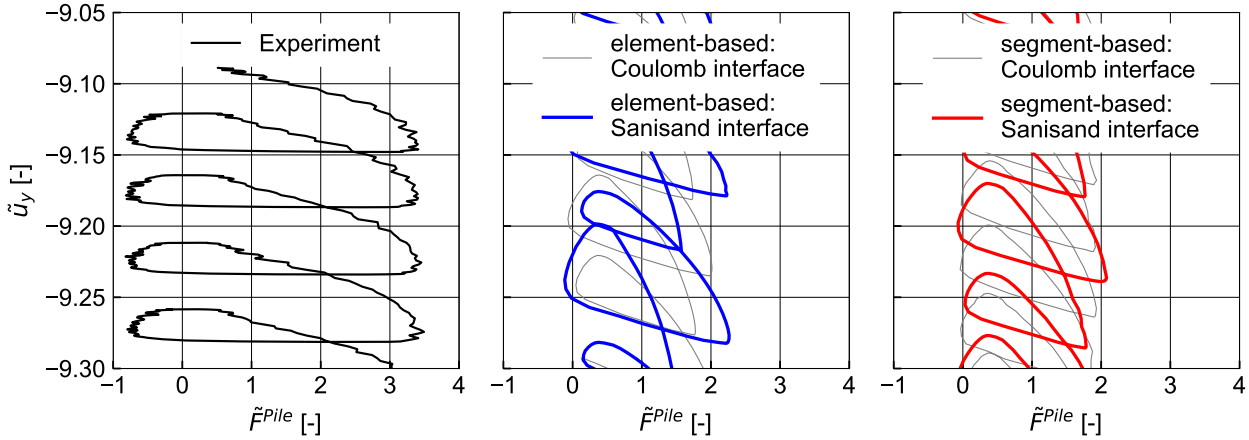

Figure 8.16: Normalised pile displacement $\tilde{u}_y$ vs. normalised pile force $\tilde{F}^{Pile}$ during time frame *S3* (marked in Fig. 8.13) for the values measured in the experiment and the simulations using the EBM and the SBM contact discretisation technique in combination with the Coulomb and the Sanisand interface model, respectively

more integration points is discussed later). The magnitude of minimum and maximum forces predicted by the two mortar methods is comparable, however. In addition, the differences between the constitutive interface models are found to be almost negligible for time frame *S*2. This is not unexpected since for smooth soil-structure interfaces such as is the case for the aluminium pile utilised in the experiment, the constitutive interface behaviour is very similar to shearing of an initially loose soil sample (i.e. no peak in the τ-γ plot prior to the critical state and almost no dilatancy/constant dilatancy angle). These characteristics can be described well by the Coulomb model. In addition, due to the increase in pore water pressure caused by the vibration of the pile, the effective stress in the vicinity of the pile shaft is significantly reduced, limiting the maximum frictional stresses that can be mobilised and thus the overall influence of the friction model.

As has been observed in Figs. 8.13 and 8.14, the differences between the two mortar techniques in terms of pile penetration increase with increasing time of vibration. In line with this, the differences in terms of force between vibrator and pile also increase accordingly, as is visible from Fig. 8.16 displaying the results for time frame *S3*. Due to the lower displacement amplitude in every second cycle observed in Fig. 8.14, the $\tilde{u}_y$ vs. $\tilde{F}^{Pile}$ plot obtained using the EBM method shows a much smaller amplitude of normalised pile force for every second cycle, being more pronounced in case of the Sanisand interface model. In contrast, a more regular course is obtained using the segment-based technique for both interface models. The results of the segment-based technique are also in better accordance with the experimental results, since

they show a regular course of force as well. However, a tiny irregularity within the first visible cycle is encountered using the SBM technique. This can (at least partially) be explained by the distortion of the finite elements close to the pile shoulder as is shown and discussed later for Fig. 8.19.

Figure 8.17 depicts the $\tilde{u}_y$ vs. $\tilde{F}^{Pile}$ plot for the time frame *S3* using the two discretisation techniques with the Coulomb and the hypoplastic interface model, respectively. Compared to the Sanisand interface model, for both contact discretisation techniques a more regular development of $\tilde{F}^{Pile}$ is observed. The differences between the two mortar methods are also much less pronounced compared to the simulations using the Sanisand interface model.

In order to assess the influence of the number of integration points used for the EBM discretisation, the normalised pile displacement $\tilde{u}_y$ vs. normalised pile force $\tilde{F}^{Pile}$ during time frame *S3* is compared for simulations using the Coulomb and the Sanisand interface models with three and five integration points per element edge in Fig. 8.18. Note that in contrast to the SBM technique, the total number of integration points stays constant throughout the simulation since the number of elements at the surface pair does not change. Note in addition that for most states during the driving process, the simulation with the element-based technique and five integration points per element surface still results in a lower total number of integration points of the surface pair, since for the segment-based method much more points are generated at the pile surface, having much larger elements than the soil surface (for mesh of the pile

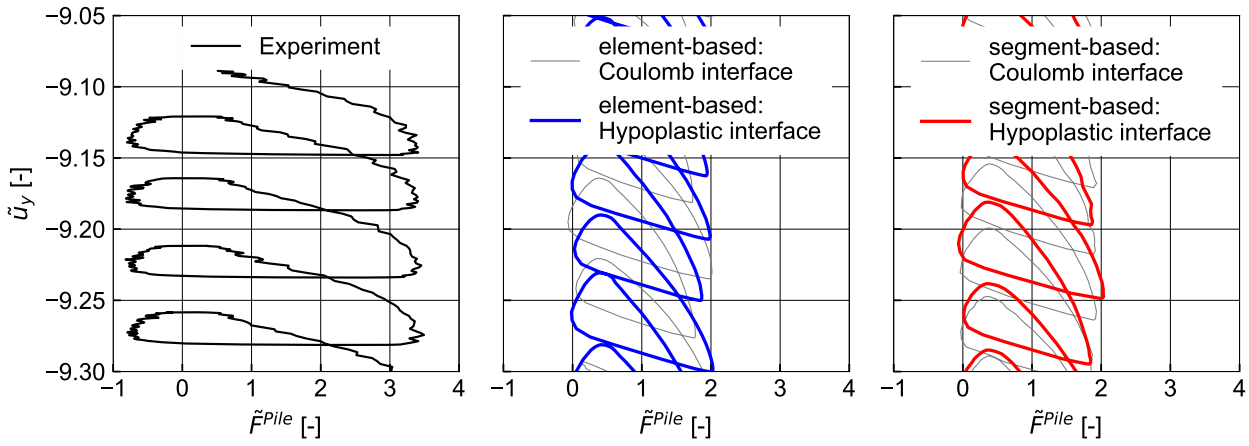

Figure 8.17: Normalised pile displacement $\tilde{u}_y$ vs. normalised pile force $\tilde{F}^{Pile}$ during time frame *S3* (marked in Fig. 8.13) for the values measured in the experiment and the simulations using the EBM and the SBM contact discretisation technique in combination with the Coulomb and the hypoplastic interface model, respectively

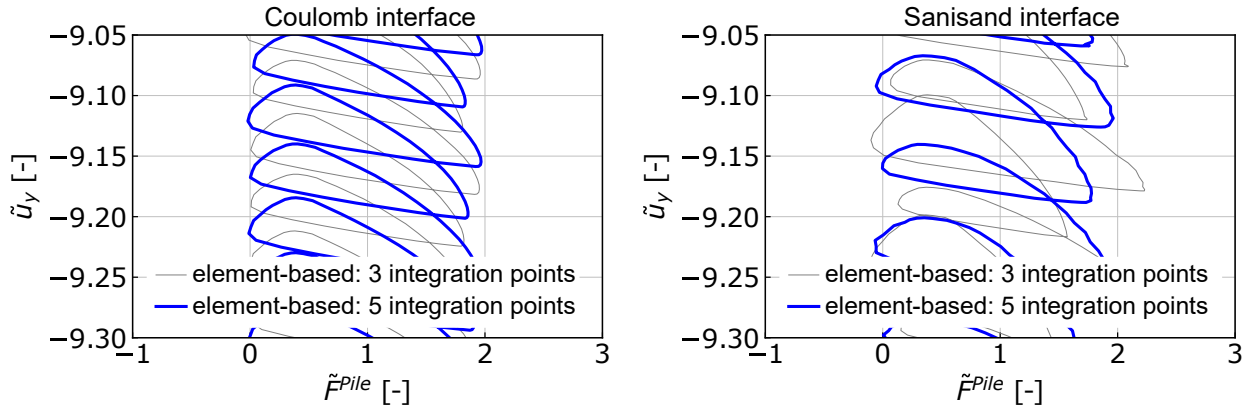

Figure 8.18: Normalised pile displacement $\tilde{u}_y$ vs. normalised pile force $\tilde{F}^{Pile}$ during time frame *S3* (marked in Fig. 8.13) for the simulations using the EBM contact discretisation technique in combination with the Coulomb and the Sanisand interface model and different number of integration points of the mortar contact

tip see Fig. 8.19). The comparison of the simulations with different numbers of integration points shows that the influence is rather small for the Coulomb interface model, but quite large for the Sanisand interface model. Using five integration points instead of three results in a more regular development of $\tilde{F}^{Pile}$ and less differences in the maximum values between subsequent cycles. However, some irregularities within individual cycles are visible. As has been mentioned earlier, they are believed to be (at least partially) caused by the distortion of the finite elements close to the pile shoulder as is discussed later on the basis of Fig. 8.19.

Overall, the results for the EBM method with five integration points are similar to those for the corresponding simulation using the segment-based method given in Fig. 8.16. Hence, the better performance of the segment-based method mentioned earlier can partly be traced back to the larger number of integration points and not to the method itself.

The left-hand side of Fig. 8.19 displays the spatial distribution of the effective horizontal stress acting in the vicinity of the pile tip for the two mortar contact discretisation techniques using the Coulomb friction model at a time of vibration of 1.31 s (end of time frame *S*1). The deformed configuration without a deformation scale factor is given. A distortion of the finite elements close to the pile shoulder is visible, which is believed to cause some of the aforementioned irregularities in the predicted forces (see e.g. Fig. 8.16 and Fig. 8.18). This could be remedied by employing re-meshing algorithms or large-deformation techniques (e.g. ALE algorithms). However, these numerical schemes add complexity and potentially additional numerical problems, for why "only" an updated Lagrangian scheme is used. High values of

effective horizontal stress are observed at the pile shoulder for both contact discretisation techniques. Considering the small dimensions of the model tests, these values are judged to be quite high, representing stress conditions which would also be expected for the installation of much larger piles (e.g. several decimetres in diameter). The plots on the right-hand side of Fig. 8.19 depict the effective horizontal, effective vertical and shear stress along the pile surface with respect to the vertical coordinate (starting from the bottom of the soil container) for the two different mortar techniques. The element-based technique shows slightly higher values and less regular distributions of the stress components, the latter in particular for the distribution of shear stress. The higher stresses visible for the element-based technique also agree well with the lower pile penetration rate observed in Fig. 8.13 and Fig. 8.14 compared to the SBM technique. Overall, however, the differences in stress are found to be rather small.

Very low values of effective stress are visible at the pile shaft above the pile shoulder. However, it has to be taken into account that the initial effective stress prior to the pile installation process is only -1 to -2 kPa (depending on the normal stress component) at the considered depth. Therefore, once the pile tip has passed the soil, a significant reduction of effective

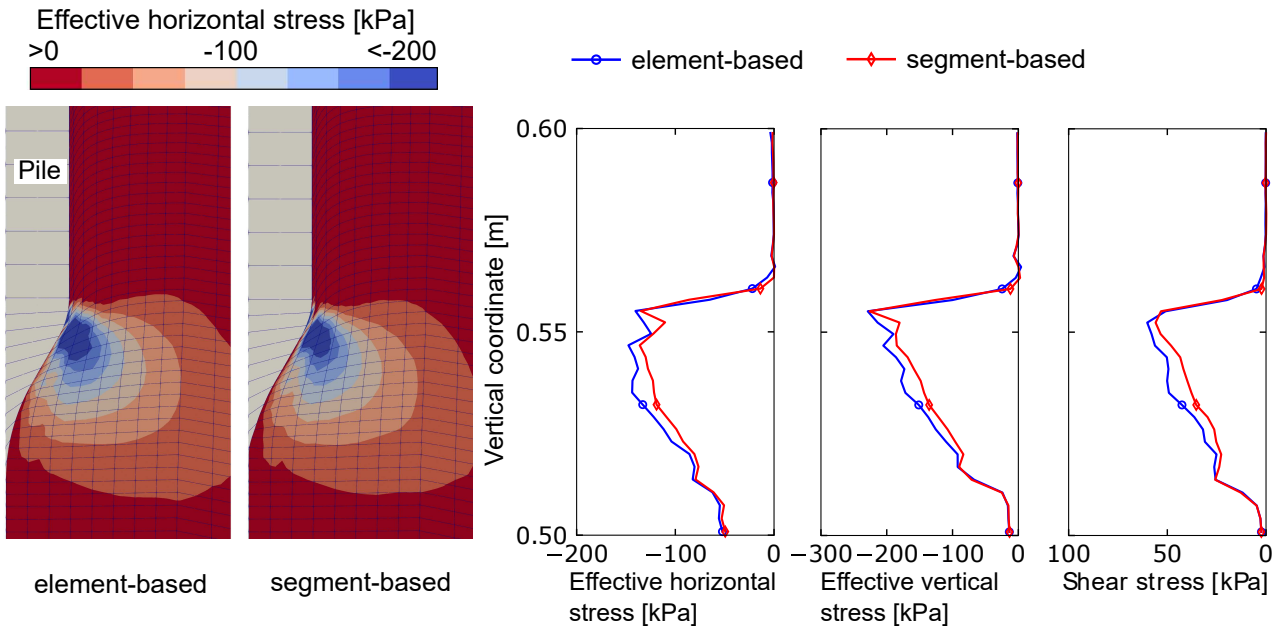

Figure 8.19: Spatial distributions of effective horizontal stress acting in the vicinity of the pile tip at a time of vibration of 1.31 s (end of time frame $S1$) for the simulations using the EBM and the SBM contact discretisation with the Coulomb friction model. In addition, the distributions of effective horizontal, effective vertical and shear stresses with respect to the vertical coordinate, starting from the bottom of the container, are given along the pile surface for the two mortar techniques.

stresses is to be expected.

Table 8.6 gives the number of iterations and the time spent in the contact routines for the different simulations. Note that all simulations are performed using four native cores and the same clock-speed. The number of required iterations is similar for the simulations using the Coulomb interface models. This is because during the dynamic pile driving process, convergence is achieved within the first iteration for almost all increments. In contrast, the time spent in the contact routines, including all procedures involving contacts (contact search, contact discretisation, calculation and integration of contact stress, assembling of contact forces), depends on the mortar method and the interface model adopted. Note that nearly all time-consuming processes of both mortar methods are performed with multiple threads. However, the parallelisation is slightly more efficient for the SBM approach, since the same strategies for parallelisation as used for regular finite elements can be applied, reducing overhead compared to the element-based approach. Unsurprisingly, for the Coulomb interface model the SBM method takes approximately 1.5 times longer than the EBM method using 3 integration points per finite element edge, which is due to the larger number of surface points at which the contact stress is evaluated and integrated. In addition, the evaluation of the segments has to be performed, which is not necessary with the EBM method. Compared to the total simulation time (approximately 27000 s), however, the differences in time required for the contact

Simulation	No. of iterations	Time contact [s]
Element-based: Coulomb interface	7016	277
Element-based (5 igp): Coulomb interface	7017	499
Segment-based: Coulomb interface	7017	450
Element-based: Hypoplastic interface	7080	416
Segment-based: Hypoplastic interface	7015	610
Element-based: Sanisand interface	9115	1568
Segment-based: Sanisand interface	7677	1355

Table 8.6: Number of iterations and (physical) time spent in the contact routines for the different simulations. The time spent in the (continuum) element loop is approximately 16000 s and the time needed to solve the system-of-equations approximately 10000 s for the simulations using the Coulomb interface model. The total time is approximately 27000 s for the simulations using the Coulomb interface model. The contact routines, element loop and the solver are all run with four native cores (one Intel®Core™ i9 9900K processor with four cores run with the base-frequency of 3.6 GHz without utilising Hyper-threading is used).

routines are almost negligible. Using five integration points per finite element edge for the element-based technique results in slightly more time spent in the contact routine compared to the segment-based approach using the same number of integration points per segment.

The simulation using the hypoplastic interface model requires more time for the contact routines compared to the Coulomb interface model, for both mortar techniques. In addition, a slightly larger number of iterations is required in case of the element-based approach. Similar to the differences observed for the Coulomb interface model, the SBM method takes approximately 1.5 times longer than the EBM method due to the larger number of integration points. However, compared to the total time of the simulation (slightly larger than 27000 s for both simulations), these differences are judged insignificant. In contrast, using the Sanisand interface model results in far more iterations and longer times spent in the contact routines, in particular for the element-based approach. This fits well to the course of force depicted in Fig. 8.16, for which strong irregularities are observed using the element-based approach.

8.2.4 Inspection of the hydro-mechanically coupled CEL method

The application of the hydro-mechanically coupled Coupled Eulerian-Lagrangian (CEL) method (see Section 4.6.2) to the vibratory pile driving tests is presented in the following (note that the results have already been published by the author in [351]). A slightly different set of parameters of the hypoplastic model is used for the simulations presented in this section, since the parameters given in Table 8.2 have been obtained from an optimised calibration conducted after the publication of [351]. The parameters adopted for the simulations presented in this section are given in [351] and are identical to those used in [349, 67].

The numerical model adopted for the CEL simulations is displayed in Fig. 8.20. The red volume indicates the initially material-empty elements whereas the blue elements are initially material-filled. The height of the initially material-filled volume is identical to the height of the soil in the model tests. During the pile driving the soil might heave, in which case the initially empty Eulerian elements are filled with material. Note that only once an element is filled with material it contributes to the global force equilibrium.

The pile is modelled rigidly using Lagrangian elements. The bottom boundary of the Eulerian region is constrained in vertical direction, the back in both horizontal directions and the boundaries in the symmetry axis in the direction normal to them. The top of the Eulerian region is made permeable by imposing zero excess pore water pressure. Every other boundary of the model is impermeable.

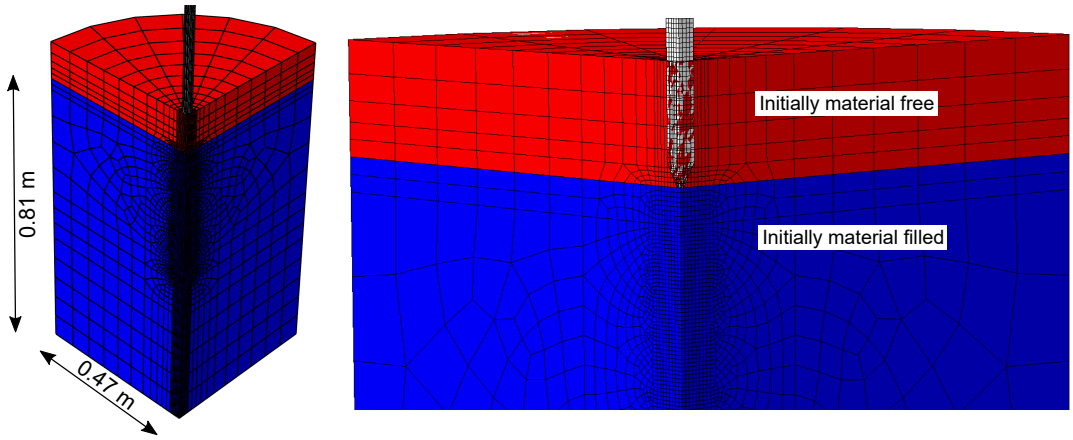

Figure 8.20: Finite element model for the CEL simulation. The blue volume indicates initially material-filled elements. The additional red area could be filled during the driving process if the soil moves into it.

The pile tip is located directly on top of the material-filled region of the model before the simulation starts. The Eulerian elements below the pile tip have a small size while the mesh gets coarser with greater distance to the pile. A variation of element size in the vicinity of the pile has proven that the results are not strongly dependent on the mesh size. Even though the problem is axisymmetric, three-dimensional elements have to be used as the CEL method available in `Abaqus` does not support two-dimensional analyses. Note that the ALE method implemented in `Abaqus` supports 2D or axisymmetric analyses but was found to be less suitable for the modelling of the large-deformations occurring during pile driving compared to the CEL method. The masses and forces of the half-axisymmetric experimental set-up have been scaled to fit to the quarter model presented in Fig. 8.20.

Friction between pile and soil is considered using a Coulomb friction model with a friction coefficient of $\mu = 0.125$. This approximately corresponds to the assumed friction coefficient of $\mu = 0.25$ (compared to the previous section a slightly higher value is assumed to better highlight the differences to frictionless simulations) in the model tests since total normal stresses are used for the computation of the shear stresses in the pile-soil interface and the ratio between the initial effective and the initial total stress is approximately 2. This is due to the inability of `Abaqus` to distinguish between effective and total normal contact stress in dynamic analyses. Furthermore, using the CEL method, `Abaqus` does not allow the use of user-defined contact models to modify the calculation of (frictional) contact forces. Obviously, the friction forces calculated are not correct if the pore water pressure changes significantly along the pile-soil interface. In order to evaluate the influence of the friction coefficient, an

additional simulation assuming a frictionless contact ($\mu = 0$) is performed.

As has been outlined in Section 4.6.2, an explicit time integration scheme is applied using the CEL method. The critical time increment

$$\Delta t_{\text{crit}} = \lambda \frac{L_{\min}}{v_c} \tag{8.4}$$

represents the largest possible time increment for which numerical stability is still secured. $L_{\min}$ is the smallest element dimension, v_c is the compression wave velocity (of the solid-water mixture) of this element and λ is the critical time scaling parameter. The compression wave velocity is defined by

$$v_c = \sqrt{\frac{D + \bar{K}^w/n}{\rho^{\text{tot}}}} \tag{8.5}$$

with $D = E\dfrac{(1-\nu)}{(1+\nu)(1-2\nu)}$. Considering the stress level at the half height of the test device, $D \approx 6000$ kPa is calculated for "Karlsruhe Sand". Using the bulk modulus of water $\bar{K}^w = 2.2$ GPa, the compression wave velocity is $v_c \approx 1672$ m/s. In the present case, elements with dimensions smaller than 4 mm exist in the model, which define the minimum length in Eq. (8.4). Using these values and setting $\lambda = 1$, the maximum stable time increment is $\Delta t_{\text{crit}} \approx 2 \cdot 10^{-6}$ s. During the analysis, this value will reduce further since the soil stiffness increases due to induced stresses by the pile installation process (see Fig. 8.19).

Since the computational effort running the simulation using this value for the critical time increment would exceed computational resources, and considering that a saturation of $S = 1$ is unrealistic for the sand placement method applied in the model tests, an air inclusion of 5 % is assumed, resulting in a degree of saturation of $S = 0,95$. This leads to a reduction of the bulk modulus of the pore water from 2.2 GPa to approximately 5 MPa and thus a reduced compression wave velocity of $v_c \approx 97$ m/s. Simulations with a bulk modulus of 2.2 GPa lead to similar pile penetration rates but to slightly larger excess pore water pressures during the driving process as is demonstrated in [351].

A reduction of the critical time increment by the factor $\lambda = 0.8$ is applied in the simulations. Similar to implicit analyses, the influence of the time increment size should be investigated in explicit analyses in order to secure that the solution remains (nearly) unchanged if smaller time steps are chosen such that non-linear effects are properly accounted for. Additional simulations proved that even the choice of a factor $\lambda = 0.5$ does not change the results of the simulation significantly. Eq. (8.4) also indicates that the critical time increment is a function of the size of the discretized domain which is problematic in case small-scale model tests are simulated

since the element size is generally smaller compared to the real-scale problem. As mentioned previously, elements with very small dimensions exist in the model. They strongly reduce the stable time increment and make the analysis extremely time-consuming. This, however, is a drawback mainly encountered in the analysis of small scale tests, being of minor relevance for the simulations of real-scale problems presented in Section 8.3.2. Since using an explicit time integration scheme is a rather unusual choice for the solution of hydro-mechanically coupled problems it is worth mentioning here that other researches have also applied explicit time integration methods for hydro-mechanically coupled problems before (see e.g. [434, 34, 261]). Apart from the decreased critical time increment due to the increased wave velocity in case of a hydro-mechanically coupled problem, oscillations in pore water pressure are reported when using an explicit integration scheme in [261]. Similar observations are made for the wave propagation in a poro-elastic 1D column using the hydro-mechanically coupled explicit analysis in Section 4.6. However, the oscillations are noticeably reduced by increasing the number of elements.

The comparison of the normalised pile displacement over the vibration time between the measured values, the fully Lagrangian simulation and the simulation using the CEL method is displayed in Fig. 8.21a,b. Using the Coulomb model for both analyses, two different friction coefficients $\mu = 0$ and $\mu = 0.25$ are compared. Note that only the mean trend of displacement is given in case of the experiment. In case of the frictionless contact, both numerical methods are in good accordance with each other and with the experimental data. In case of $\mu = 0.25$ the CEL method predicts slightly less pile penetration compared to the fully Lagrangian simulation towards the end of the test. Compared to the frictionless contact a better agreement between Lagrangian simulation and experiment is achieved using $\mu = 0.25$ which is best visible towards the end of the vibration process. A slight deviation at the beginning of the test is observed independently of the chosen friction coefficient as the rate of pile penetration is overestimated in the numerical simulations.

An enlarged section of the normalised pile displacement vs. time of vibration plot for the frictionless case is presented in Fig. 8.21c in order to identify the pile movement during individual cycles. Both simulations with $\mu = 0$ show a slightly too large upwards movement within the cycles in comparison to the experiment. The downwards movement is reproduced almost perfectly by the simulations. Interestingly, the CEL method shows a slightly different amplitude in every second cycle. It can be concluded that the results of the CEL simulations fit reasonably well to the outcomes of the Lagrangian simulations in terms of pile displacement. The influence of pile-soil interface friction is less in case of the Lagrangian simulation,

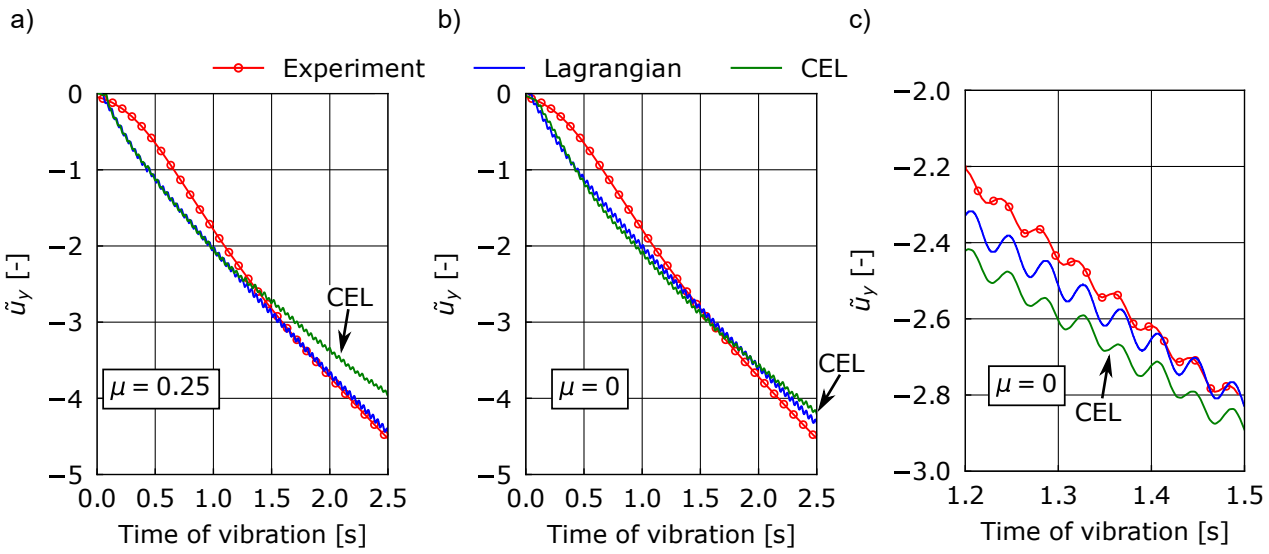

Figure 8.21: Comparison of normalised pile displacement over time of vibration between the measured values and the simulations using Lagrangian elements and the CEL method, respectively. For the simulations using Lagrangian elements and the CEL method the friction coefficients $\mu = 0$ and $\mu = 0.25$ are compared. Due to the reasons explained above $\mu = 0.125$ has to be set into approach in the CEL simulations to achieve contact friction conditions being equivalent to $\mu = 0.25$ in the Lagrangian simulations. Figure c) shows an enlarged section of the pile penetration vs. time of vibration plot for the frictionless case.

which can be traced back to the erroneous calculation of frictional contact stress in case of the CEL simulation. However, the influence of friction is not large for either of the two applied numerical methods.

Figure 8.22a displays the development of pore water pressure at transducer PPT A recorded in the experiment and the corresponding results of the simulations using the Lagrangian and the CEL model, respectively. The simulations with a friction coefficient of $\mu = 0.25$ are considered. The periodic pile movement is very well visible in the recorded pore water pressure. When the pile tip passes the transducer at around 0.8 s, the pore water pressure recorded in the experiments oscillates with the highest amplitudes which reduce subsequently. Almost no increase in the mean trend of the pore water pressure is observed. Thus, the pore water pressure is mainly oscillating around the hydrostatic value. As has already been elaborated on in Section 8.2.2, the simulation using the Lagrangian model is able to reproduce this development in a qualitative manner but predicts too small amplitudes of the pore water pressure. This is more pronounced for the simulation in this section, caused by the lower value of the bulk modulus of pore water adopted, as can be seen from the comparison with Fig. 8.11. Furthermore, a doubling of frequency is observed in the curve of pore water pressure vs. time, with a smaller

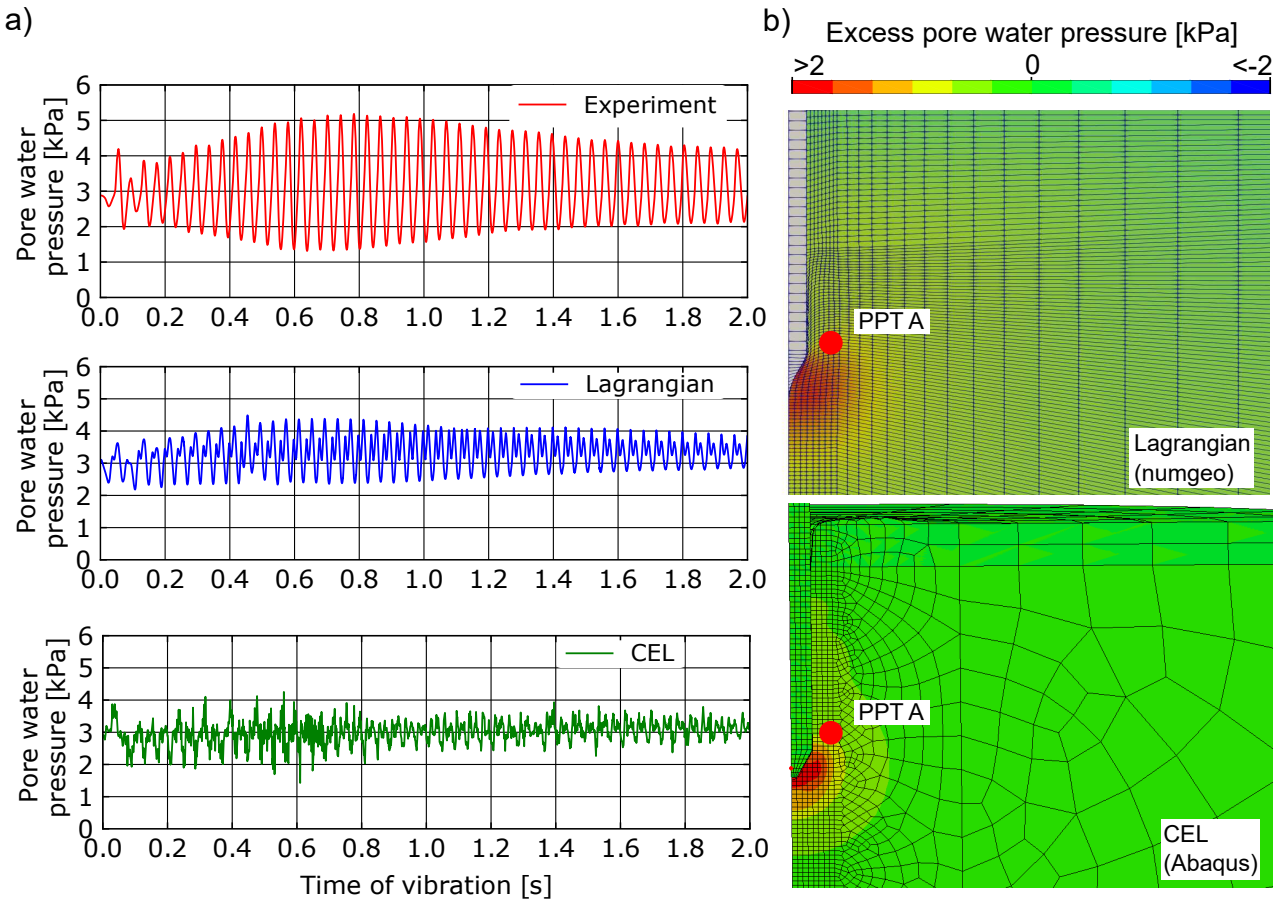

Figure 8.22: a) Development of pore water pressure recorded at PPT A for the measurements, the simulation using the Lagrangian model and the CEL model. b) Fields of the excess pore water pressure during pile driving ($t \approx 1.15$ s) using the Lagrangian model and the CEL method, respectively.

amplitude in every second cycle which is not in accordance with the experiment. The results of the simulation using the CEL model show an irregular development of pore water pressure which differs from the one observed in the Lagrangian simulation. The periodic movement of the pile is not well represented and oscillations are visible. The oscillations can be partly traced back to the application of an explicit time integration scheme. Despite these oscillations, the amplitudes of pore water pressure are comparable to the ones of the Lagrangian simulation. Similar to the simulation using the Lagrangian model, the amplitudes of pore water pressure are too small compared to the measurements. This is notably improved by using the same set of parameters of the hypoplastic model as in the previous section, as is demonstrated in Fig. 8.11.

The field of excess pore water pressure during driving ($t \approx 1.15$ s) of the pile is given in Fig. 8.22b for the simulations using the Lagrangian and the CEL model, respectively. The results are quantitatively and qualitatively in accordance. Both simulations show considerable increase in pore water pressure in the vicinity of the pile tip.

It is concluded that the hydro-mechanically coupled CEL method is suitable for the numerical analysis of vibratory pile driving in water-saturated sand. It is further applied in Section 8.3.2 for the simulation of the vibratory driving process of real-scale piles.

8.3 Influence of the installation process on the response of piles subjected to lateral (high-cyclic) loading in sand

After validation of the numerical tools used for the simulation of the pile installation process in the previous sections, the influence of the pile installation process in sand on the pile response under subsequent (cyclic) loading following the installation is investigated in the next sections. The back-analysis of small scale model tests on piles in dry sand subjected to high-cyclic lateral loading is presented in Section 8.3.1. The influence of vibratory and impact driving in water-saturated dense sand on the pile response to subsequent loading is investigated in Section 8.3.2. Finally, the conclusions of these studies are summarised in Section 8.3.3 and put into relation to investigations of the author published earlier.

8.3.1 Back-analysis of the model tests by Leblanc et al.

The simulation of the installation and subsequent lateral high-cyclic loading of piles in small scale model tests performed by Leblanc et al. [206] is presented in the following (note that the results have already been published by the author in [351]).

The geometric specifications of the model tests are shown in Fig. 8.23. A copper pile with a diameter of $D = 0.08$ m, a wall thickness of $t = 0.002$ m and an embedment length of $L = 0.36$ m was used. The pile was driven into the soil using a plastic hammer. Dry yellow Leighton-Buzzard sand was applied as the test material. It was poured into the container from a low drop height in order to achieve a loose initial state. Tests with two different initial relative densities, $D_{r0} = 4$ % and $D_{r0} = 38$ %, were performed. The lateral loading of the

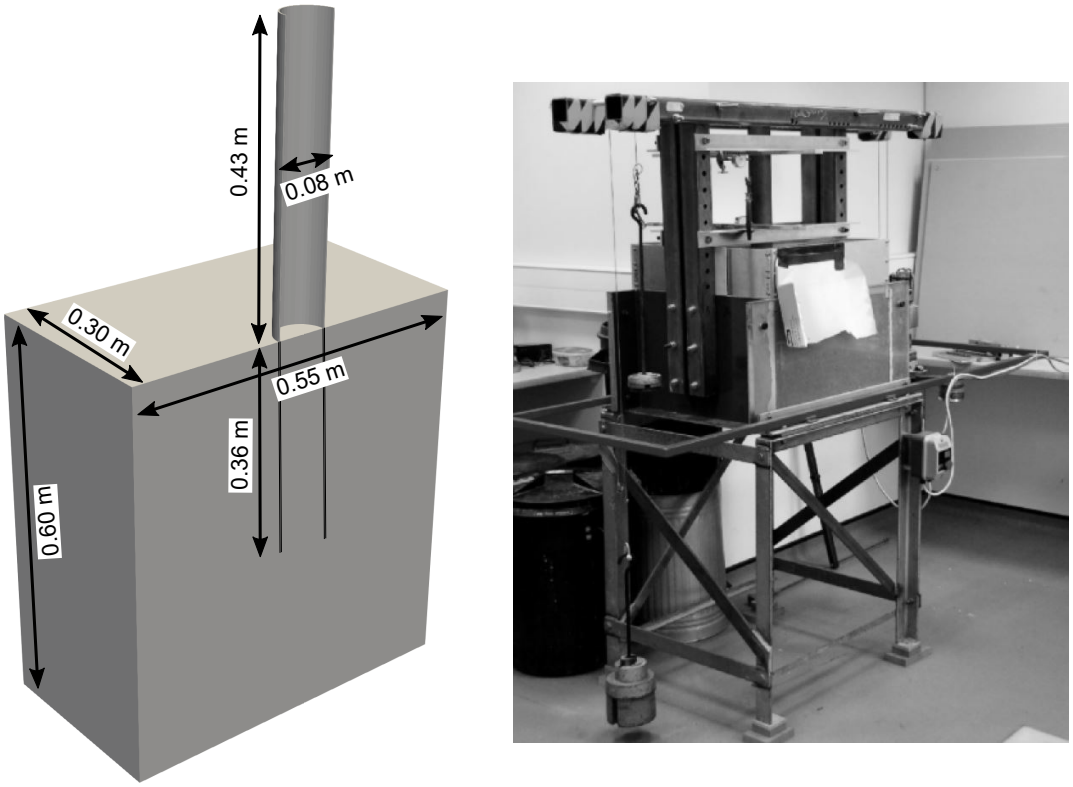

Figure 8.23: Schematic sketch of the model tests and picture of the device (reprinted from [206])

pile was applied in a height of $e = 0.43$ m above the ground surface. Different tests with varying amplitude and mean value of cyclic (harmonic) loading were conducted. The number of applied cycles varied between $N = 8,000$ and $N = 20,000$ in the tests studied in the back-analysis. In the back-analysis, for both initial relative densities, the installation of the pile, a monotonic loading test to determine the lateral capacity and at least one lateral cyclic loading test are considered. For the initial relative density of $D_{r0} = 38$ % several cyclic loading tests with varying loading amplitude are simulated.

In order to determine the material constants for yellow Leighton-Buzzard sand, an extensive laboratory testing program has been conducted. Several oedometric compression tests, drained monotonic triaxial tests with low stress level, undrained cyclic triaxial tests and a drained triaxial test with high-cyclic loading were performed. The complete calibration of the parameters of the hypoplastic model with intergranular strain extension for the yellow Leighton-Buzzard sand can be found in [351]. The parameters are given in Table 8.7. The parameters of the HCA model are provided in Table 8.8. Note that only the parameters C_{N1}, C_{N2} and C_{N3} of the HCA model, which describe the development of accumulated strain with increasing num-

φ_c	e_{i0}	e_{c0}	e_{d0}	h_s	n	α	β	R	m_R	m_T	β_R	χ
33.3 °	0.930	0.809	0.507	$1.9 \cdot 10^7$ kPa	0.191	0.223	-1.3	10^{-4}	4	2	0.1	4.6

Table 8.7: Parameters of Hypoplasticity with intergranular strain extension for yellow Leighton-Buzzard sand

C_{ampl}	C_e	C_p	C_Y	C_{N1} $[10^{-4}]$	C_{N2}	C_{N3} $[10^{-5}]$
1.7	0.482	0.38	2.69	3.1	0.063	3.7

Table 8.8: Parameters of the HCA model for yellow Leighton-Buzzard sand

ber of cycles, are determined based on the high-cyclic triaxial test on yellow Leighton-Buzzard sand. The results of this test and the curve-fit to determine C_{N1}, C_{N2} and C_{N3} are shown in Fig. 8.24c. The remaining parameters are obtained following the procedures described in [419] by estimation based on the median grain size d_{50}, the uniformity coefficient C_U and minimum void ratio $e_{\min}$.

Simulation of the installation process

The numerical model used for the simulation of pile installation into dry sand applies the CEL method and is displayed in Fig. 8.24a. The red volume is initially free of material but could be filled if the soil heaves during the driving process. The blue volume is initially fully filled by material. Green and yellow volumes indicate partially filled elements. The material-filled volume has the same dimensions as the sand container used in the experiment displayed in Fig. 8.23. Exploiting the symmetry of the BVP, a quarter model is considered for the simulation of the installation process to reduce the computational costs.

The initial relative densities are set identical to the values in the model tests, that means 4 % and 38 %, respectively. The hypoplastic model with intergranular strain extension and the parameters listed in Table 8.7 are used. The pile is modelled as rigid body. Friction between pile and soil is considered using a Coulomb friction model. The wall friction angle is assumed to be 2/3 of the critical friction angle of the soil. Note that the proposed constitutive interface models based on the hypoplastic or the Sanisand model can not be applied for the simulation of the installation of the pile due to restrictions by the commercial finite element program `Abaqus`. However, the problem of total vs. effective normal contact stress for the calculation of friction mentioned in the previous section does not exist for the simulations in this section

since no pore water is present.

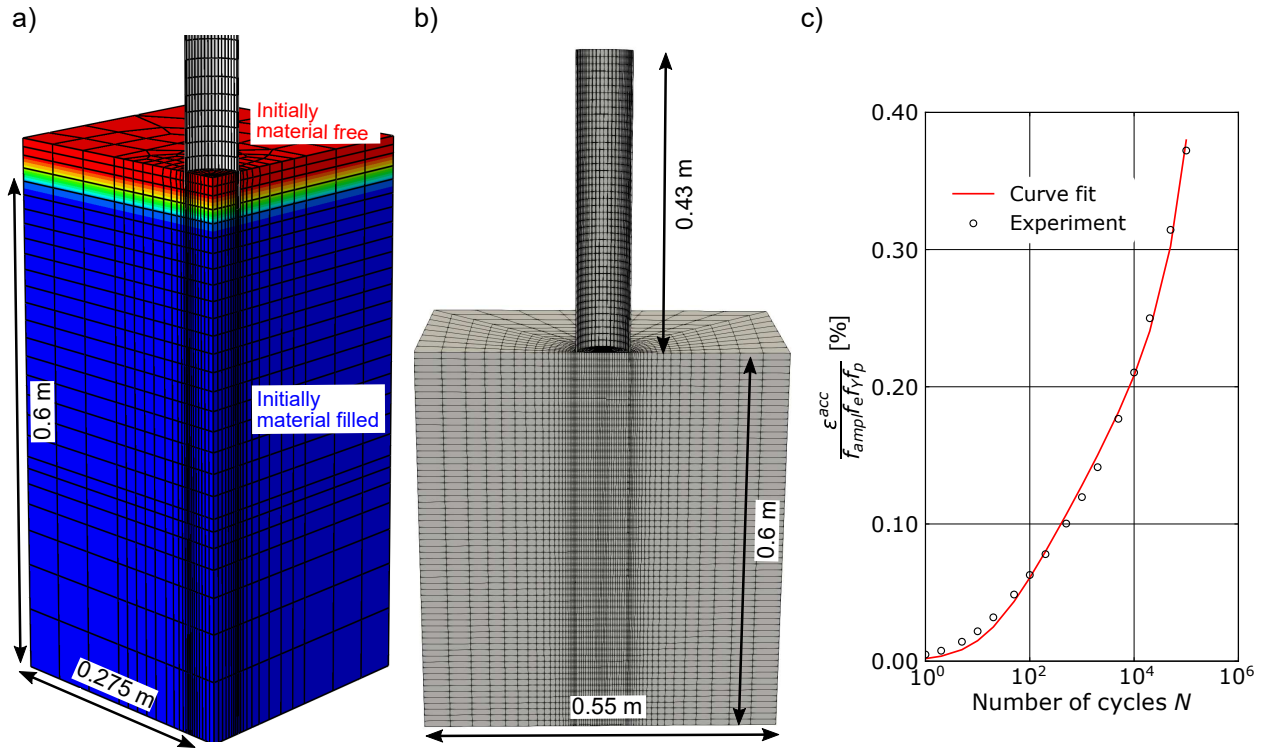

Figure 8.24: a) Numerical model for the simulation of the installation process. b) Numerical model for the simulation of the high-cyclic loading. The initial volume fraction is displayed for the CEL model. The blue volume indicates initially fully material-filled elements while the red volume indicates initially material-free elements. The determination of the parameters C_{N1}, C_{N2} and C_{N3} of the HCA model based on a drained triaxial test with high-cyclic loading on yellow Leighton-Buzzard sand is displayed in plot c).

In the model tests performed by Leblanc et al. the pile was driven into the soil with a plastic hammer. Even though the number of strokes needed to drive the pile to its final embedment depth is known, the specification of the hammer and the drop height is unknown. Since the differences in the lateral cyclic response of piles installed either by jacking or impact driving in dry or ideally drained soils were found insignificant in previous research of the author (see [353, 352]), the pile is jacked into the soil in the simulation assuming that the change in the soil surrounding the pile is similar to impact driving. Note that in an experimental study reported in [114, 112], impact driven piles were found to have a higher resistance to subsequent monotonic lateral loading compared to jacked piles. In order to investigate how large the influence of the method of installation is in the present case, additional simulations considering

impact driving were performed and reported by the author in [351]. Even though the impact driven pile exhibited slightly larger resistance to lateral monotonic loading compared to the jacked pile, the relative difference between the two installation techniques was found to be small. Therefore, the simulation of pile installation using jacking appears to be justified in the present case. A jacking speed of 0.06 m/s is assumed in the simulations. Inertia effects are considered and an explicit time integration scheme is used.

The development of relative density during the driving process for the simulation of the test with an initial relative density of $D_{r0} = 38$ % is depicted in Fig. 8.25. Note that throughout the work, results obtained using the CEL method are never displayed with a deformation scale factor. The current location of the material is depicted. The spatial field is displayed for different stages of the simulation and the current depth of embedment t is given. The soil near the top surface heaves and reaches a very loose state. In the vicinity of the pile tip the soil tends to densify considerably. This is more pronounced inside of the pile compared to the outside. In addition, the densified zone is restricted to soil close to the pile shaft. With increasing distance to the outer shaft of the pile, the relative density decreases and reaches values lower than the initial relative density. The development of relative density shown in Fig. 8.25 is comparable to the results of simulations of impact driving or jacking of real-scale piles reported in [353, 352], in case of simulations with a similar initial relative density. The qualitative change in relative density caused by the installation process is thus comparable for small-scale model tests and real-scale problems.

The change of mean effective stress during the driving process is shown in Fig. 8.26. A strong increase in pressure with values above 100 kPa is observed below the pile tip. During the driving process, the area of high pressures increases and eventually reaches the fixed bottom of the model. While the stress increases below the pile tip, a strong decrease alongside the (outer) pile shaft is observed. This effect has already been introduced in Chapter 2 and is discussed in more detail in Section 8.3.2 for the pile installation process in water-saturated soil.

The results of the pile installation for the test with an initial relative density of $D_{r0} = 4$ % are presented and discussed in [351]. A strong compaction and stress increase in the vicinity of the pile tip is observed similar to the test with an initial relative density of $D_{r0} = 38$ %.

For the simulation of the lateral loading of the pile presented in the following, an implicit Lagrangian simulation is performed using `numgeo` since the high-cycle phase with the HCA model can not be simulated using an explicit time integration scheme. Therefore, the state of the soil resulting from the simulation of the installation is transferred from the CEL model to

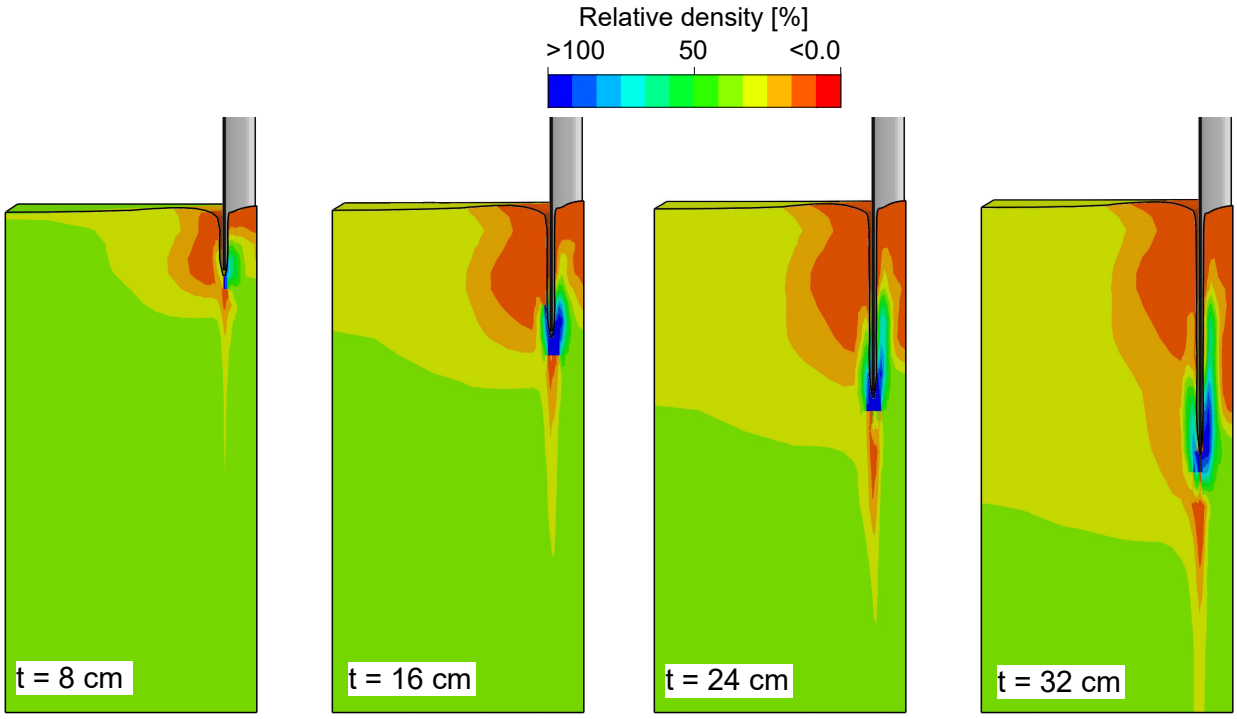

Figure 8.25: Development of relative density during the driving process for the test with an initial relative density of $D_{r0} = 38$ %. The embedment depth t is given for each stage of the installation process.

a model with Lagrangian elements as described in the following.

Lateral loading of the pile following the installation

Linearly interpolated 3D Lagrangian elements with reduced integration are used for the soil. Elements with reduced integration are beneficial in simulations with the HCA model as artificial self-stresses are avoided [270]. An hourglass stiffness of 100 kPa is used for all calculations to suppress any hourglass deformation modes. Simulations with much lower (20 kPa) or much higher values (300 kPa) for the hourglass stiffness did not reveal any differences in terms of pile rotation. The model including the mesh is displayed in Fig 8.24b. Due to the unidirectional lateral loading it is sufficient to model only one half of the model test making use of the symmetry. The finite element model is discretised using approximately 60,000 nodes and 50,000 elements. The pile is modelled deformable and the material properties of copper ($E = 1 \cdot 10^8$ kPa and $\nu = 0.3$) are used.

The contact between pile and soil is discretised using the EBM method with 4 integration points per finite element face and the contact constraints are enforced by the penalty method.

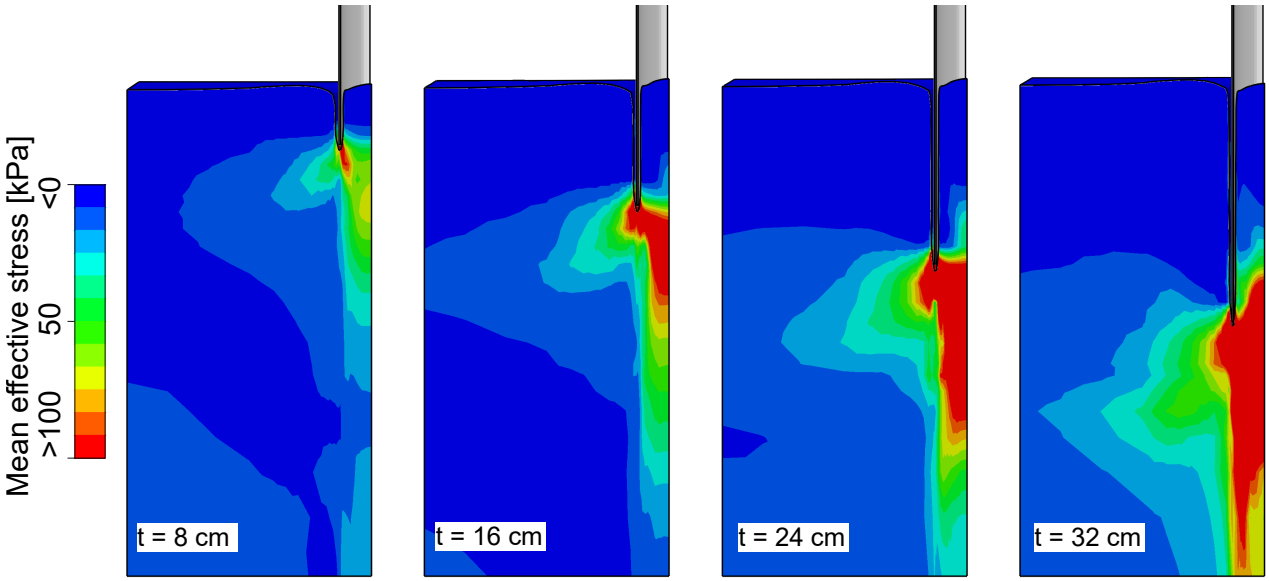

Figure 8.26: Development of mean effective stress during the driving process for the test with an initial relative density of $D_{r0} = 38$ %

The penalty factor in normal direction is calculated based on the material stiffness of the continuum element closest to the contact point. By default, the penalty factor is thirty times the trace of the stiffness. This ensures that the penetration of the soil into the pile is minimal and the normal contact constraint is enforced properly. A stiffness dependent penalty factor is superior in terms of convergence to a spatially constant value in the present simulations due to the change of soil stiffness with respect to the pile embedment depth (i.e. highest stiffness at the base, especially for the simulation incorporating the installation process). Friction is considered using a Coulomb model with a wall friction angle of 2/3 of the critical friction angle of the soil. Investigations using the proposed hypoplastic interface element reported by the author in [356] show only little influence of the constitutive contact model on the lateral response of the pile for both monotonic and cyclic loading. Therefore, these results are not discussed in detail here and a Coulomb interface model is used.

A stabilising pressure of 0.05 kPa is applied on the ground surface in order to avoid zero pressure in the soil elements close to the surface. This additional surface pressure does not influence the results of the simulations, which was proven by simulations without any surface pressure. Simulations with a higher value of surface pressure, e.g. 0.5 kPa, show a considerable influence and lead to a decreased pile rotation when the pile is subjected to lateral loading. Due to the large deformations in the monotonic tests and in the cyclic tests with large amplitudes, a geometrically non-linear calculation is performed.

The state variables of the soil after the installation are transferred from the integration points

in the CEL model to the closest integration points in the Lagrangian model. The stress, void ratio and the intergranular strain tensor are transferred. Note that the influence of considering the intergranular strain tensor resulting from the installation process is much more pronounced for monotonic lateral loading compared to cyclic lateral loading (under the assumption that the magnitude of the monotonic lateral loading is higher). This is because for monotonic loading, the soil volume contributing to the resistance of the pile continuously increases with increasing lateral deflection of the pile. Since the intergranular strain tensor is also altered in greater distance from the pile by the installation process, its influence on the lateral resistance decreases only little with ongoing lateral loading. In contrast, the influence of the change in the intergranular strain on the results of the cyclic loading is less pronounced, since the soil volume contributing to mobilising resistance stays nearly constant after the first cycle.

The deformation of the soil caused by the installation process is not considered in the Lagrangian model as the material movements are judged insignificant compared to the influence of the change in state variables. In a distance of 0.005 m around the pile the soil has settled by approximately 0.008 m ($= 0.1 \cdot D$). In greater distance to the pile as well as inside of the pile a maximum heave of approximately 0.004 m ($= 0.05 \cdot D$) is observed.

It is important to note that the stress state resulting from the simulation of installation depicted in Fig. 8.26 is not in static equilibrium since considerable inertia forces are still present at the end of the CEL simulation (no additional resting period after the installation is considered). In addition, the mapping procedure also adds inaccuracies leading to further unbalanced forces. Thus, the stress will change slightly once the soil state is imported into the Lagrangian model and the soil is free to move. An additional calculation step is included to bring the model in static equilibrium prior to the lateral loading of the pile.

In order to evaluate the influence of the installation process on the results of the lateral loading of the pile, an additional wished-in-place (WIP) simulation is performed, assuming initial K_0 stress conditions and a homogeneous distribution of void ratio.

Prior to the cyclic tests, a monotonic loading test has been performed by Leblanc et al. in order to determine the static moment capacity $\tilde{M}_R$. The non-dimensional moment $\tilde{M}$ is defined by [206]

$$\tilde{M} = \frac{M}{L^3 D \gamma}, \tag{8.6}$$

where M is the applied moment, L and D are the embedded length and the diameter of the pile, respectively, and γ is the specific unit weight of the (dry) soil. The non-dimensional

rotation $\tilde{\theta}$ is defined by [206]

$$\tilde{\theta} = \theta \sqrt{\frac{p_a}{L\gamma}}. \tag{8.7}$$

Therein θ is the rotation of the pile and $p_a \approx 100$ kPa is the atmospheric pressure.

The non-dimensional moment vs. the non-dimensional rotation for the experiment and the simulations with and without consideration of the installation is given in Fig. 8.27, for the initial relative densities of $D_{r0} = 38$ % and $D_{r0} = 4$ %, respectively. Leblanc et al. defined the ultimate-limit-state (ULS) rotation of the pile to be $\tilde{\theta} = 0.0698$ rad $= 4°$, corresponding to a static non-dimensional moment capacity of $\tilde{M}_R \approx 1.24$ for $D_{r0} = 38$ % and $\tilde{M}_R \approx 0.6$ for $D_{r0} = 4$ %.

It can be seen that the simulations without consideration of the installation process underestimate the resistance of the pile for both initial densities. This is especially pronounced during the first half of the loading process. Thus, the initial stiffness of the pile is predicted too low compared to the experiment. For the initial relative density of $D_{r0} = 38$ % the non-dimensional moment at the ULS rotation $\tilde{\theta} = 0.0698$ rad in the simulation is approximately 25 % lower than the corresponding measured value. The results of the simulation considering the installation process are in better accordance with the experimental data even though the pile resistance at the end of the test is still slightly underestimated. In case of the test with an initial relative density of $D_{r0} = 4$ % the initial stiffness is underestimated by both simulation types but the final resistance is reproduced quite well by the simulation taking into account the installation process.

Based on the significant differences between the simulations, it is concluded that the installation-induced changes of soil state considerably influence the pile response to monotonic lateral loading. However, wished-in-place conditions are a conservative assumption in terms of pile displacement. The stiffness and hence the natural frequency of the pile are underestimated in that case. Similar conclusions were drawn for the simulation of real-scale piles reported in [353].

As has been outlined in Chapter 2, the study reported in [114] has investigated the influence of the pile installation on its response to lateral loading by performing the installation process at 1 g and 100 g, respectively. The relative increase in the lateral soil resistance due to the installation process observed in [114] is qualitatively and quantitatively similar to the differences found in the numerical results presented in Fig. 8.27.

Based on the static moment capacity M_R obtained from the tests with monotonic loading,

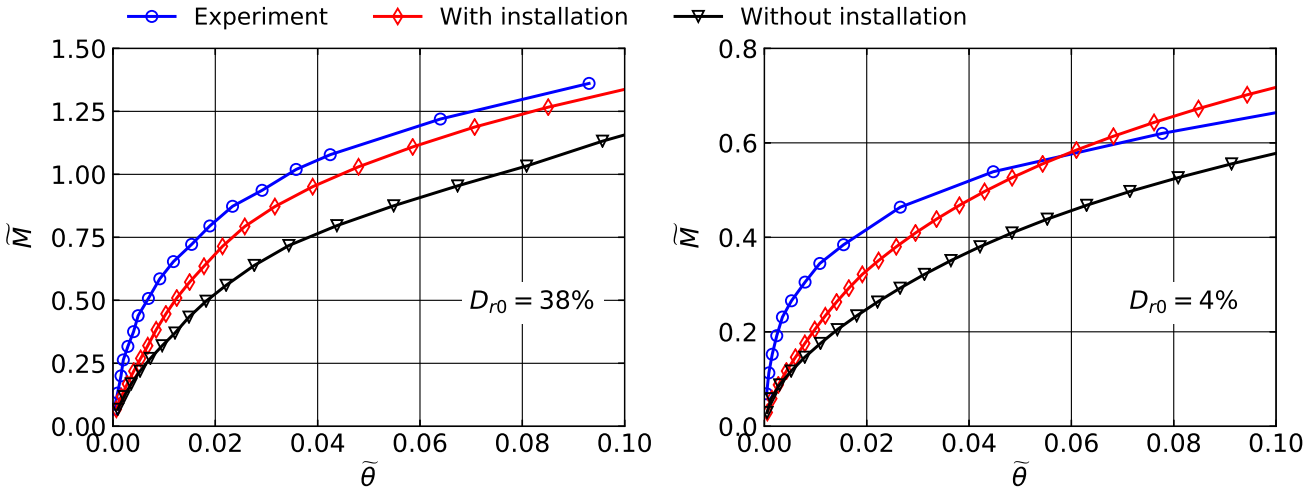

Figure 8.27: Results of the monotonic loading tests: Comparison of the curves of non-dimensional moment $\tilde{M}$ vs. non-dimensional rotation $\tilde{\theta}$ measured in the experiments and obtained from the simulations with and without consideration of the installation process, respectively. The diagram on the left-hand side refers to an initial relative density of $D_{r0} = 38$ %, that on the right-hand side to $D_{r0} = 4$ %.

two parameters ζ_b and ζ_c are used to characterise the cyclic loading [206]

$$\zeta_b = \frac{M_{\max}}{M_R} \quad \text{and} \quad \zeta_c = \frac{M_{\min}}{M_{\max}}. \tag{8.8}$$

$M_{\max}$ and $M_{\min}$ are the maximum and minimum moments in a sinusoidal load cycle. The static moment capacities M_R measured in the model tests are used for the calculation of the load amplitudes in the simulations.

The results in terms of the change of rotation $\Delta\theta$ at the pile head with respect to the first load cycle divided by the static rotation θ_s vs. the number of cycles N for test No. 17 ($D_{r0} = 38$ %, $\zeta_b = 0.4$ and $\zeta_c = 0$) are given in Fig. 8.28. The values measured in the model tests and those obtained from the simulations with and without the consideration of the installation process, respectively, are compared. Note that in the experiment θ_s has been determined at the point of maximum load application in the first cycle and $\Delta\theta$ has been also measured with respect to the point of maximum load application. In the simulations, however, θ_s is the rotation after the first complete cycle and $\Delta\theta$ is the change in rotation with respect to the rotation at the end of the first cycle. This is because the HCA model calculates the trend of deformation under the average loads, and $\Delta\theta$ can thus not be quantified at the point of maximum load application during a cycle. This doesn't influence the comparison between experiment and simulation as long as the rotation amplitude in an individual cycle does not change considerably during

the long-term loading, which is not the case for the simulations presented in this section. Note that θ_s in the simulations is slightly higher than in the experiments as has been shown by the simulations of the monotonic tests displayed in Fig. 8.27. These differences are more pronounced in case of the simulation without considering installation. Therefore, the ratio $\Delta\theta/\theta_s$ may be too small in the simulations compared to the experiments due to a weaker monotonic response of the pile in the simulations, and not because the accumulation is too low in the HCA phase.

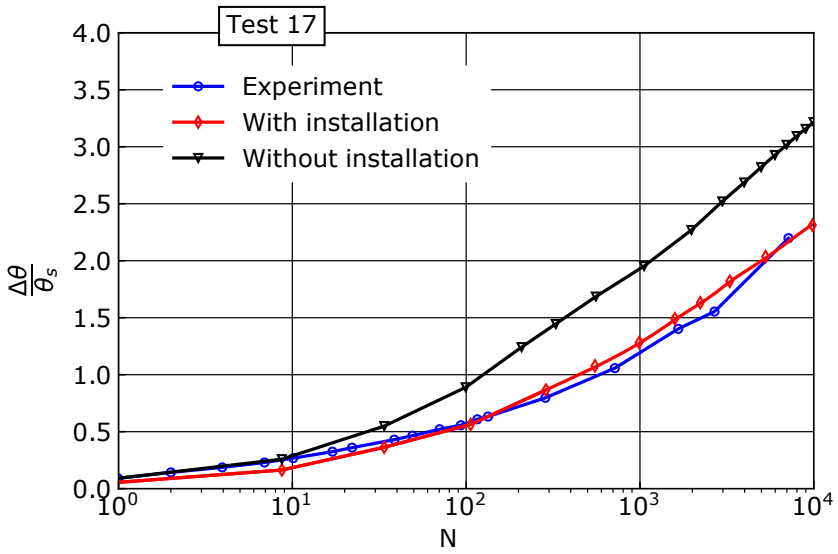

Figure 8.28: Change of rotation $\Delta\theta$ divided by the static rotation θ_s as a function of the number of cycles N measured in test No. 17 of Leblanc et al. [206] ($D_{r0} = 38$ %, $\zeta_b = 0.4$ and $\zeta_c = 0$) and obtained from the simulations with and without consideration of the installation process, respectively

From Fig. 8.28, it can be concluded that the simulation without consideration of the installation process overestimates the accumulated rotation measured in the experiment. The simulation incorporating the installation on the other hand reproduces the measurements very well. The simulation neglecting the installation predicts approximately 50 % higher values of $\Delta\theta/\theta_s$ at the end of the test compared to the measurements as well as compared to the simulation with incorporation of the installation process.

The spatial field of the strain amplitude for the simulations with and without incorporation of the installation, respectively, is given in Fig. 8.29a for test No. 17. Note that the deformed state after application of the second load cycle is displayed. It is evident that the area with

strain amplitudes larger than 0.1 % is greater at both sides of the pile in case of the simulation without installation compared to the simulation with consideration of the installation-induced changes in the soil state. Since higher values of the strain amplitude result in higher rates of strain accumulation calculated by the HCA model (disproportionate relationship with the exponent $C_{\text{ampl}} = 1.7$), larger accumulation rates are predicted in the simulation without consideration of the installation process leading to a larger pile rotation.

The spatial field of relative density after the application of 10,000 loading cycles for the simulations with and without installation, respectively, is given for test No. 17 in Fig. 8.29b. The deformed configuration is displayed. No deformation-scaling factor is used. The increased pile rotation in case of the simulation without consideration of the installation process is well visible in comparison to the simulation incorporating the installation process. In both cases a strong decrease in soil density accompanied by a heave of the soil around the pile at the ground surface is predicted by the simulations. The heave is slightly greater in case of the simulation without consideration of the installation process. While the relative density in the top half of the model is similar for both calculations, much higher D_r values are present in the vicinity of the pile tip in case of the simulation incorporating the installation process. As discussed previously based on Fig. 8.25, this high density is caused by the installation process of the pile. The density distribution in the vicinity of the pile tip is hardly changed by the application of the 10,000 loading cycles, so that the installation-induced changes in the soil state are still well visible. With ongoing cyclic loading the influence of the installation is assumed to decrease and the spatial fields of density and stress of the simulation without and with installation, respectively, equalize, as has been shown by the author in [353]. In the study presented in [353], however, 5 million loading cycles are applied. Therefore, this aforementioned equalisation may take several million load cycles to occur.

The results for test No. 18 with the same density but a higher load amplitude ($D_{r0} = 38$ %, $\zeta_b = 0.52$ and $\zeta_c = 0$) in terms of $\Delta\theta/\theta_s$ vs. N are given in Fig. 8.30a. Note that the simulation without considering installation aborted due to the large deformations towards the end of the simulation ($N \approx 5,000$). Similar to test No. 17, the simulation without incorporation of the installation process overestimates the accumulated pile rotation. The simulation with installation reproduces the measured values well. The simulation without consideration of the installation process predicts approximately 45 % higher values of $\Delta\theta/\theta_s$ at $N \approx 5,000$ in comparison to the simulation incorporating the installation process. Compared to the measurements, the simulation neglecting the installation process shows values being 50 % higher at $N \approx 5,000$.

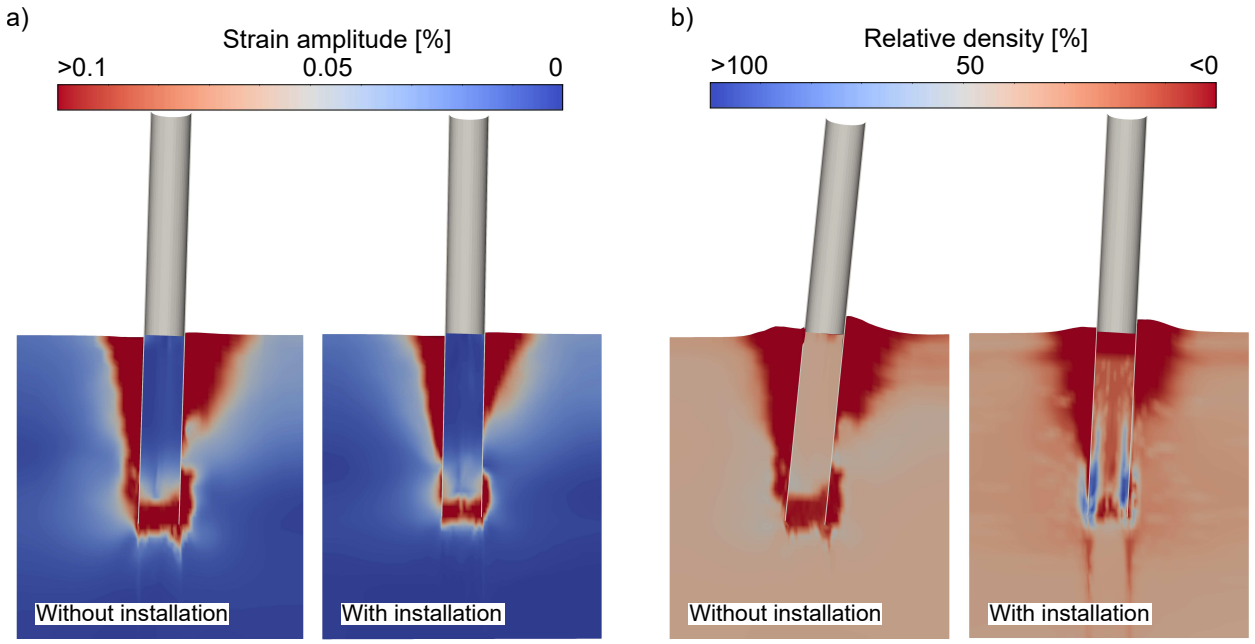

Figure 8.29: a) Deformed shape and spatial field of the strain amplitude after the second loading cycle for test No. 17 and the simulations with and without consideration of the installation process, respectively. No deformation-scale factor is used. b) Deformed shape and spatial field of the relative density after application of 10,000 cycles for test No. 17 and the simulations without and with consideration of the installation process, respectively. Again, no deformation-scale factor is used.

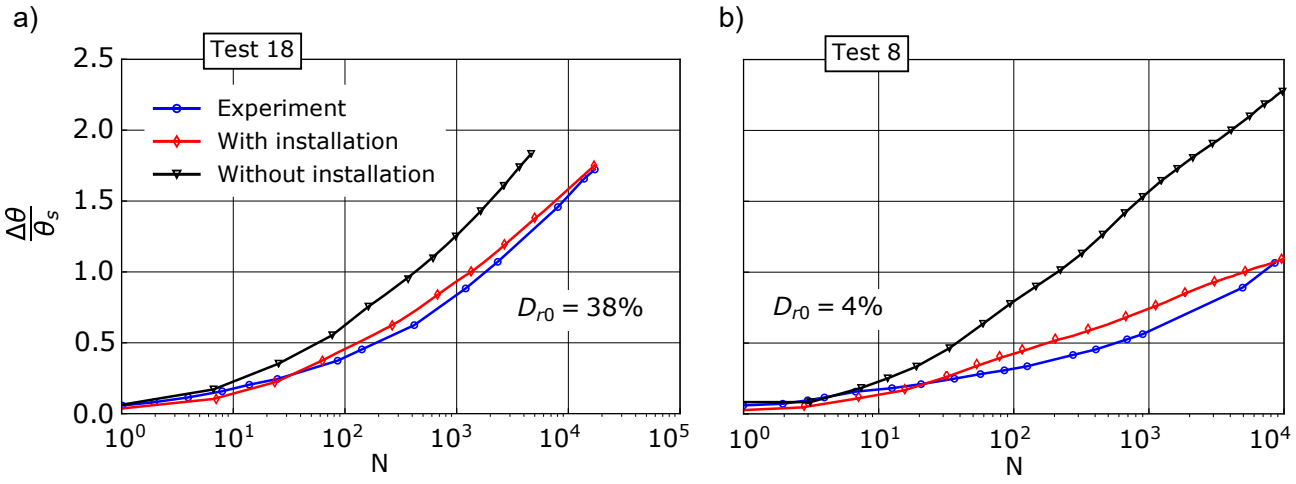

Figure 8.30: a) Change of rotation $\Delta\theta$ divided by the static rotation θ_s vs. number of cycles N measured in test No. 18 ($D_{r0} = 38$ %, $\zeta_b = 0.52$ and $\zeta_c = 0$) and obtained from the simulations with and without consideration of the installation process, respectively. b) The same as plot a) but for test No. 8 ($D_{r0} = 4$ %, $\zeta_b = 0.34$ and $\zeta_c = 0$).

The results for test No. 8 with a very low initial relative density and a lower load amplitude ($D_{r0} = 4$ %, $\zeta_b = 0.34$ and $\zeta_c = 0$) are displayed in Fig. 8.30b. In accordance with the previous findings from the tests with an initial relative density of $D_{r0} = 38$ % a higher accumulation of rotation is observed for the simulation without consideration of the installation. The simulation with incorporation of the installation process reproduces the measurements well. Compared to the tests with higher initial density ($D_{r0} = 38$ %) the difference between the two simulation types is considerably larger for $D_{r0} = 4$ %.

The back-analysis of the model tests performed by Leblanc et al. [206] shows that the incorporation of the installation process in the numerical simulations has a distinct influence on the predicted pile response under subsequent monotonic or cyclic lateral loading. The simulations without consideration of the installation process overestimated the rotation of the pile subjected to monotonic lateral loading. The simulations incorporating the installation-induced changes of soil state lead to a better accordance with the measurements and higher pile resistance. The cyclic loading tests with up to 20,000 cycles revealed that the accumulated pile rotation is influenced by the installation process as well. The simulations neglecting the installation-induced changes of soil state overestimated the pile rotation compared to the measurements. The simulations with incorporation of the installation process lead to a better agreement with the experimental results and exhibited less accumulation compared to the simulations without considering the installation process.

The herein presented simulations of the model tests by Leblanc et al. [206] are also documented in [359] using Sanisand instead of the hypoplastic model for both the installation of the pile and the subsequent (monotonic) lateral loading. Despite a careful calibration of the parameters of the Sanisand model using the same laboratory test data as for the hypoplastic model, the results in term of relative density and stress following the pile installation process differed considerably. Sanisand predicted less increase in effective stress and less densification of the soil in the vicinity of the pile tip. In line with these observations, the influence of the installation process on the subsequent lateral loading was found to be less pronounced than for the herein presented simulations using the hypoplastic model.

In addition to the model tests by Leblanc et al., the tests by Richards et al. [316], where almost the same test set-up has been used, are simulated. In contrast to the tests by Leblanc et al., initially medium dense to dense conditions ($D_{r0} = 60$ %) and two-directional lateral cyclic loading have been considered. The back-analysis of these tests is documented by the author in [350] and is not discussed here in detail. The same conclusions regarding the influence of the installation process on the response of the pile to subsequent lateral loading are drawn, despite the higher initial density. Similar differences between wished-in-place simulations and those

incorporating the installation-induced soil changes are found for the tests with two-directional loading as reported for the uni-directional tests presented here.

8.3.2 Long-term behaviour of vibratory vs. impact driven piles for OWT foundations

As has been outlined in the introduction and in Chapter 2, there is an increasing interest in the investigation of the applicability of vibratory driving for the installation of monopile foundations for OWTs. It is, however, yet unclear if the current design practices for the lateral loading of the foundation can be applied to vibratory driven piles since the methods applied are based on experience from impact driven piles. A comparative study of the two installation techniques is presented in the following, focussing on the investigation of the influence of the drainage conditions during driving.

Pile installation

The numerical model used for the simulation of the pile installation process is depicted in Fig. 8.31. The soil is discretised using Eulerian elements. The extension of the CEL method allowing for partially drained analysis as proposed in Section 4.6.2 and already applied in Section 8.2.4 is utilised. Since the soil can also heave during the pile installation, an additional, initially material-empty, volume above the seabed is considered which can be filled by material (red area in Fig. 8.31). To minimise the impact of artificial reflections of outwards travelling waves at the fixed boundaries of the model, a distance of 80 m from the pile to the outer boundary is chosen. In addition, the node-to-node distances increase with increasing distance to the pile, which leads to a progressive loss of higher frequency waves (see field of acceleration on the right-hand side of Fig. 8.31).

The size of the soil elements in the vicinity of the pile is chosen equal to the wall thickness of the pile, such that the pile occupies exactly one Eulerian element across its wall section as it penetrates the soil. The time increment is chosen to be identical to the critical time increment defined by the Courant-Friedrichs-Levy condition. During the simulation, this results in a time increment of approximately 10^{-4} s.

In case of the partially drained simulations, additional boundary conditions for the excess pore water pressure are necessary. In the present study, the top surface of the soil allows for dissipation of excess pore water pressures during the installation. Note that once elements are

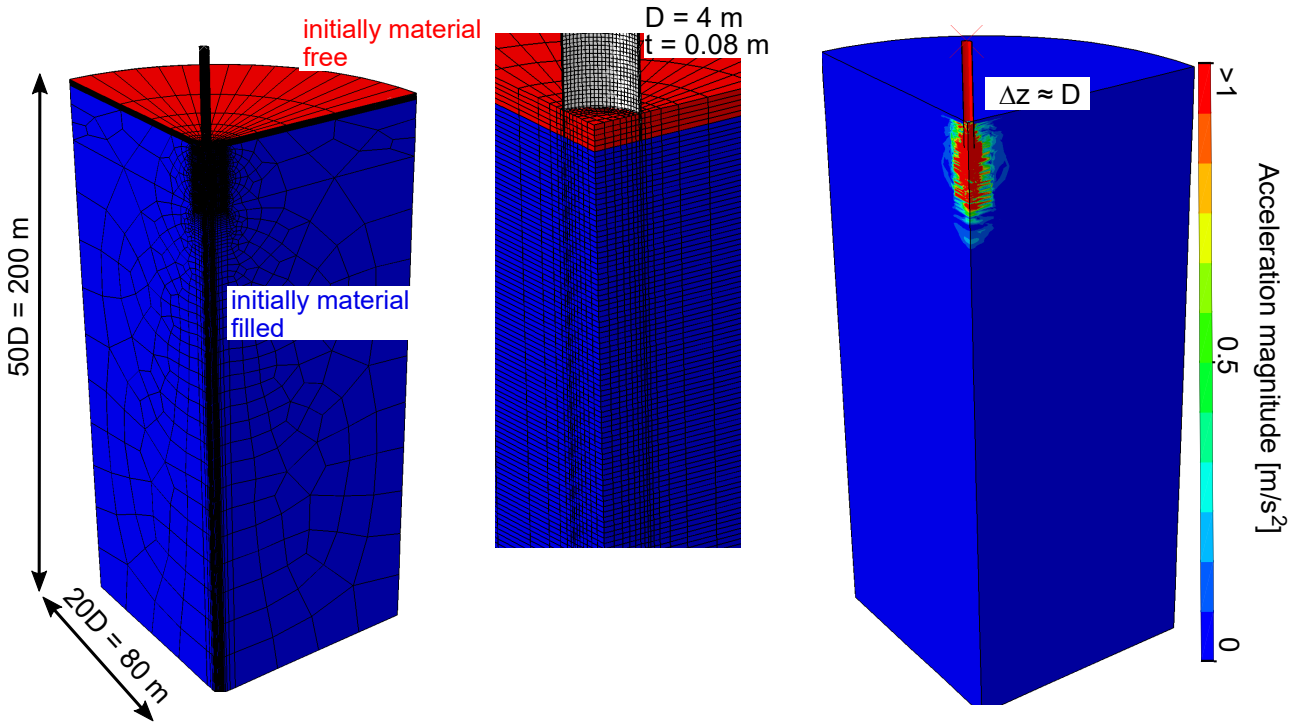

Figure 8.31: Model for the simulation of the pile installation process and spatial distribution of the acceleration magnitude (gravity is subtracted) during the driving process at a pile penetration of approximately $\Delta z = D$

no longer filled with material, no water flow through these elements is possible anymore. Since the soil around the pile settles during driving, no drainage would be possible alongside this newly formed material boundary. Therefore, zero excess pore water pressure is assigned for the top 0.3 m to allow for drainage even if the soil surface around the pile moves downwards.

For all simulations, a pile with a diameter of $D = 4$ m and a wall thickness of $t = 0.08$ m is considered. The soil is assumed to be "Karlsruhe fine sand". The hypoplastic model with intergranular strain extension with parameters given in Table 8.9 is used.

Initially medium dense ($D_{r0} = 50$ %) and dense soil conditions ($D_{r0} = 70$ %) are considered. The focus of the study is on the initially dense conditions, since it is the practically more relevant case for the offshore environment. The applied driving forces are chosen such that the penetration rate of the pile is comparable for both installation techniques and that the targeted final embedment depth can be achieved within a reasonable computational time. Note that compared to the pile installation process of monopiles in reality, for which the driving process may involve tens of thousands of hammer blows, only a limited number can be numerically simulated. A vibratory driving frequency of 30 Hz and an amplitude (single) of 1200 kN is set (all values for a full pile). The impact driving frequency is 0.65 Hz and

φ_c [-]	e_{i0} [-]	e_{c0} [-]	e_{d0} [-]	h_s [MPa]	n [-]	α [-]	β [-]	R [-]	m_R [-]	m_T [-]	β_R [-]	χ [-]
33.1°	1.212	1.054	0.677	4000	0.27	0.14	2.5	10^{-4}	2.4	1.2	0.1	6.0

Table 8.9: Parameters of the hypoplastic model with intergranular strain extension for "Karlsruhe fine sand"

the load magnitude 2400 kN. The impact force is active for 10 ms. In addition to the pile weight, a static load resulting from the driver and an additional extension of the pile, which is not modelled explicitly, of 2000 kN is considered for both installation techniques. The chosen specifications are typical values for vibratory drivers and hydro-hammers used by the industry for the driving of large offshore piles (see for instance the specifications of vibratory drivers offered by the company `PVE` and the hydro-hammers offered by the company `IHC`).

Friction between pile and soil is considered using a Coulomb friction model with a friction coefficient of 0.5 (a factor of 0.25 is set in the definitions of the analysis, as is explained in Section 8.2.4), which is a value typically found for surfaces of piles used for offshore foundations [307]. Note that the shortcoming regarding the incorporation of soil-structure interface friction mentioned in Section 8.2.4, where it is not possible to distinguish between effective and total normal contact stresses, can be circumvented to some extent. For this, the friction coefficient is defined as temperature (= Δp^w)-dependent, reducing with increasing excess pore water pressure (Δp^w). The friction coefficient μ is calculated by:

$$\mu = \begin{cases} 0.25 & \text{if } \Delta p^w \leq 0 \text{ kPa} \\ 0.25 \cdot \dfrac{(100 \text{ kPa} - \Delta p^w)}{100 \text{ kPa}} & \text{if } 0 \text{ kPa} < \Delta p^w \leq 100 \text{ kPa} \\ 0 & \text{if } \Delta p^w > 100 \text{ kPa} \end{cases} \tag{8.9}$$

Obviously, Eq. (8.9) is only a rough estimation of the correct friction coefficient μ for a given total normal stress t_N.

In addition to the modification of the friction coefficient, the maximum frictional stress is restricted to $t_{T,crit} = 100$ kPa for all performed simulations (see Fig. 8.32 for an illustration of $t_{T,crit}$ using the Coulomb friction model). It is believed that for such high normal and shear stresses, particle breakage limits the maximum frictional stresses that can develop [273]. Moreover, since `Abaqus` uses the definition of a relative tangential displacement ($u_{T,crit}$, see Fig. 8.32) required to fully mobilise the maximum shear stresses $t_{T,crit}$, defining the tangential

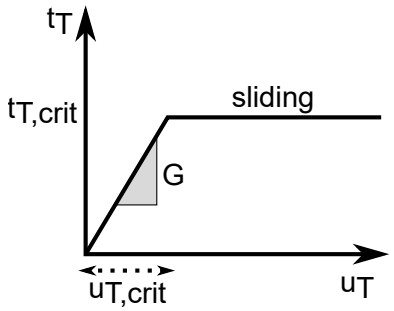

Figure 8.32: Illustration of the Coulomb friction model using the tangential penalty factor G

penalty factor of the frictional contact G, the aforementioned shortcoming of total vs. effective normal stresses is only relevant for $\mu t_N < t_{T,crit}$. This is because the value of G is not influenced by the product μt_N in case of $\mu t_N > t_{T,crit}$ (see Fig. 8.32). Therefore, the frictional stresses are correctly calculated for any given value of u_T for $\mu t_N > 100$ kPa.

As has been shown in Section 6.10.7, where interface shear tests were simulated with perfectly rough conditions, assuming $\mu = \tan(\varphi_c)$ gives the same results in terms of shear stress as simulations with shared nodes at the soil-structure interface (i.e. the nodes of the soil can not move relative tangentially to the structure). This is because the relative tangential movement between soil and structure than occurs in the continuum, since it is the "weak link" in that case. Similarly, if the friction coefficient is larger than the tangential of the internal friction angle, shear bands in the continuum occur. Therefore, the above mentioned error in calculation of t_T using total stresses can not lead to a strong overestimation of frictional stresses in case of $\mu = 0.5 \approx \tan(\varphi_c)$, since they are limited by the continuum resistance, which is in turn governed by effective stresses.

It is also conceivable to apply a fixed tangential penalty factor G and assume $\mu \to \infty$, forcing shear bands to occur in the continuum, using `Abaqus`. In this case, the normal contact stress t_N does not influence t_T at all. However, the assumption of $\mu \to \infty$ is only valid for rough surfaces with $\mu \approx \tan(\varphi_{\text{mob}})$, such that the continuum is the "weak link" in any case.

An isotropic hydraulic conductivity of $k^w = 10^{-3}$ m/s is assumed as the reference case. Additional simulations assuming ideally drained conditions (i.e. water-saturated conditions but perfect drainage) and a hydraulic conductivity of $k^w = 10^{-4}$ m/s are performed as well. To evaluate the drainage conditions during driving, the dimensionless factor π_1 introduced in Eq. (4.71) is used. The characteristic length l used in Eq. (4.71) is assumed to be identical to the embedded pile length of 10 m in the present case. The compression wave velocity is $v_c = 1700$ m/s and the total density $\rho^{\text{tot}} = 1.86$ t/m^3. The values obtained for π_1 for the different pile installation simulations are summarised in Table 8.10. In addition, the drainage conditions

Simulation	π_1	Drainage conditions
VD ($k^w = 10^{-3}$ m/s)	0.028	nearly undrained
VD ($k^w = 10^{-4}$ m/s)	0.003	undrained
ID ($k^w = 10^{-3}$ m/s)	0.131	partially drained
ID ($k^w = 10^{-4}$ m/s)	0.013	nearly undrained

Table 8.10: Drainage conditions for the different pile installation simulations (VD: Vibratory Driving; ID: Impact Driving) using the dimensionless factor π_1 and the diagram provided in [450]

according to the diagram provided by [450] are given. Note that in [450] values of $\pi_1 < 10^{-2}$ are regarded to allow for the assumption of ideally undrained conditions, while values larger 10^2 are considered to result in ideally drained conditions. In between, the response is considered to be partially drained. Since the (static) load magnitude is not considered in π_1, the conditions given in Table 8.10 might not realistically reflect the actual conditions. However, it is believed that the evaluation of π_1 at least allows to compare the drainage conditions between the different installation techniques. From Table 8.10 it is evident that the vibratory driving process leads to nearly undrained conditions, while for the impact driven pile at least for the higher value of hydraulic conductivity a larger influence by the consolidation process is expected. The conditions for the vibratory driven pile with $k^w = 10^{-3}$ m/s are similar to the impact driven pile with $k^w = 10^{-4}$ m/s, even though in case of the vibratory driven pile less influence from the consolidation process is expected.

The targeted embedment depth of the pile is 10 m. While the impact driven pile needs approximately 30 s to reach this depth, the vibratory driven pile requires approximately 33 s. While these installation times are regarded as rather short compared to the installation of real offshore piles, the company `Cape Holland`, specialised on vibratory pile driving of monopiles for OWTs, reports driving times of only 15 minutes to reach penetration depths of 24 m for even larger piles ($D = 6.5$ m) [170]. Therefore, the obtained pile penetrations rates are judged to be not unrealistic in general, taking into account that the considered specifications of the pile drivers correspond to those with the highest power available in the industry, which are used for driving of larger piles than considered here.

The pile penetration vs. time of driving plot for the vibratory driven piles is given in the left-hand plot of Fig. 8.33 for different values of hydraulic conductivity and drainage conditions. Only the results of simulations with initially dense soil conditions ($D_{r0} = 70$ %) are shown.

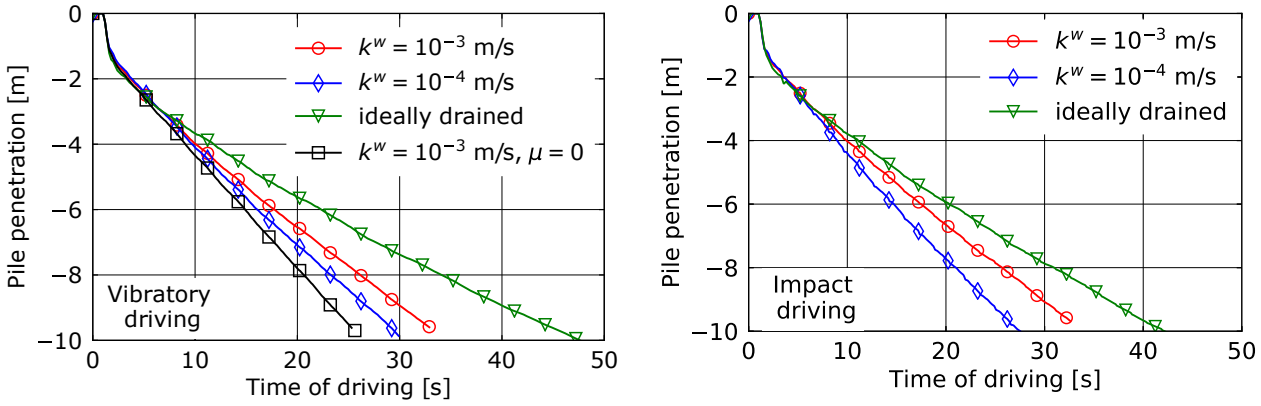

Figure 8.33: Pile penetration vs. time of vibration using vibratory pile driving for different values of hydraulic conductivity k^w for vibratory driving (left plot) and impact driving (right plot). In case of vibratory driving an additional simulation with frictionless contact ($\mu = 0$) is given.

Note that not for all cases the targeted embedment depth of 10 m is reached due to numerical instabilities and increasing soil material not satisfying the contact conditions (i.e. soil material entering volume which is already occupied by the pile) towards the end of the simulation. As explained in Section 4.6 this is a general problem of Eulerian techniques since the material interfaces have to be reconstructed within partially material filled elements. Approximately 30 cm are missing for the simulations with a hydraulic conductivity of $k^w = 10^{-3}$ m/s for both installation techniques.

As expected, the lower the hydraulic conductivity, the higher is the penetration rate. The assumption of ideally drained conditions leads to lower penetration rates, since no reduction of the soil strength due to a loss of effective stress occurs. The influence of the hydraulic conductivity and the drainage conditions on the pile penetration rate is quantitatively and qualitatively the same for the impact driven piles, as can be seen from the right-hand plot of Fig. 8.33. Given the chosen specifications of the pile drivers, the impact driven piles show a slightly faster penetration compared to vibratory driving piles. For the ideally drained simulations, nearly 1500 cycles of the vibrator are required to achieve an embedment depth of 10 m, whereas approximately 27 strokes are needed in case of impact driving. The difference in number of cycles experienced by the soil needs to be borne in mind for the results discussion.

To evaluate the influence of the frictional contact, an additional simulation assuming a frictionless contact ($\mu = 0$) in case of vibratory driving is depicted in the left-hand plot of Fig. 8.33. In comparison to the corresponding simulation with friction ($k^w = 10^{-3}$ m/s), the simulation with $\mu = 0$ gives a higher penetration rate. However, the simulation does also not reach

the targeted embedment depth of 10 m due to non-convergence.

The spatial distributions of effective radial stress, excess pore water pressure and relative density for impact and vibratory driving (with friction) using a hydraulic conductivity of $k^w = 10^{-3}$ m/s are depicted in Fig. 8.34. Note that the geotechnical sign convention is used for the effective radial stress in this section. Only the simulations with initially dense soil conditions ($D_{r0} = 70$ %) are considered. Large values of effective stress in the vicinity of the pile tip are observed for both installation techniques. With increasing distance h from the pile tip (directed to the ground surface), the effective radial stress reduces drastically and reaches values lower than the effective radial stress prior to the installation. As visible in Fig. 8.34, the vibratory driven pile shows a somewhat lower increase in effective stress below the pile tip compared to the impact driven pile, due to larger excess pore water pressure. While the area of soil showing large excess pore water pressure is similar for both installation techniques, the magnitudes are larger in the vicinity of the pile tip for the vibratory driven pile. The spatial distribution of relative density shows that compaction of the soil close to the outer pile shaft occurs for both installation techniques. In addition, compaction below the pile tip is observed. In contrast, very loose states are reached in the soil close to the inner pile shaft for both installation methods. A very thin line of loose soil can also be identified close to the outer pile shaft, which is discussed in detail later. However, these elements are only partially filled by material, and the soil state in the immediate proximity of the pile should in general be considered with care using the CEL method.

Compared to the vibratory driven pile, the compacted soil volume at the outer shaft is larger for the impact driven pile, which is most relevant for the response of the pile to subsequent lateral loading. However, a higher degree of compaction is observed inside the pile in case of vibratory driving.

The fields of effective radial stress and relative density for the ideally drained simulations are given in Fig. 8.35. Compared to the distributions obtained from the partially drained simulations provided in Fig. 8.34, the effective radial stress in the vicinity of the pile tip is much larger. In line with this observation the soil inside the pile does not heave as is observed in Fig. 8.34. Again, the vibratory driven pile shows a smaller increase in effective stress in the soil close to the pile tip, but the differences between the installation methods are much less pronounced than in case of the partially drained conditions. Similar to the partially drained simulations the radial stress is reduced at the pile shaft once the pile tip has passed the soil.

For both installation techniques the compaction of the soil close to the pile tip is slightly more pronounced for the ideally drained conditions compared to the simulations assuming a

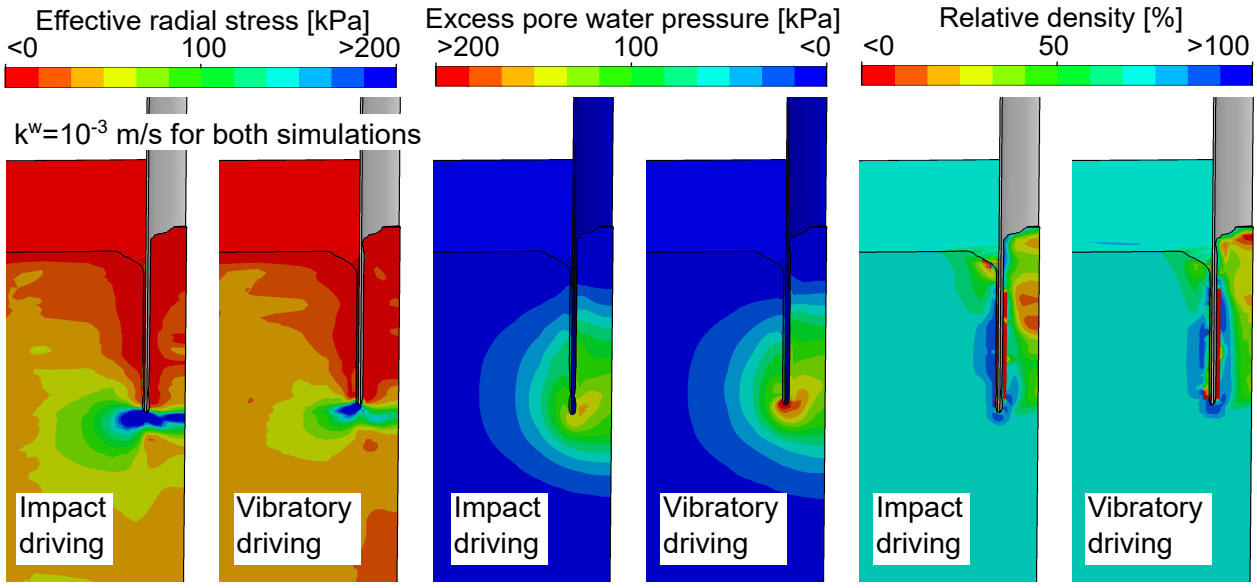

Figure 8.34: Spatial distributions of effective radial stress, excess pore water pressure and relative density at a pile penetration depth of approximately 9.7 m using impact and vibratory pile driving, respectively

hydraulic conductivity of $k^w = 10^{-3}$ m/s. In contrast to the partially drained simulations, no loosening of the soil close to the pile shaft inside the pile occurs. The soil inside the pile close to the axis of symmetry shows a strong reduction of relative density for both pile installation techniques, which is more pronounced for the ideally drained conditions compared to the partially drained case. In addition, much higher effective radial stresses develop inside of the pile close to the pile tip in case of ideally drained conditions, indicating a (partially) plugged state. Therefore, despite the greater loosening of the soil close to the ground surface inside the pile in case of ideally drained conditions, less heaving of the soil occurs inside the pile compared to the simulation assuming a hydraulic conductivity of $k^w = 10^{-3}$ m/s.

The spatial distributions for the installation using a hydraulic conductivity of $k^w = 10^{-4}$ m/s are depicted in Fig. 8.36. As expected, the consideration of a lower hydraulic conductivity leads to larger excess pore water pressures and less compaction of the soil in the vicinity of the pile tip. Somewhat surprisingly, the effective radial stress in greater distance to the pile shaft is larger for both installation techniques compared to the simulations using a hydraulic conductivity of $k^w = 10^{-3}$ m/s given in Fig. 8.34. This is due to the development of negative excess pore water pressure in greater distance to the pile shaft, increasing the effective stress. This negative excess pore water pressure is discussed later in more detail on the basis of Fig. 8.39. Figure 8.36 also shows the aforementioned problem of soil not satisfying the contact

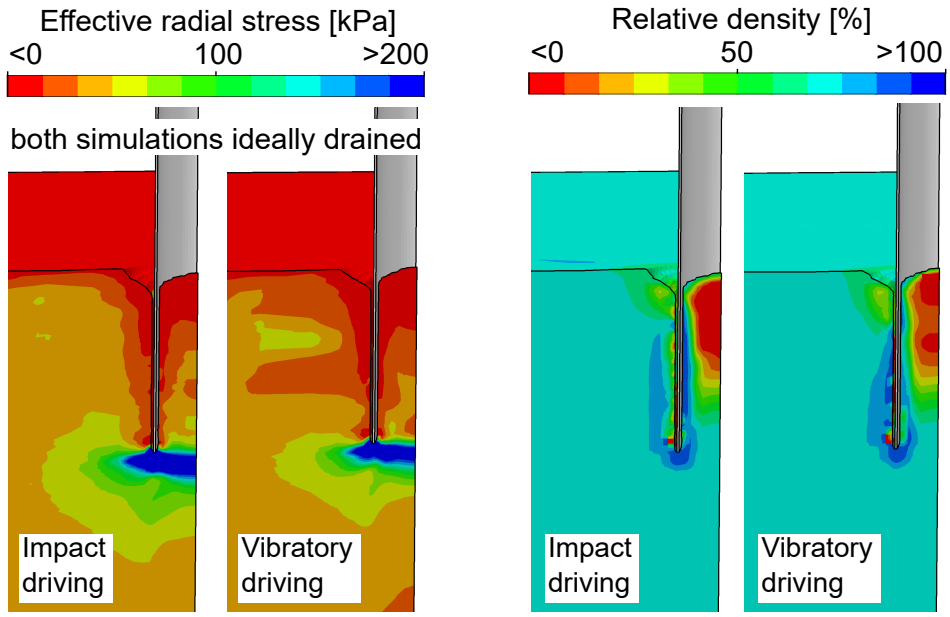

Figure 8.35: Spatial distributions of effective radial stress and relative density at a pile penetration depth of approximately 10 m using impact and vibratory pile driving, respectively. Ideally drained conditions are assumed.

conditions with the pile any more, as soil inside of the pile starts penetrating into the pile at the ground surface. This, however, is believed to be not only caused by the contact algorithms, but also by the hypoplastic model. For mean effective stresses approaching zero, a correction of the stress state is performed in the implementation of the hypoplastic model [353]. Therefore, the contact traction might not be correctly reflected in the internal stress of the element (i.e. the internal stress is not in equilibrium with the external contact traction), causing the violation of the contact constraints.

The influence of frictional contact on the spatial distributions of effective radial stress, excess pore water pressure and relative density is investigated in Fig. 8.37. An additional simulation of vibratory pile driving assuming a hydraulic conductivity of $k^w = 10^{-3}$ m/s and a friction coefficient of $\mu = 0$ is analysed for this purpose and compared to the corresponding simulation considering friction. Unsurprisingly, larger effective stress below the pile tip is observed in case of $\mu = 0$. Despite the negligence of friction, the h/R effect occurs as well. Less excess pore water pressure and less compaction is observed for the frictionless simulation. Due to the reduced effective radial stress (the mean effective stress reduces accordingly) at the pile shaft, the soil is in a very dense state, showing strong dilatancy under (larger) shear strains. Therefore, it would be expected that the application of the frictionless contact results in less dilatancy compared to the simulation with friction, since the soil at the pile shaft is not sheared. However, if the

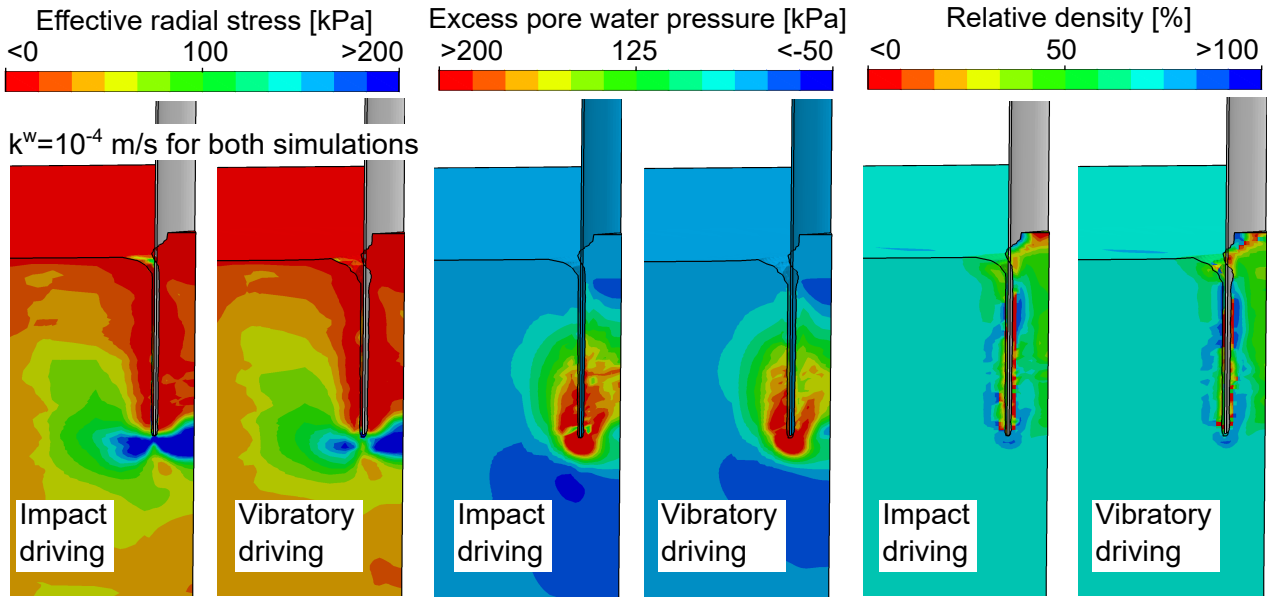

Figure 8.36: Spatial distributions of effective radial stress, excess pore water pressure and relative density at a pile penetration depth of approximately 10 m using impact and vibratory pile driving, respectively. A hydraulic conductivity of $k^w = 10^{-4}$ m/s is assumed.

soil experiences lower values of shear strain following the passing of the pile tip, as expected in greater distance from the pile shaft, contractancy occurs for the dense soil conditions. This fits to the distribution of relative density for the simulation with friction, showing the greatest compaction in greater distance to the outer pile shaft (approximately in a distance of $R/4$). In the immediate vicinity less compaction is observed, which can be explained by higher shear strains, resulting in dilatancy. Both the contractancy in greater distance and the dilatancy in the vicinity of the pile shaft are not existent for the simulation without friction since the soil is not sheared following the passing of the pile tip.

It is worth mentioning that it is known from experimental studies that sand subjected to cyclic shearing shows less dilatancy (and more pronounced contractancy) compared to monotonic shearing [406]. This agrees well with the observations from the comparison of the two installation techniques discussed previously (however, one may argue that the effect can only be described as well as the Hypoplasticity with intergranular strain is able to). Due to the higher number of cycles the soil experiences, more contractancy at the pile shaft occurs in case of vibratory driving compared to the impact driving. This leads to higher excess pore water pressures in case of partially drained conditions (see in particular Fig. 8.34 and Fig. 8.38 discussed in the following), but higher compaction in case of ideally drained conditions (see Fig. 8.35) for the vibratory driven pile.

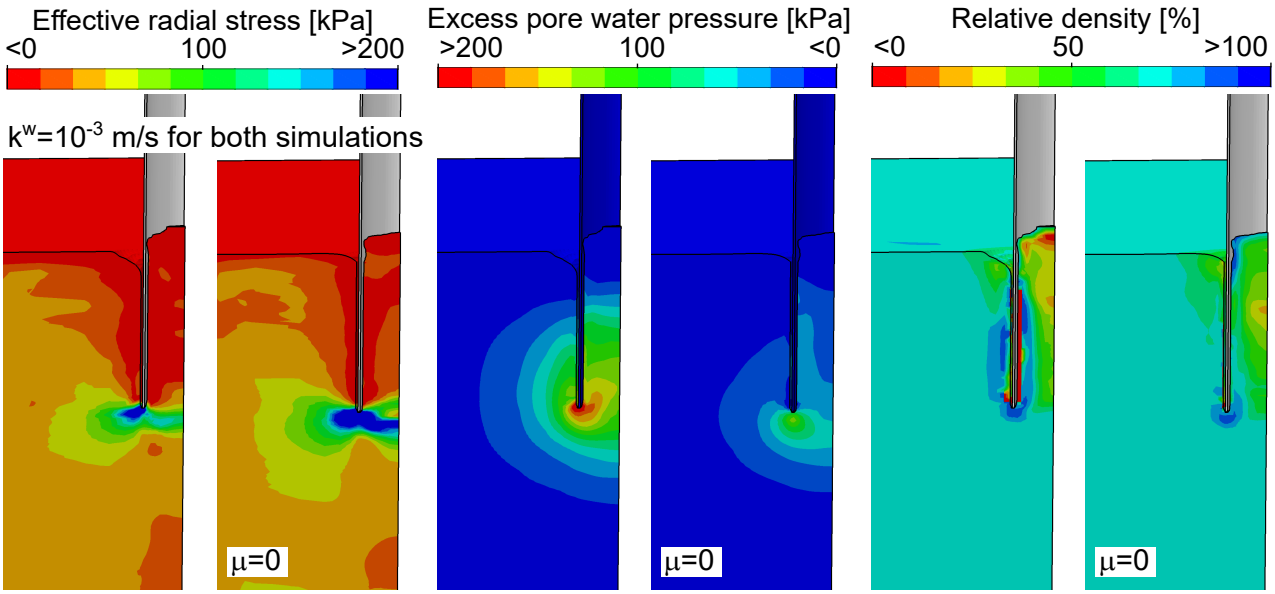

Figure 8.37: Spatial distributions of effective radial stress, excess pore water pressure and relative density at a pile penetration depth of approximately 9.7 m using vibratory pile driving with or without ($\mu = 0$) consideration of friction, respectively. A hydraulic conductivity of $k^w = 10^{-3}$ m/s is used.

The distributions of effective radial stress and excess pore water pressure with distance to the outer pile shaft for a soil depth of 5 m is given for different values of h/R (see Section 2.1.1) in Fig 8.38. Since the depth is constant, the elements or nodes for which the quantities are evaluated do not change. The results from the simulations using a hydraulic conductivity of $k^w = 10^{-3}$ m/s for both installation techniques are shown (the vibratory driven pile with frictional contact is considered). At passing of the pile tip ($h/R = 0$), the effective radial stress increases significantly for both installation techniques. Values larger than the initial effective radial stress are reached even for a distance from the pile of 5 m. The vibratory driven pile shows slightly lower values of effective radial stress and higher values of excess pore water pressure compared to the impact driven pile. Once the pile has passed the soil by 1 m ($h/R = 0.5$), a sharp reduction of effective radial stress nearby the pile occurs, while the excess pore water pressure remains nearly unchanged. Effective stress values close to zero are observed in the vicinity of the pile shaft for both installation techniques. This effect has been discussed in Section 2.1.1 and is well known from experimental studies on jacked or impact driven piles (performed mostly in dry sand, however). To date, this effect has not been investigated in detail for vibratory driven piles in water-saturated sand. In addition, to the author's best knowledge, no experimental study considering water-saturated and realistic stress conditions has investigated by local stress measurements if the h/R effect is quantitatively comparable

for the two installation techniques.

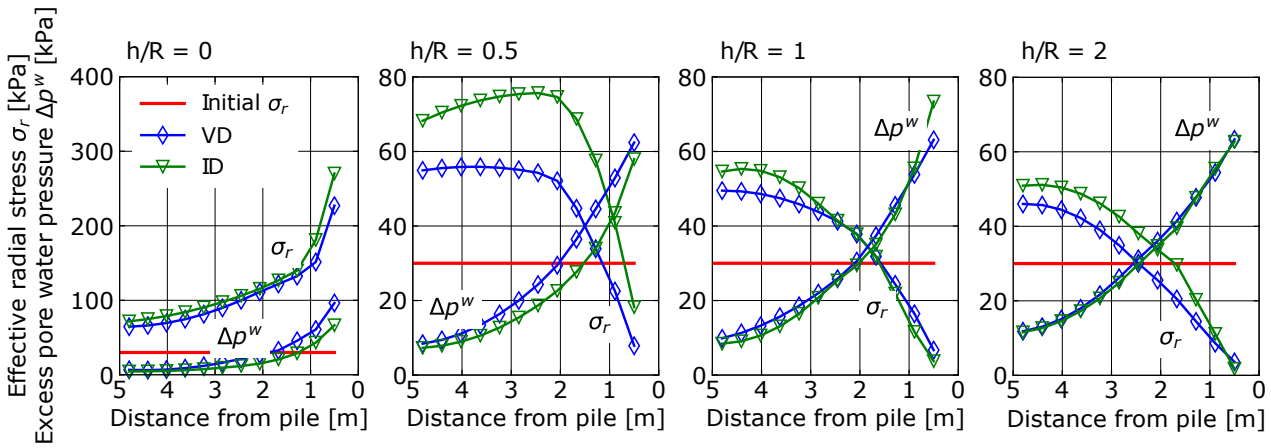

Figure 8.38: Effective radial stress and excess pore water pressure vs. radial distance from the pile in a depth of 5 m at different values of h/R for vibratory (VD) and impact driving (ID), respectively. A hydraulic conductivity of $k^w = 10^{-3}$ m/s is used in both cases.

The simulations indicate that the h/R effect is qualitatively similar for impact and vibratory driven piles. In case of the impact driven pile, larger effective radial stress is observed at $h/R = 0.5$ compared to the vibratory driven pile. However, for $h/R = 1$, both installation techniques show similar values of effective radial stress. The comparison of the stress at $h/R = 0.5$ with $h/R = 1$ shows that both installation techniques lead to a reduction of effective radial stress in the soil close to the pile shaft with increasing distance from the pile tip, i.e. the h/R effect. Interestingly, the effect is found to be quantitatively very similar for both installation techniques, considering the change in effective radial stress from $h/R = 0$ to $h/R = 1$. However, comparing the distributions of $h/R = 0$ with $h/R = 0.5$, the general consensus that the cyclic shearing exerted by vibratory driving leads to a stronger reduction in effective radial stress with increasing value of h/R compared to impact driving is confirmed. This is due to the stronger contractancy of the soil during (high-)cyclic interface shearing, as has been discussed previously. The distribution of the effective radial stress at $h/R = 2$ confirms the stronger stress reduction in case of vibratory driving. While the effective radial stress in case of the vibratory driven pile reduces further, the stress in case of the impact driven pile is not changed considerably compared to the distribution at $h/R = 1$.

To examine the influence of the hydraulic conductivity on the distribution of effective radial stress and excess pore water pressure with distance to the (outer) pile shaft, the results for

vibratory driving using a hydraulic conductivity of $k^w = 10^{-3}$ m/s and $k^w = 10^{-4}$ m/s are compared in Fig. 8.39. For every vertical distance from the pile tip h/R the excess pore water pressure close to the pile is much larger for $k^w = 10^{-4}$ m/s compared to $k^w = 10^{-3}$ m/s. However, at a greater horizontal distance $> 1 - 3$ m from the pile shaft, the excess pore water pressure is less for $k^w = 10^{-4}$ m/s compared to $k^w = 10^{-3}$ m/s for every value of h/R, reaching even negative values. With increasing value of h/R the distance from the pile tip at which the lower hydraulic conductivity results in less excess pore water pressure increases and is approximately 2.5 m for $h/R = 2$. In line with the lower value of excess pore water pressure, the effective radial stress is larger for $k^w = 10^{-4}$ m/s for greater distances from the pile shaft compared to $k^w = 10^{-3}$ m/s. This has already been observed from the spatial distribution of effective radial stress given in Fig. 8.36, where larger values of effective stress than in Fig. 8.34 are visible in greater distance to the pile shaft. Close to the pile shaft, similar values of effective radial stress are observed for both values of hydraulic conductivity independent of h/R. Very low values of radial effective stress are reached, indicating a complete loss of soil stiffness. In greater distance from the pile shaft, the h/R effect is stronger for the simulation with a lower value of hydraulic conductivity since the increase in effective radial stress and subsequent drop once the pile has passed the soil in the considered depth is much larger compared to the higher hydraulic conductivity. However, considering the larger excess pore water pressure of the simulation with $k^w = 10^{-4}$ m/s, the final stress distributions once the driving has stopped and consolidation is finished are estimated to be comparable.

The main findings from the simulations of pile installation can be summarised as follows:

- Considering partially drained conditions, the impact driven piles show a slightly larger increase in effective radial stress compared to the vibratory driven piles. In addition, a slightly stronger compaction in the vicinity of the pile tip occurs.

- Assuming ideally drained conditions, the opposite tendencies are observed for the change in relative density, i.e. the vibratory driven pile leads to a slightly higher compaction.

- Both installation techniques exhibit the h/R effect (i.e. reduction of effective radial stress with increasing distance h from the pile tip), being more pronounced for a lower value of hydraulic conductivity. The reduction of radial effective stress in the soil following the passing of the pile tip is slightly more pronounced for the vibratory driven pile.

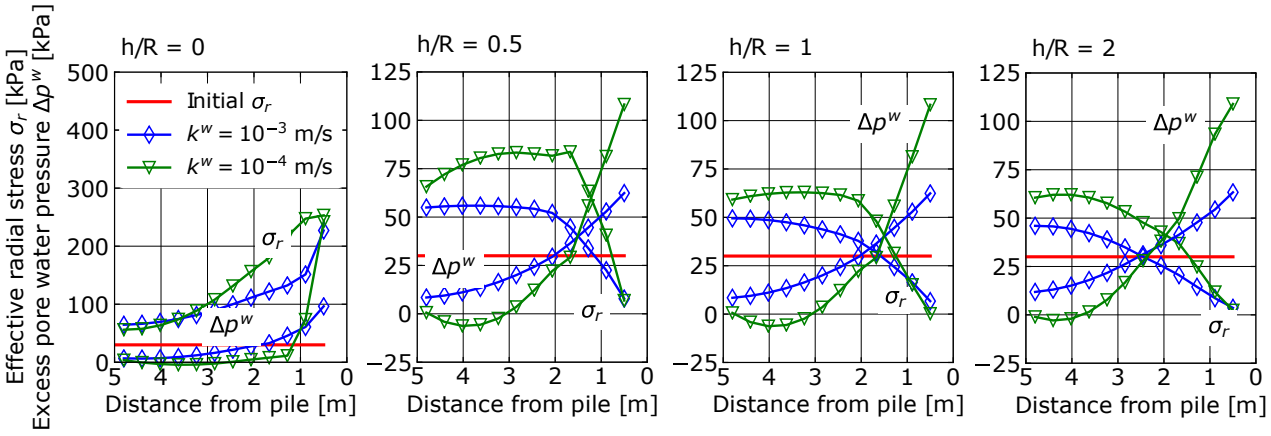

Figure 8.39: Effective radial stress and excess pore water pressure vs. radial distance from the pile in a depth of 5 m at different values of h/R for vibratory driving using a hydraulic conductivity of $k^w = 10^{-3}$ m/s and $k^w = 10^{-4}$ m/s, respectively

Lateral loading following the installation

As has already been explained in the previous section, a fully Lagrangian finite element model is used for the analysis of the high-cyclic loading following the installation since comparatively small deformations occur for which no large-deformation technique is required. For the soil, three-dimensional **u**-p finite elements with 27 nodes discretising the displacement **u** of the solid phase and 8 nodes discretising the pore water pressure p^w are utilised (termed `u27p8` element in `numgeo`, see Section 4.5). Hence, quadratic interpolation functions are used for the solid displacement while linear interpolation functions are used for the pore water pressure (i.e. Taylor-Hood element formulation [378]). The `u27p8` element is superior to the `u20p8` element in contact analyses as has been demonstrated in Section 6.6. As has already been mentioned in Section 6.6, the `u27p8` elements can not be integrated with less than 27 integration points without showing communicable hourglass modes. Since fully integrated elements can lead to numerical self-stress using constitutive models such as the HCA model [270], preliminary simulations using linearly interpolated, reduced integrated and hourglass-enhanced elements were performed and the results were compared to the `u27p8` elements. For a comparable number of global DOFs, the solutions were found to coincide, hence proving the suitability of the `u27p8` element for simulations with the HCA model. This agrees with the general finding that (tri-)quadratic elements do not tend to suffer from locking effects, to which artificial self-stresses also belong [85, 71].

For the pile, `u27` elements are used. The contact between soil and pile is discretised using the EBM contact discretisation technique with 9 integration points per finite element face. A

simple Coulomb friction model with the same parameters as applied for the simulation of the installation is used.

The state variables (density/void ratio, effective stress and excess pore water pressure) of the soil at the end of the simulation of the installation are imported into the Lagrangian model by means of a nearest-neighbour search of the integration points of both models. Only the simulations with frictional contact are considered. For the pile installation simulations which did not reach the targeted embedment depth of 10 m (see Fig. 8.33), the spatial distribution is shifted by the missing penetration depth of 30 cm to achieve 10 m. The missing information of the soil state at the ground surface is obtained by assuming that it is identical to the state of the soil resulting from the installation at the top surface. The same mapping procedure as explained in [156, 113, 359] is applied. Since the `u27p8` elements have 27 integration points, the nearest-neighbour search is performed for every individual integration point. Note that the deformation of the soil is not transferred since its influence is judged insignificant compared to the influence of the change of state variables. In addition to the simulations in Section 8.3.1, the excess pore water pressure is transferred to the Lagrangian model. The consolidation process prior to the application of lateral loading is taken into account, since it is assumed that there is sufficient time between the end of the pile installation process and the start of the service of the structure for excess pore water pressures to dissipate. The lateral loading starts once hydrostatic conditions are achieved. Note that the intergranular strain tensor is not transferred. It changes rapidly during the installation process and its distribution depends on the current load phase of the pile driver (e.g. downwards or upwards directed cyclic movement of the vibrator). In addition, since the consolidation process following the installation is considered, the strain resulting from the dissipation of excess pore water pressure is believed to erase the small strain history of the installation process.

The adopted finite element model is given in Fig. 8.40. The field of pore water pressure following the installation by vibratory driving using a hydraulic conductivity of $k^w = 10^{-3}$ m/s is shown as an example. In addition to simulations incorporating the installation-induced soil changes, WIP simulations are also performed, for which a constant distribution of density, a K_0 stress state and a hydrostatic pore water pressure distribution are assumed as initial state.

The characteristics of the (high-cyclic) lateral loading phase following the installation process are identical for all considered specifications of the installation. The following steps are performed:

1. Following the transfer of the void ratio, the effective stress and, if applicable, the excess pore water pressure, the soil-pile system is allowed to deform such that static force

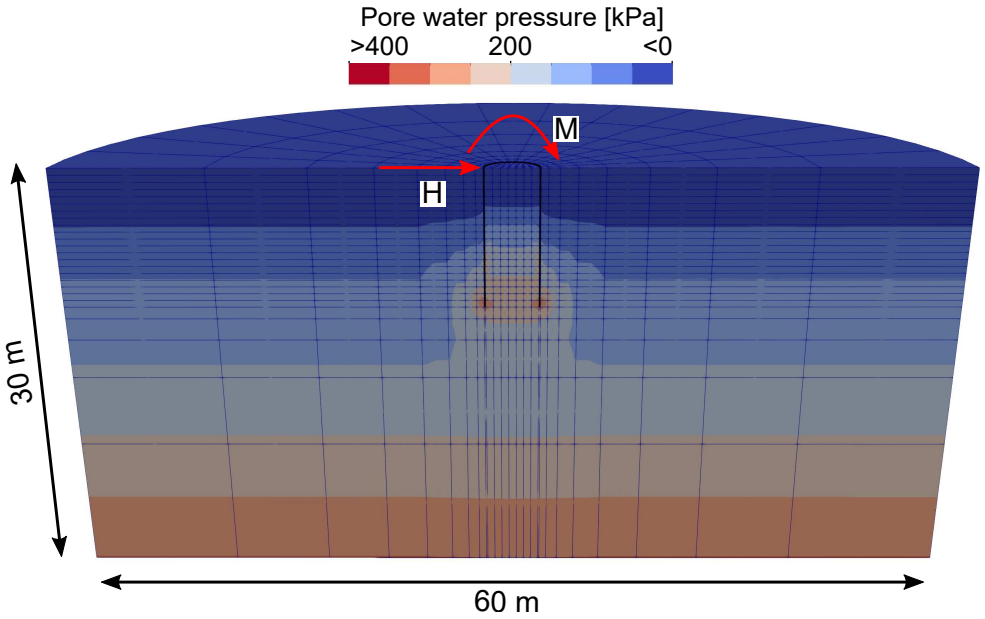

Figure 8.40: Numerical model used for the analysis of the lateral loading of the pile following the installation process and transferred spatial distribution of pore water pressure following the installation by vibratory pile driving using a hydraulic conductivity of $k^w = 10^{-3}$ m/s. Note that only the exterior nodes of the finite elements are visible.

equilibrium is achieved. This is necessary since the system is not in static force equilibrium at the end of the installation process. As a result, the soil shows a maximum of ≈ 5 mm of displacement in this calculation phase. For the WIP simulation, only the contact between pile and soil is initialized in this step.

2. For the simulations with partial drainage, a consolidation analysis is performed prior to the loading of the pile. 10^4 s are considered, which is a sufficient time for dissipation of all excess pore pressure for both values of hydraulic conductivity ($k^w = 10^{-3}$ m/s and $k^w = 10^{-4}$ m/s).

3. The pile is loaded vertically with a magnitude of 3 MN, accounting for the weight of the structure carried by the pile. The magnitude is chosen such that, taking into account the differences in embedment length, a 5-MW offshore wind turbine exerting a weight of 1200 t and being embedded into the seabed by 40 m is considered. This is consistent with the pile size and embedment ratio considered here.

4. Application of the mean value of horizontal loading, which is set to $H_{\mathrm{av}} = 200$ kN, and a mean value of moment $M_{\mathrm{av}} = 4.8$ MNm, both applied at the mudline (all loads for a full 3D model). The lever arm is thus 24 m. The magnitude of the load is chosen based on the

monotonic load capacity of the piles, which is discussed in more detail on the basis of Fig. 8.41 later. The mean value of moment for the cyclic loading amounts approximately 10 % of the moment obtained at a pile head rotation of 1° for the pile with the largest moment resistance (i.e. the impact driven pile assuming ideally drained conditions). This and all following steps are performed assuming ideally drained conditions in order to investigate the influence of the different conditions during the pile installation process alone.

5. Application of the first load cycle with a horizontal load amplitude $H_{\text{ampl}} = 200$ kN and a moment amplitude of $M_{\text{ampl}} = 4.8$ MNm. Since the simulations are performed ideally drained and no inertia effects are considered, the rate of loading can be chosen arbitrarily (as long as the increment size is small enough to adequately capture the path-dependency of the constitutive model).

6. Repetition of the previous step while the strain path in every integration point is recorded. The strain amplitude is calculated at the end of the step.

7. Simulation of 10^6 additional load cycles using the HCA model applying only the average loading H_{av} and M_{av}.

In analogy to the simulation of the installation process, the hypoplastic model with intergranular strain extension and the parameters of "Karlsruhe fine sand" provided in Table 8.9 are utilised for the first six steps. The parameters of the HCA model for "Karlsruhe Fine Sand" given in Table 8.11 are used in the last step.

Prior to the simulations considering high-cyclic loading, a monotonic loading is simulated to determine the maximum moment resistance of the pile for each configuration. Only the steps 1-4 are performed, but the horizontal force and the moment are linearly increased until a rotation at the pile head of 1° is reached in step 4. The results of the monotonic loading tests are given in Fig. 8.41. Note that only the simulations with initially dense soil conditions ($D_{r0} = 70$ %) are considered.

The simulations following the installation assuming ideally drained conditions result in the highest resistance of the pile. This is true for both installation techniques, but the impact

C_{ampl}	C_e	C_p	C_Y	C_{N1}	C_{N2}	C_{N3}
1.33	0.60	0.23	1.68	$2.95{\cdot}10^{-4}$	0.41	$1.9 \cdot 10^{-5}$

Table 8.11: Parameters of the HCA model for "Karlsruhe Fine Sand" [406]

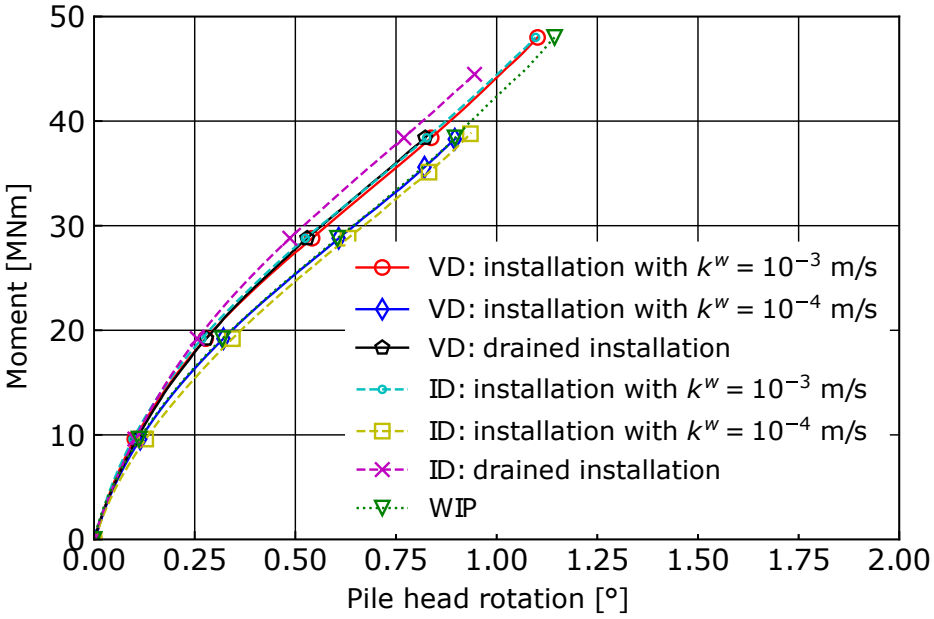

Figure 8.41: Results of the simulations with monotonic loading of the pile. The moment vs. pile head rotation for the vibratory (VD) and impact driven (ID) piles using different values of hydraulic conductivity as well as ideally drained conditions during the installation is presented. In addition, the results of a simulation without consideration of the installation process (WIP) are shown. Note that not all simulations reached 1° of pile head rotation due to non-convergence.

driven pile exhibits a slightly larger stiffness compared to the vibratory driven pile. These trends do not necessarily contradict the findings from the spatial distributions shown and discussed on the basis of Fig. 8.35, where the vibratory driven pile showed slightly stronger compaction of the soil close to the pile shaft, since the effective radial stress was less for the vibratory driven pile at the same time. With decreasing hydraulic conductivity during the installation, the resistance of the pile to subsequent lateral loading decreases, being slightly more pronounced for the impact driven piles. The assumption of WIP conditions results in a lower lateral capacity than obtained for drained vibratory or impact driven piles. Accounting for the effects of the coupled pore fluid-stress response during the installation leads to a lateral response comparable to that of a WIP pile. Overall though the influence of the installation process on the monotonic pile response is less significant for the high ratio of pile diameter and wall thickness D/t considered here than in cases with lower D/t (for simulations with lower ratio D/t see [353, 351, 47, 204, 113]). Therefore, the assumption of WIP conditions for piles with a larger D/t ratio, such as for instance assumed by recent numerical studies reported e.g. in [58, 175], seems to be justified for the specifications considered in the present investigation.

However, this conclusion does certainly depend on many different influencing factors (initial density, type of soil, etc.) in addition to the D/t ratio and is not believed to be generally applicable.

It is worth mentioning that a numerical study on the response of vibratory and impact driven piles to subsequent monotonic loading reported in [156] also did not find significant differences between the two installation techniques regarding the lateral loading response. Ideally drained behaviour was assumed during the pile installation process in this study. However, compared to the results presented in this work, no h/R effect was observed in case of impact driving.

The left-hand plot of Fig. 8.42 displays the pile head rotation with respect to number of applied load cycles for the vibratory driven piles using different values of hydraulic conductivity as well as for a simulation of the installation process assuming ideally drained conditions. The results of a WIP simulation are also provided for comparison. As expected from the installation-induced soil changes, the drainage conditions during the installation process influence the subsequent response to the high-cyclic lateral loading considerably. The better the drainage during the installation, the lower the accumulated pile head rotations after the application of one million load cycles. This is mainly attributed to the higher degree of compaction of the soil if the water can dissipate faster during the installation process.

Very similar observations can be made for the impact driven piles, as is visible from the right-hand plot of Fig. 8.42. Interestingly, assuming ideally drained conditions the impact driven pile shows a larger permanent pile head rotation after $N = 10^6$ cycles compared to the corresponding vibratory driven pile. This does not necessarily contradict the results of the monotonic loading tests, where for larger values of pile head rotation the drained impact driven pile showed the largest resistance, since for the magnitude of the cyclic load the drained impact driven pile does not give the lowest rotation (see Fig. 8.41). In addition, the tendencies observed from the monotonic loading are in general not necessarily transferable to cyclic loading. This is in particular the case for the present simulations, since two different constitutive models (Hypoplasticity with intergranular strain and the HCA model) are used, for which differences in soil state variables caused by the installation may (quantitatively) lead to different responses of the pile (e.g. the change in density due to the installation has a larger influence for one constitutive model than the other).

The lower accumulation of the vibratory driven pile assuming ideally drained conditions compared to the corresponding impact driven pile is in line with the field of relative density given in Fig. 8.35, where the vibratory driven pile showed stronger compaction of the soil in the vicinity of the pile tip compared to the impact driven pile. This explains why in [204]

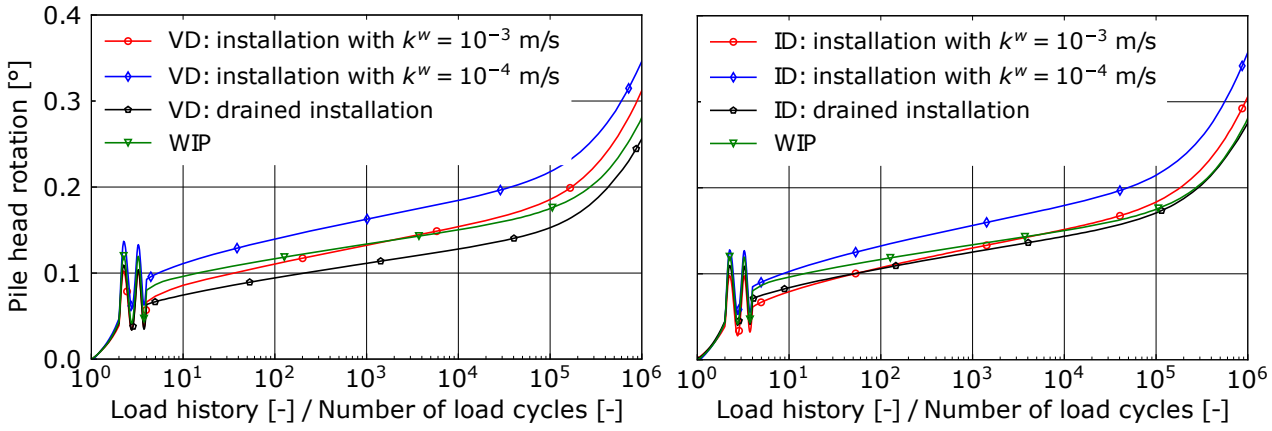

Figure 8.42: Pile head rotation with respect to the number of load cycles for vibratory (VD) and impact driven (ID) piles assuming partially drained conditions with different values of hydraulic conductivity or ideally drained conditions during the installation. In addition, the results of a simulation without consideration of the installation process (WIP) are displayed.

vibratory driven piles are reported to show a lower accumulation of deformation compared to impact driven piles, since the installation has been performed ideally drained. Similarly, a higher stiffness to lateral monotonic loading of vibratory driven piles compared to impact driven piles observed in a recent field test campaign reported in [18], where the piles have been installed in unsaturated soils, can be explained by the stronger compaction occurring without the presence of pore water.

Assuming a hydraulic conductivity of $k^w = 10^{-3}$ m/s or $k^w = 10^{-4}$ m/s during the installation process, the vibratory driven piles tend to show a slightly higher rotation at the beginning of the high-cycle phase compared to the impact driven piles. However, at $N = 10^6$ cycles similar pile head rotations are obtained for both the vibratory and the impact driven piles. These results have to be interpreted keeping in mind that the pile penetration rate of the vibratory driven piles is lower than the one of the impact driven piles. Since the drainage conditions during driving show a considerable influence on the response to subsequent loading, the differences in the pile penetration rate might also cause the impact driven piles to show more lateral deformations relative to the vibratory driven piles.

Compared to the differences found between vibratory and impact driving assuming ideally drained conditions during the installation process, the differences between the installation techniques is less for the simulations considering partial drainage during driving. This is in particular the case for a larger number of load cycles.

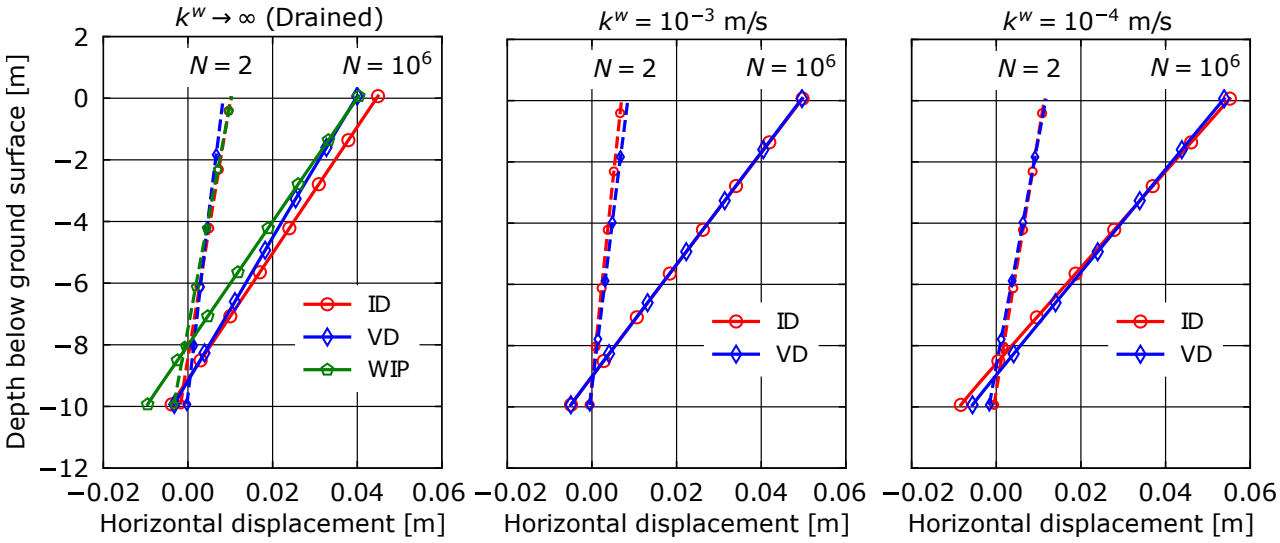

Figure 8.43: Lateral deflection lines for vibratory (VD) and impact driven (ID) piles at $N = 2$ and at $N = 10^6$ cycles assuming different values of hydraulic conductivity as well as ideally drained conditions during the installation. In addition, the results of a simulation without consideration of the installation process (WIP) are displayed.

To better illustrate the differences in the pile behaviour due to the different initial conditions, the lateral deflection lines at $N = 2$ and at $N = 10^6$ cycles are shown in Fig. 8.43. In agreement with previous research [353], the consideration of the installation process results in a deeper position of the point of rotation (zero horizontal displacement) regardless of the number of load cycles, the installation technique, and the drainage conditions. This indicates that the pile installation decreases the soil stiffness near the ground surface while it is increased close to the pile tip. These trends are consistent with the spatial distributions of effective radial stress and relative density after the pile installation process discussed earlier.

Figure 8.43 also shows that there is no clear trend for the influence of the installation technique, as it depends on the drainage conditions during driving. As already discussed earlier, the vibratory driven pile exhibits less deflection in case of ideally drained conditions during driving. The influence of the installation technique is less for the partially drained conditions, in particular for $N = 10^6$ cycles. Similar observations have been made in the 1 g small-scale model tests reported in [169], where piles have been subjected to $N = 10^3$ lateral load cycles following impact and vibratory pile driving in water-saturated sand (initial relative density of approximately 75 % and hydraulic conductivity of approximately $5 \cdot 10^{-4}$ m/s).

The spatial distributions of the strain amplitude calculated based on the recorded strain path during the second load cycle are given in Fig. 8.44 for the vibratory driven pile ($k^w = 10^{-3}$ m/s) and the WIP simulation. In accordance with a preceding study on piles with a large L/D

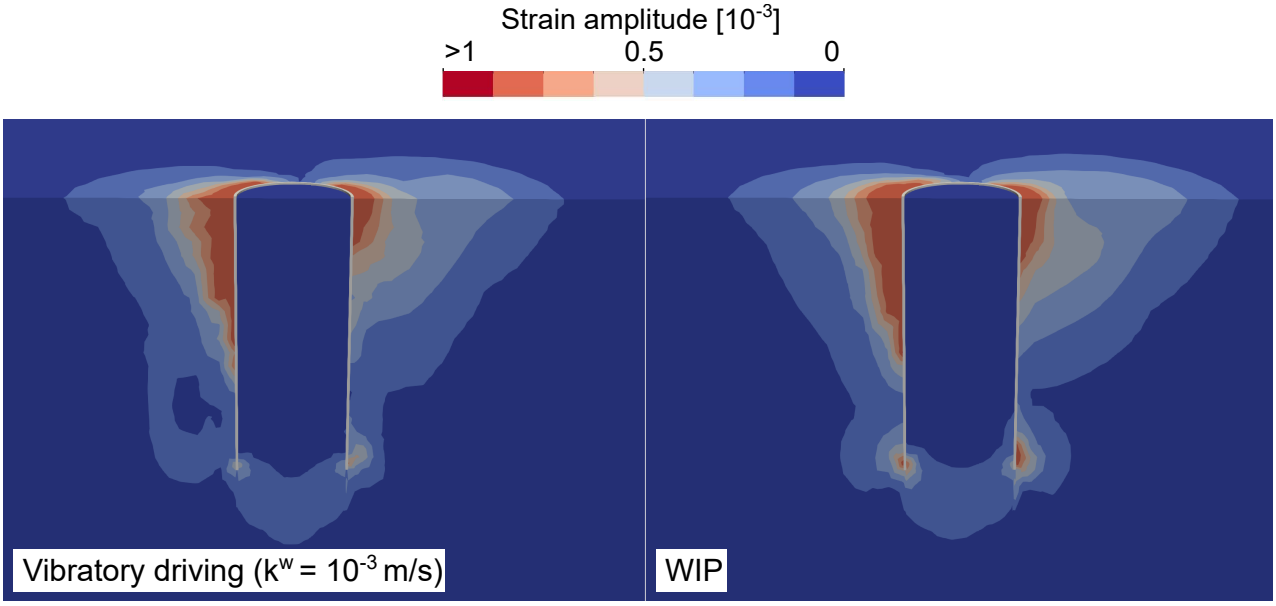

Figure 8.44: Spatial distribution of the strain amplitude recorded from the second load cycle for the vibratory driven pile ($k^w = 10^{-3}$ m/s) and the WIP simulation, respectively

ratio reported in [353], the consideration of the installation process results in lower values of the strain amplitude close to the pile tip. This is due to the increased stiffness resulting from the effective stress increase and compaction caused by the installation process. Around the pile head, however, the distributions are similar for both simulations.

The fields of relative density and horizontal effective stress after the application of one million load cycles are depicted in Fig. 8.45 for the vibratory driven pile ($k^w = 10^{-3}$ m/s) and the WIP simulation. Despite being initially dense, the soil around the outer pile head tends to compact due to the cyclic loading in both simulations. In case of the vibratory driven pile the alteration of the field of relative density caused by the installation process is still very well visible. As has been demonstrated in [353], an assimilation of the fields of relative density of the simulations incorporating and neglecting the installation occurs with increasing number of cycles, which eventually leads to similar accumulation rates for both simulation types. Thus, with ongoing cyclic loading, the influence of installation-induced changes in relative density reduces. The distribution of effective horizontal stress is similar for both initial conditions at $N = 10^6$, with both piles showing a reduction in effective stress where the soil is unloaded due to the lateral loading (left upper and right lower part of the pile). An increased effective horizontal stress below the pile tip is observed for both simulations.

Previous research has found a large influence of the initial relative density of the soil prior to the

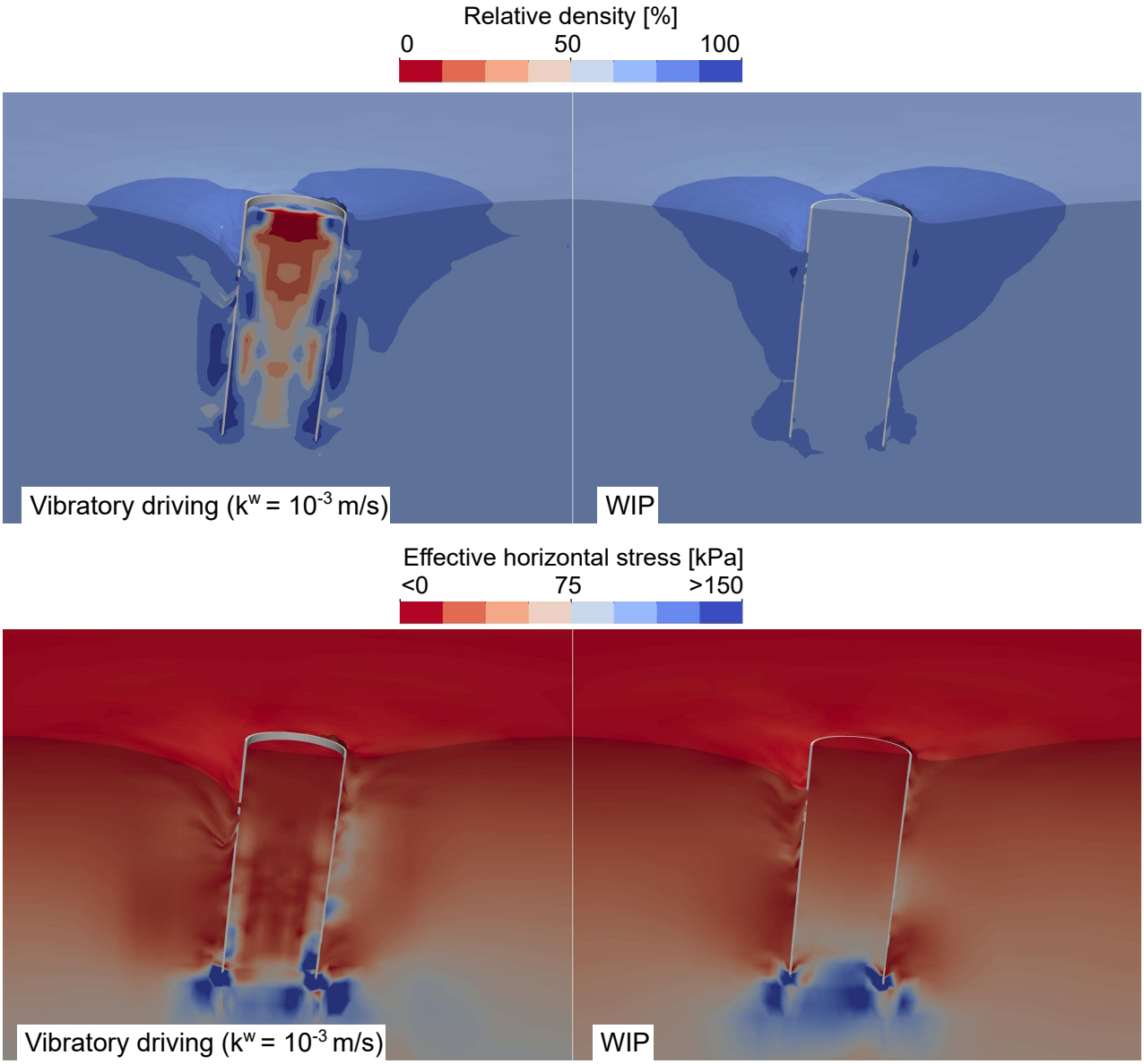

Figure 8.45: Spatial distribution of relative density and the effective horizontal stress for the vibratory driven pile ($k^w = 10^{-3}$ m/s) and the WIP simulation after application of 10^6 lateral load cycles, respectively. The deformed configuration with a scale factor of 20 is displayed.

installation process on the differences between simulations that neglect installation and those considering it [353, 113]. However, these studies were limited to ideally drained conditions and to either impact driven or jacked piles. To investigate how the pile installation process affects the pile response to cyclic lateral loading in medium dense sand, additional simulations of the installation process are performed with an initial relative density of $D_{r0} = 50$ % and assuming a hydraulic conductivity of $k^w = 10^{-3}$ m/s. To achieve pile penetration rates similar to the $D_{r0} = 70$ % case, both the impact load and the force amplitude of the vibratory driver are

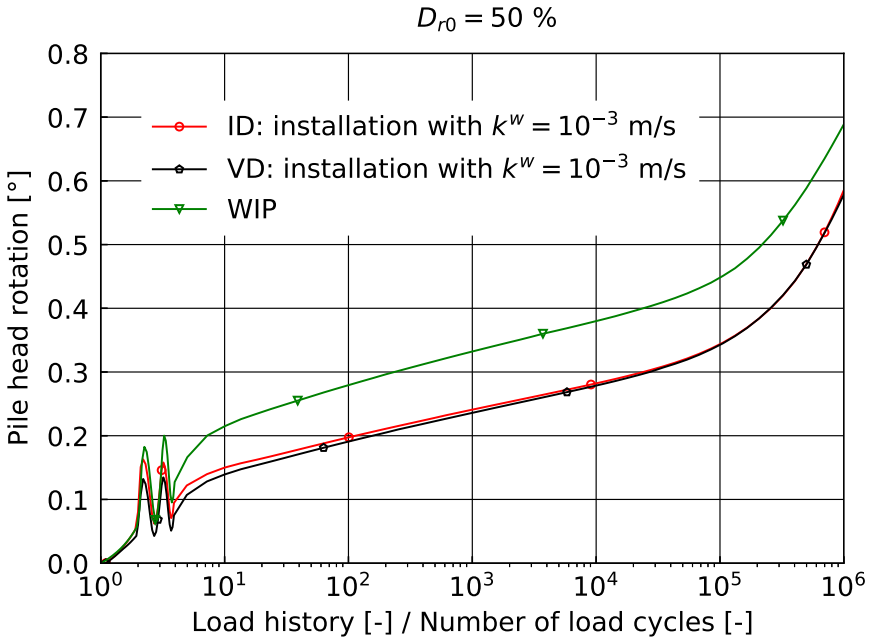

Figure 8.46: Pile head rotation as a function of the number of load cycles for vibratory (VD) and impact driven (ID) piles assuming a hydraulic conductivity of $k^w = 10^{-3}$ m/s and an initial relative density of $D_{r0} = 50$ % prior to installation. In addition, the results of a simulation without consideration of the installation process (WIP) are displayed.

scaled by 2/3. With this loading, approximately 25 s are required to achieve a penetration of 10 m for both installation techniques. The spatial distributions of the state variables following the installation process are similar to those in case of initially dense soil conditions, but the compaction of the sand is generally greater and the effective radial stress close to the pile tip less. Slightly larger excess pore water pressures develop in addition. Following the installation process, the piles were subjected to the same cyclic loading as for the case with $D_{r0} = 70$ %. The resulting curves of pile head rotation vs. number of load cycles are shown in Fig. 8.46 for an impact driven (ID), a vibratory driven (VD) and a WIP pile. Note that in the case of the WIP pile, a homogeneous initial relative density of $D_{r0} = 50$ % is assumed. Consistent with previous research [353], the assumption of WIP conditions in case of initially medium dense soil results in higher accumulated pile deformations compared to the simulations that consider the installation process. A stronger influence of the consideration of the installation process compared to the initially dense condition is found. In line with the observations for $D_{r0} = 70$ %, the differences between the two studied installation methods are found to be rather small, with the impact driven pile showing slightly larger pile head rotations at low numbers of lateral load cycles.

8.3.3 Conclusions from the investigation of the influence of the installation process on the behaviour of piles subjected to (high-cyclic) loading

The findings of the investigations on the influence of the installation process on the response of piles to subsequent (high-cyclic) loading presented in Sections 8.3.1 and 8.3.2 as well as from additional studies published by the author in [353, 352, 356, 350, 351] can be summarised as follows:

- From the simulations of the small-scale model tests in dry sand it can be concluded that the installation process causes a stiffer pile response and less accumulation of deformation when subjected to cyclic loading for both initially loose and initially dense sand (see Section 8.3.1 and [350, 351]).

- The installation of real-scale piles ($D = 4$ m) in water-saturated initially loose sand also leads to a stiffer pile response and less accumulation for both impact driven and jacked piles [352]. This also holds true for vibratory and impact driven piles in medium dense sand as shown in Fig. 8.46. Assuming ideally drained conditions during the installation process, for both cases of initially medium dense and dense soil conditions, the consideration of the installation induced soil changes results in less deformations of the pile ($D = 2$ m) when subjected to horizontal (monotonic or low-cyclic) loading [353]. However, considering high-cyclic loading with up to 5 million loading cycles, more accumulation of lateral deformation occurred for simulations incorporating the installation process in case of initially dense soil conditions. Opposite tendencies were observed for initially medium dense soil conditions [353].

- For the installation in initially dense water-saturated sand these observations are found not to be valid for all studied cases (see Section 8.3.2). The differences between wished-in-place simulations and simulations with incorporation of the installation induced soil changes are smaller and the hydraulic conductivity influences the impact of the installation process on the long-term behaviour of the pile strongly. The assumption that wished-in-place conditions are conservative for all cases cannot be confirmed, in particular if the simulation of the installation is performed considering excess pore water pressures. Vibratory driven piles show similar accumulation of deformation as impact driven piles when subjected to lateral high-cyclic loading following the installation considering partially drained conditions. However, with the selected pile driver specifications, the

vibratory driving process takes slightly longer than impact driving, resulting in slightly more time for excess pore water pressures to dissipate.

8.4 Application of the adaptive strain amplitude to monopile foundations subjected to cyclic loading under partially drained conditions

The simulations presented in the previous section have assumed ideally drained behaviour of the soil during the HCA phase. This is justified for the applied hydraulic conductivity in the range of $k^w \approx 10^{-3}$ m/s and the low frequency of the load typically encountered for offshore foundations. However, the assumption of ideally drained behaviour can be challenged if the hydraulic conductivity is lower. In such cases, the cyclic loading is accompanied by a change in the pore water pressure, which can greatly influence the strain amplitude as has been demonstrated in [357]. The application of the adaptive strain amplitude definition proposed in Section 5.2.2, allowing for an incorporation of the change in strain amplitude, is presented in the following. In addition, the submodel analysis as described in Section 5.2.2 is investigated and compared to simulations applying "conventional" update cycles. Note that the simulations presented in this section have already been published by the author in [355].

The finite element model of the monopile is displayed in Fig. 8.47. In analogy to the previous section, `u27p8` elements are used for the soil and `u27` elements for the pile. Every boundary of the model except the symmetry plane allows for drainage ($\dot{p}^w = 0$). The model is vertically constrained at the bottom, in y-direction in the symmetry axis and in the x- and y-direction at its back. The pile is modelled elastically with typical material properties of steel. It has a length of 30 m, a diameter of 5 m and a wall thickness of 8 cm.

The EBM contact discretisation method with 9 integration points per finite element face as described in Section 6.3 is used for the contact discretisation. Coulomb friction with a friction coefficient of 0.5 is applied.

Installation effects are not taken into account in the simulations since the investigation of the adaptive strain amplitude is focused. The Sanisand model and the HCA model with the parameters calibrated for "Karlsruhe fine sand" are adopted. Up to now, the HCA model has been mainly used in combination with Hypolasticity with intergranular strain. The motivation to use Sanisand is due to its popularity among researcher and to show the universality of the

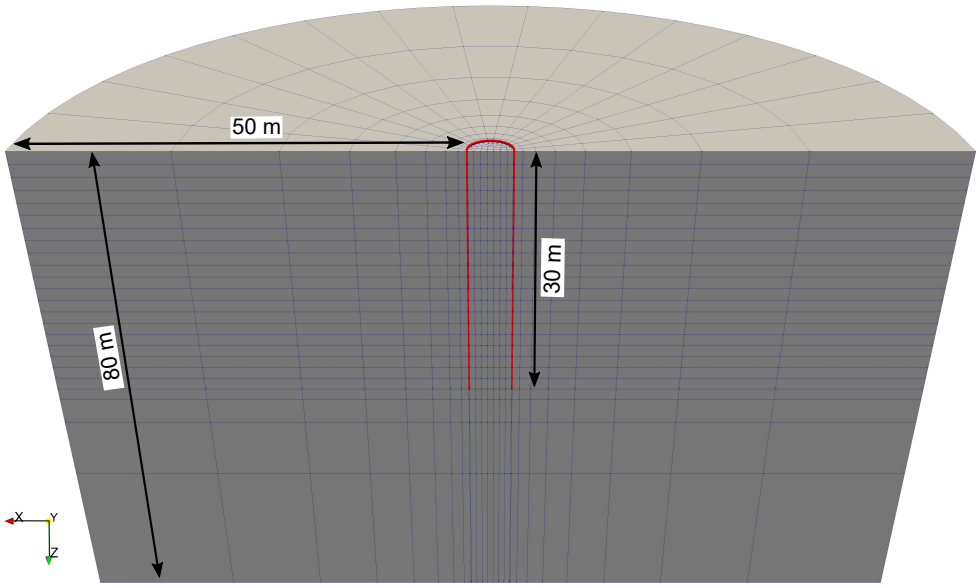

Figure 8.47: Finite element model of the monopile used for the investigation of the adaptive strain amplitude and the submodel analysis. Note that only the exterior nodes of the elements are visible.

HCA model. The parameters of Sanisand have been determined in [407] and are provided in Table 8.12. The parameters of the HCA model have already been supplied in Table 8.11.

p_a	e_0	λ_c	ξ	M_c	c	m	G_0
100 kPa	1.103	0.122	0.205	1.34	0.7	0.05	150.0
ν	h_0	c_h	n_b	A_0	n_d	$z_{\max}$	c_z
0.05	10.5	0.75	1.2	0.9	2.0	20.0	10000

Table 8.12: Parameters of the Sanisand model for "Karlsruhe Fine Sand" [407]

The initial relative density is assumed to be 60 %. The loading of the monopile is chosen according to [357], where a parametric study on monopile foundations using the HCA model has been performed. A sinusoidal load with a frequency of 1 Hz, a mean value of the moment of $M^{\text{av}} = 30$ MNm and an amplitude of $M^{\text{ampl}} = 30$ MNm is applied at the pile head (10 cm above the seabed). The lever arm of the horizontal force resulting from wind and water waves is assumed to be 30 m. The chosen magnitude of the cyclic load is approximately 10 % of the ultimate resistance of the pile determined based on monotonic loading up to a pile rotation

of 2° (see [357] again). The motivation to consider the rather high loading frequency is due to greater build-up of excess pore water pressure leading to a greater change in the effective stress and thus strain amplitude. The developed adaptive strain amplitude is therefore expected to influence the predicted long-term behaviour of the monopile strongly. Hydraulic conductivities of $k^w = 10^{-4}$ m/s and $k^w = 10^{-5}$ m/s are considered in the analyses.

The field of excess pore water pressure for the simulation using a constant strain amplitude and a hydraulic conductivity of $k^w = 10^{-5}$ m/s is given at $N = 1, 10, 10^2, 10^3, 10^4$ in Fig. 8.48. Considerable excess pore water pressures with magnitudes up to 100 kPa are visible around the upper part of the pile at $N = 1$. Slightly negative values are observed closer to the pile tip. The accumulation of excess pore water pressure increases with the start of the HCA phase ($N = 2$) and a much greater soil volume shows large excess pore water pressure at $N = 10$ compared to the distribution at $N = 1$. A heart-shaped distribution with zero excess pore water pressure close to the seabed due to the imposed boundary conditions $\dot{p}^w = 0$ at the top of the model is observed. The excess pore water pressure tends to decrease with further cyclic loading as is visible from the distribution at $N = 10^2$. The heart-shaped distribution is replaced by a V-shaped distribution. Since the rate of volumetric strain accumulation predicted by the HCA model decreases with ongoing cyclic loading, the consolidation process eventually out-paces the accumulation of excess pore water pressure, which is well visible from the distributions at $N = 10^3$ and $N = 10^4$. Only small excess pore water pressure exists at $N = 10^3$ and a hydrostatic distribution is observed at $N = 10^4$. Note that all displayed distributions show the excess pore water pressure at average loading.

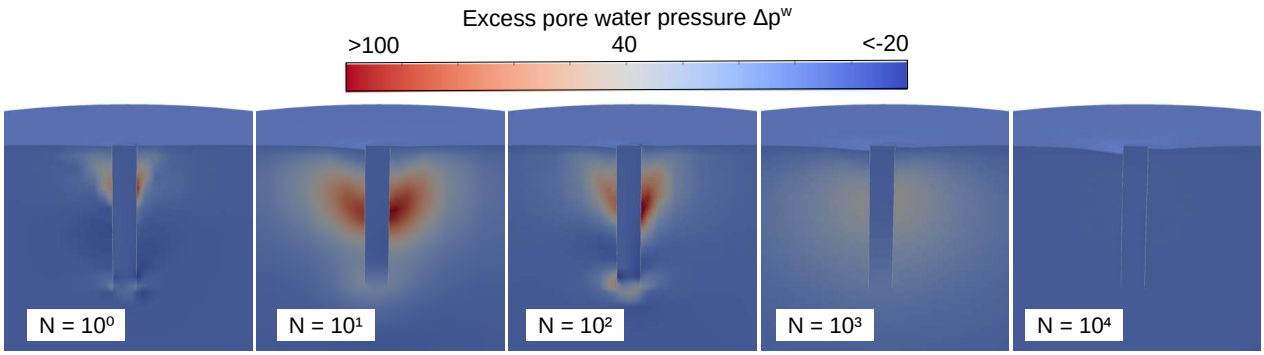

Figure 8.48: Field of excess pore water pressure at $N = 1, 10^1, 10^2, 10^3, 10^4$ for the simulation with constant strain amplitude using a hydraulic conductivity of $k^w = 10^{-5}$ m/s. The deformed configuration using a deformation scale factor of 10 is displayed.

As has been outlined earlier, the build-up of excess pore water pressure leads to an increase in strain amplitude due to reduction of the soil stiffness. Fig. 8.48 shows that the excess pore water pressure strongly varies spatially as well as with number of loading cycles. This in turn also suggests a strong variation of the strain amplitude. The next sections examine the suitability of the different approaches proposed in Section 5.2.2 to account for the change in strain amplitude.

8.4.1 Comparison submodel vs. update cycles

Prior to the application of the adaptive strain amplitude, the advantages of a submodel analysis over an analysis incorporating update cycles are highlighted. Figure 8.49 displays the horizontal pile head displacement with respect to time (equivalent to the number of cycles after 3 s) for the simulation with a constant strain amplitude and the simulations updating the strain amplitude either in a submodel analysis or by incorporation of update cycles, respectively. The final pile head rotation θ is given in Fig. 8.49 as well. The strain amplitude is updated at $N = 10^2$, 10^3, 10^4, 10^5. Therefore, the results of all three simulations coincided up to $N = 10^2$. In case of the simulation with update cycles the incorporation of regular cycles is visible by the almost vertical lines at $N = 10^2$, 10^3, 10^4, 10^5 representing the displacement during the individual cycles. Both simulations updating the strain amplitude show larger horizontal pile head displacement at $N = 10^3$ compared to the simulation with constant $\varepsilon^{\mathrm{ampl}}$. Hence, the updated strain amplitude at $N = 10^2$ is larger and/or a greater soil volume shows larger strain amplitudes compared to $\varepsilon^{\mathrm{ampl}}$ at $N = 2$ due to the increase in excess pore water pressure predicted by the HCA model. With ongoing cyclic loading the simulations with $\varepsilon^{\mathrm{ampl}} \neq$ const. show a larger increase of u_x^{pile} compared to the simulation with constant $\varepsilon^{\mathrm{ampl}}$. Towards the end of the simulation, however, the accumulation rates of the simulations incorporating the change in strain amplitude are slightly lower than those of the simulation with constant $\varepsilon^{\mathrm{ampl}}$.

Compared to the simulation using the submodel analysis, the simulation employing update cycles shows numerical instabilities following the *regular* cycles visible for instance by a drop in u_x^{pile} directly after the update at $N = 10^2$. This is caused by the transition from the conventional low-cycle to the high-cycle mode requiring small time increments due to larger accumulation rates and the sudden change of soil stiffness (switching from the Sanisand to the HCA model). These small time increments lead to oscillations in pore water pressure since, for the **u**-p formulation, the conditioning of the element matrix gets worse with decreasing time increment. Such instabilities are absent in the simulation using the submodel analysis since the high-cycle mode is not interrupted and the simulation can continue with larger increments.

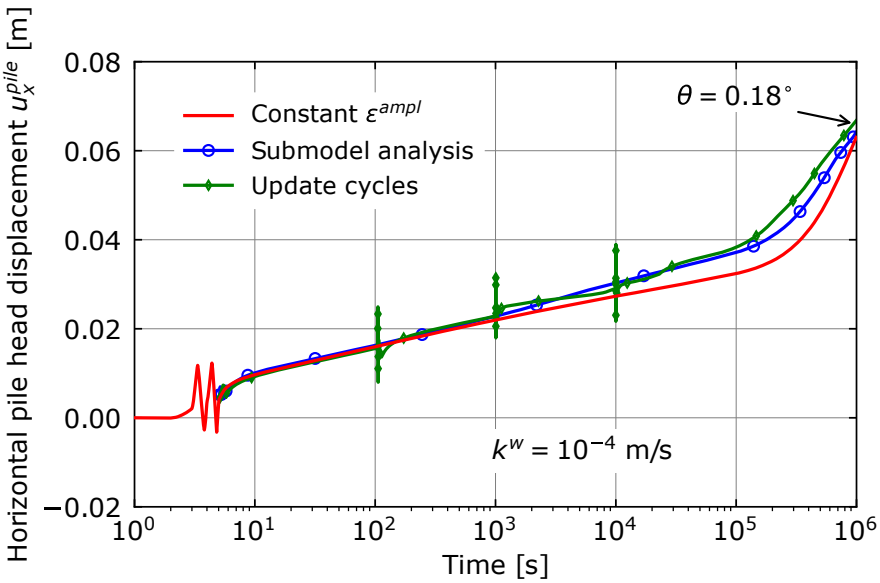

Figure 8.49: Horizontal pile head displacement with respect to time (equivalent to the number of cycles after 3 s) for the simulation assuming a constant $\varepsilon^{\text{ampl}}$ and the simulations updating $\varepsilon^{\text{ampl}}$ after $N = 10^2$, 10^3, 10^4, 10^5 in a submodel analysis or by incorporation of update cycles

8.4.2 Application of the adaptive strain amplitude

The horizontal pile head displacement with respect to time using the adaptive strain amplitude is compared to the simulation assuming a constant $\varepsilon^{\text{ampl}}$ and the submodel analysis in Fig. 8.50a for simulations with a hydraulic conductivity of $k^w = 10^{-4}$ m/s. A characteristic length of $l_c = 1$ m, influencing the number and the weighting of adjacent integration points considered in the smoothing of the field of the strain amplitude, is used for the simulation with adaptive strain amplitude. An investigation of the influence of the characteristic length and a comparison of the field of strain amplitude before and after smoothing is presented in Section 8.4.3. Simulations using characteristic lengths of $l_c = 0.5$ m and $l_c = 2$ m proved that the characteristic length hardly influences the results in terms of pile head displacement u_x^{pile}.

In both simulations with $\varepsilon^{\text{ampl}} \neq$ const. the strain amplitude is updated at $N = 10^2$, 10^3, 10^4, 10^5. The simulations with non-constant $\varepsilon^{\text{ampl}}$ are in good accordance, confirming the suitability of the novel approach with adaptive strain amplitude. Slightly larger pile head displacements are obtained using the adaptive strain amplitude compared to the simulation employing the submodel analysis at the end of the simulation. Taking into consideration the deviations of the two approaches for the triaxial test observed in Fig. 5.4 these differences between the much more complex simulations of the monopile are acceptable.

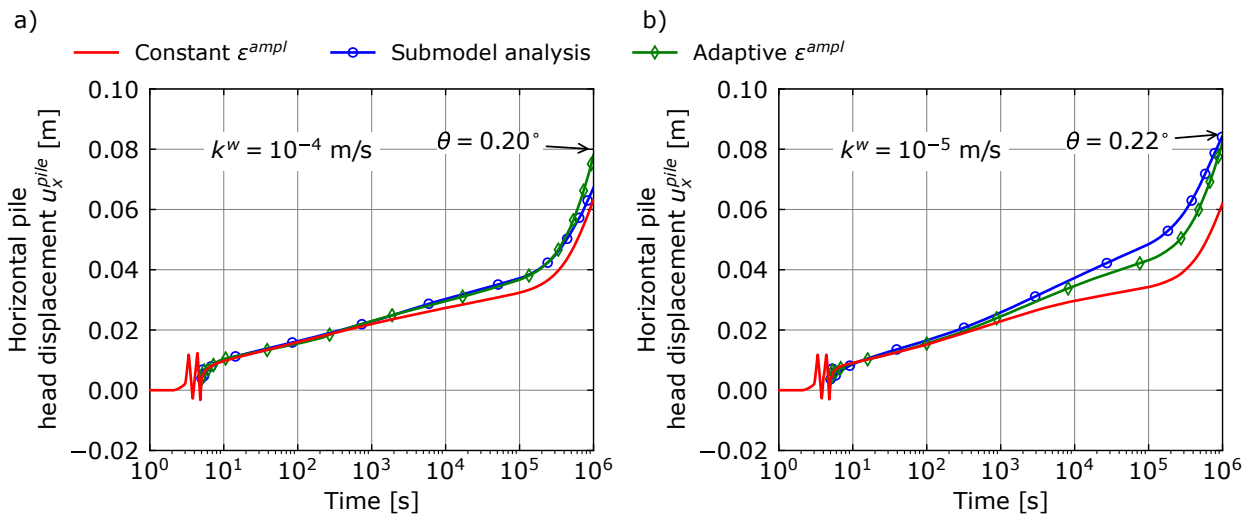

Figure 8.50: Horizontal pile head displacement with respect to time (equivalent to the number of cycles after 3 s) for the simulations with and without update of the strain amplitude employing the different approaches to calculate the updated $\varepsilon^{\text{ampl}}$ using a hydraulic conductivity of $k^w = 10^{-4}$ m/s and $k^w = 10^{-5}$ m/s, respectively

The simulations with a hydraulic conductivity of $k^w = 10^{-5}$ m/s show a stronger influence of the change in strain amplitude on the displacement of the pile head as is visible from Fig. 8.50b. Much higher accumulation rates of the pile head displacement are observed for the simulations with updated strain amplitude. The simulations with $\varepsilon^{\text{ampl}} \neq$ const. are in good agreement with each other except between $10^4 < N < 10^5$, where the simulation using the adaptive strain amplitude shows less displacement. Compared to the differences between the simulation with constant $\varepsilon^{\text{ampl}}$ and those updating $\varepsilon^{\text{ampl}}$ these deviations are judged acceptable.

As has been outline in the introduction, one motivation to prefer the adaptive strain amplitude over the application of update cycles or the submodel analysis is the reduced computational effort. For the simulations displayed in Fig. 8.50a) a total time of 3.6 h is required for the simulation with $\varepsilon^{\text{ampl}} =$ const.[1], 4.3 h for the simulation with adaptive strain amplitude and 6.7 h for the submodel analysis. The simulation with update cycles displayed in Fig. 8.49 takes almost nine hours due to a considerably larger number of required increments and the numerical instabilities already described in detail. These durations clearly demonstrate the advantage of the adaptive strain amplitude over the other two techniques.

The spatial distribution of the strain amplitude at $N = 10^2$, 10^3, 10^4, 10^5 for the simulation with adaptive strain amplitude and the simulation using the submodel analysis for the update

[1]One Intel Core™ i9 9900K processor with two threads has been used.

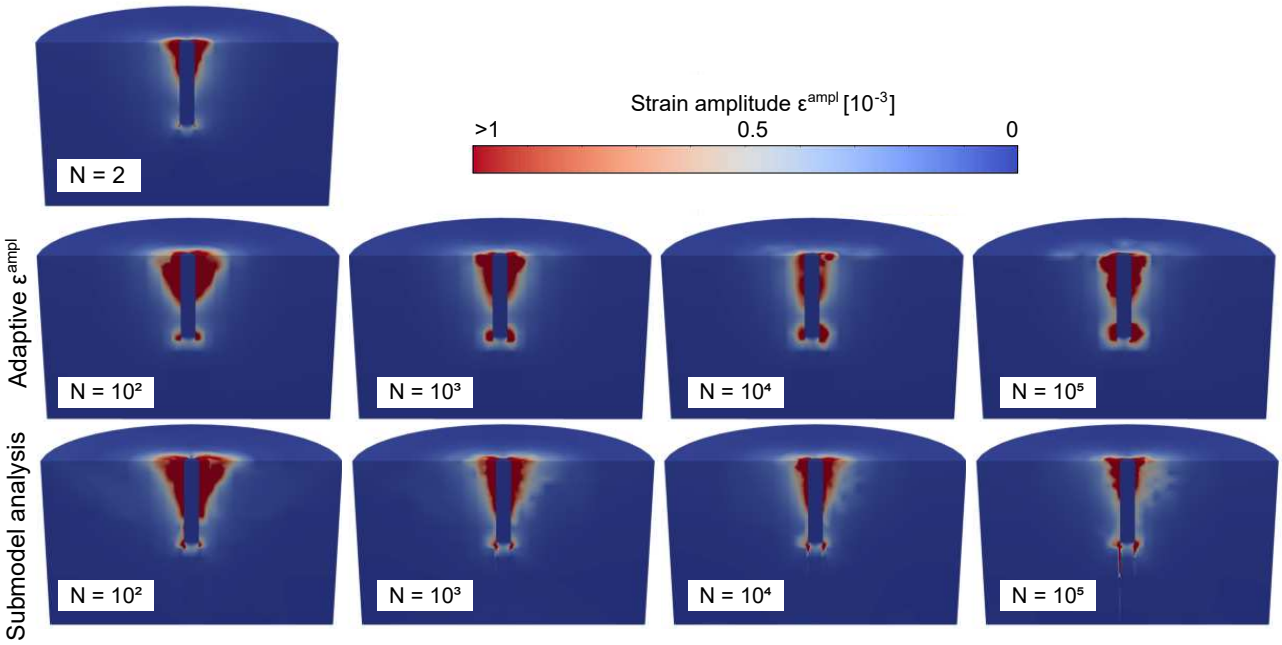

Figure 8.51: Field of strain amplitude at $N = 10^2, 10^3, 10^4, 10^5$ for the simulation with adaptive strain amplitude and the simulation employing the submodel analysis using a hydraulic conductivity of $k^w = 10^{-5}$ m/s.

of $\varepsilon^{\text{ampl}}$ is given in Fig. 8.51. Compared to the distribution at $N = 2$, the volume of soil with large strain amplitudes ($\varepsilon^{\text{ampl}} > 10^{-3}$) is greatly increased for both simulations at $N = 10^2$. The increase is mainly caused by the excess pore water pressure accumulating during the cyclic loading as is visible from Fig. 8.48. Compared to the submodel analysis, which is showing a wedge-like distribution of $\varepsilon^{\text{ampl}}$, the simulation employing the adaptive strain amplitude leads to a more sphere-like distribution of larger strain amplitudes in the vicinity of the pile head. At the second update ($N = 10^3$) the soil volume with large strain amplitudes reduces compared to $N = 10^2$ due to the reduction of excess pore water pressure by consolidation. Compared to the distribution at the previous update, the differences in terms of $\varepsilon^{\text{ampl}}$ between the two simulations are reduced. The simulation with adaptive strain amplitude shows noticeably larger strain amplitudes at the pile tip. With ongoing cyclic loading the volume with large strain amplitudes tends to decrease for both simulations, which is visible from the distributions at $N = 10^4$ and $N = 10^5$.

Having shown that the adaptive strain amplitude gives similar results as the simulation using the submodel analysis and hence having validated the proposed scheme, simulations with an update every 10th calculation increment are performed. Since the increment size gets progressively larger with increasing calculation time, a more frequent update with respect to the number of cycles at the beginning of the high-cycle mode is made. This is reasonable

since the strain amplitude changes the most at the beginning of the high-cycle mode due to larger accumulation rates and hence greater changes in the pore water pressure. Approximately 300 increments are necessary for the simulation of $N = 10^6$ cycles. The strain amplitude is thus updated 30 times. Such a frequent update of the strain amplitude is not feasible with the submodel analysis due to the considerable calculation time spent for the regular cycles.

The results of the simulations with an update every 10th increment are given in Fig. 8.52 using a hydraulic conductivity of $k^w = 10^{-4}$ m/s and $k^w = 10^{-5}$ m/s, respectively. Additionally, the simulations with an update at $N = 10^2$, 10^3, 10^4, 10^5 using the adaptive strain amplitude definition and the simulations with constant $\varepsilon^{\text{ampl}}$ are depicted. As expected, the more frequent update of the strain amplitude results in larger values for the pile head displacement u_x^{pile}. This effect is more prominent for the lower hydraulic conductivity. The pile head displacement u_x^{pile} at $N = 10^6$ is approximately factor 1.4 larger for the simulation with an update every 10th increment compared to the simulation with constant strain amplitude in case of $k^w = 10^{-5}$ m/s, highlighting the importance of the incorporation of the change in strain amplitude.

The developed adaptive strain amplitude allows to investigate how many updates of the strain amplitude are necessary such that the solution remains unchanged by the update frequency. Similar investigations have been carried out by the authors in [357] but using update cycles

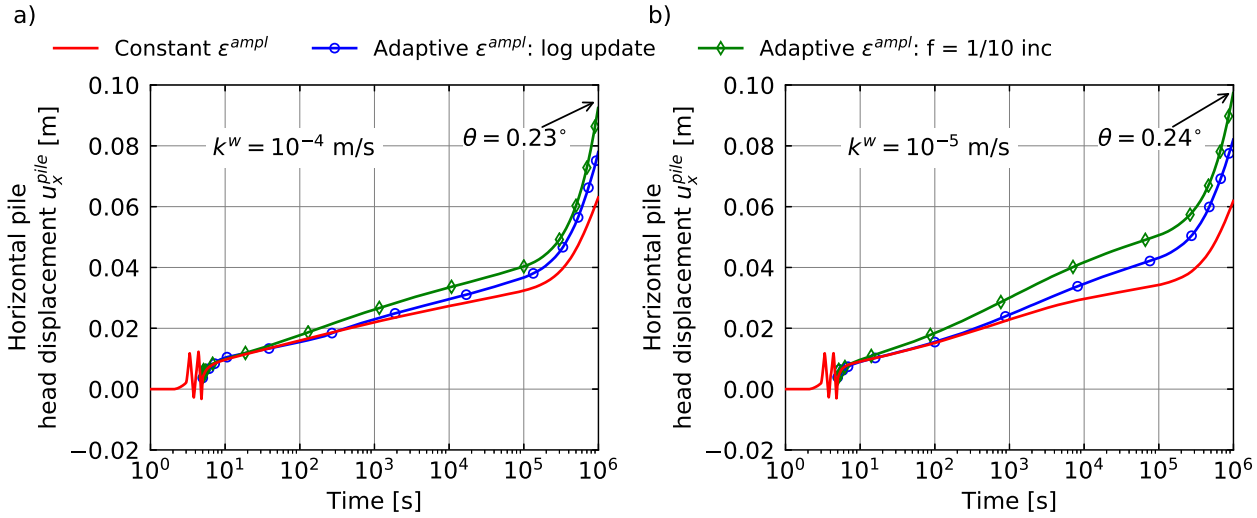

Figure 8.52: Horizontal pile head displacement with respect to time (equivalent to the number of cycles after 3 s) for the simulations with and without update of the strain amplitude using a hydraulic conductivity of $k^w = 10^{-4}$ m/s and $k^w = 10^{-5}$ m/s, respectively. The strain amplitude is updated at $N = 10^2$, 10^3, 10^4, 10^5 (log update) or every 10th increment ($f = 1/10$ inc).

and ideally drained conditions. Due to the large computational effort when applying many update cycles, an update was only performed at $N = 10$, 20, 50, 10^2, $2 \cdot 10^2$, $5 \cdot 10^2$, 10^3, $2 \cdot 10^3$, $5 \cdot 10^3$, 10^4, 10^5 in that previous study.

Using the adaptive strain amplitude, simulations with an update every increment, every 5th and every 10th increment are performed. Again, approximately 300 increments are required to simulate $N = 10^6$ cycles meaning that the strain amplitude is updated 300 times, 60 times and 30 times, respectively. The results of these simulations are compared to the simulation assuming a constant $\varepsilon^{\text{ampl}}$ in Fig. 8.53 in terms of horizontal pile head displacement u_x^{pile} using $k^w = 10^{-5}$ m/s. Up to $N = 10^5$ the solution in terms of u_x^{pile} is not altered by the different frequencies used for the update. From $N = 10^5$ to $N = 10^6$ the simulation with an update every 5th increment shows slightly less displacement compared to the other two simulations with $\varepsilon^{\text{ampl}} \neq$ const. Based on these results it is concluded that using an update every 10th increment is already sufficient to reach convergence in terms of necessary updates of the strain amplitude. It is expected that the update is less often required for higher hydraulic conductivity but most likely more often in case of less permeable soils. Similarly, more updates will be necessary for initially loose soil compared to a dense initial state in case of drained

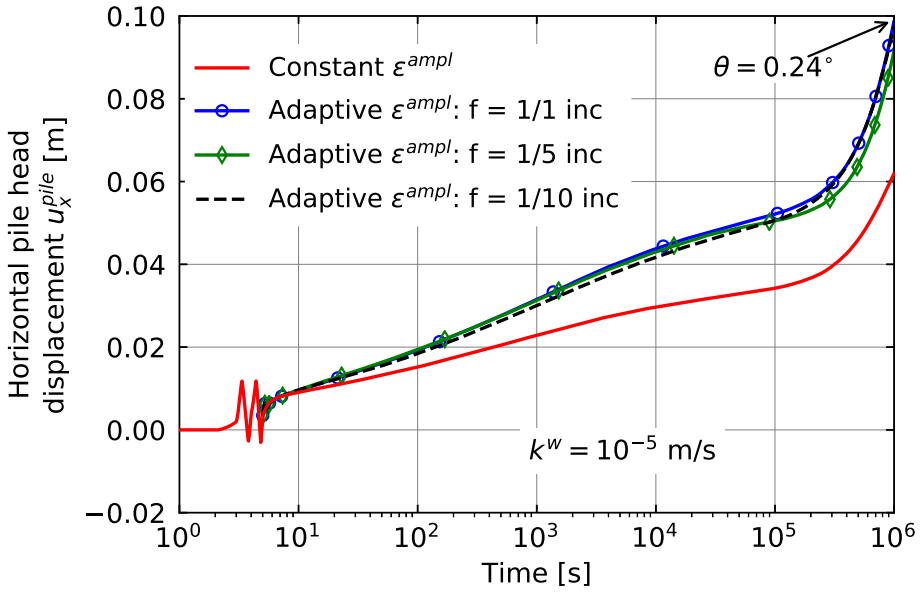

Figure 8.53: Horizontal pile head displacement with respect to time (equivalent to the number of cycles after 3 s) for the simulations with constant $\varepsilon^{\text{ampl}}$ and adaptive $\varepsilon^{\text{ampl}}$ updated every increment ($f = 1/1$ inc), every 5th increment ($f = 1/5$ inc) and every 10th increment ($f = 1/10$ inc) using a hydraulic conductivity of $k^w = 10^{-5}$ m/s

conditions since the cyclic loading results in compaction of the loose soil (at least for the BVP of the monopile) and hence an increase in soil stiffness. Such influences due to the change in density can also be accounted for using the proposed adaptive strain amplitude definition.

Based on the results presented in this section, the consideration of the change of the strain amplitude using the adaptive strain amplitude is judged important for partially drained analyses, since the negligence leads to less deformations. Therefore, the results are not conservative assuming a constant value of the strain amplitude or updating it only seldom.

8.4.3 Spatial smoothing of the strain amplitude

The importance of the nonlocal smoothing of the strain amplitude is illustrated by Fig. 8.54, displaying the spatial distribution of $\varepsilon^{\text{ampl}}$ using the adaptive strain amplitude prior to smoothing (left) and after smoothing (right) employing a characteristic length of $l_c = 1$ m. The field prior to smoothing shows large gradients of the strain amplitude in some elements close to the surface which are noticeably reduced after the smoothing process.

A comparison of the horizontal pile head displacement with respect to time using a hydraulic conductivity of $k^w = 10^{-5}$ m/s for simulations with

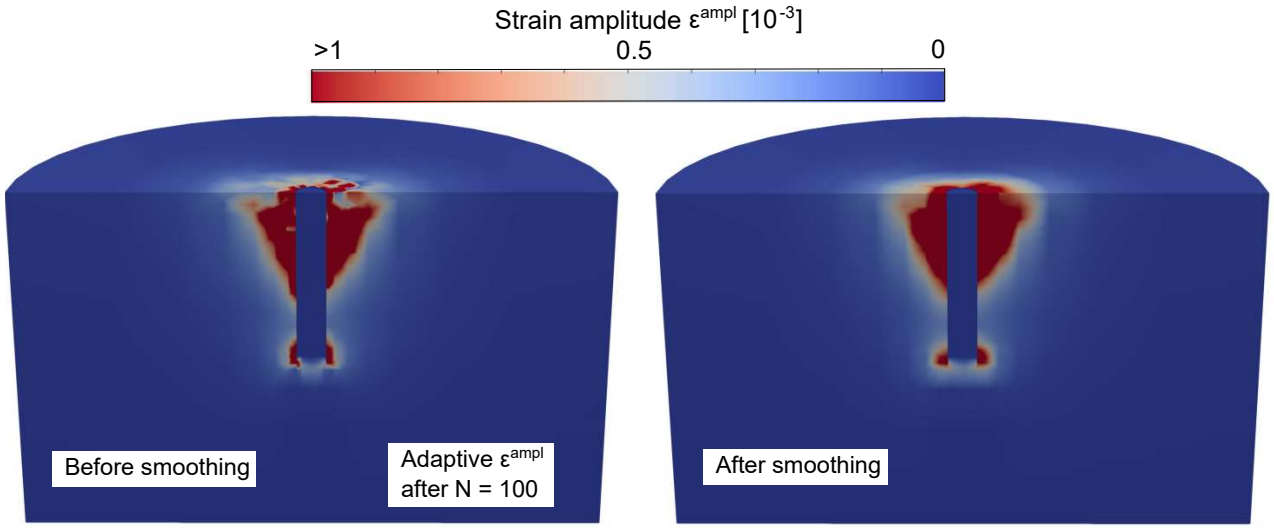

Figure 8.54: Field of strain amplitude at $N = 10^2$ (after the first update of the strain amplitude) for the simulations with adaptive strain amplitude using a hydraulic conductivity of $k^w = 10^{-5}$ m/s before and after the nonlocal smoothing procedure employing a characteristic length of $l_c = 1$ m

- constant strain amplitude
- adaptive strain amplitude updated at $N = 10^2$, 10^3, 10^4, 10^5 and smoothed using a characteristic length of $l_c = 1$ m
- adaptive strain amplitude updated at $N = 10^2$, 10^3, 10^4, 10^5 but no smoothing

is provided in Fig. 8.55a. The simulations with an update of the strain amplitude are in accordance up to $N = 10^4$ but the simulation without smoothing gives much less pile head displacement u_x^{pile} for larger number of cycles. This is due to the localisation of large strain amplitudes in a few integration points while neighbouring integration points show merely small values. As has been outlined in Section 5.2.2, this is caused by the self-reinforcing or positive feedback phenomenon, which tends to cause increasing localisation of $\varepsilon^{\text{ampl}}$ with each update.

A comparison of simulations with different values of the characteristic length l_c is given in Fig. 8.55b. Only small differences between the simulations are observed. The characteristic length of $l_c = 1$ m used for the analyses presented in the Section 8.4.2 is hence judged as suitable.

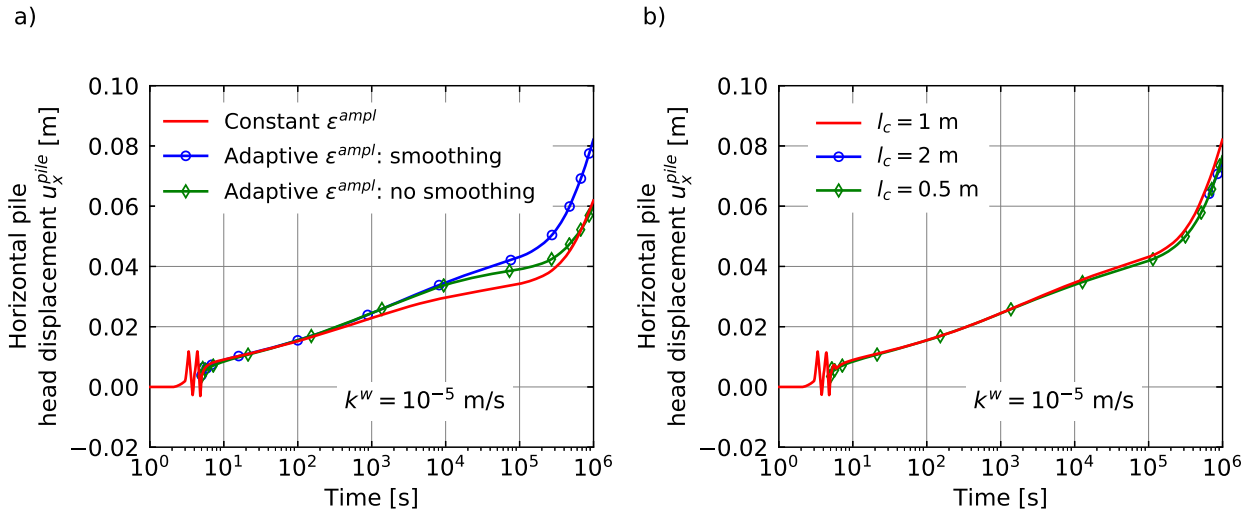

Figure 8.55: Horizontal pile head displacement with respect to time (equivalent to number of cycles after 3 s) for simulations using a hydraulic conductivity of $k^w = 10^{-5}$ m/s. A comparison of simulations with nonlocal smoothing ($l_c = 1$ m) and without any smoothing is provided in a). Different characteristic lengths l_c for the nonlocal smoothing of the strain amplitude are compared in b).

8.5 Validation of the HCA model for clay using centrifuge tests on monopiles subjected to cyclic lateral loading

In order to show the feasibility of the HCA model for clay presented in Section 5.1.2 for the analysis of OWT foundations subjected to lateral cyclic loading, a back-analysis of centrifuge tests performed by Yang et al. [431] on soft kaolin clay is presented in the following. Note that the results of these simulations have already been published in [358].

The considered centrifuge tests have been performed at Zhejiang University in 2019. All quantities are given in model scale in the following. A strongbox with internal dimensions of 1.2 $\times$ 0.9 $\times$ 1.0 m and Malaysia kaolin clay (plastic limit w_P = 35 %, liquid limit w_L = 80 % and plasticity index I_P = 45 %), which is a standard material of the National University of Singapore, have been used.

The soil sample was prepared by mixing dry kaolin powder with water using a soil-mixing machine and subjecting the slurry to 8 hours of consolidation in the centrifuge at 100 g. For these tests, water and not a fluid with a higher viscosity has been used as pore fluid. Following the consolidation of the clay, the centrifuge was stopped and the pile was pushed into the soil. The aluminium pile had an outer diameter of 0.059 m, a wall thickness of 0.0022 m and an embedded length of 0.55 m. Once the pile had been installed at 1 g, the soil including the pile were subjected to 100 g for one hour in order to allow for any settlement around the pile.

Following the resting period, the pile was laterally loaded at 0.23 m above the ground surface. Three cyclic load packages with varying amplitude and average loading with 100 cycles each and a frequency of 0.2 Hz have then been applied. 30 s of consolidation between the packages has been allowed. Only the first two cyclic loading packages are considered for the back-analysis since the third package with the largest amplitudes led to large pile head displacements (approximately 1 m in prototype scale) for which a large-deformation numerical method should be applied.

The finite element model of the centrifuge test is displayed in Fig. 8.56. The simulations are performed in model scale. In order to incorporate the change in pore water pressure as well as consolidation effects, the `u27p8` element formulation as introduced in Section 6.6 is used. The pile is modelled using `u27` elements. The `u27` elements are beneficial for the simulation of bending of stiff materials as they do not suffer from shear-locking problems as linearly

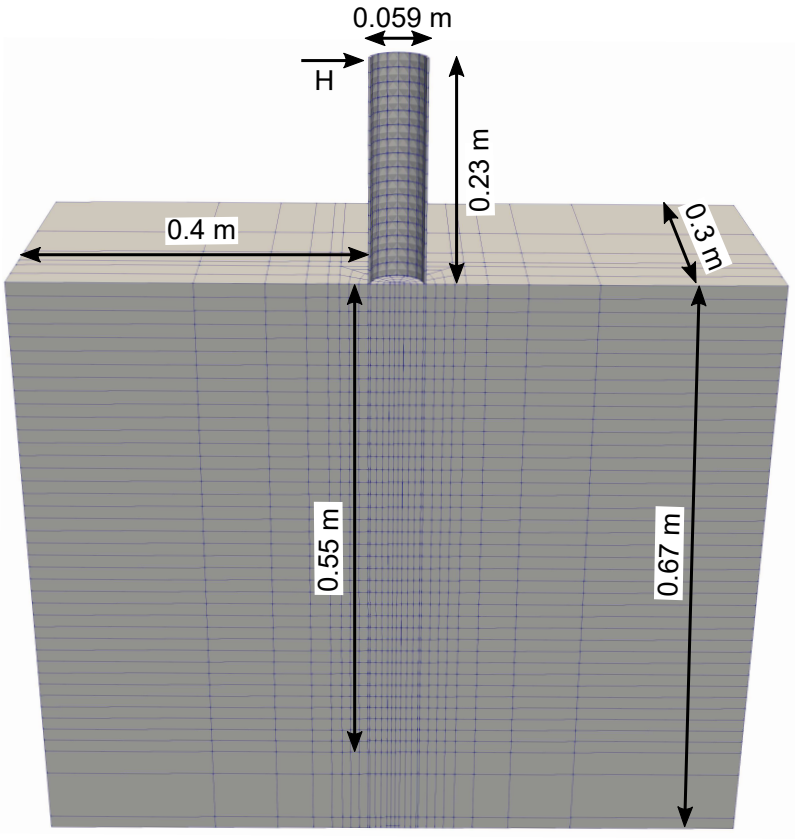

Figure 8.56: Finite element model of the centrifuge test. Note that only the exterior nodes are displayed.

interpolated elements do. The displayed finite element mesh depicts only the corner nodes of the elements.

The EBM method with 9 integration points per finite element face is used for the contact discretisation. A stiffness-dependent penalty factor (30 times the trace of the stiffness tensor of the adjacent continuum) is used to enforce the normal contact constraints. A Coulomb friction model with a friction coefficient of 0.2 is applied (note that effective normal stresses are used for the calculation of friction). A bulk modulus of the pore water of 2.2 GPa is assumed. The permeability of the Malaysian kaolin clay is $K^{\mathrm{Perm}} = \eta^w k^w / \gamma^w = 2 \cdot 10^{-15}$ m^2 (assuming the dynamic viscosity of water to be $\eta^w = 1 \cdot 10^{-6}$ kPas). With the increased gravity in the centrifuge test, this resulted in a hydraulic conductivity of $k^w \approx 2 \cdot 10^{-6}$ m/s during the testing. Installation effects are not taken into account in the simulations since in the experiment the pile has been jacked into the soil at 1 g. Due to the increase of gravity to 100 g, the influence of the installation on the initial soil state is assumed to decrease significantly. The initial overconsolidation ratio prior to the spin-up of the centrifuge is assumed to be one. The lateral stress coefficient is set to $K_0 = 0.5$.

For the low-cycle part of the simulations, the anisotropic visco-ISA (AVISA) model [374] is used. This is a rate-dependent model for fine-grained soils able to reproduce small-strain effects, inherent anisotropy as well as the influence of the overconsolidation ratio. The strain rate dependency is reproduced by incorporating a third strain rate mechanism (in addition to the elastic and hypoplastic strain rate), which can be switched off in case of low-plasticity fine-grained soils. The parameters of the AVISA model are partially determined for the Malaysian kaolin clay ($w_P = 35\,\%,\ w_L = 80\,\%$) used in the centrifuge tests (parameters of the MCC model: λ, κ, ν_h and M_c obtained from [221]) or are assumed to lie between the parameters calibrated for a kaolin clay with lower plasticity ($w_P = 12.2\,\%,\ w_L = 47.2\,\%$) and those for the more plastic Lower Rhine Clay ($w_P = 34\,\%,\ w_L = 56.1\,\%$) reported in [374, 373].

The utilised set of parameters is given in Table 8.13, whereby further details about the correlations used for the calibration as well as the numerical calculation of an oedometric compression test can be found in [358].

It it worth mentioning that using the HCA model for clay, the influence of the conventional model is much lower than in case of the HCA model for sand since the influence of the strain amplitude, calculated by the conventional model, is much lower due to the smaller values of the parameter C_{ampl} of the amplitude function f_{ampl}. The soil inside the pile is modelled elastically since it is only involved in a rigid deformation when the pile rotates and does not influence the pile response. Preliminary simulations showed that an elastic stiffness of 10,000 kPa and a Poisson's ratio of 0.3 are appropriate values. The parameters of the HCA model for clay given in Table 8.14 are applied for the simulations, which have been determined using test data of "Karlsruhe kaolin" [406]. Unfortunately, no cyclic triaxial test data is available for the Malaysian kaolin clay.

During the high-cycle phase of the HCA model, the change of the strain amplitude $\varepsilon^{\text{ampl}}$ due to the change in the soil stiffness caused by the cyclic loading is taken into account using the adaptive strain amplitude definition. In accordance with the findings of the previous section, a characteristic length of $l_c = 1$ m is used for the nonlocal smoothing algorithm. The reference

λ [-]	κ [-]	ν_h [-]	α [-]	M_c [-]	e_{i0} [-]	f_{b0} [-]	I_v [-]	R [-]	m_R [-]	d [-]	β_0 [-]	χ_0 [-]	$\chi_{\max}$ [-]	C_a [-]
0.244	0.053	0.25	1.2	0.9	2.34	2	0.015	10^{-4}	5	3	0.1	5	30	0.005

Table 8.13: Parameters of the AVISA model for Malaysian kaolin clay used in the simulations of the centrifuge tests

C_{ampl}	C_{N1}	C_{N2}	C_{N3}	C_e	C_η	C_{OCR}
0.6	0.00115	0.8	0.0	-0.97	2.9	0.5

Table 8.14: HCA model parameters for "Karlsruhe kaolin" [406]

and updated soil stiffness required for the update of the strain amplitude is calculated using the stiffness tensor defined in Eq. (5.23).

The simulations are performed in the following steps:

1. Application of the self-weight of the soil and pile at 1 g.
2. Application of increased gravity by the centrifuge (spin-up of the centrifuge).
3. Application of the average value of the lateral force $H^{\text{av}} = 62.5$ N linearly increasing over a time span of 3 s.
4. Calculation of the first cycle, using the AVISA model. The average load H^{av} is superposed by a sinusoidal cyclic load with the amplitude $H^{\text{ampl}} = 37.5$ N.
5. Calculation of the second cycle, using the AVISA model. During this second cycle, the strain path is recorded in each integration point. The spatial field of the strain amplitude $\varepsilon^{\text{ampl}}$ is determined from that strain path.
6. Calculation of permanent deformations due to $N = 100$ further cycles using the HCA model. The load is kept constant at its average value H^{av} while the permanent deformations due to the cyclic loading are predicted by the HCA model. During the high-cyclic loading, the strain amplitude is updated every 10th calculation increment (approximately at $N = 3,\ 8,\ 15,\ 40,\ 90$). Taking into account the frequency of the cyclic loading of 0.2 Hz, 500 s are simulated in the high-cycle phase.
7. 30 s of consolidation are allowed before application of the next package of cycles. Only H^{av} is applied in this phase.
8. Repetition of steps 3-6 using the load magnitudes of the second package of cyclic loads ($H^{\text{av}} = 110$ N and $H^{\text{ampl}} = 65$ N).

As has been done in the study by Yang et al. [431], the results are evaluated in prototype scale. The pile head displacement measured at the point of load application is given in Fig. 8.57 for

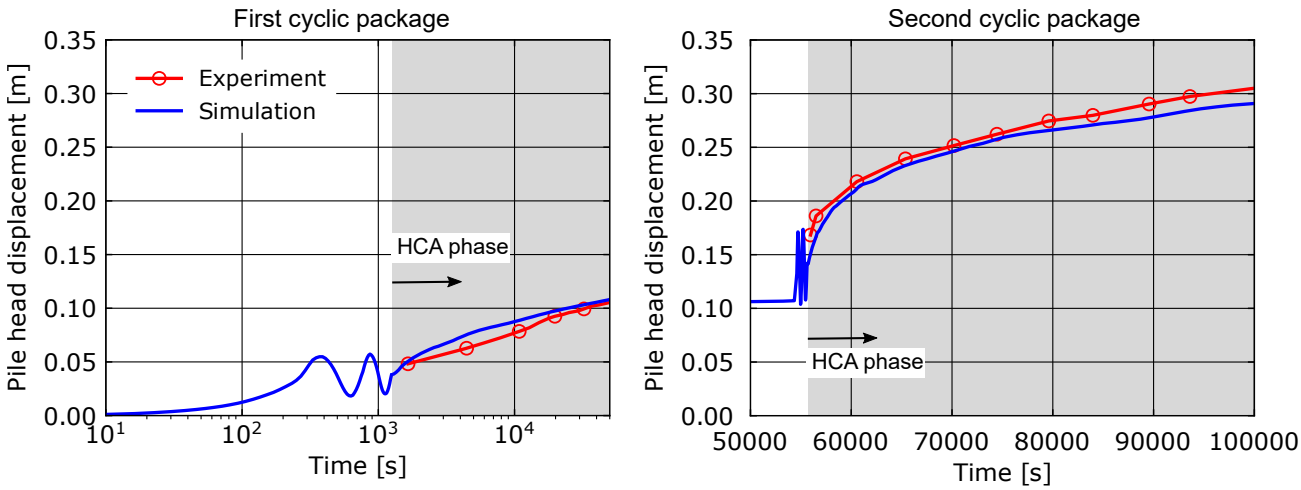

Figure 8.57: Displacement of the pile head versus time for the measurements and the results of the simulation, respectively

the measurements as well as for the results of the simulation. The results of the experiment are displayed as mean pile head displacement beginning after the end of the second load cycle (note that the data of the experiment for a low number of cycles is not available for which reason the curve starts at $N \approx 3$). The measured displacement after the first two cycles of the first cyclic loading package (see the plot on the left-hand side of Fig. 8.57) is slightly underestimated by the simulation using the AVISA model, which yields approximately 0.04 m. The subsequent HCA phase starts at $t = 1,300$ s ($N = 2$) and first predicts a comparatively fast accumulation which slows down after approximately $\approx 1,500$ s. Afterwards an almost linear increase of the pile head displacement with time (or the number of cycles, respectively) is observed in the diagram with log-linear scale. The pile head displacement predicted by the simulation fits well to the measurements even though the final displacement is slightly lower in case of the experiment.

For the second load package two individual cycles are simulated again using AVISA. Due to the larger loading magnitudes, larger displacement amplitudes are observed compared to the cyclic loading of the first package (see the plot on the right-hand side of Fig. 8.57). Consequently, the strain amplitude is larger leading to a higher accumulation rate of the HCA model in the subsequent high-cycle phase. The accumulation of pile head displacement predicted by the HCA model during this phase fits well to the values recorded in the experiment.

The curves of bending moment vs. the height of the pile after $N = 1$ and $N = 90$ cycles are given in Fig. 8.58. The mudline is located at a vertical coordinate of 0 m. The distribution after one cycle shows that the simulation underestimates the magnitude of the bending moment

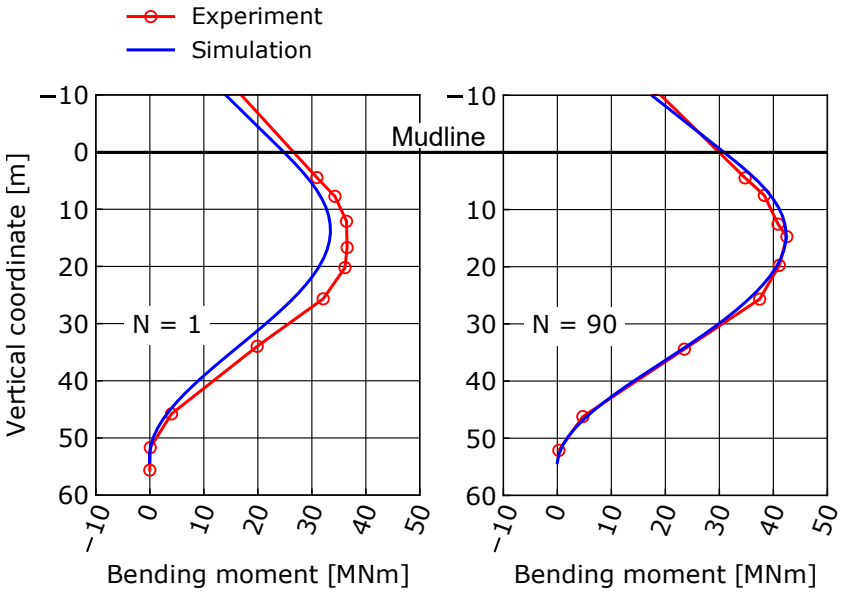

Figure 8.58: Comparison of the bending moment along the pile between the measurements made in the experiment and the results of the simulations after $N = 1$ and $N = 90$ cycles

slightly but captures the general shape of the measured curve very well. After the application of 90 cycles both the bending moment measured in the experiment and the one obtained from the simulation have increased in magnitude. This increase is more pronounced in case of the simulation. The accordance at $N = 90$ between the measurements and the results of the simulation is almost perfect.

Figure 8.59 displays the spatial distribution of the strain amplitude $\varepsilon^{\text{ampl}}$ at $N = 2$ and $N = 90$ for the first cyclic load package (top part of figure). The largest strain amplitudes with values above 0.1 % occur at the soil surface in the vicinity of the pile. Thus, the function f_{ampl} is largest at this location. As has been explained earlier, the change in the strain amplitude is taken into account using the adaptive strain amplitude definition. The spatial distribution of the strain amplitude following the last update performed during the first cyclic load package (at $N = 90$) shows that the strain amplitude has changed only slightly due to the application of 90 cycles. Moderately larger values are obtained at the left-hand side of the pile (the average loading of the pile is applied to the right) compared to the distribution at $N = 2$. The strain amplitude is much larger for the second cyclic load package as is visible from the lower part of Fig. 8.59. During the second cyclic load package, the change of the strain amplitude is larger compared to the first cyclic load package as is visible from the distribution at $N = 90$. Therefore, the consideration of the change in strain amplitude in the simulation with the HCA model is judged mandatory for the cyclic loading with larger amplitudes but is of less

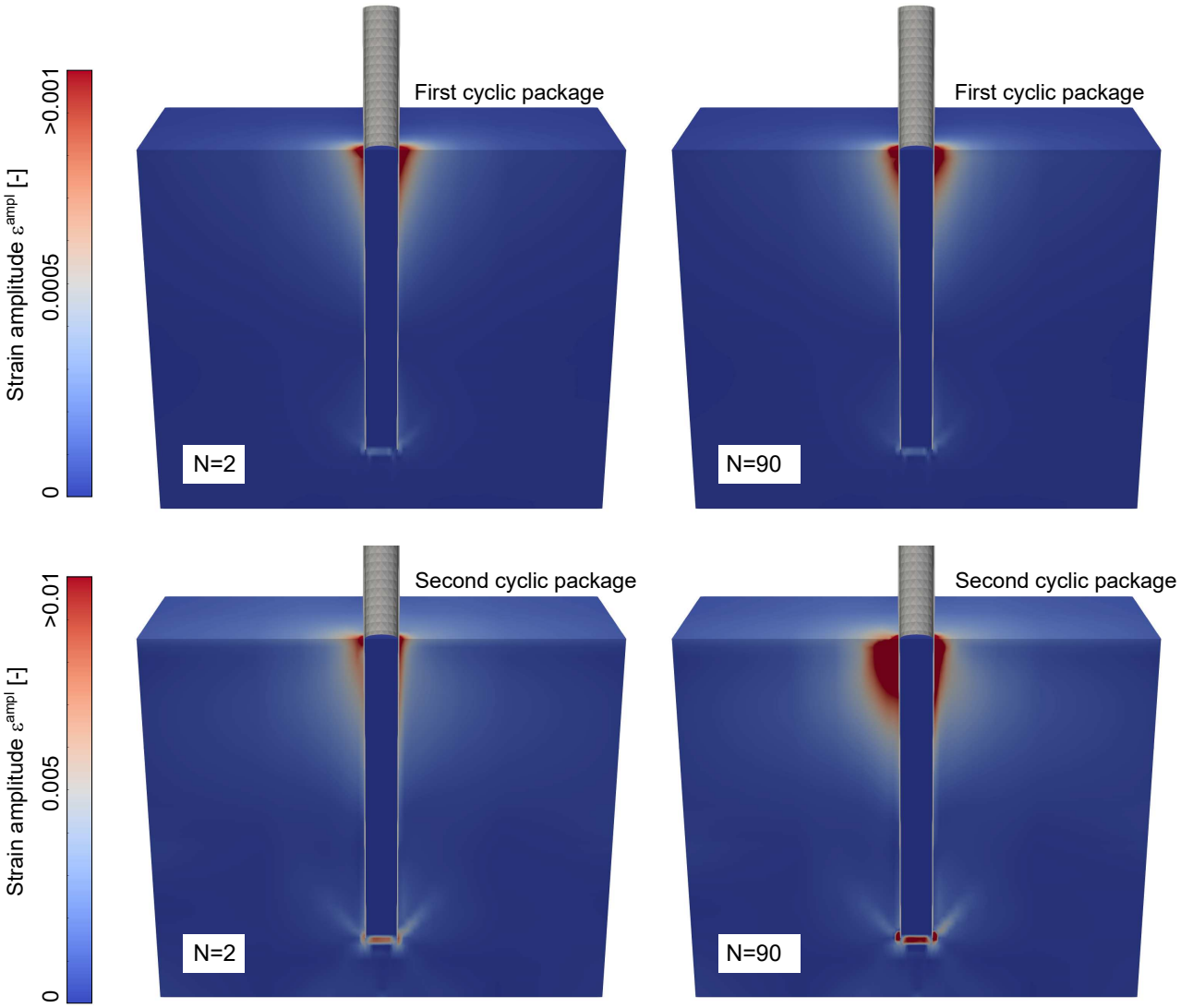

Figure 8.59: Spatial distribution of the strain amplitude at $N = 2$ and $N = 90$ for the first cyclic load package (top part of figure) and the second package (lower part of figure). Note the different scale of the legends.

importance for the cyclic load package with lower load magnitude. This is reasonable since the cyclic loading with higher magnitude causes larger increase in excess pore water pressure and consequently a more pronounced reduction in soil stiffness leading to larger strain amplitudes.

The function f_η, describing the dependence of the rate of accumulation on the average stress ratio η^{av}, shows large values alongside the left-hand side of the pile at the start of the HCA phase as is visible from Fig. 8.60. Since the pile is loaded to the right, the horizontal effective stress is reduced on its left, which leads to large average stress ratios η^{av}. From the factors influencing the rate of strain accumulation, f_η varies the most in magnitude over the calculated

domain. While the factor f_e takes values in the range of 0.8 to 1.3, f_η varies from 0 to values above 60. f_{ampl} has a comparably modest influence with values in the range of 0 to 2 (for the first cyclic load package). f_{OCR} takes values reaching from 1 to 2 due to the change in the overconsolidation ratio prior to the HCA phase caused by the first two cycles of loading.

The fields of excess pore water pressure ratio ($\Delta p^w/p_0$) at the beginning of the HCA phase (at $N = 2$) and at the end of the simulation (at $N = 100$) are given in Fig. 8.61 for the first cyclic load package. At $N = 2$ an increased pore water pressure in the upper half of the soil on the right-hand side of the pile (where the soil is pushed by the pile) is evident, while a decrease is observed in the soil on the left-hand side (where the soil is unloaded). After the application of 100 cycles, a significant increase of the soil area near the ground surface affected by large excess pore water pressures is observed. The increase in excess pore water pressure is due to the tendency of the soil to compact around the pile when subjected to cyclic loading. The consolidation process taking place simultaneously is, however, not fast enough to allow free drainage of the pore water.

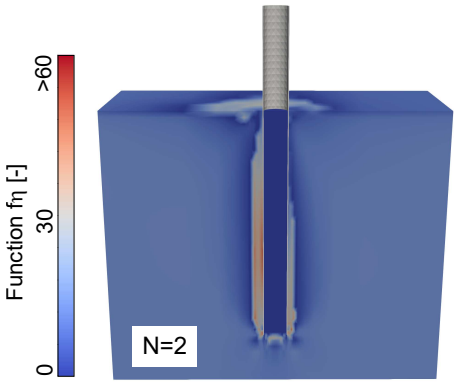

Figure 8.60: Spatial distribution of the function f_η directly at the start of the HCA phase ($N = 2$) of the first cyclic load package

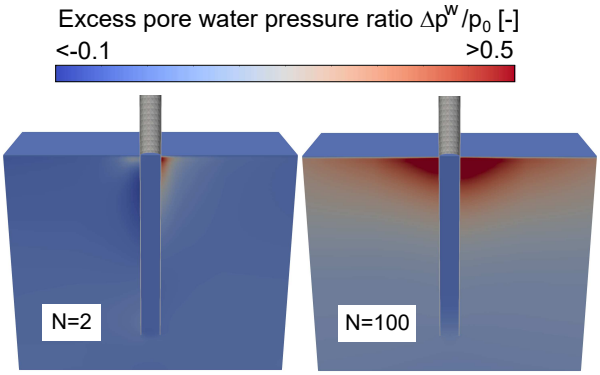

Figure 8.61: Spatial distribution of the excess pore water pressure ratio at $N = 2$ (left) and at the end of the HCA phase at $N = 100$ cycles (right) for the first cyclic load package

8.6 Parametric study on the long-term deformations of monopile foundations in kaolin clay

A parametric study on the long-term behaviour of monopile foundations for OWTs in clay using the HCA model for clay is presented in this section. A similar study considering sandy soil has already been published by the author in [357].

The numerical model of a monopile with a diameter of $D = 5$ m, a length $L = 30$ m and a wall thickness $t = 8$ cm is the same as employed for the analysis of the adaptive strain amplitude (Section 5.2.2) given in Fig. 8.47. `u27p8` elements are used to discretise the soil. The soil volume has a height of 80 m and a radius of 50 m. No effects due to the pile installation process are taken into account for the simulations presented in this section. The influence of the installation process on the response to subsequent lateral loading of piles in clay is investigated in Section 8.7.

The Coulomb friction model with a wall friction angle of $\delta = \varphi_c$ is used. The top, back and bottom borders of the model allow any excess pore water pressure to dissipate. The lateral and vertical loading is applied to a rigid extension of the pile above the seabed of 0.2 m. A lever arm of $h = 30$ m with respect to the point of load application of the resulting horizontal load due to water and wind waves is assumed. For all simulations an initial lateral stress coefficient of $K_0 = 0.5$ and a lithostatic stress distribution are set. The grain density is $\bar{\rho}^s = 2.6$ g/cm^3.

For the monotonic and low-cycle phase, the AVISA model with the constitutive parameters for "Karlsruhe kaolin" is used. The parameters are given in Table 8.15 and the calibration of the parameters is documented in [373, 374]. The initial void ratio e_0 is calculated using

$$e_0 = e(z = 0 \text{ m}) - \lambda \cdot \log \Big[p(z) \cdot \text{OCR}_0 \Big], \tag{8.10}$$

where $e(z = 0 \text{ m}) = 1.76$ is the void ratio at the seabed and λ is the virgin compression index. An initial overconsolidation ratio of $\text{OCR}_0 = 1$ is assumed.

In order to determine meaningful values of the cyclic loading magnitude, the pile is subjected to monotonic loading first to identify its ultimate resistance. The required loading to reach a pile head rotation of $\theta = 2°$ is applied in a transient simulation over a time span of 10 s. A hydraulic conductivity of $k^w = 10^{-8}$ m/s is assumed. Based on these values, the response of the soil is assumed to be nearly undrained during the monotonic loading. The spatial distribution of excess pore water pressures due to monotonic loading up to a pile head rotation of $\theta = 2°$ displayed in Fig. 8.62a shows large excess pore water pressure at the left-hand side of the

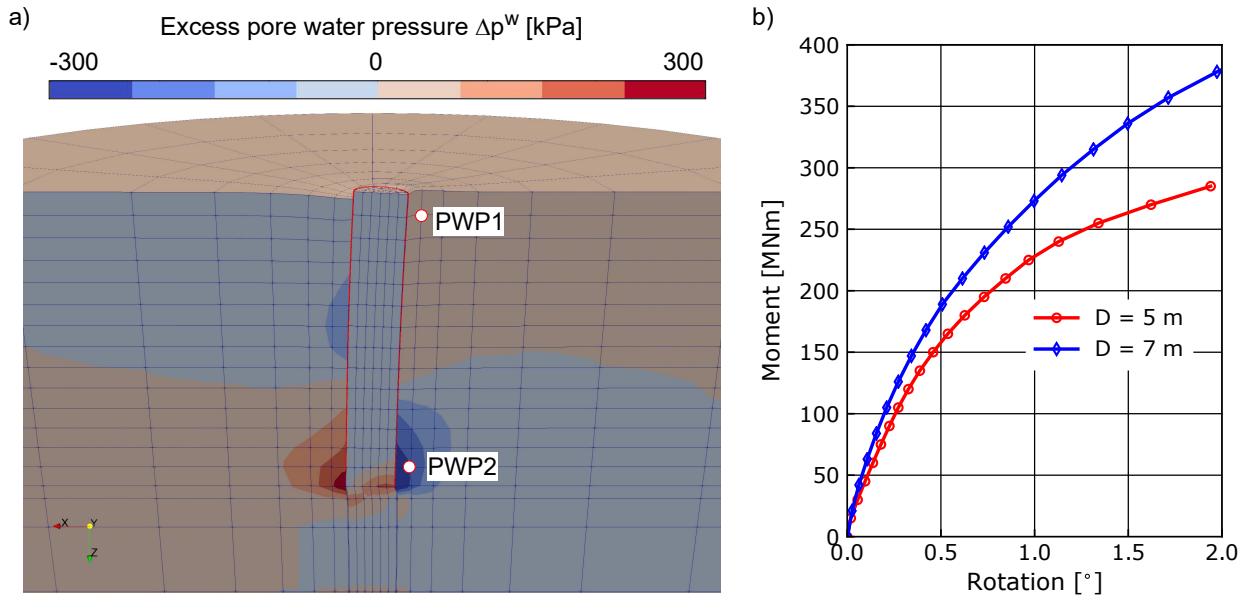

Figure 8.62: a) Spatial distribution of excess pore water pressure at a rotation of the monopile ($D = 5$ m) of $\theta = 2°$ (deformation scale factor 3). b) Corresponding moment-rotation curves for monopiles with a diameter of $D = 5$ m or $D = 7$ m.

pile tip. On the other hand, negative excess pore water pressures with values of up to -300 kPa are observed at the right-hand side of the pile tip. However, considering that the free water table is approximately 20-30 m above the seabed, the total pore water pressure is still approximately 200-300 kPa at the pile tip. The relation between applied moment and rotation of the pile head (determined at the pile head extension above the seabed) is given in the plot in Fig. 8.62b for a monopile with a diameter of $D = 5$ m and of $D = 7$ m, respectively. The ultimate resistance is assumed to be reached at a rotation of $\theta = 2°$. Note that the resulting moment corresponds to a full model. For the determination of the cyclic loading, an ultimate moment of $M^R = 300$ MNm for $D = 5$ m is assumed. For the monopile with a diameter of $D = 7$ m, $M^R = 375$ MNm is obtained. The ratio of the maximum moments $M^R(D = 7$ m$)/M^R(D = 5$ m$) = 1.25$ is less than the ratio of the diameters $7/5 = 1.4$. This is important to note, since the loading of the piles is linearly scaled with respect to their diameter in the following.

For piles with a diameter of $D = 5$ m and a length of $L = 30$ m a cyclic loading amplitude of $M^{\text{ampl}} = 15$ MNm $= 5\ \% \cdot M^R$ and an average value of $M^{\text{av}} = M^{\text{ampl}}$ is set. The horizontal loading is calculated using the lever arm $h = 30$ m: $H^{\text{ampl}} = M^{\text{ampl}}/h$ and $H^{\text{av}} = M^{\text{av}}/h$. For piles with larger diameter or length, both the amplitude and the average values are scaled linearly with respect to the corresponding difference in geometry. The frequency of cyclic

λ [-]	κ [-]	ν_h [-]	α [-]	M_c [-]	e_{i0} [-]	f_{b0} [-]	I_v [-]	R [-]	m_R [-]	d [-]	β_0 [-]	χ_0 [-]	$\chi_{\max}$ [-]	C_a [-]
0.13	0.05	0.3	1.8	1	1.76	1.5	0.015	10^{-4}	3	3	0.076	7	40	0.001

Table 8.15: Parameters of the AVISA Model for "Karlsruhe kaolin" used in the simulations of the monopile [373, 374]

loading is assumed to be 0.1 Hz, which is a typical value found for frequencies of wind and water waves in the offshore environment. In contrast to the simulations performed in Section 8.3.2, the loading to the average values M^{av} and H^{av} is performed in a transient analysis over a time of 10 s. This is done because the value of M^R was also obtained by a transient analysis, as opposed to the simulations in Section 8.3.2.

In order to evaluate the influence of the change in strain amplitude during the high-cycle phase of the simulation, a comparison of the pile head displacements for simulations assuming values of hydraulic conductivity of $k^w = 10^{-6}$ m/s and $k^w = 10^{-9}$ m/s, respectively, is given in Fig. 8.63. Simulations with and without application of the adaptive strain amplitude definition according to Section 5.2.2 are compared. The update is performed every 10th increment in accordance with the conclusions drawn in Section 8.4 regarding the required frequency of the update. As has been done in the previous section, the reference and updated soil stiffness used for the update of the strain amplitude is calculated using the stiffness tensor defined in Eq. (5.23). In order to distinguish between the displacement caused by the accumulated strain $\boldsymbol{\varepsilon}^{\text{acc}}$ calculated by the HCA equations and the displacement due to dissipation of the excess pore water pressure caused by the loading to the average values and the first two cycles, an additional simulation setting $\boldsymbol{\varepsilon}^{\text{acc}} = \mathbf{0}$ is depicted in grey. In addition, the development of excess pore water pressures for the two points marked in Fig. 8.62 is given for the two simulations employing the adaptive strain amplitude on the right-hand side of Fig. 8.63. For both values of hydraulic conductivity the consideration of the change in strain amplitude leads to a larger accumulation of permanent horizontal pile head displacements. Therefore, the tendency is in accordance with the tendencies observed for monopiles in sandy soils investigated in Section 8.4. However, despite the much lower hydraulic conductivity and thus larger increase in excess pore water pressure during the high-cycle phase, the influence of the change in $\varepsilon^{\text{ampl}}$ on the horizontal pile displacement is comparatively small. This is due to the lower C_{ampl} value for clay compared to sand as already mentioned in Section 8.5.

The influence of the consideration of the change in strain amplitude is larger for the lower value of hydraulic conductivity, in particular for times larger than $\approx 5 \cdot 10^5$ s. Much higher

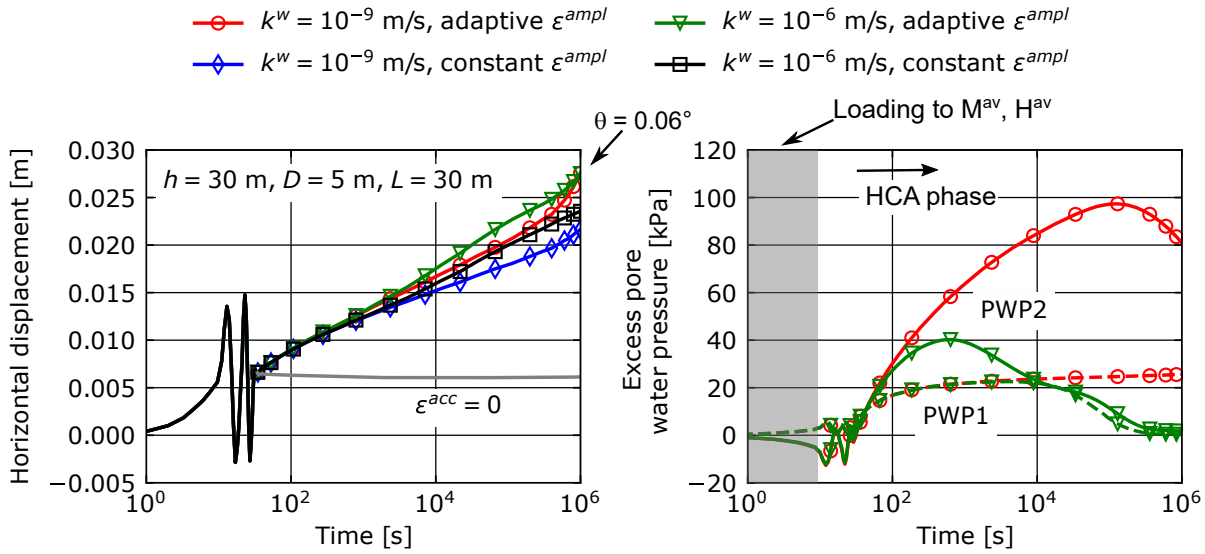

Figure 8.63: Horizontal pile head displacement for simulations with and without consideration of the change in strain amplitude during the HCA phase assuming values of hydraulic conductivity of 10^{-6} m/s and 10^{-9} m/s, respectively. An additional simulation without any strain accumulation calculated by the HCA equations ($\boldsymbol{\varepsilon}^{\mathrm{acc}} = \mathbf{0}$) is displayed in grey. The right-hand plot shows the development of excess pore water pressures for the two points marked in Fig. 8.62 for the two simulations employing the adaptive strain amplitude definition.

accumulation rates are observed for the simulation with adaptive strain amplitude and $k^w = 10^{-9}$ m/s compared to all other simulations. Similar, but much less pronounced, the simulation with adaptive strain amplitude and $k^w = 10^{-6}$ m/s shows higher accumulation rates compared to the corresponding simulation assuming a constant strain amplitude towards the end of the simulation. A final pile head rotation of $\theta = 0.06°$ is observed for both simulations utilising the adaptive strain amplitude definition.

Unsurprisingly, the consideration of a hydraulic conductivity of $k^w = 10^{-9}$ m/s results in a delayed dissipation of excess pore water pressures compared to a value of $k^w = 10^{-6}$ m/s, which can be seen from the right-hand side of Fig. 8.63. Up to a time of $\approx 1 \cdot 10^2$ s, the increase in point PWP2 is almost identical for both simulations. In case of the simulation with a value of $k^w = 10^{-9}$ m/s the accumulation rate of excess pore water pressures is higher than the corresponding rate of dissipation up to a time of $\approx 1 \cdot 10^5$ s, whereas the drop of excess pore water pressure already starts at a time of $\approx 5 \cdot 10^2$ s for $k^w = 10^{-6}$ m/s. Only the simulation with higher value of k^w reaches hydrostatic conditions in both points within the considered simulation time.

To investigate the influence of the adaptive strain amplitude for a different pile geometry, a

simulation of a monopile with a length of $L = 42$ m and a diameter of $D = 5$ m using a constant strain amplitude is compared to a simulation with adaptive strain amplitude definition. All load magnitudes are increased linearly with respect to the pile with $L = 30$ m. The motivation to consider another pile geometry for the investigation of the influence of the adaptive strain amplitude is due to the larger displacement amplitude of the pile near the ground surface for the longer pile, resulting in larger values of strain amplitude. A hydraulic conductivity of $k^w = 10^{-8}$ m/s is assumed. The resulting lateral deflection lines of the monopile are displayed in Fig. 8.64 at $N = 2$ (dashed) and at $N = 10^4$ (solid). In addition, the final pile head rotation θ is given for the simulation with adaptive strain amplitude. The consideration of the change in strain amplitude leads to slightly larger lateral deformation at $N = 10^4$ compared to the simulation with constant $\varepsilon^{\text{ampl}}$, which is in accordance with the tendencies of the previously discussed simulations. Figure 8.65 displays the field of the strain amplitude at $N = 2,\ 10^2,\ 10^3,\ 10^4$ for the simulation with adaptive strain amplitude. The spatial distribution at $N = 2$ is the same for both simulations, with or without adaptive strain amplitude. Employing the adaptive strain amplitude definition, a large increase in strain amplitude from $N = 2$ to $N = 10^2$ is visible. From $N = 10^2$ to $N = 10^4$ $\varepsilon^{\text{ampl}}$ increases further but less than from $N = 2$ to $N = 10^2$. The change in the spatial distribution is similar to the one observed for the simulations considering sand presented in Section 8.4.

Despite the large change in $\varepsilon^{\text{ampl}}$ only modest influence on the horizontal pile displacement is found. For all further calculations $\varepsilon^{\text{ampl}} = \text{const.}$ is assumed, acknowledging that the accumulation during the high-cycle phase might be underestimated. This is because the pile deflection lines are evaluated at $N = 10^4$ in the following, for which the influence of the consideration of the change in strain amplitude is little according to the results given in Fig 8.63. A hydraulic conductivity of $k^w = 10^{-8}$ m/s is assumed for all subsequent simulations.

The influence of the pile length on the long-term behaviour of the pile is investigated in the left-hand plot of Fig. 8.66. Again, the dashed lines represent the horizontal pile displacement at $N = 2$ cycles and the solid lines at $N = 10^4$ cycles. In order to take into account a larger loading magnitude due to the increased stiffness of the pile-soil system, the applied cyclic and average moment are linearly scaled with respect to the pile length. However, the diameter and the lever arm are held constant. Somewhat surprisingly, the pile with a length of $L = 30$ m shows the lowest value of horizontal displacement at $N = 2$ but the largest horizontal displacement at $N = 10^4$ cycles. This is because the larger lateral resistance near the pile tip of the longer piles gets activated only for larger pile head deformations, increasing the overall resistance with ongoing cyclic loading stronger than for the shorter pile. The simulation with a length

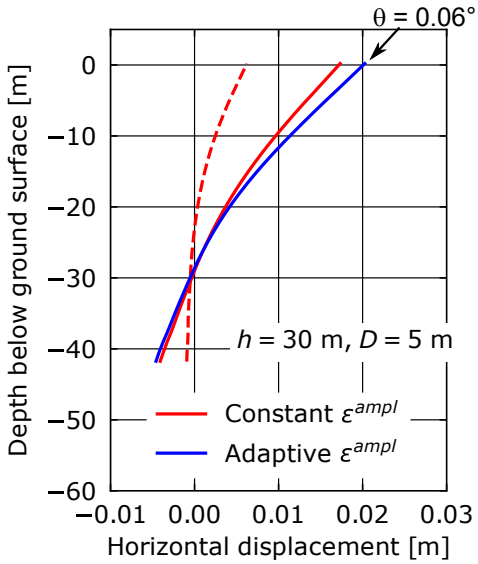

Figure 8.64: Comparison of the lateral deflection curves of monopiles at $N = 2$ (dashed) and at $N = 10^4$ (solid). The simulations are performed with constant $\varepsilon^{\text{ampl}}$ or with adaptive $\varepsilon^{\text{ampl}}$ with an update every 10th increment. A diameter $D = 5$ m, a lever arm $h = 30$ m, a monopile length of $L = 42$ m and a wall thickness of $t = 8$ cm are set for both simulations.

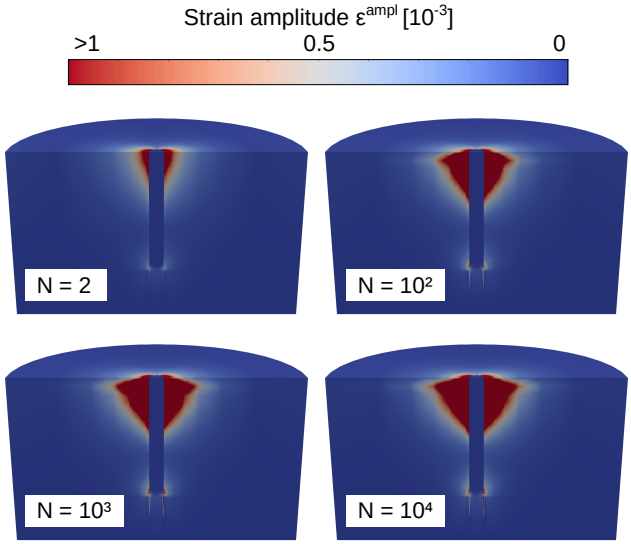

Figure 8.65: Fields of strain amplitude at $N = 2,\ 10^2,\ 10^3,\ 10^4$ for the simulation with adaptive strain amplitude with the lateral deflection line given in Fig. 8.64

of $L = 30$ m shows almost no bending of the pile at $N = 10^4$ compared to the other two piles.

Simulations considering different pile diameters of $D = \{5, 7, 9\}$ m but a constant pile length of $L = 30$ m and lever arm of $h = 30$ m are displayed in the right-hand plot of Fig. 8.66. Note that the average and amplitude values of the moment are again increased linearly with respect to the pile diameter. Similar to the results of the variation of the pile length, under the given loading conditions an increase in pile diameter does not necessarily reduce the lateral pile deflection. The piles with $D = \{7, 9\}$ m both show larger displacement at $N = 2$ cycles compared to the pile with $D = 5$ m. The same holds true for the deflection lines at $N = 10^4$ cycles. The pile with a diameter of $D = 9$ m tilts slightly less than the pile with $D = 7$ m. These findings are in accordance with the results for the monotonic loading of the pile since the ultimate moment increases less than linear with increasing pile diameter. In a similar study on monopiles in sand presented by the author in [357], the pile deflection decreased significantly

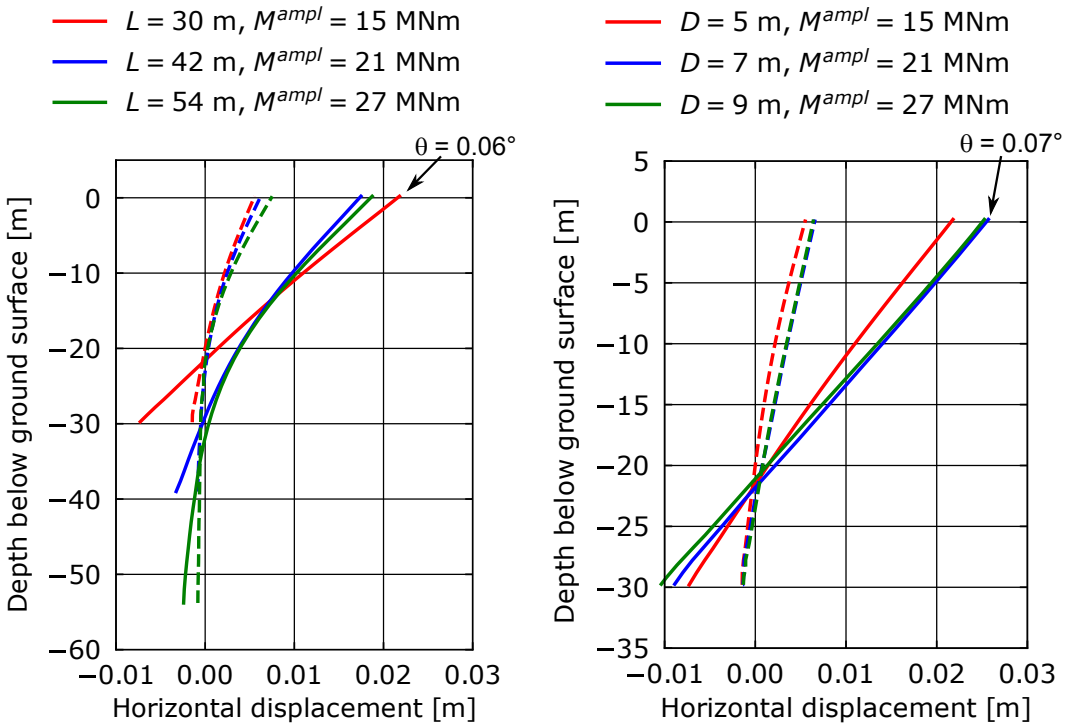

Figure 8.66: Comparison of the lateral deflection curves of monopiles with different lengths L (left-hand plot) or different diameters D (right-hand plot) at $N = 2$ (dashed) and at $N = 10^4$ (solid). The cyclic loading magnitude is increased linearly with increasing pile length or increasing pile diameter ($M^{\mathrm{av}} = M^{\mathrm{ampl}}$). A wall thickness of $t = 8$ cm is set in all simulations. The diameter is $D = 5$ m for the variation of L and the length is $L = 30$ m for the variation of D.

with increasing diameter despite the linear increasing load magnitude.

The influence of the wall thickness of the pile is investigated in Fig. 8.67. A small reduction in permanent deformation of the pile with a wall thickness of $t = 10$ cm is observed at $N = 2$ and $N = 10^4$ cycles compared to the pile with $t = 8$ cm.

Finally, the influence of layered soils composed of sand and clay layers on the long-term behaviour of the pile is investigated in Fig. 8.68. Two configurations of layered subsoil are investigated: either the upper 6 m of soil consist of sand and the lower 74 m of clay or reverse. The sandy soil is modelled using the Sanisand model for the low-cycle phase and the HCA model for sand for the high-cycle phase. For both constitutive models the material parameters of "Karlsruhe fine sand" are used (see Table 8.12 for the parameters of Sanisand and Table 8.11 for the parameters of the HCA model for sand). Initially medium dense ($D_{r0} = 60$ %)

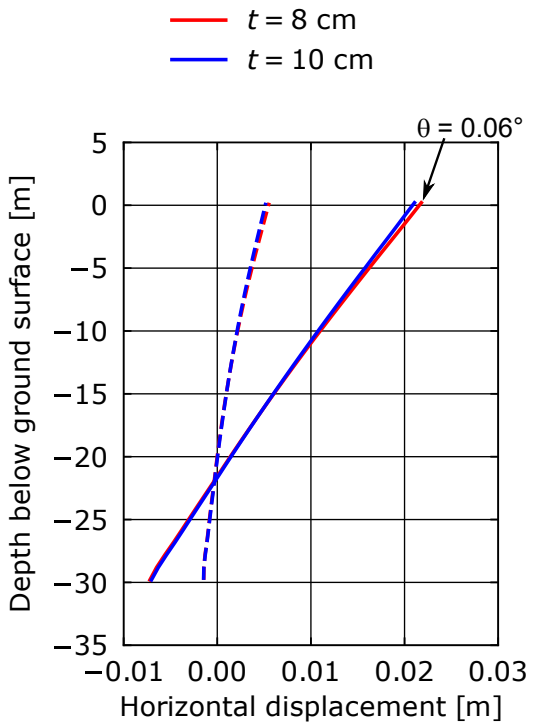

Figure 8.67: Comparison of the lateral deflection curves of monopiles with different wall thicknesses t at $N = 2$ (dashed) and at $N = 10^4$ (solid). A diameter $D = 5$ m and a monopile length of $L = 30$ m are set for both simulations.

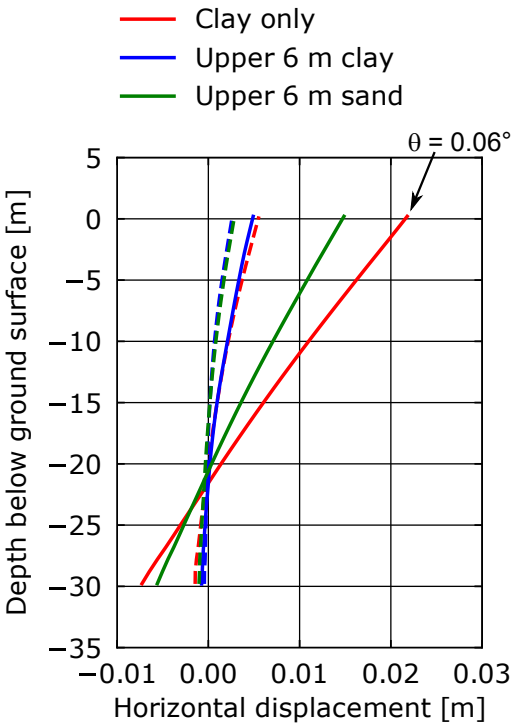

Figure 8.68: Comparison of the lateral deflection curves of monopiles at $N = 2$ (dashed) and at $N = 10^4$ (solid) for layered subsoil with different configurations. Simulations considering clay only, a 6 m thick layer of clay at the ground surface with sand below and a 6 m thick layer of sand at the ground surface with clay below are displayed. A diameter $D = 5$ m and a monopile length of $L = 30$ m are set in all cases.

conditions and a hydraulic conductivity of $k^w = 10^{-4}$ m/s are assumed for the sand. The initial conditions are defined analogously to the definitions used for the analyses presented in Section 8.4. Unsurprisingly, the consideration of a sand layer reduces the deformations of the pile significantly. For the configuration with an upper clay layer of 6 m, the lowest horizontal displacement at $N = 2$ and $N = 10^4$ of all simulations is found. The deflection line at $N = 2$ is similar for both simulations with layered soil but the deformation at $N = 10^4$ is significantly larger for the configuration with the sand layer at the ground surface.

8.7 Installation and subsequent lateral loading of monopile foundations in clay

The influence of the installation process of monopile foundations in clay on their response to subsequent lateral loading is investigated in the following. Up to now, no such study has been documented in the literature. Despite a large number of numerical studies on piles in clay subjected to lateral loading (see, for example, [224, 279, 441]), the assumption of WIP conditions has never been shown to be justified.

So far, pile installation processes in clay have mainly been investigated using analytical or simplified numerical methods. Particularly noteworthy are the cavity expansion methods (see, for example, [305, 208, 10, 315, 80, 142, 219]), which assume changes in soil state due to the installation process in radial direction only, and the strain path methods (see, for example, [33, 327, 426, 264]), which additionally consider a dependence in vertical direction. [88] presented an approach using thin plane strain discs, modelling the soil with a rather sophisticated hypoplastic clay model and assuming ideally undrained conditions. Earlier applications of FE techniques to the analysis of cone penetration tests, considering the "complete" installation process in one model, can be found in [336]. Recent studies of cone penetration tests in clay utilising particle FE techniques are reported in [253, 153, 445].

No attempt has yet been made to simulate the complete installation process of open-profile piles in clay considering partially drained conditions. Such analyses are discussed in the following.

8.7.1 Simulation of the installation process

The CEL model used in Section 8.3.2 is adopted. In contrast to the previous two sections, the (standard) Modified-Cam-Clay (MCC) model [317] instead of the AVISA model is used as constitutive model. This is because the MCC model was found to be numerically more robust for the simulation of the installation using the hydro-mechanically coupled CEL method. Since only monotonic jacking is considered as installation technique, the MCC model is judged to be sufficient to study the installation-induced changes in the soil state. Note that a user-defined implementation of the MCC model is employed since the hydro-mechanically coupled extension of the CEL method only works with user-materials in `Abaqus`. The model is implemented by the author using a radial-return mapping algorithm as proposed in [55].

Analogously to the simulations presented in the previous section, "Karlsruhe kaolin" with the

λ	κ	ν	M
0.13	0.05	0.3	1

Table 8.16: Material parameters of "Karlsruhe kaolin" for the MCC model [373]

material properties summarised in Table 8.16 for the MCC model is considered as soil. The same critical stress ratio $M(\varphi_c = 25°) = 1$ is used for compression and extension, respectively.

Different values of initial OCR are studied. In overconsolidated soils, the influence of OCR on the lateral stress coefficient K_0 should be considered. K_0 is calculated using the relation

$$K_0 = [1 - \sin(\varphi_c)] \cdot \mathrm{OCR}^{\sin(\varphi_c)} \tag{8.11}$$

proposed in [250], which has been applied in [212, 338] as well. A hydraulic conductivity of k^w = 10^{-8} m/s is assumed. The installation is performed velocity controlled with a value of 0.3 m/s. The jacking velocity influences only the inertia forces and the consolidation.

Note that the choice of the height of free water table is of great importance for the simulation of the installation in clay, since cavitation has to be accounted for. Numerically, cavitation is considered by the following equation:

$$\frac{n}{\bar{K}^w}\dot{p}^w = \begin{cases} -\mathrm{div}\left\{ \dfrac{K^{\mathrm{Perm}}}{\eta^w} \left[-\mathrm{grad}(p^w) + \bar{\rho}^w \left(\boldsymbol{b} - \ddot{\boldsymbol{u}}^s \right) \right] \right\} - \mathrm{div}(\dot{\boldsymbol{u}}^s) & \text{if } p^w + \dot{p}^w \Delta t \geq -100 \text{ kPa} \\ 0 & \text{if } p^w + \dot{p}^w \Delta t < -100 \text{ kPa} \end{cases} \tag{8.12}$$

Eq. (8.12) is essentially the mass balance of the pore water for fully saturated conditions. Therein, n is the porosity, $\bar{K}^w$ is the bulk modulus of the pore water, $\dot{p}^w$ is the rate of pore water pressure, K^{Perm} is the permeability of the soil, η^w is the dynamic viscosity of the water, p^w is the pore water pressure relative to the atmospheric pressure (assumed to be 100 kPa), $\bar{\rho}^w$ is the density of water, $\boldsymbol{b}$ is the gravity vector, $\ddot{\boldsymbol{u}}^s$ is the acceleration of the solid phase, $\dot{\boldsymbol{u}}^s$ is the velocity of the solid phase and Δt is the time increment. Unless mentioned otherwise, the water level is assumed to be 10 m above the seabed. This shallow water depth is chosen because, as will be explained below, a pile penetration depth of only 8 m is achieved.

The simulations are performed assuming a frictionless contact, except one simulation for which the Coulomb friction model with a friction coefficient of $\mu = 0.25$ is used (a value of 0.125 is set in the definitions of the analysis, see Section 8.3.2). In analogy to the simulations of the installation of piles in sand in Section 8.3.2, the incorrect consideration of effective normal

contact stresses in hydro-mechanically coupled CEL simulations with `Abaqus` is circumvented to some extent by defining a temperature ($= \Delta p^w$)-dependent friction coefficient, reducing with increasing excess pore water pressure Δp^w. The same Eq. (8.9) is applied and the frictional stress is limited to $t_{T,crit} = 100$ kPa as well.

In Fig. 8.69a the pile penetration versus the jacking force is shown for different initial OCR values. All four simulations are performed assuming a frictionless contact ($\mu = 0$) and a water level above the seabed of $H^w = 10$ m. As expected, the higher the initial value of OCR, the higher is the jacking force required to reach the targeted penetration depth. A comparison with a simulation considering a friction coefficient of $\mu = 0.25$ for an initial OCR of 3 is shown in Fig. 8.69b. The influence of the friction of the pile shaft is rather small, which justifies the use of a frictionless contact for the other simulations. The frictionless contact is preferred due to improved numerical stability. To investigate the influence of cavitation, Fig. 8.69c depicts the results of a simulation where the water table is assumed to be at ground surface level ($H^w = 0$ m) for an initial OCR of 6. Since the negative excess pore water pressure can reach smaller values in the case of $H^w = 10$ m compared to $H^w = 0$ m, a higher pile resistance is observed for $H^w = 10$ m.

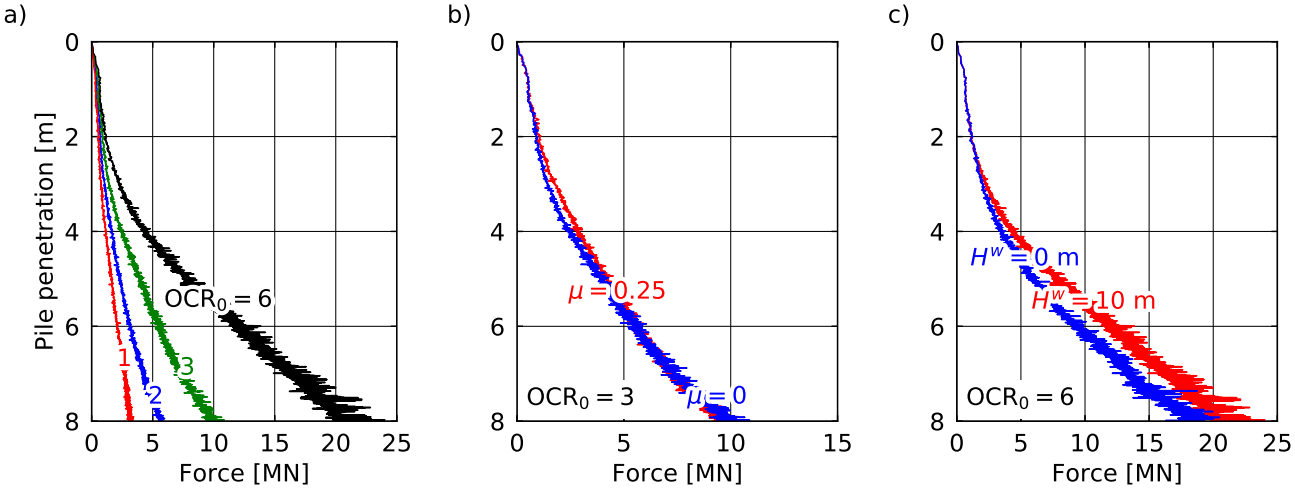

Figure 8.69: Pile penetration vs. jacking force for different values of initial OCR (a), different values of friction coefficient μ (b) and different heights H^w of water table above the seabed (c)

The spatial distributions of excess pore water pressure, effective radial stress and OCR are shown in Fig. 8.70 for initial values of OCR of $\text{OCR}_0 = 2$ and $\text{OCR}_0 = 6$. Note that the geotechnical sign convention is used for the effective radial stress. For $\text{OCR}_0 = 6$, a much

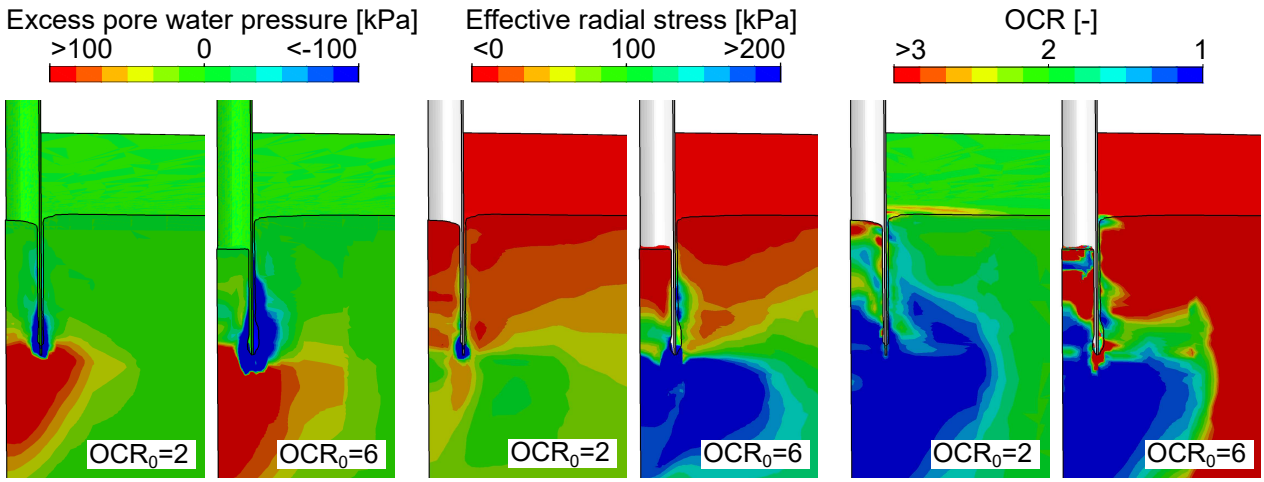

Figure 8.70: Spatial distributions of excess pore water pressure, effective radial stress and OCR at a pile penetration depth of 8 m for an initial OCR of $OCR_0 = 2$ and $OCR_0 = 6$, respectively

larger area with negative excess pore water pressures is observed at the pile shaft. In addition, slightly larger positive excess pore water pressures are generated below the pile tip. The soil inside the pile tends to move downwards with the pile in the case of $OCR_0 = 6$, which is not the case for $OCR_0 = 2$. Large differences between the two simulations are also observed for the field of effective radial stress. In the case of $OCR_0 = 6$, much higher values occur near the pile. While the effective stress below the pile tip is reduced for the lower value of the initial OCR, opposite trends are observed for the higher initial OCR. The higher values of effective radial stress and negative excess pore water pressure are not unexpected considering that the jacking force given in Fig. 8.69a is also much higher for $OCR_0 = 6$. Due to the larger negative excess pore water pressure at the pile shaft for $OCR_0 = 6$, the effective radial stress at the pile shaft increases much more compared to the simulation assuming $OCR_0 = 2$. However, for a larger distance from the pile shaft, both simulations show a strong decrease of the effective radial stress compared to the initial value (h/R effect). The reduction of the radial stress with increasing h/R is more pronounced in the case of $OCR_0 = 2$. For the installation of piles in sand [404, 403, 183, 433], the negative excess pore water pressures tend not to be as large as in clay (or are not existent at all), for why the effective radial stress is lowest at the pile shaft. This is not the case for an installation in clay, where in particular the simulation with a higher initial value of OCR shows large values of effective stress at the pile shaft due to negative excess pore water pressure. The spatial distribution of OCR demonstrates that the installation process drastically reduces the initial OCR below the pile tip for both the initially slightly overconsolidated ($OCR_0 = 2$) and the initially more overconsolidated ($OCR_0 = 6$)

soil. This is due to the fact that the mean effective stress increases significantly below the pile tip for both simulations, particularly the vertical component of the effective stress tensor. In agreement with the observed effective stress ratios at the pile shaft, larger OCR values relative to the initial values are observed for $\mathrm{OCR}_0 = 2$ as the effective stresses decrease. This is less pronounced in the simulation with $\mathrm{OCR}_0 = 6$, which is due to the larger negative excess pore water pressures already mentioned.

Fig. 8.71 shows the spatial distributions of excess pore water pressure, effective radial stress and OCR for a simulation with an initial OCR of 3 assuming a frictionless contact and a friction coefficient of $\mu = 0.25$, respectively. The frictionless simulation with $\mathrm{OCR}_0 = 3$ shows similar trends in the spatial distributions as observed in Fig. 8.70 for $\mathrm{OCR}_0 = 2$ and $\mathrm{OCR}_0 = 6$. Slightly larger negative excess pore water pressures, larger effective radial stresses and lower OCR values are encountered at the pile shaft compared to the simulation with $\mathrm{OCR}_0 = 2$. Between the frictionless simulation and the simulation setting $\mu = 0.25$ in Fig. 8.71 only minor differences are observed. When friction is taken into account, slightly larger effective radial stresses are obtained near the pile shaft. Accordingly, somewhat lower values for OCR are found in this area. Overall, however, the differences are rather small, which justifies the assumption of a frictionless contact.

Plots of the normalised effective radial stress $\sigma_r/\sigma_{r,0}$ and normalised excess pore water pressure p^w/p_0^w (including the pressure from the free water table $H^w = 10$ m above the seabed) with distance to the (outer) pile shaft for a depth of 5.2 m below the seabed are given for different values of h/R in Fig. 8.72 for initial values of $\mathrm{OCR}_0 = 2$ and $\mathrm{OCR}_0 = 6$. For each value of h/R, the spatial distribution of effective radial stress for $\mathrm{OCR}_0 = 2$ is given. In addition, the line along which $\sigma_r/\sigma_{r,0}$ and p^w/p_0^w are evaluated is depicted in Fig. 8.72.

When passing the pile tip ($h/R = 0$), the effective radial stress increases significantly at greater distance from the pile shaft for both initial values of OCR. In the immediate vicinity, however, there is a sharp decrease, which is limited to a very small soil zone. At greater distances from the pile tip, values greater than the initial effective radial stress are reached, which is more pronounced in the case of the simulation with a higher initial OCR. In the case of $\mathrm{OCR}_0 = 6$, the trend of the normalised pore water pressure p^w/p_0^w is qualitatively very similar to that of the effective radial stress. For $\mathrm{OCR}_0 = 2$ and for larger values of h/R, opposite trends are observed, as can be seen from the plots for $h/R = 0.7$. For this depth, both simulations show qualitatively similar trends for both the effective radial stress and the excess pore water pressure. As observed earlier, the higher initial OCR value leads to higher negative pore water pressures and thus higher effective radial stresses near the pile shaft. At

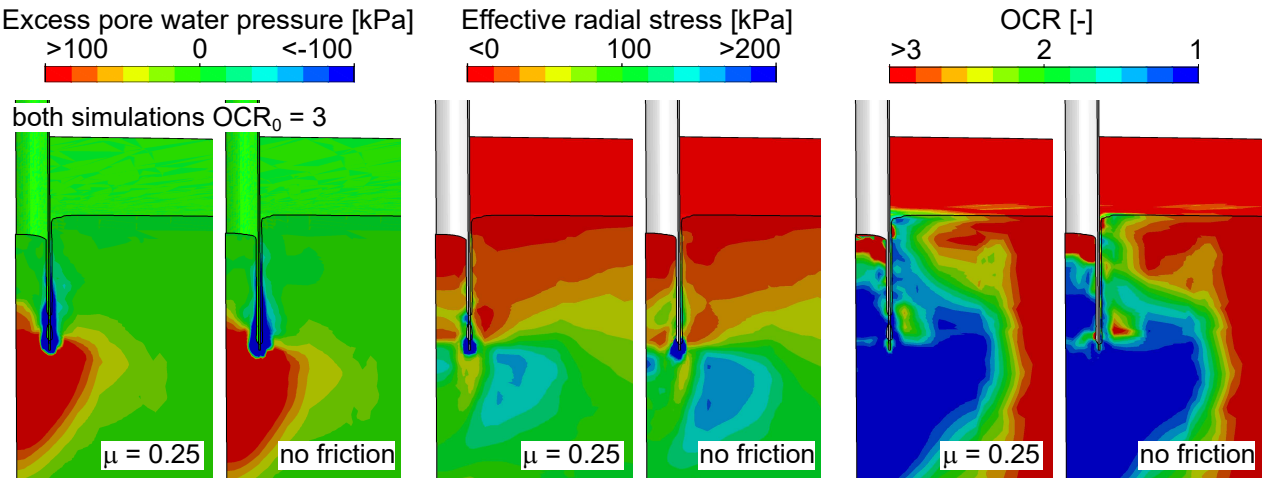

Figure 8.71: Spatial distributions of excess pore water pressure, effective radial stress and OCR at a pile penetration depth of 8 m for an initial OCR of $OCR_0 = 3$ assuming a frictionless contact or a friction coefficient of $\mu = 0.25$

greater distance from the pile shaft, almost no excess pore water pressures occur in either simulation and the effective radial stress decreases from $h/R = 0$ to $h/R = 0.7$. The decrease with increasing distance from the pile continues as pile penetration progresses, as can be seen from the diagram for $h/R = 1.7$. While in the simulation with $OCR_0 = 2$ the values of the effective radial stress are almost identical to the initial values even near the pile shaft, the effective radial stress near the pile shaft continues to increase in the case of $OCR_0 = 6$. This increase occurs despite a decrease in the negative excess pore water pressures.

Compared to the pile installation process in sand, where the effective radial stress tends to decrease near the pile shaft with increasing h/R, piles in clay show an opposite tendency, especially for higher values of initial OCR. This is consistent with research reported in [211, 51, 210], which found higher effective stresses for higher values of initial OCR prior to installation.

8.7.2 Lateral loading following the installation process

Monotonic lateral loading following the installation

A schematic representation of the studied example of an offshore wind turbine founded on a monopile is shown in Fig. 8.73a. The load due to wind and water waves is assumed to act at identical frequency, so it is sufficient to consider only a total horizontal force acting 8 m above the seabed. The adopted FE model is given in Fig. 8.73b, in conjunction with the field of excess pore water pressure following the installation with an initial OCR of 3.

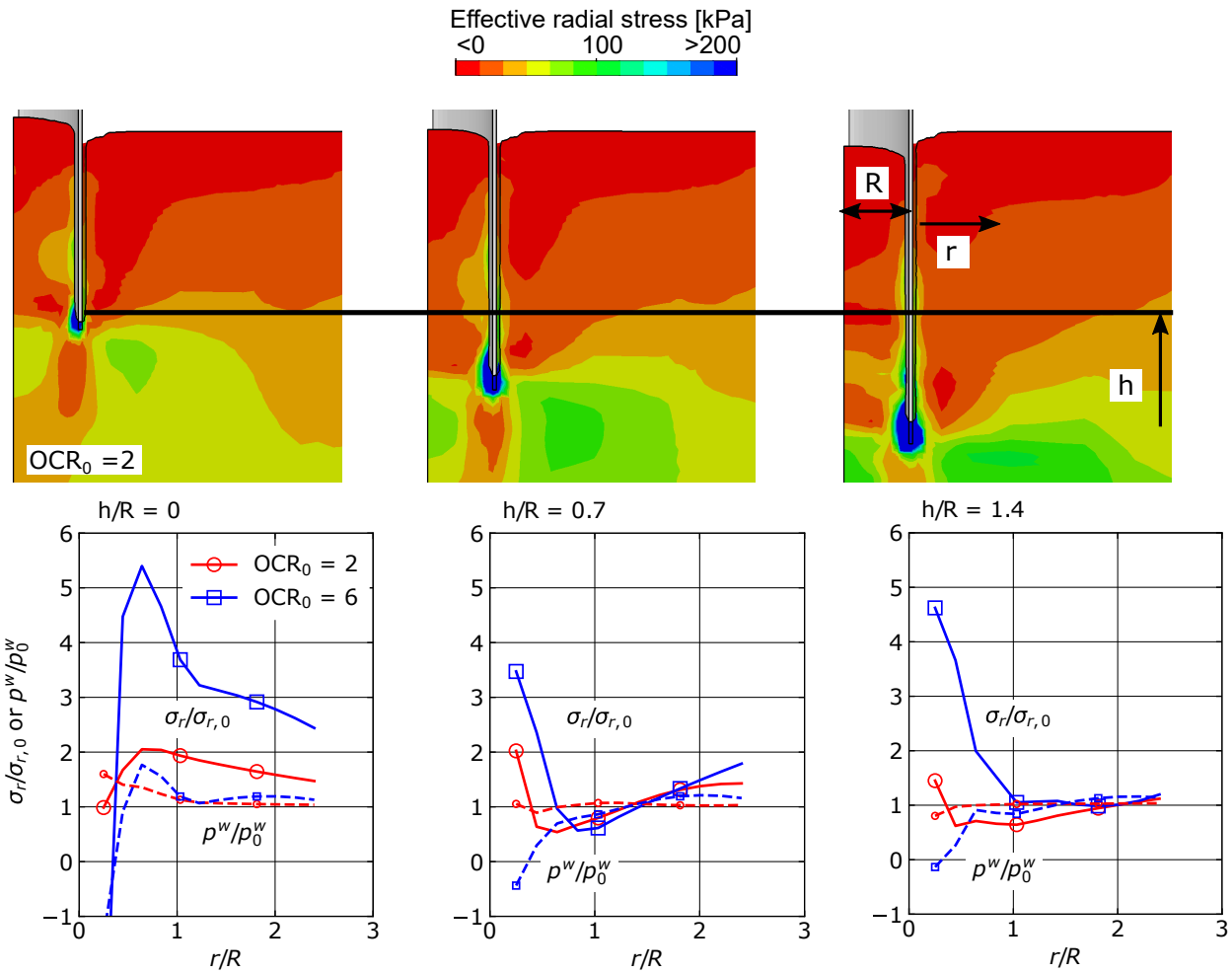

Figure 8.72: Spatial distribution of effective radial stress and corresponding plots of normalised effective radial stress $\sigma_r/\sigma_{r,0}$ (solid) and normalised excess pore water pressure p^w/p_0^w (dashed) vs. normalised radial distance r/R from the pile shaft in a depth of 5.2 m at different values of h/R for an initial OCR of $\mathrm{OCR}_0 = 2$ and $\mathrm{OCR}_0 = 6$

In addition to the simulations that take into account the installation-induced soil changes, WIP simulations are carried out. For these analyses, a constant density, a K_0-stress state and a hydrostatic pore water pressure distribution are assumed. The same relationship between the initial OCR and K_0 given by Eq. (8.11) is used.

The same procedures as described in Section 8.3.2 are applied for the analysis of lateral loading following the installation process. However, for the consolidation phase prior to lateral loading, $2 \cdot 10^6$ s $\approx$ 25 days are considered in order to secure that all excess pore water pressures caused by the installation process are dissipated. The average time to install the pile and turbine of the offshore wind turbine in reality is about 5 days [199]. Therefore, the pile could be loaded

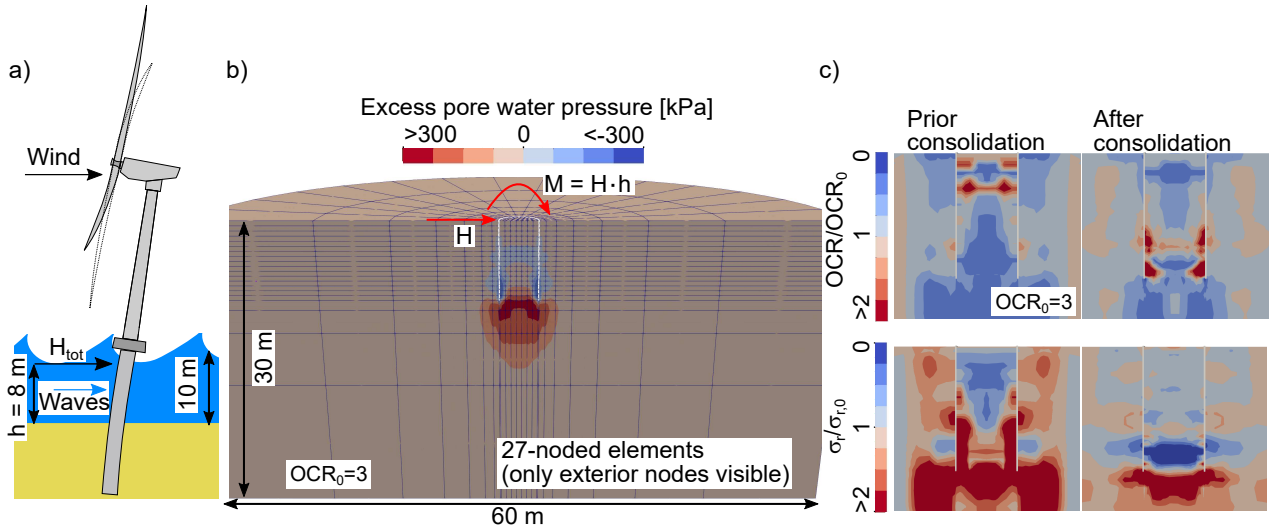

Figure 8.73: a) Schematic of an offshore wind turbine and assumed lever arm h of the combined horizontal force of wind and water waves. b) Numerical model to analyse the lateral loading of the pile after installation and the transferred spatial distribution of the excess pore water pressure after jacking with an initial OCR of 3. Note that only the outer nodes of the finite elements are visible. c) Spatial distributions of normalised OCR and normalised horizontal effective stress $\sigma_r/\sigma_{r,0}$ before and after the consolidation process for the jacked pile with $\mathrm{OCR}_0 = 3$.

by wind and water waves before the hydrostatic conditions are reached. Such a scenario is not considered in order to allow a clear comparison with the WIP simulations, which also assume hydrostatic conditions.

Since only 8 m of penetration depth are achieved for the piles in clay, the pile in the fully Lagrangian analysis in `numgeo` has also only a length of 8 m. The remaining geometrical specifications are analogous to those used in Section 8.3.2. The MCC model is employed for the monotonic loading as well as for the low-cycle phase preceding the simulation of the high-cycle phase with the HCA model for clay. The same material parameters as for the simulation of the installation process are adopted.

The following steps are performed for the monotonic loading of the piles:

1. After transferring the void ratio, effective stress, OCR and excess pore water pressure, a consolidation analysis is performed before loading the pile. $2 \cdot 10^6$ s $\approx$ 25 days are considered, which is sufficient time for the dissipation of all excess pore pressure. The soil-pile system is allowed to deform such that static force equilibrium is achieved. This is necessary because the system is not in static force equilibrium at the end of the instal-

lation process due to inertial forces. As a result, the soil shows a maximum displacement of ≈ 5 mm in this calculation phase. For the WIP simulation, only the contact between pile and soil is initialised in this step.

2. The pile is loaded vertically with a magnitude of 0.2 MN to account for the weight of the structure supported by the pile. Compared to the vertical loads in real wind farms, this load is rather small, even if the lower embedment length is accounted for. This is because in the WIP simulations, larger values of vertical load lead to very large vertical displacements of up to 1 m for $\mathrm{OCR}_0 = 1$, indicating a failure of the pile that cannot be modelled with a fully Lagrangian model. This is not the case for the jacked pile, where only small vertical displacements are observed (≈ 4 cm for the jacked pile vs. ≈ 40 cm for the WIP simulation in case of $\mathrm{OCR}_0 = 1$ and a load of 0.2 MN). These results already demonstrate the importance of considering the installation process, since the application of a realistic vertical load is not possible in case of the WIP simulations.

3. The moment applied at seabed level, see Fig. 8.73a, is linearly increased until a rotation of 4° is reached at the pile head. Assuming a lever arm of 8 m, the horizontal load is increased linearly at the same time. This step is carried out either assuming ideally drained conditions or partially drained conditions with a hydraulic conductivity of $k^w = 10^{-8}$ m/s. In the latter case, the loading required for a pile head rotation of 2° is approximately reached at 10 s of loading, resulting in nearly ideally undrained conditions during loading.

Figure 8.73c shows the spatial distributions of normalised OCR ($\mathrm{OCR}/\mathrm{OCR}_0$) and normalised horizontal effective stress $\sigma_r/\sigma_{r,0}$ before and after the consolidation phase performed in step 1 for the simulation assuming an initial OCR of 3. The fields before consolidation correspond to the transferred fields from the installation simulation. The consolidation process changes both fields significantly. As the negative excess pore water pressure dissipates at the pile shaft, the effective radial stress decreases, leading to an increase in OCR, especially inside the pile. At greater distances from the pile shaft, values greater than $\mathrm{OCR}_0 = 3$ are also achieved. In addition, an increase in OCR below the pile tip is observed. Here, two opposing effects are at work, namely the increase in effective stress due to dissipation of the positive excess pore water pressure and the decrease of the effective stress due to the unloading of the pile by releasing the jacking force. Apparently, the second effect outweighs the first. Figure 8.73c shows that strong installation-induced changes in the soil state are present even after consolidation is completed.

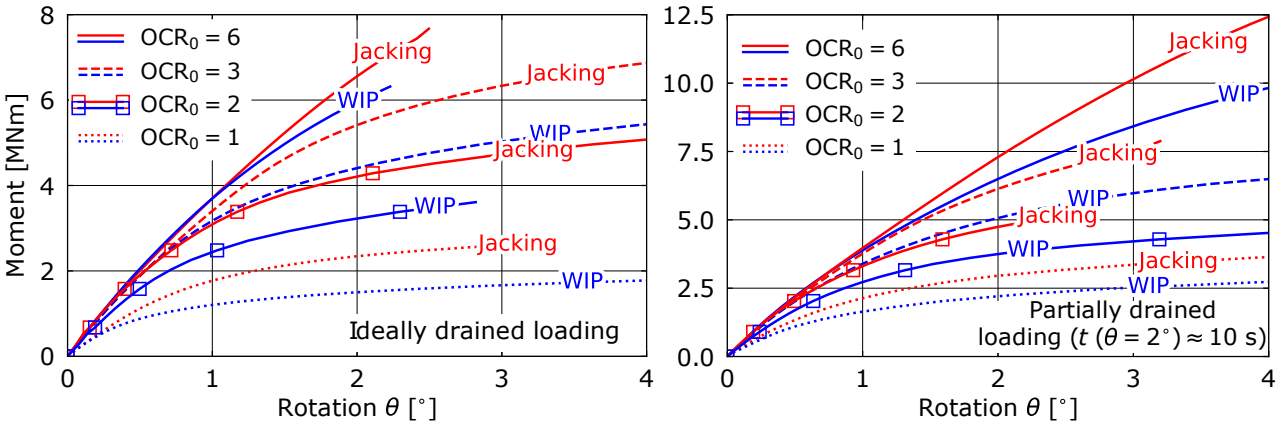

Figure 8.74: Comparison of moment vs. rotation plots of jacked and WIP piles assuming ideally drained conditions (left-hand plot) and partially drained conditions (right-hand plot), respectively, for different values of initial OCR (moments are given for a full 3D model)

The results of the monotonic load tests for four different values of initial OCR are shown in Fig. 8.74. Two different loading scenarios are investigated. Either the load is increased linearly, assuming ideally drained conditions (left-hand plot) or partially drained conditions (right-hand plot). Note that some simulations do not converge when the load is increased further, which is why not all results are shown up to a rotation of 4°. Not surprisingly, accounting for partially drained conditions (including the change in pore water pressure) results in higher pile head moments, as negative excess pore water pressure significantly increases resistance. This is more pronounced for larger values of OCR_0. Very similar responses for jacked and WIP piles are observed for the initial phase of monotonic loading for both drainage conditions. However, at high values of rotation, the WIP piles exhibit lower resistance than the jacked piles. This is true for all values of OCR_0 and becomes even more evident for higher values of initial overconsolidation ratio. The larger OCR_0, the greater is the rotation at which the jacked piles and the WIP piles begin to diverge. These results indicate that the assumption of WIP conditions is conservative with respect to pile rotation and that the stiffness of the soil-pile system at small rotations, an important aspect for the design of offshore wind turbine foundations, is not significantly affected by the installation-related changes in soil state.

High-cyclic lateral loading following the installation

After the first and second step in which the vertical load is applied (see the steps performed for the monotonic loading), the simulations with high-cyclic lateral loading are performed in

the following steps:

3. Application of the average value of the moment M^{av} and the average value of the horizontal load H^{av}. Both the moment and the horizontal load are applied at the level of the seabed, see Fig. 8.73a. Depending on the initial value of OCR, different load magnitudes are studied. The considered loading scenarios are listed in Table 8.17. For each case, the ratio of the average value of moment M^{av} to the moment resistance M^R at a rotation of 2° for the jacked pile is given. M^R is obtained from the drained monotonic tests displayed in Fig. 8.74. The magnitudes of M^{av} and H^{av} are identical for both the jacked and WIP piles. This step is performed ideally drained, assuming that there is sufficient time for any excess pore water pressures caused by the average loading to dissipate before the cyclic loading starts.

4. Application of the first load cycle with a horizontal load amplitude $H^{\text{ampl}} = H^{\text{av}}$ and a moment amplitude of $M^{\text{ampl}} = M^{\text{av}}$ (see Table 8.17). This and all subsequent steps are carried out considering partially drained conditions, i.e. excess pore water pressures and consolidation processes. A frequency of 0.1 Hz for the cyclic loading is assumed.

5. Repetition of the previous step, recording the strain path at each integration point of each soil element of the model. The strain amplitude is calculated at the end of the step

OCR_0	$M^R(\theta = 2°)$ [MNm]	$M^{\text{av}} = M^{\text{ampl}}$ [MNm]	$M^{\text{av}} / M^R(\theta = 2°)$
1	2.5	0.25	0.1
		0.5	0.2
2	4.2	0.25	0.06
		0.5	0.12
3	5.5	0.5	0.09
		0.75	0.14
6	6.5	0.75	0.12
		1.5	0.23

Table 8.17: Values of the average moment M^{av} and the amplitude of the moment M^{ampl} used for the analyses of the high-cyclic loading of the piles. Two different cases are considered for each initial value of OCR_0. In addition, for each cyclic loading scenario, the moment resistance M^R at a rotation of 2° (see left-hand plot of Fig. 8.74) for the jacked piles and the corresponding ratio of M^{av}/M^R are given.

based on the recorded strain path.

6. Simulation of 10^6 additional load cycles using the HCA model, applying only the average load H^{av} and M^{av}. To simulate $N = 10^6$ cycles with a frequency of 0.1 Hz, a total time of 10^7 s is considered. The strain amplitude is updated in every 10th calculation increment using the adaptive strain amplitude with a characteristic length of $l_c = 1$ m. This corresponds to updates at $N \approx \{3,\ 5,\ 12,\ 30,\ 100,\ 300,\ 10^3,\ 3 \cdot 10^3,\ 10^4,\ 3 \cdot 10^4,\ 8 \cdot 10^4,\ 2 \cdot 10^5,\ 4 \cdot 10^5,\ 5 \cdot 10^5,\ 6 \cdot 10^5,\ 6 \cdot 10^5,\ 8 \cdot 10^5\}$.

The normalised horizontal pile head displacement u/D as a function of time for the simulations with an initial OCR of 1 is shown in Fig. 8.75a and for an initial OCR of 2 in Fig. 8.75b for the jacked and the WIP piles, respectively. Two different values for the moment $M^{\mathrm{ampl}} = M^{\mathrm{av}}$ (and thus the horizontal load $H^{\mathrm{ampl}} = H^{\mathrm{av}}$) are compared. In the simulation with $\mathrm{OCR}_0 = 1$ and $M^{\mathrm{ampl}} = M^{\mathrm{av}} = 0.25$ MNm, the installation process influences both the short-term ($N \leq 10$) and the long-term ($N > 10$) response only insignificantly. However, the simulation taking into account the installation process leads to slightly larger pile head displacements in the long term. For the simulation with $\mathrm{OCR}_0 = 1$ and $M^{\mathrm{ampl}} = M^{\mathrm{av}} = 0.5$ MNm, the assumption of WIP initial conditions leads to larger short- and long-term displacements. Very large values of pile head rotation are already reached at $N = 10^2$ (10^3 s), leading to non-convergence of the simulation.

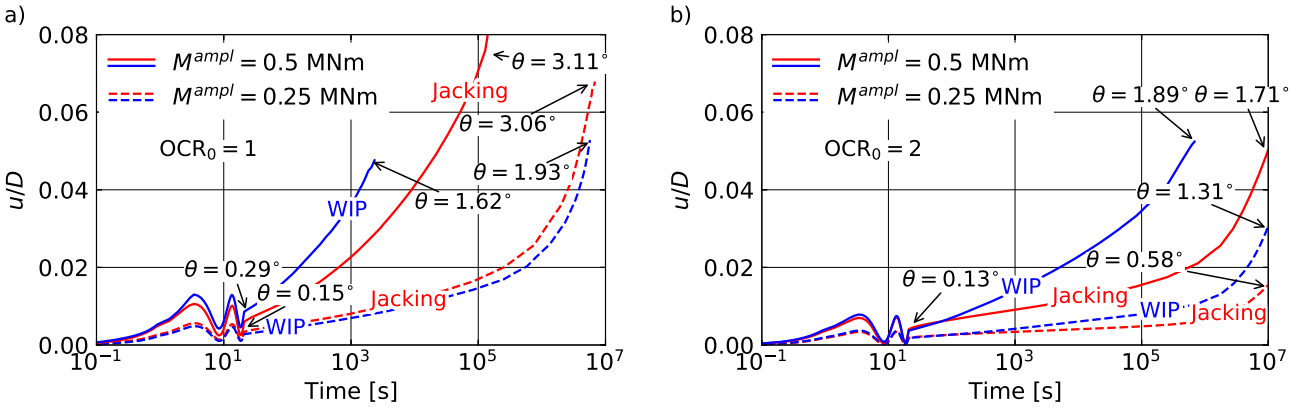

Figure 8.75: Comparison of normalised horizontal pile head displacement u/D vs. time plots of jacked and WIP piles for an initial OCR of 1 (a) and 2 (b). The load magnitudes are either $M^{\mathrm{ampl}} = M^{\mathrm{av}} = 0.5$ MNm and $H^{\mathrm{ampl}} = H^{\mathrm{av}} = 0.5/8$ MN (solid lines) or $M^{\mathrm{ampl}} = M^{\mathrm{av}} = 0.25$ MNm and $H^{\mathrm{ampl}} = H^{\mathrm{av}} = 0.25/8$ MN (dashed lines). The pile head rotation θ is given at $N = 2$ and at the end of the HCA phase.

A much larger influence of the installation process is found for an initial OCR value of 2, as can be seen from Fig. 8.75b. While both jacked and WIP piles result in similar pile head displacements for both load magnitudes in the short-term, the WIP simulations predict much greater deformations in the long-term. This is more pronounced for the higher load magnitudes.

Very similar observations can be made for the simulations with $OCR_0 = 3$, as can be seen from Fig. 8.76a. The negligence of the installation process leads to significantly larger deformations in the long-term for both load magnitudes. In contrast to the simulation with $OCR_0 = 2$, however, the WIP simulations result in somewhat smaller deformations in the short-term ($N \leq 10$). This is also evident from the results of the simulation with an initial OCR of 6, given in Fig. 8.76b. The WIP simulation results in lower pile head displacement up to $N = 10^2$ (10^3 s) for $M^{ampl} = M^{av} = 1.5$ MNm, but a much higher accumulation of deformations for larger numbers of load cycles. Similar but less pronounced tendencies are observed for the simulations with lower load magnitude. However, more load cycles are required before the WIP simulation shows larger deformations compared to the jacked pile.

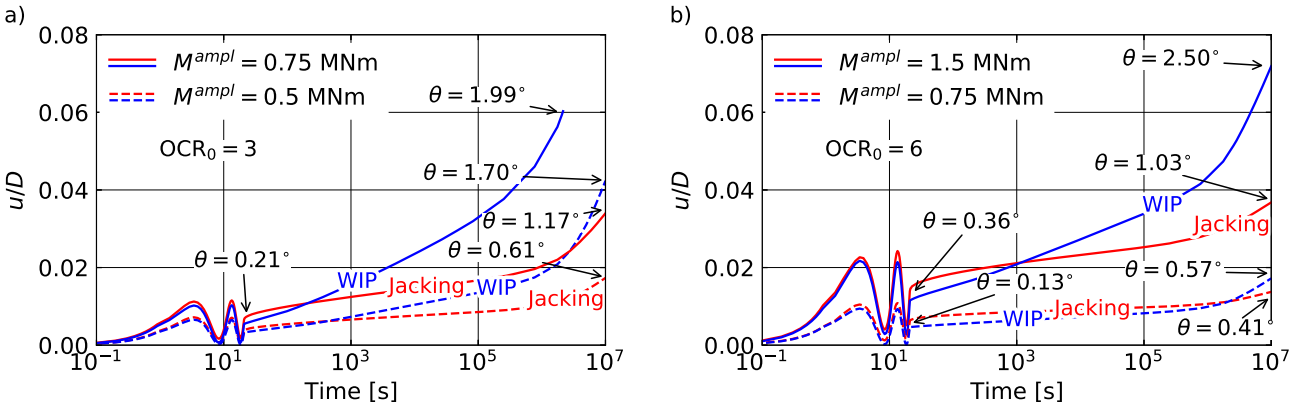

Figure 8.76: Comparison of normalised horizontal pile head displacement u/D vs. time plots of jacked and WIP piles for an initial OCR of 3 (a) and 6 (b). For $OCR_0 = 3$, the load magnitudes are either $M^{ampl} = M^{av} = 0.75$ MNm and $H^{ampl} = H^{av} = 0.75/8$ MN (solid lines) or $M^{ampl} = M^{av} = 0.5$ MNm and $H^{ampl} = H^{av} = 0.5/8$ MN (dashed lines). For $OCR_0 = 6$, the load magnitudes are either $M^{ampl} = M^{av} = 1.5$ MNm and $H^{ampl} = H^{av} = 1.5/8$ MN (solid lines) or $M^{ampl} = M^{av} = 0.75$ MNm and $H^{ampl} = H^{av} = 0.75/8$ MN (dashed lines). The pile head rotation θ is given at $N = 2$ and at the end of the HCA phase.

Overall, the simulations show that the installation has a significant influence on the long-term behaviour of the pile, especially for overconsolidated soils. The assumption of WIP conditions

tends to lead to higher accumulation rates and is therefore judged conservative with respect to the long-term cyclic behaviour of the pile. However, with increasing OCR, WIP conditions result in lower pile head displacements in the short term. Compared to the long-term cyclic behaviour, these differences between the two simulation types are smaller in the short-term.

To investigate by which effects the differences between the two simulation types are caused, the spatial distributions of the normalised mean effective stress (p/p_0) and OCR/OCR$_0$ at different times and numbers of cycles of the analyses, respectively, are given in Fig. 8.77a,b for the simulations with OCR$_0$ = 3. At $N = 2$, the mean effective stress in the case of the jacked pile is much higher at the pile tip and at the mean height of the pile compared to the WIP simulation. At $N = 10^5$, the mean effective stress is reduced significantly in the vicinity to the pile shaft for both analyses, but less for the jacked pile. At the same time, the spatial distribution of OCR shows much larger values around the pile shaft for the jacked pile as well. Since the mean effective stress at the outer pile shaft is initially larger in the case of the jacked pile, the potential increase in OCR is much larger with continued cyclic loading. Considering that the installation in clay with a higher initial OCR results in a large increase in effective stresses (see Fig. 8.70), but subsequent cyclic lateral loading results in a similarly

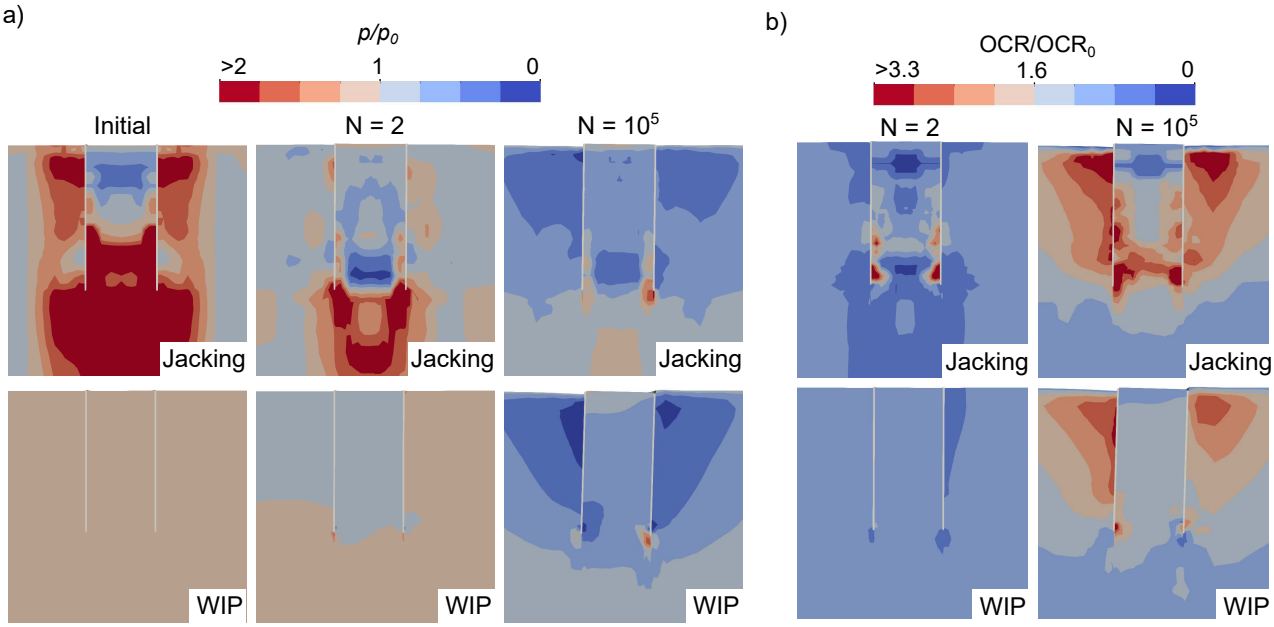

Figure 8.77: a) Spatial distributions of normalised mean effective stress p/p_0 for jacked and WIP piles at different times of the analyses. b) Spatial distributions of OCR/OCR$_0$ for the same simulations at $N = 2$ and $N = 10^5$. The deformed configurations without a scale factor are displayed (OCR$_0$ = 3 for all simulations).

large decrease in mean effective stresses, the OCR under cyclic lateral loading increases more for the jacked pile compared to the WIP simulation. Such a decrease in mean effective stress under cyclic lateral loading of piles in clay is also frequently observed in experiments and field tests, resulting in a reduction in the stiffness of the soil-pile system [299, 220, 200].

The spatial distributions of the strain amplitude at different numbers of load cycles are given in Fig. 8.78 for the jacked and WIP pile with $OCR_0 = 3$. As mentioned earlier, the strain amplitude is calculated from the second load cycle and updated several times during the high-cycle phase using the adaptive strain amplitude definition. This definition takes into account the change in soil stiffness due to changes in effective stress and void ratio. Since both the

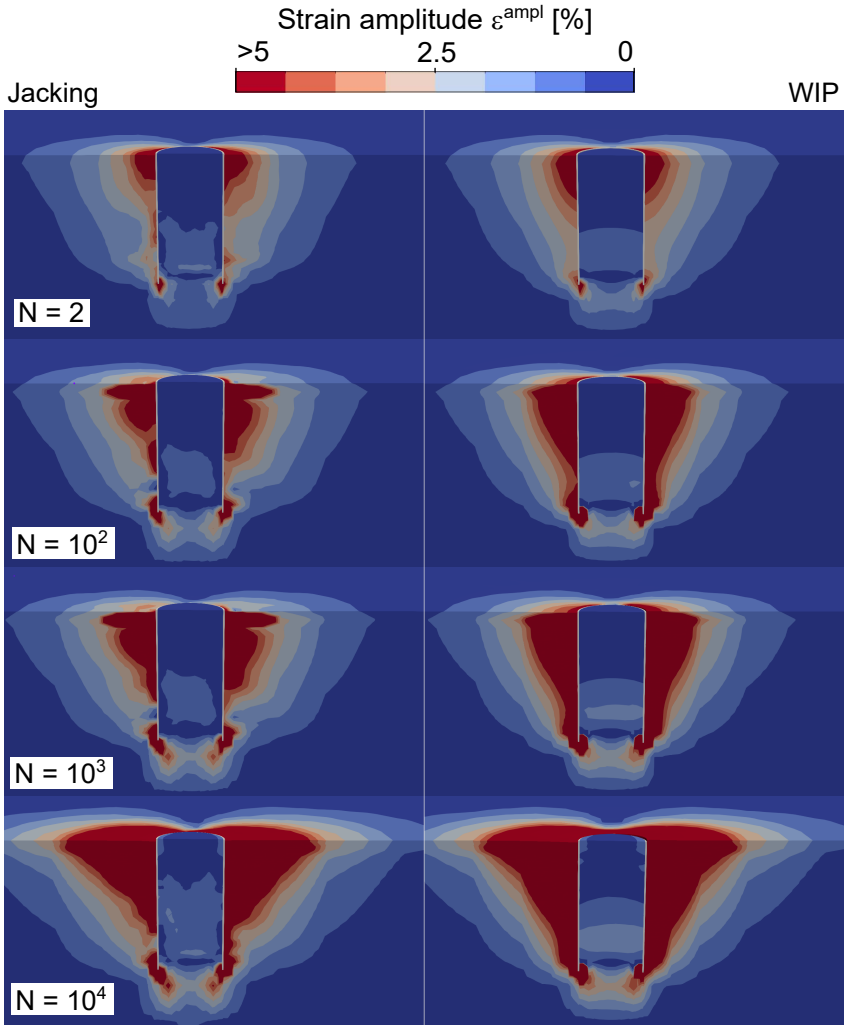

Figure 8.78: Spatial distribution of the strain amplitude at different numbers of load cycles for the jacked and WIP pile with $OCR_0 = 3$. The deformed configurations without a scale factor are displayed.

mean effective stress and the void ratio decrease during the high-cyclic loading (see Fig. 8.77 for the mean effective stress), the stiffness decreases as well. This results in a continuous increase of the strain amplitude with increasing number of load cycles. In accordance with the spatial distribution of the normalised mean effective stress given in Fig. 8.77, the strain amplitude for the jacked pile increases less compared to the WIP simulation. This is especially the case in the lower third of the pile. Around the pile head, the differences in the change in strain amplitude are less pronounced, with both distributions being comparable at $N = 10^4$. Therefore, the large differences between the two simulation types in the long-term behaviour of the pile observed in Fig. 8.76a are not due to differences in strain amplitude, but primarily caused by differences in OCR, as mentioned earlier.

The spatial distributions of the normalised excess pore water pressure $\Delta p^w / p_0^w$ (including the pressure from the free water table 10 m above the seabed) at different numbers of load cycles are given in Fig. 8.79 for $\mathrm{OCR}_0 = 3$. The WIP simulation predicts a higher accumulation of excess pore water pressures compared to the jacked pile. This is most prominent for the soil below the pile tip, where the jacked pile shows initially much higher values of mean effective stress compared to the WIP simulation (see Fig. 8.77).

The adaptive strain amplitude definition is used to account for the influence of the change in soil stiffness during the high-cycle phase on the strain amplitude calculated from the second load cycle. The significance of updating the strain amplitude is discussed in the following. Figure 8.80 shows the normalised horizontal displacement u/D of jacked piles with an initial OCR of 3 assuming a constant strain amplitude during the high-cycle phase (*const.* $\varepsilon^{\mathrm{ampl}}$) or using the adaptive strain amplitude definition ($\varepsilon^{\mathrm{ampl}}(N)$). As mentioned earlier, the strain amplitude is updated every 10th calculation increment during the high-cycle phase, giving a total of almost 20 updates.

Figure 8.80 shows that the assumption of a constant strain amplitude is justified up to $N = 10^4$ (10^5 s), but leads to a much lower accumulation of permanent pile head displacements for a larger number of load cycles. This is consistent with the spatial distribution of the strain amplitude given in Fig. 8.78, which shows the largest increase from $N = 10^3$ to $N = 10^4$. As explained earlier, the increase in strain amplitude is due to the decrease in mean effective stress and void ratio during the high-cyclic loading, which leads to a decrease in soil stiffness (and hence in stiffness of the soil-pile system as well). Figure 8.80 demonstrates that the assumption of a constant strain amplitude is not conservative, especially for a larger number of load cycles. Therefore, updating the strain amplitude for the HCA model for clay is considered mandatory when a large number of load cycles must be considered.

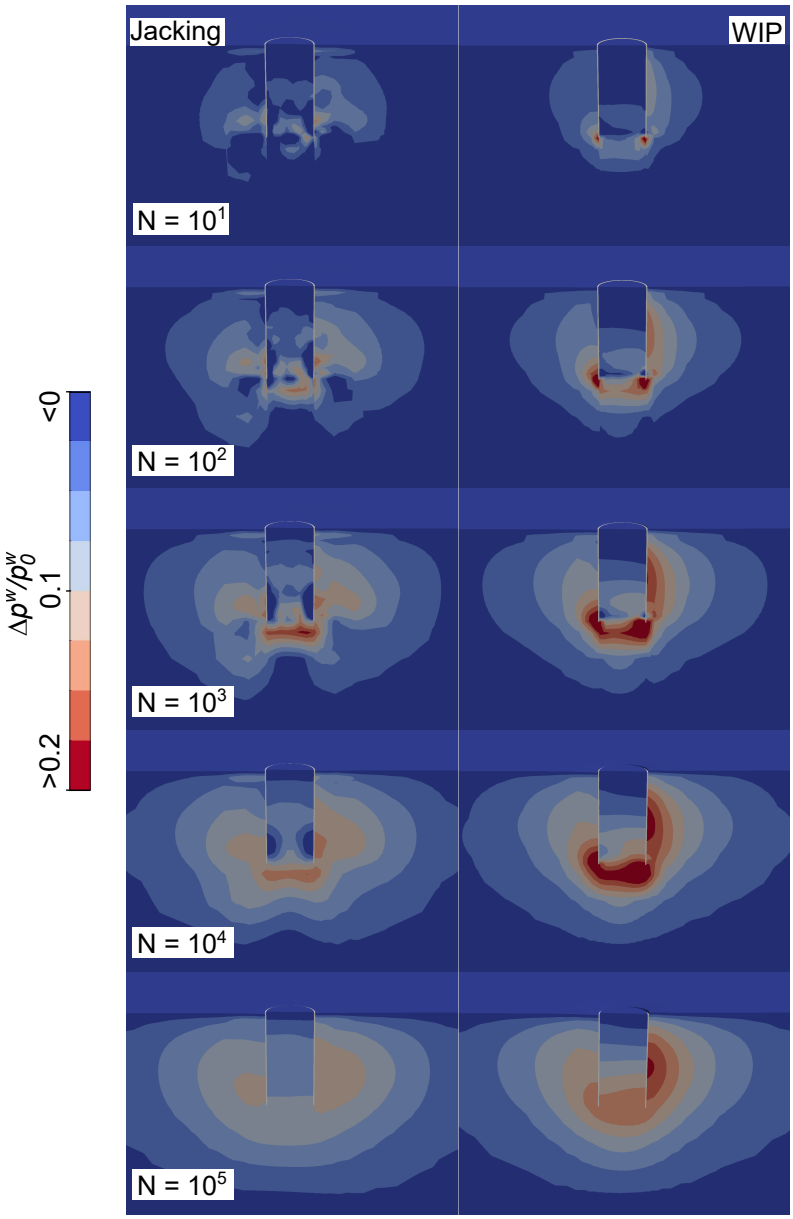

Figure 8.79: Spatial distribution of the normalised excess pore water pressure $\Delta p^w/p_0^w$ at different numbers of load cycles for the jacked and WIP pile with $\mathrm{OCR}_0 = 3$. The deformed configurations without a scale factor are displayed.

Overall, based on these simulations the influence of the installation on the response of the pile to lateral loading is judged to be comparatively small for the initial phase of monotonic or cyclic loading. For larger rotations or larger numbers of load cycles the jacked piles exhibit a larger resistance compared to the WIP piles. Therefore, in terms of resistance, WIP simulations are judged conservative. However, as has been shown for the installation of piles in sandy soils, these conclusions are certainly not universally valid. Strong influence of the

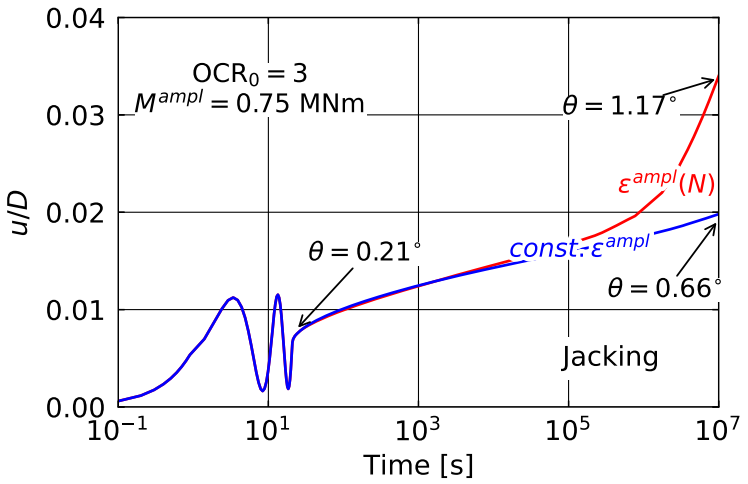

Figure 8.80: Comparison of normalised horizontal pile head displacement u/D vs. time plots of jacked piles for an initial OCR of 3 assuming a constant strain amplitude during the high-cycle phase (*const.* $\varepsilon^{\mathrm{ampl}}$) or using the adaptive strain amplitude definition ($\varepsilon^{\mathrm{ampl}}(N)$). The load magnitudes are $M^{\mathrm{ampl}} = M^{\mathrm{av}} = 0.75$ MNm and $H^{\mathrm{ampl}} = H^{\mathrm{av}} = 0.75/8$ MN.

drainage conditions during installation, the installation technique and specifications (including influence of the pile penetration rate), the pile geometry and the initial soil conditions is expected. In addition, the simulations performed utilise a rather simple constitutive model for the monotonic and low-cycle phase. Future work should investigate if the drawn conclusions hold also when employing more complex constitutive models, able to account for effects due to cyclic loading and anisotropy (e.g. the AVISA model).

Chapter 9

Summary and outlook

9.1 Summary

9.1.1 Hydro-mechanically coupled finite elements and investigation of relative acceleration

A five-phase model for the continuum-mechanics description of the soil has been adopted, allowing to consider free and residual fluid phases. Three phases (namely the solid, the free pore water and the free pore air) were assumed to move relative to each other. The governing equations for such a formulation have been derived and were discretised spatially using the finite element method in a Lagrangian framework. An implicit **u**-p-(p)-**U**-(**U**) element formulation has been derived and implemented, which discretises the displacement of the solid phase as well as the fluid pressures and the fluid displacements of the pore water and pore air phase. Existing finite element formulations are based on a **u**-p-(p) formulation, which does not discretise the pore fluid displacements. In the framework of the **u**-p-(p) formulation it is assumed that all phases have the same acceleration, which is a valid assumption only in case of modest dynamic wave frequencies and low hydraulic conductivity. No such assumption is required in case of the **u**-p-(p)-**U**-(**U**) formulation. Since there exists a lack of clarity in the literature regarding the influence of relative acceleration (and hence the applicability of the **u**-p-(p) formulation), a novel scheme to estimate the error made using the assumption of identical accelerations has been proposed. For this purpose, a semi-analytical solution for the wave propagation in a fluid-saturated 1D column has been developed, which, in contrast to existing solutions, takes into account the relative acceleration. It was then shown that for specific loading conditions this semi-analytical solution allows to express the influence of the

relative acceleration solely in terms of the highest wave frequency and hydraulic conductivity. The existing method to estimate the influence of relative acceleration requires to define a so-called characteristic length, which has no physical meaning and can be difficult to estimate. Using the novel approach, a threshold value of frequency of 50 Hz was identified at which relative acceleration still can be neglected. Lower values of frequency showed only insignificant influence of relative acceleration. In addition, only for a hydraulic conductivity larger than $\approx 5 \cdot 10^{-4}$ m/s any influence of relative acceleration was found.

The implementation of a **u**-p-(p)-**U**-(**U**) formulation in the finite element program `numgeo` and the comparison to other finite element formulations such as the **u**-p-(p) and the **u**-**U**-(**U**) formulation was presented. The element formulations have been validated based on the derived semi-analytical solution.

A hydro-mechanically coupled finite element formulation based on an Eulerian framework, which allows to simulate BVPs with large-deformations, and an explicit time integration using the commercial finite element program `Abaqus` has been proposed as an extension of an existing approach. The novelty of the proposed scheme lies in the consideration of the acceleration of the fluid phase, which has been neglected in the original approach. The proposed hydro-mechanically coupled Eulerian method showed a good accordance with the previously derived semi-analytical solution (in dependence of the number of finite elements used for the Eulerian calculation).

9.1.2 Constitutive models

Different advanced constitutive models for low-cyclic as well as high-cyclic loading have been implemented and partly extended in the framework of this thesis. The hypoplastic model with intergranular strain extension and the Sanisand model have been implemented anew in order to improve the numerical stability for the analysis of pile driving. The high-cycle accumulation (HCA) model for sand has also been implemented anew in order to enhance its convergence ratio in comparison to the existing implementation. In addition to the HCA model for sand, the HCA model for clay proposed in [406] has been implemented using a plastic strain rate based on the Modified-Cam-Clay model.

The HCA models have been extended by an adaptive strain amplitude, which enables to consider the change of soil stiffness on the strain amplitude during the high-cycle phase without the need to perform update cycles. A scaling with respect to the change in soil stiffness during high-cyclic loading was proposed, which, however, had to be combined with a nonlocal smoothing algorithm following the update of the strain amplitude in order to avoid localisation

of strain accumulation. The simulation of undrained cyclic triaxial tests showed that the application of the adaptive strain amplitude leads to a better approximation of the increase of excess pore water pressure as well as the strain amplitude measured in the experiment in comparison to simulations using update cycles.

9.1.3 Contact mechanics

In order to allow for numerical analyses involving contacting bodies using the in-house code `numgeo`, different mortar contact discretisation techniques were developed and implemented. An element-based mortar (EBM) discretisation technique allowing for the numerical analysis involving large deformations and non-matching surface meshes has been implemented for 2D and 3D analyses. A segment-based mortar (SBM) discretisation technique for 2D analyses has been developed as well. The SBM technique divides the surface pair into finite segments with arbitrary order of integration, allowing, in contrast to to simpler contact discretisation techniques, for an exact integration of contact stress. Additional notes about the application of so-called serendipity elements in contact analyses were made and the superior convergence behaviour of elements using tri-quadratic interpolation functions was demonstrated. A numerical differentiation scheme to evaluate the left-hand-side of the contact contributions was proposed, which does not require the analytical derivation of the contact contributions with respect to the primary (spatially discretised) variables. Such a scheme is of great importance for the application of advanced constitutive interface models, for which an analytical derivation can be impossible.

In the second part of the chapter, novel formulations for advanced constitutive interface models for granular media have been developed and tested. Constitutive models such as Hypoplasticity with intergranular strain extension and the Sanisand model can be directly applied as interface models using the presented approaches. In order to obtain the stress state in the interface, an extrapolation of the stress from the adjacent continuum to the interface has been proposed, which avoids jumps in the stress between interface and continuum being the case using existing approaches. This allows to satisfy boundary conditions not only for the continuum but also for the interface as well as enables to consider all normal strain components in the interface zone. In addition to interface models based on the hypoplastic and the Sanisand model, a model for high-cyclic interface shearing based on the HCA model for sand has been developed. This model allows to take into account the accumulation of permanent strain in the interface during a high-cycle loading phase. The proposed models have then been applied to the simulation of simple monotonic and cyclic interface shear tests. The novel interface formulation was found to

give realistic normal stress conditions in the interface zone, while the existing approach resulted in a strong jump in the stress tensor between interface and continuum. The suitability of the HCA interface formulation has been demonstrated by the back-analysis of cyclic interface shear tests with up to 50 cycles.

9.1.4 Finite element program `numgeo`

The proposed numerical schemes have been implemented into the in-house finite element program `numgeo`, developed by Machaček [242] and the author of this thesis. Some details on the implementation of the numerical schemes, especially with regard to parallel computation, have been provided. In order to show the performance of the code, comparisons with the commercial finite element code `Abaqus` were presented. The results of both finite element programs were in good accordance, proving the functionality of `numgeo`. The (compiled) program including user manuals can be downloaded from `www.numgeo.de`.

9.1.5 Verification of the developed methods and investigation of the influence of pile installation on the response to subsequent loading

The developed interface formulation for the application of (advanced) continuum soil models as interface models has been used for the simulation of large-scale cyclic interface shear tests. Compared to simulations using a simple Coulomb friction model, simulations using the hypoplastic interface model were in better agreement with the measurements of the experiment. Using the Sanisand interface model, an even better accordance could be achieved. Both advanced interface models were found to be able to capture the different interface behaviour at un- and reloading, which is not possible using the Coulomb friction model. Compared to the interface formulation by Stutz et al. [366], the novel formulation was able to predict the large increase in normal and shear stress at the reloading phase, which were found to be a result of the increased vertical stresses in the adjacent continuum. Since the approach by Stutz et al. considers the adjacent continuum stress only indirectly, it resulted in a worse accordance with the measurement of the experiments.

The different finite element and contact discretisation techniques have been applied to the analysis of vibratory pile driving tests in water-saturated sand. In a first comparison, simulations using the developed **u**-p-(p)-**U**-(**U**) formulation have been compared to simulations

using the **u**-p-(p) formulation in order to investigate the influence of relative acceleration. In accordance to the novel method for the evaluation of the applicability of the **u**-p-(p) formulation derived based on the semi-analytical approach, no large influence of relative acceleration was found, in spite of the high hydraulic conductivity ($\approx 1 \cdot 10^{-3}$ m/s) and simultaneously high vibratory driving frequency (25 Hz). Hence, the **u**-p-(p) formulation was found to be a suitable element formulation for the analysis of vibratory pile driving in water-saturated soil.

Following, the two mortar contact discretisation techniques (SBM and EBM methods) were compared for the simulation of the vibratory pile driving tests using the Coulomb friction model and the developed hypoplastic and Sanisand interface models. The following conclusions were drawn from these simulations:

- The SBM contact discretisation proved to be more robust in terms of numerical stability compared to the EBM method. This was especially evident with respect to the predicted force between the vibrator and the pile head in the simulations using the Sanisand interface model, for which the EBM method showed stronger irregularities, which were absent when applying the segment-based technique. The results using the SBM method were observed to be in better agreement with the measured forces. However, using the EBM method with a larger number of integration points per finite element edge resulted in less irregularities, giving pile forces similar to the segment-based approach.

- Following these conclusions, it is apparent that the contact discretisation technique plays a key role in obtaining numerically stable results for the analysis of pile installation processes.

- In terms of computational performance, the SBM contact discretisation was found to be comparable to the EBM method, if a comparable number of integration points was used.

- The comparison of simulations using a hypoplastic and a Sanisand interface model with simulations using a simple Coulomb friction model showed that despite the smooth surface of the pile the constitutive interface model influenced the predicted pile penetration during the vibratory driving. In terms of force between the vibrator and the pile head, however, almost no influence from the constitutive interface model was found.

In a last study on the vibratory pile driving tests, the proposed hydro-mechanically coupled Eulerian finite element formulation has been applied and compared to the results using the hydro-mechanically coupled Lagrangian finite elements. In terms of pile penetration, a

satisfying accordance between the Eulerian and the Lagrangian simulations was found. The development of excess pore water pressure, however, was found to be represented worse using the Eulerian formulation, which was traced back to the explicit time integration applied.

The influence of the pile installation on its response to subsequent lateral (high-)cyclic loading was investigated first by the back-analysis of small-scale model tests on monopiles subjected to 10,000 lateral load cycles. The installation of the pile was simulated using the Coupled Eulerian-Lagrangian (CEL) method. A significant increase in the effective stress and a strong compaction of the soil in the vicinity of the pile tip were observed. Following its installation, the pile was first subjected to monotonic lateral loading and simulations with and without consideration of the installation-induced changes in soil state were compared. The piles with incorporation of the installation process showed much larger lateral resistance for both, initially medium dense and initially loose sand. A much better agreement between the results of the model tests and the simulations with consideration of the installation process was found compared to the wished-in-place (WIP) simulations. Similar observations were made for the analysis of the pile when subjected to high-cyclic lateral loading. The simulations without consideration of the installation process overestimated the rotation of the pile compared to the measurements made in the model tests, which was more pronounced in case of the initially loose sand. The simulations with installation were in good agreement with the measurements.

A specific investigation of the effect of installation by vibratory driving compared to impact driving of real-scale piles for OWTs in initially dense sand showed that the magnitude of the effective radial stress acting in the soil close to the pile shaft is less following the installation by vibration. A stronger increase of excess pore water pressure was observed for the vibratory driven pile. In line with these observations, the vibratory driven pile showed less densification in the soil close to the pile for partially drained conditions. However, if ideally drained conditions were assumed, the vibratory driven piles showed stronger compaction of the soil close to the pile tip compared to impact driven piles. For both installation techniques the h/R effect, i.e. decreasing magnitude of the effective radial stress with increasing distance h from the pile tip, has been observed. Close to the pile shaft the effective stress was comparable for both installation techniques, but in case of the impact driven piles the soil in greater distance showed a larger magnitude of effective radial stress. Unsurprisingly, the lower the hydraulic conductivity of soil, the higher the excess pore water pressure and the less the compaction of the soil close to the pile tip. However, in greater distance from the pile shaft, the magnitude of the radial effective stress was found to be larger for lower values of hydraulic conductivity due to the development of negative excess pore water pressure. Following the installation process, the lateral high-cyclic loading of the pile, representing wind and water load faced by offshore

pile foundations, was simulated using the high-cycle accumulation (HCA) model and assuming ideally drained conditions for this phase. The permanent pile head rotations after one million loading cycles were comparable for both impact and vibratory driven piles, if the hydraulic conductivity of the soil was $k^w = 10^{-3}$ m/s. However, if the installation was simulated assuming ideally drained conditions, the vibratory driven pile showed less pile head rotation after one million lateral load cycles, which was traced back to greater compaction of the soil caused by the installation process compared to the impact driven pile. For a lower hydraulic conductivity of $k^w = 10^{-4}$ m/s the lateral deformation of the pile was larger compared to $k^w = 10^{-3}$ m/s for both installation techniques. In general, the better the drainage during driving, the less pile head rotation occurred during the high-cyclic loading following the installation process. The results of the study indicate that both installation techniques, vibratory and impact driving, result in comparable long-term deformations if the pile is subjected to high-cyclic lateral loading after the installation. However, the simulations of impact driving gave a slightly higher rate of pile penetration during the installation process compared to vibratory driving, resulting in worse drainage conditions. Therefore, if identical pile penetration rates would have been achieved, less long-term deformations of the impact driven piles would be expected.

The numerical studies on a monopile under partially drained high-cyclic lateral loading with large changes in pore water pressure during the high-cycle mode of the simulation with the HCA model showed that the proposed schemes for the adaptive strain amplitude give similar results as simulations incorporating update cycles. The adaptive strain amplitude, however, allows for a much more frequent update of the strain amplitude and much less numerical effort compared to update cycles. It was demonstrated that the solution in terms of permanent lateral pile displacement was unaffected by the frequency of the update of the strain amplitude if the updates were performed more frequently than every 10th calculation increment. Simulations with an update every increment did not change the solution. The influence of the characteristic length used for the nonlocal smoothing of the strain amplitude following its update was found to be negligible for values chosen in a meaningful range.

The HCA model for clay proposed in [406] was validated by the back-analysis of centrifuge tests on monopiles in water-saturated kaolin subjected to lateral cyclic loading. The adaptive strain amplitude was used to incorporate the change in strain amplitude during the high-cycle phase of the simulation. Both the accumulated deformations as well as the change of bending moment with number of applied load cycles were well reproduced using the HCA model for clay. A parametric study on the long-term behaviour of monopile foundations for OWTs founded in clay using the HCA model for clay showed that an increase in the diameter of the pile is not leading to a reduction in permanent lateral deflection after 10,000 loading

cycles in case the cyclic loading amplitude is linearly scaled with respect to the diameter of the pile. An increase in pile length on the other hand leads to a reduction in permanent deformations even if the loading is increased proportionally to the increasing pile length. As expected, the consideration of sand layers significantly reduces the accumulation of permanent deformations.

Lastly, the influence of the pile installation process on the response to subsequent (high-cyclic) loading was investigated for clayey soils. The following conclusions were drawn from these investigations:

- The pile installation process in clay reduces the initial OCR values in overconsolidated soils considerably, in particular below the pile tip. Large values of negative excess pore water pressure are observed close to the pile shaft, which are larger at higher values of initial OCR. The effective radial stress increases significantly below the pile tip for initially overconsolidated soils, but much less for normally consolidated conditions. The h/R effect, i.e. the reduction in effective radial stress at the pile shaft with increasing pile penetration depth, is more pronounced at lower values of initial OCR, but much less than in sandy soils due to the aforementioned negative excess pore water pressures at the pile shaft. For larger values of initial OCR even opposite tendencies, i.e. an increase in effective radial stress with increasing pile penetration depth, was observed.

- Cavitation can limit the pile resistance during installation and is important to be accounted for. This is more important for larger values of initial OCR.

- The consolidation process after installation leads to a decrease in effective stress near the pile shaft as negative excess pore water pressures dissipate in case of initially overconsolidated soils. At the same time, OCR increases, even at a greater distance from the pile shaft.

- Compared to the simulations neglecting the installation process, the monotonic lateral loading behaviour of jacked piles was found to be comparable for smaller values of pile head rotation. However, higher resistance was found for larger rotations in the simulations that considered the installation process. The greater the initial OCR prior to installation, the greater the rotation at which jacked and WIP piles began to diverge.

- When the pile was subjected to 10^6 lateral load cycles, simulations that neglected the installation process resulted in a much higher accumulation of lateral pile deformations

at larger numbers of load cycles ($N > 100$). This was especially pronounced for initially overconsolidated soils. For initially normally consolidated soils, installation did not change the pile response as much.

- With increasing initial OCR, neglecting the installation process resulted in lower pile deformations at a low number of load cycles ($N \leq 100$).

- The cyclic lateral loading after the consolidation process further reduced the effective stresses on the pile shaft while OCR increased. The increase in OCR is much more pronounced when the pile installation process is taken into account. This is particularly the case for initially overconsolidated soils, as the effective stress increased more during the installation process compared to normally consolidated initial conditions.

These results indicate that the practice of neglecting the installation process, i.e. assumption of wished-in-place conditions, is not necessarily justified for piles in clay. This is especially true for initially overconsolidated soils and a larger number of lateral load cycles, as is the case with piles in the offshore environment. However, in almost all cases investigated, neglecting the installation process resulted in higher pile displacements and is therefore conservative. In addition, the stiffness of the soil-pile system at small rotations, influencing the natural frequency of the structure, was found to be comparable for jacked and wished-in-place piles.

9.2 Outlook

- A large-deformation technique should be implemented in `numgeo` in order to allow for the application of the developed numerical tools also for the simulation of pile installation without having to resort to e.g. a zipper technique to avoid mesh distortion. The Coupled Eulerian-Lagrangian method applied in this work showed a weak performance in terms of predicted pore fluid pressure due to the explicit time integration scheme. In addition, with increasing pile penetration, for some points on the soil-pile interface the contact conditions were not satisfied any more. An implicit large-deformation technique based on a re-meshing method such as the RITSS (Remeshing and Interpolation Technique with Small-Strain) method [176, 398, 381, 397] is hence favoured for the implementation in `numgeo`.

- Having implemented a large-deformation technique in `numgeo`, the proposed constitutive interface models could be used for the simulation of the installation of (open-profile) piles

and compared to the results using a simple Coulomb contact. Such simulations are not possible using the large-deformation techniques implemented in `Abaqus`, because the proposed interface formulation requires an open-source finite element code.

- The adaptive strain amplitude definition can be used to improve the performance of the HCA models for irregular cyclic loading with frequently changing cyclic load magnitudes. Up to now, irregular cyclic load histories have been roughly grouped into a limited number of cyclic load packages with comparable amplitudes (and periods) based on Miner's rule (for ideally drained conditions). The adaptive strain amplitude definition allows to consider a much larger number of cyclic load packages (and hence a refined analysis) because the strain amplitude has to be calculated only once for each load amplitude. A repetition of a cyclic load package following some interposed loading can then be simulated using the initial strain amplitude updated employing the adaptive strain amplitude definition. Future work will investigate the applicability of the presented approach for such irregular cyclic load histories, in particular for partially drained conditions.

- High-cyclic interface shear tests with varying surface roughness are necessary to further validate the proposed HCA model for interfaces. Thus far, no comprehensive experimental study with more than ≈ 100 load cycles exists. Future work in this direction is desirable.

- The installation process by vibratory pile driving could be simulated using the HCA model for sand for the continuum as well as for the interface. So far, only the continuum has been modelled using the HCA model in such analyses [278, 276].

- For the simulation of the installation of a real monopile by impact driving, several tens of thousands of hammer blows are needed to be taken into account. With the approaches used in the present work, such simulations are not possible due to the large computational effort. An approach with implicit time integration applying the HCA model for the installation could be studied in the future.

- The proposed HCA interface model could be applied for the analysis of the long-term behaviour of monopile foundations and compared to simulations using a simple Coulomb contact model.

- A simplified incorporation of the installation-induced soil changes in simulations studying the vertical or lateral response of driven piles is desirable since the numerical simulation of the installation process is complex and time consuming.

- Effects due to grain crushing should be incorporated in the pile driving simulations since large effective stresses (> 1000 kPa) occur in the vicinity of the pile tip. Future work could focus on the investigation of the influence of grain grushing using the constitutive models proposed e.g. in [64, 291].
- The simulation of the installation of piles in clay and the subsequent (monotonic or low-cyclic) loading should be performed with more advanced constitutive models. Different initial soil conditions, loading scenarios and pile geometries could be investigated as well. In addition, different installation techniques could be investigated, since field tests shown an influence of the installation method on the development of the decisive soil state variables during driving [136].

Appendix A

Constitutive models

A.1 The hypoplastic model with intergranular strain extension and its implementation

The objective stress rate $\mathring{\boldsymbol{\sigma}}$ is calculated from

$$\mathring{\boldsymbol{\sigma}} = \mathsf{M} : \dot{\boldsymbol{\varepsilon}} \tag{A.1}$$

where $\dot{\boldsymbol{\varepsilon}}$ is the strain rate. The stiffness tensor M is defined by [269]

$$\mathsf{M} = \left[\rho^{\chi} m_T + (1-\rho^{\chi}) m_R\right]\mathsf{L} + \begin{cases} \rho^{\chi}(1-m_T)\mathsf{L} : \vec{\mathbf{h}} \otimes \vec{\mathbf{h}} + \rho^{\chi}\mathbf{N}\vec{\mathbf{h}} & \text{for} \quad \vec{\mathbf{h}} : \dot{\boldsymbol{\varepsilon}} > 0 \\ \rho^{\chi}(m_R - m_T)\mathsf{L} : \vec{\mathbf{h}} \otimes \vec{\mathbf{h}} & \qquad\quad \vec{\mathbf{h}} : \dot{\boldsymbol{\varepsilon}} \leq 0 \end{cases} \tag{A.2}$$

with the intergranular strain tensor $\mathbf{h}$, its degree of mobilization ρ and its direction $\vec{\mathbf{h}}$ defined as

$$\rho = \frac{\|\mathbf{h}\|}{R} \quad \text{and} \quad \vec{\mathbf{h}} = \frac{\mathbf{h}}{\|\mathbf{h}\|}. \tag{A.3}$$

χ, m_T, m_R and R are material parameters controlling the influence of the intergranular strain. The evolution law of the intergranular strain $\mathbf{h}$ is [269]

$$\mathring{\mathbf{h}} = \begin{cases} (\mathsf{I} - \vec{\mathbf{h}} \otimes \vec{\mathbf{h}} \rho^{\beta_r}) : \dot{\boldsymbol{\varepsilon}} & \text{for} \quad \vec{\mathbf{h}} : \dot{\boldsymbol{\varepsilon}} > 0 \\ \dot{\boldsymbol{\varepsilon}} & \qquad\quad \vec{\mathbf{h}} : \dot{\boldsymbol{\varepsilon}} \leq 0 \end{cases} \tag{A.4}$$

where β_R is another material parameter and I is the fourth-order identity tensor. The stiffness tensors L and $\mathbf{N}$ are given by the following equations [423]:

$$\mathsf{L} = f_b f_e \frac{1}{\mathrm{tr}(\hat{\boldsymbol{\sigma}} \cdot \hat{\boldsymbol{\sigma}})} (F^2 \mathsf{I} + a^2 \hat{\boldsymbol{\sigma}} \otimes \hat{\boldsymbol{\sigma}}) \tag{A.5}$$

$$\mathbf{N} = f_b f_e f_d \frac{Fa}{\mathrm{tr}(\hat{\boldsymbol{\sigma}} \cdot \hat{\boldsymbol{\sigma}})} (\hat{\boldsymbol{\sigma}} + \hat{\boldsymbol{\sigma}}^*) \tag{A.6}$$

Therein $\hat{\boldsymbol{\sigma}} = \dfrac{\boldsymbol{\sigma}}{\mathrm{tr}\boldsymbol{\sigma}}$ and $\hat{\boldsymbol{\sigma}}^* = \hat{\boldsymbol{\sigma}} - \frac{1}{3}\mathbf{I}$ are used. The scalar factors are defined by

$$a = \frac{\sqrt{3}(3 - \sin\varphi_c)}{2\sqrt{2}\sin\varphi_c} \ , \ f_d = \left(\frac{e - e_d}{e_c - e_d}\right)^{\alpha} \ , \ f_e = \left(\frac{e_c}{e}\right)^{\beta} \tag{A.7}$$

and

$$f_b = \frac{h_s}{n}\left(\frac{e_{i0}}{e_{c0}}\right)^{\beta} \frac{1 + e_i}{e_i}\left(\frac{3p}{h_s}\right)^{1-n}\left[3 + a^2 - a\sqrt{3}\left(\frac{e_{i0} - e_{d0}}{e_{c0} - e_{d0}}\right)^{\alpha}\right]^{-1}. \tag{A.8}$$

φ_c, h_s, n, e_{i0}, e_{d0}, e_{c0}, α and β are parameters and e is the actual void ratio. The pressure-dependent void ratios e_i, e_c and e_d in Eq. (A.7), describing the loosest, the critical and the densest state, are calculated using the following relation [37]

$$\frac{e_i}{e_{i0}} = \frac{e_c}{e_{c0}} = \frac{e_d}{e_{d0}} = \exp\left[-\left(\frac{3p}{h_s}\right)^n\right]. \tag{A.9}$$

p is the mean effective stress. The scalar factor F in Eq. (A.5) and Eq. (A.6) is given by

$$F = \sqrt{\frac{1}{8}\tan(\psi)^2 + \frac{2 - \tan(\psi)^2}{2 + \sqrt{2}\tan(\psi)\cos(3\theta)}} - \frac{1}{2\sqrt{2}}\tan(\psi), \tag{A.10}$$

with $\tan(\psi) = \sqrt{3}\|\hat{\boldsymbol{\sigma}}^*\|$ and

$$\cos(3\theta) = -\sqrt{6}\frac{\mathrm{tr}(\hat{\boldsymbol{\sigma}}^* \cdot \hat{\boldsymbol{\sigma}}^* \cdot \hat{\boldsymbol{\sigma}}^*)}{[\mathrm{tr}(\hat{\boldsymbol{\sigma}}^* \cdot \hat{\boldsymbol{\sigma}}^*)]^{3/2}}. \tag{A.11}$$

The present implementation uses an adaptive explicit Euler scheme to integrate the stress rate within a sub-stepping method and with error control (see the modified Euler method used in [96, 97, 119] proposed by [343]). The error of the explicit scheme within every sub-increment is calculated and the sub-step size is reduced if the error is too large. Likewise, the sub-step size is increased if the error is small. The integration of stress and the determination of the error of the explicit scheme is given by Algorithm 4.

In addition to the adaptive explicit Euler scheme, an implicit integration scheme using numerical differentiation is programmed. For the implicit integration, the derivation of the stress

Algorithm 4: Integration of the stress rate using an adaptive explicit Euler scheme with error control

Result: Updated stress $\boldsymbol{\sigma}^{(i+1)}$ and state variables $\mathbf{h}^{(i+1)},\ e^{(i+1)}$

1 **for** $i = 0, 1, 2, ..$ *until* $t^{(i+1)} = 1$ **do**

2 Calculate sub-increment of strain $\Delta\boldsymbol{\varepsilon}^{(i+1)} = \Delta\boldsymbol{\varepsilon}\Delta t^{(i)}$

3 Calculate sub-increment of stress $\Delta\boldsymbol{\sigma}^{(i+1),1} = \mathsf{M}(\boldsymbol{\sigma}^{(i)}, \mathbf{h}^{(i)}, e^{(i)}) : \Delta\boldsymbol{\varepsilon}^{(i+1)}$

4 Update stress using $\boldsymbol{\sigma}^{(i+1),1} = \boldsymbol{\sigma}^{(i)} + \Delta\boldsymbol{\sigma}^{(i+1),1}$

5 Calculate sub-increment of stress $\Delta\boldsymbol{\sigma}^{(i+1),2} = \mathsf{M}(\boldsymbol{\sigma}^{(i+1),1}, \mathbf{h}^{(i)}, e^{(i)}) : \Delta\boldsymbol{\varepsilon}^{(i+1)}$

6 Calculate error defined by

$$R^{(i)} = \frac{\|\Delta\boldsymbol{\sigma}^{(i+1),1}\| - \|\Delta\boldsymbol{\sigma}^{(i+1),2}\|}{\|\Delta\boldsymbol{\sigma}^{(i+1),1}\|}$$

7 **if** $R^{(i)} < tol$ **then**

8 Update sub-increment time $t^{(i+1)} = t^{(i)} + \Delta t^{(i)}$

9 Increase dimensionless time increment using:

$$\Delta t^{(i+1)} = t^{(i)} \cdot \min\left\{0.9\left(\frac{tol}{R^{(i)}}\right)^{0.5}; 2.0\right\} \quad \text{with} \quad \Delta t^{(i+1)} < 1 - t^{(i)}$$

10 Update stress $\boldsymbol{\sigma}^{(i+1)} = \boldsymbol{\sigma}^{(i)} + \frac{1}{2}(\Delta\boldsymbol{\sigma}^{(i+1),1} + \Delta\boldsymbol{\sigma}^{(i+1),2})$

11 Update other state variables $\mathbf{h}^{(i+1)},\ e^{(i+1)}$

12 Go to line 1

13 **else**

14 Reduce dimensionless time increment using:

$$\Delta t^{(i+1)} = t^{(i)} \cdot \max\left\{0.9\left(\frac{tol}{R^{(i)}}\right)^{0.5}; 0.1\right\}$$

15 Go to line 1

16 **end**

17 **end**

increment $\Delta\boldsymbol{\sigma}$ with respect of the strain increment $\Delta\boldsymbol{\varepsilon}$ is required. An analytical derivation is not possible for the hypoplastic model [120]. A numerical differentiation scheme proposed by [120, 119] is therefore used. In analogy to Eq. (6.55), the derivative is rewritten to

$$\frac{\partial \Delta\boldsymbol{\sigma}}{\partial \Delta\boldsymbol{\varepsilon}} = \big(\mathbf{J}\big)_i. \tag{A.12}$$

The increment in stress $\Delta\boldsymbol{\sigma}$ is a function of the strain increment $\Delta\boldsymbol{\varepsilon}$, of the stress $\boldsymbol{\sigma}$ and of state variables $\boldsymbol{\alpha}$, i.e. $\Delta\boldsymbol{\sigma}(\Delta\boldsymbol{\varepsilon}, \boldsymbol{\sigma}, \boldsymbol{\alpha})$. The state variables change with respect to strain, stress and the state variables $\boldsymbol{\alpha}(\Delta\boldsymbol{\varepsilon}, \boldsymbol{\sigma}, \boldsymbol{\alpha})$ described by the function $\mathbf{F}(\Delta\boldsymbol{\varepsilon}, \boldsymbol{\sigma}, \boldsymbol{\alpha})$. In this case, the derivative has to incorporate the change with respect to these variables as well. The derivative can be expressed by

$$\frac{\mathrm{d}}{\mathrm{d}t}\big(\mathbf{J}\big)_i = \frac{1}{\vartheta}\Big[\Delta\boldsymbol{\sigma}\Big(\Delta\boldsymbol{\varepsilon} + \vartheta\mathbf{I}_i, \boldsymbol{\sigma} + \vartheta\big(\mathbf{J}\big)_i, \boldsymbol{\alpha} + \vartheta\big(\mathbf{G}\big)_i\Big) - \Delta\boldsymbol{\sigma}\big(\Delta\boldsymbol{\varepsilon}, \boldsymbol{\sigma}, \boldsymbol{\alpha}\big)\Big], \tag{A.13}$$

where

$$\frac{\mathrm{d}}{\mathrm{d}t}\big(\mathbf{G}\big)_i = \frac{1}{\vartheta}\Big[\mathbf{F}(\Delta\boldsymbol{\varepsilon} + \vartheta\mathbf{I}_i, \boldsymbol{\sigma} + \vartheta\big(\mathbf{J}\big)_i, \boldsymbol{\alpha} + \vartheta\big(\mathbf{G}\big)_i) - \mathbf{F}(\Delta\boldsymbol{\varepsilon}, \boldsymbol{\sigma}, \boldsymbol{\alpha})\Big]. \tag{A.14}$$

In Eqs. (A.13, A.14), the perturbation ϑ is used. Following [120], ϑ can be estimated using

$$\vartheta = \max(1, ||\Delta\boldsymbol{\varepsilon}||) \cdot \sqrt{EPS}, \tag{A.15}$$

wherein $EPS \approx 10^{-16}$ is the machine precision. The advantage of the implicit scheme is not only a larger stable increment in the sub-increment of strain but also the obtained consistent Jacobian required by the global Newton-Raphson scheme (see Eq. 4.24). The evaluation of Eq. (A.13), however, requires to compute the update of stress 5 (2D) or 7 (3D) times within each sub-increment and is hence computationally expensive. Experience shows that the explicit Euler-scheme with error control is computational superior to the implicit integration using numerical differentiation for most BVPs, which has also been observed in [61] for an elasto-plastic bounding surface model.

Two additional implementations are tested and compared to the new implementation: the one by Niemunis[1], which has been used extensively at the Institute of Soil Mechanics and Rock Mechanics at the KIT, and the one by Tamagnini et al., available from `www.soilmodels.com`. The implementation by Niemunis uses an explicit sub-stepping scheme with error control, the one by Tamagnini et al. uses an implicit scheme calculating the Jacobian by the above discussed numerical differentiation scheme. The novel implementation uses the explicit adaptive Euler-scheme with error control.

[1]This implementation has originally been written by Prof. A. Niemunis but was modified by many different researchers making the code hard to read and prone to errors

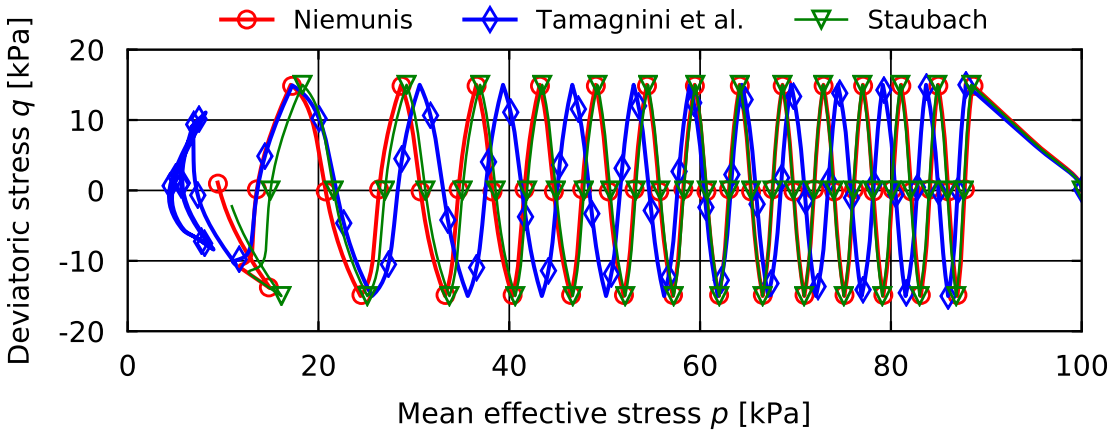

Figure A.1: Comparison of the results of the simulations of an undrained cyclic triaxial test using the implementations of the hypoplastic model by Niemunis, by Tamagnini et al. and the present one (Staubach)

A cyclic undrained triaxial test is simulated using the three different implementations and identical parameters. The results are given in Fig. A.1. The new implementation and the one by Niemunis are in good accordance. A slightly faster accumulation of pore water pressure is observed using the implementation by Niemunis. The implementation by Tamagnini et al. gives considerably faster relaxation of the mean effective stress compared to the other two implementations.

A.2 Constitutive equations of Sanisand and its implementation

Building on the original Sanisand version of 2004 [82], many extensions have been proposed. [202] proposed an extension by an anisotropic elasticity. A version with a closed cap of the yield surface was developed by [375] such that plastic strains can occur for stress paths with constant stress ratio. Furthermore, [83] presented a reformulation where the model has no elastic range. For an extension by a memory surface to allow for the simulation of several thousands of loading cycles the reader is referred to [225, 226] and for an enhanced performance under cyclic loading in general to [227]. In addition, an extension by a memory surface and semifluidised states has been proposed by [35, 430] and by [290] taking into account the evolving fabric anisotropy of sand. Despite these extensions, the original version remains a very frequently used constitutive model due to its proven robustness in various numerical studies (see e.g. [189] and [359]).

Different implementations of the version of 2004 exist and are partly freely available (e.g. the implementation by Tamagnini, Martinelli and Miriano from `www.soilmodels.com`). These implementations were tested in the course of the present work but were found to be numerically not stable for the simulation of e.g. vibratory pile driving. Therefore, a new implementation is written by the author.

In the following, the implemented equations used for the simulations with the Sanisand model are given. They are identical to those presented in [82]. The objective stress rate is calculated using

$$\mathring{\boldsymbol{\sigma}} = \mathsf{E}^{\mathsf{ep}} : \dot{\boldsymbol{\varepsilon}}. \tag{A.16}$$

The elasto-plastic stiffness E^{ep} is calculated by

$$\mathsf{E}^{ep} = 2G(\mathsf{I} - \frac{1}{3}\mathbf{1}\otimes\mathbf{1}) + K\mathbf{1}\otimes\mathbf{1} - \langle L\rangle\dot{\boldsymbol{\varepsilon}}^{-1}\big(2G\big[B\boldsymbol{n} - C(\boldsymbol{n}^2 - \frac{1}{3}\mathbf{1})\big] + KD\mathbf{1}\big). \tag{A.17}$$

$\langle \sqcup \rangle$ are the Macaulay-brackets. The scalar elastic stiffness parameters G and K in Eq. (A.17) are defined by

$$G = G_0\ p_{atm}\frac{(2.97-e)^2}{1+e}\left(\frac{p}{p_{\mathrm{atm}}}\right)^{\frac{1}{2}} \quad \text{and} \quad K = \frac{2(1+\nu)}{3(1-2\nu)}G. \tag{A.18}$$

G_0, p_{atm} and ν are material parameters.

The plastic multiplier L is larger than zero if the yield surface defined by

$$f = \left[(\boldsymbol{\sigma}^* - p\boldsymbol{\alpha}) : (\boldsymbol{\sigma}^* - p\boldsymbol{\alpha})\right]^{\frac{1}{2}} - \sqrt{\frac{2}{3}}pm < 0 \tag{A.19}$$

is no longer satisfied, i.e. the trial stress is outside the elastic range. Eq. (A.19) represents a wedge in the 2D stress space. The back-stress tensor $\boldsymbol{\alpha}$ defines the centre of the wedge and m is the opening of the wedge. For stress states inside of wedge, a hypo-elastic material response follows.

The plastic multiplicator L is given by

$$L = \frac{2G\boldsymbol{n} : \dot{\boldsymbol{\varepsilon}}^* - \boldsymbol{n} : \mathbf{r}\ \mathrm{tr}(\dot{\boldsymbol{\varepsilon}})}{K_p 2G(B - C\mathrm{tr}\ \boldsymbol{n}^3) - KD\boldsymbol{n} : \mathbf{r}}, \tag{A.20}$$

where

$$\boldsymbol{n} = \frac{\boldsymbol{\sigma}^*/p - \boldsymbol{\alpha}}{\sqrt{2/3}pm}. \tag{A.21}$$

K_p is a hardening variable and defined as

$$K_p = \frac{2}{3} ph(\boldsymbol{\alpha}_\theta^b - \boldsymbol{\alpha}) : \boldsymbol{n} \tag{A.22}$$

where h is

$$h = \frac{G_0 h_0 (1 - c_h e) \left(\dfrac{p}{p_{\text{atm}}} \right)^{-1/2}}{(\boldsymbol{\alpha} - \boldsymbol{\alpha}_{\text{ini}}) : \boldsymbol{n}} \tag{A.23}$$

and $\boldsymbol{\alpha}_\theta^b$ is

$$\boldsymbol{\alpha}_\theta^b = \sqrt{\frac{2}{3}} \Big[g(\theta, c) M e^{-n_b \psi} - m \Big] \boldsymbol{n}. \tag{A.24}$$

M is the stress ratio at the critical state, n_b and m are parameters and ψ is the state parameter defined as

$$\psi = e - e_c = e - e_0 + \lambda_c \, (p_c / p_{\text{atm}})^{\xi}. \tag{A.25}$$

Using $c = \dfrac{M_e}{M_c}$, $g(\theta, c)$ is

$$g(\theta, c) = \frac{2c}{(1 + c) - (1 - c)\cos(3\theta)}, \tag{A.26}$$

with $\cos(3\theta) = \sqrt{6}\text{tr}(\boldsymbol{n}^3)$. The dilatancy D is defined by

$$D = A_d (\boldsymbol{\alpha}_\theta^d - \boldsymbol{\alpha}) : \boldsymbol{n}, \tag{A.27}$$

where α_θ^d is calculated using

$$\boldsymbol{\alpha}_\theta^d = \sqrt{\frac{2}{3}} \Big[g(\theta, c) M e^{n_d \psi} - m \Big] \boldsymbol{n} \tag{A.28}$$

and A_d by

$$A_d = A_0 (1 + \langle \boldsymbol{z} : \boldsymbol{n} \rangle). \tag{A.29}$$

The change of the fabric-dilatancy tensor $\boldsymbol{z}$ with plastic volumetric strain increment is defined by

$$d\boldsymbol{z} = -c_z \langle -d\varepsilon_v^p \rangle (z_{\max} \boldsymbol{n} + \boldsymbol{z}). \tag{A.30}$$

Lastly, the change of the back-stress tensor $\boldsymbol{\alpha}$ is

$$d\boldsymbol{\alpha} = \frac{2}{3} \langle L \rangle h (\boldsymbol{\alpha}_\theta^b - \boldsymbol{\alpha}). \tag{A.31}$$

The initial back-stress tensor $\boldsymbol{\alpha}_{\text{ini}}$ is updated to $\boldsymbol{\alpha}$ in case of a load reversal which occurs in case of $(\boldsymbol{\alpha} - \boldsymbol{\alpha}_{\text{ini}}) : \boldsymbol{n} < 0$. B and C in Eq. (A.20) are defined by

$$B = 1 + \frac{3 - 3c}{2c} g \cos(3\theta) \quad \text{and} \quad C = 3\sqrt{\frac{3}{2}} \frac{1 - c}{c} g. \tag{A.32}$$

Sanisand is implemented in an explicit scheme. To avoid any violation of Eq. (A.19) and to take into account the incremental non-linearity, a sub-stepping scheme is applied. The strain increment is divided into several (up to 50,000) smaller increments ensuring numerical stability. In most cases, rapid convergence of the return-mapping algorithm is achieved. For some stress states, however, the return-mapping algorithm may diverge. Since it is neither desirable that the calculation is aborted in such a case nor that the simulation continues with an un-satisfied yield criterion, a rigorous correction of the back-stress tensor $\boldsymbol{\alpha}$ is proposed. For a given stress state, the yield surface is exactly satisfied, i.e. the stress state is on the yield locus, in case of

$$\boldsymbol{\alpha} = \frac{\mathbf{s}}{p} - \boldsymbol{n}\sqrt{\frac{2}{3}} m, \tag{A.33}$$

with $\boldsymbol{n}$ being defined by

$$\boldsymbol{n} = (\mathbf{s} - p\boldsymbol{\alpha})^{\rightarrow}. \tag{A.34}$$

In Eq. (A.34) the definition $(\sqcup)^{\rightarrow} = \sqcup / \| \sqcup \|$ holds. Using $\boldsymbol{n} : \boldsymbol{n} = 1$ it is evident that f in Eq. (A.19) is zero when setting $\boldsymbol{\alpha}$ according to Eq. (A.33). Of course, this artificial adjustment of the back-stress tensor $\boldsymbol{\alpha}$ influences the material response and it has to be secured that it is performed only rarely. Figure A.2 displays the change of deviatoric stress

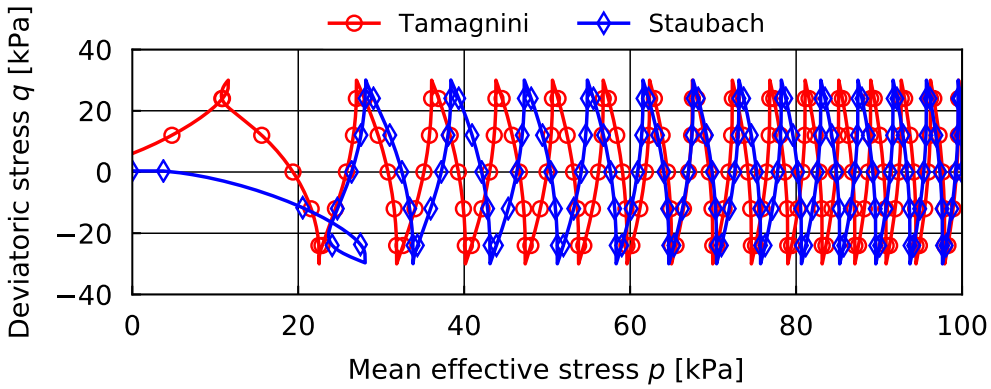

Figure A.2: Comparison of the results of the simulations of an undrained cyclic triaxial test using the Sanisand implementation by Tamagnini et al. and the implementation used in this thesis (Staubach)

with respect to mean effective pressure for simulations of an undrained cyclic triaxial test on an initially medium dense sample with an isotropic initial mean effective stress of $p_0 = 100$ kPa. The implementation of Tamagnini et al. and the present one are used. Identical constitutive parameters are employed. The new implementation shows a faster relaxation of effective stress, especially between cycle 3 to cycle 5. These differences can partly be traced back to different employed integration schemes of stress and state variables, leading to a deviation in case of a larger number of computed increments.

Appendix B

Finite element operations and contact mechanics

B.1 Tri-quadratic Lagrangian interpolation functions

The interpolation functions used for the `u27` element introduced in Section 6.6 are supplied in Table B.1. The derivatives with respect to the local coordinates are not given here explicitly, but can be easily calculated. The location of the integration points and weights of the `u27` element are calculated according to Eqs. (4.10, 4.11).

B.2 Partial derivatives of contact contributions for the mortar contact discretisations

The analytical calculation of the partial derivatives of the contact contributions with respect to the primary variables (only the **u**-p formulation is considered) is presented in the following. The derivatives of both the SBM and the EBM contact discretisation techniques are covered. First, the derivatives of the normal vector (Section B.2.1), the local convective coordinates and integration area (Section B.2.2) and the normal contact stress (Section B.2.5) are calculated. Following, the complete contributions to the LHS are presented in Section B.2.6 for the normal contact force and in Section B.2.7 for the tangential force components.

$N_1 = \frac{1}{8}\xi(\xi-1)\eta(\eta-1)\zeta(\zeta-1)$	$N_{10} = \frac{1}{8}\xi(\xi+1)(1-\eta^2)\zeta(\zeta-1)$	$N_{19} = \frac{1}{8}(1-\xi^2)\eta(\eta+1)\zeta(\zeta+1)$
$N_2 = \frac{1}{8}\xi(\xi+1)\eta(\eta-1)\zeta(\zeta-1)$	$N_{11} = \frac{1}{8}(1-\xi^2)\eta(\eta+1)\zeta(\zeta-1)$	$N_{20} = \frac{1}{8}\xi(\xi-1)(1-\eta^2)\zeta(\zeta+1)$
$N_3 = \frac{1}{8}\xi(\xi+1)\eta(\eta+1)\zeta(\zeta-1)$	$N_{12} = \frac{1}{8}\xi(\xi-1)(1-\eta^2)\zeta(\zeta-1)$	$N_{21} = \frac{1}{8}(1-\xi^2)(1-\eta^2)\zeta(\zeta-1)$
$N_4 = \frac{1}{8}\xi(\xi-1)\eta(\eta+1)\zeta(\zeta-1)$	$N_{13} = \frac{1}{8}\xi(\xi-1)\eta(\eta-1)(1-\zeta^2)$	$N_{22} = \frac{1}{8}(1-\xi^2)\eta(\eta-1)(1-\zeta^2)$
$N_5 = \frac{1}{8}\xi(\xi-1)\eta(\eta-1)\zeta(\zeta+1)$	$N_{14} = \frac{1}{8}\xi(\xi+1)\eta(\eta-1)(1-\zeta^2)$	$N_{23} = \frac{1}{8}\xi(\xi+1)(1-\eta^2)(1-\zeta^2)$
$N_6 = \frac{1}{8}\xi(\xi+1)\eta(\eta-1)\zeta(\zeta+1)$	$N_{15} = \frac{1}{8}\xi(\xi+1)\eta(\eta+1)(1-\zeta^2)$	$N_{24} = \frac{1}{8}(1-\xi^2)\eta(\eta+1)(1-\zeta^2)$
$N_7 = \frac{1}{8}\xi(\xi+1)\eta(\eta+1)\zeta(\zeta+1)$	$N_{16} = \frac{1}{8}\xi(\xi-1)\eta(\eta+1)(1-\zeta^2)$	$N_{25} = \frac{1}{8}\xi(\xi-1)(1-\eta^2)(1-\zeta^2)$
$N_8 = \frac{1}{8}\xi(\xi-1)\eta(\eta+1)\zeta(\zeta+1)$	$N_{17} = \frac{1}{8}(1-\xi^2)\eta(\eta-1)\zeta(\zeta+1)$	$N_{26} = \frac{1}{8}(1-\xi^2)(1-\eta^2)\zeta(\zeta+1)$
$N_9 = \frac{1}{8}(1-\xi^2)\eta(\eta-1)\zeta(\zeta-1)$	$N_{18} = \frac{1}{8}\xi(\xi+1)(1-\eta^2)\zeta(\zeta+1)$	$N_{27} = \frac{1}{8}(1-\xi^2)(1-\eta^2)(1-\zeta^2)$

Table B.1: Tri-quadratic Lagrangian interpolation functions in three local dimensions (ξ, η, ζ) used for the `u27` element

B.2.1 Derivatives of the normal vector

The derivative of the normal vector is formulated generally such that it holds independently of the contact discretisation. In case of the SBM method or the EBM discretisation with direct projection to the location of the integration points, the expressions have to be evaluated for ξ_{igp} and η_{igp}.

Recalling the general definition of the normal vector introduced in Eq. (4.4) and introducing the non-normalised normal vector $\hat{\boldsymbol{n}}(\xi,\eta)$

$$\boldsymbol{n}(\xi,\eta) = \frac{\sum_I^{\text{nnode}} \dfrac{\partial N_I(\xi,\eta)}{\partial \xi}\boldsymbol{x}_I \times \sum_I^{\text{nnode}} \dfrac{\partial N_I(\xi,\eta)}{\partial \eta}\boldsymbol{x}_I}{\left\| \sum_I^{\text{nnode}} \dfrac{\partial N_I(\xi,\eta)}{\partial \xi}\boldsymbol{x}_I \times \sum_I^{\text{nnode}} \dfrac{\partial N_I(\xi,\eta)}{\partial \eta}\boldsymbol{x}_I \right\|} = [\hat{\boldsymbol{n}}(\xi,\eta)]^{\rightarrow} \tag{B.1}$$

the derivation with respect to the displacement is defined by

$$\frac{\partial \boldsymbol{n}(\xi,\eta)}{\partial \boldsymbol{u}_J} = \frac{\dfrac{\partial \hat{\boldsymbol{n}}(\xi,\eta)}{\partial \boldsymbol{u}_J}}{\|\hat{\boldsymbol{n}}\|} - \frac{\left[\hat{\boldsymbol{n}} \cdot \dfrac{\partial \hat{\boldsymbol{n}}(\xi,\eta)}{\partial \boldsymbol{u}_J}\right]\hat{\boldsymbol{n}}}{\|\hat{\boldsymbol{n}}\|^3}. \tag{B.2}$$

In Eq. (B.2), the differential Δ of the norm of a vector $\sqcup$ defined by

$$\Delta\| \sqcup \| = \frac{\sqcup \cdot \Delta \sqcup}{\| \sqcup \|} \tag{B.3}$$

is used. $\dfrac{\partial \hat{\boldsymbol{n}}(\xi,\eta)}{\partial \boldsymbol{u}_J}$ is defined by

$$\frac{\partial \hat{\boldsymbol{n}}(\xi,\eta)}{\partial \boldsymbol{u}_J} = \frac{\partial}{\partial \boldsymbol{u}_J}\Big[\sum_I^{\text{nnode}} \frac{\partial N_I(\xi,\eta)}{\partial \xi}\boldsymbol{x}_I \times \sum_I^{\text{nnode}} \frac{\partial N_I(\xi,\eta)}{\partial \eta}\boldsymbol{x}_I\Big]. \tag{B.4}$$

Using the relation $\dfrac{\partial}{\partial \boldsymbol{a}}\big(\boldsymbol{a}\times\boldsymbol{b}\big) = -[\boldsymbol{B}]$, where $[\boldsymbol{B}] = skew(\boldsymbol{b})$ is defined by

$$[\boldsymbol{B}] = \begin{bmatrix} 0 & -b_3 & b_2 \\ b_3 & 0 & -b_1 \\ -b_2 & b_1 & 0 \end{bmatrix} \tag{B.5}$$

and $\dfrac{\partial}{\partial \boldsymbol{b}}\big(\boldsymbol{a}\times\boldsymbol{b}\big) = [\boldsymbol{A}] = skew(\boldsymbol{a})$, Eq. (B.4) becomes

$$\begin{aligned}\frac{\partial \hat{\boldsymbol{n}}(\xi,\eta)}{\partial \boldsymbol{u}_J} =& \Big[\sum_I^{\text{nnode}} \frac{\partial N_I(\xi,\eta)}{\partial \xi} skew(\boldsymbol{x}_I)\Big]\frac{dN_J(\xi,\eta)}{\partial \eta} \\ &- \Big[\sum_I^{\text{nnode}} \frac{\partial N_I(\xi,\eta)}{\partial \eta} skew(\boldsymbol{x}_I)\Big]\frac{\partial N_J(\xi,\eta)}{\partial \xi}.\end{aligned} \tag{B.6}$$

In general, $\dfrac{\partial \hat{\boldsymbol{n}}(\xi,\eta)}{\partial \boldsymbol{u}_J}$ is unsymmetric. For every location ξ,η on a finite element face, Eq. (B.6) is computed for the displacement $\boldsymbol{u}_J$ of every node J of the face. Component-wise, Eq. (B.6) can be written by

$$\begin{aligned}\frac{\partial \hat{\boldsymbol{n}}(\xi,\eta)}{\partial \boldsymbol{u}_J} &= \frac{\partial}{\partial \boldsymbol{u}_J}\begin{bmatrix} \sum_I^{\text{n}} \frac{\partial N_I}{\partial \xi}x_{2,I}\sum_I^{\text{n}} \frac{\partial N_I}{\partial \eta}x_{3,I} - \sum_I^{\text{n}} \frac{\partial N_I}{\partial \xi}x_{3,I}\sum_I^{\text{n}} \frac{\partial N_I}{\partial \eta}x_{2,I} \\ \sum_I^{\text{n}} \frac{\partial N_I}{\partial \xi}x_{3,I}\sum_I^{\text{n}} \frac{\partial N_I}{\partial \eta}x_{1,I} - \sum_I^{\text{n}} \frac{\partial N_I}{\partial \xi}x_{1,I}\sum_I^{\text{n}} \frac{\partial N_I}{\partial \eta}x_{3,I} \\ \sum_I^{\text{n}} \frac{\partial N_I}{\partial \xi}x_{1,I}\sum_I^{\text{n}} \frac{\partial N_I}{\partial \eta}x_{2,I} - \sum_I^{\text{n}} \frac{\partial N_I}{\partial \xi}x_{2,I}\sum_I^{\text{n}} \frac{\partial N_I}{\partial \eta}x_{1,I} \end{bmatrix} \\ &= \left[\begin{array}{c|c} 0 & \sum_I^{\text{n}} \frac{\partial N_I}{\partial \xi}x_{2,I}\frac{\partial N_J}{\partial \eta} - \frac{\partial N_J}{\partial \xi}\sum_I^{\text{n}} \frac{\partial N_I}{\partial \eta}x_{2,I} \\ \hline \frac{\partial N_J}{\partial \xi}\sum_I^{\text{n}} \frac{\partial N_I}{\partial \eta}x_{3,I} - \sum_I^{\text{n}} \frac{\partial N_I}{\partial \xi}x_{3,I}\frac{\partial N_J}{\partial \eta} & \frac{\partial N_J}{\partial \xi}\sum_I^{\text{n}} \frac{\partial N_I}{\partial \eta}x_{1,I} - \sum_I^{\text{n}} \frac{\partial N_I}{\partial \xi}x_{1,I}\frac{\partial N_J}{\partial \eta} \\ \hline \sum_I^{\text{n}} \frac{\partial N_I}{\partial \xi}x_{1,I}\frac{\partial N_J}{\partial \eta} - \frac{\partial N_J}{\partial \xi}\sum_I^{\text{n}} \frac{\partial N_I}{\partial \eta}x_{1,I} & 0 \end{array}\right].\end{aligned} \tag{B.7}$$

In a similar way the derivative of the tangential vector is obtained.

B.2.2 Derivatives of the convective coordinate

The goal is to derive an explicit expression for the derivative of the convective coordinate $\bar{\xi}^{(i)}$ ($i = \{1, 2\}$) with respect to the displacement of node I. The term used for the calculation of the convective coordinate in 2D analyses $\boldsymbol{g}_I \cdot \boldsymbol{x}^{(2)}_{,\xi}(\bar{\xi}^{(2)}) = \Big[\sum_J^{\text{nnode}} N^{(2)}_J(\bar{\xi}^{(2)}) \boldsymbol{x}^{(2)}_J - \boldsymbol{x}^{(1)}_I \Big] \cdot \boldsymbol{x}^{(2)}_{,\xi}(\bar{\xi}^{(2)})$ can be differentiated by $\boldsymbol{u}^{(1)}_I$ yielding

$$\frac{\partial}{\partial \boldsymbol{u}^{(1)}_I} \Bigg\{ \Big[\sum_J^{\text{nnode}} N^{(2)}_J(\bar{\xi}^{(2)}) \boldsymbol{x}^{(2)}_J - \boldsymbol{x}^{(1)}_I \Big] \cdot \boldsymbol{x}^{(2)}_{,\xi}(\bar{\xi}^{(2)}) \Bigg\} = \boldsymbol{0}. \tag{B.8}$$

Using the chain-rule, the following expression is obtained

$$\begin{aligned} &\Big[\sum_J^{\text{nnode}} \frac{\partial}{\partial \bar{\xi}^{(2)}} N^{(2)}_J(\bar{\xi}^{(2)}) \boldsymbol{x}^{(2)}_J \frac{\partial \bar{\xi}^{(2)}}{\partial \boldsymbol{u}^{(1)}_I} + \sum_J^{\text{nnode}} N^{(2)}_J(\bar{\xi}^{(2)}) \frac{\partial \boldsymbol{x}^{(2)}_J}{\partial \boldsymbol{u}^{(1)}_I} - \frac{\partial \boldsymbol{x}^{(1)}_I}{\partial \boldsymbol{u}^{(1)}_I} \Big] \cdot \sum_J^{\text{nnode}} N^{(2)}_{J,\xi}(\bar{\xi}^{(2)}) \boldsymbol{x}^{(2)}_J \\ &+ \boldsymbol{g}_I \cdot \sum_J^{\text{nnode}} \frac{\partial}{\partial \bar{\xi}^{(2)}} N^{(2)}_{J,\xi}(\bar{\xi}^{(2)}) \frac{\partial \bar{\xi}^{(2)}}{\partial \boldsymbol{u}^{(1)}_I} \boldsymbol{x}^{(2)}_J + \boldsymbol{g}_I \cdot \sum_J^{\text{nnode}} N^{(2)}_{J,\xi}(\bar{\xi}^{(2)}) \frac{\partial \boldsymbol{x}^{(2)}_J}{\partial \boldsymbol{u}^{(1)}_I} = \boldsymbol{0}. \end{aligned} \tag{B.9}$$

Simplifying and rearranging yields

$$\begin{aligned} &\Big[\sum_J^{\text{nnode}} N^{(2)}_{J,\xi}(\bar{\xi}^{(2)}) \boldsymbol{x}^{(2)}_J \cdot \sum_J^{\text{nnode}} N^{(2)}_{J,\xi}(\bar{\xi}^{(2)}) \boldsymbol{x}^{(2)}_J + \boldsymbol{g}_I \cdot \sum_J^{\text{nnode}} N^{(2)}_{J,\xi\xi}(\bar{\xi}^{(2)}) \boldsymbol{x}^{(2)}_J \Big] \frac{\partial \bar{\xi}^{(2)}}{\partial \boldsymbol{u}^{(1)}_I} \\ &+ \sum_J^{\text{nnode}} N^{(2)}_J(\bar{\xi}^{(2)}) \frac{\partial \boldsymbol{x}^{(2)}_J}{\partial \boldsymbol{u}^{(1)}_I} \cdot \sum_J^{\text{nnode}} N^{(2)}_{J,\xi}(\bar{\xi}^{(2)}) \boldsymbol{x}^{(2)}_J - \sum_J^{\text{nnode}} N^{(2)}_{J,\xi}(\bar{\xi}^{(2)}) \boldsymbol{x}^{(2)}_J \\ &+ \boldsymbol{g}_I \cdot \sum_J^{\text{nnode}} N^{(2)}_{J,\xi}(\bar{\xi}^{(2)}) \frac{\partial \boldsymbol{x}^{(2)}_J}{\partial \boldsymbol{u}^{(1)}_I} = \boldsymbol{0}. \end{aligned} \tag{B.10}$$

Solving for $\dfrac{\partial \bar{\xi}^{(2)}}{\partial \boldsymbol{u}^{(1)}_I}$ and considering that $\dfrac{\partial \boldsymbol{x}^{(2)}_J}{\partial \boldsymbol{u}^{(1)}_I} = \boldsymbol{0}$ holds results in

$$\frac{\partial \bar{\xi}^{(2)}}{\partial \boldsymbol{u}^{(1)}_I} = - \frac{- \sum_J^{\text{nnode}} N^{(2)}_{J,\xi}(\bar{\xi}^{(2)}) \boldsymbol{x}^{(2)}_J}{\sum_J^{\text{nnode}} N^{(2)}_{J,\xi}(\bar{\xi}^{(2)}) \boldsymbol{x}^{(2)}_J \cdot \sum_J^{\text{nnode}} N^{(2)}_{J,\xi}(\bar{\xi}^{(2)}) \boldsymbol{x}^{(2)}_J + \boldsymbol{g}_I \cdot \sum_J^{\text{nnode}} N^{(2)}_{J,\xi\xi}(\bar{\xi}^{(2)}) \boldsymbol{x}^{(2)}_J}. \tag{B.11}$$

Proceeding analogously but differentiating with respect to $\boldsymbol{u}^{(2)}_J$ gives

$$\frac{\partial \bar{\xi}^{(2)}}{\partial \boldsymbol{u}^{(2)}_J} = - \frac{N^{(2)}_J(\bar{\xi}^{(2)}) \sum_J^{\text{nnode}} N^{(2)}_{J,\xi}(\bar{\xi}^{(2)}) \boldsymbol{x}^{(2)}_J + \boldsymbol{g}_I N^{(2)}_{J,\xi}(\bar{\xi}^{(2)})}{\sum_J^{\text{nnode}} N^{(2)}_{J,\xi}(\bar{\xi}^{(2)}) \boldsymbol{x}^{(2)}_J \cdot \sum_J^{\text{nnode}} N^{(2)}_{J,\xi}(\bar{\xi}^{(2)}) \boldsymbol{x}^{(2)}_J + \boldsymbol{g}_I \cdot \sum_J^{\text{nnode}} N^{(2)}_{J,\xi\xi}(\bar{\xi}^{(2)}) \boldsymbol{x}^{(2)}_J}. \tag{B.12}$$

The derivatives of $\bar{\xi}^{(1)}$ are obtained likewise utilising Eq. (6.29) for the EBM contact discretisation and Eq. (6.37) in case of the SBM technique. The derivatives of the vector of local

convective coordinates $\bar{\boldsymbol{\xi}}^{(i)} = \left[\bar{\xi}^{(i)}, \bar{\eta}^{(i)}\right]^T$ for 3D analyses are calculated analogously giving the 2×3 matrix $\dfrac{\partial \bar{\boldsymbol{\xi}}^{(i)}}{\partial \boldsymbol{u}_J^{(j)}}$.

B.2.3 Derivatives of local segment coordinates

For the SBM contact discretisation, the derivative of the local coordinates of the segment are required. The derivative of the local coordinate of the finite element given in terms of the local coordinate of the segment calculated using Eq. (6.40) with respect to the node displacement is for quadratically interpolated finite elements given by

$$\frac{\partial \xi^{(i)}(\eta)}{\partial \boldsymbol{u}_I^{(i)}} = -\frac{1}{2}\eta(1-\eta)\frac{\partial \xi_a^{(i)}}{\partial \boldsymbol{u}_I^{(i)}} + \frac{1}{2}\eta(1+\eta)\frac{\partial \xi_b^{(i)}}{\partial \boldsymbol{u}_I^{(i)}} + (1-\eta^2)\frac{\partial \xi_c^{(i)}}{\partial \boldsymbol{u}_I^{(i)}}. \tag{B.13}$$

The derivatives of the local convective coordinates at the segment borders ($\xi_a^{(i)}$ and $\xi_b^{(i)}$) can be obtained with the formulas that have been derived in the previous section. $\dfrac{\partial \xi_c^{(1)}}{\partial \boldsymbol{u}_I^{(i)}}$ is defined by

$$\frac{\partial \xi_c^{(1)}}{\partial \boldsymbol{u}_I^{(i)}} = \Big(\frac{\partial \xi_a^{(1)}}{\partial \boldsymbol{u}_I^{(i)}} + \frac{\partial \xi_b^{(1)}}{\partial \boldsymbol{u}_I^{(i)}}\Big)/2. \tag{B.14}$$

B.2.4 Derivatives of the integration area and volume

For 2D analyses using the SBM contact discretisation, the derivative of $j_{\text{igp}}^{(i)} = \left|\left|\dfrac{\partial \boldsymbol{x}^{(i)}(\xi_{\text{igp}})}{\partial \xi^{(i)}}\right|\right| \dfrac{\partial \xi^{(i)}(\eta_{\text{igp}})}{\partial \eta}$ with respect to the node displacement is required. The derivative depends on the interpolation order of the finite elements. For quadratically interpolated elements, the second term of $j_{\text{igp}}^{(i)}$ is

$$\frac{\partial \xi^{(i)}(\eta_{\text{igp}})}{\partial \eta} = -\frac{1}{2}(1-\eta_{\text{igp}})\xi_a^{(i)} + \frac{1}{2}\eta_{\text{igp}}\xi_a^{(i)} + \frac{1}{2}(1+\eta_{\text{igp}})\xi_b^{(i)} + \frac{1}{2}\eta_{\text{igp}}\xi_b^{(i)} + (1-2\eta_{\text{igp}})\xi_c^{(i)} \tag{B.15}$$

and the derivative with respect to the displacement is consequently given by

$$\begin{aligned}\frac{\partial \partial \xi^{(i)}(\eta_{\text{igp}})}{\partial \boldsymbol{u}_I^{(i)} \partial \eta} = &-\frac{1}{2}(1-\eta_{\text{igp}})\frac{\partial \xi_a^{(i)}}{\partial \boldsymbol{u}_I^{(i)}} + \frac{1}{2}\eta_{\text{igp}}\frac{\partial \xi_a^{(i)}}{\partial \boldsymbol{u}_I^{(i)}} + \frac{1}{2}(1+\eta_{\text{igp}})\frac{\partial \xi_b^{(i)}}{\partial \boldsymbol{u}_I^{(i)}} \\ &+ \frac{1}{2}\eta_{\text{igp}}\frac{\partial \xi_b^{(i)}}{\partial \boldsymbol{u}_I^{(i)}} + (1-2\eta_{\text{igp}})\frac{\partial \xi_c^{(i)}}{\partial \boldsymbol{u}_I^{(i)}}.\end{aligned} \tag{B.16}$$

Recalling Eq. (B.3), the first term of Eq. (B.15) for quadratically or higher order interpolated elements is defined by

$$\frac{\partial}{\partial \boldsymbol{u}_I^{(i)}}\left|\left|\frac{\partial \boldsymbol{x}^{(i)}(\xi_{\text{igp}})}{\partial \xi^{(i)}}\right|\right| = \frac{\partial \boldsymbol{x}^{(i)}(\xi_{\text{igp}})}{\partial \xi^{(i)}} \cdot \frac{\partial}{\partial \boldsymbol{u}_I^{(i)}} \frac{\partial \boldsymbol{x}^{(i)}(\xi_{\text{igp}})}{\partial \xi^{(i)}} / \left|\left|\frac{\partial \boldsymbol{x}^{(i)}(\xi_{\text{igp}})}{\partial \xi^{(i)}}\right|\right|. \tag{B.17}$$

For the EBM contact discretisation, only the first term of $j_{\text{igp}}^{(i)}$ is relevant and hence only the derivative given in Eq. (B.15) is required.

For 3D analyses the derivative of the determinant of the 2 x 2 matrix $\mathbf{J}(\xi_{\text{igp}}, \eta_{\text{igp}})$ given by Eq. (4.2) is required for the integration of surfaces since $j_{\text{igp}} = \det \mathbf{J}(\xi_{\text{igp}}, \eta_{\text{igp}})$ holds. In general, the derivative of the determinant of a matrix with respect to itself is its transposed adjugate (Jacobi's formula). Hence, differentiating with respect to the displacement, the required derivative is defined by

$$\frac{\partial \det \mathbf{J}}{\partial \boldsymbol{u}_J} = \text{adj}[\mathbf{J}(\xi_{\text{igp}}, \eta_{\text{igp}})]^T : \frac{\partial \mathbf{J}(\xi_{\text{igp}}, \eta_{\text{igp}})}{\partial \boldsymbol{u}_J}. \tag{B.18}$$

For the implementation, it is convenient to write Eq. (B.18) component-wise, viz.

$$\frac{\partial \det \mathbf{J}}{\partial \boldsymbol{u}_J} = \frac{\partial}{\partial \boldsymbol{u}_J}\left[\sum_I^{\text{n}} \frac{\partial N_I}{\partial \xi} x_{1,I} \sum_I^{\text{n}} \frac{\partial N_I}{\partial \eta} x_{2,I} - \sum_I^{\text{n}} \frac{\partial N_I}{\partial \xi} x_{2,I} \sum_I^{\text{n}} \frac{\partial N_I}{\partial \eta} x_{1,I}\right] \tag{B.19}$$

$$= \begin{bmatrix} \frac{\partial N_J}{\partial \xi} \sum_I^{\text{n}} \frac{\partial N_I}{\partial \eta} x_{2,I} - \frac{\partial N_J}{\partial \eta} \sum_I^{\text{n}} \frac{\partial N_I}{\partial \xi} x_{2,I} \\ \frac{\partial N_J}{\partial \eta} \sum_I^{\text{n}} \frac{\partial N_I}{\partial \xi} x_{1,I} - \frac{\partial N_J}{\partial \xi} \sum_I^{\text{n}} \frac{\partial N_I}{\partial \eta} x_{1,I} \end{bmatrix}. \tag{B.20}$$

Note that the interpolation functions in Eq. (B.19) are evaluated at the location of the integration points of the finite element face ξ_{igp} and η_{igp}.

For 3D analyses in an updated Lagrangian framework the derivative of the determinant of the 3 x 3 matrix $\mathbf{J}(\xi_{\text{igp}}, \eta_{\text{igp}}, \zeta_{\text{igp}})$ is required when integrating 3D finite elements. Again, Jacobi's formula is used yielding

$$\frac{\partial \det \mathbf{J}}{\partial \boldsymbol{u}_J} = \text{adj}[\mathbf{J}(\xi_{\text{igp}}, \eta_{\text{igp}}, \zeta_{\text{igp}})]^T : \frac{\partial \mathbf{J}(\xi_{\text{igp}}, \eta_{\text{igp}}, \zeta_{\text{igp}})}{\partial \boldsymbol{u}_J}. \tag{B.21}$$

In analogy to Eq. (B.19), it is convenient to differentiate the determinant of $\mathbf{J}$ before writing

the results component-wise required for the implementation, viz.

$$\begin{aligned}\frac{\partial \det \mathbf{J}}{\partial \boldsymbol{u}_J} =& \frac{\partial}{\partial \boldsymbol{u}_J}\Bigg[\sum_I^{\mathrm{n}} \frac{\partial N_I}{\partial \xi} x_{1,I} \sum_I^{\mathrm{n}} \frac{\partial N_I}{\partial \eta} x_{2,I} \sum_I^{\mathrm{n}} \frac{\partial N_I}{\partial \zeta} x_{3,I} \\ &- \sum_I^{\mathrm{n}} \frac{\partial N_I}{\partial \xi} x_{1,I} \sum_I^{\mathrm{n}} \frac{\partial N_I}{\partial \eta} x_{3,I} \sum_I^{\mathrm{n}} \frac{\partial N_I}{\partial \zeta} x_{2,I} - \sum_I^{\mathrm{n}} \frac{\partial N_I}{\partial \xi} x_{2,I} \sum_I^{\mathrm{n}} \frac{\partial N_I}{\partial \eta} x_{1,I} \sum_I^{\mathrm{n}} \frac{\partial N_I}{\partial \zeta} x_{3,I} \\ &+ \sum_I^{\mathrm{n}} \frac{\partial N_I}{\partial \xi} x_{2,I} \sum_I^{\mathrm{n}} \frac{\partial N_I}{\partial \eta} x_{3,I} \sum_I^{\mathrm{n}} \frac{\partial N_I}{\partial \zeta} x_{1,I} + \sum_I^{\mathrm{n}} \frac{\partial N_I}{\partial \xi} x_{3,I} \sum_I^{\mathrm{n}} \frac{\partial N_I}{\partial \eta} x_{1,I} \sum_I^{\mathrm{n}} \frac{\partial N_I}{\partial \zeta} x_{2,I} \\ &- \sum_I^{\mathrm{n}} \frac{\partial N_I}{\partial \xi} x_{3,I} \sum_I^{\mathrm{n}} \frac{\partial N_I}{\partial \eta} x_{2,I} \sum_I^{\mathrm{n}} \frac{\partial N_I}{\partial \zeta} x_{1,I}\Bigg]. \end{aligned} \tag{B.22}$$

Note that the determinant of a matrix is equivalent to the determinant of its transposed. Eq. (B.22) yields

$$\begin{aligned}\frac{\partial \det \mathbf{J}}{\partial \boldsymbol{u}_J} =& \begin{bmatrix} \frac{\partial N_J}{\partial \xi} \sum_I^{\mathrm{n}} \frac{\partial N_I}{\partial \eta} x_{2,I} \sum_I^{\mathrm{n}} \frac{\partial N_I}{\partial \zeta} x_{3,I} - \frac{\partial N_J}{\partial \xi} \sum_I^{\mathrm{n}} \frac{\partial N_I}{\partial \eta} x_{3,I} \sum_I^{\mathrm{n}} \frac{\partial N_I}{\partial \zeta} x_{2,I} \\ \frac{\partial N_J}{\partial \eta} \sum_I^{\mathrm{n}} \frac{\partial N_I}{\partial \xi} x_{1,I} \sum_I^{\mathrm{n}} \frac{\partial N_I}{\partial \zeta} x_{3,I} - \frac{\partial N_J}{\partial \zeta} \sum_I^{\mathrm{n}} \frac{\partial N_I}{\partial \xi} x_{1,I} \sum_I^{\mathrm{n}} \frac{\partial N_I}{\partial \eta} x_{3,I} \\ \frac{\partial N_J}{\partial \zeta} \sum_I^{\mathrm{n}} \frac{\partial N_I}{\partial \xi} x_{1,I} \sum_I^{\mathrm{n}} \frac{\partial N_I}{\partial \eta} x_{2,I} - \frac{\partial N_J}{\partial \eta} \sum_I^{\mathrm{n}} \frac{\partial N_I}{\partial \xi} x_{1,I} \sum_I^{\mathrm{n}} \frac{\partial N_I}{\partial \zeta} x_{2,I} \end{bmatrix} \\ &+ \begin{bmatrix} -\frac{\partial N_J}{\partial \eta} \sum_I^{\mathrm{n}} \frac{\partial N_I}{\partial \xi} x_{2,I} \sum_I^{\mathrm{n}} \frac{\partial N_I}{\partial \zeta} x_{3,I} + \frac{\partial N_J}{\partial \zeta} \sum_I^{\mathrm{n}} \frac{\partial N_I}{\partial \xi} x_{2,I} \sum_I^{\mathrm{n}} \frac{\partial N_I}{\partial \eta} x_{3,I} \\ -\frac{\partial N_J}{\partial \xi} \sum_I^{\mathrm{n}} \frac{\partial N_I}{\partial \eta} x_{1,I} \sum_I^{\mathrm{n}} \frac{\partial N_I}{\partial \zeta} x_{3,I} + \frac{\partial N_J}{\partial \zeta} \sum_I^{\mathrm{n}} \frac{\partial N_I}{\partial \eta} x_{3,I} \sum_I^{\mathrm{n}} \frac{\partial N_I}{\partial \xi} x_{1,I} \\ -\frac{\partial N_J}{\partial \zeta} \sum_I^{\mathrm{n}} \frac{\partial N_I}{\partial \xi} x_{2,I} \sum_I^{\mathrm{n}} \frac{\partial N_I}{\partial \eta} x_{1,I} + \frac{\partial N_J}{\partial \eta} \sum_I^{\mathrm{n}} \frac{\partial N_I}{\partial \xi} x_{2,I} \sum_I^{\mathrm{n}} \frac{\partial N_I}{\partial \zeta} x_{1,I} \end{bmatrix} \\ &+ \begin{bmatrix} \frac{\partial N_J}{\partial \eta} \sum_I^{\mathrm{n}} \frac{\partial N_I}{\partial \xi} x_{3,I} \sum_I^{\mathrm{n}} \frac{\partial N_I}{\partial \zeta} x_{2,I} - \frac{\partial N_J}{\partial \zeta} \sum_I^{\mathrm{n}} \frac{\partial N_I}{\partial \xi} x_{3,I} \sum_I^{\mathrm{n}} \frac{\partial N_I}{\partial \eta} x_{2,I} \\ \frac{\partial N_J}{\partial \zeta} \sum_I^{\mathrm{n}} \frac{\partial N_I}{\partial \xi} x_{3,I} \sum_I^{\mathrm{n}} \frac{\partial N_I}{\partial \eta} x_{1,I} - \frac{\partial N_J}{\partial \eta} \sum_I^{\mathrm{n}} \frac{\partial N_I}{\partial \xi} x_{3,I} \sum_I^{\mathrm{n}} \frac{\partial N_I}{\partial \zeta} x_{1,I} \\ \frac{\partial N_J}{\partial \xi} \sum_I^{\mathrm{n}} \frac{\partial N_I}{\partial \eta} x_{1,I} \sum_I^{\mathrm{n}} \frac{\partial N_I}{\partial \zeta} x_{2,I} - \frac{\partial N_J}{\partial \eta} \sum_I^{\mathrm{n}} \frac{\partial N_I}{\partial \xi} x_{2,I} \sum_I^{\mathrm{n}} \frac{\partial N_I}{\partial \zeta} x_{1,I} \end{bmatrix}. \end{aligned} \tag{B.23}$$

Again, the interpolation functions in Eq. (B.23) are evaluated at $\xi_{\mathrm{igp}},\ \eta_{\mathrm{igp}},\ \zeta_{\mathrm{igp}}$.

B.2.5 Normal contact contributions and derivative of the normal contact stress

SBM discretisation technique

Assuming a frictionless case using the penalty regularisation ($t_{N,\mathrm{igp}} = \varepsilon g_{N,\mathrm{igp}}$, $\boldsymbol{t}_{T,\mathrm{igp}}^{(i)} = \mathbf{0}$), the contact contribution to the RHS using the SBM discretisation technique given by Eq. (6.51)

is rewritten to

$$\boldsymbol{r}_{N,I}^{(i),\,\mathrm{SBM}} = \sum_{\mathrm{igp}}^{\mathrm{ngp}} N_I^{(i)}[\xi^{(i)}(\eta_{\mathrm{igp}})] t_{N,\mathrm{igp}} \boldsymbol{n}_{\mathrm{igp}}^{(i)} w_{\mathrm{igp}} j_{\mathrm{igp}}^{(i)}. \tag{B.24}$$

Note that the scalar normal contact stress is identical for both surfaces i. Using the penalty regularisation, the normal contact stress is calculated using Eq. (6.45) yielding

$$\begin{aligned} t_{N,\mathrm{igp}} = \varepsilon g_{N,\mathrm{igp}} &= \varepsilon \big(\boldsymbol{x}_{\mathrm{igp}}^{(2)} - \boldsymbol{x}_{\mathrm{igp}}^{(1)} \big) \cdot \boldsymbol{n}_{\mathrm{igp}}^{(1)} \\ &= \varepsilon \Big\{ \sum_{I}^{\mathrm{nnode}} N_I^{\mathrm{seg}}[\xi^{(2)}(\eta_{\mathrm{igp}})] \boldsymbol{x}_I^{(2)} - \sum_{J}^{\mathrm{nnode}} N_J^{\mathrm{seg}}[\xi^{(1)}(\eta_{\mathrm{igp}})] \boldsymbol{x}_J^{(1)} \Big\} \cdot \boldsymbol{n}_{\mathrm{igp}}^{(1)}. \end{aligned} \tag{B.25}$$

The derivative of the normal contact stress $t_{N,\mathrm{igp}}$ with respect to the corresponding displacement $\boldsymbol{u}_J^{(i)}$ for $i = 1$ is

$$\begin{aligned} \frac{\partial t_{N,\mathrm{igp}}}{\partial \boldsymbol{u}_J^{(1)}} &= -\varepsilon N_J^{\mathrm{seg}}[\xi^{(1)}(\eta_{\mathrm{igp}})] \boldsymbol{n}_{\mathrm{igp}}^{(1)} + \varepsilon \big(\boldsymbol{x}_{\mathrm{igp}}^{(2)} - \boldsymbol{x}_{\mathrm{igp}}^{(1)} \big) \cdot \frac{\partial \boldsymbol{n}_{\mathrm{igp}}^{(1)}}{\partial \boldsymbol{u}_J^{(1)}} \\ &\quad + \varepsilon \Big\{ \sum_{I}^{\mathrm{nnode}} N_{I,\xi}^{\mathrm{seg}}[\xi^{(2)}(\eta_{\mathrm{igp}})] \frac{\partial \xi^{(2)}}{\partial \boldsymbol{u}_J^{(1)}} \otimes \boldsymbol{x}_I^{(2)} - \sum_{J}^{\mathrm{nnode}} N_{J,\xi}^{\mathrm{seg}}[\xi^{(1)}(\eta_{\mathrm{igp}})] \frac{\partial \xi^{(1)}}{\partial \boldsymbol{u}_J^{(1)}} \otimes \boldsymbol{x}_J^{(1)} \Big\} \cdot \boldsymbol{n}_{\mathrm{igp}}^{(1)} \end{aligned} \tag{B.26}$$

and for $i = 2$

$$\begin{aligned} \frac{\partial t_{N,\mathrm{igp}}}{\partial \boldsymbol{u}_I^{(2)}} &= \varepsilon N_I^{\mathrm{seg}}[\xi^{(2)}(\eta_{\mathrm{igp}})] \boldsymbol{n}_{\mathrm{igp}}^{(1)} + \varepsilon \big(\boldsymbol{x}_{\mathrm{igp}}^{(2)} - \boldsymbol{x}_{\mathrm{igp}}^{(1)} \big) \cdot \frac{\partial \boldsymbol{n}_{\mathrm{igp}}^{(1)}}{\partial \boldsymbol{u}_I^{(2)}} \\ &\quad + \varepsilon \Big\{ \sum_{I}^{\mathrm{nnode}} N_{I,\xi}^{\mathrm{seg}}[\xi^{(2)}(\eta_{\mathrm{igp}})] \frac{\partial \xi^{(2)}}{\partial \boldsymbol{u}_J^{(2)}} \otimes \boldsymbol{x}_I^{(2)} - \sum_{J}^{\mathrm{nnode}} N_{J,\xi}^{\mathrm{seg}}[\xi^{(1)}(\eta_{\mathrm{igp}})] \frac{\partial \xi^{(1)}}{\partial \boldsymbol{u}_J^{(2)}} \otimes \boldsymbol{x}_J^{(1)} \Big\} \cdot \boldsymbol{n}_{\mathrm{igp}}^{(1)}. \end{aligned} \tag{B.27}$$

The required derivatives of the local finite element coordinates depending on the local segment coordinate and of the normal vector have already been derived previously.

EBM discretisation technique

The contact contribution to the RHS using the EBM discretisation technique is given in analogy to Eq. (B.24) by

$$\boldsymbol{r}_{N,I}^{(i),\,\mathrm{EBM}} = \sum_{\mathrm{igp}}^{\mathrm{ngp}} N_I^{(i)}(\xi_{\mathrm{igp}}^{(i)}) t_{N,\mathrm{igp}}^{(i)} \boldsymbol{n}_{\mathrm{igp}}^{(i)} w_{\mathrm{igp}}^{(i)} j_{\mathrm{igp}}^{(i)} \tag{B.28}$$

if the normal contact stress is evaluated directly for the integration points (see Section 6.3). Note that the integration points used in Eq. (B.28) are the actual integration points located on the finite element edges or faces. In addition, every term in Eq. (B.28) is different for the different surfaces $i = \{1, 2\}$. If the projection is performed to the nodes instead to integration points of the paired surface, Eq. (B.28) is rewritten to

$$\boldsymbol{r}_{N,I}^{(i),\,\mathrm{EBM}} = \sum_{\mathrm{igp}}^{\mathrm{ngp}} N_I^{(i)}(\xi_{\mathrm{igp}}^{(i)}) \Big[\sum_{I}^{\mathrm{nnode}} N_I^{(i)}(\xi_{\mathrm{igp}}^{(i)}) t_{N,I}^{(i)} \Big] \boldsymbol{n}_{\mathrm{igp}}^{(i)} w_{\mathrm{igp}}^{(i)} j_{\mathrm{igp}}^{(i)}, \tag{B.29}$$

where the normal contact stress is first interpolated to the integration points of the edge or surface of the finite element.

The derivative of the normal contact stress $t_{N,\mathrm{igp}}^{(i)}$ at the integration point with respect to the corresponding displacement $\boldsymbol{u}_I^{(i)}$ for $i = \{1, 2\}$ and $j = \{2, 1\}$ is

$$\begin{aligned} \frac{\partial t_{N,\mathrm{igp}}^{(i)}}{\partial \boldsymbol{u}_I^{(i)}} = &-\varepsilon N_I^{(i)}(\xi_{\mathrm{igp}}^{(i)}) \boldsymbol{n}^{(j)}(\bar{\xi}_{\mathrm{igp}}^{(j)}) + \varepsilon \Big[\sum_{J}^{\mathrm{nnode}} N_{J,\xi}^{(j)}(\bar{\xi}_{\mathrm{igp}}^{(j)}) \frac{\partial \xi^{(j)}}{\partial \boldsymbol{u}_I^{(i)}} \otimes \boldsymbol{x}_J^{(j)} - \sum_{I}^{\mathrm{nnode}} N_{I,\xi}^{(i)}(\xi_{\mathrm{igp}}^{(i)}) \frac{\partial \xi^{(i)}}{\partial \boldsymbol{u}_I^{(i)}} \otimes \boldsymbol{x}_I^{(i)} \Big] \\ &\cdot \boldsymbol{n}^{(j)}(\bar{\xi}_{\mathrm{igp}}^{(j)}) + \varepsilon \Big[\sum_{J}^{\mathrm{nnode}} N_J^{(j)}(\bar{\xi}_{\mathrm{igp}}^{(j)}) \boldsymbol{x}_J^{(j)} - \sum_{I}^{\mathrm{nnode}} N_I^{(i)}(\xi_{\mathrm{igp}}^{(i)}) \boldsymbol{x}_I^{(i)} \Big] \cdot \frac{\partial \boldsymbol{n}^{(j)}(\bar{\xi}_{\mathrm{igp}}^{(j)})}{\partial \boldsymbol{u}_I^{(i)}}. \end{aligned} \tag{B.30}$$

In Eq. (B.30), $\bar{\xi}_{\mathrm{igp}}^{(j)}$ is the convective coordinate of surface j giving the minimum distance to the integration point of the paired surface i. Likewise,

$$\begin{aligned} \frac{\partial t_{N,\mathrm{igp}}^{(i)}}{\partial \boldsymbol{u}_J^{(j)}} = &\varepsilon N_J^{(j)}(\bar{\xi}_{\mathrm{igp}}^{(j)}) \boldsymbol{n}^{(j)}(\bar{\xi}_{\mathrm{igp}}^{(j)}) + \varepsilon \Big[\sum_{J}^{\mathrm{nnode}} N_{J,\xi}^{(j)}(\bar{\xi}_{\mathrm{igp}}^{(j)}) \frac{\partial \xi^{(j)}}{\partial \boldsymbol{u}_J^{(j)}} \otimes \boldsymbol{x}_J^{(j)} - \sum_{I}^{\mathrm{nnode}} N_{I,\xi}^{(i)}(\xi_{\mathrm{igp}}^{(i)}) \frac{\partial \xi^{(i)}}{\partial \boldsymbol{u}_J^{(j)}} \otimes \boldsymbol{x}_I^{(i)} \Big] \\ &\cdot \boldsymbol{n}^{(j)}(\bar{\xi}_{\mathrm{igp}}^{(j)}) + \varepsilon \Big[\sum_{J}^{\mathrm{nnode}} N_J^{(j)}(\bar{\xi}_{\mathrm{igp}}^{(j)}) \boldsymbol{x}_J^{(j)} - \sum_{I}^{\mathrm{nnode}} N_I^{(i)}(\xi_{\mathrm{igp}}^{(i)}) \boldsymbol{x}_I^{(i)} \Big] \cdot \frac{\partial \boldsymbol{n}^{(j)}(\bar{\xi}_{\mathrm{igp}}^{(j)})}{\partial \boldsymbol{u}_J^{(j)}} \end{aligned} \tag{B.31}$$

is obtained.

When using Eq. (B.29) to integrate the contact contributions, the derivatives given by Eqs. (B.30, B.26) hold if the quantities evaluated at the integration points are replaced by the values at the nodes.

B.2.6 Derivatives of normal contact contributions to the LHS

Using Eqs. (B.26, B.2, B.15, B.16), the normal contact contribution to the LHS of node I of the slave surface with respect to the displacement of a node I at the slave surface using the

SBM contact discretisation is given by

$$\begin{aligned}\frac{\partial \boldsymbol{r}_{N,I}^{(1),\,\mathrm{SBM}}}{\partial \boldsymbol{u}_I^{(1)}} = \sum_{\mathrm{igp}}^{\mathrm{ngp}} \Bigg\{ & N_I^{(1)}[\xi^{(1)}(\eta_{\mathrm{igp}})] \frac{\partial t_{N,\mathrm{igp}}}{\partial \boldsymbol{u}_I^{(1)}} \otimes \boldsymbol{n}_{\mathrm{igp}}^{(1)} w_{\mathrm{igp}} j_{\mathrm{igp}}^{(1)} \\ & + N_{I,\xi}^{(1)}[\xi^{(1)}(\eta_{\mathrm{igp}})] \frac{\partial \xi^{(1)}(\eta_{\mathrm{igp}})}{\partial \boldsymbol{u}_I^{(1)}} \otimes \boldsymbol{n}_{\mathrm{igp}}^{(1)} t_{N,\mathrm{igp}} w_{\mathrm{igp}} j_{\mathrm{igp}}^{(1)} \\ & + N_I^{(1)}[\xi^{(1)}(\eta_{\mathrm{igp}})] t_{N,\mathrm{igp}} \frac{\partial \boldsymbol{n}_{\mathrm{igp}}^{(1)}}{\partial \boldsymbol{u}_I^{(1)}} w_{\mathrm{igp}} j_{\mathrm{igp}}^{(1)} + N_I^{(1)}[\xi^{(1)}(\eta_{\mathrm{igp}})] t_{N,\mathrm{igp}} w_{\mathrm{igp}} \boldsymbol{n}_{\mathrm{igp}}^{(1)} \otimes \Bigg[\frac{\partial \boldsymbol{x}^{(1)}(\xi_{\mathrm{igp}})}{\partial \xi^{(1)}} \\ & \cdot \frac{\partial \partial \boldsymbol{x}^{(1)}(\xi_{\mathrm{igp}})}{\partial \boldsymbol{u}_I^{(1)} \partial \xi^{(1)}} \frac{\partial \xi^{(1)}(\eta_{\mathrm{igp}})}{\partial \eta} \Big/ \Big|\Big| \frac{\partial \boldsymbol{x}^{(1)}(\xi_{\mathrm{igp}})}{\partial \xi^{(1)}} \Big|\Big| + \Big|\Big| \frac{\partial \boldsymbol{x}^{(1)}(\xi_{\mathrm{igp}})}{\partial \xi^{(1)}} \Big|\Big| \frac{\partial \partial \xi^{(1)}(\eta_{\mathrm{igp}})}{\partial \boldsymbol{u}_I^{(1)} \partial \eta} \Bigg] \Bigg\}. \end{aligned} \tag{B.32}$$

$\dfrac{\partial \boldsymbol{r}_{N,I}^{(2)}}{\partial \boldsymbol{u}_I^{(2)}}$ is obtained analogously. In addition, the terms $\dfrac{\partial \boldsymbol{r}_{N,I}^{(1)}}{\partial \boldsymbol{u}_J^{(2)}}$ and $\dfrac{\partial \boldsymbol{r}_{N,J}^{(2)}}{\partial \boldsymbol{u}_I^{(1)}}$ have to be accounted for, which consider the change of the contact forces with respect to the displacement of the paired surface node.

Using the EBM contact discretisation in 2D analyses, the derivative corresponding to Eq. (B.32) is given by

$$\begin{aligned}\frac{\partial \boldsymbol{r}_{N,I}^{(1),\,\mathrm{EBM}}}{\partial \boldsymbol{u}_I^{(1)}} = \sum_{\mathrm{igp}}^{\mathrm{ngp}} \Bigg\{ & N_I^{(1)}(\xi_{\mathrm{igp}}^{(1)}) \frac{\partial t_{N,\mathrm{igp}}^{(1)}}{\partial \boldsymbol{u}_I^{(1)}} \otimes \boldsymbol{n}_{\mathrm{igp}}^{(1)} w_{\mathrm{igp}}^{(1)} j_{\mathrm{igp}}^{(1)} + N_I^{(1)}(\xi_{\mathrm{igp}}^{(1)}) t_{N,\mathrm{igp}}^{(1)} \frac{\partial \boldsymbol{n}_{\mathrm{igp}}^{(1)}}{\partial \boldsymbol{u}_I^{(1)}} w_{\mathrm{igp}}^{(1)} j_{\mathrm{igp}}^{(1)} \\ & + N_I^{(1)}(\xi_{\mathrm{igp}}^{(1)}) t_{N,\mathrm{igp}}^{(1)} w_{\mathrm{igp}}^{(1)} \boldsymbol{n}_{\mathrm{igp}}^{(1)} \otimes \frac{\partial \boldsymbol{x}^{(1)}(\xi_{\mathrm{igp}})}{\partial \xi^{(1)}} \cdot \frac{\partial \partial \boldsymbol{x}^{(1)}(\xi_{\mathrm{igp}})}{\partial \boldsymbol{u}_I^{(1)} \partial \xi^{(1)}} \Big/ \Big|\Big| \frac{\partial \boldsymbol{x}^{(1)}(\xi_{\mathrm{igp}})}{\partial \xi^{(1)}} \Big|\Big| \Bigg\}. \end{aligned} \tag{B.33}$$

B.2.7 Derivatives of tangential contact contributions to the LHS

For three-dimensional analyses, the contribution to the force equilibrium of the frictional contact forces $\boldsymbol{r}_{T,I}^{(i)}$ for the SBM contact discretisation technique is given by

$$\boldsymbol{r}_{T,I}^{(i),\,\mathrm{SBM}} = \sum_{\alpha}^{\mathrm{ndim\text{-}1}} \sum_{\mathrm{igp}}^{\mathrm{ngp}} N_I^{(i)}[\xi^{(i)}(\eta_{\mathrm{igp}})] t_{T,\mathrm{igp},\alpha}^{(i)} \boldsymbol{\tau}_{\mathrm{igp},\alpha}^{(i)} w_{\mathrm{igp}}^{(i)} j_{\mathrm{igp}}^{(i)} \quad \text{for} \quad i = \{1, 2\}, \tag{B.34}$$

where the subscript α denotes the local direction (ξ, η). For the EBM discretisation $N_I^{(i)}[\xi^{(i)}(\eta_{\mathrm{igp}})]$ is replaced by $N_I^{(i)}(\xi_{\mathrm{igp}}^{(i)})$.

The tangential contact stress is a function of the tangential gap and can also be a function of the effective normal contact stress $t'_{N,\mathrm{igp}}$. The derivative with respect to the displacement is

given by

$$\frac{\partial t^{(i)}_{T,\mathrm{igp},\alpha}}{\partial \boldsymbol{u}^{(i)}_I} = \frac{\partial t^{(i)}_{T,\mathrm{igp},\alpha}}{\partial t'_{N,\mathrm{igp}}} \frac{\partial t'_{N,\mathrm{igp}}}{\partial \boldsymbol{u}^{(i)}_I} + \frac{\partial t^{(i)}_{T,\mathrm{igp},\alpha}}{\partial g_{T,\mathrm{igp},\alpha}} \frac{\partial g_{T,\mathrm{igp},\alpha}}{\partial \boldsymbol{u}^{(i)}_I} \quad \text{for} \quad i = \{1, 2\}. \tag{B.35}$$

The derivatives $\dfrac{\partial t^{(i)}_{T,\mathrm{igp},\alpha}}{\partial t'_{N,\mathrm{igp}}}$ and $\dfrac{\partial t^{(i)}_{T,\mathrm{igp},\alpha}}{\partial g_{T,\mathrm{igp},\alpha}}$ are calculated in dependence of the friction model used. They can be found in the literature for the Coulomb friction model [424] and are obtained using the constitutive Jacobian $\dfrac{\partial \Delta\boldsymbol{\sigma}}{\partial \Delta\boldsymbol{\varepsilon}}$ in case of the hypoplastic and Sanisand friction model (see also Eq. (6.90)). $\dfrac{\partial g_{N,\mathrm{igp}}}{\partial \boldsymbol{u}^{(i)}_I}$ can directly be obtained by Eqs. (B.26, B.27) detaching the penalty factor ε for the SBM contact discretisation and by Eqs. (B.30, B.31) for the EBM technique. $\dfrac{\partial g_{T,\mathrm{igp},\alpha}}{\partial \boldsymbol{u}^{(1)}_I}$ for the SBM contact discretisation is given in analogy to Eq. (B.26) by

$$\begin{aligned}\frac{\partial g_{T,\mathrm{igp},\alpha}}{\partial \boldsymbol{u}^{(1)}_I} =& - N_I[\xi^{(1)}(\eta_{\mathrm{igp}})]\boldsymbol{\tau}^{(1)}_{\mathrm{igp},\alpha} + \left(\boldsymbol{x}^{(2)}_{\mathrm{igp}} - \boldsymbol{x}^{(1)}_{\mathrm{igp}}\right) \cdot \frac{\partial \boldsymbol{\tau}^{(1)}_{\mathrm{igp},\alpha}}{\partial \boldsymbol{u}^{(1)}_I} \\ &+ \left\{ \sum_I^{\mathrm{nnode}} N_{I,\xi}[\xi^{(2)}(\eta_{\mathrm{igp}})] \frac{\partial \xi^{(2)}}{\partial \boldsymbol{u}^{(1)}_I} \otimes \boldsymbol{x}^{(2)}_I - \sum_J^{\mathrm{nnode}} N_{J,\xi}[\xi^{(1)}(\eta_{\mathrm{igp}})] \frac{\partial \xi^{(1)}}{\partial \boldsymbol{u}^{(1)}_I} \otimes \boldsymbol{x}^{(1)}_J \right\} \cdot \boldsymbol{\tau}^{(1)}_{\mathrm{igp},\alpha}.\end{aligned} \tag{B.36}$$

The derivative with respect to $\boldsymbol{u}^{(2)}_I$ and for the EBM contact discretisation are obtained likewise. The derivatives of the tangential vectors are obtained in analogy to the derivative of the normal vector in Section B.2.1. The remaining derivatives of Eq. (B.34) are obtained analogously to Eqs. (B.32, B.33) for the SBM and the EBM contact discretisation techniques, respectively.

Equation (B.34) also depends on the pore water pressure p^w since the effective normal contact stress is used for the update of the tangential stress. Defining the effective normal contact stress $t'_{N,\mathrm{igp}}$ at the integration points of the segment by (see Eq. 6.43)

$$t'_{N,\mathrm{igp}} = t_{N,\mathrm{igp}} + p^w_{\mathrm{igp}} = \sum_L^{\mathrm{nnode}} N^{\mathrm{seg}}_L(\eta_{\mathrm{igp}})(t_{N,L} + p^w_L), \tag{B.37}$$

where the interpolation from the nodes introduced in Eq. (6.42) is used, the derivative with respect to the pore water pressure p^w_K at node K is

$$\frac{\partial t'_{N,\mathrm{igp}}}{\partial p^w_K} = N^{\mathrm{seg}}_K(\eta_{\mathrm{igp}}). \tag{B.38}$$

Finally, this defines the derivative of the tangential stress with respect to p^w_K

$$\frac{\partial t^{(i)}_{T,\mathrm{igp}}}{\partial p^w_K} = \frac{\partial t^{(i)}_{T,\mathrm{igp}}}{\partial t'_{N,\mathrm{igp}}} \frac{\partial t'_{N,\mathrm{igp}}}{\partial p^w_K}. \tag{B.39}$$

Appendix C

Additional analyses of the vibratory pile driving tests

C.1 Simulations using an iterative solver

In addition to direct solvers, different iterative solvers and preconditioners are tested in the framework of this thesis. The application of mixed (hydro-mechanically coupled) elements leads to ill-conditioned sattle-point matrices for which a solution can be difficult to obtain. The success of the iterative solving procedure strongly depends on the feasibility of the preconditioner. [138] compared different preconditioners for ill-conditioned sattle-point problems and found the multilevel incomplete LU factorization (MILU) to be the most stable one. An incomplete LU factorization approximates a matrix $\mathbf{A}$ by

$$\mathbf{A} = \tilde{\mathbf{L}}\tilde{\mathbf{U}}. \tag{C.1}$$

Typically, many entries in $\tilde{\mathbf{L}}$ and $\tilde{\mathbf{U}}$ are assumed zero if they are below a predefined drop-tolerance in order to save computational resources. A serial MILU preconditioner is implemented in ILUPACK [50], which has been added to `numgeo` by the author. Machaček has implemented different iterative solvers (GMRES and different BICGSTAB solvers) in `numgeo`, which can be used in combination with MILU.

The simulations of the vibratory pile driving model tests presented in Section 8.2 (which were performed with the direct solver `MUMPS`) are repeated with GMRES in combination with MILU in order to evaluate the feasibility of iterative solvers for hydro-mechanically coupled BVPs (**u**-p elements are used) in combination with contact constraints. Note that no reordering of DOFs is applied, i.e. the DOFs of the individual nodes are continuously listed. Initial studies

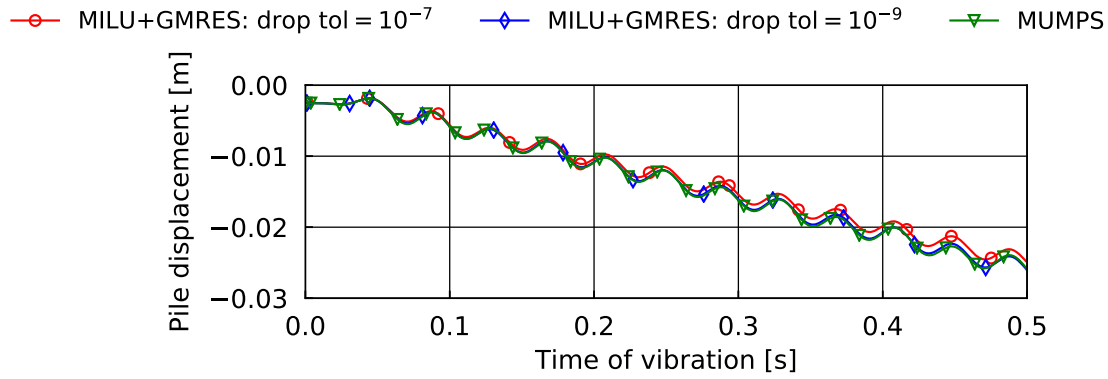

Figure C.1: Results of a vibratory pile driving simulation using **u**-p elements and different solvers. The iterative solver GMRES in combination with the MILU preconditioner is used with different drop-tolerances. The results are compared to results using the direct solver `MUMPS`.

showed that the drop-tolerance of the MILU preconditioner has significant influence on the results of the simulation and the convergence ratio of the solver. Considerably smaller values than typically assumed for applications in solid mechanics are necessary. The results of the simulation of the vibratory pile driving test in terms of pile penetration vs. vibration time using different solvers and drop-tolerances for the preconditioner are given in Fig. C.1.

For a drop-tolerance of 10^{-7} the solution obtained using the iterative solver shows a well visible deviation from the results using the direct solver (`MUMPS`). Only for a lower drop-tolerance of 10^{-9} the results of the different solvers coincide. Due to the low value of the drop-tolerance, the preconditioning is computationally more expensive. For a drop-tolerance of 10^{-9}, the preconditioning alone takes approximately 10 times longer than the overall solving process using `MUMPS`. Thus, the direct solver is judged to be better suited for the considered BVP. Similar conclusions are also drawn for BVPs with a much larger number of DOFs (e.g. simulations of shaking table tests with $\approx 400,000$ DOFs). It is worth mentioning that simulations using other preconditioners (e.g. ILUT or ILUTP [138]) did not converge at all.

C.2 Influence of a porosity-dependent hydraulic conductivity

In Section 8.2.3, the Kozeny/Carman equation is used to consider the influence of the change in porosity on the hydraulic conductivity k^w for the analysis of the vibratory pile driving tests.

The spatial distributions of the hydraulic conductivity at 2 s and at 6.35 s of vibratory driving are given on the left-hand side of Fig. C.2. It is well visible that due to the loosening of the soil close to the pile shaft the hydraulic conductivity increases approximately by a factor 2 in that zone. This creates a preferred dissipation path for excess pore water pressure in the vicinity of the pile. Due to compaction of the soil at greater distances from the pile shaft the hydraulic conductivity slightly decreases there, which leads to a large gradient of k^w with respect to the radial distance from the pile shaft. The plot on the right-hand side of Fig. C.2 compares the normalised pile penetration (see Eq. (8.1)) vs. vibration time from simulations using either a constant hydraulic conductivity $k^w = 1.1 \cdot 10^{-3}$ m/s (corresponding to the value obtained using the Kozeny/Carman equation with the initial value of porosity) or the Kozeny/Carman equation ($k^w(n)$). The SBM contact discretisation with Coulomb friction is applied in both cases. While for the first 3 s the results of both simulations coincide, the simulation assuming a constant value of k^w leads to less pile penetration towards the end of the driving phase. This can be explained by the high gradient of k^w for the simulation with $k^w(n)$ resulting in worse drainage conditions in radial direction in the vicinity of the pile tip. Therefore, higher excess pore water pressures develop in the vicinity of the pile tip for the simulation using the Kozeny/Carman equation. This is demonstrated in Fig. C.3, where the normalised excess pore water pressure $\Delta p^w / p_0^w$ at PPT B (see Fig. 8.8) measured in the experiment and obtained from the simulations using either a constant hydraulic conductivity k^w or the Kozeny/Carman equation ($k^w(n)$) is displayed. Δp^w denotes the change in pore water pressure relative to the hydrostatic pore water pressure p_0^w. At the time of vibration the pile tip passes the transducer (at approximately 5.6 s for $k^w(n)$ and 5.9 s for the constant value of k^w) the simulation with $k^w(n)$ shows slightly larger values of $\Delta p^w / p_0^w$ compared to the simulation with a constant value of k^w. However, even before the pile tip reaches PPT B, the consideration of the variable hydraulic conductivity leads to larger excess pore water pressures, which also fit better to the measured values compared to the simulation with constant k^w.

In addition to the higher excess pore water pressure developing in case of $k^w(n)$, the shear stress that can be mobilised at the pile shaft is also lower, since the upward directed flow of pore water tangentially to the pile-soil interface close to the pile shaft reduces the effective stress in the interface zone.

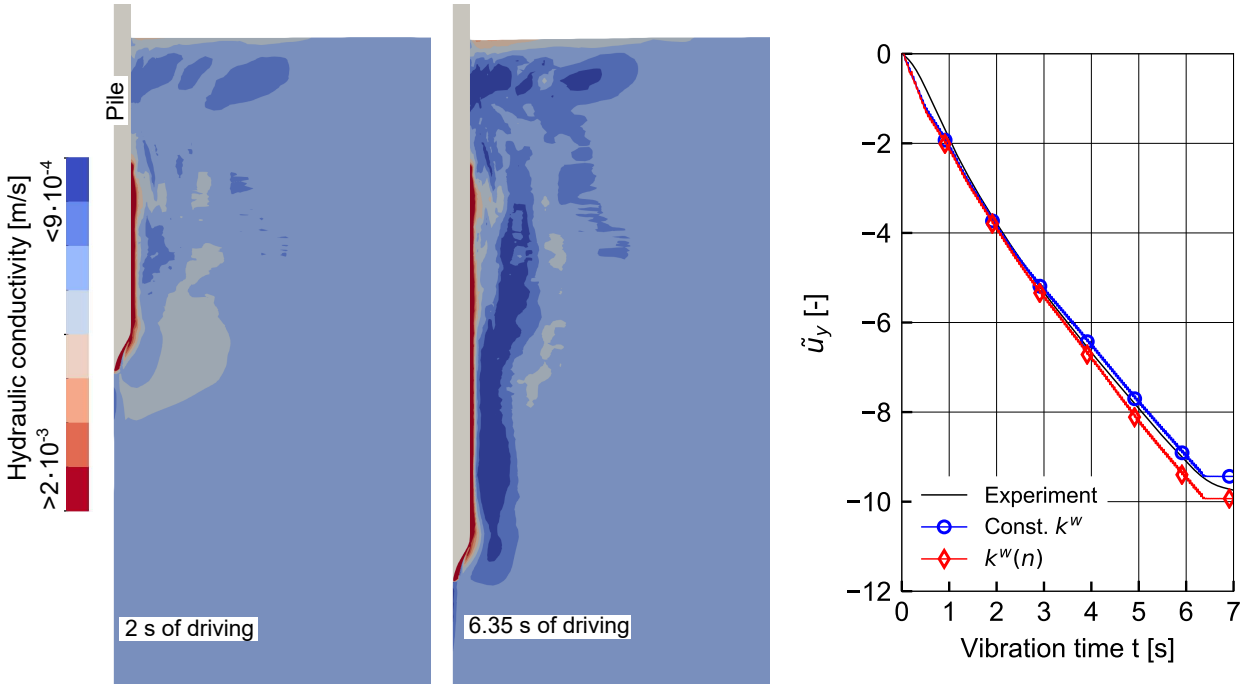

Figure C.2: Spatial distribution of hydraulic conductivity at 2 s and at the end of driving (6.35 s) using the Kozeny/Carman equation (left) and normalised pile penetration vs. vibration time utilising either a constant hydraulic conductivity k^w or the Kozeny/Carman equation ($k^w(n)$) for simulations with the segment-based mortar technique and Coulomb friction (right)

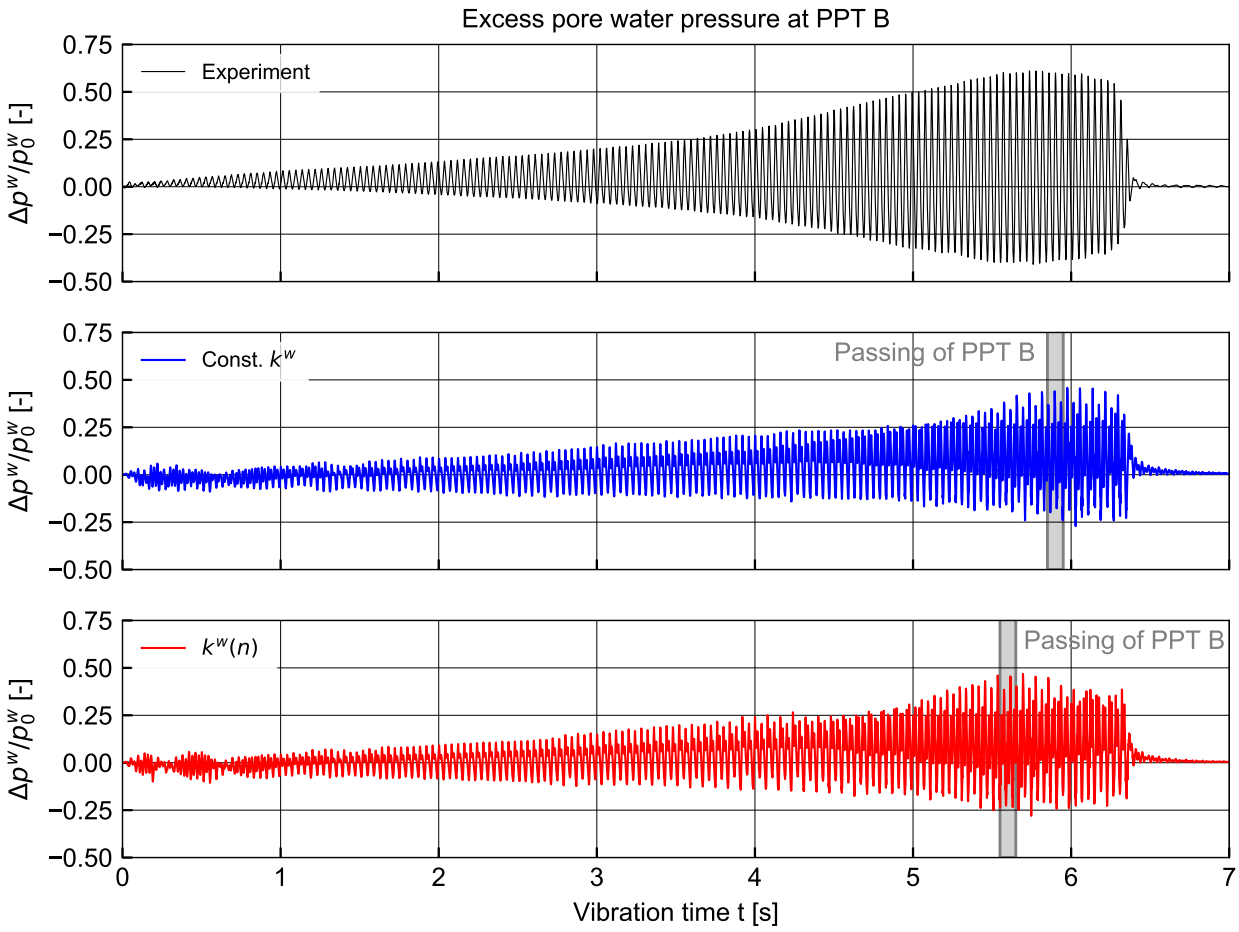

Figure C.3: Normalised excess pore water pressure at PPT B (see Fig. 8.8) for the values measured in the experiment and the simulations using either a constant hydraulic conductivity k^w or the Kozeny/Carman equation ($k^w(n)$)

Bibliography

[1] C. N. Abadie, B. W. Byrne, and G. T. Houlsby. "Rigid pile response to cyclic lateral loading: laboratory tests". In: *Géotechnique* 69.10 (2019), pp. 863–876.

[2] N. El-Abbasi and K. J. Bathe. "Stability and patch test performance of contact discretizations and a new solution algorithm". In: *Computers and Structures* 79.16 (June 2001), pp. 1473–1486. ISSN: 00457949. DOI: 10.1016/S0045-7949(01)00048-7.

[3] K. Abe, K. Soga, and S. Bandara. "Material Point Method for Coupled Hydromechanical Problems". In: *Journal of Geotechnical and Geoenvironmental Engineering* 140.3 (2014), p. 04013033. ISSN: 1090-0241. DOI: 10.1061/(asce)gt.1943-5606.0001011.

[4] M. Achmus, Y.-S. Kuo, and K. Abdel-Rahman. "Zur Bemessung von Monopiles für zyklische Lasten". In: *Der Bauingenieur* 83 (2008), pp. 303–311.

[5] M. Achmus, K. Schmoor, V. Herwig, and B. Matlock. "Lateral bearing behaviour of vibro- and impact-driven large-diameter piles in dense sand". In: *Geotechnik* 43.3 (Aug. 2020), pp. 147–159. DOI: 10.1002/gete.202000006.

[6] M. Achmus, Y. S. Kuo, and K. Abdel-Rahman. "Behavior of monopile foundations under cyclic lateral load". In: *Computers and Geotechnics* 36.5 (2009), pp. 725–735. ISSN: 0266352X. DOI: 10.1016/j.compgeo.2008.12.003.

[7] M. Achmus, K. Thieken, J. E. Saathoff, M. Terceros, and J. Albiker. "Un- and reloading stiffness of monopile foundations in sand". In: *Applied Ocean Research* 84 (Mar. 2019), pp. 62–73. ISSN: 01411187. DOI: 10.1016/j.apor.2019.01.001.

[8] M. Achmus and F. T. Worden. "Geotechnische Aspekte der Bemessung der Gründungs-Konstruktionen von Offshore-Windenergieanlagen". In: *Bauingenieur* 87.JUL/AUG (2012), pp. 331–341. ISSN: 00056650.

[9] A. S. Alawneh and A. A. Sharo. "Estimation of long-term set-up of driven piles in sand". In: *Geomechanics and Geoengineering* 15.4 (Oct. 2020), pp. 281–296. ISSN: 1748-6025. DOI: 10.1080/17486025.2019.1641630.

[10] A. Ali, T. Meier, and I. Herle. "Numerical investigation of undrained cavity expansion in fine-grained soils". In: *Acta Geotechnica* 6.1 (2011), pp. 31–40. ISSN: 18611133. DOI: 10.1007/s11440-011-0133-8.

[11] E. E. Alonso, A. Gens, and A. Josa. "A constitutive model for partially saturated soils". In: *Géotechnique* 40.3 (1990), pp. 405–430.

[12] E. E. Alonso, J. M. Pereira, J. Vaunat, and S. Olivella. "A microstructurally based effective stress for unsaturated soils". In: *Géotechnique* 60.12 (2010), pp. 913–925.

[13] A. P. I. American Petroleum Institute. *Recommended Practice for Planning, Designing and Constructing Fixed Offshore Platforms - Working Stress Design*. API RP 2A - WSD, Washington CD, USA. 2000.

[14] P. R. Amestoy, A. Buttari, J. Y. L'Excellent, and T. Mary. "Performance and scalability of the block low-rank multifrontal factorization on multicore architectures". In: *ACM Transactions on Mathematical Software* 45.1 (2019), pp. 1–26. ISSN: 15577295. DOI: 10.1145/3242094.

[15] K. H. Andersen. "Bearing capacity under cyclic loading - offshore, along the coast, and on land. The 21st Bjerrum Lecture presented in Oslo, 23 November 2007". In: *Canadian Geotechnical Journal* 46.5 (2009), pp. 513–535.

[16] K. H. Andersen. "Cyclic soil parameters for offshore foundation design". In: *3rd International Symposium on Frontiers in Offshore Geotechnics (ISFOG), Oslo*. Ed. by Meyer. 2015, pp. 5–82.

[17] L. Andresen and H. X. Khoa. "LDFE analysis of installation effects for offshore anchors and foundations". In: *Installation Effects in Geotechnical Engineering*. Ed. by Hicks. 2013, pp. 162–168.

[18] I. Anusic, B. M. Lehane, G. R. Eiksund, and M. A. Liingaard. "Influence of installation method on static lateral response of displacement piles in sand". In: *Geotechnique Letters* 9.3 (2019), pp. 193–197. ISSN: 20452543. DOI: 10.1680/jgele.18.00191.

[19] API. *Recommended Practice for Planning , Designing and Constructing Fixed Offshore Platforms — Working Stress Design*. 2A-WSD RP2AWSD, Errata and Supplement 3, Washington DC, USA. 2007. arXiv: arXiv:1011.1669v3.

[20] L. P. Argani and A. Gajo. "A novel insight into vertical ground motion modelling in earthquake engineering". In: *International Journal for Numerical and Analytical Methods in Geomechanics* (Nov. 2021). ISSN: 0363-9061. DOI: https://doi.org/10.1002/nag.3295.

[21] M. Arnold. *Application of the intergranular strain concept to the hypoplastic modelling of non-adhesive interfaces*. Vol. 1. Conference IACMAG, 1-6 October, Goa- India, 2008, pp. 747–754. ISBN: 9781622761760.

[22] M. Arnold and I. Herle. "Hypoplastic description of the frictional behaviour of contacts". In: *Proceedings of the 6th European Conference on Numerical Methods in Geotechnical Engineering - Numerical Methods in Geotechnical Engineering*. Ed. by H. Schweiger. 2006, pp. 101–106. ISBN: 0415408229. DOI: 10.1201/9781439833766.ch14.

[23] M. Arshad and B. C. O'Kelly. "Model Studies on Monopile Behavior under Long-Term Repeated Lateral Loading". In: *International Journal of Geomechanics* 17.1 (Jan. 2017), p. 04016040. ISSN: 1532-3641. DOI: 10.1061/(ASCE)GM.1943-5622.0000679.

[24] M. Ashour and G. Norris. "Modeling lateral soil-pile response based on soil-pile interaction". In: *Journal of Geotechnical and Geoenvironmental Engineering, ASCE* 126.5 (2000), pp. 420–428.

[25] M. Ashour, G. Norris, and S. Elfass. *Analysis of laterally loaded long or intermediate drilled shafts of small or large diameter in layered soil*. Tech. rep. CCEER 04-05. Department of Civil Engineering, University of Nevada, Reno, 2004.

[26] M. Ashour, G. Norris, and P. Pilling. "Lateral loading of a pile in layered soil using the strain wedge model". In: *Journal of Geotechnical and Geoenvironmental Engineering, ASCE* 124.4 (1998), pp. 303–315.

[27] D. Aubram. "Development and experimental validation of an Arbitrary Lagrangian-Eulerian (ALE) method for soil mechanics". In: *Geotechnik* 38.3 (2015), pp. 193–204.

[28] D. Aubram, F. Rackwitz, P. Wriggers, and S. A. Savidis. "An ALE method for penetration into sand utilizing optimization-based mesh motion". In: *Computers and Geotechnics* 65 (Apr. 2015), pp. 241–249. ISSN: 18737633. DOI: 10.1016/j.compgeo.2014.12.012.

[29] D. Aubram. "Explicitly coupled consolidation analysis using piecewise constant pressure". In: *Acta Geotechnica* 15.4 (2020), pp. 1031–1037. ISSN: 18611133. DOI: 10.1007/s11440-019-00792-z.

[30] D. Aubram, S. A. Savidis, and F. Rackwitz. "Theory and numerical modeling of geomechanical multi-material flow". In: *Lecture Notes in Applied and Computational Mechanics*. Ed. by T. Triantafyllidis. Vol. 80. Springer, 2016, pp. 187–229. DOI: 10.1007/978-3-319-23159-4_10.

[31] C. E. Augarde, S. J. Lee, and D. Loukidis. "Numerical modelling of large deformation problems in geotechnical engineering: A state-of-the-art review". In: *Soils and Foundations* (2021). ISSN: 0038-0806. DOI: https://doi.org/10.1016/j.sandf.2021.08.007.

[32] M. Bakroon, R. Daryaei, D. Aubram, and F. Rackwitz. "Multi-Material Arbitrary Lagrangian-Eulerian and Coupled Eulerian-Lagrangian methods for large deformation geotechnical problems". In: Numerical Methods in Geotechnical Engineering IX: Proceedings of the 9th European Conference on Numerical Methods in Geotechnical Engineering (NUMGE 2018), 2018, pp. 673–681.

[33] M. Baligh. "Strain Path Method". In: *Journal of Geotechnical Engineering* 111.9 (Sept. 1985), pp. 1108–1136. DOI: 10.1061/(ASCE)0733-9410(1985)111:9(1108).

[34] S. Bandara and K. Soga. "Coupling of soil deformation and pore fluid flow using material point method". In: *Computers and Geotechnics* 63 (2015), pp. 199–214. ISSN: 18737633. DOI: 10.1016/j.compgeo.2014.09.009.

[35] A. R. Barrero, M. Taiebat, and Y. F. Dafalias. "Modeling cyclic shearing of sands in the semifluidized state". In: *International Journal for Numerical and Analytical Methods in Geomechanics* 44.3 (2020), pp. 371–388. ISSN: 10969853. DOI: 10.1002/nag.3007.

[36] K. J. Bathe. *Finite Element Procedures*. Prentice Hall, 2006. ISBN: 9780979004902.

[37] E. Bauer. *Zum mechanischen Verhalten granularer Stoffe unter vorwiegend odometrischer Beanspruchung.* Dissertation, Institut für Bodenmechanik und Felsmechanik der Universität Fridericiana in Karlsruhe, Heft Nr. 130. 1992.

[38] E. Bauer and B. Ebrahimian. "Investigations of granular specimen size effect in interface shear box test using a micro-polar continuum description". In: *International Journal for Numerical and Analytical Methods in Geomechanics* 45.17 (Dec. 2021), pp. 2467–2489. ISSN: 0363-9061. DOI: https://doi.org/10.1002/nag.3273.

[39] M. Bayat, L. V. Andersen, L. B. Ibsen, and J. Clausen. "Influence of pore water in the seabed on dynamic response of offshore wind turbines on monopiles". In: *Soil Dynamics and Earthquake Engineering* 100 (Sept. 2017), pp. 233–248. ISSN: 02677261. DOI: 10.1016/j.soildyn.2017.06.001.

[40] S. M. Bayton, J. A. Black, and R. T. Klinkvort. "Centrifuge modelling of long term cyclic lateral loading on monopiles". In: *Physical Modelling in Geotechnics*. Vol. 1. 2018, pp. 689–694. ISBN: 9781138559752. DOI: 10.1201/9780429438660-103.

[41] Z. P. Bažant and M. Jirásek. "Nonlocal Integral Formulations of Plasticity and Damage: Survey of Progress". In: *Perspectives in Civil Engineering: Commemorating the 150th Anniversary of the American Society of Civil Engineers* 128.11 (Nov. 2003), pp. 21–51. ISSN: 0733-9399. DOI: 10.1061/(asce)0733-9399(2002)128:11(1119).

[42] H. di Benedetto, M. Blanc, S. Tiouajni, and A. Ezaoui. "Elastoplastic model with loading memory surfaces (LMS) for monotonic and cyclic behaviour of geomaterials". In: *International Journal for Numerical and Analytical Methods in Geomechanics* 38.14 (2014), pp. 1477–1502. ISSN: 10969853. DOI: 10.1002/nag.2265.

[43] D. J. Benson. "Computational methods in Lagrangian and Eulerian hydrocodes". In: *Computer Methods in Applied Mechanics and Engineering* 99.2 (1992), pp. 235–394. ISSN: 0045-7825.

[44] D. J. Benson and S. Okazawa. "Contact in a multi-material Eulerian finite element formulation". In: *Computer Methods in Applied Mechanics and Engineering* 193.39 (2004), pp. 4277–4298. ISSN: 0045-7825.

[45] P. V. D. Berg. "Analysis of soil penetration". PhD thesis. Delft University of Technology, 1994, pp. 133–143.

[46] C. Bernardi, Y. Maday, and A. T. Patera. "A new nonconforming approach to domain decomposition: The mortar element method." In: *Nonlinear partial differential equations and their applications. College de France Seminar, volume XI. Lectures presented at the weekly seminar on applied mathematics*. Ed. by H. Brezia and J. Lions. Pitman, 1994, pp. 13–51. ISBN: 0-582-23800-5.

[47] B. Bienen, S. Fan, M. Schröder, and M. F. Randolph. "Effect of the installation process on monopile lateral response". In: *Proceedings of the Institution of Civil Engineers - Geotechnical Engineering* (Sept. 2021), pp. 1–19. ISSN: 1353-2618. DOI: 10.1680/jgeen.20.00219.

[48] R. de Boer and J. Bluhm. "Eine Theorie fürs Grobe und Feine". In: *Essener Unikate 23/2004* (2004).

[49] C. Bojanowski. "Numerical modeling of large deformations in soil structure interaction problems using FE, EFG, SPH, and MM-ALE formulations". In: *Archive of Applied Mechanics* 84.5 (2014), pp. 743–755. ISSN: 1432-0681. DOI: 10.1007/s00419-014-0830-5.

[50] M. Bollhöfer and Y. Saad. *ILUPACK preconditioning software package*. 2011. URL: http://ilupack.tu-bs.de.

[51] A. J. Bond and R. J. Jardine. "Effects of installing displacement piles in a high OCR clay". In: *Geotechnique* 41.3 (1991), pp. 341–363. ISSN: 17517656. DOI: 10.1680/geot.1991.41.3.341.

[52] J. Bonet and R. D. Wood. *Nonlinear continuum mechanics for finite element analysis, 2nd edition*. 2nd ed. Vol. 9780521838. Cambridge: Cambridge University Press, 2008, pp. 1–318. ISBN: 9780511755446. DOI: 10.1017/CBO9780511755446.

[53] R. I. Borja, C. H. Lin, and F. J. Montans. "Cam-Clay Plasticity, Part IV: Implicit integration of anisotropic bounding surface model with nonlinear hyperelasticity and ellipsoidal loading function". In: *Computer Methods in Applied Mechanics and Engineering* 190.26-27 (2001), pp. 3293–3323.

[54] R. I. Borja. "On the mechanical energy and effective stress in saturated and unsaturated porous continua". In: *International Journal of Solids and Structures* 43.6 (2006), pp. 1764–1786. ISSN: 0020-7683. DOI: https://doi.org/10.1016/j.ijsolstr.2005.04.045.

[55] R. I. Borja and S. R. Lee. "Cam-Clay plasticity, Part 1: Implicit integration of elastoplastic constitutive relations". In: *Computer Methods in Applied Mechanics and Engineering* 78.1 (Jan. 1990), pp. 49–72. ISSN: 00457825. DOI: 10.1016/0045-7825(90)90152-C.

[56] R. Buczkowski. "21-Node hexahedral isoparametric element for analysis of contact problems". In: *Communications in Numerical Methods in Engineering* 14 (1998), pp. 681–692. DOI: 10.1002/(SICI)1099-0887(199807)14:7<681::AID-CNM182>3.0.CO;2-T.

[57] F. Burali d'Arezzo, S. Haigh, M. Talesnick, and Y. Ishihara. "Measuring horizontal stresses during jacked pile installation". In: *Proceedings of the Institution of Civil Engineers - Geotechnical Engineering* 168.4 (2015), pp. 306–318.

[58] H. J. Burd, D. M. G. Taborda, L. Zdravković, C. N. Abadie, B. W. Byrne, G. T. Houlsby, K. G. Gavin, D. J. P. Igoe, R. J. Jardine, C. M. Martin, R. A. McAdam, A. M. G. Pedro, and D. M. Potts. "PISA design model for monopiles for offshore wind turbines: application to a marine sand". In: *Géotechnique* 70.11 (Nov. 2020), pp. 1048–1066. ISSN: 0016-8505. DOI: 10.1680/jgeot.18.P.277.

[59] S. Burlon, H. Mroueh, and J. P. Cao. "'Skipped cycles' method for studying cyclic loading and soil-structure interface". In: *Computers and Geotechnics* 61 (2014), pp. 209–220. ISSN: 0266352X. DOI: 10.1016/j.compgeo.2014.05.007.

[60] P. C. Carman. "Permeability of saturated sands, soils and clays". In: *The Journal of Agricultural Science* 29.2 (1939), pp. 262–273. ISSN: 14695146. DOI: 10.1017/S0021859600051789.

[61] C. Carow and F. Rackwitz. "Comparison of implicit and explicit numerical integration schemes for a bounding surface soil model without elastic range". In: *Computers and Geotechnics* 140 (2021), p. 104206. ISSN: 0266352X. DOI: 10.1016/j.compgeo.2021.104206.

[62] A. Carstensen, T. Pucker, and J. Grabe. "Numerical model to predict the displacement of piles under cyclic lateral loading using a new hypoplastic spring element". In: *Computers and Geotechnics* 101 (2018), pp. 217–223. ISSN: 18737633. DOI: 10.1016/j.compgeo.2018.05.001.

[63] F. Ceccato and P. Simonini. "Numerical study of partially drained penetration and pore pressure dissipation in piezocone test". In: *Acta Geotechnica* 12.1 (2017), pp. 195–209. ISSN: 18611133. DOI: 10.1007/s11440-016-0448-6.

[64] M. Cecconi, A. DeSimone, C. Tamagnini, and G. M. Viggiani. "A constitutive model for granular materials with grain crushing and its application to a pyroclastic soil". In: *International Journal for Numerical and Analytical Methods in Geomechanics* 26.15 (2002), pp. 1531–1560. ISSN: 03639061. DOI: 10.1002/nag.257.

[65] S. H. Chong. "Numerical simulation of offshore foundations subjected to repetitive loads". In: *Ocean Engineering* 142 (2017), pp. 470–477. ISSN: 00298018. DOI: 10.1016/j.oceaneng.2017.07.031.

[66] F. C. Chow, R. J. Jardine, J. F. Nauroy, and F. Brucy. "Time-related increases in the shaft capacities of driven piles in sand". In: *Geotechnique* 47.2 (1997), pp. 353–361. ISSN: 00168505. DOI: 10.1680/geot.1997.47.2.353.

[67] S. Chrisopoulos. "Contributions to the Numerical Modelling of Vibratory Pile Driving in Saturated Soil". PhD thesis. Dissertation, Publications of the Institute of Soil Mechanics and Rock Mechanics, Karlsruhe Institute of Technology, Issue No. 184, 2018.

[68] S. Chrisopoulos, V. A. Osinov, and T. Triantafyllidis. "Dynamic Problem for the Deformation of Saturated Soil in the Vicinity of a Vibrating Pile Toe". In: *Holistic Simulation of Geotechnical Installation Processes: Benchmarks and Simulations*. Ed. by T. Triantafyllidis. Cham: Springer International Publishing, 2016, pp. 53–67. DOI: 10.1007/978-3-319-23159-4_3.

[69] S. Chrisopoulos and J. Vogelsang. "A finite element benchmark study based on experimental modeling of vibratory pile driving in saturated sand". In: *Soil Dynamics and Earthquake Engineering* 122 (2019), pp. 248–260. ISSN: 0267-7261. DOI: https://doi.org/10.1016/j.soildyn.2019.01.001.

[70] M. O. Ciantia, M. Arroyo, J. Butlanska, and A. Gens. "DEM modelling of cone penetration tests in a double-porosity crushable granular material". In: *Computers and Geotechnics* 73 (2016), pp. 109–127. ISSN: 18737633. DOI: 10.1016/j.compgeo.2015.12.001.

[71] R. D. Cook, D. S. Malkus, M. E. Plesha, and R. J. Witt. *Concepts and Applications of Finite Element Analysis*. John Wiley & Sons, 2007. ISBN: 0470088214.

[72] R. W. Cooke and G. Price. "Strains and Displacements around Friction Piles". In: *8th International Conference on Soil Mechanics and Foundation Engineering (Moscow)*. 1973, pp. 53–60.

[73] M. R. Coop and C. P. Wroth. "Field studies of an instrumented model pile in clay". In: *Geotechnique* 39.4 (1989), pp. 679–696. ISSN: 00168505. DOI: 10.1680/geot.1989.39.4.679.

[74] S. Corciulo, O. Zanoli, and F. Pisanò. "Transient response of offshore wind turbines on monopiles in sand: role of cyclic hydro–mechanical soil behaviour". In: *Computers and Geotechnics* 83 (2017), pp. 221–238. ISSN: 18737633. DOI: 10.1016/j.compgeo.2016.11.010.

[75] R. O. Cudmani. *Statische, alternierende und dynamische Penetration in nichtbindige Böden*. Dissertation, Publications of the Institute of Soil Mechanics and Rock Mechanics, Karlsruhe Institute of Technology, Issue No. 152. 2001.

[76] P. Cuéllar, M. Baeßler, and W. Rücker. "Ratcheting convective cells of sand grains around offshore piles under cyclic lateral loads". In: *Granular Matter* 11.6 (2009), pp. 379–390.

[77] P. Cuéllar, S. Georgi, M. Baeßler, and W. Rücker. "On the quasi-static granular convective flow and sand densification around pile foundations under cyclic lateral loading". In: *Granular Matter* 14.1 (2012), pp. 11–25.

[78] P. Cuéllar, P. Mira, M. Pastor, J. A. Fernández Merodo, M. Baeßler, and W. Rücker. "A numerical model for the transient analysis of offshore foundations under cyclic loading". In: *Computers and Geotechnics* 59 (2014), pp. 75–86.

[79] V. P. Cuéllar. *Pile foundations for offshore wind turbines : numerical and experimental investigations on the behaviour under short- term and long-term cyclic loading*. Veröffentlichungen des Grundbauinstituts der TU Berlin, Heft Nr. 52. 2011.

[80] J. Cui, J. Li, and G. Zhao. "Long-term time-dependent load-settlement characteristics of a driven pile in clay". In: *Computers and Geotechnics* 112 (2019), pp. 41–50. ISSN: 0266-352X. DOI: https://doi.org/10.1016/j.compgeo.2019.04.007.

[81] P. A. Cyril, S. T. Kok, M. K. Song, A. Chan, J. Y. Wong, and W. K. Choong. "Smooth particle hydrodynamics for the analysis of stresses in soil around Jack-in Pile". In: *European Journal of Environmental and Civil Engineering* (Aug. 2019), pp. 1–27. ISSN: 19648189. DOI: 10.1080/19648189.2019.1649198.

[82] Y. F. Dafalias and M. T. Manzari. "Simple Plasticity Sand Model Accounting for Fabric Change Effects". In: *Journal of Engineering Mechanics* 130.6 (2004), pp. 622–634. ISSN: 0733-9399. DOI: 10.1061/(asce)0733-9399(2004)130:6(622).

[83] Y. F. Dafalias and M. Taiebat. "SANISAND-Z: zero elastic range sand plasticity model". In: *Géotechnique* 66.12 (2016), pp. 999–1013. DOI: 10.1680/jgeot.15.P.271.

[84] M. Damgaard, M. Bayat, L. V. Andersen, and L. B. Ibsen. "Assessment of the dynamic behaviour of saturated soil subjected to cyclic loading from offshore monopile wind turbine foundations". In: *Computers and Geotechnics* 61 (2014), pp. 116–126. ISSN: 0266352X. DOI: 10.1016/j.compgeo.2014.05.008.

[85] K. T. Danielson and J. L. O'Daniel. "Reliable second-order hexahedral elements for explicit methods in nonlinear solid dynamics". In: *International Journal for Numerical Methods in Engineering* 85.9 (2011), pp. 1073–1102. ISSN: 00295981. DOI: 10.1002/nme.3003.

[86] R. Daryaei, M. Bakroon, D. Aubram, and F. Rackwitz. "Numerical evaluation of the soil behavior during pipe-pile installation using impact and vibratory driving in sand". In: *Soil Dynamics and Earthquake Engineering* 134 (2020), p. 106177. ISSN: 02677261. DOI: 10.1016/j.soildyn.2020.106177.

[87] H. De Chaunac. "Numerical investigation of the set-up around the shaft of a driven pile in clay". Phd thesis. Université catholique de Louvain, Belgium, 2015.

[88] H. De Chaunac and A. Holeyman. "Numerical analysis of the set-up around the shaft of a closed-ended pile driven in clay". In: *Geotechnique* 68.4 (2018), pp. 332–344. ISSN: 17517656. DOI: 10.1680/jgeot.16.P.229.

[89] A. De Nicola and M. F. Randolph. "The plugging behaviour of driven and jacked piles in sand". In: *Geotechnique* 47.4 (1997), pp. 841–856. ISSN: 00168505. DOI: 10.1680/geot.1997.47.4.841.

[90] J. T. DeJong, M. F. Randolph, and D. J. White. "Interface load transfer degradation during cyclic loading: a microscale investigation". In: *Soils Found.* 43.4 (2003), pp. 81–93.

[91] J. T. DeJong and Z. J. Westgate. "Role of Initial State, Material Properties, and Confinement Condition on Local and Global Soil-Structure Interface Behavior". In: *Journal of Geotechnical and Geoenvironmental Engineering* 135.11 (Nov. 2009), pp. 1646–1660. ISSN: 1090-0241. DOI: 10.1061/(asce)1090-0241(2009)135:11(1646).

[92] J. T. DeJong, D. J. White, and M. F. Randolph. "Microscale Observation and Modeling of Soil-Structure Interface Behavior Using Particle Image Velocimetry". In: *Soils and Foundations* 46.1 (Feb. 2006), pp. 15–28. ISSN: 00380806. DOI: 10.3208/sandf.46.15.

[93] C. S. Desai, E. C. Drumm, and M. M. Zaman. "Cyclic testing and modeling of interfaces". In: *Journal of Geotechnical Engineering* 111.6 (June 1985), pp. 793–815. ISSN: 0733-9410. DOI: 10.1061/(ASCE)0733-9410(1985)111:6(793).

[94] DGGT. *Empfehlungen des Arbeitskreises "Pfaehle" der Deutschen Gesellschaft für Geotechnik e.V., 2. Auflage*. 2012.

[95] J. Dijkstra, W. Broere, and O. M. Heeres. "Numerical simulation of pile installation". In: *Computers and Geotechnics* 38.5 (2011), pp. 612–622. ISSN: 0266-352X. DOI: https://doi.org/10.1016/j.compgeo.2011.04.004.

[96] K. Z. Ding, Q.-H. Qin, and M. Cardew-Hall. "Substepping algorithms with stress correction for the simulation of sheet metal forming process". In: *International Journal of Mechanical Sciences* 49.11 (2007), pp. 1289–1308. ISSN: 0020-7403. DOI: https://doi.org/10.1016/j.ijmecsci.2007.03.010.

[97] Y. Ding, W. Huang, D. Sheng, and S. W. Sloan. "Numerical study on finite element implementation of hypoplastic models". In: *Computers and Geotechnics* 68 (July 2015), pp. 78–90. ISSN: 18737633. DOI: 10.1016/j.compgeo.2015.04.003.

[98] P. Doherty and K. Gavin. "Shaft Capacity of Open-Ended Piles in Clay". In: *Journal of Geotechnical and Geoenvironmental Engineering* 137.11 (Nov. 2011), pp. 1090–1102. ISSN: 1090-0241. DOI: 10.1061/(ASCE)GT.1943-5606.0000528.

[99] P. Doherty and K. Gavin. "The Shaft Capacity of Displacement Piles in Clay: A State of the Art Review". In: *Geotechnical and Geological Engineering* 29.4 (July 2011), pp. 389–410. ISSN: 0960-3182. DOI: 10.1007/s10706-010-9389-2.

[100] A. I. Dumitrescu, A. Corfdir, and R. Frank. "Influence of the Anisotropy of Confining Stress on the Sand/Steel Interface Behaviour in a Cylinder Shear Apparatus". In: *Soils and Foundations* 49.2 (2009), pp. 167–174. ISSN: 0038-0806. DOI: https://doi.org/10.3208/sandf.49.167.

[101] T. W. Dunnavant and M. W. O'neill. "Experimental P-Y Model For Submerged, Stiff Clay". In: *Journal of Geotechnical Engineering* 115.1 (1989), pp. 95–114. ISSN: 0733-9410. DOI: 10.1061/(ASCE)0733-9410(1989)115:1(95).

[102] J. Duque, M. Ochmański, D. Mašín, Y. Hong, and L. Wang. "On the behavior of monopiles subjected to multiple episodes of cyclic loading and reconsolidation in cohesive soils". In: *Computers and Geotechnics* 134 (June 2021), p. 104049. ISSN: 0266352X. DOI: 10.1016/j.compgeo.2021.104049.

[103] G. J. Dyson and M. F. Randolph. "Monotonic Lateral Loading of Piles in Calcareous Sand". In: *Journal of Geotechnical and Geoenvironmental Engineering* 127.4 (2001), pp. 346–352. DOI: 10.1061/(ASCE)1090-0241(2001)127:4(346).

[104] W. Ehlers and P. Blome. "On Porous Soil Materials Saturated with a Compressible Pore-fluid Mixture". In: *ZAMM - Journal of Applied Mathematics and Mechanics / Zeitschrift für Angewandte Mathematik und Mechanik* 80.S1 (2000), pp. 141–144. ISSN: 1521-4001. DOI: 10.1002/zamm.20000801336.

[105] W. Ehlers and J. Bluhm. *Porous Media: Theory, Experiments and Numerical Applications*. Springer Berlin Heidelberg, 2013. ISBN: 9783662049990.

[106] W. Ehlers, T. Graf, and S. Diebels. "On the Description of Partially Saturated Soils by the Theory of Porous Media". In: *PAMM* 2.1 (2003), pp. 230–231. ISSN: 1617-7061. DOI: 10.1002/pamm.200310100.

[107] A. C. Eringen. "On nonlocal plasticity". In: *International Journal of Engineering Science* 19.12 (1981), pp. 1461–1474. ISSN: 00207225. DOI: 10.1016/0020-7225(81)90072-0.

[108] J. van Esch, D. Stolle, and J. Jassim I. "Finite element method for coupled dynamic flow-deformation simulation". In: *2nd International Symposium on Computational Geomechanics (ComGeo II)*. Croatia, Apr. 2011.

[109] K. Fakharian. "Three Dimensional Monotonic and Cyclic Behaviour of sand-steel interfaces: Testing and Modeling". PhD thesis. University of Ottawa, 1996, pp. 1–283.

[110] K. Fakharian and E. Evgin. "Cyclic Simple-Shear Behavior of Sand-Steel Interfaces under Constant Normal Stiffness Condition". In: *Journal of Geotechnical and Geoenvironmental Engineering* 123.12 (1997), pp. 1096–1105. ISSN: 1090-0241. DOI: 10.1061/(asce)1090-0241(1997)123:12(1096).

[111] R. S. Falk. *Mixed and Hybrid Finite Element Methods (Franco Brezzi and Michel Fortin)*. Vol. 35. 3. Springer Science & Business Media, 1993, pp. 514–517. DOI: 10.1137/1035113.

[112] S. Fan. "Effect of the installation process on the subsequent response of monopiles under lateral loading in sand". PhD thesis. The University of Western Australia, 2020. DOI: 10.26182/3dyy-r158.

[113] S. Fan, B. Bienen, and M. F. Randolph. "Effects of Monopile Installation on Subsequent Lateral Response in Sand. II: Lateral Loading". In: *Journal of Geotechnical and Geoenvironmental Engineering* 147.5 (May 2021), p. 04021022. ISSN: 1090-0241. DOI: 10.1061/(ASCE)GT.1943-5606.0002504.

[114] S. Fan, B. Bienen, and M. F. Randolph. "Centrifuge study on effect of installation method on lateral response of monopiles in sand". In: *International Journal of Physical Modelling in Geotechnics* 21.1 (2021), pp. 40–52. ISSN: 20426550. DOI: 10.1680/jphmg.19.00013.

[115] S. Fan, B. Bienen, and M. F. Randolph. "Effects of Monopile Installation on Subsequent Lateral Response in Sand. I: Pile Installation". In: *Journal of Geotechnical and Geoenvironmental Engineering* 147.5 (2021), p. 04021021. ISSN: 1090-0241. DOI: 10.1061/(asce)gt.1943-5606.0002467.

[116] P. Farah, W. A. Wall, and A. Popp. "A mortar finite element approach for point, line, and surface contact". In: *International Journal for Numerical Methods in Engineering* 114.3 (2018), pp. 255–291. ISSN: 10970207. DOI: 10.1002/nme.5743.

[117] P. Farah, A. Popp, and W. A. Wall. "Segment-based vs. Element-based integration for mortar methods in computational contact mechanics". In: *Computational Mechanics* 55.1 (2015), pp. 209–228. ISSN: 01787675. DOI: 10.1007/s00466-014-1093-2.

[118] B. Farhadi and A. Lashkari. "Influence of soil inherent anisotropy on behavior of crushed sand-steel interfaces". In: *Soils and Foundations* 57.1 (2017), pp. 111–125. ISSN: 0038-0806. DOI: https://doi.org/10.1016/j.sandf.2017.01.008.

[119] W. Fellin, M. Mittendorfer, and A. Ostermann. "Adaptive integration of constitutive rate equations". In: *Computers and Geotechnics* 36.5 (June 2009), pp. 698–708. ISSN: 0266352X. DOI: 10.1016/j.compgeo.2008.11.006.

[120] W. Fellin and A. Ostermann. "Consistent tangent operators for constitutive rate equations". In: *International Journal for Numerical and Analytical Methods in Geomechanics* 26.12 (Oct. 2002), pp. 1213–1233. ISSN: 03639061. DOI: 10.1002/nag.242.

[121] D. K. Feng, J. M. Zhang, and L. J. Deng. "Three-dimensional monotonic and cyclic behavior of a gravel-steel interface from large-scale simple-shear tests". In: *Canadian Geotechnical Journal* 55.11 (Mar. 2018), pp. 1657–1667. ISSN: 12086010. DOI: 10.1139/cgj-2018-0065.

[122] K. A. Fischer and P. Wriggers. "Frictionless 2D contact formulations for finite deformations based on the mortar method". In: *Computational Mechanics* 36.3 (2005), pp. 226–244. ISSN: 01787675. DOI: 10.1007/s00466-005-0660-y.

[123] K. A. Fischer, D. Sheng, and A. J. Abbo. "Modeling of pile installation using contact mechanics and quadratic elements". In: *Computers and Geotechnics* 34.6 (Nov. 2007), pp. 449–461. ISSN: 0266352X. DOI: 10.1016/j.compgeo.2007.01.003.

[124] K. A. Fischer and P. Wriggers. "Mortar based frictional contact formulation for higher order interpolations using the moving friction cone". In: *Computer Methods in Applied Mechanics and Engineering* 195.37-40 (2006), pp. 5020–5036. ISSN: 00457825. DOI: 10.1016/j.cma.2005.09.025.

[125] D. G. Fredlund, H. Rahardjo, and M. D. Fredlund. *Unsaturated Soil Mechanics in Engineering Practice*. John Wiley & Sons, Inc., 2012. ISBN: 9781118133590. DOI: 10.1002/9781118280492.

[126] D. Frick and M. Achmus. "An experimental study on the parameters affecting the cyclic lateral response of monopiles for offshore wind turbines in sand". In: *Soils and Foundations* 60.6 (Dec. 2020), pp. 1570–1587. ISSN: 00380806. DOI: 10.1016/j.sandf.2020.10.004.

[127] W. Fuentes. *Contributions in mechanical modelling of fill material*. Dissertation, Publications of the Institute of Soil Mechanics and Rock Mechanics, Karlsruhe Institute of Technology, Issue No. 179. 2014.

[128] W. Fuentes and T. Triantafyllidis. "ISA model: A constitutive model for soils with yield surface in the intergranular strain space". In: *International Journal for Numerical and Analytical Methods in Geomechanics* 39.11 (Aug. 2015), pp. 1235–1254. ISSN: 03639061. DOI: 10.1002/nag.2370.

[129] W. Fuentes and T. Triantafyllidis. "On the effective stress for unsaturated soils with residual water". In: *Géotechnique* 63.16 (2013), pp. 1451–1455.

[130] W. Fuentes, M. Gil, and G. Rivillas. "A p–y Model for Large Diameter Monopiles in Sands Subjected to Lateral Loading under Static and Long-Term Cyclic Conditions". In: *Journal of Geotechnical and Geoenvironmental Engineering* 147.2 (Feb. 2021), p. 04020164. ISSN: 1090-0241. DOI: 10.1061/(asce)gt.1943-5606.0002448.

[131] M. A. Gabr, T. Lunne, and J. J. Powell. "P-y Analysis of Laterally Loaded Piles in Clay Using DMT". In: *Journal of Geotechnical Engineering* 120.5 (May 1994), pp. 816–837. DOI: 10.1061/(ASCE)0733-9410(1994)120:5(816).

[132] A. Gajo and L. Mongiovi. "An analytical solution for the transient response of saturated linear elastic porous media". In: *International Journal for Numerical and Analytical Methods in Geomechanics* 19.6 (1995), pp. 399–413. ISSN: 10969853. DOI: 10.1002/nag.1610190603.

[133] V. Galavi, M. Martinelli, A. Elkadi, P. Ghasemi, and R. Thijssen. "Numerical simulation of impact driven offshore monopiles using the material point method". In: *Proceedings of the XVII ECSMGE-2019*. 2019. DOI: 10.32075/17ECSMGE-2019-0758.

[134] V. Galavi and H. F. Schweiger. "Nonlocal Multilaminate Model for Strain Softening Analysis". In: *International Journal of Geomechanics* 10.1 (Feb. 2010), pp. 30–44. ISSN: 1532-3641. DOI: 10.1061/(asce)1532-3641(2010)10:1(30).

[135] K. Gavin, R. Jardine, K. Karlsrud, and B. Lehane. "The effects of pile ageing on the shaft capacity of offshore piles in sand". In: *Frontiers in Offshore Geotechnics III - Proceedings of the 3rd International Symposium on Frontiers in Offshore Geotechnics, ISFOG 2015*. CRC Press / Balkema, 2015, pp. 129–151. ISBN: 9781138028500.

[136] K. Gavin, D. Gallagher, P. Doherty, and B. McCabe. "Field investigation of the effect of installation method on the shaft resistance of piles in clay". In: *Canadian Geotechnical Journal* 47.7 (June 2010), pp. 730–741. ISSN: 0008-3674. DOI: 10.1139/T09-146.

[137] M. T. van Genuchten. "A Closed-form Equation for Predicting the Hydraulic Conductivity of Unsaturated Soils". In: *Soil Science Society of America Journal* 44.5 (1980), pp. 892–898. ISSN: 1435-0661. DOI: 10.2136/sssaj1980.03615995004400050002x.

[138] A. Ghai, C. Lu, and X. Jiao. "A comparison of preconditioned Krylov subspace methods for large-scale nonsymmetric linear systems". In: *Numerical Linear Algebra with Applications* 26.1 (2019), e2215. DOI: https://doi.org/10.1002/nla.2215.

[139] V. N. Ghionna and G. Mortara. "An elastoplastic model for sand-structure interface behaviour". In: *Geotechnique* 52.1 (2002), pp. 41–50. ISSN: 00168505. DOI: 10.1680/geot.2002.52.1.41.

[140] J. Ghorbani, M. Nazem, J. Kodikara, and P. Wriggers. "Finite element solution for static and dynamic interactions of cylindrical rigid objects and unsaturated granular soils". In: *Computer Methods in Applied Mechanics and Engineering* 384 (2021), p. 113974. ISSN: 0045-7825. DOI: https://doi.org/10.1016/j.cma.2021.113974.

[141] S. Giridharan, S. Gowda, D. F. Stolle, and C. Moormann. "Comparison of UBCSAND and Hypoplastic soil model predictions using the Material Point Method". In: *Soils and Foundations* 60.4 (2020), pp. 989–1000. ISSN: 00380806. DOI: 10.1016/j.sandf.2020.06.001.

[142] W. Gong, L. Li, S. Zhang, and J. Li. "Long-term setup of a displacement pile in clay: An analytical framework". In: *Ocean Engineering* 218 (2020), p. 108143. ISSN: 0029-8018. DOI: https://doi.org/10.1016/j.oceaneng.2020.108143.

[143] K. M. Göttsche, U. Steinhagen, and P. M. Juhl. "Numerical evaluation of pile vibration and noise emission during offshore pile driving". In: *Applied Acoustics* 99 (Dec. 2015), pp. 51–59. ISSN: 1872910X. DOI: 10.1016/j.apacoust.2015.05.008.

[144] J. Grabe and T. Pucker. "Improvement of bearing capacity of vibratory driven open-ended tubular piles". In: *Frontiers in Offshore Geotechnics III - Proceedings of the 3rd International Symposium on Frontiers in Offshore Geotechnics, ISFOG 2015*. 2015, pp. 551–556. ISBN: 9781138028500. DOI: 10.1201/b18442-70.

[145] J. Grabe and K.-P. Mahutka. "Finite-Elemente-Analyse zur Vibrationsrammung von Pfählen". In: *Bautechnik* 82.9 (2005), pp. 632–640. ISSN: 1437-0999. DOI: 10.1002/bate.200590192.

[146] T. Graf and W. Ehlers. "On the Theoretical and Numerical Modelling of Unsaturated Soil". In: *PAMM* 3.1 (2003), pp. 278–279. ISSN: 1617-7061. DOI: 10.1002/pamm.200310411.

[147] S. Gutjahr. "Optimierte Berechnung von nicht gestützten Baugrubenwänden in Sand". PhD thesis. Universität Dortmund, Oct. 2003.

[148] M. B. Halvorsen, B. M. Casper, C. M. Woodley, T. J. Carlson, and A. N. Popper. "Threshold for onset of injury in Chinook salmon from exposure to impulsive pile driving sounds." eng. In: *PloS one* 7.6 (2012), e38968. ISSN: 1932-6203 (Electronic). DOI: 10.1371/journal.pone.0038968.

[149] F. Hamad. "Formulation of the axisymmetric CPDI with application to pile driving in sand". In: *Computers and Geotechnics* 74 (2016), pp. 141–150. ISSN: 18737633. DOI: 10.1016/j.compgeo.2016.01.003.

[150] T. Hamann. "Zur Modellierung wassergesättigter Böden unter dynamischer Belastung und großen Bodenverformungen am Beispiel der Pfahleinbringung". PhD thesis. Publications of the Institute of Geotechnical Engineering and Construction Management, University of Hamburg, 2015.

[151] T. Hamann, G. Qiu, and J. Grabe. "Application of a Coupled Eulerian-Lagrangian approach on pile installation problems under partially drained conditions". In: *Computers and Geotechnics* 63 (2015), pp. 279–290. ISSN: 0266-352X. DOI: https://doi.org/10.1016/j.compgeo.2014.10.006.

[152] M. N. Haque and E. J. Steward. "Evaluation of Pile Setup Phenomenon for Driven Piles in Alabama". In: *Geo-Congress 2020*. Reston, VA: American Society of Civil Engineers, Feb. 2020, pp. 200–208. ISBN: 9780784482780. DOI: 10.1061/9780784482780.019.

[153] L. Hauser and H. F. Schweiger. "Numerical study on undrained cone penetration in structured soil using G-PFEM". In: *Computers and Geotechnics* 133 (2021), p. 104061. ISSN: 18737633. DOI: 10.1016/j.compgeo.2021.104061.

[154] M. Haustein, A. Gladkyy, and R. Schwarze. "Discrete element modeling of deformable particles in YADE". In: *SoftwareX* 6 (Jan. 2017), pp. 118–123. ISSN: 23527110. DOI: 10.1016/j.softx.2017.05.001.

[155] E. P. Heerema. "Predicting pile driveability: Heather as an illustration of the "friction fatigue" theory". In: *Society of Petroleum Engineers - SPE European Petroleum Conference 1978* 13 (1978), pp. 413–422. DOI: 10.2118/8084-ms.

[156] E. Heins and J. Grabe. "Class-A-prediction of lateral pile deformation with respect to vibratory and impact pile driving". In: *Computers and Geotechnics* 86 (2017), pp. 108–119. ISSN: 18737633. DOI: 10.1016/j.compgeo.2017.01.007.

[157] E. Heins, M. F. Randolph, B. Bienen, and J. Grabe. "Effect of installation method on static and dynamic load test response for piles in sand". In: *International Journal of Physical Modelling in Geotechnics* 20.1 (2020), pp. 1–23. ISSN: 20426550. DOI: 10.1680/jphmg.18.00028.

[158] S. Henke and J. Grabe. "Numerical investigation of soil plugging inside open-ended piles with respect to the installation method". In: *Acta Geotechnica* 3.3 (2008), pp. 215–223.

[159] S. Henke. "Influence of pile installation on adjacent structures". In: *International Journal for Numerical and Analytical Methods in Geomechanics* 34.11 (Aug. 2010), pp. 1191–1210. ISSN: 03639061. DOI: 10.1002/nag.859.

[160] S. Henke and B. Bienen. "Investigation of the influence of the installation method on the soil plugging behaviour of a tubular pile". In: *Physical Modelling in Geotechnics - Proceedings of the 8th International Conference on Physical Modelling in Geotechnics 2014, ICPMG 2014*. Vol. 2. 2014, pp. 681–687. ISBN: 9781138022225. DOI: 10.1201/b16200-94.

[161] S. Henke. "Untersuchungen zur Pfropfenbildung infolge der Installation offener Profile in granularen Böden". Habilitation. Hamburg-Harburg: Veröffentlichungen des Instituts für Geotechnik und Baubetrieb, 2014.

[162] S. Henke and B. Bienen. "Centrifuge tests investigating the influence of pile cross-section on pile driving resistance of open-ended piles". In: *International Journal of Physical Modelling in Geotechnics* 13.2 (2013), pp. 50–62. ISSN: 1346213X. DOI: 10.1680/ijpmg.12.00012.

[163] S. Henke and J. Grabe. "Field measurements regarding the influence of the installation method on soil plugging in tubular piles". In: *Acta Geotechnica* 8.3 (2013), pp. 335–352. ISSN: 18611133. DOI: 10.1007/s11440-012-0191-6.

[164] S. Henke, M. Milatz, and J. Grabe. "Numerical simulations of acoustic emissions due to offshore-pile installation". In: *PAMM* 11.1 (2011), pp. 629–630. DOI: https://doi.org/10.1002/pamm.201110304.

[165] Henke, S., Grabe, J. "Numerische Untersuchungen zur Pfropfenbildung in offenen Profilen in Abhängigkeit des Einbringverfahrens". In: *Bautechnik* 85.8 (2008), pp. 521–529.

[166] I. Herle and K. Nübel. "Hypoplastic description of the interface behaviour". In: *Numerical models in geomechanics. Proceedings of the 7th international symposium, Graz, September 1999.* Ed. by G. Pande, S. Pietruszczak, and H. Schweiger. 1999, pp. 53–58. ISBN: 9058090957.

[167] C. Hesch and P. Betsch. "Transient three-dimensional contact problems: Mortar method. Mixed methods and conserving integration". In: *Computational Mechanics* 48.4 (2011), pp. 461–475. ISSN: 01787675. DOI: 10.1007/s00466-011-0583-8.

[168] H. M. Hilber, T. J. Hughes, and R. L. Taylor. "Improved numerical dissipation for time integration algorithms in structural dynamics". In: *Earthquake Engineering & Structural Dynamics* 5.3 (1977), pp. 283–292. ISSN: 10969845. DOI: 10.1002/eqe.4290050306.

[169] B. Hoffmann, J. Labenski, and C. Moormann. "Effects of Vibratory Driving of Monopiles on Soil Conditions and Their Cyclic Lateral Load Bearing Behavior". In: *4th International Symposium on Frontiers in Offshore Geotechnics*. Vol. 49. 0. 2020, pp. 714–724.

[170] C. HOLLAND. *Monopile installation, Maasvlakte 2, Rotterdam (2018)*. 2020.

[171] Y. Hong, B. He, L. Z. Wang, Z. Wang, C. W. Ng, and D. Mašín. "Cyclic lateral response and failure mechanisms of semi-rigid pile in soft clay: Centrifuge tests and numerical modelling". In: *Canadian Geotechnical Journal* 54.6 (2017), pp. 806–824. ISSN: 12086010. DOI: 10.1139/cgj-2016-0356.

[172] Hottinger Bruel & Kjaer (Netherlands). *HBK strain gauges measure vibration of new pile driving method for offshore wind turbines*. 2020.

[173] G. T. Houlsby, C. N. Abadie, W. J. Beuckelaers, and B. W. Byrne. "A model for nonlinear hysteretic and ratcheting behaviour". In: *International Journal of Solids and Structures* 120 (2017), pp. 67–80. ISSN: 00207683. DOI: 10.1016/j.ijsolstr.2017.04.031.

[174] L. Hu and J. Pu. "Testing and Modeling of Soil-Structure Interface". In: *Journal of Geotechnical and Geoenvironmental Engineering* 130.8 (Aug. 2004), pp. 851–860. ISSN: 1090-0241. DOI: 10.1061/(asce)1090-0241(2004)130:8(851).

[175] Q. Hu, F. Han, M. Prezzi, R. Salgado, and M. Zhao. "Lateral load response of large-diameter monopiles in sand". In: *Géotechnique* 0.0 (2021), pp. 1–16. ISSN: 0016-8505. DOI: 10.1680/jgeot.20.00002.

[176] Y. Hu and M. F. Randolph. "A practical numerical approach for large deformation problems in soil". In: *International Journal for Numerical and Analytical Methods in Geomechanics* 22.5 (1998), pp. 327–350. ISSN: 03639061. DOI: 10.1002/(SICI)1096-9853(199805)22:5<327::AID-NAG920>3.0.CO;2-X.

[177] M. Huang, Y. Chen, and X. Gu. "Discrete element modeling of soil-structure interface behavior under cyclic loading". In: *Computers and Geotechnics* 107 (2019), pp. 14–24. ISSN: 0266-352X. DOI: https://doi.org/10.1016/j.compgeo.2018.11.022.

[178] T. J. Hughes and J. Winget. "Finite rotation effects in numerical integration of rate constitutive equations arising in large deformation analysis". In: *International Journal for Numerical Methods in Engineering* 15.12 (1980), pp. 1862–1867. ISSN: 10970207. DOI: 10.1002/nme.1620151210.

[179] S. R. Idelsohn, E. Onate, and F. Del Pin. "The particle finite element method: A powerful tool to solve incompressible flows with free-surfaces and breaking waves". In: *International Journal for Numerical Methods in Engineering* 61.7 (2004), pp. 964–989. ISSN: 00295981. DOI: 10.1002/nme.1096.

[180] B. M. Irons. "Quadrature rules for brick based finite elements". In: *International Journal for Numerical Methods in Engineering* 3.2 (1971), pp. 293–294. DOI: https://doi.org/10.1002/nme.1620030213.

[181] R. J. Jardine, B. T. Zhu, P. Foray, and Z. X. Yang. "Measurement of stresses around closed-ended displacement piles in sand". In: *Géotechnique* 63.1 (2013), pp. 1–17. DOI: 10.1680/geot.9.P.137.

[182] R. J. Jardine and J. R. Standing. "Field axial cyclic loading experiments on piles driven in sand". In: *Soils and Foundations* 52.4 (2012), pp. 723–736. ISSN: 00380806. DOI: 10.1016/j.sandf.2012.07.012.

[183] R. J. Jardine, B. T. Zhu, P. Foray, and Z. X. Yang. "Interpretation of stress measurements made around closed-ended displacement piles in sand". In: *Geotechnique* 63.8 (2013), pp. 613–627. ISSN: 00168505. DOI: 10.1680/geot.9.P.138.

[184] G. Jaumann. "Geschlossenes System physikalischer und chemischer Differentialgesetze". In: *Sitzber. Akad. Wiss. Wien (IIa)* 120 (1911), pp. 385–530.

[185] B. Jeremic, Z. Cheng, M. Taiebat, and Y. Dafalias. "Numerical simulation of fully saturated porous materials". In: *International Journal for Numerical and Analytical Methods in Geomechanics* 32 (2008), pp. 1635–1660.

[186] M. Jirásek and S. Rolshoven. "Comparison of integral-type nonlocal plasticity models for strain-softening materials". In: *International Journal of Engineering Science* 41.13-14 (2003), pp. 1553–1602. ISSN: 00207225. DOI: 10.1016/S0020-7225(03)00027-2.

[187] K. L. Johnson. *Contact Mechanics*. Cambridge University Press, 1987. ISBN: 9780521347969.

[188] H. P. Jostad, B. M. Dahl, A. Page, N. Sivasithamparam, and H. Sturm. "Evaluation of soil models for improved design of offshore wind turbine foundations in dense sand". In: *Geotechnique* 70.8 (2020), pp. 682–699. ISSN: 17517656. DOI: 10.1680/jgeot.19.TI.034.

[189] E. Kementzetzidis, S. Corciulo, W. G. Versteijlen, and F. Pisanò. "Geotechnical aspects of offshore wind turbine dynamics from 3D non-linear soil-structure simulations". In: *Soil Dynamics and Earthquake Engineering* 120 (May 2019), pp. 181–199. ISSN: 02677261. DOI: 10.1016/j.soildyn.2019.01.037.

[190] E. Kementzetzidis, A. V. Metrikine, W. G. Versteijlen, and F. Pisanò. "Frequency effects in the dynamic lateral stiffness of monopiles in sand: Insight from field tests and 3D FE modelling". In: *Geotechnique* 71.9 (2021), pp. 812–825. ISSN: 17517656. DOI: 10.1680/jgeot.19.TI.024.

[191] K. Kim, B. Nam, and H. Youn. "Effect of Cyclic Loading on the Lateral Behavior of Offshore Monopiles Using the Strain Wedge Model". In: *Mathematical Problems in Engineering* 2015 (2015), pp. 1–12. DOI: 10.1155/2015/485319.

[192] I. Kimmig. "Untersuchungen zur Verdichtungsprognose von Sand bei der Rütteldruckverdichtung". PhD thesis. Publications of the Institute of Soil Mechanics and Rock Mechanics, Karlsruhe Institute of Technology, Issue No. 190, 2021, p. 218.

[193] H. Kishida and M. Uesugi. "Tests of the interface between sand and steel in the simple shear apparatus". In: *Geotechnique* 37.1 (1987), pp. 45–52. ISSN: 17517656. DOI: 10.1680/geot.1987.37.1.45.

[194] Klinkvort. *Centrifuge modelling of drained lateral pile-soil response.* PhD thesis, Department of Civil Engineering, Technical University of Denmark. 2012.

[195] L. Knittel. "Verhalten granularer Böden unter mehrdimensionaler zyklischer Beanspruchung". PhD thesis. Institut für Bodenmechanik und Felsmechanik am KIT, Heft-Nr. 188, 2020.

[196] D. Kong, J. Zhu, Y. Long, B. Zhu, Q. Yang, Y. Gao, and Y. Chen. "Centrifuge modelling on monotonic and cyclic lateral behaviour of monopiles in kaolin clay". In: *Géotechnique* 0.0 (2022), pp. 1–14. DOI: 10.1680/jgeot.19.P.402.

[197] Kozeny Josef. *Über kapillare Leitung des Wassers im Boden.* Vol. 136. 2a. Hölder-Pichler-Tempsky, A.-G.[Abt.]: Akad. d. Wiss., 1927, pp. 271–306.

[198] J. Labenski and C. Moormann. "Lateral bearing behaviour of vibratory-driven monopiles: A modified p-y approach based on experimental observations of scaled model tests". In: *17th European Conference on Soil Mechanics and Geotechnical Engineering, ECSMGE 2019 - Proceedings* 2019-Septe (2019), pp. 1867–1874. DOI: 10.32075/17ECSMGE-2019-0350.

[199] R. Lacal-Arántegui, J. M. Yusta, and J. A. Domínguez-Navarro. "Offshore wind installation: Analysing the evidence behind improvements in installation time". In: *Renewable and Sustainable Energy Reviews* 92 (2018), pp. 133–145. ISSN: 1364-0321. DOI: https://doi.org/10.1016/j.rser.2018.04.044.

[200] Y. Lai, L. Wang, Y. Hong, and B. He. "Centrifuge modeling of the cyclic lateral behavior of large-diameter monopiles in soft clay: Effects of episodic cycling and reconsolidation". In: *Ocean Engineering* 200 (2020), p. 107048. ISSN: 00298018. DOI: 10.1016/j.oceaneng.2020.107048.

[201] A. Lashkari. "A plasticity model for sand-structure interfaces". In: *Journal of Central South University of Technology (English Edition)* 19.4 (2012), pp. 1098–1108. ISSN: 10059784. DOI: 10.1007/s11771-012-1115-1.

[202] A. Lashkari. "A SANISAND model with anisotropic elasticity". In: *Soil Dynamics and Earthquake Engineering* 30.12 (2010), pp. 1462–1477. ISSN: 0267-7261. DOI: https://doi.org/10.1016/j.soildyn.2010.06.015.

[203] T. A. Laursen, M. A. Puso, and J. Sanders. "Mortar contact formulations for deformable-deformable contact: Past contributions and new extensions for enriched and embedded interface formulations". In: *Computer Methods in Applied Mechanics and Engineering* 205-208.1 (2012), pp. 3–15. ISSN: 00457825. DOI: 10.1016/j.cma.2010.09.006.

[204] V. H. Le, F. Remspecher, and F. Rackwitz. "Development of numerical models for the long-term behaviour of monopile foundations under cyclic loading considering the installation effects". In: *Soil Dynamics and Earthquake Engineering* 150 (2021), p. 106927. ISSN: 02677261. DOI: 10.1016/j.soildyn.2021.106927.

[205] C. Leblanc, B. W. Byrne, and G. T. Houlsby. "Response of stiff piles in sand to random two-way lateral loading". In: *Géotechnique* 60.2 (2010), pp. 79–90.

[206] C. Leblanc, G. T. Houlsby, and B. W. Byrne. "Response of stiff piles in sand to long-term cyclic lateral loading". In: *Géotechnique* 60.2 (2010), pp. 79–90.

[207] W. Lee, D. Kim, R. Salgado, and M. Zaheer. "Setup of Driven Piles in Layered Soil". In: *Soils and Foundations* 50.5 (2010), pp. 585–598. ISSN: 0038-0806. DOI: https://doi.org/10.3208/sandf.50.585.

[208] B. M. Lehane and D. R. Gill. "Displacement fields induced by penetrometer installation in an artificial soil". In: *International Journal of Physical Modelling in Geotechnics* 4.1 (2004), pp. 25–36. DOI: 10.1680/ijpmg.2004.040103.

[209] B. M. Lehane, R. Jardine, A. J. Bond, and R. Frank. "Mechanisms of Shaft Friction in Sand from Instrumented Pile Tests". In: *Journal of Geotechnical Engineering* 119.1 (Jan. 1993), pp. 19–35. DOI: 10.1061/(ASCE)0733-9410(1993)119:1(19).

[210] B. M. Lehane and R. J. Jardine. "Displacement pile behaviour in glacial clay". In: *Canadian Geotechnical Journal* 31.1 (1994), pp. 79–90. ISSN: 00083674. DOI: 10.1139/t94-009.

[211] B. M. Lehane and R. J. Jardine. "Displacement-pile behaviour in a soft marine clay". In: *Canadian Geotechnical Journal* 31.2 (1994), pp. 181–191. ISSN: 00083674. DOI: 10.1139/t94-024.

[212] B. M. Lehane, C. O'Loughlin, C. Gaudin, and M. F. Randolph. "Rate effects on penetrometer resistance in kaolin". In: *Géotechnique* 59.1 (2009), pp. 41–52. DOI: 10.1680/geot.2007.00072.

[213] C. Li, R. I. Borja, and R. A. Regueiro. "Dynamics of porous media at finite strain". In: *Computer Methods in Applied Mechanics and Engineering* 193.36 (2004), pp. 3837–3870. ISSN: 0045-7825.

[214] L. Li, W. Wu, M. Hesham El Naggar, G. Mei, and R. Liang. "DEM analysis of the sand plug behavior during the installation process of open-ended pile". In: *Computers and Geotechnics* 109 (2019), pp. 23–33. ISSN: 0266-352X. DOI: https://doi.org/10.1016/j.compgeo.2019.01.014.

[215] S. Li, Y. Zhang, and H. P. Jostad. "Drainage conditions around monopiles in sand". In: *Applied Ocean Research* 86 (2019), pp. 111–116. ISSN: 01411187. DOI: 10.1016/j.apor.2019.01.024.

[216] Y. Li, P. Wu, Z. Xia, Q. Yang, G. Flores, H. Jiang, M. Kamon, and B. Yu. "Changes in residual air saturation after thorough drainage processes in an air-water fine sandy medium". In: *Journal of Hydrology* 519.PA (2014), pp. 271–283. ISSN: 00221694. DOI: 10.1016/j.jhydrol.2014.07.019.

[217] J. Liang and J. Liang. "A user-defined element for dynamic analysis of saturated porous media in ABAQUS". In: *Computers and Geotechnics* 126 (2020), p. 103693. ISSN: 0266-352X. DOI: https://doi.org/10.1016/j.compgeo.2020.103693.

[218] J. Liang, G. Zhang, Z. Ba, and J. Liang. "Development of a 3D fluid-saturated element for dynamic analysis of two-phase media in ABAQUS based on u-U formed equations". In: *Computers and Geotechnics* 139 (2021), p. 104377. ISSN: 0266-352X. DOI: https://doi.org/10.1016/j.compgeo.2021.104377.

[219] L. Liang and L. Jingpei. "Analysis of Shaft Resistance Setup of Driven Piles in Soft Sensitive Clays Considering Soil Consolidation and Creep". In: *International Journal of Geomechanics* 21.11 (Nov. 2021), p. 4021216. DOI: 10.1061/(ASCE)GM.1943-5622.0002147.

[220] W. Liao, J. Zhang, J. Wu, and K. Yan. "Response of flexible monopile in marine clay under cyclic lateral load". In: *Ocean Engineering* 147 (2018), pp. 89–106. ISSN: 00298018. DOI: 10.1016/j.oceaneng.2017.10.022.

[221] G. Lim. "Stabilisation of an excavation by an embedded improved soil layer". PhD thesis. National University of Singapore, 2003, p. 219.

[222] J. Lim and B. Lehane. "Interpretation difficulties of pile set-up in sand". In: *Frontiers in Offshore Geotechnics III*. CRC Press, May 2015, pp. 605–611. ISBN: 9781138028500. DOI: 10.1201/b18442-79.

[223] J. K. Lim and B. Lehane. "Characterisation of the effects of time on the shaft friction of displacement piles in sand". In: *Géotechnique* 64.6 (2014), pp. 476–485. DOI: 10.1680/geot.13.P.220.

[224] C. Lin, J. Han, C. Bennett, and R. L. Parsons. "Analysis of laterally loaded piles in soft clay considering scour-hole dimensions". In: *Ocean Engineering* 111 (2016), pp. 461–470. ISSN: 0029-8018. DOI: https://doi.org/10.1016/j.oceaneng.2015.11.029.

[225] H. Y. Liu, J. A. Abell, A. Diambra, and F. Pisano. "Modelling the cyclic ratcheting of sands through memory-enhanced bounding surface plasticity". In: *Géotechnique* 69.9 (2019), pp. 783–800. DOI: 10.1680/jgeot.17.P.307.

[226] H. Y. Liu and F. Pisano. "Prediction of oedometer terminal densities through a memory-enhanced cyclic model for sand". In: *Geotechnique Letters* 9.2 (2019), pp. 81–88. DOI: 10.1680/jgele.18.00187.

[227] H. Liu, A. Diambra, J. A. Abell, and F. Pisanò. "Memory-Enhanced Plasticity Modeling of Sand Behavior under Undrained Cyclic Loading". In: *Journal of Geotechnical and Geoenvironmental Engineering* 146.11 (2020), p. 04020122. ISSN: 1090-0241. DOI: 10.1061/(asce)gt.1943-5606.0002362.

[228] H. Liu, E. Kementzetzidis, J. A. Abell, and F. Pisanò. "From cyclic sand ratcheting to tilt accumulation of offshore monopiles: 3D FE modelling using SANISAND-MS". In: *Géotechnique* 0.0 (2021), pp. 1–16. ISSN: 0016-8505. DOI: 10.1680/jgeot.20.p.029.

[229] J. Liu, D. Zou, and X. Kong. "A three-dimensional state-dependent model of soil-structure interface for monotonic and cyclic loadings". In: *Computers and Geotechnics* 61 (Sept. 2014), pp. 166–177. ISSN: 0266352X. DOI: 10.1016/j.compgeo.2014.05.012.

[230] J. Liu, D. Zou, and X. Kong. "A two-mechanism soil-structure interface model for three-dimensional cyclic loading". In: *International Journal for Numerical and Analytical Methods in Geomechanics* 44.15 (Oct. 2020), pp. 2042–2069. ISSN: 0363-9061. DOI: https://doi.org/10.1002/nag.3118.

[231] W. Liu, Y. Tian, and M. J. Cassidy. "An interface to numerically model undrained soil-structure interactions". In: *Computers and Geotechnics* 138 (Oct. 2021), p. 104327. ISSN: 18737633. DOI: 10.1016/j.compgeo.2021.104327.

[232] D. S. Liyanapathirana. "Arbitrary Lagrangian Eulerian based finite element analysis of cone penetration in soft clay". In: *Computers and Geotechnics* 36.5 (2009), pp. 851–860. ISSN: 0266352X. DOI: 10.1016/j.compgeo.2009.01.006.

[233] D. Lombardi, S. Bhattacharya, and D. Muir Wood. "Dynamic soil-structure interaction of monopile supported wind turbines in cohesive soil". In: *Soil Dynamics and Earthquake Engineering* 49 (2013), pp. 165–180. ISSN: 02677261. DOI: 10.1016/j.soildyn.2013.01.015.

[234] S. López-Querol, J. A. Fernández-Merodo, P. Mira, and M. Pastor. "Numerical modelling of dynamic consolidation on granular soils". In: *International Journal for Numerical and Analytical Methods in Geomechanics* 32.12 (2008), pp. 1431–1457. ISSN: 03639061. DOI: 10.1002/nag.676.

[235] C. Lubich. "Convolution quadrature and discretized operational calculus. II". In: *Numerische Mathematik* 52.4 (July 1988), pp. 413–425. ISSN: 0029599X. DOI: 10.1007/BF01462237.

[236] G. Ma, Y. Chen, F. Yao, W. Zhou, and Q. Wang. "Evolution of particle size and shape towards a steady state: Insights from FDEM simulations of crushable granular materials". In: *Computers and Geotechnics* 112 (2019), pp. 147–158. ISSN: 18737633. DOI: 10.1016/j.compgeo.2019.04.022.

[237] J. Machacek, P. Staubach, M. Tafili, H. Zachert, and T. Wichtmann. "Performance of different constitutive soil models: from element tests to the simulation of vibratory pile driving tests". In: *16th edition of the International Conference on Computational Plasticity*. CIMNE, 2021. DOI: 10.23967/complas.2021.057.

[238] J. Machaček and P. Staubach. "numgeo: A finite-element program for the simulation of hydro-mechanically coupled geotechnical processes". In: *Fachsektionstage Geotechnik 2021*. DGGT, 2021.

[239] J. Machaček, T. Wichtmann, H. Zachert, and T. Triantafyllidis. "Long-term settlements of a ship lock: measurements vs. FE-prediction using a high cycle accumulation model". In: *Computers and Geotechnics* 97.5 (2018), pp. 222–232.

[240] J. Machaček, P. Staubach, M. Tafili, H. Zachert, and T. Wichtmann. "Investigation of three sophisticated constitutive soil models: From numerical formulations to element tests and the analysis of vibratory pile driving tests". In: *Computers and Geotechnics* 138 (2021), p. 104276. ISSN: 18737633. DOI: 10.1016/j.compgeo.2021.104276.

[241] J. Machaček, T. Triantafyllidis, and P. Staubach. "Fully coupled simulation of an opencast mine subjected to earthquake loading". In: *Soil Dynamics and Earthquake Engineering* 115 (2018), pp. 853–867. ISSN: 02677261. DOI: 10.1016/j.soildyn.2018.09.016.

[242] J. Machaček. *Contributions to the Numerical Modelling of Saturated and Unsaturated Soils*. Dissertation, Publications of the Institute of Soil Mechanics and Rock Mechanics, Karlsruhe Institute of Technology, Issue No. 187. 2020.

[243] J. Machaček. "Entwicklung und Implementierung eines dreieckförmigen Dreiphasen-Bodenelementes für ebene Verformungsanalysen sowie Simulierung von Randwertproblemen mit Teilsättigung". Masterarbeit am Institut für Bodenmechanik und Felsmechanik am Karlsruher Institut für Technologie (KIT). 2016.

[244] J. Machaček and T. Triantafyllidis. "Numerical investigation of a partially saturated opencast mine subjected to earthquake loading". In: *Aktuelle Forschung in der Bodenmechanik 2018*. Springer, 2018.

[245] K.-P. Mahutka. "Zur Verdichtung von rolligen Böden infolge dynamischer Pfahleinbringung und durch Oberflächenrüttler". PhD thesis. Hamburg University of Technology, Heft 15, 2007.

[246] M. Martinelli and V. Galavi. "Investigation of the Material Point Method in the simulation of Cone Penetration Tests in dry sand". In: *Computers and Geotechnics* 130 (2021), p. 103923. ISSN: 18737633. DOI: 10.1016/j.compgeo.2020.103923.

[247] A. Martinez, J. D. Frost, and G. L. Hebeler. "Experimental study of shear zones formed at sand/steel interfaces in axial and torsional axisymmetric tests". In: *Geotechnical Testing Journal* 38.4 (July 2015), pp. 409–426. ISSN: 01496115. DOI: 10.1520/GTJ20140266.

[248] H. Matlock. "Correlations for design of laterally loaded piles in soft clay". In: *Proceedings of the Annual Offshore Technology Conference*. Vol. 1970-April. Offshore Technology Conference Inc., Houston, 1970, OTC–1204–MS. ISBN: 9781555637095. DOI: 10.4043/1204-ms.

[249] H. Matsuoka and T. Nakai. "A new failure criterion for soils in three-dimensional stresses". In: *Deformation and Failure of Granular Materials*. 1982, pp. 253–263.

[250] P. Mayne and F. H. Kulhawy. "K-OCR relationships in soil". In: *Journal of Geotechnical Engineering* 108 (1982), pp. 851–872.

[251] H. I. Meyer and A. O. Garder. *Mechanics of two immiscible fluids in porous media*. Vol. 25. 11. Water Resources Publication, 1954, pp. 1400–1406. ISBN: 9780918334831. DOI: 10.1063/1.1721576.

[252] L. Monforte, A. Gens, M. Arroyo, M. Mánica, and J. M. Carbonell. "Analysis of cone penetration in brittle liquefiable soils". In: *Computers and Geotechnics* 134 (2021), p. 104123. ISSN: 18737633. DOI: 10.1016/j.compgeo.2021.104123.

[253] L. Monforte, M. Arroyo, J. M. Carbonell, and A. Gens. "Coupled effective stress analysis of insertion problems in geotechnics with the Particle Finite Element Method". In: *Computers and Geotechnics* 101 (2018), pp. 114–129. ISSN: 18737633. DOI: 10.1016/j.compgeo.2018.04.002.

[254] L. Monforte, P. Navas, J. M. Carbonell, M. Arroyo, and A. Gens. "Low-order stabilized finite element for the full Biot formulation in soil mechanics at finite strain". In: *International Journal for Numerical and Analytical Methods in Geomechanics* 43.7 (2019), pp. 1488–1515. DOI: https://doi.org/10.1002/nag.2923.

[255] C. Moormann, S. Gowda, and S. Giridharan. "Numerical simulation of open ended pile installation in saturated sand". In: *Springer Series in Geomechanics and Geoengineering*. Ed. by A. Ferrari and L. Laloui. Vol. 0. 217729. Cham: Springer International Publishing, 2019, pp. 459–466. ISBN: 978-3-319-99670-7. DOI: 10.1007/978-3-319-99670-7_57.

[256] G. Mortara and A. Mangiola. "Cyclic shear stress degradation and post-cyclic behaviour from sand-steel interface direct shear tests". In: *Canadian Geotechnical Journal* 44.7 (2007), pp. 739–752.

[257] G. Mortara, M. Boulon, and V. N. Ghionna. "A 2-D constitutive model for cyclic interface behaviour". In: *International Journal for Numerical and Analytical Methods in Geomechanics* 26.11 (2002), pp. 1071–1096. ISSN: 03639061. DOI: 10.1002/nag.236.

[258] H.-B. Mühlhaus and I. Vardoulakis. "The thickness of shear bands in granular materials". In: *Géotechnique* 37.3 (1987), pp. 271–283.

[259] S. S. Nagula, Y. W. Hwang, S. Dashti, and J. Grabe. "Numerical investigation of liquefaction mitigation potential with vibroflotation". In: *Soil Dynamics and Earthquake Engineering* 146 (2021), p. 106736. ISSN: 02677261. DOI: 10.1016/j.soildyn.2021.106736.

[260] A. Nardelli, P. P. Cacciari, and M. M. Futai. "Sand-concrete interface response: The role of surface texture and confinement conditions". In: *Soils and Foundations* 59.6 (2019), pp. 1675–1694. ISSN: 0038-0806. DOI: https://doi.org/10.1016/j.sandf.2019.05.013.

[261] P. Navas, L. Sanavia, S. López-Querol, and R. C. Yu. "Explicit meshfree solution for large deformation dynamic problems in saturated porous media". In: *Acta Geotechnica* 13.2 (2018), pp. 227–242. ISSN: 18611133. DOI: 10.1007/s11440-017-0612-7.

[262] A. G. Neto and P. Wriggers. "Discrete element model for general polyhedra". In: *Computational Particle Mechanics* (2021). ISSN: 21964386. DOI: 10.1007/s40571-021-00415-z.

[263] H. V. Nguyen and D. F. Durso. "Absorption of Water By Fiber Webs: an Illustration of Diffusion Transport." In: *Tappi Journal* 66.12 (1983), pp. 76–79. ISSN: 07341415.

[264] Q. Ni, C. C. Hird, and I. Guymer. "Physical modelling of pile penetration in clay using transparent soil and particle image velocimetry". In: *Géotechnique* 60.2 (2010), pp. 121–132. DOI: 10.1680/geot.8.P.052.

[265] A. Niemunis. *Extended hypoplastic models for soils*. Habilitation, Publications of the Institute of Foundation Engineering and Soil Mechanics, Ruhr-University Bochum, Issue No. 34. 2003.

[266] A. Niemunis and M. Cudny. "On FE modelling of fully saturated soils". In: *Proceedings of the 11th Baltic Sea Geotechnical Conference* (2008), pp. 659–674.

[267] A. Niemunis, T. Wichtmann, Y. Petryna, and T. Triantafyllidis. "Stochastic modelling of settlements due to cyclic loading for soil-structure interaction". In: *Proceedings of Session 14 on Structural Damage and Lifetime Assessment of the ICOSSAR05 Conference in Rome*. 2005.

[268] A. Niemunis, T. Wichtmann, and T. Triantafyllidis. "A high-cycle accumulation model for sand". In: *Computers and Geotechnics* 32.4 (2005), pp. 245–263.

[269] A. Niemunis and I. Herle. "Hypoplastic model for cohesionless soils with elastic strain range". In: *Mechanics of Cohesive-Frictional Materials* 2.4 (1997), pp. 279–299. ISSN: 10825010. DOI: 10.1002/(SICI)1099-1484(199710)2:4<279::AID-CFM29>3.0.CO;2-8.

[270] A. Niemunis and I. Melikayeva. "Improved integration of high-cycle accumulated strain using hierarchical and EAS finite elements". In: *Lecture Notes in Applied and Computational Mechanics*. Ed. by T. Triantafyllidis. Vol. 77. Cham: Springer International Publishing, 2015, pp. 181–205. DOI: 10.1007/978-3-319-18170-7_10.

[271] A. Niemunis. *Über die Anwendung der Kontinuumstheorie auf bodenmechanische Probleme*. Vorlesungsskript, Institut für Bodenmechanik und Felsmechanik, Karlsruher Institut für Technologie. 2019.

[272] A. Niemunis and T. Wichtmann. "Separation of time scales in the HCA model for sand". In: *Acta Geophysica* 62.5 (2014), pp. 1127–1145. ISSN: 18957455. DOI: 10.2478/s11600-014-0221-x.

[273] Y. Nonyuki and O. Hidetoshi. *Sand-Steel Interface Friction Related to Soil Crushability*. Jan. 2005. DOI: doi:10.1061/40797(172)36.

[274] G. M. Norris. "Theoretically based BEF laterally loaded pile analysis". In: *Proc. 3rd Int. Conf on Numerical Methods in Offshore Piling, Nantes, France*. 1986, pp. 361–386.

[275] V. A. Osinov. "Numerical Modelling of the Effective-Stress Evolution in Saturated Soil Around a Vibrating Pile Toe". In: *Holistic Simulation of Geotechnical Installation Processes: Numerical and Physical Modelling*. Ed. by T. Triantafyllidis. Cham: Springer International Publishing, 2015, pp. 133–147. ISBN: 978-3-319-18170-7. DOI: 10.1007/978-3-319-18170-7_7.

[276] V. A. Osinov, S. Chrisopoulos, and C. E. Grandas Tavera. "Vibration-induced stress changes in saturated soil: a high-cycle problem". In: *Lecture Notes in Applied and Computational Mechanics. Vol. 80. Holistic Simulation of Geotechnical Installation Processes - Benchmarks and Simulations*. Ed. by T. Triantafyllidis. Springer, 2015, pp. 69–84.

[277] V. A. Osinov, S. Chrisopoulos, and T. Triantafyllidis. "Numerical study of the deformation of saturated soil in the vicinity of a vibrating pile". In: *Acta Geotechnica* 8.4 (Aug. 2013), pp. 439–446. ISSN: 1861-1133. DOI: 10.1007/s11440-012-0190-7.

[278] V. A. Osinov. "Application of a high-cycle accumulation model to the analysis of soil liquefaction around a vibrating pile toe". In: *Acta Geotechnica* 8.6 (2013), pp. 675–684. ISSN: 18611133. DOI: 10.1007/s11440-013-0215-x.

[279] A. M. Page, G. Grimstad, G. Eiksund, and H. Jostad. "A macro-element pile foundation model for integrated analyses of monopile-based offshore wind turbines". In: *Ocean Engineering* 167 (2018), pp. 23–35. ISSN: 0029-8018. DOI: https://doi.org/10.1016/j.oceaneng.2018.08.019.

[280] A. M. Page, G. Grimstad, G. R. Eiksund, and H. P. Jostad. "A macro-element model for multidirectional cyclic lateral loading of monopiles in clay". In: *Computers and Geotechnics* 106 (2019), pp. 314–326. ISSN: 18737633. DOI: 10.1016/j.compgeo.2018.11.007.

[281] A. M. Page, R. T. Klinkvort, S. Bayton, Y. Zhang, and H. P. Jostad. "A procedure for predicting the permanent rotation of monopiles in sand supporting offshore wind turbines". In: *Marine Structures* 75 (Jan. 2021), p. 102813. ISSN: 09518339. DOI: 10.1016/j.marstruc.2020.102813.

[282] K. Paik and R. Salgado. "Effect of Pile Installation Method on Pipe Pile Behavior in Sands". In: *Geotechnical Testing Journal* 27 (2004), pp. 78–88.

[283] H. W. Pan, W. J. Xu, and B. Y. Zhang. "Numerical method for the triaxial test of granular materials based on computational contact mechanics". In: *Computers and Geotechnics* 138 (Oct. 2021), p. 104343. ISSN: 18737633. DOI: 10.1016/j.compgeo.2021.104343.

[284] L. Pang, C. Jiang, X. Ding, H. Chen, and L. Deng. "A parameter calibration method in two-surface elastoplastic model for sand-structure interface under monotonic shear loading". In: *Computers and Geotechnics* 134 (2021), p. 104115. ISSN: 0266-352X. DOI: https://doi.org/10.1016/j.compgeo.2021.104115.

[285] P. Papadopoulos and R. L. Taylor. "A mixed formulation for the finite element solution of contact problems". In: *Computer Methods in Applied Mechanics and Engineering* 94.3 (1992), pp. 373–389. ISSN: 00457825. DOI: 10.1016/0045-7825(92)90061-N.

[286] C. Pasten, H. Shin, and J. C. Santamarina. "Long-term foundation response to repetitive loading". In: *Journal of Geotechnical and Geoenvironmental Engineering, ASCE* 140.4 (2014).

[287] S. K. Patra and S. Haldar. "Long-term behavior of monopile supported offshore wind turbines in silty sand". In: *16th Asian Regional Conference on Soil Mechanics and Geotechnical Engineering, ARC 2019* 5.2 (2020), pp. 80–84. ISSN: 2095-0349.

[288] R. H. Peerlings, M. G. Geers, R. De Borst, and W. A. Brekelmans. "A critical comparison of nonlocal and gradient-enhanced softening continua". In: *International Journal of Solids and Structures* 38.44-45 (Oct. 2001), pp. 7723–7746. ISSN: 00207683. DOI: 10.1016/S0020-7683(01)00087-7.

[289] C. J. Permann, D. R. Gaston, D. Andrš, R. W. Carlsen, F. Kong, A. D. Lindsay, J. M. Miller, J. W. Peterson, A. E. Slaughter, R. H. Stogner, and R. C. Martineau. "MOOSE: Enabling massively parallel multiphysics simulation". In: *SoftwareX* 11 (2020), p. 100430. ISSN: 23527110. DOI: 10.1016/j.softx.2020.100430. arXiv: 1911.04488.

[290] A. L. Petalas, Y. F. Dafalias, and A. G. Papadimitriou. "SANISAND-F: Sand constitutive model with evolving fabric anisotropy". In: *International Journal of Solids and Structures* 188-189 (2020), pp. 12–31. ISSN: 00207683. DOI: 10.1016/j.ijsolstr.2019.09.005.

[291] N. T. Phuong, A. Rohe, R. B. Brinkgreve, and A. F. van Tol. "Hypoplastic model for crushable sand". In: *Soils and Foundations* 58.3 (2018), pp. 615–626. ISSN: 00380806. DOI: 10.1016/j.sandf.2018.02.022.

[292] N. T. Phuong, A. F. Van Tol, A. S. Elkadi, and A. Rohe. "Modelling of pile installation using the material point method (MPM)". In: *Numerical Methods in Geotechnical Engineering - Proceedings of the 8th European Conference on Numerical Methods in Geotechnical Engineering, NUMGE 2014*. Ed. by Hicks, Brinkgreve, and Rohe. Vol. 1. 2014, pp. 271–276. ISBN: 9781138026872. DOI: 10.1201/b17017-50.

[293] H. J. Pincus, J. Tabucanon, D. Airey, and H. Poulos. "Pile Skin Friction in Sands from Constant Normal Stiffness Tests". In: *Geotechnical Testing Journal* 18.3 (1995), pp. 350–364. DOI: 10.1520/GTJ11004J.

[294] M. Poblete, W. Fuentes, and T. Triantafyllidis. "On the simulation of multidimensional cyclic loading with intergranular strain". In: *Acta Geotechnica* 11.6 (2016), pp. 1263–1285.

[295] V. L. Popov. *Kontaktmechanik und Reibung: ein Lehr- und Anwendungsbuch von der Nanotribologie bis zur numerischen Simulation*. Springer, 2009. ISBN: 9783540888369.

[296] A. Popp. "Mortar Methods for Computational Contact Mechanics and General Interface Problems". Dissertation. München: Technische Universität München, 2012.

[297] A. Popp, M. W. Gee, and W. A. Wall. "A finite deformation mortar contact formulation using a primal-dual active set strategy". In: *International Journal for Numerical Methods in Engineering* 79.11 (2009), pp. 1354–1391. ISSN: 00295981. DOI: 10.1002/nme.2614.

[298] A. Popp, M. Gitterle, M. W. Gee, and W. A. Wall. "A dual mortar approach for 3D finite deformation contact with consistent linearization". In: *International Journal for Numerical Methods in Engineering* 83.11 (2010), pp. 1428–1465. ISSN: 00295981. DOI: 10.1002/nme.2866.

[299] A. Puech and J. Garnier. "Behavior of Piles Subject to Cyclic Lateral Loading". In: *Design of Piles Under Cyclic Loading*. John Wiley & Sons, Ltd, 2017. Chap. 8, pp. 233–297. ISBN: 9781119469018. DOI: 10.1002/9781119469018.ch8.

[300] A. Puech and J. Garnier. "Design of Piles Subject to Cyclic Lateral Loading". In: *Design of Piles Under Cyclic Loading*. John Wiley & Sons, Ltd, 2017. Chap. 9, pp. 299–346. ISBN: 9781119469018. DOI: 10.1002/9781119469018.ch9.

[301] M. A. Puso and T. A. Laursen. "A mortar segment-to-segment frictional contact method for large deformations". In: *Computer Methods in Applied Mechanics and Engineering* 193.45-47 (Nov. 2004), pp. 4891–4913. ISSN: 00457825. DOI: 10.1016/j.cma.2004.06.001.

[302] M. A. Puso, T. A. Laursen, and J. Solberg. "A segment-to-segment mortar contact method for quadratic elements and large deformations". In: *Computer Methods in Applied Mechanics and Engineering* 197.6-8 (2008), pp. 555–566. ISSN: 00457825. DOI: 10.1016/j.cma.2007.08.009.

[303] G. Qiu, S. Henke, and J. Grabe. "Application of a Coupled Eulerian-Lagrangian Approach on Geomechanical Problems Involving Large Deformation". In: *Computers and Geotechnics* 38 (2011), pp. 30–39.

[304] M. F. Randolph. "Science and empiricism in pile foundation design". In: *Géotechnique* 53.10 (Dec. 2003), pp. 847–875. ISSN: 0016-8505. DOI: 10.1680/geot.2003.53.10.847.

[305] M. F. Randolph, J. P. Carter, and C. P. Wroth. "Driven piles in clay-the effects of installation and subsequent consolidation". In: *Géotechnique* 29.4 (1979), pp. 361–393. DOI: 10.1680/geot.1979.29.4.361.

[306] M. F. Randolph, E. C. Leong, and G. T. Houlsby. "One-dimensional analysis of soil plugs in pipe piles". In: *Geotechnique* 41.4 (1991), pp. 587–598. ISSN: 17517656. DOI: 10.1680/geot.1991.41.4.587.

[307] M. Randolph and S. Gourvenec. *Offshore geotechnical engineering*. CRC Press, July 2017, pp. 1–528. ISBN: 9781351988919. DOI: 10.1201/9781315272474.

[308] D. Rathod, D. Nigitha, and K. T. Krishnanunni. "Experimental Investigation of the Behavior of Monopile under Asymmetric Two-Way Cyclic Lateral Loads". In: *International Journal of Geomechanics* 21.3 (Mar. 2021), p. 06021001. ISSN: 1532-3641. DOI: 10.1061/(asce)gm.1943-5622.0001920.

[309] N. Ravichandran. "A framework-based finite element approach for solving large deformation problems in multi-phase porous media". PhD thesis. University of Oklahoma, 2005.

[310] N. Ravichandran and K. K. Muraleetharan. "Dynamics of unsaturated soils using various finite element formulations". In: *International Journal for Numerical and Analytical Methods in Geomechanics* 33.5 (2009), pp. 611–631. ISSN: 1096-9853. DOI: 10.1002/nag.737.

[311] N. Ravichandran, K. K. Muraleetharan, L. M. Taylor, and K. D. Mish. "Uniform Gradient Element Formulation with Hourglass Control Scheme for Solving Fully Coupled Finite-Element Equations for Saturated Soils". In: *International Journal of Geomechanics* 16.1 (Feb. 2016), p. 04015019. ISSN: 1532-3641. DOI: 10.1061/(asce)gm.1943-5622.0000490.

[312] D. Rebstock. "Verspannung und Entspannung von Sand entlang von Baukörpern". PhD thesis. Karlsruher Institut für Technologie (KIT), 2011. DOI: 10.5445/IR/1000023891.

[313] L. C. Reese, W. R. Cox, and F. D. Koop. *Field testing and analysis of laterally loaded piles in stiff clay*. Tech. rep. paper 2312. Offshore Technology Centre, Dallas, 1975.

[314] P. G. Reinhall, T. Dardis, and J. Hampden. *Underwater Noise Reduction of Marine Pile Driving Using a Double Pile: Vashon Ferry Terminal Test*. English. Ed. by W. S. T. Center. 2015.

[315] M. Rezania, M. Mousavi Nezhad, H. Zanganeh, J. Castro, and N. Sivasithamparam. "Modeling Pile Setup in Natural Clay Deposit Considering Soil Anisotropy, Structure, and Creep Effects: Case Study". In: *International Journal of Geomechanics* 17.3 (Mar. 2017), p. 04016075. ISSN: 1532-3641. DOI: 10.1061/(ASCE)GM.1943-5622.0000774.

[316] I. A. Richards, B. W. Byrne, and G. T. Houlsby. "Monopile rotation under complex cyclic lateral loading in sand". In: *Geotechnique* 70.10 (2020), pp. 916–930. ISSN: 17517656. DOI: 10.1680/jgeot.18.P.302.

[317] K. H. Roscoe and J. B. Burland. "On the generalized stress-strain behaviour of wet clays". In: *Engineering plasticity*. Ed. by J. Heyman and F. A. Leckie. Cambridge University Press, 1968, pp. 535–609.

[318] C. Rudolph, B. Bienen, and J. Grabe. "Effect of variation of the loading direction on the displacement accumulation of large-diameter piles under cyclic lateral loading in sand". In: *Canadian Geotechnical Journal* 51.10 (2014), pp. 1196–1206.

[319] C. Rudolph and J. Grabe. "Untersuchungen zu zyklisch horizontal belasteten Pfählen bei veränderlicher Lastrichtung". In: *Bautechnik* 36.2 (2013), pp. 90–95.

[320] C. Rudolph. "Untersuchungen zur Drift von Pfählen unter zyklischer, lateraler Last aus veränderlicher Richtung". PhD thesis. Veröffentlichungen des Instituts für Geotechnik und Baubetrieb der Technischen Universität Hamburg, 2015. ISBN: 3936310343.

[321] M. Saberi, C. D. Annan, and J. M. Konrad. "On the mechanics and modeling of interfaces between granular soils and structural materials". In: *Archives of Civil and Mechanical Engineering* 18.4 (2018), pp. 1562–1579. ISSN: 16449665. DOI: 10.1016/j.acme.2018.06.003.

[322] M. Saberi, C. D. Annan, and J. M. Konrad. "Three-dimensional constitutive model for cyclic behavior of soil-structure interfaces". In: *Soil Dynamics and Earthquake Engineering* 134 (July 2020), p. 106162. ISSN: 02677261. DOI: 10.1016/j.soildyn.2020.106162.

[323] M. Saberi, C. D. Annan, J. M. Konrad, and A. Lashkari. "A critical state two-surface plasticity model for gravelly soil-structure interfaces under monotonic and cyclic loading". In: *Computers and Geotechnics* 80 (2016), pp. 71–82. ISSN: 18737633. DOI: 10.1016/j.compgeo.2016.06.011.

[324] M. Saberi, C.-D. Annan, and J.-M. Konrad. "Implementation of a soil-structure interface constitutive model for application in geo-structures". In: *Soil Dynamics and Earthquake Engineering* 116 (2019), pp. 714–731. ISSN: 0267-7261. DOI: https://doi.org/10.1016/j.soildyn.2018.11.001.

[325] H. Sabetamal, J. P. Carter, M. Nazem, and S. W. Sloan. "Coupled analysis of dynamically penetrating anchors". In: *Computers and Geotechnics* 77 (July 2016), pp. 26–44. ISSN: 18737633. DOI: 10.1016/j.compgeo.2016.04.005.

[326] H. Sabetamal, M. Nazem, S. W. Sloan, and J. P. Carter. "Frictionless contact formulation for dynamic analysis of nonlinear saturated porous media based on the mortar method". In: *International Journal for Numerical and Analytical Methods in Geomechanics* 40.1 (Jan. 2016), pp. 25–61. ISSN: 10969853. DOI: 10.1002/nag.2386.

[327] C. Sagaseta, A. J. Whittle, and M. Santagata. "Deformation analysis of shallow penetration in clay". In: *International Journal for Numerical and Analytical Methods in Geomechanics* 21.10 (Oct. 1997), pp. 687–719. ISSN: 0363-9061. DOI: 10.1002/(SICI)1096-9853(199710)21:10<687::AID-NAG897>3.0.CO;2-3.

[328] R. Salgado, D. Loukidis, G. Abou-Jaoude, and Y. Zhang. "The role of soil stiffness non-linearity in 1D pile driving simulations". In: *Géotechnique* 65.3 (2015), pp. 169–187. DOI: 10.1680/geot.13.P.124.

[329] V. A. Sawant, S. K. Shukla, N. Sivakugan, and B. M. Das. "Insight into pile set-up and load carrying capacity of driven piles". In: *International Journal of Geotechnical Engineering* 7.1 (2013), pp. 71–83. ISSN: 19387879. DOI: 10.1179/1938636212Z.0000000004.

[330] M. Schanz and A. H. Cheng. "Transient wave propagation in a one-dimensional poroelastic column". In: *Acta Mechanica* 145.1-4 (2000), pp. 1–18. ISSN: 00015970. DOI: 10.1007/BF01453641.

[331] M. Schanz, W. Ye, and J. Xiao. "Comparison of the convolution quadrature method and enhanced inverse FFT with application in elastodynamic boundary element method". In: *Computational Mechanics* 57.4 (2016), pp. 523–536. ISSN: 01787675. DOI: 10.1007/s00466-015-1237-z.

[332] B. A. Schrefler, L. Simoni, L. Xikui, and O. C. Zienkiewicz. *Mechanics of Partially Saturated Porous Media*. Springer Vienna, 1990.

[333] B. A. Schrefler and R. Scotta. "A fully coupled dynamic model for two-phase fluid flow in deformable porous media". In: *Computer Methods in Applied Mechanics and Engineering* 190.24-25 (2001), pp. 3223–3246. ISSN: 00457825. DOI: 10.1016/S0045-7825(00)00390-X.

[334] B. Schümann. "Beitrag zum dynamischen Dreiphasenmodell für Boden auf Basis der Finite-Elemente-Methode". PhD thesis. Veröffentlichungen des Instituts für Geotechnik und Baubetrieb der Technischen Universität Hamburg, 2015.

[335] I. Shahrour and F. Rezaie. "An Elastoplastic Constitutive Relation for the Soil-Structure Interface under Cyclic Loading". In: *Computers and Geotechnics* 21.1 (1997), pp. 21–39. ISSN: 0266352X. DOI: 10.1016/S0266-352X(97)00001-3.

[336] D. Sheng, K. D. Eigenbrod, and P. Wriggers. "Finite element analysis of pile installation using large-slip frictional contact". In: *Computers and Geotechnics* 32.1 (2005), pp. 17–26. ISSN: 0266-352X. DOI: https://doi.org/10.1016/j.compgeo.2004.10.004.

[337] L. Shi, H. Sun, Y. Cai, C. Xu, and P. Wang. "Validity of fully drained, fully undrained and u–p formulations for modeling a poroelastic half-space under a moving harmonic point load". In: *Soil Dynamics and Earthquake Engineering* 42 (2012), pp. 292–301. ISSN: 0267-7261. DOI: https://doi.org/10.1016/j.soildyn.2012.06.016.

[338] M. F. Silva, D. J. White, and M. D. Bolton. "An analytical study of the effect of penetration rate on piezocone tests in clay". In: 30.6 (2006), pp. 501–527. DOI: https://doi.org/10.1002/nag.490.

[339] J. C. Simo, P. Wriggers, and R. L. Taylor. "A perturbed Lagrangian formulation for the finite element solution of contact problems". In: *Computer Methods in Applied Mechanics and Engineering* 50.2 (1985), pp. 163–180. ISSN: 00457825. DOI: 10.1016/0045-7825(85)90088-X.

[340] A. Simulia Dassault Systemes. *Abaqus 2017*. 2017.

[341] V. Singh, S. Stanier, B. Bienen, and M. F. Randolph. "Modelling the behaviour of sensitive clays experiencing large deformations using non-local regularisation techniques". In: *Computers and Geotechnics* 133 (2021), p. 104025. ISSN: 18737633. DOI: 10.1016/j.compgeo.2021.104025.

[342] S. Sitzmann. "Robust Algorithms for Contact Problems with Constitutive Contact Laws". PhD thesis. Friedrich-Alexander-Universität Erlangen-Nürnberg, 2016, p. 144.

[343] S. W. Sloan. "Substepping schemes for the numerical integration of elastoplastic stress-strain relations". In: *International Journal for Numerical Methods in Engineering* 24.5 (1987), pp. 893–911. DOI: https://doi.org/10.1002/nme.1620240505.

[344] K. Soga, E. Alonso, A. Yerro, K. Kumar, and S. Bandara. "Trends in large-deformation analysis of landslide mass movements with particular emphasis on the material point method". In: *Geotechnique* 66.3 (2016), pp. 248–273. ISSN: 17517656. DOI: 10.1680/jgeot.15.LM.005.

[345] M. Soleimani and C. Weissenfels. "Numerical simulation of pile installations in a hypoplastic framework using an SPH based method". In: *Computers and Geotechnics* 133 (2021), p. 104006. ISSN: 0266-352X. DOI: https://doi.org/10.1016/j.compgeo.2021.104006.

[346] O. Solf. *Zum mechanischen Verhalten von zyklisch belasteten Offshore-Gründungen*. Dissertation, Veröffentlichungen des Institutes für Bodenmechanik und Felsmechanik am Karlsruher Institut für Technologie, Heft 176. 2012.

[347] P. Staubach. "Beitrag zur numerischen Untersuchung dynamischer geotechnischer Fragestellungen unter vollständig und teilweise gesättigten Bedingungen". Masterarbeit. Institut für Bodenmechanik und Felsmechanik am Karlsruher Institut für Technologie (KIT), 2018.

[348] P. Staubach and J. Machaček. "Einfluss der Relativbeschleunigung bei dynamischer Beanspruchung von Mehrphasenmedien am Beispiel der Vibrationsrammung". In: *Fachsektionstage Geotechnik*. Deutsche Gesellschaft für Geotechnik e.V. (DGGT), 2019, pp. 340–345. ISBN: 978-3-946039-06-8.

[349] P. Staubach and J. Machaček. "Influence of relative acceleration in saturated sand: Analytical approach and simulation of vibratory pile driving tests". In: *Computers and Geotechnics* 112 (Aug. 2019), pp. 173–184. ISSN: 0266352X. DOI: 10.1016/j.compgeo.2019.03.027.

[350] P. Staubach, J. Machaček, L. Rentzsch, and T. Wichtmann. "Impact of the installation process on piles subjected to lateral high-cyclic loading: back-analysis of model tests using a high-cycle accumulation model". In: *Proceedings of the 7th International Young Geotechnical Engineers Conference, 29 April - 1 May 2022, Sydney, Australia*. Ed. by Brendan Scott. Sydney: Australian Geomechanics Society, 2022, pp. 485–490.

[351] P. Staubach, J. Machaček, R. Sharif, and T. Wichtmann. "Back-analysis of model tests on piles in sand subjected to long-term lateral cyclic loading: Impact of the pile installation and application of the HCA model". In: *Computers and Geotechnics* 134 (June 2021), p. 104018. ISSN: 0266352X. DOI: 10.1016/j.compgeo.2021.104018.

[352] P. Staubach, J. Machaček, and T. Wichtmann. "Impact of the installation on the long-term behaviour of offshore wind turbine pile foundations". In: *4th International Symposium on Frontiers in Offshore Geotechnics,* Taylor & Francis Group, London, UK, 2020, pp. 573–583.

[353] P. Staubach, J. Machaček, M. C. Moscoso, and T. Wichtmann. "Impact of the installation on the long-term cyclic behaviour of piles in sand: A numerical study". In: *Soil Dynamics and Earthquake Engineering* 138 (2020), p. 106223. ISSN: 02677261. DOI: 10.1016/j.soildyn.2020.106223.

[354] P. Staubach, J. Machaček, J. Skowronek, and T. Wichtmann. "Vibratory pile driving in water-saturated sand: Back-analysis of model tests using a hydro-mechanically coupled CEL method". In: *Soils and Foundations* 61.1 (Feb. 2021), pp. 144–159. ISSN: 00380806. DOI: 10.1016/j.sandf.2020.11.005.

[355] P. Staubach, J. Machaček, L. Tschirschky, and T. Wichtmann. "Enhancement of a high-cycle accumulation model by an adaptive strain amplitude and its application to monopile foundations". In: *International Journal for Numerical and Analytical Methods in Geomechanics* 46.2 (Feb. 2022), pp. 315–338. ISSN: 0363-9061. DOI: 10.1002/nag.3301.

[356] P. Staubach, J. Machaček, and T. Wichtmann. "Impact of the constitutive contact model on the simulation of model tests on monopiles with high-cyclic loading". In: *Proceedings of the 20th International Conference on Soil Mechanics and Geotechnical Engineering, Sydney 2021*. Sydney, 2022, pp. 2685–2690.

[357] P. Staubach and T. Wichtmann. "Long-term deformations of monopile foundations for offshore wind turbines studied with a high-cycle accumulation model". In: *Computers and Geotechnics* 124 (Aug. 2020), p. 103553. ISSN: 0266352X. DOI: 10.1016/j.compgeo.2020.103553.

[358] P. Staubach, J. Machaček, M. Tafili, and T. Wichtmann. "A high-cycle accumulation model for clay and its application to monopile foundations". In: *Acta Geotechnica* 17.3 (Mar. 2022), pp. 677–698. ISSN: 1861-1125. DOI: 10.1007/s11440-021-01446-9.

[359] P. Staubach, J. Machaček, and T. Wichtmann. "Large-deformation analysis of pile installation with subsequent lateral loading: Sanisand vs. Hypoplasticity". In: *Soil Dynamics and Earthquake Engineering* 151 (Dec. 2021), p. 106964. ISSN: 02677261. DOI: 10.1016/j.soildyn.2021.106964.

[360] P. Staubach, J. Machaček, and T. Wichtmann. "Mortar contact discretisation methods incorporating interface models based on Hypoplasticity and Sanisand: Application to vibratory pile driving". In: *Computers and Geotechnics* 146 (June 2022), p. 104677. ISSN: 0266352X. DOI: 10.1016/j.compgeo.2022.104677.

[361] P. Staubach, J. Machaček, and T. Wichtmann. "Novel approach to apply existing constitutive soil models to the modelling of interfaces". In: *International Journal for Numerical and Analytical Methods in Geomechanics* 46.7 (May 2022), pp. 1241–1271. ISSN: 0363-9061. DOI: 10.1002/nag.3344.

[362] P. Stein, J. Gattermann, E. Daumlechner, N. Hinzmann, and J. Stahlmann. *ZykLaMP Großmaßstäbliche Modellversuche zur lateralen Tragfähigkeit offener Stahlrohrpfähle unter zyklischer Belastung bei verschiedenen Einbringverfahren*. Report, Nov. 2020. DOI: 10.2314/KXP:1757076905.

[363] D. A. Stonestrom and J. Rubin. "Air permeability and trapped-air content in two soils". In: *Water Resources Research* 25.9 (1989), pp. 1959–1969. ISSN: 1944-7973. DOI: 10.1029/WR025i009p01959.

[364] D. A. Stonestrom and J. Rubin. "Water content dependence of trapped air in two soils". In: *Water Resources Research* 25.9 (1989), pp. 1947–1958. ISSN: 1944-7973. DOI: 10.1029/WR025i009p01947.

[365] H. Stutz. "Hypoplastic Models for Soil-Structure Interfaces : Modelling and Implementation". PhD thesis. Faculty of Mathematics and Natural Sciences at Kiel University, 2016.

[366] H. Stutz, D. Mašín, A. S. Sattari, and F. Wuttke. "A general approach to model interfaces using existing soil constitutive models application to hypoplasticity". In: *Computers and Geotechnics* 87 (July 2017), pp. 115–127. ISSN: 18737633. DOI: 10.1016/j.compgeo.2017.02.010.

[367] H. Stutz, D. Mašín, and F. Wuttke. "Enhancement of a hypoplastic model for granular soil-structure interface behaviour". In: *Acta Geotechnica* 11.6 (2016), pp. 1249–1261. ISSN: 18611133. DOI: 10.1007/s11440-016-0440-1.

[368] H. Stutz and F. Wuttke. "Hypoplastic modeling of soil-structure interfaces in offshore applications". In: *Journal of Zhejiang University: Science A* 19.8 (Aug. 2018), pp. 624–637. ISSN: 18621775. DOI: 10.1631/jzus.A1700469.

[369] H. Stutz and D. Mašín. "Hypoplastic interface models for fine-grained soils". In: *International Journal for Numerical and Analytical Methods in Geomechanics* 41.2 (2017), pp. 284–303. ISSN: 10969853. DOI: 10.1002/nag.2561.

[370] F. C. Summersgill, S. Kontoe, and D. M. Potts. "On the use of nonlocal regularisation in slope stability problems". In: *Computers and Geotechnics* 82 (Feb. 2017), pp. 187–200. ISSN: 18737633. DOI: 10.1016/j.compgeo.2016.10.016.

[371] I. E. Sutherland and G. W. Hodgman. "Reentrant Polygon Clipping". In: *Communications of the ACM* 17.1 (1974), pp. 32–42. ISSN: 15577317. DOI: 10.1145/360767.360802.

[372] D. Systems simulia. *Abaqus 6.14 theory guide*. 2014.

[373] M. Tafili. *On the behaviour of cohesive soils: Constitutive description and experimental observations*. Dissertation, Publications of the Institute of Soil Mechanics and Rock Mechanics, Karlsruhe Institute of Technology, Issue No. 186. 2020.

[374] M. Tafili and T. Triantafyllidis. "AVISA: Anisotropic Visco ISA model and its performance at cyclic loading". In: *Acta Geotechnica* 15 (2020), pp. 2395–2413.

[375] M. Taiebat and Y. F. Dafalias. "SANISAND: Simple anisotropic sand plasticity model". In: *International Journal for Numerical and Analytical Methods in Geomechanics* 32.8 (2008), pp. 915–948. DOI: 10.1002/nag.651.

[376] H. E. Tasan. "Prognose der Verschiebungen von zyklisch lateral belasteten Monopiles in geschichteten Böden". In: *Der Bauingenieur* 6 (2012), pp. 297–305.

[377] H. E. Tasan, F. Rackwitz, and R. Glasenapp. "Ein Bemessungsmodell für Monopilegründungen unter zyklischen Horizontallasten". In: *Bautechnik* 88.5 (2011), pp. 301–318.

[378] C. Taylor and P. Hood. "A numerical solution of the Navier-Stokes equations using the finite element technique". In: *Computers and Fluids* 1.1 (1973), pp. 73–100. ISSN: 00457930. DOI: 10.1016/0045-7930(73)90027-3.

[379] J. Tejchman and A. Niemunis. "FE-studies on Shear Localization in an Anistropic Micro-polar Hypoplastic Granular Material". In: *Granular Matter* 8.3-4 (Aug. 2006), pp. 205–220. ISSN: 1434-5021. DOI: 10.1007/s10035-006-0009-z.

[380] The Overseas Coastal Area Development Institute of Japan. *Technical Standards and Commentaries for Port and Harbour Facilities in Japan*. 3-2-4 Kasumigaseki, Chiyoda-ku, Tokyo, 100-0013, Japan, 2002.

[381] Y. Tian, M. J. Cassidy, M. F. Randolph, D. Wang, and C. Gaudin. "A simple implementation of RITSS and its application in large deformation analysis". In: *Computers and Geotechnics* 56 (2014), pp. 160–167. ISSN: 0266352X. DOI: 10.1016/j.compgeo.2013.12.001.

[382] A. Tolooiyan and K. Gavin. "Modelling the Cone Penetration Test in sand using Cavity Expansion and Arbitrary Lagrangian Eulerian Finite Element Methods". In: *Computers and Geotechnics* 38.4 (2011), pp. 482–490. ISSN: 0266352X. DOI: 10.1016/j.compgeo.2011.02.012.

[383] D. Tovar-Valencia Ruben, C. Galvis-Castro Ayda, M. Prezzi, and R. Salgado. "Short-Term Setup of Jacked Piles in a Calibration Chamber". In: *Journal of Geotechnical and Geoenvironmental Engineering* 144.12 (Dec. 2018), p. 4018092. DOI: 10.1061/(ASCE)GT.1943-5606.0001984.

[384] P. Truong and B. M. Lehane. "Effects of pile shape and pile end condition on the lateral response of displacement piles in soft clay". In: *Géotechnique* 68.9 (2018), pp. 794–804. DOI: 10.1680/jgeot.16.P.291.

[385] P. Truong, B. M. Lehane, V. Zania, and R. T. Klinkvort. "Empirical approach based on centrifuge testing for cyclic deformations of laterally loaded piles in sand". In: *Geotechnique* 69.2 (2019), pp. 133–145. ISSN: 17517656. DOI: 10.1680/jgeot.17.P.203.

[386] A. Tsetas, S. S. Gomez, A. Tsouvalas, K. van Beek, F. S. Tehrani, E. Kementzetzidis, F. Pisano, A. Elkadi, M. Segeren, T. Molenkamp, and A. V. Metrikine. "Experimental identification of the dynamic behaviour of pile-soil system installed by means of three different pile-driving techniques". In: *Eurodyn 2020: XI International Conference on Structural Dynamics* (2020), pp. 3005–3015. DOI: 10.47964/1120.9245.20367.

[387] C. H. C. Tsuha, P. Y. Foray, R. J. Jardine, Z. X. Yang, M. Silva, and S. Rimoy. "Behaviour of displacement piles in sand under cyclic axial loading". In: *Soils Found.* 52.3 (2012), pp. 393–410.

[388] M. Tur, F. J. Fuenmayor, and P. Wriggers. "A mortar-based frictional contact formulation for large deformations using Lagrange multipliers". In: *Computer Methods in Applied Mechanics and Engineering* 198.37 (2009), pp. 2860–2873. ISSN: 0045-7825. DOI: https://doi.org/10.1016/j.cma.2009.04.007.

[389] UBA. *Empfehlung von Lärmschutzwerten bei der Errichtung von Offshore-Windenergieanlagen (OWEA)*. 2011.

[390] I. Vardoulakis and J. Sulem. *Bifurcation analysis in geomechanics*. CRC Press, 1995. ISBN: 0751402141. DOI: 10.4324/9780203697030.

[391] J. Vogelsang, G. Huber, and T. Triantafyllidis. "A large-scale soil-structure interface testing device". In: *Geotechnical Testing Journal, ASTM* 36.5 (2013), pp. 613–625.

[392] J. Vogelsang, G. Huber, T. Triantafyllidis, and Bender. "Interpretation of vibratory pile penetration based on Digital Image Correlation". In: *Springer International Publishing Switzerland* (2015), pp. 31–51.

[393] J. Vogelsang. "Untersuchungen zu den Mechanismen der Pfahlrammung". PhD thesis. Veröffentlichung des Instituts für Bodenmechanik und Felsmechanik am Karlsruher Institut für Technologie (KIT), Heft 182, 2016.

[394] J. Vogelsang, G. Huber, and T. Triantafyllidis. "Experimental Investigation of Vibratory Pile Driving in Saturated Sand". In: *Holistic Simulation of Geotechnical Installation Processes: Theoretical Results and Applications*. Ed. by T. Triantafyllidis. Cham: Springer International Publishing, 2017, pp. 101–123. ISBN: 978-3-319-52590-7. DOI: 10.1007/978-3-319-52590-7_4.

[395] J. Walker and H. S. Yu. "Adaptive finite element analysis of cone penetration in clay". In: *Acta Geotechnica* 1.1 (2006), pp. 43–57. ISSN: 1861-1125. DOI: 10.1007/s11440-006-0005-9.

[396] J. Waltz. "Operator splitting and time accuracy in Lagrange plus remap solution methods". In: *Journal of Computational Physics* 253 (2013), pp. 247–258. ISSN: 0021-9991. DOI: https://doi.org/10.1016/j.jcp.2013.07.016.

[397] D. Wang, B. Bienen, M. Nazem, Y. Tian, J. Zheng, T. Pucker, and M. F. Randolph. "Large deformation finite element analyses in geotechnical engineering". In: *Computers and Geotechnics* 65 (Apr. 2015), pp. 104–114. DOI: 10.1016/j.compgeo.2014.12.005.

[398] D. Wang, Y. Hu, and M. F. Randolph. "Three-Dimensional Large Deformation Finite-Element Analysis of Plate Anchors in Uniform Clay". In: *Journal of Geotechnical and Geoenvironmental Engineering* 136.2 (Feb. 2010), pp. 355–365. ISSN: 1090-0241. DOI: 10.1061/(asce)gt.1943-5606.0000210.

[399] C. Weißenfels and P. Wriggers. "Methods to project plasticity models onto the contact surface applied to soil structure interactions". In: *Computers and Geotechnics* 65 (2015), pp. 187–198. ISSN: 0266-352X. DOI: https://doi.org/10.1016/j.compgeo.2014.11.015.

[400] C. Weißenfels, A. B. Harish, and P. Wriggers. "Strategies to Apply Soil Models Directly as Friction Laws in Soil Structure Interactions". In: *Holistic Simulation of Geotechnical Installation Processes: Theoretical Results and Applications*. Ed. by T. Triantafyllidis. Cham: Springer International Publishing, 2017, pp. 216–236. ISBN: 978-3-319-52590-7. DOI: 10.1007/978-3-319-52590-7_9.

[401] K. Westermann, H. Zachert, and T. Wichtmann. "Vergleich von Ansätzen zur Prognose der Langzeitverformungen von OWEA-Monopilegründungen in Sand. Teil 2: Simulationen und Schlussfolgerungen". In: *Bautechnik* 91.5 (2014), pp. 324–332.

[402] K. Westermann, H. Zachert, and T. Wichtmann. "Vergleich von Ansätzen zur Prognose der Langzeitverformungen von OWEA-Monopilegründungen in Sand". In: *Bautechnik* 91.5 (May 2014), pp. 324–332. ISSN: 09328351. DOI: 10.1002/bate.201400015.

[403] D. J. White and M. D. Bolton. "Displacement and strain paths during plane-strain model pile installation in sand". In: *Géotechnique* 54.6 (2004), pp. 375–397. DOI: 10.1680/geot.2004.54.6.375.

[404] D. J. White and B. M. Lehane. "Friction fatigue on displacement piles in sand". In: *Geotechnique* 54.10 (2004), pp. 645–658. ISSN: 00168505. DOI: 10.1680/geot.2004.54.10.645.

[405] T. Wichtmann. *Explicit accumulation model for non-cohesive soils under cyclic loading*. PhD thesis, Publications of the Institute of Foundation Engineering and Soil Mechanics, Ruhr-University Bochum, Issue No. 38. 2005.

[406] T. Wichtmann. *Soil Behaviour Under Cyclic Loading: Experimental Observations, Constitutive Description and Applications*. Habilitation, Institute of Soil Mechanics and Rock Mechanics, Karlsruhe Institute of Technology, Issue No. 181, 2016.

[407] T. Wichtmann, W. Fuentes, and T. Triantafyllidis. "Inspection of three sophisticated constitutive models based on monotonic and cyclic tests on fine sand: Hypoplasticity vs. Sanisand vs. ISA". In: *Soil Dynamics and Earthquake Engineering* 124 (2019), pp. 172–183. ISSN: 0267-7261. DOI: https://doi.org/10.1016/j.soildyn.2019.05.001.

[408] T. Wichtmann and L. Knittel. "Behaviour of granular soils under uni- and multidimensional drained high-cyclic loading". In: *Recent Developments of Soil Mechanics and Geotechnics in Theory and Practice*. Ed. by T. Triantafyllidis. Springer, 2019, pp. 136–165.

[409] T. Wichtmann, A. Niemunis, and T. Triantafyllidis. "Experimental evidence of a unique flow rule of non-cohesive soils under high-cyclic loading". In: *Acta Geotechnica* 1.1 (2006), pp. 59–73.

[410] T. Wichtmann, A. Niemunis, and T. Triantafyllidis. "On the "elastic" stiffness in a high-cycle accumulation model for sand: a comparison of drained and undrained cyclic triaxial tests". In: *Canadian Geotechnical Journal* 47.7 (2010), pp. 791–805.

[411] T. Wichtmann, A. Niemunis, and T. Triantafyllidis. "On the determination of a set of material constants for a high-cycle accumulation model for non-cohesive soils". In: *Int. J. Numer. Anal. Meth. Geomech.* 34.4 (2010), pp. 409–440.

[412] T. Wichtmann, A. Niemunis, and T. Triantafyllidis. "On the influence of the polarization and the shape of the strain loop on strain accumulation in sand under high-cyclic loading". In: *Soil Dynamics and Earthquake Engineering* 27.1 (2007), pp. 14–28.

[413] T. Wichtmann, A. Niemunis, and T. Triantafyllidis. "Strain accumulation in sand due to cyclic loading: drained cyclic tests with triaxial extension". In: *Soil Dynamics and Earthquake Engineering* 27.1 (2007), pp. 42–48.

[414] T. Wichtmann, A. Niemunis, and T. Triantafyllidis. "Strain accumulation in sand due to cyclic loading: drained triaxial tests". In: *Soil Dynamics and Earthquake Engineering* 25.12 (2005), pp. 967–979.

[415] T. Wichtmann, A. Niemunis, and T. Triantafyllidis. "Validation and calibration of a high-cycle accumulation model based on cyclic triaxial tests on eight sands". In: *Soils and Foundations* 49.5 (2009), pp. 711–728.

[416] T. Wichtmann, A. Niemunis, and T. Triantafyllidis. "On the "elastic stiffness" in a high-cycle accumulation model - continued investigations". In: *Canadian Geotechnical Journal* 50.12 (2013), pp. 1260–1272.

[417] T. Wichtmann and T. Triantafyllidis. "Inspection of a high-cycle accumulation model for large numbers of cycles (N = 2 million)". In: *Soil Dynamics and Earthquake Engineering* 75 (2015), pp. 199–210.

[418] T. Wichtmann and T. Triantafyllidis. "Monotonic and cyclic tests on Kaolin - a database for the development, calibration and verification of constitutive models for cohesive soils with focus to cyclic loading". In: *Acta Geotechnica* 13.5 (2018), pp. 1103–1128.

[419] T. Wichtmann, A. Niemunis, and T. Triantafyllidis. "Improved simplified calibration procedure for a high-cycle accumulation model". In: *Soil Dynamics and Earthquake Engineering* 70.3 (2015), pp. 118–132. ISSN: 02677261. DOI: 10.1016/j.soildyn.2014.12.011.

[420] T. Wichtmann and T. Triantafyllidis. "On the influence of multiple polarization changes on the cumulative deformations in sand under drained high-cyclic loading". In: *Geotechnical Testing Journal* 43.1 (2019), pp. 208–227. ISSN: 01496115. DOI: 10.1520/GTJ20170298.

[421] T. Wichtmann, A. Niemunis, and T. Triantafyllidis. "Flow rule in a high-cycle accumulation model backed by cyclic test data of 22 sands". In: *Acta Geotechnica* 9.4 (2014), pp. 695–709. ISSN: 18611133. DOI: 10.1007/s11440-014-0302-7.

[422] B. I. Wohlmuth. *Iterative Solvers Based on Domain Decomposition*. Springer-Verlag Berlin Heidelberg, 2001, pp. 85–176. ISBN: 354041083X. DOI: 10.1007/978-3-642-56767-4_2.

[423] P.-A. von Wolffersdorff. "A hypoplastic relation for granular materials with a predefined limit state surface". In: *Mechanics of Cohesive-Frictional Materials* 1 (1996), pp. 251–271.

[424] P. Wriggers. *Computational Contact Mechanics*. Springer Berlin Heidelberg, 2006. ISBN: 9783540326090.

[425] P. Wriggers. *Computational contact mechanics*. Vol. 67. Lecture Notes in Applied and Computational Mechanics. Berlin, Heidelberg: Springer Berlin Heidelberg, 2006, pp. 1–518. ISBN: 3540326081. DOI: 10.1007/978-3-540-32609-0.

[426] X. T. Xu, H. L. Liu, and B. M. Lehane. "Pipe pile installation effects in soft clay". In: *Proceedings of the Institution of Civil Engineers - Geotechnical Engineering* 159.4 (Oct. 2006), pp. 285–296. ISSN: 1353-2618. DOI: 10.1680/geng.2006.159.4.285.

[427] B. Yang and T. A. Laursen. "A large deformation mortar formulation of self contact with finite sliding". In: *Computer Methods in Applied Mechanics and Engineering* 197.6-8 (Jan. 2008), pp. 756–772. ISSN: 00457825. DOI: 10.1016/j.cma.2007.09.004.

[428] B. Yang, T. A. Laursen, and X. Meng. "Two dimensional mortar contact methods for large deformation frictional sliding". In: *International Journal for Numerical Methods in Engineering* 62.9 (Mar. 2005), pp. 1183–1225. ISSN: 00295981. DOI: 10.1002/nme.1222.

[429] J. Yang and Z. Y. Yin. "Soil-structure interface modeling with the nonlinear incremental approach". In: *International Journal for Numerical and Analytical Methods in Geomechanics* 45.10 (July 2021), pp. 1381–1404. ISSN: 10969853. DOI: 10.1002/nag.3206.

[430] M. Yang, M. Taiebat, and Y. F. Dafalias. "SANISAND-MSf: a sand plasticity model with memory surface and semifluidised state". In: *Géotechnique* (Dec. 2020), pp. 1–20. ISSN: 0016-8505. DOI: 10.1680/jgeot.19.P.363.

[431] Q. Yang, Y. Gao, D. Kong, and B. Zhu. "Centrifuge modelling of lateral loading behaviour of a semi-rigid Monopile in soft clay". In: *Marine Georesources and Geotechnology* 37.10 (2019), pp. 1205–1216. ISSN: 15210618. DOI: 10.1080/1064119X.2018.1545004.

[432] Z. Yang, R. Jardine, B. Zhu, C. Tsuha, and P. Foray. "Sand grain crushing and interface shearing during displacement pile installation in sand". In: *Géotechnique* 60.6 (2010), pp. 469–482. DOI: 10.1680/geot.2010.60.6.469.

[433] Z. X. Yang, Y. Y. Gao, R. J. Jardine, W. B. Guo, and D. Wang. "Large Deformation Finite-Element Simulation of Displacement-Pile Installation Experiments in Sand". In: *Journal of Geotechnical and Geoenvironmental Engineering* 146.6 (2020), p. 4020044. DOI: 10.1061/(ASCE)GT.1943-5606.0002271.

[434] F. J. Ye, S. H. Goh, and F. H. Lee. "A method to solve Biot's u-U formulation for soil dynamics applications using the ABAQUS/explicit platform". In: *Numerical Methods in Geotechnical Engineering - Proceedings of the 7th European Conference on Numerical Methods in Geotechnical Engineering*. Ed. by Benz and Nordal. 2010, pp. 417–422. ISBN: 9780415592390. DOI: 10.1201/b10551-79.

[435] H. Zachert. *Zur Gebrauchstauglichkeit von Gründungen für Offshore-Windenergieanlagen*. Dissertation, Publications of the Institute of Soil Mechanics and Rock Mechanics, Karlsruhe Institute of Technology, Issue No. 180. 2015.

[436] H. Zachert, T. Wichtmann, P. Kudella, T. Triantafyllidis, and U. Hartwig. "Validation of a high cycle accumulation model via FE-simulations of a full-scale test on a gravity base foundation for offshore wind turbines". In: *International Wind Engineering Conference, IWEC 2014, Hannover*. 2014.

[437] H. Zachert, T. Wichtmann, T. Triantafyllidis, and U. Hartwig. "Simulation of a full-scale test on a Gravity Base Foundation for Offshore Wind Turbines using a High Cycle Accumulation Model". In: *3rd International Symposium on Frontiers in Offshore Geotechnics (ISFOG), Oslo*. 2015.

[438] H. Zachert, T. Wichtmann, P. Kudella, and T. Triantafyllidis. "Inspection of a high-cycle accumulation model for sand based on recalculations of a full-scale test on a gravity base foundation for offshore wind turbines". In: *Computers and Geotechnics* 126 (2020), p. 103727. ISSN: 18737633. DOI: 10.1016/j.compgeo.2020.103727.

[439] S. Zaremba. "Sur une forme perfectionée de la théorie de la relaxation". In: *Bull. Int. Acad. Sci. Cracovie* (1903), pp. 594–614.

[440] G. Zavarise and P. Wriggers. "A segment-to-segment contact strategy". In: *Mathematical and Computer Modelling* 28.4-8 (1998), pp. 497–515. ISSN: 08957177. DOI: 10.1016/S0895-7177(98)00138-1.

[441] L. Zdravkovic, D. M. Taborda, D. M. Potts, D. Abadias, H. J. Burd, B. W. Byrne, K. G. Gavin, G. T. Houlsby, R. J. Jardine, C. M. Martin, R. A. McAdam, and E. Ushev. "Finite-element modelling of laterally loaded piles in a stiff glacial clay till at Cowden". In: *Geotechnique* 70.11 (2020), pp. 999–1013. ISSN: 17517656. DOI: 10.1680/jgeot.18.PISA.005.

[442] G. Zhang and J.-M. Zhang. "Unified Modeling of Monotonic and Cyclic Behavior of Interface between Structure and Gravelly Soil". In: *Soils and Foundations* 48.2 (2008), pp. 231–245.

[443] G. Zhang and J. M. Zhang. "Large-scale monotonic and cyclic tests of interface between geotextile and gravelly soil". In: *Soils and Foundations* 49.1 (Feb. 2009), pp. 75–84. ISSN: 00380806. DOI: 10.3208/sandf.49.75.

[444] N. Zhang and T. M. Evans. "Three dimensional discrete element method simulations of interface shear". In: *Soils and Foundations* 58.4 (2018), pp. 941–956. ISSN: 0038-0806. DOI: https://doi.org/10.1016/j.sandf.2018.05.010.

[445] W. Zhang, J. qiang Zou, X. wei Zhang, W. hai Yuan, and W. Wu. "Interpretation of cone penetration test in clay with smoothed particle finite element method". In: *Acta Geotechnica* 16.8 (Aug. 2021), pp. 2593–2607. ISSN: 18611133. DOI: 10.1007/s11440-021-01217-6.

[446] Y. Zhang, K. H. Andersen, and P. Jeanjean. "Verification of a framework for cyclic p-y curves in clay by hindcast of Sabine River, SOLCYP and centrifuge laterally loaded pile tests". In: *Applied Ocean Research* 97 (2020), p. 102085. ISSN: 01411187. DOI: 10.1016/j.apor.2020.102085.

[447] Y. Zhang, K. H. Andersen, P. Jeanjean, K. Karlsrud, and T. Haugen. "Validation of Monotonic and Cyclic p-y Framework by Lateral Pile Load Tests in Stiff, Overconsolidated Clay at the Haga Site". In: *Journal of Geotechnical and Geoenvironmental Engineering* 146.9 (2020), p. 04020080. ISSN: 1090-0241. DOI: 10.1061/(asce)gt.1943-5606.0002318.

[448] B. Zhu, Z.-j. Zhu, T. Li, J.-c. Liu, and Y.-f. Liu. "Field Tests of Offshore Driven Piles Subjected to Lateral Monotonic and Cyclic Loads in Soft Clay". In: *Journal of Waterway, Port, Coastal, and Ocean Engineering* 143.5 (2017), p. 05017003. ISSN: 0733-950X. DOI: 10.1061/(asce)ww.1943-5460.0000399.

[449] H.-X. Zhu, W.-H. Zhou, X.-Y. Jing, and Z.-Y. Yin. "Observations on fabric evolution to a common micromechanical state at the soil-structure interface". In: *International Journal for Numerical and Analytical Methods in Geomechanics* 43.15 (Oct. 2019), pp. 2449–2470. ISSN: 0363-9061. DOI: https://doi.org/10.1002/nag.2989.

[450] O. C. Zienkiewicz, C. T. Chang, and P. Bettess. "Drained, undrained, consolidating and dynamic behaviour assumptions in soils". In: *Geotechnique* 30.4 (1980), pp. 385–395.

[451] O. C. Zienkiewicz and T. Shiomi. "Dynamic behaviour of saturated porous media: The generalized Biot formulation and its numerical solution". In: *International Journal for Numerical and Analytical Methods in Geomechanics* 8.1 (1984), pp. 71–96. ISSN: 1096-9853. DOI: 10.1002/nag.1610080106.

[452] O. C. Zienkiewicz and R. L. Taylor. *The finite element method; 5th ed.* Oxford: Butterworth, 2000.

[453] O. C. Zienkiewicz, H. C. Chan, M. Pastor, B. A. Schrefler, and T. Shiomi. *Computational Geomechanics with Special Reference to Earthquake Engineering*. Vol. 613. Wiley, 1999. ISBN: 0471982857.

Schriftenreihe des Instituts für Grundbau, Wasserwesen und Verkehrswesen der Ruhr-Universität Bochum

Herausgeber: H.L. Jessberger

1 (1979) **Hans Ludwig Jessberger**
Grundbau und Bodenmechanik an der Ruhr-Universität Bochum

2 (1978) **Joachim Klein**
Nichtlineares Kriechen von künstlich gefrorenem Emschermergel

3 (1979) **Heinz-Joachim Gödecke**
Die Dynamische Intensivverdichtung wenig wasserdurchlässiger Böden

4 (1979) **Poul V. Lade**
Three Dimensional Stress-Strain Behaviour and Modeling of Soils

5 (1979) **Roland Pusch**
Creep of soils

6 (1979) **Norbert Diekmann**
Zeitabhängiges, nichtlineares Spannungs-Verformungsverhalten von gefrorenem Schluff unter triaxialer Belastung

7 (1979) **Rudolf Dörr**
Zeitabhängiges Setzungsverhalten von Gründungen in Schnee, Firn und Eis der Antarktis am Beispiel der deutschen Georg-von-Neumayer- und Filchner-Station

8 (1984) **Ulrich Güttler**
Beurteilung des Steifigkeits- und Nachverdichtungsverhaltens von ungebundenen Mineralstoffen

9 (1986) **Peter Jordan**
Einfluss der Belastungsfrequenz und der partiellen Entwässerungs-möglichkeiten auf die Verflüssigung von Feinsand

10 (1986) **Eugen Makowski**
Modellierung der künstlichen Bodenvereisung im grundwasserdurchströmten Untergrund mit der Methode der finiten Elemente

11 (1986) **Reinhard A. Beine**
Verdichtungswirkung der Fallmasse auf Lastausbreitung in nichtbindigem Boden bei der Dynamischen Intensivverdichtung

12 (1986) **Wolfgang Ebel**
Einfluss des Spannungspfades auf das Spannungs-Verformungsverhalten von gefrorenem Schluff im Hinblick auf die Berechnung von Gefrierschächten

13 (1987) **Uwe Stoffers**
Berechnungen und Zentrifugen-Modellversuche zur Verformungsabhängigkeit der Ausbaubeanspruchung von Tunnelausbauten in Lockergestein

14 (1988) **Gerhard Thiel**
Steifigkeit und Dämpfung von wassergesättigtem Feinsand unter Erdbebenbelastung

15 (1991) **Mahmud Thaher**
Tragverhalten von Pfahl-Platten-Gründungen im bindigen Baugrund,
Berechnungsmodelle und Zentrifugen-Modellversuche

Schriftenreihe des Instituts für Grundbau der Ruhr-Universität Bochum

Herausgeber: H.L. Jessberger

16 (1992) **Rainer Scherbeck**
Geotechnisches Verhalten mineralischer Deponieabdichtungsschichten
bei ungleichförmiger Verformungswirkung

17 (1992) **Martin M. Bizialiele**
Torsional Cyclic Loading Response of a Single Pile in Sand

18 (1993) **Michael Kotthaus**
Zum Tragverhalten von horizontal belasteten Pfahlreihen aus langen Pfählen in Sand

19 (1993) **Ulrich Mann**
Stofftransport durch mineralische Deponieabdichtungen:
Versuchsmethodik und Berechnungsverfahren

20 (1992) **Festschrift anlässlich des 60. Geburtstages von**
Prof. Dr.-Ing. H. L. Jessberger
20 Jahre Grundbau und Bodenmechanik an der Ruhr-Universität Bochum

21 (1993) **Stephan Demmert**
Analyse des Emissionsverhaltens einer Kombinationsabdichtung im Rahmen der
Risikobetrachtung von Abfalldeponien

22 (1994) **Diethard König**
Beanspruchung von Tunnel- und Schachtausbauten in kohäsionslosem Lockergestein
unter Berücksichtigung der Verformung im Boden

23 (1995) **Thomas Neteler**
Bewertungsmodell für die nutzungsbezogene Auswahl von Verfahren zur Altlastensanierung

24 (1995) **Ralph Kockel**
Scherfestigkeit von Mischabfall im Hinblick auf die Standsicherheit von Deponien

25 (1996) **Jan Laue**
Zur Setzung von Flachfundamenten auf Sand unter wiederholten Lastereignissen

26 (1996) **Gunnar Heibrock**
Zur Rissbildung durch Austrocknung in mineralischen Abdichtungsschichten
an der Basis von Deponien

27 (1996) **Thomas Siemer**
Zentrifugen-Modellversuche zur dynamischen Wechselwirkung zwischen Bauwerken
und Baugrund infolge stoßartiger Belastung

28 (1996) **Viswanadham V. S. Bhamidipati**
Geosynthetic Reinforced Mineral Sealing Layers of Landfills

29 (1997) **Frank Trappmann**
Abschätzung von technischem Risiko und Energiebedarf bei Sanierungsmaßnahmen für Altlasten

30 (1997) **André Schürmann**
Zum Erddruck auf unverankerte flexible Verbauwände

31 (1997) **Jessberger, H. L. (Herausgeber)**
Environment Geotechnics, Report of ISSMGE Technical Committee TC 5 on Environmental Geotechnics

Schriftenreihe des Institutes für Grundbau und Bodenmechanik der Ruhr-Universität Bochum

Herausgeber: Th. Triantafyllidis

32 (2000) **Triantafyllidis, Th. (Herausgeber)**
Boden unter fast zyklischer Belastung: Erfahrung und Forschungsergebnisse (Workshop)

33 (2002) **Christof Gehle**
Bruch- und Scherverhalten von Gesteinstrennflächen mit dazwischenliegenden Materialbrücken

34 (2003) **Andrzej Niemunis**
Extended hypoplastic models for soils

35 (2004) **Christiane Hof**
Über das Verpressankertragverhalten unter kalklösendem Kohlensäureangriff

36 (2004) **René Schäfer**
Einfluss der Herstellungsmethode auf das Verformungsverhalten von Schlitzwänden in weichen bindigen Böden

37 (2005) **Henning Wolf**
Zur Scherfugenbänderung granularer Materialien unter Extensionsbeanspruchung

38 (2005) **Torsten Wichtmann**
Explicit accumulation model for non-cohesive soils under cyclic loading

39 (2008) **Christoph M. Loreck**
Die Entwicklung des Frischbetondruckes bei der Herstellung von Schlitzwänden

40 (2008) **Igor Arsic**
Über die Bettung von Rohrleitungen in Flüssigböden

41 (2009) **Anna Arwanitaki**
Über das Kontaktverhalten zwischen einer Zweiphasenschlitzwand und nichtbindigen Böden

Schriftenreihe des Lehrstuhls für Grundbau, Boden- und Felsmechanik der Ruhr-Universität Bochum

Herausgeber: T. Schanz

42 (2009) **Yvonne Lins**
Hydro-Mechanical Properties of Partially Saturated Sand

43 (2010) **Tom Schanz (Herausgeber)**
Geotechnische Herausforderungen beim Umbau des Emscher-Systems,
Beiträge zum RuhrGeo Tag 2010

44 (2010) **Jamal Alabdullah**
Testing Unsaturated Soil for Plane Strain Conditions: A New Double-Wall Biaxial Device

45 (2011) **Lars Röchter**
Systeme paralleler Scherbänder unter Extension im ebenen Verformungszustand

46 (2011) **Yasir Al-Badran**
Volumetric Yielding Behavior of Unsaturated Fine-Grained Soils

47 (2011) **Usque ad finem**
Selected research papers

48 (2012) **Muhammad Ibrar Khan**
Hydraulic Conductivity of Moderate and Highly Dense Expansive Clays

49 (2014) **Long Nguyen-Tuan**
Coupled Thermo-Hydro-Mechanical Analysis: Experimental and Back Analysis

50 (2014) **Tom Schanz (Herausgeber)**
Ende des Steinkohlenbergbaus im Ruhrrevier: Realität und Perspektiven für die Geotechnik, Beiträge zum RuhrGeo Tag 2014

51 (2014) **Usque ad finem**
Selected research papers

52 (2014) **Houman Soleimani Fard**
Study on the Hydro-Mechanical Behaviour of Fiber Reinforced Fine Grained Soils with Application to the Preservation of Historical Monuments

53 (2014) **Wiebke Baille**
Hydro-Mechanical Behavior of Clays - Significance of Mineralogy

54 (2014) **Qasim Abdulkarem Jassim Al-Obaidi**
Hydro-Mechanical Behavior of Collapsible Soils

55 (2015) **Veselin Zarev**
Model Identification for the Adaption of Numerical Simulation Models - Application to Mechanized Shield Tunneling

56 (2015) **Meisam Goudarzy**
Micro and Macro Mechanical Assessment of Small and Intermediate Strain Properties of Granular Material

57 (2016) **Oliver Detert**
Analyse einer selbstregulierenden interaktiven Membrangründung für Schüttkörper auf geringtragfähigen Böden

58 (2016) **Yang Yang**
Analyses of Heat Transfer and Temperature-induced Behaviour in Geotechnics

59 (2016) **Alborz Pourzargar**
Application of suction stress concept to partially saturated compacted soils

60 (2017) **Hanna Haase**
Multiscale analysis of clay-polymer composites for Geoenvironmental applications

61 (2017) **Kavan Khaledi**
Constitutive modeling of rock salt with application to energy storage caverns

62 (2017) **Nina Silvia Müthing**
On the consolidation behavior of fine-grained soils under cyclic loading

63 (2017) **Elham Mahmoudi**
Probabilistic analysis of a rock salt cavern with application to energy storage systems

64 (2017) **Negar Rahemi**
Evaluation of liquefaction behavior of sandy soils using critical state soil mechanics and instability concept

65 (2018) **Chenyang Zhao**
A contribution to modeling of mechanized tunnel excavation

66 (2018) **Tom Schanz (Herausgeber)**
Innovationen im Spezialtiefbau und in der Umweltgeotechnik,
Beiträge zum RuhrGeo Tag 2018

67 (2019) **Linzhi Lang**
Hydro-Mechanical Behaviour of Bentonite-Based Materials Used for Disposal of Radioactive Wastes

68 (2019) **Usama Al-Anbaki**
Hydraulic Interaction of Soil and Nonwoven Geotextiles under Unsaturated Conditions

69 (2019) **Abhishek Rawat**
Coupled Hydro-mechanical Behavior of a Compacted Bentonite-Sand Mixture: Experimental and Numerical Investigations

Schriftenreihe des Lehrstuhls für Bodenmechanik, Grundbau und Umweltgeotechnik der Ruhr-Universität Bochum

Herausgeber: T. Wichtmann

70 (2019) **Mahmoud Qarmout**
Tunnel face stability using Kinematical Element Method (KEM)

71 (2021) **Raoul Hölter**
Optimal Experimental Design in Geotechnical Engineering

72 (2022) **Wolfgang Lieske**
Impact of polymer constitution on the hydro-mechanical behaviour of modified bentonite for the application in geotechnical and geoenvironmental engineering

73 (2022) **Patrick Staubach**
Contributions to the numerical modelling of pile installation processes and high-cyclic loading of soils